Charles University in Prague
Faculty of Mathematics and Physics

DOCTORAL THESIS

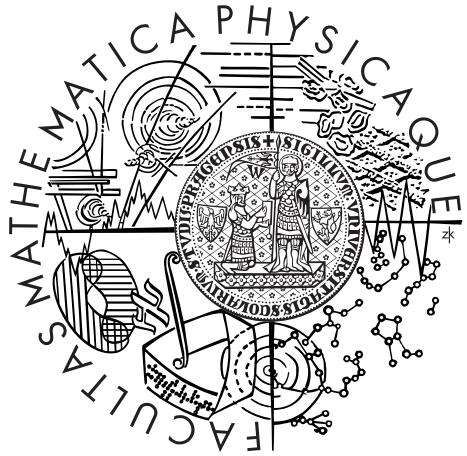

Petr Pokorný

Dynamics of small bodies of the Solar System: from dust particles to asteroids

Astronomical Institute, Charles University, Prague

Supervisor of the doctoral thesis:	prof. RNDr. David Vokrouhlický, DrSc.
Study programme:	Physics
Specialization:	Theoretical Physics, Astronomy and Astrophysics

Prague 2014

I would like to thank to everyone who helped me to accomplish one of the most difficult feats in my life. Since the variety of their contribution and effort is more than complex, let me omit their names and thank them personally.

I declare that I carried out this doctoral thesis independently, and only with the cited sources, literature and other professional sources.

I understand that my work relates to the rights and obligations under the Act No. 121/2000 Coll., the Copyright Act, as amended, in particular the fact that the Charles University in Prague has the right to conclude a license agreement on the use of this work as a school work pursuant to Section 60 paragraph 1 of the Copyright Act.

In Prague date ..... signature of the author

Název práce: Pohyb malých těles sluneční soustavy: od prachových částic k asteroidům

Autor: Petr Pokorný

Katedra: Astronomický ústav Univerzity Karlovy

Vedoucí disertační práce: prof. RNDr. David Vokrouhlický, DrSc., Astronomický ústav Univerzity Karlovy

Abstrakt: V této práci se zaměřujeme na dvě rozdílná témata: výpočet pravděpodobností srážek mezi dvěma tělesy a dynamiku sporadických meteoroidů ve sluneční soustavě. Výpočet kolizních pravděpodobností ve sluneční soustavě je jedním z důležitých problémů v moderní nebeské mechanice. Zobecňujeme klasické teorie pojednávající o kolizicích mezi dvěma tělesy publikované Öpikem, Wetherillem, nebo Greenbergem, započtením Kozaiovy-Lidovovy oscilace, tj. mechanismu, který významně mění excentricity a sklony drah těles ve sluneční soustavě. Sporadické meteory jsou cílem různých studií po mnoho desetiletí a poskytují významný zdroj dat. V této dizertační práci konstruujeme stacionární modely pro všechny známé zdroje pozorované ve sporadickém meteorickém komplexu, které jsou založené na nejnovějších a nejpřesnějších datech poskytnutých zařízením Canadian Meteor Orbit Radar (CMOR). Naše modely, využívající nejnovějších teorií o kometárních populacích ve sluneční soustavě, přesně popisují pozorovanou populaci sporadického pozadí. Naše výsledky jsou ve shodě s pozorováním družic *IRAS* a *LDEF*.

Klíčová slova: nebeská mechanika, malá tělesa sluneční soustavy, meteory

Title: Dynamics of small bodies of the Solar System: from dust particles to asteroids

Author: Petr Pokorný

Department: Astronomical Insitute, Charles University, Prague

Supervisor: prof. RNDr. David Vokrouhlický, DrSc., Astronomical Insitute, Charles University, Prague

Abstract: In this thesis, we study two different topics: collisional probability between two bodies and dynamics of the sporadic meteoroids in the Solar System. Determination of the collision probabilities in the Solar System is one of the important problems in modern celestial mechanics. Here, we generalize classical theories of the collisions between two bodies by Öpik, Wetherill or Greenberg by including the Kozai-Lidov oscillations, a mechanism that significantly change orbital eccentricity and inclination in the Solar System. Sporadic meteors have been studied for many decades providing a wealthy resource of data. Here, we build dynamical steady-state models for all known populations observed in the sporadic meteoroid complex based on the latest and most precise data provided by Canadian Meteor Orbit Radar (CMOR). Our models using the latest theories for cometary populations in the Solar System accurately describe observed sporadic background population. Our results are in agreement with observations provided by space probes *IRAS* and *LDEF*.

Keywords: celestial mechanics, small bodies of the Solar System, meteors

Contents

Introduction

This thesis presents a our research and results we achieved in two different topics: dynamics of the sporadic meteoroids in the Solar System and determination of the collisional probability between two bodies. While at the first glance these topics may not share many common features, the advancement in the correct evaluation of the collisional probability between Earth and dust particles provided us an important tool for building a satisfactory steady-state model for the sporadic meteoroid complex. Our research led to five publications in peer-reviewed journals, namely Astrophysical Journal and Icarus. This thesis is organized as a guidebook that connects particular papers together, provides overview and major conclusions for the studied topics. Our intention is to provide to reader a general overview of the topic with emphasized important ideas and procedures leading to our final conclusions. Published papers are attached to the thesis and their contents are not rewritten but only commented, which we find the best ratio between clarity and length of the text.

Since the first man looked up to the night sky and saw a falling star, the mankind was wondering: where these falling stars were coming from and will there be more and bigger of them? The second part of the question was already answered by dinosaurs long time ago (Bottke et al., 2007), but they obviously didn't leave any message. During a brief history of mankind there were several events yielding enough power to pose a threat to citywide regions, in the last century e.g., Tunguska event in 1908 (see, Trayner, 1997, for a great review of the event and its most possible cause), Caruçá event in 1930 (Bailey et al., 1995), or the most recent Chelyabinsk event in 2013 (Brown et al., 2013). The best precaution against these hazardous objects, called near-Earth objects (NEOs), is to know about them long enough before they hit the planet. Current technology prohibits us from moving the entire planet, thus the only hope is to change the orbit of the projectile (see e.g., the NEOShield project, Harris et al., 2012). Even with the most advanced current telescopes we are not able to see all NEOs in the Solar System that may pose a threat in near future. Models for NEOs developed by (Bottke et al., 2002), and further improved by (Granvik et al., 2013), provide a substantial agreement with an observed population and also give us an estimate for bodies invisible to contemporary telescopes.

One of the most fundamental pieces of information is a knowledge of the collisional probability between possible hazardous object and the Earth. To estimate the true collisional probability one can fill the ellipsoid of the orbital elements errors with clones of an investigated body and propagate them in time. This method is rather time demanding and not applicable for larger populations of bodies, and also works only for shorter timescales because of the stochastic nature of the problem. Many scientists dealt (see references in papers A and B) with this problem in more statistical way, evaluating a mean collisional probability between target and projectile that was averaged over a timescale longer than timescale of a secular evolution of the projectile orbit. This approach is very convenient and efficient for many different problems in the modern celestial mechanics, such as collisions of primordial populations of bodies in the Solar System with planets (Bottke et al., 2012), statistical evaluation of the collisions in the asteroid belt (Farinella and Davis, 1992), or determination of the mass influx onto the Earth from various sources of dust particles in the Solar System (Nesvorný et al., 2010). Deep knowledge of the collisional theories is an essential part of their proper application to the studied problem, because many simplifications and assumptions are needed for a fast, but still

accurate to the highest possible degree, algorithm. We developed a generalization of the standard works of Öpik (1951); Wetherill (1967); Kessler (1981); Greenberg (1982) eliminating an assumption of no secular variation of eccentricity and inclination of the projectile. Many objects in the Solar System follow orbits experiencing Kozai oscillations that may significantly change their eccentricities and inclinations in several thousands years. We adopt the crudest approximation of the Kozai oscillations, which provides our new theory an advantage over the previous standard theories, allow us to more precisely determine the collisional probability for bodies, where these standard theories might fail, while achieving the same results in situations, where assumptions of standard theories are valid. Our work is summarized in Chap. 1 and papers A and B.

Every day the Earth's atmosphere is showered by countless small particles of asteroidal and cometary origin. Born in the various places in the vast space of the Solar System, extending from the Sun to the Oort cloud, these particles, called meteoroids, experience a gravitational attraction of the Sun and planets in the Solar System, effects of the solar radiation, or pressure of the solar wind. En route from many prolific sources of the dust particles in the Solar System, such as Jupiter-family comets, Halley-type comets, Oort cloud comets, or the asteroid belt, they must overcome a suite of obstacles. Only a small fraction of the original population released from comets pass through an invisible, though very effective, barrier of Jupiter, survive long enough inside the zodiacal cloud without a destructive collision with their smaller, but more abundant, counterparts, and finally acquire an orbit that intersects Earth's orbit at exact time and position to be detected by ground-based of space-borne systems. Larger meteoroids, while passing through the Earth's atmosphere, experience a significant friction that causes them to ablate and produce a visible streak of light (Vondrak et al., 2008). Many of these meteors can be observed by a naked eye, and thousands of visual meteors are observed every day by projects like Cameras for Allsky Meteor Surveillance (CAMS) (Jenniskens et al., 2011). A large fraction of meteoroids is smaller than it is required for a detection by the most advanced meteor hunting visual systems. Seemingly left to their own final fate in evaporation in the atmosphere or impacting the Earth's surface, these particles invisible to the visual systems interact with molecules of air and produce a train of ionization several kilometers long. Several radar systems around the world can using the specular reflection from these trains observe these bodies, and accurately determine their orbits before entering the atmosphere.

Using decades of analysis of the radar observation datasets two different components of the Earth's meteor complex were distinguished: (1) particles associated with meteor streams impacting the Earth at discrete and well-defined time windows lasting typically several days (e.g., Brown et al., 2008, 2010), and (2) sporadic meteor background (e.g., Jones and Brown, 1993). While stream meteors are well known in the general public, in fact, the sporadic meteors dominate the time-integrated flux at Earth by about a factor 10 (Jones and Brown, 1993). Stream meteors can be usually easily linked to their parent body, on the other hand, orbits of the sporadic component of meteoroids hitting the Earth are , due to hundreds thousand years of dynamical evolution, completely different from the distribution of the orbital elements of their parent bodies. Sporadic meteoroids impact the Earth from various directions on the sky during the whole year, however, the geometry of their flux, as seen from the Earth, is not isotropic, and rather they are grouped into certain concentrations of radiant positions with a wide range of impact velocities. The most of the particles observable at the Earth in the sporadic meteoroid complex belong to one of the three groups: (1) the helion/anti-helion sources, (2) the north/south apex

sources, and (3) the north/south toroidal sources. This is caused by a limited number of source populations for the sporadic particles in the Solar System, combined with Earth's heliocentric motion. Long-term dynamical evolution makes finding groups of parent bodies difficult and requires a proper, and time-demanding, modeling (Wiegert et al., 2009; Nesvorný et al., 2010) with many dead ends of research. At the beginning of our research, we dared to set a bold objective: to develop a steady state models able to explain the most of observed structures of the sporadic meteoroid background population, match the observed distributions of the orbital elements, radiant positions, comply with constraints given by both ground-based and space-borne systems, and use only realistic and properly modeled populations of the dust producing bodies. We review our modeling effort in Chap. 2 and papers C, D, and E.

1. Contributions to the collision probability theory

In this chapter, we review our two papers dealing with the collisional probability between two celestial bodies on bound heliocentric orbits, present our motivation, and also some blind branches of our research. Our goal is to provide a standalone theory developed from the basic principles, which was not possible to fully describe in our papers. Simulations and tests performed to prove validity of our theories are extensively described in both papers, and thus we are not repeating these parts in the following text and address the reader directly to the papers.

Papers reviewed in this chapter:

Paper A: Vokrouhlický, D., **Pokorný, P**, & Nesvorný, D., 2012, Öpik-type collision probability for high-inclination orbits, *Icarus*, 219, 150.
Paper B: **Pokorný, P.**, Vokrouhlický, D., 2013, Öpik-type collision probability for high-inclination orbits: Targets on eccentric orbits, *Icarus*, 226, 682.

1.1 Introduction and motivation

As stated in the Introduction, many problems in the celestial mechanics require a correct determination of the probability with which two bodies could collide. Since the precise calculation of a set of differential equations describing motion of gravitationally interacting bodies is not an easy task even for current computers, there was, and we believe there also will be, a considerable demand for an analytic solution of a similar problem, even when we assume a very simplified scenario. In this chapter, we focus on an evaluation of collision probability averaged over the secular orbital timescale.

The first drop in the ocean was a paper published by Öpik (1951). This rather geometrical work allowed to estimate collisional probabilities in the Solar System in almost no time, and even though more than 50 years old is still used by many contemporary scientists. Öpik, however, adopted slightly restrictive assumptions: the target is on circular non-inclined orbit[1] and the projectile is assumed to have the constant semimajor axis a, the eccentricity e, and the inclination i, while remaining Euler angles, the longitude of the ascending node Ω and the argument of pericenter ω undergo an uniform precession. Fig. 1.1 shows an evolution of the eccentricity and inclination of two bodies, the minor planet 1 Ceres (dashed lines), and the comet 96P/Machholz (solid lines). We immediately see that Öpik's assumptions are violated by behavior of 96P/Machholz which undergoes strong variations in e and I. Such behavior is described as Kozai-Lidov oscillations (Lidov, 1961; Kozai, 1962) and will be more precisely discussed in Sec. 1.2. Even for 1 Ceres with very small values of e and I the body do not conserve the initial values in time, however, the variations are small enough to keep Öpik's assumptions valid.

Therefore, Öpik's approach cannot be used for targets on highly inclined orbits, or those have large values of eccentricity, because the original assumptions are violated and

[1] By a non-inclined orbit, we always mean that the orbit is coplanar to the local reference plane, e.g., the Laplace plane in the Solar System

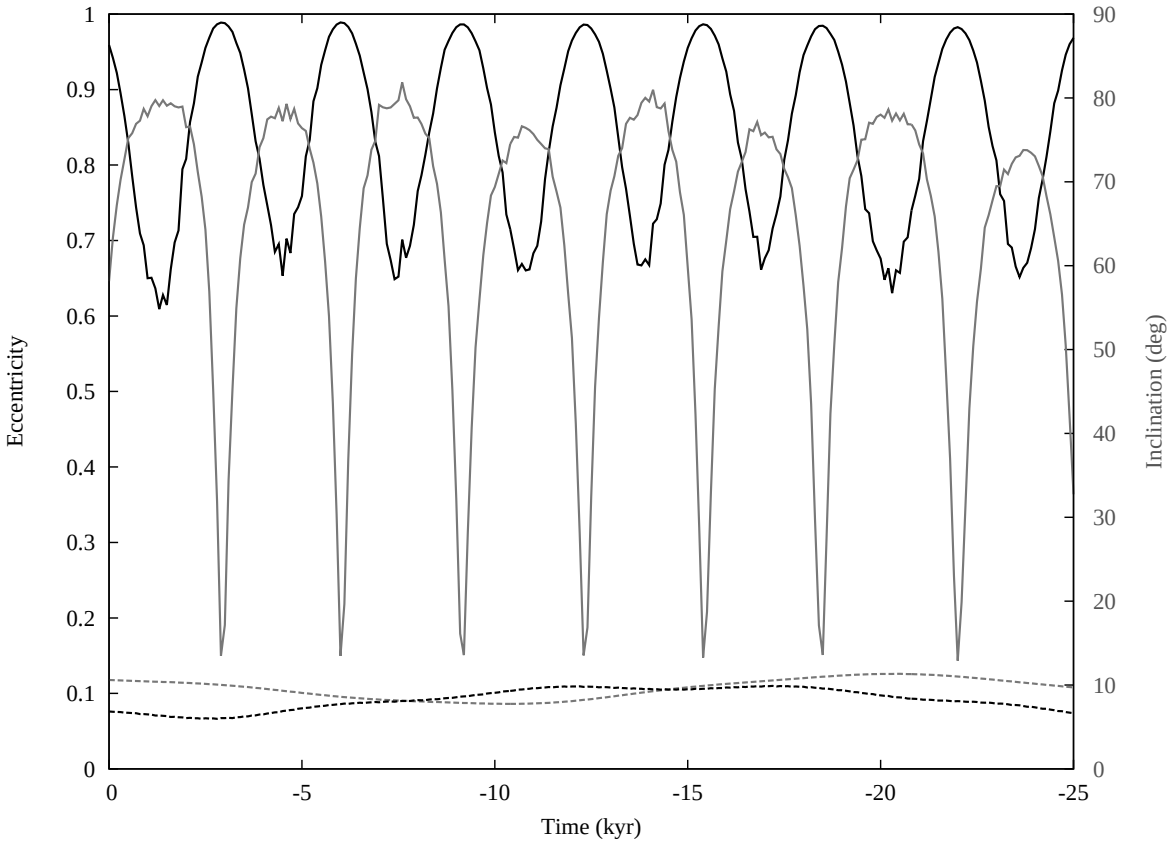

Figure 1.1: Evolution of eccentricity (black lines) and inclination (gray lines) of 1 Ceres (dashed lines) and 96P/Machholz (solid lines) in backward time. While 1 Ceres undergoes only small variations in e and I, 96P/Machholz experiences Kozai-Lidov oscillations leading to severe changes of both eccentricity and inclination with ~ 4000 y period. Initial orbital elements a, e and I for 1 Ceres: $a = 2.783$ au, $e = 0.0820$, $I = 10.562°$ and for 96P/Machholz: $a = 3.037$ au, $e = 0.9590$, $I = 58.145°$.

the evaluation method may fail. Öpik also presented a rough correction factor for targets on elliptic orbits, however, still based on circular motion of the target. Wetherill (1967) improved Öpik's original theory and made it valid bodies, where both are on arbitrary bound orbits. Still the theory assumed uniform distribution of the apsidal and nodal longitudes and also no variations of e and I in time. Greenberg (1982) found a flaw of Wetherill's approach noting a wrong assumption of uniform probability distribution of true anomaly for both target and projectile. This assumption may introduce an error comparable with eccentricities of the bodies. Greenberg presented a corrected version of Wetherill's approach and his theory is used by the many of researchers today.

Kessler (1981) presented a different, more geometrical method using a concept of a spatial density, average number of objects found in a unit volume in space. One of the advantages of this method is that it could be used for evaluating collision probability of an artificial spacecraft with different bodies in the Solar System, because the target is represented by its position and velocity vectors instead of orbital elements. However, the theory still assumes constant values of e and I and uniform precession of nodes for both target and projectile. In consequence, all presented theories give comparable results if used correctly for bodies that are not violating the original assumptions, however, may fail in situation, when the original assumptions are not satisfied.

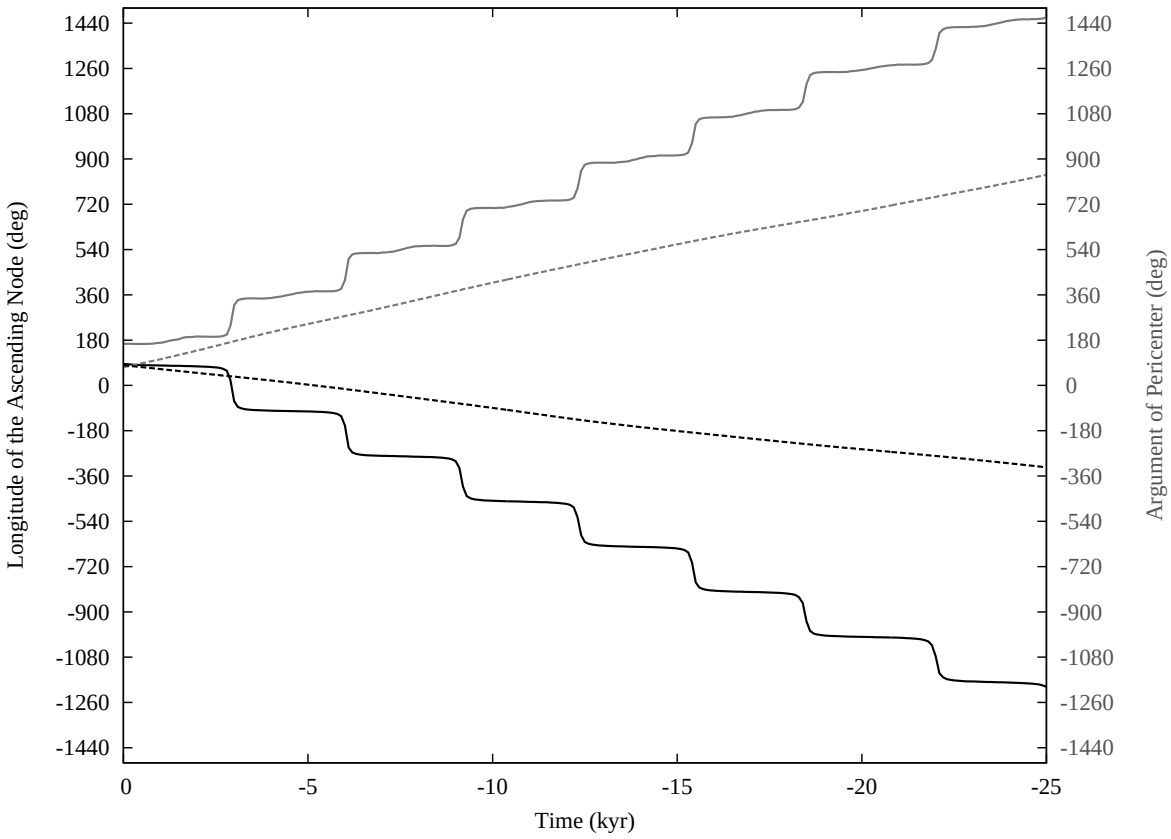

Figure 1.2: Evolution of longitude of the ascending node (black lines) and argument of pericenter (gray lines) of 1 Ceres (dashed lines) and 96P/Machholz (solid lines) in time. While 1 Ceres undergoes only slow uniform precession in Ω and ω, 96P/Machholz experiences Kozai-Lidov oscillations leading to non-uniform changes of both Ω and ω with $\sim$ 8000 y period, where the period is two times slower than for e and I due to the symmetries of the problem.

We have mentioned that many scientists sought the best solution for the collisions of two bodies in the Solar System. Our goal was to overcome the common assumptions of these all theories, namely the invariance of e and I in time. At the first glance, it seemed simple to incorporate a perturbing body causing Kozai-Lidov oscillations of the projectile and also possibly of the target, however, a few months of calculations convinced us that our original task was not simple at all. We especially focused on Kessler's theory because it gives a considerable freedom for the target body, and the theory itself is understandable and straightforward. We must admit that the exact analytical solution of latitude dependence of spatial density of a projectile's orbit undergoing Kozai-Lidov oscillations remains unknown to us even for the most simple setup of the bodies (Sun–projectile–perturber). This task may be solved numerically, which, however, was not the goal we intended to achieve. On the other hand, detailed study of Kessler's theory allowed us to obtain an analytical solution for collision probabilities for projectiles on hyperbolic orbits, which will be further investigated in future.

Our main goal was thus completely redefined. We chose the simplest scenario with Sun as a center of gravity, circular non-inclined target (e.g. idealized Earth), projectile on bound heliocentric orbit, and perturbing body on circular non-inclined orbit (e.g., idealized Jupiter). Then, if the first step was analytically solvable, proceed to more complex orbits of the target, perturber and add more perturbing bodies.

1.2 Kozai-Lidov dynamics

In this section, we briefly recall fundamental ideas of the Kozai-Lidov model for the secular evolution of the projectile orbit. We omit a more detailed study because the mechanism was extensively presented by numerous authors (Lidov, 1961; Kozai, 1962; Thomas and Morbidelli, 1996; Gronchi and Milani, 1998, 1999; Morbidelli, 2002) and restrict our explanation only to the simple setup of the problem.

1.2.1 Quadrupole approximation of the perturbing function

Consider a simple scenario: a projectile (e.g., asteroid or comet) is moving through the idealized Solar System where only the Sun and Jupiter are present. The projectile's mass m is negligible in comparison with mass of Jupiter m_{J} or mass of the Sun $m_{\odot}$. Coordinates of Jupiter, and those of projectile, are referred to the center of the Sun. We can write the Hamiltonian $\mathcal{H}$ for this system as

$$\mathcal{H} = m\mathcal{H}_0 + m\mathcal{P} \,, \tag{1.1}$$

$$\mathcal{H}_0 = -\frac{\mathcal{G}m_{\odot}}{2a} \,, \tag{1.2}$$

$$\mathcal{P} = -\mathcal{G}m_{\mathrm{J}} \left(\frac{1}{|\mathbf{r} - \mathbf{r_J}|} - \frac{\mathbf{r}.\mathbf{r_J}}{r_{\mathrm{J}}^3} \right) \,, \tag{1.3}$$

where $\mathcal{H}_0$ is an unperturbed Keplerian part of $\mathcal{H}$, $\mathcal{P}$ is the planetary perturbation of Jupiter, a is the semimajor axis of projectile, $\mathcal{G}$ is the gravitational constant, r and r_{J} are the heliocentric distances of the projectile and Jupiter, and $\mathbf{r}$ and $\mathbf{r}_{\mathrm{J}}$ are respectively the

heliocentric vectors of projectile and Jupiter defined as

$$\mathbf{r} = a\left[(\cos E - e)\,\mathbf{e_P} + \eta \sin E \mathbf{e_Q}\right] , \tag{1.4}$$

$$\mathbf{e_P} = \begin{pmatrix} \cos\Omega\cos\omega - \sin\Omega\sin\omega\cos I \\ \sin\Omega\cos\omega + \cos\Omega\sin\omega\cos I \\ \sin I\sin\omega \end{pmatrix} , \tag{1.5}$$

$$\mathbf{e_Q} = \begin{pmatrix} -\cos\Omega\sin\omega - \sin\Omega\cos\omega\cos I \\ -\sin\Omega\sin\omega + \cos\Omega\cos\omega\cos I \\ \sin I\cos\omega \end{pmatrix} , \tag{1.6}$$

where u is the eccentric anomaly, e the eccentricity, $\eta^2 = 1 - e^2$, I the inclination, Ω the longitude of the ascending node, and ω the argument of pericenter. Function $\mathcal{P}$ can be expressed using Legendre polynomials $P_n(\cos S)$:

$$\mathcal{P} = -\mathcal{G}m_{\mathrm{J}}\left(\frac{1}{r_{\mathrm{J}}}\sum_{n\geq 1}\left(\frac{r}{r_{\mathrm{J}}}\right)^n P_n(\cos S) - \frac{r\cos S}{{r_{\mathrm{J}}}^2}\right) , \tag{1.7}$$

where $\mathbf{r}.\mathbf{r}_{\mathrm{J}} = r r_{\mathrm{J}} \cos S$. At the moment, we restrict our investigation only to terms up to the quadrupole part of $\mathcal{P}$, where we consider only $P_1(\cos S) = \cos S$ and $P_2(\cos S) = 1/2(3\cos^2 S - 1)$ are present. Thus we readily get

$$\mathcal{P} = -\mathcal{G}m_{\mathrm{J}}\frac{1}{2}\frac{r^2}{r_{\mathrm{J}}^3}\left(3\cos^2 S - 1\right) = -\mathcal{G}\frac{m_{\mathrm{J}}}{r_{\mathrm{J}}}\frac{1}{2}\frac{r^2}{r_{\mathrm{J}}^2}\left[3\left(\frac{\mathbf{r}.\mathbf{r_J}}{r r_{\mathrm{J}}}\right)^2 - 1\right] . \tag{1.8}$$

Since we are mainly interested in the secular evolution of the orbital elements, we need to eliminate fast angles, mean anomalies l and l_{J}, from the perturbation function $\mathcal{P}$. This is achieved by integrating the function $\mathcal{P}$ over the whole range of l and l_{J} with an assumption that values of both mean anomalies are uniformly distributed in time. This, so called averaging technique, can be expressed in the integral from as follows

$$\overline{\mathcal{P}} = \frac{1}{4\pi^2}\int_{-\pi}^{\pi}\int_{-\pi}^{\pi}\mathcal{P}\mathrm{d}l_{\mathrm{J}}\mathrm{d}l , \tag{1.9}$$

where it is convenient to use following transformations

$$l \rightarrow u, \mathrm{d}l = \frac{r}{a}\mathrm{d}u , \tag{1.10}$$

$$l_{\mathrm{J}} \rightarrow f_{\mathrm{J}}, \mathrm{d}l_{\mathrm{J}} = \frac{1}{\eta_{\mathrm{J}}}\left(\frac{r_{\mathrm{J}}}{a_{\mathrm{J}}}\right)^2 \mathrm{d}f_{\mathrm{J}} , \tag{1.11}$$

where a_{J} is the semimajor axis of Jupiter, $\eta_{\mathrm{J}} = \sqrt{1 - e_{\mathrm{J}}}$, e_{J} is the eccentricity of Jupiter, and f_{J} is the true anomaly of Jupiter. The calculation is straightforward since the odd terms of sines and cosines vanish. Finally, we obtain an averaged perturbation function $\overline{\mathcal{P}}$ as follows

$$\overline{\mathcal{P}} = -\frac{\mathcal{G}m_{\mathrm{J}}}{16 a_{\mathrm{J}}\eta_{\mathrm{J}}}\left(\frac{a}{a_{\mathrm{J}}\eta_{\mathrm{J}}}\right)^2\left[\left(2 + 3e^2\right)\left(3\cos^2 I - 1\right) + 15e^2\sin^2 I\cos 2\omega\right]$$

$$= -\frac{1}{16}\Gamma C , \tag{1.12}$$

$$\Gamma = \frac{\mathcal{G}m_{\mathrm{J}}}{a_{\mathrm{J}}\eta_{\mathrm{J}}}\left(\frac{a}{a_{\mathrm{J}}\eta_{\mathrm{J}}}\right)^2 , \tag{1.13}$$

$$C = \left[\left(2 + 3e^2\right)\left(3\cos^2 I - 1\right) + 15e^2\sin^2 I\cos 2\omega\right] , \tag{1.14}$$

where $\overline{\mathcal{P}}$ is an integral of motion in our approximation, because $\overline{\mathcal{P}}$ is derived directly from the Hamiltonian $\mathcal{H}$ and does not explicitly depend on time variable.

Dynamical equations for the Keplerian orbital elements are thus easily derived from the Lagrangian equations of the perturbation theory (see, e.g., pp. 306 in Bertotti et al., 2003)

$$\begin{aligned}
\frac{da}{dt} &= -\frac{2}{na}\frac{\partial\overline{\mathcal{P}}}{\partial l} = 0 && (1.15)\\
\frac{de}{dt} &= \frac{\eta}{ena^2}\frac{\partial\overline{\mathcal{P}}}{\partial\omega} - \frac{\eta^2}{ena^2}\frac{\partial\overline{\mathcal{P}}}{\partial l} = \Gamma^\star\frac{15\eta}{8e}\left(e^2\sin^2 I\sin 2\omega\right) && (1.16)\\
\frac{dI}{dt} &= \frac{1}{na^2\eta}\left(\frac{1}{\sin I}\frac{\partial\overline{\mathcal{P}}}{\partial\Omega} - \cot I\frac{\partial\overline{\mathcal{P}}}{\partial\omega}\right) = -\Gamma^\star\frac{15}{16\eta}\left(e^2\sin 2I\sin 2\omega\right) && (1.17)\\
\frac{d\Omega}{dt} &= -\frac{1}{na^2\eta\sin I}\frac{\partial\overline{\mathcal{P}}}{\partial I} = \Gamma^\star\frac{3}{8}\frac{\cos I}{na^2\eta}\left(-2-3e^2+5e^2\cos 2\omega\right) && (1.18)\\
\frac{d\omega}{dt} &= -\frac{\eta}{ena^2}\frac{\partial\overline{\mathcal{P}}}{\partial e} + \frac{1}{na^2\eta}\cot I\frac{\partial\overline{\mathcal{P}}}{\partial I} = \\
&= -\frac{3}{8\eta}\Gamma^\star\left(\eta^2 - 5\cos^2 I + 5\left(\cos^2 I-\eta^2\right)\cos 2\omega\right) && (1.19)\\
\frac{dl}{dt} &= n + \frac{2}{na}\frac{\partial\overline{\mathcal{P}}}{\partial a} + \frac{\eta^2}{ena^2}\frac{\partial\overline{\mathcal{P}}}{\partial e}\\
&= n - \frac{1}{4}\Gamma^\star C - \frac{3\eta^2}{8}\Gamma\left(3\cos^2 I - 1 + 5\sin^2 I\cos 2\omega\right) && (1.20)
\end{aligned}$$

with

$$\Gamma^\star = \frac{\Gamma}{na^2}\ . \qquad (1.21)$$

These equations give us two additional integrals of motion

$$\begin{aligned}
a &= \text{const}\ , && (1.22)\\
c &= \eta\cos I = \text{const} \Leftrightarrow \frac{e}{\eta}\frac{de}{dt}\cos I - \eta\sin I\frac{dI}{dt} = 0\ , && (1.23)
\end{aligned}$$

where Eq. (1.23) comes simply from Eqs. (1.16) and (1.17). We should also note an order of magnitude of the neglected secular terms in our quadrupole approximation. The order of magnitude of the octupole term, $n = 3$, in Eq. (1.7), is proportional to $(a/a_{\rm J}\cdot e\cdot e_{\rm J})$. Kozai (1962) neglected Jupiter's eccentricity, thus all odd-order terms were dropped from the disturbing function. Recent observations show that some exoplanetary systems contain planets with retrograde orbits, which can be explained by adding the octupole term to the dynamical equations. Derivation and some interesting dynamical consequences of the octupole term will be discussed in Sec. 1.2.2. The magnitude of the $n = 4$ term, the hexadecapole term, is proportional to $(a/a_{\rm J})^2$, where this term provides only corrections to the quadrupole term, and does not imply significantly different dynamical evolution to the quadrupole term, contrary to the octupole term.

Now, we briefly investigate a meaning of integral C (Eq. 1.14). Since the integral c ties eccentricity e and inclination I together, we may substitute one of them and process our analysis only in two-dimensional space of parameters (e,ω). Dynamical evolution of e and ω thus strictly follows $C = \text{const}$ isoline. Let us denote two new variables that are more convenient for description of the problems where eccentricity approaches zero

$$\begin{aligned}
k &= e\cos\omega\ ,\\
h &= e\sin\omega\ ,
\end{aligned} \qquad (1.24)$$

which gives us a new form of the integral C

$$\begin{aligned}\mathcal{H}(k,h) = \left(2+3k^2+3h^2\right)\left(\frac{3c^2}{1-k^2-h^2}-1\right) \\ +15\left(k^2-h^2\right)\left(1-\frac{c^2}{1-k^2-h^2}\right) = C\ .\end{aligned} \tag{1.25}$$

Fig. 1.3 shows the evolution of e and ω given by the Hamiltonian from Eq. (1.2) on six surfaces with different values $c = \text{const}$. Each surface in Fig. 1.3 is defined by the maximal value of the inclination $I_{\max} = \arccos(c)$, corresponding to $e = 0$. For small values of $I_{\max} = 5^\circ, 25^\circ$, the level curves of $C(k,h)$ are very close to circles changing to ovals with increasing value of $I_{\max}$. This means that the argument of perihelion ω circulates over 360 degrees and eccentricity e remains during the whole secular cycle of ω almost constant. By consequence, also inclination I does not experience any significant changes.

For $I_{\max} = 35^\circ$, the level curves are elongated along h axis. The argument of perihelion ω still circulates, however, values of eccentricity e oscillate more significantly, acquiring the maximum values for $\omega = 90^\circ$ and 270°, where, on the other hand, the inclination I assumes the minimum value.

When the maximal value of the inclination is higher than a critical value $I_{\max} \geq I_{\text{crit}} = 39.2^\circ$, the topology of the C isolines changes severely. The origin in (k,h) plane, where $e = 0$, becomes an unstable equilibrium point. A separatrices plotted with solid bold black lines in Fig. 1.3 divides the phase space into three different parts: a region that is still similar to previous cases where ω still circulates over 360 degrees, and two regions where ω librates around either 90 or 270 degrees (the precession stops and ω is not able to overcome the barrier represented by $h = 0$ level). This behavior is usually called *Kozai oscillations* or *Kozai-Lidov oscillations*.

Increasing $I_{\max}$ causes the Kozai oscillations to become stronger, meaning that the difference between maximum and minimum values of e and I become larger. This may pose severe consequences for bodies with low present values of e because during their secular cycle their orbit can cross the orbits of the planets in the Solar System.

Now, we proceed to an analysis of $C(k,h)$, which will give us another insight to the behavior of the orbits depicted in Fig. 1.3. At first we analyze a behavior of $C(k,h)$ along the h axis. On the h axis lie two stationary points for $I_{\max} \geq I_{\text{crit}}$ and also the saddle point of the separatrix. We seek extremes of $C(0,h)$ that we easily obtain by its first derivative

$$\begin{aligned}C(0,h) &= \frac{(2+3h^2)(3c^2-1-h^2)-15h^2(1-c^2-h^2)}{1-h^2} \\ \frac{\partial C(0,h)}{\partial h} &= 0 \Leftrightarrow h(3h^4-6h^2+3-5c^2) = 0\ ,\end{aligned} \tag{1.26}$$

which lead to three different solutions: $h = 0$ and $h_\pm = \pm\sqrt{1-c\sqrt{5/3}}$ (we assume $-1 < h < 1$). The solution $h_\pm$ gives us positions of the stationary points and also the critical value of the c integral for which $h_\pm > 0 \Leftrightarrow c > c_{\text{crit}} = \sqrt{3/5}$ thus the critical value for the maximal value of the inclination is $I > I_{\text{crit}} = \arccos(\sqrt{3/5}) = 39.2^\circ$. The separatrix is represented by $C(0,0) = 2(3c^2-1)$ isoline where bodies with $C > C(0,0)$ circulate over 360 degrees in ω while bodies with $C < C(0,0)$ enter the forced stationary mode around $h_\pm$.

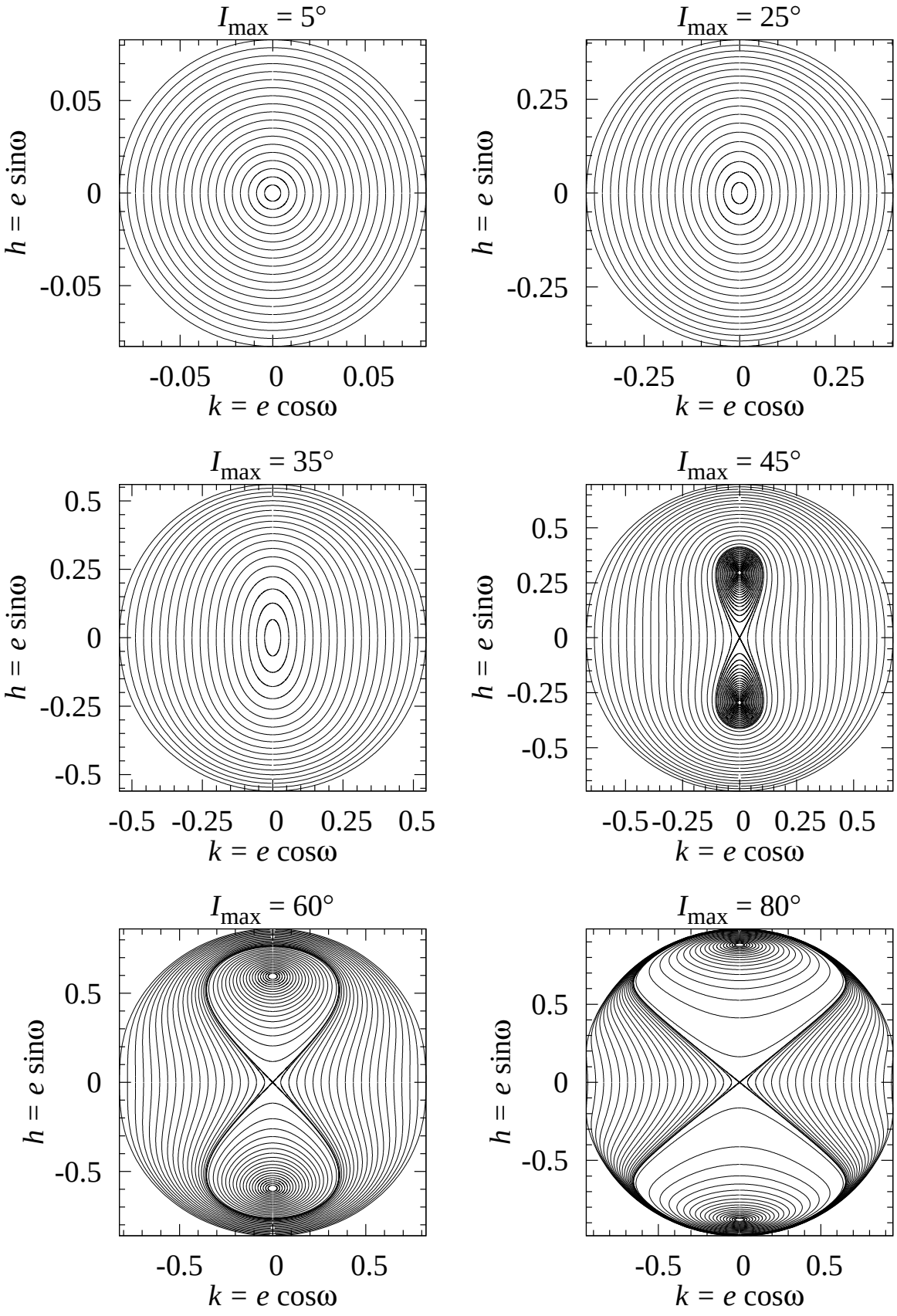

Figure 1.3: Portraits of possible C isolines for different values of $I_{\max}$. The inclination $I_{\max}$ corresponding to $e = 0$ is shown on the top of each panel. The separatrix corresponding to $e_{\min} = 0$ is plotted with solid bold black line.

The existence of the Kozai oscillations depends only on a value of c, in other words, on the initial conditions of the orbit. Its existence does not depend on the mass of the perturbing body, however, the mass of the perturbing body influences a timescale of this effect, and may lead to extremely long timescales for low-mass perturbers.

The derivation of the characteristic timescale $T_{\rm Kozai}$ of the Kozai oscillations can be found e.g., in Kinoshita and Nakai (2007). Since Kinoshita and Nakai (2007) used a different formalism, we express this derivation in our variables in the following paragraph.

From the topology of C-isolines know that the argument of pericenter ω circulates around origin for certain values of C and c. To obtain characteristic timescale $T_{\rm Kozai}$ of the Kozai oscillations, we thus must solve one of the dynamical equations and look for the period defined by two moments when a given variable assumes the same value.

In the following paragraph we will search for a solution of following equation

$$X = \eta^2 , \tag{1.27}$$

$$\frac{dX}{dt} = 2\eta\frac{d\eta}{dt} = -2e\frac{de}{dt} = -\frac{15\eta}{4}e^2\sin^2 I\sin 2\omega . \tag{1.28}$$

Using Eq. (1.23) we get

$$\frac{dX}{dt} = -\frac{15}{4\sqrt{X}}(1-X)(X-c^2)\sin 2\omega , \tag{1.29}$$

which is a differential equation that depends on two variables X and ω. Now, we eliminate ω from Eq. (1.29). The C integral is a constant of motion, thus we may search its value for $\omega_0 = 0°$, where the second term in Eq. (1.25) vanishes

$$C = 10 - 12X_0 + 6c^2 , \tag{1.30}$$

where $X_0 = 1 - e_0^2$, and also for $\omega_0 = 0°$ we have also I_0 and η_0. From Eq. (1.16) we see that e_0 is the minimum value for a given orbit. Combining Eqs. (1.25) and (1.30) we obtain

$$\cos 2\omega = \frac{-X^2 + X(5 + 5c^2 - 4X_0) - 5c^2}{5(1-X)(X-c^2)} = \cos^2\omega - \sin^2\omega . \tag{1.31}$$

From Eq. (1.31) we get

$$\cos^2\omega = \frac{1+\cos 2\omega}{2} = \frac{-3X^2 + X(5+5c^2-2X_0) - 5c^2}{5(1-X)(X-c^2)} , \tag{1.32}$$

$$\sin^2\omega = \frac{1-\cos 2\omega}{2} = \frac{2X(X_0 - X)}{5(1-X)(X-c^2)} . \tag{1.33}$$

$$\tag{1.34}$$

This allows us to substitute ω with X

$$\frac{dX}{dt} = -\frac{3}{2}\sqrt{2(X_0 - X)(-3X^2 + X(5+5c^2-2X_0) - 5c^2)} . \tag{1.35}$$

Since $(-3X^2 + X(5+5c^2-2X_0) - 5c^2)$ is a quadratic equation, we easily find its roots

$$X_{1,2} = \frac{-(5+5c^2-2X_0) \pm \sqrt{(5+5c^2-2X_0)^2 - 60c^2}}{-6} , \tag{1.36}$$

$$X_1 X_2 = \frac{5}{3}c^2 , \tag{1.37}$$

$$X_1 + X_2 = \frac{5+5c^2-2X_0}{3} , \tag{1.38}$$

and thus we obtain

$$\frac{dX}{dt} = -\frac{3}{2}\sqrt{2(X_0 - X)(X - X_1)(X_2 - X)} \,. \tag{1.39}$$

Eq. (1.39) is a nonlinear ordinary differential equation, that can be solved by a straightforward quadrature. The solution can be expressed with the Jacobi elliptic functions

$$X = X_0 + (X_1 - X_0)\mathrm{cn}^2\Theta \,, \tag{1.40}$$

where

$$\Theta = \frac{2K}{\pi}\left(n_\omega t + \frac{\pi}{2}\right) \,, \tag{1.41}$$

$$n_\omega = = \frac{3\sqrt{6}\pi}{128K}\Gamma^\star\sqrt{X_2 - X_1} \tag{1.42}$$

The expression $K(k)$ in Eqs. (1.41) and (1.42) is the complete elliptic integral of the first kind

$$K(k) = \int_0^{\frac{\pi}{2}} \frac{d\Theta}{\sqrt{1 - k^2\sin^2\Theta}} \,, \tag{1.43}$$

where k is the modulus

$$k^2 = \frac{X_0 - X_1}{X_2 - X_1} \,. \tag{1.44}$$

Finally, the characteristic timescale T_{Kozai} of the Kozai oscillations is

$$T_{\mathrm{Kozai}} = \frac{512\sqrt{2}K(k)}{3\sqrt{3}\sqrt{\alpha_2 - \alpha_0}\Gamma^\star} \,, \tag{1.45}$$

where $\Gamma^\star$ comes from Eq. (1.21). In the Solar System this value may range from thousands of years, e.g., for 96P/Machholz $T_{\mathrm{Kozai}} = 6314$ yr to several hundred thousand years for hypothetical body with $a = 1$ AU, $e = 0$ and $I = 60^\circ$, which would have $T_{\mathrm{Kozai}} = 326,000$ yr.

1.2.2 Octupole Term in the Kozai-Lidov Dynamics

In previous section, we studied Kozai-Lidov oscillations only in quadrupole approximation which, although very simplified, give very interesting results and dynamical consequences. Now, we will briefly investigate influence of the octupole term in the planetary perturbation function $\mathcal{P}$ by simply adding $n = 3$ term in Eq. (1.7). The octupole part $\mathcal{P}_{\mathrm{oct}}$ reads

$$\mathcal{P}_{\mathrm{oct}} = -\mathcal{G}m_{\mathrm{J}}\frac{1}{2}\frac{r^3}{r_{\mathrm{J}}^4}\left(5\cos^3 S - 3\cos S\right) = -\mathcal{G}\frac{m_{\mathrm{J}}}{r_{\mathrm{J}}}\frac{1}{2}\frac{r^3}{r_{\mathrm{J}}^3}\left[5\left(\frac{\mathbf{r}.\mathbf{r_J}}{rr_{\mathrm{J}}}\right)^3 - 3\left(\frac{\mathbf{r}.\mathbf{r_J}}{rr_{\mathrm{J}}}\right)\right] \,. \tag{1.46}$$

We use the same averaging technique as in case of the quadrupole part, and after a slight algebra we obtain the averaged octupole term in the planetary perturbation function $\overline{\mathcal{P}_{\mathrm{oct}}}$ that reads

$$\begin{aligned}\overline{\mathcal{P}_{\mathrm{oct}}} = & -\frac{\mathcal{G}m_{\mathrm{J}}}{a_{\mathrm{J}}\eta_{\mathrm{J}}}\left(\frac{a}{a_{\mathrm{J}}\eta_{\mathrm{J}}}\right)^3\frac{15}{32}ee_{\mathrm{J}}\{(\cos\Omega\cos\omega - \sin\Omega\sin\omega\cos I) \\ & [-16 - 12e^2 + (15 + 20e^2)(1 - \sin^2 I\sin^2\omega) - 15\eta^2(1 - \sin^2 I\cos^2\omega)] \\ & -10\cos I\eta^2(-\sin\Omega\sin\omega + \cos\Omega\cos\omega\cos I)\} \,.\end{aligned} \tag{1.47}$$

From Eq. (1.47) we see that the $\overline{\mathcal{P}_{\rm oct}}$ is a linear function of eccentricity $e_{\rm J}$ of the perturbing body. Since in the Solar System all massive planets have very low eccentricities $e_{\rm J} \leq 0.05$ the effects of the octupole part of the perturbation functions are dampened and can be omitted in the first-order approximation. However, for larger values of $e_{\rm J}$ the magnitude of $\overline{\mathcal{P}_{\rm oct}}$ cannot be neglected and must be treated correctly. The octupole extension of the perturbation potential has been used in studies of secular evolution of hierarchical triple star systems (Krymolowski and Mazeh, 1999; Ford et al., 2000), dynamics of the binary black holes (Blaes et al., 2002), or newly discovered exoplanetary systems with eccentric Jovian-mass planets (Lee and Peale, 2003; Katz et al., 2011).

Let us briefly discuss some dynamical consequences, that cannot be described by using the quadrupole term only. First of all, we see that longitude of the ascending node does not vanish in Eq. (1.47), which implies that $c = \eta \cos I$ is no longer constant in time, and we lose one of the integrals of motion. Moreover, this also implies that C-level isolines, now more complicated, are no more closed curves in (k, h) plane. Due to this, there is no expression for a characteristic timescale of this effect, however, for small eccentricities of the perturbing body we may assume that the characteristic timescale is similar to $T_{\rm Kozai}$ derived from the quadrupole term only.

The most interesting dynamical consequence of the octupole term extension is a dynamical evolution of the inclination I of the perturbed body. During last few years many extrasolar Jovian-mass planets were discovered, and about 25 per cent of them have a retrograde orbit with respect to the stellar rotation (Naoz et al., 2011). As we learned in previous section, the Kozai oscillations restricted to the quadrupole term cannot excite prograde bodies over $I = 90°$. Also, according to Fabrycky and Tremaine (2007) even though the perturbations from a binary star companion can produce very high inclinations, they are not able to explain the existence of retrograde orbits of the planets. Thus, there must exist a secular perturbation that pushes the originally prograde planet to the retrograde orbit. Katz et al. (2011) showed that when the octupole term extension is taken into account, the inclination may oscillate around $I = 90°$ when specific conditions are fulfilled (see, Fig. 2 in Katz et al., 2011, or Fig. 1.4). We recall, the stabilization of the exoplanet orbits in the retrograde domain is further assisted by the tidal effects, mainly by the eccentricity dampening (Correia et al., 2013).

1.3 Circular orbit of the target – paper A

The main goal of this and the following sections is to provide reader a more detailed description of our theory, than it was possible in paper A (Vokrouhlický et al., 2012) and paper B (Pokorný and Vokrouhlický, 2013). Here, we to use notation and formalism similar to the quoted papers.

Our first step was to develop a generalization of the original work of Öpik (1951). The configuration of the system, we investigate here, is very simple; we assume a massless target on a circular coplanar orbit and a massless projectile on a bound heliocentric orbit, where the motion of the target is influenced only by the mass of the Sun, while the projectile is also influenced by gravity of the perturbing body, that is assumed to be on an circular coplanar orbit. The orbit of the projectile lies inside the orbit of the perturbing body and their orbits never intersect (this may occur due to the Kozai oscillations even though the initial conditions indicated no crossing between projectile and perturbing body). This scenario may seem very artificial and academical, however, Sun-Earth-Jupiter and e.g., the comet 2P/Encke greatly fits our assumptions, and the

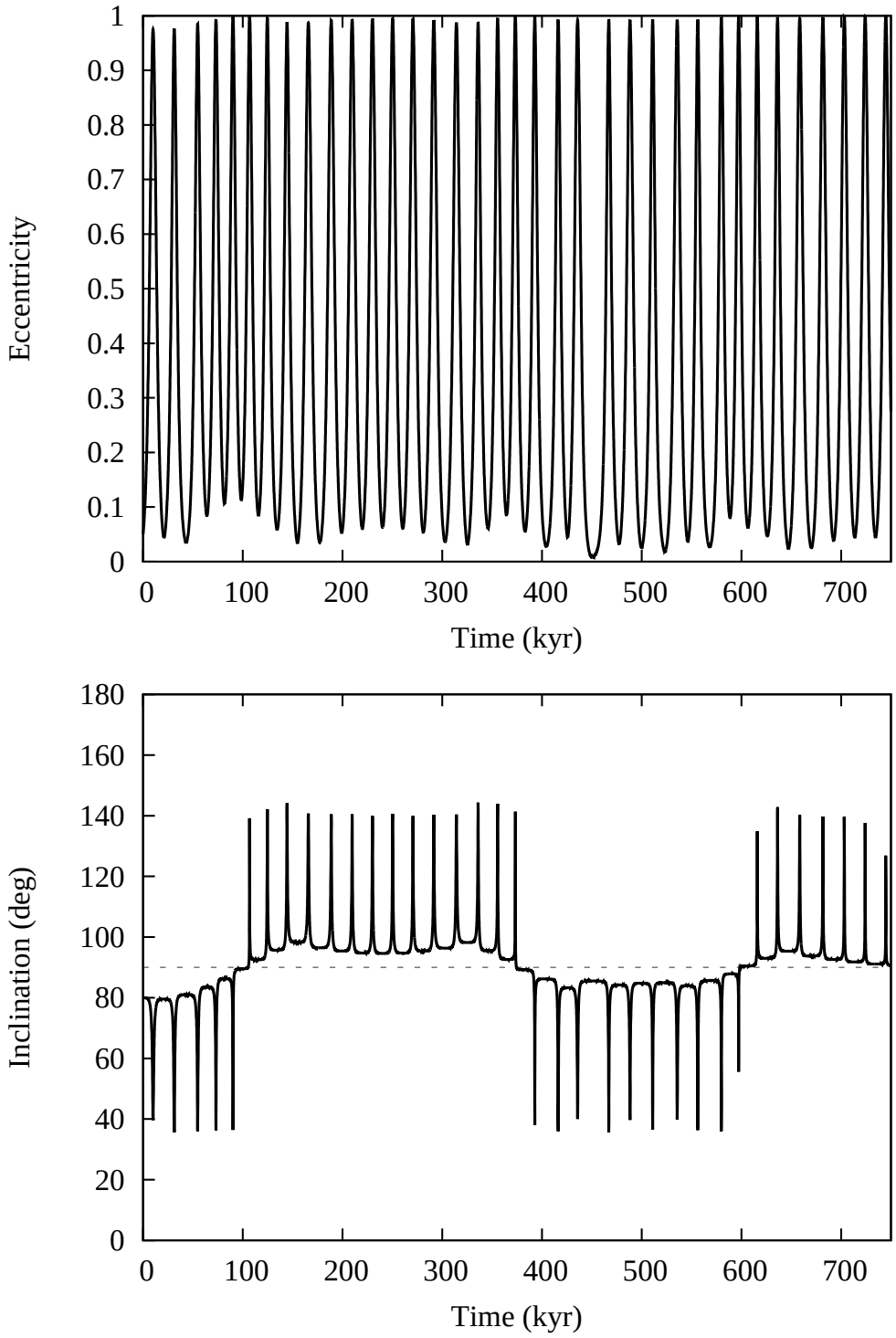

Figure 1.4: Evolution of eccentricity (top panel) and inclination (bottom panel) of a test particle influenced by gravitational effects of the Sun, and eccentric giant planet ten times massive than the Jupiter. While the quadrupole part of the perturbing function $\overline{P}$ causes short periodic oscillations in e and I, the octupole part of $\overline{P}$ forces the test particle to change the orientation of the orbit from prograde to retrograde and vice-versa. Note, that the secular effects of the octupole part of $\overline{P}$ are applied on much longer timescales than the secular effects of the quadrupole part. Global dynamical behavior of e remains unchanged when the inclination crosses $I = 90°$. Initial orbital elements a, e and I for the test particle: $a = 1.0$ au, $e = 0.05$, $I = 80°$ and for the giant planet: $a = 5.2$ au, $e = 0.25$, $I = 0.1°$.

value of its integral $c = 0.52$ is low enough to force changes of e and I caused by Kozai oscillations.

Our main motivation for the development of a more general method of the collisional probability evaluation was an unresolved problem of the origin of the toroidal population observed in the sporadic meteoroid complex. Toroidal meteors are known for their very peculiar orbits in the Solar System. Their mean inclination is very high $\sim 70°$, while the mean eccentricity is rather low, where the majority of the observed meteors has $e < 0.4$, and almost all of them have semimajor axis lower than 3 AU. Due to the very high inclinations all toroidal particles undergo Kozai-Lidov oscillations, and thus the estimates of the original theories could provide misleading results.

1.3.1 Mathematical introduction, reference frame and notation

As the target revolves on a circular coplanar orbit at constant heliocentric distance r_0 around the center of gravity, the intersection of the orbits of the target and projectile may occur only in the orbital plane of the target (X, Y). This determines the true anomaly f of the projectile at intersection points, because Z coordinate of the target (e.g., pp. 307 in Bertotti et al., 2003) is always zero at all intersection points

$$0 = Z = r \sin(\omega + f) \sin I \ , \tag{1.48}$$

which gives two solutions: $f_{\rm node} = -\omega$ for the intersection at the ascending node and $f_{\rm node} = \pi - \omega$ for the descending node. These intersections occur at heliocentric distance $r(f_{\rm node})$ thus

$$r(f_{\rm node}) = \frac{a\eta^2}{1 + e\cos f_{\rm node}} = \frac{a\eta^2}{1 \pm e\cos\omega} = r_0 \ , \tag{1.49}$$

where the upper sign holds for the intersection at the ascending node and the lower sign for the intersection at the descending node. It is useful to rewrite Eq. (1.49) to non-singular variables k and h

$$\left(k \pm \frac{\alpha}{2}\right)^2 + h^2 = 1 - \alpha + \frac{\alpha^2}{4} \ , \tag{1.50}$$

where parameter $\alpha = r_0/a$. This equation describes a circle with the origin at $(\pm\alpha/2, 0)$ in (k, h) plane for ascending and descending node, respectively, and the radius of the circle equal to $\sqrt{1 - \alpha + \alpha^2/4}$.

Now, let us investigate the orbit of the projectile near the nodal intersection points. Introduce an orthonormal triad $(\mathbf{e}_r, \mathbf{e}_\phi, \mathbf{e}_z)$ composed of three unit vectors with the origin at ascending and descending nodes. The vector $\mathbf{e}_r$ points to the radial direction, $\mathbf{e}_\phi$, normal to $\mathbf{e}_r$ both residing in the orbit plane (X, Y), and $\mathbf{e}_z$ is the orthonormal complement and points along the axis Z of the inertial frame. In our definition, the radial and longitudinal directions at the ascending node are opposite to their values at the descending node.

Similarly to Eqs. (1.4), (1.5) and(1.6) we define the heliocentric position vector $\mathbf{r}$ that describes the elliptic orbit as follows

$$\mathbf{r}(f) = r(f) \left[\mathbf{a}\cos(\omega + f) + \mathbf{b}\sin(\omega + f)\right] \ , \tag{1.51}$$

where $r(f) = a\eta^2/(1 + e\cos f)$. It should be noted that Eqs. (1.4) and (1.51) are identical,

but expressed in different variables. Unit vectors $\mathbf{a}$ and $\mathbf{b}$ read

$$\mathbf{a} = \begin{pmatrix} \cos\Omega \\ \sin\Omega \\ 0 \end{pmatrix} , \tag{1.52}$$

$$\mathbf{b} = \begin{pmatrix} -\sin\Omega\cos I \\ +\cos\Omega\cos I \\ \sin I \end{pmatrix} , \tag{1.53}$$

with $\mathbf{a}$ directed along the ascending node, and $\mathbf{b}$ in the orbit plane, perpendicular to $\mathbf{a}$. At the ascending node we have $\mathbf{a} = \mathbf{e}_r$ and $\mathbf{b} = \cos I\mathbf{e}_\phi + \sin I\mathbf{e}_z$, while at the descending node we get different expression $\mathbf{a} = -\mathbf{e}_r$ and $\mathbf{b} = -\cos I\mathbf{e}_\phi + \sin I\mathbf{e}_z$. This might be a bit confusing at the first sight, however, as we see in following text, this representation proves very beneficial.

We seek a representation of $\mathbf{r}(f)$ near the ascending and descending nodes, thus we expand $\mathbf{r}(f)$ in true anomaly f, bearing in mind that $r = a\eta^2/(1 \pm e\cos\omega)$ at the nodal intersection points (the upper sign for the ascending node). Using the Taylor series expansion we obtain

$$\mathbf{r}(f) = r\mathbf{e}_r + d\mathbf{r} = r\mathbf{e}_r + r\mathbf{A}_1 df + \frac{r}{2}\mathbf{A}_2 df^2 + \mathcal{O}(df^3) , \tag{1.54}$$

where $df = f - f_{\mathrm{node}}$ is an infinitesimal increment of the true anomaly. The first term with the vectorial coefficient $\mathbf{A}_1$ represents a rectilinear approximation, while the second term with $\mathbf{A}_2$ describes a local curvature of the elliptic orbit. For the simplicity, we omit terms of higher degrees, because we assume that their increments are infinitesimally small. The expression of vectorial coefficient reads (the upper sign for the intersection at the ascending node and the lower sign for the intersection at the descending node)

$$\mathbf{A}_1 = \mp\frac{e\sin\omega}{P}\mathbf{e}_r + (\cos I\mathbf{e}_\phi \pm \sin I\mathbf{e}_z) , \tag{1.55}$$

$$\mathbf{A}_2 = -2\left[1 - \frac{3}{2P} + \frac{\eta^2}{P^2}\right]\mathbf{e}_r - 2\frac{e\sin\omega}{P}\left(\pm\cos I\mathbf{e}_\phi + \sin I\mathbf{e}_z\right) , \tag{1.56}$$

where $P = a\eta^2/r$. Using this notation we can easily express the orbital velocity of the projectile at the nodal intersection.

A similar expansion is also necessary for the description of the motion of the target body. Since in this section we assume the target body to be on and circular and coplanar heliocentric orbit, its orbital elements read (we denote variables of the target body with subscript 0); the semimajor axis $a = a_0$, the eccentricity $e = e_0 = 0$, the inclination $I = I_0 = 0$, and the argument of pericenter $\omega = \omega_0$. For the sake of simplicity and without loss of generality let us set $\omega_0 = 0$. Using Eqs. (1.55) and (1.56) we easily obtain the vectorial coefficients for the target body

$$\mathbf{A}_{10} = \mathbf{e}_\phi , \tag{1.57}$$

$$\mathbf{A}_{20} = -\mathbf{e}_r . \tag{1.58}$$

Since we deal with moving bodies it is necessary to express their orbital velocity. The orbital velocity $\mathbf{v}$ of the projectile at the nodal intersection is easily obtainable from the linear term in Eq. (1.54) and from the total derivative of the true anomaly f with respect to time t that reads

$$\frac{df}{dt} = \frac{a\eta}{r}\frac{du}{dt} = n\eta\left(\frac{a}{r}\right)^2 , \tag{1.59}$$

with the second term in Eq. (1.59) coming from the Kepler's equation $nt = u - e\sin u$, where n is the mean motion of the body, and u is the eccentric anomaly of the body. If we denote $V_0 = n_0 a_0$ as a normalization of velocity, we get for the orbital velocity of the projectile

$$\begin{aligned} \mathbf{v} &= V_0\sqrt{\frac{a_0}{r}}\sqrt{P}\mathbf{A}_1 \\ &= V_0\sqrt{\frac{a_0}{r}}\sqrt{P}\left[\mp\frac{e\sin\omega}{P}\mathbf{e}_r + (\cos I\mathbf{e}_\phi \pm \sin I\mathbf{e}_z)\right] , \end{aligned} \tag{1.60}$$

where the upper and lower signs correspond to the intersections at the ascending and descending nodes respectively. For the target body the situation is really simple, because $a_0 = r_0, P_0 = 1$, and thus

$$\mathbf{v}_0 = V_0\mathbf{e}_\phi . \tag{1.61}$$

The relative velocity vector $\mathbf{V}$ is easily obtained by subtracting velocity vector of the target body $\mathbf{v}_0$ from the projectile's velocity vector $\mathbf{v}$; note that $r = a_0$ because of the circular orbit of the target body

$$\mathbf{V} = \mathbf{v} - \mathbf{v}_0 = V_0\left(\sqrt{P}\left[\mp\frac{e\sin\omega}{P}\mathbf{e}_r + (\cos I\mathbf{e}_\phi \pm \sin I\mathbf{e}_z)\right] - \mathbf{e}_\phi\right) , \tag{1.62}$$

where the components of $\mathbf{V}$ read

$$V_r = \mp V_0\frac{e\sin\omega}{\sqrt{P}} = V_0\cos b\sin\ell , \tag{1.63}$$

$$V_\phi = V_0\left(\sqrt{P}\cos I - 1\right) = V_0\cos b\cos\ell , \tag{1.64}$$

$$V_z = \pm V_0\sqrt{P}\sin I = V_0\sin b , \tag{1.65}$$

where ℓ is a longitude and b latitude of the radiant seen by the observer on the target body (the upper sign for the intersection at the ascending node and lower sign for the descending node). This means that ℓ and b are measured from the apex direction of the target body and that $\mathbf{V}$ points toward the radiant from which the projectile impacts the target body. We recall that Eqs. (1.63), (1.64), and (1.65) express in a different notation the standard velocity components (U_x, U_y, U_z) introduced in Öpik (1951) (note that standard velocity components are normalized, thus $V_0 = 1$ in Öpik, 1951).

1.3.2 Collision probability estimation

Here, we follow approach presented by Öpik (1951) or Wetherill (1967) who defined the collision probability of a projectile with a target body as a combination of two mutually independent parts: (1) the probability P_1 that during one secular cycle of the projectile's orbit its nodal crossing is close enough to the orbit of the target body, and (2) the probability P_2 that the target body is in the sufficient proximity of the nodal crossing of the projectile's orbit. Our assumptions about the target body are satisfied in both works by Öpik or Wetherill, where Wetherill assumed more general problem of the target body on an arbitrary elliptic orbit, thus we borrow Wetherill's result (Eq. 15 in Wetherill, 1967) for P_2 that expressed in our variables reads ($r_0 = a_0$ here)

$$P_2 = \frac{R}{4a_0\sqrt{\frac{2a_0}{r_0} - 1}}\sqrt{\frac{V^2}{V^2 - V_a^2}} = \frac{R}{4a_0}\sqrt{\frac{V^2}{V^2 - V_\phi^2}} , \tag{1.66}$$

where V_a is a velocity component of the target body directing towards instantaneous apex (in the circular case $V_a = V_\phi$), $V^2 = V_r^2 + V_\phi^2 + V_z^2$ is the square of the relative velocity at the intersection point of the orbits, and R is the radius of the target body (the projectile is assumed to be negligibly small, otherwise, R would be a sum of the radii of both bodies).

Evaluation of P_1 probability is, however, completely different story. Both Öpik (1951) and Wetherill (1967) assumed that the projectile keeps its values of the eccentricity e and inclination i constant and that its argument of perihelion ω circulates uniformly. As we show in Sec. 1.2 it is not true even for orbits with very low inclination I and very low eccentricity e, however, for such values it can be accepted as a meaningful approximation. For higher values of e and I the original assumption fails, because the orbital elements change significantly at short timescales (see Fig. 1.1).

In the following text, we determine the probability P_1 for orbits influenced by Kozai-Lidov oscillations we discussed in Sec. 1.2. The exact intersection configurations of the projectile and target are determined by Eqs. (1.25) and (1.50) leading to a cubic equation for $k_\star$ (or equivalently for $h_\star$, where $\star$ symbol denotes the orbital elements at the intersection)

$$(5-3\alpha\mp3\alpha k_\star)(3c^2-\alpha\mp\alpha k_\star)+15(\alpha\pm\alpha k_\star-c^2)(2k_\star^2-1+\alpha\pm\alpha k_\star)-C\alpha(1\pm k_\star) = 0 \ , \quad (1.67)$$

which is indeed a cubic equation $a_3k_\star^3 + a_2k_\star^2 + a_1k_\star^1 + a_0 = 0$ with coefficients

$$a_3 = \pm 30\alpha \ , \quad (1.68)$$

$$a_2 = 6(3\alpha^2 + 5\alpha - 5c^2) \ , \quad (1.69)$$

$$a_1 = \pm\alpha(36\alpha - 20 - 24c^2 - C) \ , \quad (1.70)$$

$$a_0 = 30c^2 - 20\alpha + 18\alpha^2 - 24\alpha c^2 - C\alpha \ . \quad (1.71)$$

We can easily obtain $h_\star$ from Eq. (1.50), which gives us up to 8 possible impact configurations because of the inversion symmetry $h_\star \leftrightarrow -h_\star$ and the fact that the cubic equation has always even number of roots different to ±1. There is also $k_\star \leftrightarrow -k_\star$ symmetry for the impact configurations in the ascending and descending nodes of the projectile's orbit stemming directly from Eq. (1.67). The number of impact configurations is following: (1) the projectile has very low e and I thus does not exhibit changes of e and I (Fig. 2 in paper A). Such configuration gives 4 impact configurations (2 in the singular case, when $h_\star = 0$ or $k_\star = 0$). (2) projectile has sufficiently high values of e or I to undergo Kozai oscillations (Fig. 3 in paper A). This geometry provides 8 impact configurations (6 the in singular case). (3) the combination of orbital elements of the projectile forces the projectile's libration around $h_\pm = \pm\sqrt{1 - c\sqrt{5/3}}$ (see end of Sec. 1.2 for the further reference) thus having 4 impact configurations (2 in the singular case), see Fig. 3 in paper A.

We assume, similarly to Öpik and Wetherill, that the target body is considerably smaller than its semimajor axis $R \ll a_0$. This assumption is correct for all known bodies in the Solar System, and is even valid for the most extreme case of very close hot Jupiters in known exoplanetary Systems (Sahu et al., 2006). Since the radius of the target body R is finite, we expect that in a close proximity of the exact intersection point $(k_\star, h_\star)$ values in (k, h) space exist, giving distance from the intersection point smaller than R. This also means that there also exist the limiting values $k_{\rm lim}$ and $h_{\rm lim}$, for which the distance from the intersection point is equal to the radius of the target body[2] R.

[2]We expect the target body to be a sphere with radius R. More complex shapes of the target body would require further treatment.

Now, we focus on finding the limiting values $k_{\rm lim}$ and $h_{\rm lim}$. We use the same reference system defined in Sec. 1.3.1. The projectile's position is close to the nodal intersection point that is exactly at heliocentric distance a_0. Using the linear part of Eq. (1.54) we get for the distance of the projectile from the nodal intersection

$$\Delta\mathbf{r}(\lambda) = r\mathbf{A}_1\lambda + (r-a_0)\mathbf{e}_r + \mathcal{O}(\lambda^2)\ , \tag{1.72}$$

with $\lambda = df$, where df is a small increment of true anomaly f near the ascending and descending nodes. Similarly we express the target's distance from the intersection point

$$\Delta\mathbf{r}_0(\lambda_0) = a_0\mathbf{e}_\phi\lambda_0 + \mathcal{O}(\lambda_0^2)\ , \tag{1.73}$$

where we used $\lambda_0 = df_0$. Now, we easily obtain the square of the projectile-target distance

$$\begin{aligned} d^2(\lambda,\lambda_0) &= [\Delta\mathbf{r}(\lambda) - \mathbf{r}_0(\lambda_0)]\cdot[\Delta\mathbf{r}(\lambda) - \mathbf{r}_0(\lambda_0)]\ , \\ &= (r-a_0)^2 \pm 2r(r-a_0)\frac{r}{a}\frac{e\sin\omega}{\eta^2}\lambda + r^2 - 2\cos I a_0\lambda\lambda_0 + a_0^2\lambda_0^2 \\ &+ \left[\left(\frac{r}{a}\right)^2\left(\frac{e\sin\omega}{\eta^2}\right)^2\sin^2 I + \cos^2 I\right]\lambda^2 \end{aligned} \tag{1.74}$$

and we search for its minimum value $d^2_{\rm min}$ as a minimization problem in the two-dimensional space (λ,λ_0). The minimization for λ_0 is quite simple giving

$$\frac{\partial d^2_{\rm min}}{\partial\lambda_0} = 2a_0^2\lambda_0 - 2a_0\cos I\lambda = 0 \Leftrightarrow \lambda_{0_{\rm min}} = \lambda\cos I\frac{r}{a_0}\ , \tag{1.75}$$

and then the minimization for λ reads

$$d^2_{\rm min}(\lambda) = (r-a_0)^2 \pm 2r(r-a_0)\frac{r}{a}\frac{e\sin\omega}{\eta^2}\lambda \tag{1.76}$$

$$+ \ r^2\left[\left(\frac{r}{a}\right)^2\left(\frac{e\sin\omega}{\eta^2}\right)^2\lambda^2 + \sin^2 I\right]\lambda^2\ , \tag{1.77}$$

$$\frac{\partial d^2_{\rm min}(\lambda)}{\partial\lambda} = \pm 2r(r-a_0)\frac{r}{a}\frac{e\sin\omega}{\eta^2} + 2r^2\left[\left(\frac{r}{a}\right)^2\left(\frac{e\sin\omega}{\eta^2}\right)^2 + \sin^2 I\right]\lambda\ , \tag{1.78}$$

$$\frac{\partial d^2_{\rm min}(\lambda)}{\partial\lambda} = 0 \Leftrightarrow \lambda_{\rm min} = \mp\frac{(r-a_0)\frac{r}{a}\frac{e\sin\omega}{\eta^2}}{r\left(\frac{r}{a}\frac{e\sin\omega}{\eta^2}\right)^2 + \sin^2 I}\ , \tag{1.79}$$

thus the minimum distance finally yields

$$d_{\rm min} = (r-a_0)\frac{\frac{a\eta^2}{r}\sin I}{\sqrt{\left(\frac{a\eta^2}{r}\sin I\right)^2 + e^2\sin^2\omega}} = (r-a_0)\frac{P\sin I}{\sqrt{P^2\sin^2 I + e^2\sin^2\omega}}\ . \tag{1.80}$$

Now, let us scale $d_{\rm min}$ by semimajor axis a and make it equal to scaled radius of the target body $\rho = R/a$

$$\rho = \left[\eta^2 - \alpha(1\pm k)\right]\Lambda = \mathcal{K}(k,h)\ , \tag{1.81}$$

$$\Lambda = \sqrt{\frac{\eta^2 - c^2}{(\eta^2-c^2)(1\pm k)^2 + h^2\eta^2}}\ , \tag{1.82}$$

where we used $\sin^2 I = (\eta^2 - c^2)/\eta^2$ and $\alpha(1 \pm k)) = \eta^2$. Since c remains constant during the Kozai cycle and is determined by the initial conditions of the projectile's orbit, we can find the limiting values $k_{\rm lim}$ and $h_{\rm lim}$ by solving a set of two independent equations, namely Eqs. (1.25) and (1.81). This system of equations does not provide a simple analytical solution. Assuming $\rho \ll 1$ we might search for small displacements δk and δh that give $k_{\rm lim} = k_\star + \delta k$ and $h_{\rm lim} = h_\star + \delta h$. Using two-dimensional Taylor expansion of $\mathcal{H}(k,h)$ and $\mathcal{K}(k,h)$ at the point of exact intersection we get

$$\mathcal{H}(k,h) = \mathcal{H}(k_\star,h_\star) + (\partial\mathcal{H}/\partial k)_\star \delta k + (\partial\mathcal{H}/\partial h)_\star \delta h + \mathcal{O}(\delta k + \delta h)^2 = C \,, \quad (1.83)$$

$$\mathcal{K}(k,h) = \mathcal{K}(k_\star,h_\star) + (\partial\mathcal{K}/\partial k)_\star \delta k + (\partial\mathcal{K}/\partial h)_\star \delta h + \mathcal{O}(\delta k + \delta h)^2 = \rho \,. \quad (1.84)$$

Since $\mathcal{K}(k_\star,h_\star) = 0$ and $\mathcal{H}(k_\star,h_\star) = C$ we obtain for δk and δh following expressions

$$\delta k = -\rho \frac{(\partial\mathcal{H}/\partial h)_\star}{\mathcal{D}_\star} \,, \quad (1.85)$$

$$\delta h = +\rho \frac{(\partial\mathcal{H}/\partial k)_\star}{\mathcal{D}_\star} \,, \quad (1.86)$$

$$\mathcal{D} = (\partial\mathcal{K}/\partial h)_\star (\partial\mathcal{H}/\partial k)_\star - (\partial\mathcal{K}/\partial k)_\star (\partial\mathcal{H}/\partial h)_\star \,, \quad (1.87)$$

recall that the symbol $\star$ represents the exact intersection configuration. Obtaining the partial derivatives of functions $\mathcal{K}(k,h)$ and $\mathcal{H}(k,h)$ is a straightforward process, thus after a brief algebra we find

$$(\partial\mathcal{K}/\partial k)_\star = -2\left(k_\star \pm \frac{\alpha}{2}\right)\Lambda \,, \quad (1.88)$$

$$(\partial\mathcal{K}/\partial h)_\star = -2\, h_\star \Lambda \,, \quad (1.89)$$

$$(\partial\mathcal{H}/\partial k)_\star = \frac{2k_\star}{\eta_\star^2}\left[2\left(7 - 3c^2 - 12k_\star^2 + 3h_\star^2\right) + C\right] \,, \quad (1.90)$$

$$(\partial\mathcal{H}/\partial h)_\star = \frac{2h_\star}{\eta_\star^2}\left[2\left(-8 + 12c^2 + 3k_\star^2 + 18h_\star^2\right) + C\right] \,, \quad (1.91)$$

Interestingly, in the linear approximation the $(\delta k, \delta h)$ solution has also its symmetric counterpart $(-\delta k, -\delta h)$. Such displacements direct along the tangent to the isoline $\mathcal{H}(k,h) = C$ at the point of exact intersection $(k_\star, h_\star)$.

Now, we proceed to determination of the time interval $(\Delta t)_\star$ which the projectile spends in the interval ranging from $(k_\star - \delta k, h_\star - \delta h)$ to $(k_\star + \delta k, h_\star + \delta h)$, i.e. in the interval where the mutual distance of projectile and target body is smaller that the radius R of the target body. Using the Eqs. (1.16) and (1.19) we, after a brief algebra, obtain the time differentials $\frac{dk}{dt}$ and $\frac{dh}{dt}$ describing the motion of the projectile in the (k,h) plane along the C integral isoline

$$\frac{dk}{dt} = -\frac{3}{2}\Gamma^\star \eta h \left[1 + \frac{5}{2}\frac{c^2(1-k^2) - \eta^4}{\eta^4}\right] \,, \quad (1.92)$$

$$\frac{dh}{dt} = +\frac{3}{2}\Gamma^\star \eta k \left[1 + \frac{5}{2}\frac{c^2 h^2}{\eta^4}\right] \,. \quad (1.93)$$

Our linear solution of δk and δh is assumed to have values of the order $\rho(\ll 1)$, thus we adopt only a linear discretization of the Eqs. (1.92) and (1.93), namely we represent $dk \to \delta k$, $dh \to \delta h$, and $dt \to (\Delta t)_\star/2$. As we mentioned before, the solution is symmetric in δk and δh, thus we need to evaluate only one half of the collisional region. Naturally,

Eqs. (1.92) and (1.93) are evaluated at the point of exact intersection $(k_\star, h_\star)$, where both equations provide the same results, up to the terms of the second order in ρ.

However, this approach might fail when the displacements δk and δh are large. Such situation occurs when $\mathcal{D}_\star$ is very close to 0, which always occurs for intersections with $h_\star = 0$, but also when two solutions are very close to each other in (k, h) space. In such cases, we should not use our simple linearized approach and solve Eqs. (1.92) and (1.93) numerically. Our tests show that the exact value when the linear approach fails depends on the orbital elements of both projectile and target, where the absolute value of $|\mathcal{D}|$ may range from 1×10^{-3} to 5×10^{-2}; for the purpose of our code we adopted critical value $|\mathcal{D}_{\rm crit}| = 2 \times 10^{-3}$. The determination of corresponding value of $(\Delta t)_\star/2$ is then performed by a numerical integration of the Eqs. (1.92) and (1.93) from the intersection point to the limiting value of mutual distance of projectile and target body. Such approach provide validity for arbitrary orbits of both projectile and target body satisfying assumptions for which our theory is valid.

Since we now know the time $(\Delta t)_\star$ that spend both bodies in the region where the mutual collision is possible, the partial probability P_1 for a particular intersection configuration is then reads

$$P_1 = \frac{(\Delta t)_\star}{T_{\rm Kozai}} \,, \tag{1.94}$$

where $T_{\rm Kozai}$ comes from Eq. (1.45) and is the duration of the whole cycle of secular evolution of the projectile along the level curve of the C integral. Now, we can evaluate the collisional probability P of impact per one revolution of the projectile

$$P = \sum P_1 P_2 = \sum \frac{(\Delta t)_\star}{T_{\rm Kozai}} P_2(a, e_\star, I_\star) \,, \tag{1.95}$$

where the summation is performed over all possible intersection configurations for both the ascending and descending nodes. Contrary to Öpik's approach, P_1 is also a function of ω, and P_2 in our case must be evaluated for each intersection configuration independently because we do not assume e and I to be constant in time.

It is also convenient to determine an intrinsic collision probability p per unit of time and unit of cross sectional area, which we obtain by dividing P by the projectile's orbital period $T_{\rm orb}$ and square of the target's body radius R

$$p = \frac{P}{T_{\rm orb} R^2} = P \frac{\sqrt{G M_\odot}}{2\pi a^{3/2} R^2} \,, \tag{1.96}$$

where $GM_\odot$ is the standard gravitational parameter of the Sun. For a detailed comparison with the standard Öpik's theory, and interesting facts about Öpik's approximation, see paper A.

1.4 Elliptic orbit of the target – paper B

Our theory for the target on the circular coplanar orbit was a good improvement to the standard and widely used theories, providing better results and still maintaining analytical form. However, we knew, from the very beginning, that further improvements of the theory are needed. Impacts on Mercury, the most eccentric planet in the Solar System with $e_{\rm Mercury} = 0.20563$, provide very interesting resources for various scientific fields. A lack of Mercury's atmosphere, similarly to our Moon, does not provide any protection

from incoming impactors thus leaving the unprotected surface severely bombarded (see, e.g., Marchi et al., 2009, 2013, and references therein).

The Solar System experienced during its early stages a dynamical instability that produced a cataclysmic cratering events seen even in the present as basins on the Mercury or Moon. This event occurred ~ 700 Myr after the planets formed, and is known as the Late Heavy Bombardment (LHB; Gomes et al., 2005). While it is assumed that the LHB ended about 3.7 to 3.8 Gyr ago, many craters over 300 km in diameter are known either on the Earth or Moon (Wilhelms, 1987). Bottke et al. (2012) found that the LHB lasted much longer than previously thought, where the majority of the late impactors originated in the E-belt. The E-belt, now largely extinct, is an extended population of the asteroid belt between 1.7 and 2.1 au.

Even the most ambitious simulations are not able to represent the realistic abundance of bodies producing the LHB or the later cratering events caused by the E-belt population. Thus, only a small fraction of the original ensemble of bodies can be simulated, which significantly decreases the impact statistics of studied problems. During the LHB many impactors were driven to high eccentric and/or inclined orbits forcing them to experience Kozai oscillations. Since we showed, in previous section, that even the crudest approximation of the Kozai oscillations can greatly improve the determination of the collisional probabilities. Here, motivated mostly by findings of Bottke et al. (2012), we develop an extension of our original theory for the targets on the elliptic orbits. Still, we restrict the target to be coplanar with the plane of the reference, however, we expect that our generalization improves the determination accuracy of the collisional rates for the Mercury, and may become an interesting tool for many exoplanetary applications.

Our theory for a target on an elliptic coplanar orbit follows the same approach we used in Sec. 1.3, thus we do not rewrite the whole theory, but we mainly focus on differences between two theories.

We use the same reference system as in Sec. 1.3.1 and since the projectile was assumed to be on an arbitrary bound orbit, there are no changes regarding formulas describing projectile's motion. For now, we focus on the motion of the target body. We must modify Eqs. (1.57) and (1.58) describing the vectorial coefficients for the target body $\mathbf{A}_{10}$ and $\mathbf{A}_{20}$, since the eccentricity of the target body is not assumed to be equal to zero, while we still assume the inclination of the target body to be equal zero $I_0 = 0$. Thus, we obtain

$$\mathbf{A}_{10} = \mp\frac{e_0 \sin f_0}{P_0}\mathbf{e}_r + \mathbf{e}_\phi \,, \tag{1.97}$$

$$\mathbf{A}_{20} = -2\left[1 - \frac{3}{2P_0} + \frac{\eta_0^2}{P_0^2}\right]\mathbf{e}_r - 2\frac{e_0 \sin f_0}{P_0}\mathbf{e}_\phi \,, \tag{1.98}$$

where we recall $\eta_0^2 = 1 - e_0^2$ and $P_0 = a_0\eta_0^2/r_0$. Since $e_0 > 0$, we cannot assume $a_0 = r_0$ and set arbitrary value of f_0 without a loss of generality. However, r_0 is still only a function of f_0, thus we may substitute f_0 in $\mathbf{A}_{10}$ and $\mathbf{A}_{20}$ by r_0 using relation $e_0 \sin f_0 = \eta_0 R_\pm$, where

$$R_\pm = \pm\frac{\sqrt{(r_0 - r_1)(r_2 - r_0)}}{r_0} \,, \tag{1.99}$$

with $r_1 = a_0(1 - e_0)$ and $r_2 = a_0(1 + e_0)$ standing for the perihelion and aphelion distances

of the target body, respectively, thus the rewritten equations for $\mathbf{A}_{10}$ and $\mathbf{A}_{20}$ yield

$$\mathbf{A}_{10} = \frac{\eta_0 R_\pm}{P_0}\mathbf{e}_r + \mathbf{e}_\phi \,, \tag{1.100}$$

$$\mathbf{A}_{20} = -2\left[1 - \frac{3}{2P_0} + \frac{\eta_0^2}{P_0^2}\right]\mathbf{e}_r - 2\frac{\eta_0 R_\pm}{P_0}\mathbf{e}_\phi \,. \tag{1.101}$$

The upper and lower sign in $R_\pm$ corresponds to f_0 values in different parts of orbit, namely the upper sign for interval $(0, \pi)$ and the lower sign for the interval $(\pi, 2\pi)$. Please bear in mind that these signs must not be confused with signs denoting the impact configuration in the ascending and descending nodes, and need to be treated separately.

Now, we express the orbital velocity $\mathbf{v}_0$ of the target body on the elliptic orbit using Eqs. (1.60) and (1.97)

$$\mathbf{v}_0 = V_0 F \mathbf{A}_{10} = V_0(R_\pm \mathbf{e}_r + F\mathbf{e}_\phi) \,, \tag{1.102}$$

with $F = \eta_0 a_0/r_0$. From Eq. (1.60) we see, that the vector pointing to the instantaneous apex of the target's body motion is no longer parallel to vector $\mathbf{e}_\phi$. We thus, for further convenience, introduce a new orthonormal triad $(\mathbf{e}_a, \mathbf{e}_b, \mathbf{e}_z)$, where $\mathbf{e}_a$ is directed to the instantaneous apex of the target's motion, $\mathbf{e}_b = \mathbf{e}_a \times \mathbf{e}_z$, and $\mathbf{e}_z$ is still pointing along the Z axis of the inertial frame. The new triad directly results from Eq. (1.60) and reads

$$\mathbf{e}_a = \frac{R_\pm \mathbf{e}_r + F\mathbf{e}_\phi}{\sqrt{R_\pm^2 + F^2}} \,, \mathbf{e}_b = \frac{F\mathbf{e}_r - R_\pm \mathbf{e}_\phi}{\sqrt{R_\pm^2 + F^2}} \,, \tag{1.103}$$

where $R_\pm^2 + F^2 = 2(a_0/r_0) - 1$. Using the new orthonormal triad the corresponding relative velocity components yield

$$V_a = \frac{V_0}{\sqrt{R_\pm^2 + F^2}}\left[\sqrt{\frac{r_0}{r}}\sqrt{P}\left(\mp R_\pm \frac{e\sin\omega}{P} + F\cos I\right) - \left(R_\pm^2 + F^2\right)\right] \,, \tag{1.104}$$

$$V_b = \frac{V_0}{\sqrt{R_\pm^2 + F^2}}\sqrt{\frac{r_0}{r}}\sqrt{P}\left(\mp F\frac{e\sin\omega}{P} - R_\pm\cos I\right) \,, \tag{1.105}$$

$$V_z = \pm V_0\sqrt{P}\sin I \,, \tag{1.106}$$

where $V_a = \mathbf{V}\cdot\mathbf{e}_a$, $V_b = \mathbf{V}\cdot\mathbf{e}_b$, and $V_z = \mathbf{V}\cdot\mathbf{e}_z$. The longitude ℓ and latitude b of the radiant position seen by the observer then read

$$\ell = \arctan\left(\frac{V_b}{V_a}\right) \,, \tag{1.107}$$

$$b = \arcsin\left(\frac{V_z}{V_0}\right) \,. \tag{1.108}$$

The evaluation of the collision probability follows the same method as we presented in Sec. 1.3, thus we will point out only the main differences to the previous method. The distance of the target $\Delta\mathbf{r}_0$ from the point of exact intersection is different due to the non-zero eccentricity of the target body and in the elliptic case reads

$$\Delta\mathbf{r}_0(\lambda_0) = r_0\mathbf{A}_{10}\lambda_0 + \mathcal{O}(\lambda_0^2) \,, \tag{1.109}$$

where r_0 is the heliocentric distance of the intersection point. If we compare Eqs. (1.109) and (1.73), the elliptic expression for $\Delta\mathbf{r}_0$ and its circular counterpart, we see, that unlike

in the circular case, $\mathbf{A}_{10}$ has both radial and longitudinal components. Thus, we also must anticipate changes in the evaluation of the minimum mutual orbital distance $d_{\rm min}$ of the projectile and target body near the intersection point. The square of the projectile-target distance reads

$$\begin{aligned} d^2(\lambda,\lambda_0) &= [\Delta\mathbf{r}(\lambda)-\mathbf{r}_0(\lambda_0)]\cdot[\Delta\mathbf{r}(\lambda)-\mathbf{r}_0(\lambda_0)]\ , \\ &= (r-r_0)^2 \pm 2r(r-r_0)\frac{r}{a}\frac{e\sin\omega}{\eta^2}\lambda + r^2 - 2\cos I r_0\lambda\lambda_0 + r_0^2\lambda_0^2 \\ &+ \left[\left(\frac{r}{a}\right)^2\left(\frac{e\sin\omega}{\eta^2}\right)^2\sin^2 I + \cos^2 I\right]\lambda^2\ . \end{aligned} \tag{1.110}$$

We follow a similar approach used in Sec. 1.3, however, in this case the situation is more complex. First, we derive the first partial derivatives with respect to both variables (λ,λ_0)

$$\begin{aligned} \frac{1}{2}\frac{\partial d^2}{\partial\lambda} &= (X_1+X_2\lambda-X_3\lambda_0)X_2 + (r\cos I\lambda - r_0\lambda_0)r\cos I \\ &\quad + r^2\sin^2(I)\lambda = 0\ , \end{aligned} \tag{1.111}$$

$$\frac{1}{2}\frac{\partial d^2}{\partial\lambda_0} = -(X_1+X_2\lambda-X_3\lambda_0)X_3 - r_0(r\cos I\lambda - r_0\lambda_0) = 0\ , \tag{1.112}$$

where $X_1=(r-r_0)$, $X_2=\pm re\sin\omega/P$, and $X_3=r_0\eta R_\pm/P_0$. The system of Eqs. (1.111) and (1.112) has following solutions for (λ,λ_0) (using e.g., Cramer's rule)

$$\lambda = X_1\frac{X_2r_0^2 - X_3r_0r\cos I}{\Delta}\ , \tag{1.113}$$

$$\lambda_0 = X_1\frac{-X_3r^2 + X_2r_0r\cos I}{\Delta}\ , \tag{1.114}$$

$$\Delta = 2r_0rX_2X_3\cos I - r^2r_0^2\sin^2 I - r^2X_3^2 - r_0^2X_2^2\ . \tag{1.115}$$

The minimum distance $d_{\rm min}$ in the case of the target on an elliptic orbit thus reads

$$d_{\rm min} = \frac{(r-r_0)\sin I}{\sqrt{(1+\beta^2)\sin^2 I + (\gamma-\beta\cos I)^2}}\ , \tag{1.116}$$

where $\beta=r_0R_\pm/(a_0\eta_0)$ and $\gamma=\mp e\sin\omega/P$). Eq. (1.116) is obtained straightforwardly because terms in brackets in Eq. (1.110) give after the substitution of (λ,λ_0) very simple expressions. Note that $d_{\rm min}$ is a function of orbital parameters of the projectile with the nodal distance $r=a\eta^2/(1\pm e\cos\omega)$ and the heliocentric distance of the target r_0 that is assumed to be fixed.

Again, we follow the same procedure as in the circular case. The limiting impact configuration is given by $d_{\rm min}=R$, where R is the radius of the target body (for a negligible size of the projectile), thus after scaling R with the semimajor axis a of the projectile we get

$$\rho = \left[\eta^2 - \alpha(1\pm k)\right]\Lambda = \mathcal{K}(k,h)\ , \tag{1.117}$$

with

$$\Lambda = \sqrt{\frac{\eta^2-c^2}{(\eta^2-c^2)\,(1+\beta^2)\,(1\pm k)^2 + [h\eta\pm\beta c(1\pm k)]^2}}\ . \tag{1.118}$$

Using Eqs. (1.83) – (1.93), that are the same for the target on either circular or elliptic orbit, we obtain the probability P_1 which now depends also on r_0

$$P_1(r_0) = \frac{(\Delta t)_\star(r_0)}{T_{\rm Kozai}} \ , \tag{1.119}$$

thus we again express the total collisional probability P per one revolution of the projectile as

$$P(r_0) = \sum P_1 P_2 \ , \tag{1.120}$$

where we sum over all possible impact configuration denoted by $\star$ symbol. The intrinsic collisional probability $p(r_0)$ thus reads

$$p(r_0) = \frac{P(r_0)}{T_{\rm orb} R^2} \ , \tag{1.121}$$

where we again applied a normalization for the orbital period of the projectile $T_{\rm orb}$, and to the cross-section factor R^2 we adopt definition of the intrinsic collisional probability from (Öpik, 1951; Wetherill, 1967; Greenberg, 1982). Since the probability $P(r_0)$ is dimensionless, the convenient units of $p(r_0)$ are au^{-2}y^{-1}.

We derived the collisional probability P, now, for the target that is on an elliptic orbit, following the similar approach as in circular case. There are some noticeable differences, but overall both theories look almost the same. However, so far we fixed the heliocentric distance r_0 of the target body, thus we can derive using Eq. (1.120) the collisional probability for a particular value of r_0, but the target body with non-zero e may reside in the time of the collision on an arbitrary value of r_0 between the pericenter and apocenter of the target's orbit. In order to evaluate the final collisional probability $p_{\rm fin}$, we thus need to consider all possible values of r_0 in the range (r_1, r_2). Since the values of r_0 are not equally probable in time, we need to apply an appropriate weighting to $p(r_0)$. Because the true anomaly differential df of an elliptic orbit satisfies relation $df \propto dr_0/(r_0^2 |\mathbf{v} \cdot \mathbf{e_r}|) \propto dr_0/(r_0^2 R_+)$, we finally identify the weighting factor to be

$$\Psi(r_0) = \frac{a_0 \eta_0}{\pi} \frac{1}{r_0 \sqrt{(r_0 - r_1)(r_2 - r_0)}} \ . \tag{1.122}$$

The constants at the right side of Eq. (1.122) are set that the integral over the range (r_1, r_2) satisfies the normalization

$$\int_{r_1}^{r_2} \Psi(r_0) dr_0 = 1 \ . \tag{1.123}$$

We should note that one would expect also another weighting factor $dt \propto dr_0/(|\mathbf{v} \cdot \mathbf{e_r}|)$ expressing the time interval that the target body spends in the region $(r_0, r_0 + dr_0)$, however, this weighting factor is already contained in the P_2 probability. Hence, the final intrinsic collisional probability $p_{\rm fin}$ over all possible impact configurations reads

$$p_{\rm fin} = \int_{r_1}^{r_2} \Psi(r_0) p(r_0) dr_0 \ . \tag{1.124}$$

The weighting factor $\Psi(r_0)$ is apparently singular at pericenter and apocenter distance of the target body, at both lower and upper integration boundaries. Fortunately, the integral itself is finite, however, the numerical evaluation of $p_{\rm fin}$ must be performed with caution. In our code we use the standard method of the improper integrals calculation (Press et al., 2007). More specified information can be found in the Appendix Section of paper B.

1.5 Implementation of our approach

Our theory provides more complicated and not easily understandable formulas for the evaluation of the collisional probability between two bodies compared to those of Öpik (1951), or Wetherill (1967), and readers might find the theory too complex to use it without making a big effort, thus leaving our theory aside and keep using theories in situations where the original assumptions are violated. One of the crucial parts of both our papers is the comparison between the direct impacts recorded in the $N-$body simulation and the estimate of the collisional probability based on our theory. We wrote a simple code in FORTRAN 77 that provided only an intrinsic collisional probability between target and projectile. This code was later expanded and made more versatile providing radiant distribution of the impactors, orbital elements at the moment of impact (our theory cannot predict values of the longitude of the ascending node Ω and mean anomaly l because of the averaging technique used to obtain integrals of motion), impact velocities at infinity and influenced by gravitational focusing.

The code was later rewritten in FORTRAN 90 and was improved for the targets on eccentric orbits. We successfully tested our code and used it in process of writing paper (A,B and E). The most recent version of our code is presented in Appendix A and can be found at `http://sirrah.troja.mff.cuni.cz/~pokorny/Kozai/` . The code is currently used by Gerhard Hahn who is implementing it as a part of a software package for modeling a distribution of NEAs designated for the European Space Agency (ESA). The code was recently used by Alessandro Morbidelli for evaluation of the collisional probabilities between terrestrial planets and artificial population of NEAs (Granvik et al., 2013).

1.6 Conclusions and further work

We presented two extensions of the original works that were using assumptions contradictory to observed behavior of many bodies in the Solar System. Our extensions are valid even for high inclination and high eccentricity orbits of the projectiles. We restricted the orbit of the target to circular coplanar orbit (paper A) and elliptic coplanar orbit (paper B) to obtain purely analytic solution. Such solution is highly efficient because allows us to evaluate the collisional probability between two bodies with an arbitrary precision with almost no costs for computational time. This naturally led us to write a code providing intrinsic collision probability, position of radiants and impact velocities base on our work. This code is written in FORTRAN 77 and 90 (two separate versions) and is available at `http://sirrah.troja.mff.cuni.cz/~pokorny/Kozai/` .

Our approach and code was also successfully tested in a "real-life scenario", a numerical experiment of E-belt population evolution (paper B). We studied a dispersion of the original population by all eight planets in the Solar System starting at the time when all planets reached the current architecture. Using N-body code we recorded impacts of E-belt objects on every planet and directly compared them with predictions of our collision theory. Despite of fact that the investigated scenario incorporated far more complex system than assumed in our theory, the direct comparison showed good performance of our theory and fair improvement in comparison with the original theories.

Many challenging tasks are also ahead of us. A generalization to target orbits with non-zero inclination would prove useful for implication is the Solar System as collisions among objects in the asteroid belt and also in many exotic exoplanetary systems where

some planets reside on inclined orbits. Another improvement would be to adopt a more complex perturbing function $\mathcal{P}$, which would allow us to consider more perturbing bodies and allow the projectile's orbit have close encounters with them. This would improve our estimates e.g., collisions of the long-periodic comets with terrestrial planets.

2. Sporadic meteoroid complex

In this chapter, we review our work on the modeling of the sporadic meteoroid complex (SMC). We will recall crucial physical processes that influence the dynamics of the meteoroids in the Solar System. We focused mainly on a development of steady-state models for various structures in the SMC. At the very end of our research we were fortunate to obtain the whole dataset from Canadian Meteor Orbit Radar (CMOR) that, on the other hand, could not be fully analyzed and described in presented papers. In what follows, we present the whole dataset in some extend, describe observed structures, and also point out the most interesting features. In total, we presented three papers, where each of them is describing one of the most prolific sources of dust particles in the Solar System and their contribution to the meteor flux observed on the Earth.

We would like to thank Margaret and Peter Brown, and other CMOR staff, for providing the data. Their contribution allowed us to understand CMOR observations in a great detail, provided an essential input to our model presented in paper E, and allowed us to explore many interesting phenomena in this thesis.

Papers reviewed in this section:

Paper C: Nesvorný, D., Vokrouhlický, D. **Pokorný, P.**, & Janches, D., 2011, Dynamics of Dust Particles Released from Oort Cloud Comets and Their Contribution to Radar Meteors, *Astrophysical Journal*, 743, 129.
Paper D: Nesvorný, D., Janches, D., Vokrouhlický, D. **Pokorný, P.**, Bottke, W. F., & Jenniskens, P., 2011, Dynamical Model for the Zodiacal Cloud and Sporadic Meteors, *Astrophysical Journal*, 743, 129.
Paper E: **Pokorný, P.**, Vokrouhlický, D. Nesvorný, D., Campbell-Brown, M. D., & Brown, P. G., 2014, Dynamical Model for the Toroidal Sporadic Meteors, *Astrophysical Journal*, 789, 25

2.1 Introduction

The Solar System is a very dusty environment. Every second myriads of small micron sized particles are released from comets, created in cometary and asteroidal breakups and also a small portion of dust comes from the interstellar space. The Earth, passing through this dusty environment, is constantly showered with particles. Shall the dust particle be large enough, its deceleration in the Earth's atmosphere may be visually seen by observers, creating a phenomenon called meteor. The exact threshold of the detectability of the visual meteor is a complex function of its size, composition, atmospheric entry velocity, weather conditions and also sensitivity of a observing system. Modern visual meteor survey like Cameras for Allsky Meteor Surveillance (CAMS; Jenniskens et al., 2011), or Canadian Automated Meteor Observatory (CAMO; Weryk et al., 2013) observing a large portion of the sky are able to detect dust particles with radii $s \gtrsim 5$ mm (valid for the fastest meteors). Smaller dust particles decelerating in the atmosphere are not bright enough to be observed visually, however, during the deceleration they ablate, and thus ionize surrounding air, which makes them visible to powerful radar systems. Radars do not detect the particles directly, but a train of ionized air left behind the dust particle

was found to be a very effective reflector of radio waves, which allows particles with diameters of tens to hundreds micrometers to be detected (Jones et al., 2005). In the past decade, the majority of the radar meteor detections were performed by two different radar systems; Advanced Meteor Orbit Radar (AMOR; Galligan and Baggaley, 2004, 2005), and Canadian Meteor Orbit Radar (CMOR; Jones et al., 2005). Radars have many advantages over the visual observation systems, such as the independence on the weather conditions, ability to observe throughout all day regardless on the position of the Sun, and also the ability to detect much smaller particles down to hundreds or even tens micrometers, which provides an access to much richer sample of data when compared to the observations performed by a visual system in the same period of time. Both visual and radar observations provide a precise determination of the radiant location and velocity of each impacting particle, thus, in other words, provide us a complete set of the Keplerian elements for given particle. Moreover, since these systems are able to record the whole deceleration process of the particle in the atmosphere, we can also obtain information about the mass of the meteor (Verniani, 1973; Pecina and Ceplecha, 1983), which, as we show in the following sections, is an essential piece of information for our modeling efforts.

Decades of analysis of different radar or visual observations distinguished two different components of the Earth's meteoroid complex: (1) particles associated with meteor streams, and (2) particles belonging to a sporadic background. Particles belonging to the meteor streams are concentrated in the interplanetary space and are not dynamically evolved, thus revolve on the similar orbits to their parent body (see, e.g., Fernández, 2005; Jenniskens, 2006; Brown et al., 2008, 2010). These bodies impact Earth's atmosphere at discrete intervals of time that last typically for a few days. Many different techniques for meteor stream recognition were developed during the past decades, mostly comparing the orbital elements of the recorded meteors and excluding the orbits that fall outside a threshold value of similarity (e.g., Southworth and Hawkins, 1963; Jopek et al., 2006), sometimes called a discriminant criteria (D) method. Since these methods compare the orbital elements of the particles, they are used widely for both visual and radar observations. The exact values for threshold values may differ from author to author, which may lead to discovery of a new meteor stream in one dataset, while in the different dataset the same event may not pass the threshold value. The sporadic background is composed of particles that are not associated with any stream. It is generally believed that the sporadic component of the meteoroid complex is actually a dynamically evolved population of originally stream meteoroids, whose orbital elements due to the various dynamical effects became less and less similar to the orbital elements of the parent body. Such dispersion does not allow meteoroids to be distinguished individually among the various sources of the dust particles anymore. However, there must be also some intermediate dynamical state of the particles when they do not belong to the meteor streams due to the higher dispersion of the orbital elements, but, on the other hand, the nodes of the particles are still not randomly distributed, thus creating "semi-sporadic" structures in the meteoroid complex (Brown et al., 2010).

Since meteor showers provide a spectacular show, when hundreds of meteors are observable by a naked eye, many might guess that the majority of the meteor influx is brought by stream meteors. This opinion was proved to be wrong by various projects in both visual (Jones and Brown, 1993) and radar (Campbell-Brown, 2008) observations. In fact, the sporadic meteors dominate the time-integrated flux of meteors at Earth by a factor of ten (Brown et al., 2010).

2.1.1 Observations of sporadic meteoroid complex

Fig. 2.1 shows a radiant distribution map for more than a million meteors observed by CMOR in 2012 where all recognized meteor streams were removed from the dataset. We can clearly distinguish five different concentrations of meteors in the radiant map. Since CMOR is located on the northern hemisphere, its sensitivity for meteors with southern latitudes is much lower than for those with positive latitudes. From the symmetry of the impacts[1], we can also expect that there is another concentration of meteors located at -60 degrees of latitude, which was, indeed, confirmed by independent observations made by AMOR (Galligan and Baggaley, 2004).

We thus find six concentrations in the sporadic meteoroid complex, where the majority of observed meteors belong to: (1) the helion and anti-helion sources (H/AH), (2) the north and south apex sources (NA/SA), and finally (3) the north and south toroidal sources (NT/ST). The exact positions and ranges of the areas defining sources differ from author to author (e.g., Campbell-Brown, 2008; Kero et al., 2012), however, the areas greatly overlap and contain the majority of observed meteors. We define the regions similarly to Campbell-Brown (2008): (1) helion source as the rectangular region with the center at $(\ell, b) = (-60^\circ, 0^\circ)$, with longitudinal width 60° and latitudinal width 90°, (2) anti-helion source is similar to helion, but with center at $(\ell, b) = (60^\circ, 0^\circ)$, (3) north apex source is enclosed in a semicircle with radius 40° and center at $(\ell, b) = (0^\circ, 0^\circ)$, while (4) south apex source is a symmetric counterpart of the north apex with respect to the ecliptic plane, (5) north toroidal region is defined by an ellipse with center at $(\ell, b) = (0^\circ, 55^\circ)$ with semimajor axis equal to 28° and semiminor axis equal to 15°, and (6) south toroidal source is again the symmetric counterpart of the north toroidal source with respect to the ecliptic plane. Here, the longitude ℓ is measured from the apex direction, where the apex of the Earth's motion is at the origin $(\ell, b) = (0^\circ, 0^\circ)$, and the latitude b is measured from the ecliptic plane. All six sources are marked in Fig. 2.2. The main features of each source will be discussed in the following sections, namely the H/AH source in Sec. 2.9, the NA/SA source in Sec. 2.7, and the NT/ST source in Sec. 2.11.

The ground-based observations provide a vast ensemble of data, however, also many satellites and space probes were deployed in the past decades, some of which also contained instruments with an ability to measure various characteristics of the interplanetary dust particles. One of the most comprehensive observations of the terrestrial accretion rate was performed by Long Term Duration Facility (*LDEF*) experiment. Even though the experiment is almost thirty years old (see, e.g, Love and Brownlee, 1993, and references therein), the exact outcome of the experiment is still investigated (Cremonese et al., 2012), and may change in the future. According to Cremonese et al. (2012) the total mass accreted by the Earth is $(7.4 \pm 1.0) \times 10^6$ kg yr^{-1} for asteroidal sources and $(4.2 \pm 0.5) \times 10^6$ kg yr^{-1} for cometary sources. This gives us total mass approximately 15 tons per year, where the majority of mass is brought by particles with diameters around ~ 200 μm.

Meteoroids orbiting in the Solar System also emit an infrared light that can be measured by space probes. The first spacecraft that observed almost the whole sky in mid-infrared (MIR) wavelengths, and became a pioneer of modern infrared astronomy, was the Infrared Astronomical Satellite (*IRAS*; e.g., Sykes et al., 1986). Followed by Cosmic Background Explorer (*COBE*; e.g., Kelsall et al., 1998), Wide-field Infrared Survey Explorer (*WISE*; e.g., Kramer et al., 2012), or *Planck* (Planck Collaboration et al., 2013),

[1] As we show in Sec. 1.3.1, the impacts of the projectiles at the ascending nodes have always positive value of latitude, while the impacts at the descending nodes have negative values of latitude

a large amount of data was collected. Knowledge of the thermal emission in the Solar System allows us to constrain the models for the zodiacal cloud, because we can compare the emission from an artificial model population to the observations from different space satellites (see, e.g., Nesvorný et al., 2006, 2010).

Finally, many different space probes traveled through various regions of the Solar System. Some of them carried instruments, impact detectors, that were able to detect impacts of particles from diameters about 20 μm like e.g. (Pioneer 10 and 11 spacecrafts (Landgraf et al., 2002) down to micron sizes particles observed by New Horizons spacecraft (Poppe et al., 2010). Even though the statistics of such experiments are very low compared to ground-based observations, they provide valuable information about the dust distribution in the vast regions of the Solar System.

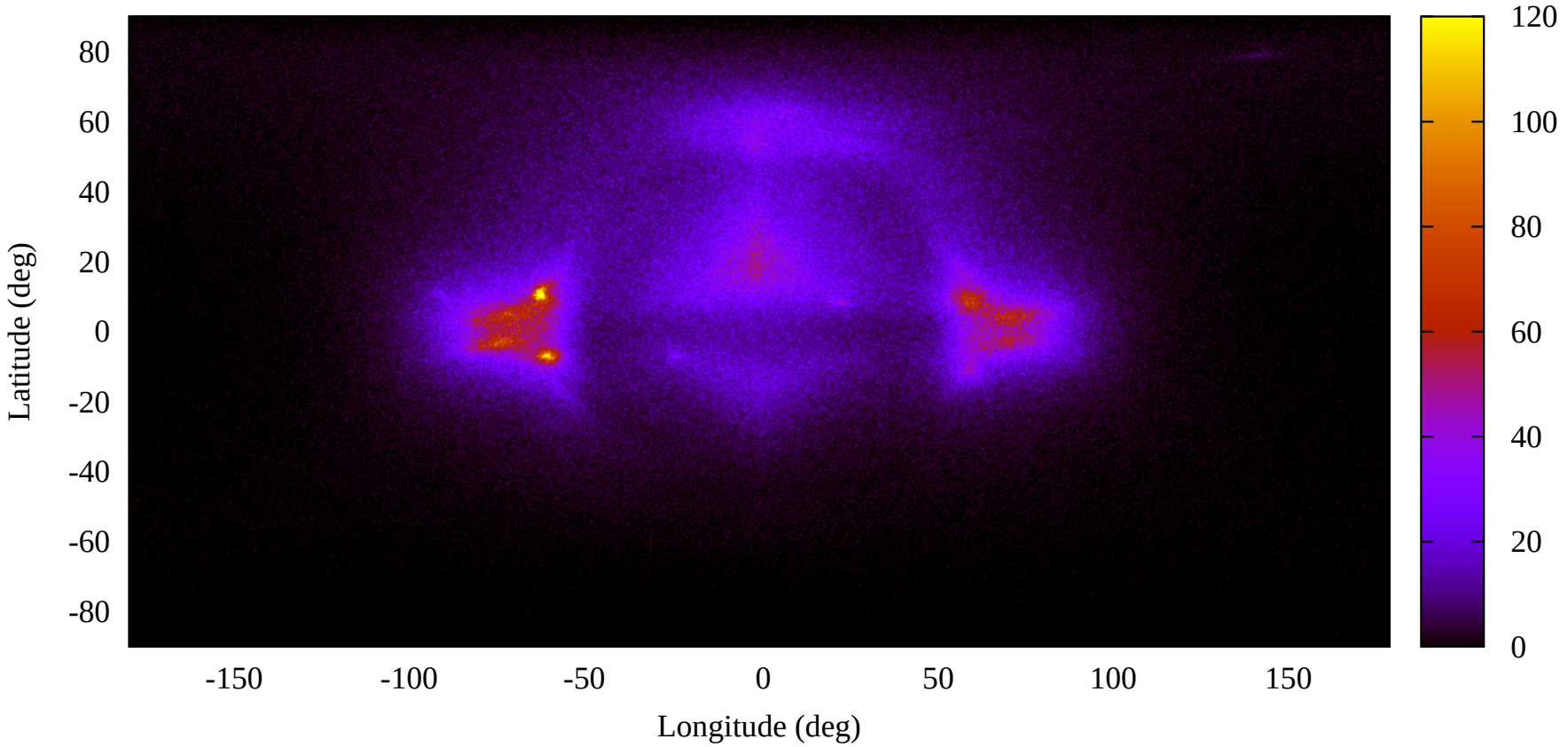

Figure 2.1: Distribution of radiant positions of 1.3 million meteors measured by Canadian Meteor Orbit Radar in 2012. The color range corresponds to the measured flux in $1^\circ \times 1^\circ$ radiant bins. Longitude is measured from the apex direction, where apex is at the origin, and latitude is measured from the ecliptic plane. CMOR is located at 43.3° northern latitude thus is not able to observe meteors coming from souther sky (roughly radiant latitudes $\lesssim -40^\circ$).

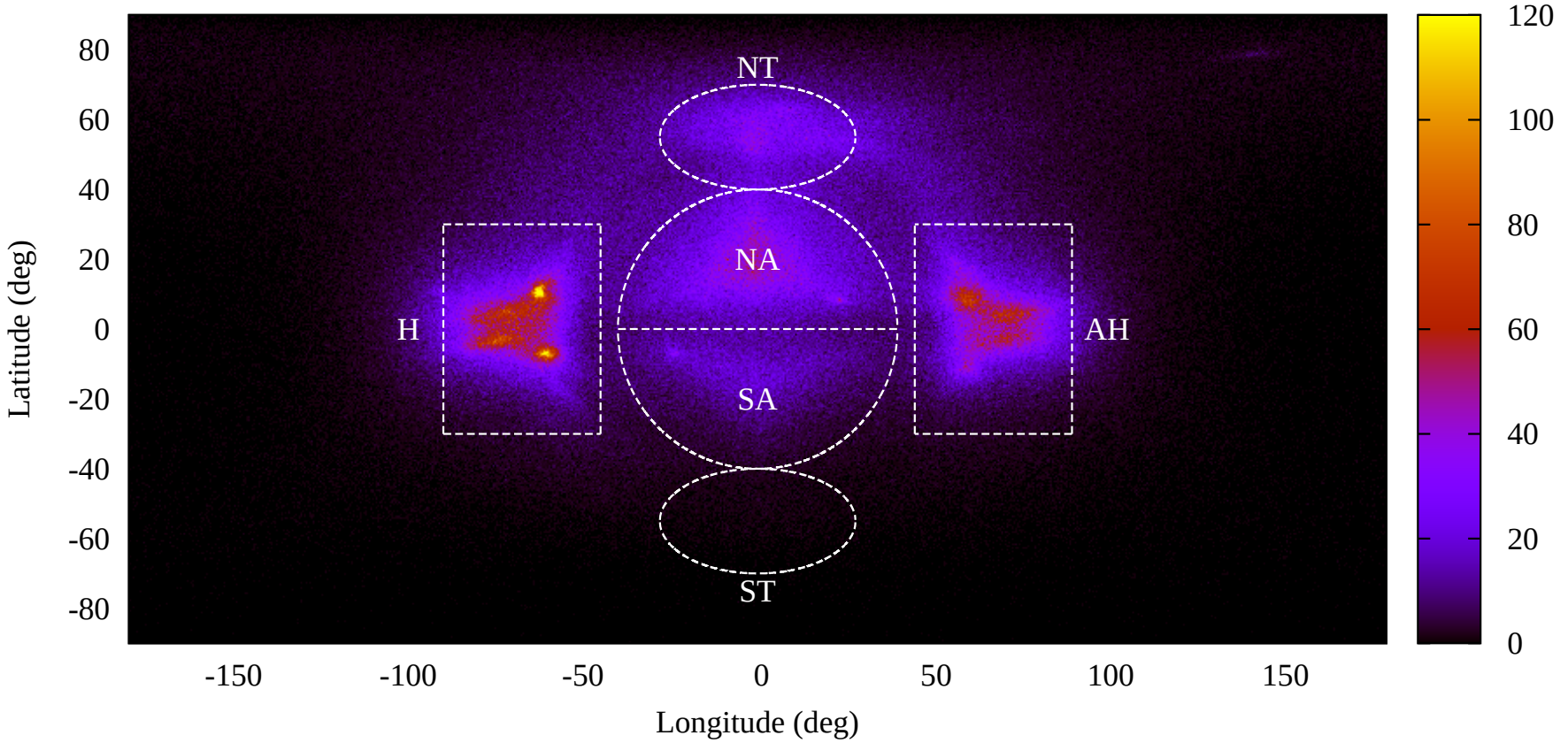

Figure 2.2: The same as in Fig. 2.1, but now with highlighted six recognized sources of the sporadic meteors (areas with white dashed borders), helion/anti-helion (H/AH) source, north/south apex source (NA/SA), and north/south toroidal source. The exact definition of the highlighted areas used throughout this work can be found in the text.

2.1.2 Modeling of sporadic meteoroid complex and motivation

In the previous chapter, we mentioned that the time-integrated flux of visual and radar meteors impacting the Earth is dominated by about a factor ten by sporadic meteors (Jones and Brown, 1993), and that sporadic meteors come mainly from six different radiants. Since the sporadic meteors are not associated with particular streams, they certainly experienced a long dynamical evolution. Once the dust particle is released from a parent body it at once feels effects of gravity of the planets, solar radiative forces, and also collisions with other small bodies in the Solar System (we will discuss these effects in more detail in Sec. 2.2). The dynamical evolution of a dust particle is, thus, a very chaotic process where even a small change in the initial conditions can cause a completely different outcome. The stochastic nature of the problem does not allow an analytical solution and needs a construction of a numerical model based on simulations of thousands of particles of various sizes originating in different parent bodies.

The first models were usually composed of simple sets of empirical equations describing the up-to-date measurements, and used only very simple assumptions for speed of meteors or their parent bodies (see, e.g., McNamara et al., 2004, for a review of NASA models). Divine (1993) model was a great improvement of the modeling efforts of the dust environment in the Solar System. It presented five populations of interplanetary and was supported by various data sources from ground-based telescopes and space probes. However, neither Divine's model, nor models of NASA (McNamara et al., 2004), and ESA (Dikarev et al., 2004), could precisely explain radiant and velocity distributions of observed sporadic meteors.

Wiegert et al. (2009) presented a study with a challenging objective to explain all six observed sources of the sporadic meteors. Authors assumed the known populations of asteroids and comets as the source regions of meteoroids and made a few assumptions (e.g., they magnified Earth's radius to 0.1 au in order to get better impact statistics) to make their model simpler and less time demanding. Their results were interesting, however, the general conclusion from this model contained several drawbacks. Authors did not perform any kind of fits, thus the agreement between model and observations is only qualitative, which is the most apparent for the toroidal concentration (Fig. 4 in Wiegert et al., 2009). Authors also conclude that a single body may dominate the contribution of the dust particles for a particular radiant region. This led Wiegert et al. (2009) to a conclusion that the parent bodies for the north toroidal source were several near-Earth asteroids (NEAs), which would have, however, pushed their dust ejection activity well above any observed values.

To summarize the situation around 2010 we may say that the radar observations recorded millions of meteors with accurate orbital elements and heliocentric velocities. Yet, the existing models were not able to accurately explain observed structures and orbital element distributions. Motivated by the considerable amount of precise data and the complexity of the problem we started to investigate dynamics of particles coming from various prolific sources of dust in the Solar System, their contribution to the sporadic complex measured at the Earth, and validity of our models keeping in mind results of Wiegert et al. (2009).

2.2 Dynamics of the dust particles in the Solar System

The dynamics of the small meteoroids is dominated by two different types of forces: the gravitational effects of all massive bodies in the Solar System, and the radiative forces caused by the Sun. In the following text, we explore the most dominant effects on the dynamics of the dust particles caused by radiative forces, while the direct effects of the gravitational attraction are not discussed in detail. The reason is simple. In our papers we study motion of dust particles in a very broad region of the Solar System which extents from the Sun up to the Oort cloud, a region thousands astronomical units far from the Sun. Such vast region is interwoven with mean motion resonances, secular resonances, particles may undergo close encounters with planets, and also in many cases dust particles experience influence of secular mechanisms like Kozai oscillations. Even a brief description of all known phenomena would fill several tens of pages, thus we refer to a few publications to provide a basic overview of the topic (Murray and Dermott, 1999; Morbidelli, 2002; Bertotti et al., 2003). However, in our models we take into account effects of gravitation forces from massive bodies. We use a standard numerical package SWIFT (Levison and Duncan, 1994) that is able to accurately simulate dynamical evolution of massive bodies and test particles on very long timescales (see also Sec. 2.4).

On the other hand, radiative forces originate only from one body, the Sun, thus we may expect that the magnitude of their effects follow a specific power-law, or even such forces could have the same effect regardless on the heliocentric distance of the body. A standard reference for an introduction to radiation forces on small particles in the Solar System is the work of Burns et al. (1979). We will introduce a notation used in this work, follow its approach, discuss several assumptions used in our numerical models based on our findings, and also add a few interesting consequences not discussed in Burns et al. (1979).

Assume a small spherical particle of a geometrical cross-section A that absorbs light incident on an area $AQ_{\rm abs}$ and scatters an amount of light that is equivalent to light incident on an area $AQ_{\rm sca}$. We thus define absorption $Q_{\rm abs}$ and scattering $Q_{\rm sca}$ coefficients which correspond to the fraction of amount of energy that is absorbed or scattered, respectively. For a given particle we define the radiation pressure coefficient

$$Q_{\rm pr} = Q_{\rm abs} + Q_{\rm sca}\left(1 - \langle\cos\alpha\rangle\right) \ , \tag{2.1}$$

where $\langle\cos\alpha\rangle$ is an anisotropy parameter that can be calculated from the Mie theory (see, e.g., Burns et al., 1979; Horvath, 2009, for a review and historical background). In our models and simulations we, for simplicity, assume $Q_{\rm pr} = 1$, which is equivalent to a perfectly absorbing particle, similarly to the case originally considered by Robertson (1937). Such particle feels a force from the solar photon radiation that can be viewed as a composition of two different parts: (1) a *radiation pressure* caused by an initial incidence of the dust particle by a momentum of the photon beam, and (2) a *Poynting-Robertson drag* caused by a reradiation of the incident energy. If we denote S as the integrated flux density (erg cm^2 s^{-1}), the total amount of incident energy on the particle per second is SA. For a moving particle in the heliocentric reference frame with velocity $\mathbf{v}$ relative to the Sun, we must make a correction for the limited speed of the light c –Doppler effect– that reads

$$S' = S\left(1 - \frac{\mathbf{v}\cdot\hat{\mathbf{S}}}{c}\right) \ , \tag{2.2}$$

where S' is a corrected integrated flux density for a moving particle and $\hat{\mathbf{S}}$ is a unit vector in the direction of the incident beam. The force F_1 equal to a momentum removed per second from the incident beam of photons is

$$F_1 = Q_{\rm pr}\frac{S'A}{c}\hat{\mathbf{S}}. \tag{2.3}$$

Now, the absorbed energy flux is continuously reradiated by the particle. We assume the reradiation process to be isotropic, because we are dealing with very small particles (centimeters in size at maximum), and thus we may consider them effectively isothermal. On the other hand, we also assume, that our theory corresponds to the geometrical optics limit, where the particle size is much larger than the incident-light wavelength. In the reference frame moving with the particle there is no net force, since the reradiation is isotropic. However, in the heliocentric reference frame the particle has velocity $\mathbf{v}$, and thus the momentum flux from the particle is

$$F_2 = -Q_{\rm pr}\frac{S'A}{c^2}\mathbf{v}. \tag{2.4}$$

The mass of the particle is conserved, thus, in fact, the particle losses its momentum and is decelerated by force F_2. The net force caused by radiation $F_{\rm rad}$ is then the vectorial sum of F_1 and F_2

$$F_{\rm rad} = Q_{\rm pr}\frac{S'A}{c^2}\left(c\hat{\mathbf{S}} - \mathbf{v}\right) = Q_{\rm pr}\frac{SA}{c}\left[\left(1 - \frac{\mathbf{v}\cdot\hat{\mathbf{S}}}{c}\right)\hat{\mathbf{S}} - \frac{\mathbf{v}}{c} + \frac{(\mathbf{v}\cdot\hat{\mathbf{S}})\mathbf{v}}{c^2}\right], \tag{2.5}$$

where the first term is the *radiation pressure* and the remaining terms are usually called *Poynting-Robertson drag*. Since the maximum velocities of the bodies in the Solar System are smaller than $\lesssim 100$ km s^{-1}, the last term in Eq. (2.5) is usually not considered.

The most of the literature finds it useful to define a ratio β between the gravitational attraction $F_{\rm grav}$ of the Sun with mass $M_\odot$ at heliocentric distance r upon a spherical particle of radius s and density ρ that reads

$$F_{\rm grav} = \frac{4\pi s^3\rho}{3}\frac{\mathcal{G}M_\odot}{r^2}, \tag{2.6}$$

where $\mathcal{G}$ gravitational constant, and the magnitude of the *radiation pressure* force $F_{\rm r}$ defined by Eq. (2.5) as

$$F_{\rm r} = Q_{\rm pr}\frac{LA}{4\pi r^2 c}, \tag{2.7}$$

where we used $S = L/4\pi r^2$ for the radiation flux density at heliocentric distance r generated by the Sun with the solar luminosity L. Then the parameter β reads

$$\beta = \frac{F_{\rm r}}{F_{\rm grav}} = \frac{3L}{16\pi\mathcal{G}M_\odot c}\frac{Q_{\rm pr}}{\rho s} = 5.7\times10^{-5}\frac{Q_{\rm pr}}{\rho s}, \tag{2.8}$$

where ρ, and s, are in units g cm^{-3}, and cm, respectively. With the parameter β the total net force caused by solar radiation upon the dust particle may be written as

$$F_{\rm rad} = \frac{\mathcal{G}M_\odot m\beta}{r^2}\left[\left(1 - \frac{\mathbf{v}\cdot\hat{\mathbf{S}}}{c}\right)\hat{\mathbf{S}} - \frac{\mathbf{v}}{c} + \frac{(\mathbf{v}\cdot\hat{\mathbf{S}})\mathbf{v}}{c^2}\right], \tag{2.9}$$

where m is the mass of the dust particle. From Eq. (2.9) we see that the *radiation pressure* directly opposes a part of the gravitational attraction of the Sun, which causes the dust particle to behave as if it were orbiting the center of gravity with mass of $(1-\beta)M_\odot$. In our simulations, we assume particles to be composed of silicates with mean density $\rho = 2.0$ g cm^{-3}, thus we have only one free parameter in determination of β from Eq. (2.8). If we are to compare our simulations with other works where different values of ρ are used, we would simply recalibrate the size of particles without losing the validity of our results.

The *radiation pressure* and *Poynting-Robertson drag* have very interesting consequences on the dynamical behavior of the dust particles. For particles with $\beta > 1$ the radiation forces are strong enough to push such bodies out of the Solar System on hyperbolic orbits. However, this occurs only for very small particles with diameters $D = 2s < 0.5$ μm. These bodies called β-meteoroids are observed by different space probes (Poppe et al., 2010), but are too small to be observed on the Earth by either radars or ground-based optical telescopes. Larger particles, with $\beta < 1$, feel lower gravity from the Sun than their parent body, for which we have $\beta = 0$, and thus their orbital elements might change at the time of ejection from the parent body.

Let us consider a parent body at heliocentric distance r moving along an orbit with the semimajor axis a, the eccentricity e and the inclination I. The heliocentric velocity $V_{\rm hel}$ of the parent body then reads

$$V_{\rm hel}^2 = \mathcal{G}M_\odot \left(\frac{2}{r} - \frac{1}{a} \right) . \tag{2.10}$$

A small dust particle released from the parent body with a negligible ejection speed at heliocentric distance r will instantly feel the effects caused by *radiation pressure*. Since we neglected the ejection speed, the heliocentric velocity of the dust particle will be the same as that of the parent body, however, with non-zero β we get

$$V_{\rm hel}^2 = \mathcal{G}(1-\beta)M_\odot \left(\frac{2}{r} - \frac{1}{a'} \right) , \tag{2.11}$$

which gives us a solution for the new semimajor axis a' of the dust particle after ejection

$$a' = a \frac{r(1-\beta)}{r - 2\beta a} . \tag{2.12}$$

Since the heliocentric position $\mathbf{r}_{\rm hel}$ and velocity vectors $\mathbf{v}_{\rm hel}$ are conserved upon ejection of the particle, the specific relative angular momentum $\mathcal{H}$ of the dust particle equal to the angular momentum of the parent body

$$\mathcal{H} = \mathbf{r} \times m\mathbf{v} = m\sqrt{\mathcal{G}M_\odot a(1-e^2)} = m\sqrt{\mathcal{G}(1-\beta)M_\odot a'(1-e'^2)} . \tag{2.13}$$

Combining Eqs. (2.12) and (2.13), we obtain the solution for the new value of eccentricity e' after the ejection of the dust particle

$$e' = \sqrt{1 - \frac{(1-e^2)(r-2\beta a)}{r(1-\beta)^2}} . \tag{2.14}$$

From Eqs. (2.12) and (2.14) we see that if $\beta > r/2a$ then the orbit of the ejected particle becomes unbound and the particle will escape from the Solar System. This factor

becomes more important for parent bodies with very large semimajor axes such as Oort Cloud Comets having $a \sim 1000$ au, thus even quite large particles with diameters of tens or hundreds of micrometers may be released on hyperbolic orbits, if the ejection occurs very close to the Sun, even though β is a small number. Finally, there is no change in inclination upon the release of the dust particle from the body, because the radiation from the Sun is emitted radially, and also since $\mathbf{r}_{\rm hel}$ and $\mathbf{v}_{\rm hel}$ are conserved, the Z-component of the specific relative angular momentum $\mathcal{H}_Z$ is also conserved, and thus

$$\mathcal{H}_Z = \mathcal{H}\cos I = \mathcal{H}\cos I' \Rightarrow I = I' \ . \tag{2.15}$$

Now, we will investigate the dynamical consequences of the radiative forces on the orbital elements, averaged over one orbital period. We describe the results presented by Wyatt and Whipple (1950) and Burns et al. (1979), that were originally obtained by Robertson (1937). The secular change of the semimajor axis due to the *Poynting-Robertson drag* reads

$$\frac{da}{dt} = -\frac{\mathcal{N}}{a}\frac{(2+3e^2)}{(1-e^2)^{3/2}} \ , \tag{2.16}$$

while the change of the eccentricity is

$$\frac{de}{dt} = -\frac{5}{2}\frac{\mathcal{N}}{a^2}\frac{e}{(1-e^2)^{1/2}} \ , \tag{2.17}$$

where $\mathcal{N} = 2.53 \times 10^{11} Q_{\rm pr}/\rho s = 4.44 \times 10^{15}\beta$, with a, ρ, and s in units cm, g cm^{-3}, and cm, respectively. There is no secular change in the inclination I, thus we may formally state that

$$\frac{dI}{dt} = 0 \ . \tag{2.18}$$

For a dust particle with $e = 0$ we can simply integrate Eq. (2.16) and get characteristic orbital decay time $t_{\rm PR}$ for a particle decaying from heliocentric distance R_1 to distance R_2

$$t_{\rm PR} = \frac{400}{\beta}(R_1^2 - R_2^2) \ , \tag{2.19}$$

where the heliocentric distances R_1 and R_2 are in astronomical units and $t_{\rm PR}$ is in years. The determination of the characteristic decay times $t_{\rm PR}$ for the non-zero eccentricity is not simple, but it is obtainable by the numerical integration of Eqs. (2.16) and (2.17). Figs. 2.3 and 2.4 show $t_{\rm PR}$ for a wide range of initial semimajor axes a and eccentricities e at the time of ejection for the dust particle with radius $s = 100$ μm and density $\rho = 2$ g cm^{-3}. Dust particles were tracked until their heliocentric distance r reached the surface of the Sun. We see that higher initial eccentricity greatly reduces the decay time, where for $e \sim 0.9$ the particles have one order of magnitude shorter dynamical lifetimes than the particles with initially zero eccentricity. This effect is very important for particles released from comets that are usually observed on very eccentric orbits. We also have to take into account the effect of radiation pressure that increases e of the dust particle upon its ejection from the comet as described by Eq. (2.14).

We should not neglect an effect of the solar wind that influences the dynamics of the dust particles in the similar manner as the radiative forces from the Sun. According to Mukai and Yamamoto (1982), the direct effect of the solar wind in the radial direction is not negligible only for very small particles with $s < 0.1$ μm, when compared to the magnitude of the radiation pressure force. However, the transverse part of the radiation

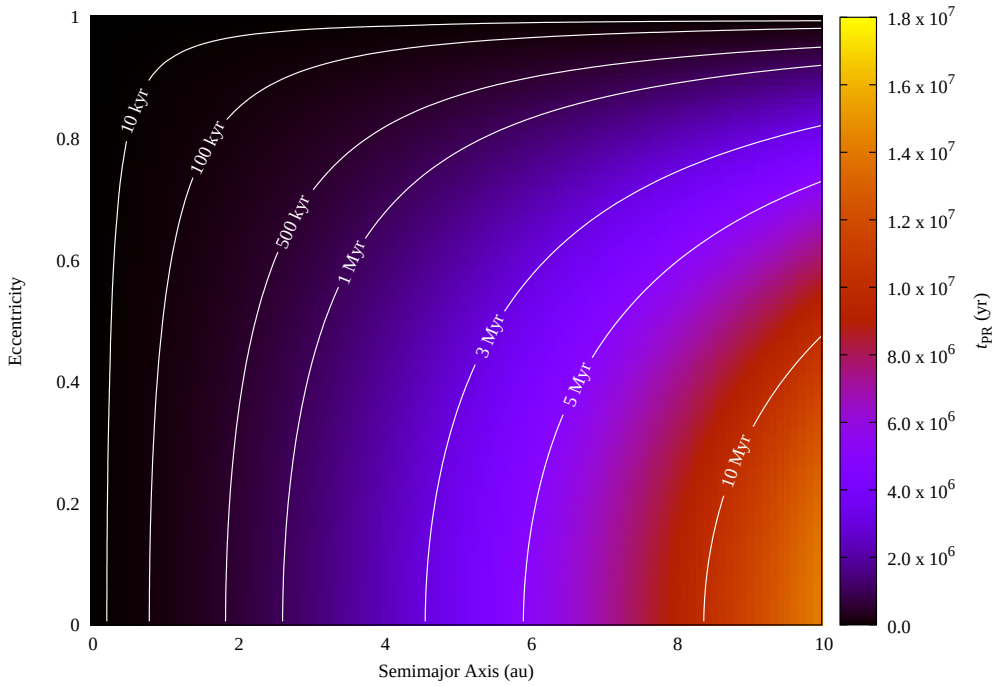

Figure 2.3: Values of characteristic decay times t_{PR} (color range) for particles with radius $s = 100$ μm and density $\rho = 2$ g cm^{-3} released with different initial orbital elements a and e. The orbital elements of the particles were tracked until the dust particle reached the heliocentric distance $r = R_{\odot}$, where $R_{\odot} = 700,000$ km is the approximate radius of the Sun. White lines represent isolines of the same value of the characteristic decay time t_{PR}.

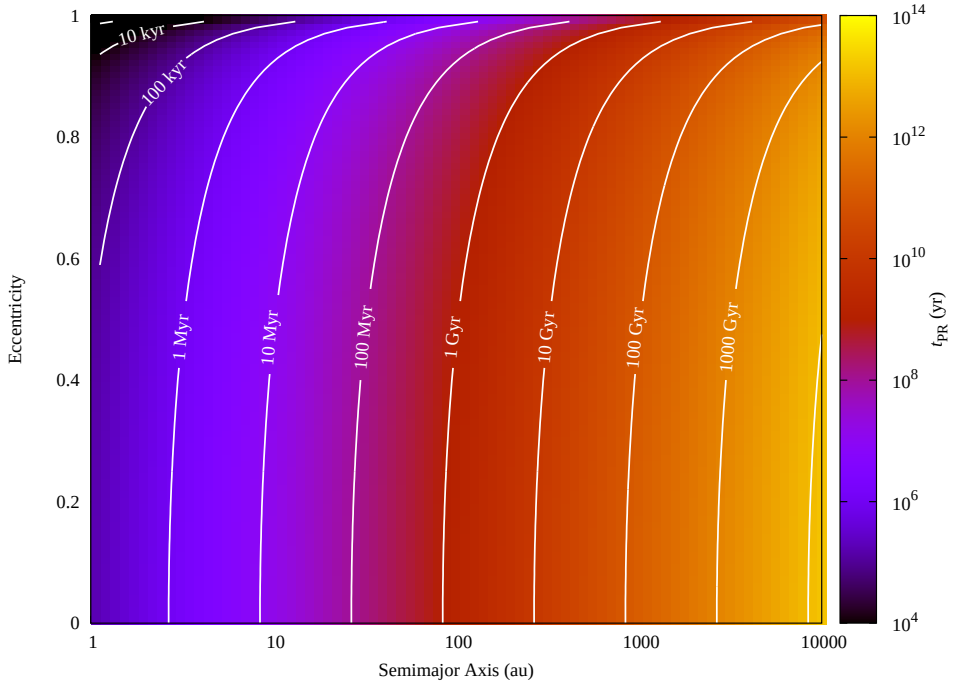

Figure 2.4: The same as in Fig. 2.3, however, now for range of semimajor axes a from 1 au up to 10, 000 au. We use logarithmic scale for the semimajor axis a and the characteristic decay time t_{PR}. Even though the parameter β is constant, regardless to heliocentric distance r of the dust particle, T_{PR} easily acquires extreme values for dust particles with $a > 100$ au.

forces, the *Poynting-Robertson drag*, is affected by the solar wind more effectively. In our simulations we use a mean value of 30% increase of the magnitude of the Poynting-Robertson drag, which is in accordance with calculations of Mukai and Yamamoto (1982) that for micron to centimeter sized bodies acquired 40% increase for prograde magnetite particles and 20% increase for retrograde magnetite particles. Again, such parameter is transferable between different simulations by changing the size of the dust particles.

In previous paragraphs we omitted several other dynamical effects caused by radiative forces that are important for larger bodies like Yarkovsky effect or YORP effect (see e.g., Burns et al., 1979; Bottke et al., 2006, for excellent review of the problem), and also effects that dominate in the close proximity of the Solar surface like differential Doppler effect (Burns et al., 1979). These effects influence the dynamics of the dust particles we study only in a negligible way.

2.3 Collisional lifetimes - theory

Collisions between dust particles and other bodies in the Solar System decrease the lifetime of the dust particles, that may be very short, as we learned in the previous section. On the other hand, dynamical lifetimes of larger particles may exceed billion years, thus there must exist a mechanism that disrupts larger, dynamically stable, particles, because the zodiacal cloud is dominated by particles with diameters $D \sim 10 - 100$ μm (Reach et al., 2003). If we want to study the evolution of large populations of dust particles in the Solar System, it is crucial to know, what the collisional lifetimes τ_{coll} of population members are. The dynamical lifetime can be much longer than the collisional lifetime τ_{coll} of the dust particles, and thus even though theoretically the particles would reach the proximity of the Sun due to the radiative forces in finite time, in reality mutual collisions can break them apart even very close to their parent bodies.

Most works today use two different approaches for an evaluation of the collisional lifetime of the small bodies in the Solar System. Model from Grün et al. (1985) gives meteoroid flux and collisional lifetimes for particles with different masses at heliocentric distance 1 au, where the results are based on various observations from different spacecraft and Earth-based detectors. If we set a radial dependence of the meteoroid flux in the Solar System, the knowledge of the collisional lifetimes at 1 au allows us to evaluate the collisional lifetime for every particle on an arbitrary orbit (see Eqs. (16)–(19) in Grün et al., 1985). We adopted Grün's model in papers C and D (see, Nesvorný et al., 2011b, for a more detailed description). Since this model is based on more than twenty years old measurements, and more recent measurements indicate that fluxes used in Grün et al. (1985) are higher than more recent values, we introduced two free parameters that shift the collisional model in mass of the particles and the magnitude of the flux. These two parameters allowed us to understand the direct effects of collisional lifetimes and supported our hypothesis that the original collisional lifetimes are much shorter than dust particles need for their evolution from the parent bodies to the Earth and to match the observational constrains.

The second model, published by Steel, Baggaley, and Elford (Steel and Baggaley, 1985; Steel, 1985; Steel and Elford, 1986), uses a slightly different approach. Instead of evaluating the collisional lifetime at certain heliocentric distance $\overline{R}$ it uses the collisional frequency evaluation method developed by Kessler (1981), tracks every particle along its orbit, and compute its collisional probability with the dust environment. Contrary to Grün's approach, it also take into account the inclination I of the studied particle, that

may be an important factor for highly inclined dust particles.

Now, we will briefly discuss a method used in paper E based on Steel's and Elford's method (Steel and Elford, 1986). Let us assume a simple model that the particles we study orbit inside a dust cloud (zodiacal cloud in the Solar System) and represent only a negligible fraction of the total amount of dust in the dust cloud, thus we omit can omit mutual collisions among studied particles. A structure of the dust cloud can be very complex, however, since our goal is to study large populations of dust particles, we use a simpler model to decrease computational demands of our model. Supported by various spacecraft measurements (e.g., Leinert et al., 1981; Mukai and Giese, 1984) we adopt the radial spatial density of the dust cloud proportional to $\overline{R}^{\,-1.3}$. Furthermore, we assume that the cloud as a doughnut-shaped structure with the mean inclination $i_{\rm ZC}$ and eccentricity $e_{\rm ZC}$. Then, we may assume that the spatial density varies with a latitude $\overline{\beta}$ with respect to the cloud as $(1-\sin\overline{\beta})$. Our simple model thus allows us to obtain spatial density $S_{\rm z}$ of the dust cloud at arbitrary position in the Solar System

$$S_{\rm z}(\overline{R},\overline{\beta}) = S_{\rm 1au}(1-\sin\overline{\beta})\overline{R}^{\,-1.3}\ , \tag{2.20}$$

where $S_{\rm 1au}$ represents the reference spatial density at 1 au. $S_{\rm 1au}$ should not be considered constant for different sizes of the dust particles, but rather as a function of the meteoroid radius. Since the mutual velocity of the dust grains easily exceeds 10 km s^{-1}, we expect that the meteoroids can be disrupted by much smaller particles. We adopt a radius ratio of 30 (see, Steel and Elford, 1986, and references therein), which we assume, for simplicity, to be valid for meteoroids of all sizes and collisions with various impact speeds. Our assumption thus means that a meteoroid with diameter $D = 3$ mm is collisionally destroyed by a particle with $D \geq 100$ μm, where collisions with smaller particles are omitted.

Table 2.3 shows the reference spatial densities at 1 au $S_{\rm 1au}$ for all particles assumed in our model adopted from Cremonese et al. (2012), where we assumed that all particles have the mean density $\rho = 2$ g cm^{-3}. We evaluate $S_{\rm 1au}$ as a sum of spatial density of asteroidal dust particles $S_{\rm 1au_{ast}}$ and cometary dust particles $S_{\rm 1au_{ast}}$ at 1 au, where the mean impact velocity for is 18.6 km s^{-1}, and 29.0 km s^{-1}, for asteroids, and comets, respectively.

Using the collision probability evaluation based on Kessler (1981), we proceed to the evaluation of probability that the meteoroid collides with a dust cloud with spatial density defined by Eq. (2.20). The meteoroid passes through the dust cloud on an elliptic orbit with constant orbital elements $a_{\rm m}$,$e_{\rm m}$,$I_{\rm m}$,$\omega_{\rm m}$; the remaining orbital elements may be omitted because of the symmetry of the problem. We divide the volume of space where the collisions can take place into small volume elements ΔU. In each of these volume elements we examine the collisions separately. Since the gravitational focusing in this situation is negligible, and also the size of the impactors is negligible in comparison with the size of the meteoroids, we assume the collision cross-section $\sigma = \pi D^2/4$. We recall, that for collisions of larger bodies such as asteroid-planet collisions, the collisional cross-section must be treated more carefully, where the gravitational focusing, and also radii of both bodies are taken into account (Öpik, 1951).

Now, assume that both particles in the dust cloud and meteoroid are moving along their orbits, then the collisional rate $P_{\Delta U}$ in the volume element will be

$$P_{\Delta U} = S_{\rm z}S_{\rm m}V\sigma\Delta U = \frac{\pi D^2}{4}S_{\rm z}S_{\rm m}V\Delta U\ , \tag{2.21}$$

D_m [μm]	$S_{1\mathrm{au}_\mathrm{ast}}$ [AU^{-3}]	$S_{1\mathrm{au}_\mathrm{com}}$ [AU^{-3}]	$S_{1\mathrm{au}}$ [AU^{-3}]
100	3.67×10^{24}	1.93×10^{24}	5.60×10^{24}
200	1.42×10^{24}	8.03×10^{23}	2.22×10^{24}
400	6.35×10^{23}	3.14×10^{23}	9.49×10^{23}
600	3.63×10^{23}	1.79×10^{23}	5.42×10^{23}
800	2.30×10^{23}	1.28×10^{23}	3.59×10^{23}
1000	1.62×10^{23}	7.08×10^{22}	2.33×10^{23}
1500	8.28×10^{22}	3.42×10^{22}	1.17×10^{23}
2000	4.79×10^{22}	2.05×10^{22}	6.84×10^{22}
3000	1.88×10^{22}	7.62×10^{21}	2.64×10^{22}
4000	8.17×10^{21}	2.71×10^{21}	1.09×10^{22}

Table 2.1: Reference spatial densities for different diameters D_m of the meteoroid at 1 au based on measurements of *LDEF* where new theory of the impact evaluation was used (Cremonese et al., 2012). The total spatial density of the dust cloud $S_{1\mathrm{au}}$ is a sum of the asteroidal $S_{1\mathrm{au}_\mathrm{ast}}$ and cometary contribution $S_{1\mathrm{au}_\mathrm{com}}$.

where S_m is the spatial density of the meteoroid in the particular volume element ΔU, and V is the relative collisional velocity. The exact derivation of S_m and V is obtained directly from Kessler's theory (Kessler, 1981) and can be found e.g, in Steel and Baggaley (1985). The total collisional probability between the dust cloud and the meteoroid is the integral of $P_{\Delta U}$ over the whole volume shared by both objects

$$P = \int_\mathrm{volume} \frac{\pi D^2}{4} S_\mathrm{z} S_\mathrm{m} V dU \ , \tag{2.22}$$

where $dU = 2\pi R^2 \cos\beta dR d\beta$. However, for the needs of the numerical solution of P we may assume, that for a given volume element ΔU the spatial densities $S_\mathrm{z}, S_\mathrm{m}$, and the velocity V remain almost constant, thus we can evaluate P as a sum of mean values of given variables in every volume element

$$P = \sum_j \frac{\pi D^2}{4} \overline{S_{\mathrm{z}j}} \ \overline{S_{\mathrm{m}j}} V_j \Delta U_j \ , \tag{2.23}$$

where the mean values for every element are denoted by bars, and $\Delta U = 2\pi \overline{R_j^2} \cos\overline{\beta_j} \Delta R \Delta\beta$. The position in orbit of the meteoroid with fixed orbital elements is, however, fully described by its true anomaly f_m, and thus we can transform the two-dimensional integration in dU to the one-dimensional integration in df_m

$$P = \pi (D/2)^2 S_{1\mathrm{au}} \int_0^{2\pi} S_\mathrm{m} (1 - \sin\beta) R^{-1.3} V 2\pi R^2 \cos\beta \delta R^\star \delta\beta^\star df_\mathrm{m} \ , \tag{2.24}$$

$$\delta R^\star = \left| \frac{R^2 e_\mathrm{m} \sin f_\mathrm{m}}{a_\mathrm{m} \eta_\mathrm{m}^2} \right| \ , \tag{2.25}$$

$$\delta\beta^\star = \left| \frac{\cos(\omega_\mathrm{m} + f_\mathrm{m}) \sin I_\mathrm{m}}{\cos\beta} \right| \ . \tag{2.26}$$

where $\eta_\mathrm{m} = \sqrt{1 - e_\mathrm{m}^2}$. The collisional lifetime τ_coll of the meteoroid passing through the dust cloud is then given by

$$\tau_\mathrm{coll} = 1/P \ . \tag{2.27}$$

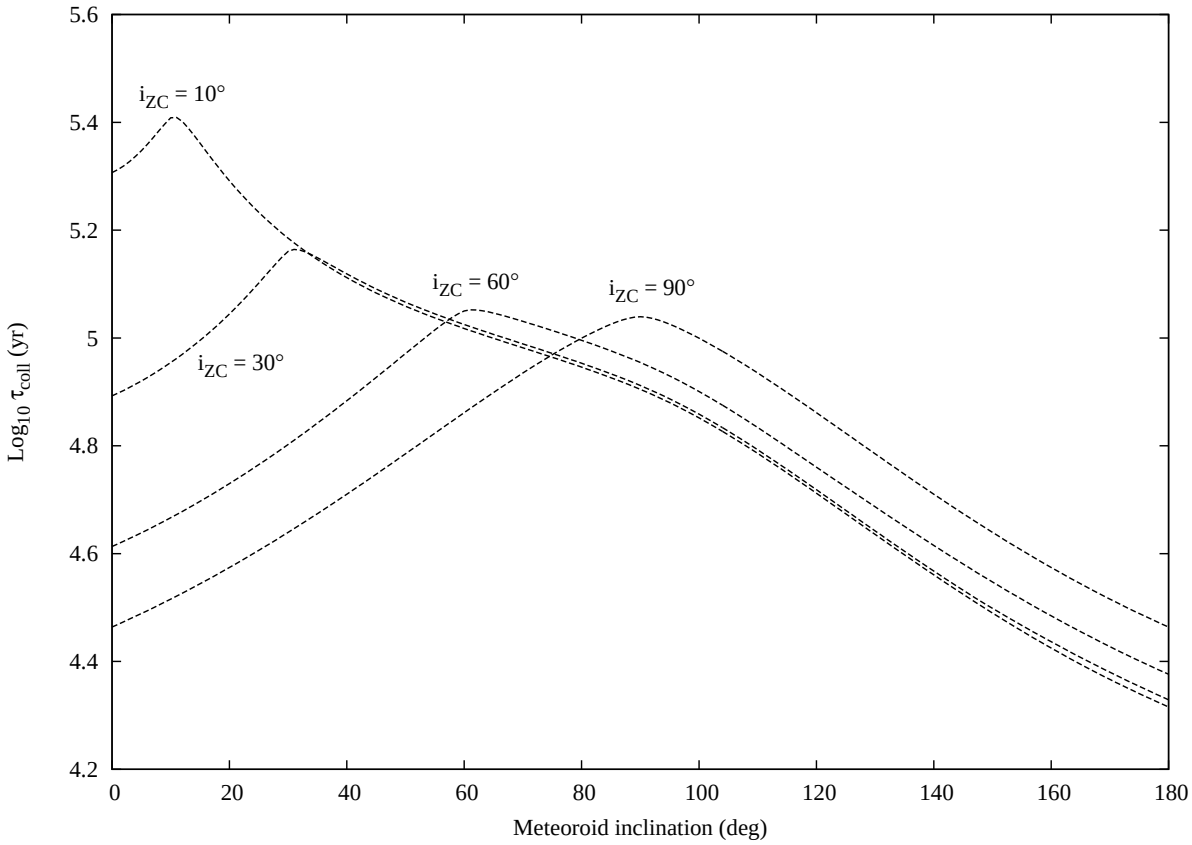

Figure 2.5: The dependence of the collisional lifetime $\tau_{\rm coll}$ on inclination of meteoroid $I_{\rm m}$ for different values of inclinations of the zodiacal dust $I_{\rm ZC}$. All curves are represented by a meteoroid with $a_{\rm m} = 1$ AU, $e_{\rm m} = 0.1$ and $\omega_{\rm m} = 0$ all particles of the dust cloud are assumed to be on circular orbits. The diameter of the meteoroid is $D_{\rm m} = 2000$ μm.

Even though we used several simplifications in our model, the exact specification of the dust cloud through its mean inclination $i_{\rm ZC}$ and eccentricity $e_{\rm ZC}$ remains unknown. Fig. 2.5 shows the dependence of the collisional lifetime $\tau_{\rm coll}$ for different values of meteoroid orbit and dust cloud inclinations. The mean eccentricity of the dust cloud is assumed to be zero, since due to the Poynting-Robertson drag the eccentricities of the dust particles in the cloud are quickly decreased, and thus we may assume that all particles in the dust cloud have circular orbits. The test meteoroid has following orbital elements: $a_{\rm m} = 1.0$ au, $e_{\rm m} = 0.1$, $\omega_{\rm m} = 0°$, with diameter $D_{\rm m} = 2000$ μm, which are the same values as in Steel and Elford (1986). We assumed four different values of $I_{\rm ZC} = 10°, 30°, 60°$ and $90°$. When the inclination of meteoroid is equal to inclination of the dust cloud the collisional lifetime is highest because the relative velocity V is minimal. We also see, that the retrograde orbits are removed from the system much faster, than the prograde ones. In paper E we use $I_{\rm ZC} = 30°$ since it is the observed mean inclination in the zodiacal cloud in the Solar System (Leinert et al., 1983).

The dependence of $\tau_{\rm coll}$ on different values of the inclination $I_{\rm m}$ and the eccentricity $e_{\rm m}$ of the meteoroid is shown in Fig. 2.6. The semimajor axis $a_{\rm m} = 1$ au and argument of pericenter $\omega_{\rm m} = 0°$ are fixed, and the mean inclination of the dust cloud is $i_{\rm ZC} = 30°$. The effect of the meteoroids eccentricity $e_{\rm m}$ is evident, the collisional lifetime $\tau_{\rm coll}$ decreases

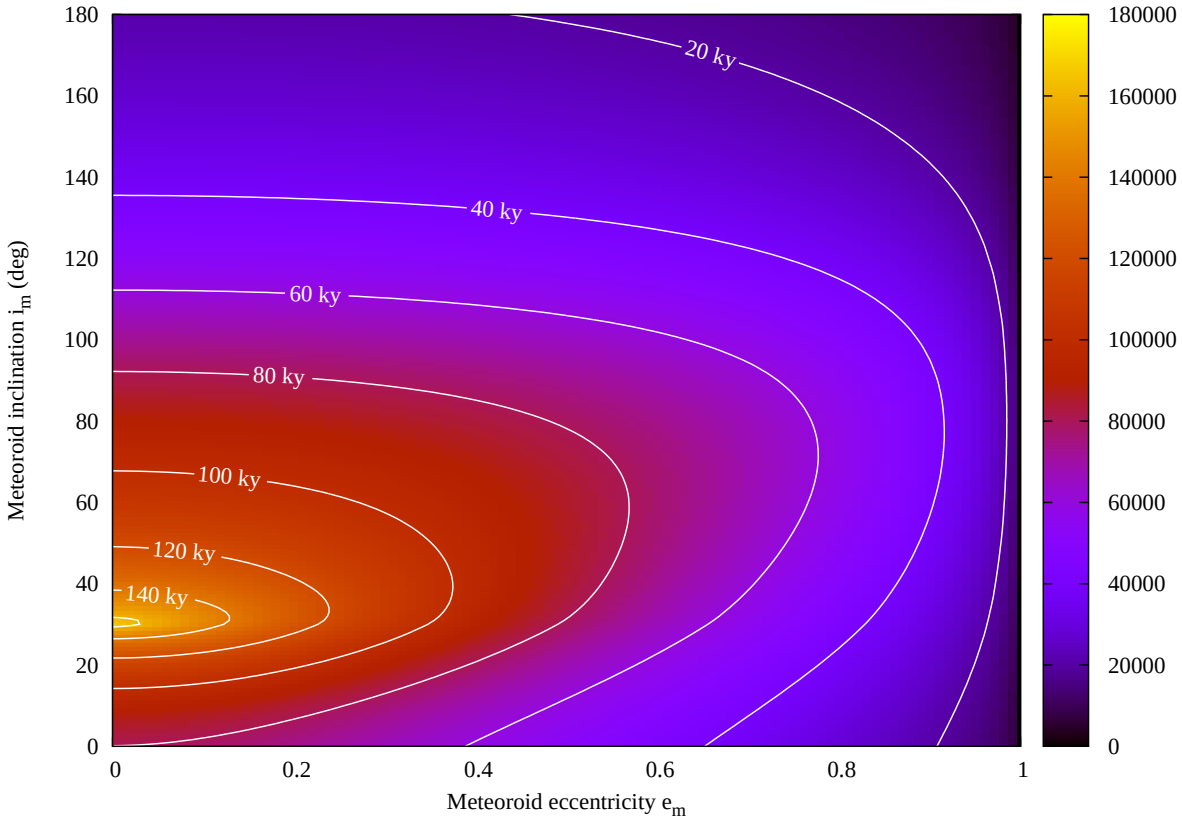

Figure 2.6: The dependence of the collisional lifetime $\tau_{\rm coll}$, represented by colors, with inclination $i_{\rm m}$ and eccentricity $e_{\rm m}$ of meteoroid. The levels of the same value of $\tau_{\rm coll}$ are represented with white lines with 20 ky steps. All points on the map are represented by a meteoroid with $a_{\rm m} = 1$ AU, $e_{\rm m} = 0.1$, $\omega_{\rm m} = 0$ and all particles of the zodiacal cloud are assumed to be on circular orbits with mean inclination $i_{\rm ZC} = 30°$. The diameter of the meteoroid is 2,000 μm.

with increasing eccentricity. Interestingly, there is almost a plateau in $\tau_{\rm coll}$ for higher eccentricities around meteoroid inclinations $I_{\rm m} \sim 70°$.

We also have to mention the variation of $\tau_{\rm coll}$ with the semimajor axis of the meteoroid $a_{\rm m}$. Perhaps unnoticed in the original work of Steel and Elford (1986), the variation can be simply expressed as $\tau_{\rm coll} \propto a_{\rm m}^{1.8}$. This is the direct consequence of our simplified model of the dust cloud, where we assumed its radial variation to be proportional to $R^{-1.3}$, and the speed of the mutual collisions $V \propto a_{\rm m}^{-0.5}$.

2.4 Numerical codes

One of the essential parts of our modeling efforts is the numerical integration of the particle orbits in the Solar System. In all presented papers all numerical simulations were performed by `swift_rmvs3` code (Levison and Duncan, 1994), where the authors effectively implemented the Wisdom-Holman mapping (Wisdom and Holman, 1991). The code itself can also deal with very close encounters between test particles and planets. All particles are considered massless in or simulations and do not influence the motion of

planets. The effects of *radiation pressure* and *Poynting-Robertson drag* are incorporated in our numerical code. While the effect of *radiation pressure* is simply adopted as a change of the mass of the Sun $M_\odot$ for $M_\odot(1-\beta)$, the effect of PR drag is added to the vectorial acceleration components. As we discussed in Sec. 2.2 the solar-wind drag force influences particles similarly to P-R drag force, thus we included it also into the numerical code by increasing the magnitude of the P-R drag by 30%.

Using the code, we track orbits of all particles as they evolve during their revolution around the Sun. In papers C and D, we took into account only seven planets of the Solar System (the Mercury was excluded and its mass was added to the mass of the Sun). In paper E, we used all eight planets, because our computational capability improved. We usually removed particles, as they reached heliocentric distance $R < 0.05$ au, for two reasons. The first reason is that we used one-day time step in our numerical simulations and orbits with smaller heliocentric distances are not properly resolved with such a timestep. The second reason is that bodies reaching such close distances to the Sun would be heated significantly and may vaporize (see, e.g., Nesvorný et al., 2011b).

In our models we track dust particles with different chemical composition. It is known, that e.g., particles released from Jupiter Family comets (JFCs) quickly lose their volatile ice layers after their ejection. We do not model the change of chemical composition of the particles and also we cannot model the size change of the dust particles caused by evaporation. Particles in our models thus remain chemically and structurally invariant during the whole simulation.

All particles in our models are tracked until they leave the Solar System on a hyperbolic orbit, impact one of the planets, or are too close to the Sun. We thus have the complete record of the particle dynamical state from its birth, after the ejection from the parent body, till its final end. However, in the real Solar System dust particles collide with each other. To incorporate these collisions we apply on the recorded ensemble of possible pathways of the dust particles at every recorded time step the collisional theory described in Sec. 2.3. Since the collisional disruption of the dust particles is a stochastic process, it is not included in the numerical integration, but it is applied subsequently, which allows us to test different theories and free parameters for the evaluation of the collisional lifetimes, and also effectively adjusting the statistics of our model by applying the collisional model with different setups of the random number generator.

Even though the computational capabilities improve every year, we are still able to handle the evolution of tens of thousands of particles within one numerical simulation. In our models, we study direct impacts onto the Earth and compare them with the various radar and optical observations of meteors. The collisional probability of a particular meteoroid with the Earth is very low, thus we usually record only units of direct impacts in our numerical simulations. This problem has two conceptually different solutions: 1) we can increase the number of simulated particles until we obtain reasonable statistics, and 2) we can evaluate for each particle at each time step its collisional probability, and determine the total collisional probability with the Earth. Since the first solution would be extremely time demanding, and also since we are considering large populations of dust particles, theories of collisional probability determination provide an elegant solution of our problem. In papers C and D, we used Greenberg's method (Greenberg, 1982), while for paper E we developed our own method described in Chap. 1, and papers A and B.

One of the constrains for our models is provided by the thermal emission of the zodiacal cloud in the Solar System. In papers D and E, we compared our model with the thermal emission observed by *IRAS* using a code named Synthetic InfraRed Telescope

(SIRT) developed by Nesvorný et al. (2006) that is able to model a thermal emission from distributions of dynamically evolving dust particles. SIRT provides IR fluxes that are comparable to space-borne IR telescope observations considering the location, pointing direction, and the epoch of observation of the telescope.

The last but not least, we construct a model of a synthetic ground-based telescope that is able to simulate the observations performed by radar systems or optical telescopes. Characterization of the sensitivity of the system is obtained through an ionization factor

$$I_{\rm ion} = \frac{m}{10^{-7}\ {\rm kg}} \left(\frac{V}{30\ {\rm km\ s^{-1}}} \right)^{3.5} , \tag{2.28}$$

where m is the mass of the meteoroid, and V its apparent velocity at the Earth (composed of the relative velocity at intersection of the particle's heliocentric orbit with the Earth and the planet's velocity vector including acceleration due to gravity). For each system we set a critical threshold $I_\star$, which means that particles with $I_{\rm ion} > I_\star$ are detected, while those with $I_{\rm ion} < I_\star$ cannot be detected by a particular system. We adopted thos approach from Wiegert et al. (2009), where authors investigated measurements of CMOR system, but the similar approach was also applied for the AMOR system, and should be applicable to other systems as well. We recall that for CMOR $I_\star \sim 1$ (Wiegert et al., 2009), for AMOR $I_\star \sim 0.001 - 0.01$ (personal communication with Margaret Campbell-Brown), and we expect that for optical systems like CAMO or CAMS $I_\star \sim 100 - 1000$. Another aspects influencing observations such as longitudinal and latitudinal dependence of detectability throughout the year, sensitivity for different radiant positions and velocities, trail echo height ceiling effect, and many more are very specific and vary from system to system, thus should be discussed carefully with the operating staff, which was e.g., performed in paper E, where we investigated CMOR observations of the north toroidal source.

2.5 Steady-state model – basics

Daily observations performed by various systems around the world provide information about meteors coming from a vast population of the bodies in the Solar System. In Sec. 2.2, we showed that the dynamical timescale of the transport from the parent body to the Earth linearly depends on the diameter of the particle D, and for the larger particles coming from distant bodies can exceed million years. It is modeled and also observed (Fernández, 2005) that comets may disrupt or become dormant in relatively short timescales, and thus the majority of meteors observed in the sporadic environment can originate from bodies that are not observable today. Observations of meteors cover only a few decades, and observations of the brightest comets cover thousand years at maximum, which forbids us to search for specific very old and today inactive or nonexistent bodies that could be the parent bodies of the sporadic meteoroids, we observe today. Thus, we have no other option than to rely on dynamical models explaining the observed populations of comets and asteroids and assume that such models based on the dynamical transfer of bodies from the e.g, Oort cloud, or Kuiper belt, are valid even when their results are extrapolated to the distant past.

For the steady-state models, we assume that structure and composition of the parent bodies remain the same. Another assumption is that the distribution of the orbital elements of the parent bodies, namely, the semimajor axis a, the eccentricity e and the inclination I, is constant in time. This means, that we assume the overall distribution

of the orbital elements (a, e, I) of e.g., HTCs one million years ago was the same as today. However, the observed population of HTCs one million years ago could be composed of bodies with different orbital elements compared to their contemporary counterparts, HTCs observed today. On the other hand, the remaining Euler angles, the longitude of the ascending node Ω, the argument of pericenter ω, and the mean anomaly l, should be taken randomly in the whole range of their possible values $(0, 2\pi)$ due to the chaotic nature of the dynamical transfer from the original population, and also due to the unknown original values of these angles (Levison et al., 2006).

Our steady-state models are created in following steps: (1) we create a certain amount of particles with orbits in accord with the modeled distribution of a particular group of the parent bodies, (2) these particles are followed in time until the whole population is eliminated, (3) then we determine for each particle at every timestep whether it is destroyed, or not, in the collision with the zodiacal cloud using a comparison of the disruption probability with a randomly generated number. However, this Monte Carlo procedure brings a stochastic element to the model, thus we typically repeat the collisional model 25 times and average over the results.

Since the particles of different sizes have different dynamical pathways due to the dependence of the PR drag on the size of the particle we need to create such steady-state models for a wide range of particle sizes. Contributions of particles of different sizes to the general model for a given group of parent bodies are then determined by the size-frequency distribution. Even though we usually start with thousands of the initial orbits for a given particle size, during its pathway through the Solar System a single particle creates thousands of imprints corresponding to every timestep with an unique set of the orbital elements, thus the steady-state population is represented by millions of individual orbits. For such a population, we can determine its dynamical lifetime, and consequently estimate a mass needed to keep the model in steady state.

Such steady-state models, however, do not allow us to predict temporal variations of the various observed features, like the well-known year variations of the north toroidal meteor concentration, because we assume the uniform distribution of Ω, ω, and l. Steady-state models cannot also predict a formation of young meteors streams because the orbital elements (Ω, ω, l) of such stream meteors are not distributed randomly, which is one of the main assumptions of our steady-state models.

Thus, in general, the steady-state models can predict only a behavior of the background population that satisfies our assumptions we presented in the previous paragraphs. As we will see, the background population corresponds to the majority of meteors observed in all six sources of sporadic meteors, and it is usually possible to separate the background from the stream-like structures, thus the development of the steady-state model represents one of the most crucial parts for the understanding sporadic meteoroid complex.

2.6 A brief overview of the 2012 CMOR dataset

Canadian Meteor Orbit Radar (CMOR) provides the most complete radar observations available today, and we were more than fortunate to get the whole dataset of the year 2012. In this section, we will briefly discuss general characteristics of the CMOR system, and also present general plots before, we proceed to the more detailed study of the three pairs of observed sources. We omit a significant portion of information that would be very similar to a comprehensive study of CMOR dataset by Campbell-Brown (2008). Instead,

we would like to present new figures that were not published, or are not commonly used in the literature, rather than mention well-known features of CMOR data.

CMOR is a radar system located in Ontario, Canada at 43.26° N, 80.77° W. It has been in operation since 2001 as a three station system, named as CMOR, while in 2009 it underwent a major upgrade that has expanded the system to six stations, and also doubled its transmit power to 15 kW, where the new facility was named CMOR II (Campbell, 2002; Campbell-Brown, 2008; Brown et al., 2012). The radar has three frequency systems running at 17.45, 29.85, and 38.15 MHz. Only the 29.85 MHz system is capable to derive the orbital elements of the observed meteor, thus, in the following text, we will present only results from this particular system. According to Campbell-Brown (2008) the limiting mass for CMOR is for a mean geocentric velocity 30 km s^{-1} about 10^{-7} kg, which is equivalent to $I_{\rm ion} \simeq 1$ (see Eq. 2.28). A detailed description of CMOR system can be found in Jones et al. (2005).

The 2012 dataset contains more than 1.3 million orbits, where for each orbit, the heliocentric ecliptic latitude and longitude of the radiant were calculated. The corrections for zenith attraction, diurnal aberration, and gravity acceleration, were taken into account in the dataset (see, Campbell, 2002, for a great review of all recognized biases in for CMOR system). All recognized meteor showers were removed from the dataset to provide the most accurate data for the sporadic population. In order to keep radiant positions constant with respect to the Earth, that orbits around the Sun on a slightly eccentric and inclined orbit, the solar longitude of the Earth λ at the time of meteor observation is subtracted from the measured ecliptic longitude, which makes the coordinates Sun-centered. In our papers C, D, E, and also here, we use a slightly different coordinates, where the apex is located at the origin of our coordinate system, and the Sun is located at longitude $-90°$. The map of the radiant distribution of the whole dataset is shown in Fig. 2.1 and six recognized sources are marked in Fig. 2.2 (see Sec. 2.1 for the definition of source regions).

The fundamental piece of information is a distribution of orbital elements and geocentric velocities for the observed meteors. Fig. 2.7 shows the distribution of the geocentric speed v_g, heliocentric semimajor axis a, inclination I, and eccentricity e for 1.3 million meteors measured by CMOR in 2012. We removed all meteors on hyperbolic orbits, thus e does not exceed unity, and $v_g < 72$ km s^{-1}, which is the hyperbolic limit in the Solar System for the particles impacting the Earth. According to Weryk and Brown (2004), most of the hyperbolic orbits are in fact very eccentric orbits that are, due to the a small error, moved to the hyperbolic regime with $e > 1$.

Fig. 2.7 also shows an approximate distribution of population with an ability of generating observed meteors. Each recorded meteor is characterized by a set of orbital elements $(a, e, I, \Omega, \omega, l)$ that allows us to evaluate its collisional probability $P_{\rm coll}$ with the Earth. We can then assign a weight $\propto 1/P_{\rm coll}$ to each observed meteor, and thus obtain a population of particles with an ability to generate observed meteor orbits. The determination of the collisional probability $P_{\rm coll}$ is performed by theory and code described in Chap. 1, and papers A and B.

The v_g distribution of all observed meteors has two visible peaks, one at ~ 30 km s^{-1} that is more dominant and is associated with the prograde meteors, and the second one around 60 km s^{-1} associated with meteors on retrograde orbits. The generating population has also two peaks, but the contribution of meteors with the lowest v_g is diminished. The peak for the prograde meteors moved to 45 km s^{-1}, while the second peak did not change significantly, moving to 65 km s^{-1}.

The semimajor axis a, shown in the top right panel in Fig. 2.7, is concentrated near 1 au, which is a direct consequence of the position of the detector, the Earth, which amplifies the collisional probability of the particles with the similar a. The number of impacts with $a > 2$ au is almost negligible, which might mean, that the parent bodies may be of an asteroidal origin. However, when we investigate the generating population, we see completely different picture. There is a peak at $a \sim 2.5$ au, but the contribution of the bodies with larger semimajor axes is not significantly lower. In fact, the slope is very shallow and implies that the majority of observed meteors must be of cometary origin.

The inclination distribution is divided to two segments, with $I < 90°$, and $I > 90°$. Near the $I = 90°$ there is a significant absence of observed meteors, which is caused by strong effect of the Kozai oscillations (see Sec. 1.2) that drives particles with polar orbits to highly eccentric modes, where these particles can be driven to heliocentric distances very close to the Sun. Flux of the meteors is dominated by prograde meteors with a prominent contribution of meteors with low inclinations. There is also a visible contribution of meteors with peculiar values of inclinations with peak near $I \sim 70°$. For retrograde meteors there is only one peak near $I \sim 150°$, however, the distribution of retrograde meteors is almost constant. Since the collisional probability strongly depends on I the importance of low inclined meteors in the generating population is decreased and orbits with $I \sim 70°$ become more prominent. This may suggest that the prograde meteors come from two different populations.

Observed meteors have wide range of eccentricities with peak at $e \sim 0.8$. The total flux is dominated by very eccentric meteors, however, the contribution of the less eccentric orbits is not negligible. The generating population is dominantly composed of very eccentric bodies. Meteoroids with very high eccentricities, and also correlated semimajor axes, have smaller P_{coll} than meteoroids with more circularized orbits, thus to populate the observed population of orbits a huge reservoir of very eccentric orbits must exist.

Since Fig. 2.7 represents only one-dimensional distributions of the geocentric impact speed and orbital elements, we are not able to see correlations between these variables. Fig. 2.8 shows two-dimensional correlations between geocentric impact speed v_g, semimajor axis a, eccentricity e and inclination I, while Fig. 2.9 shows the same correlations but for the generating populations weighted by collisional probability P_{coll} of each meteor. There is a significant difference between Fig. 2.8 and Fig. 2.9, where the most evident is a drift of generating population toward larger a and higher e. This suggests, that we have to take into account even parent bodies with $a > 20$ au, which not evident from unweighed distributions.

Fig. 2.10 shows the number of recorded particles in the CMOR dataset as a function of the solar longitude λ at the time of detection, we recall that all hyperbolic and stream meteors were excluded from our dataset. In other words, Fig. 2.10 represents the temporal variations of meteoric flux detected by CMOR in 2012. During 2012 CMOR was not fully functional for a brief period of time, which is represented by a sudden drop in the flux near $\lambda = 150°$. Many stream-like structures are visible in Fig. 2.7, and will be discussed in the following sections where we describe in more detail the data for different sources of sporadic meteors.

It is also very useful to plot distribution of the orbital elements with respect to the solar longitude λ (Figs. 2.11 and 2.12, for observed and generating populations, respectively). In Fig. 2.11 we immediately recognize a very prominent structure near solar longitude $\lambda \sim 260°$, with $v_g \sim 35$ km s^{-1}, $a \sim 1.4$ au, $e \sim 0.9$, and $I \sim 24°$. Even though all streams were removed from our dataset, we can identify this structure as a more

evolved part of Geminids meteor stream, that has almost the same orbital elements as the original stream (see, e.g., Brown et al., 2008). Further analysis shows, that these meteors, indeed, come from the similar radiant positions as the Geminids stream, which implies that the parent body of this structure is the asteroid 3200 Phaethon (Jenniskens, 2006, 2008). However, since this structure is dynamically older, it is not removed from the dataset by common techniques. The origin of Geminids dates to ∼1030 AD, when an unknown body was fragmented during a collision and left 3200 Phaethon and Geminids as products (Jenniskens, 2006), thus even the oldest particles coming from the breakup event are not old enough to be dispersed in the sporadic background. Structure with similar orbital elements can be seen also in Fig. 2.12, however, it is less prominent than in Fig. 2.11. One of the possible explanations is that the structure is not old enough to satisfy assumptions of the collisional probability theory, the random distribution of longitudes of the ascending node, and mean anomalies, thus the evaluated value P_{coll} might provide less reliable results.

On the other hand, Fig. 2.12 may be helpful to understand older structures evolved enough that their observed elements are too different from their parent body. One of such structures may be found near solar longitude $\lambda \sim 126°$, with $v_g \sim 46$ km s^{-1}, $a \sim 2 - 3$ au, $e \sim 0.99$ and $I \sim 25 - 35°$. The same structure is almost invisible in Fig. 2.11, and also the semimajor axis a of such meteors is observed near 1 au, which is given by the position of the Earth. It is known that these meteors belong to Southern δ Aquarids complex, associated with Marsden and Kracht sungrazing comets (Sekanina and Chodas, 2005; Jenniskens, 2006), however, without any modeling Fig. 2.12 gives us just a simple hint, where we could search for the parent bodies of such meteors.

Fig. 2.13 shows two-dimensional distributions of orbital elements, where color of each bin represents the mean particle diameter, and distribution of particle diameter for 1.3 million meteors measured by CMOR in 2012. The mean diameter of particles is almost constant in (a, e) plane, where for large values of a the size of particles tends to be smaller. From (a, I) plot, we see that particles with smaller semimajor axes and low inclinations are, in average, larger, which is a consequence of mutual effect of the ionization cutoff threshold that is more easily overcome by faster particles, and longer collisional lifetimes (Fig. 2.6). The correlation between e and I is readily evident from bottom left panel in Fig. 2.13. It implies that the largest particles have low eccentricities and inclinations, while meteors on retrograde orbits are much smaller, regardless on their eccentricity. The size distribution is influenced by ionization factor I introduced in Eq. (2.28). Particles with $D < 100$ μm are not detected by CMOR (we use $\rho = 2$ g cm^{-3}, and assume spherical particles to obtain D), the majority of detected meteors have diameters $400 < D < 800$ μm, and also a fraction of meteors have $D > 2000$ μm.

Wiegert et al. (2009) introduced ionization factor I_{ion} and presented the critical threshold value for CMOR $I_\star = 1$. Fig. 2.14 shows distribution of I_{ion} for all meteors measured by CMOR in 2012. We also plotted the black line representing $I_{\mathrm{ion}} = 1$ to evaluate the accuracy of $I_\star$. Only a negligible fraction is detected below $I_\star$, and we must also admit that a small error in v_g may considerably change value of ionization factor for a given meteor. Fig. 2.14 also shows that the distribution is not ideal, where one would expect a significant increase of detected meteors near $I_\star$. This might mean that Eq. (2.28) is not expressing the detectability correctly, however, we must also accept that the observations have non-zero errors, and by using the approximation expressed by Eq. (2.28) we do not incorporate a significant error to the modeling. In fact, we tested different expressions for ionization function I_{ion}, and also different values for $I_\star$ during our research of toroidal

sporadic meteors, and we concluded that even very complicated functions expressing I_{ion} do not produce a significant change to our models, when compared with rather simple expression given by Eq. (2.28).

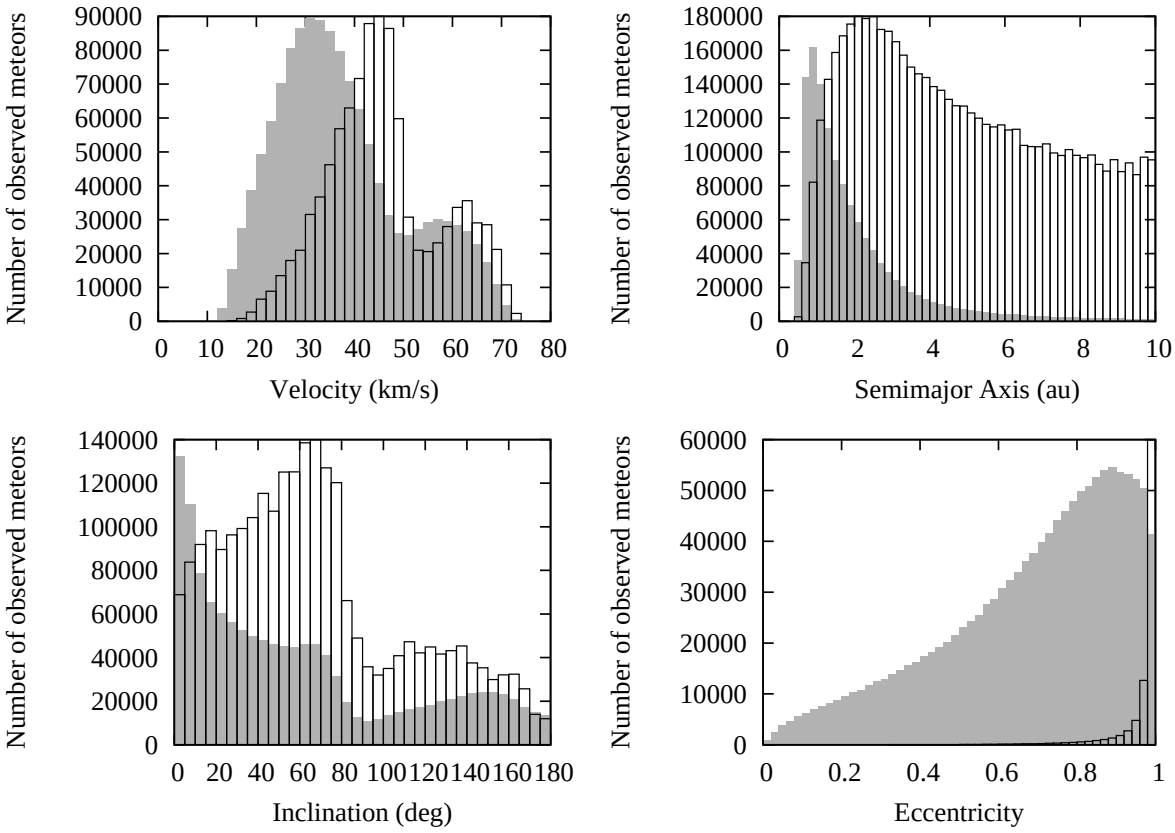

Figure 2.7: Distribution of geocentric impact speed (top left), heliocentric semimajor axis (top right), inclination (bottom left), and eccentricity (bottom right) for 1.3 million meteors measured by CMOR in 2012. The grey histograms correspond to the observed data from CMOR. The unfilled black histograms approximate the distribution of the population with an ability of generating observed meteors. The construction of the generating population is described in Sec. 2.6. The unfilled black histograms are normalized to unity. The observed and generating distributions are significantly different, which implies strong selection effects in the observed population caused by significant variation of the collisional probability of the meteoroid with the Earth for different sets of the orbital elements. The parameters of the generating population imply that the majority of observed meteors are of cometary origin, and the contribution of the asteroidal particles is rather low.

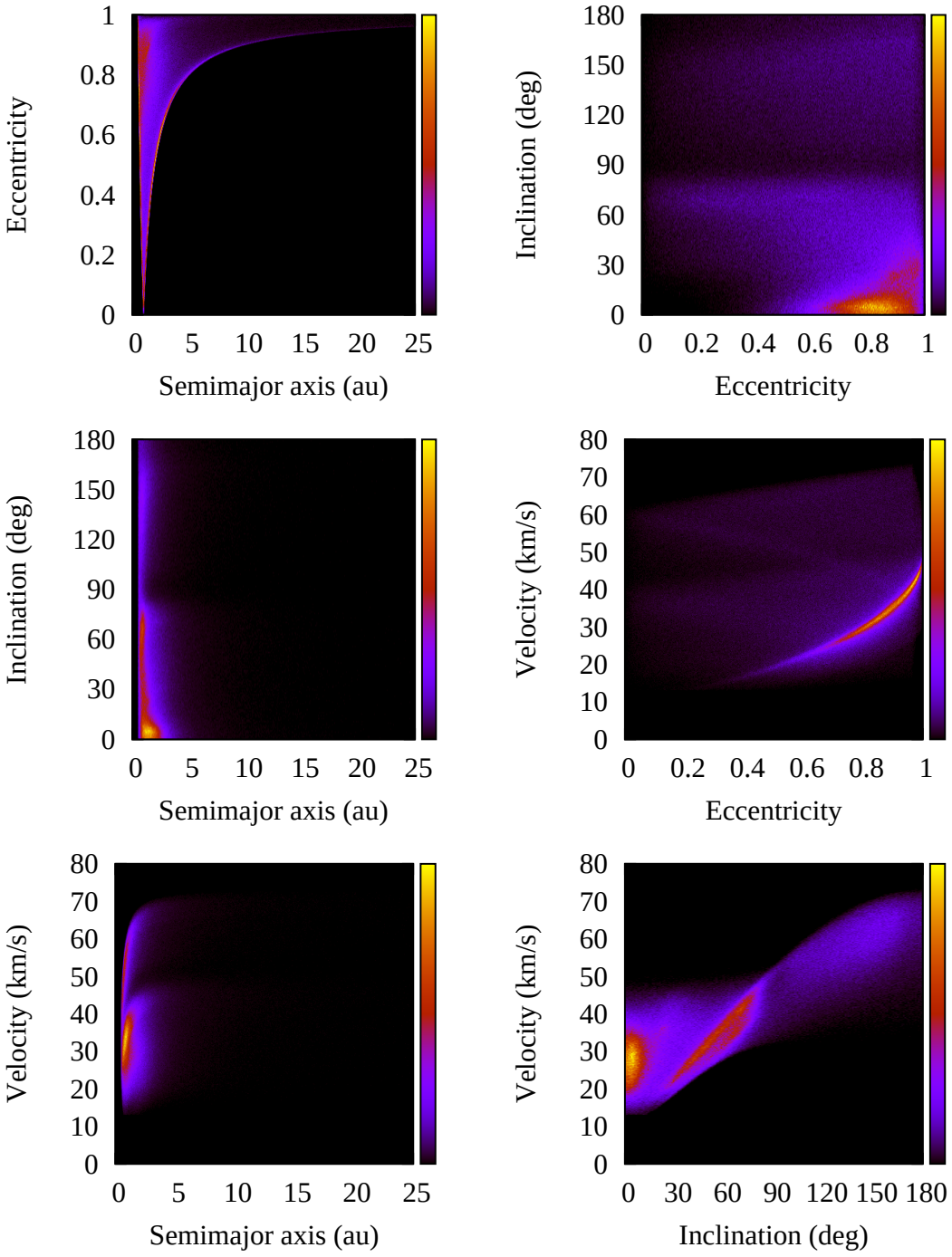

Figure 2.8: Two-dimensional distributions of semimajor axis vs eccentricity (top left), semimajor axis vs inclination (middle left), semimajor axis vs geocentric impact velocity (bottom left), eccentricity vs inclination (top right), eccentricity vs velocity (middle right), and inclination vs geocentric impact velocity (bottom right) for 1.3 million meteors measured by CMOR in 2012. The color scale represents number of meteors in each bin that was normalized to unity (the bin with the highest magnitude is equal to unity).

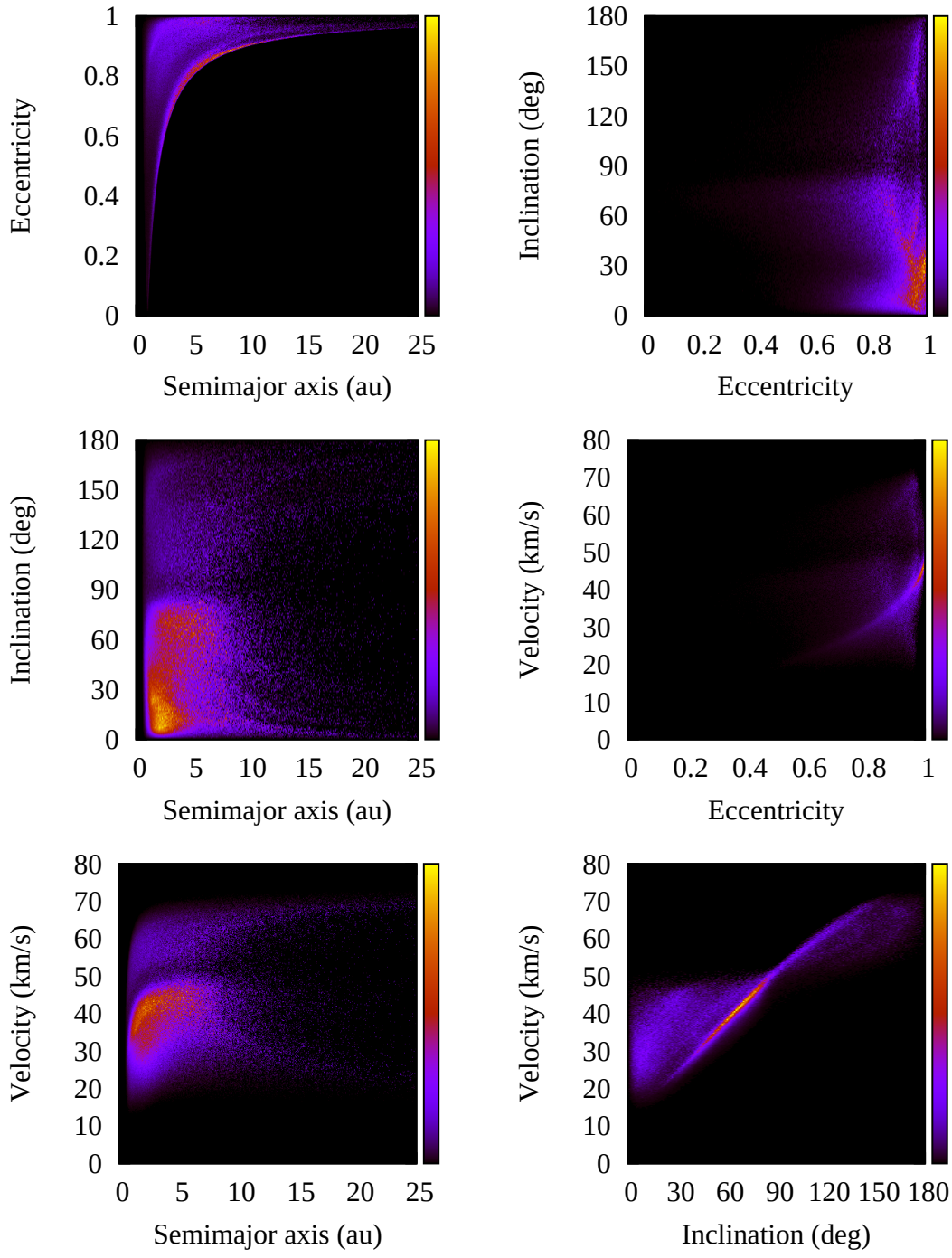

Figure 2.9: The same as in Fig. 2.8 but now weighted for the collisional probability $P_{\rm coll}$.

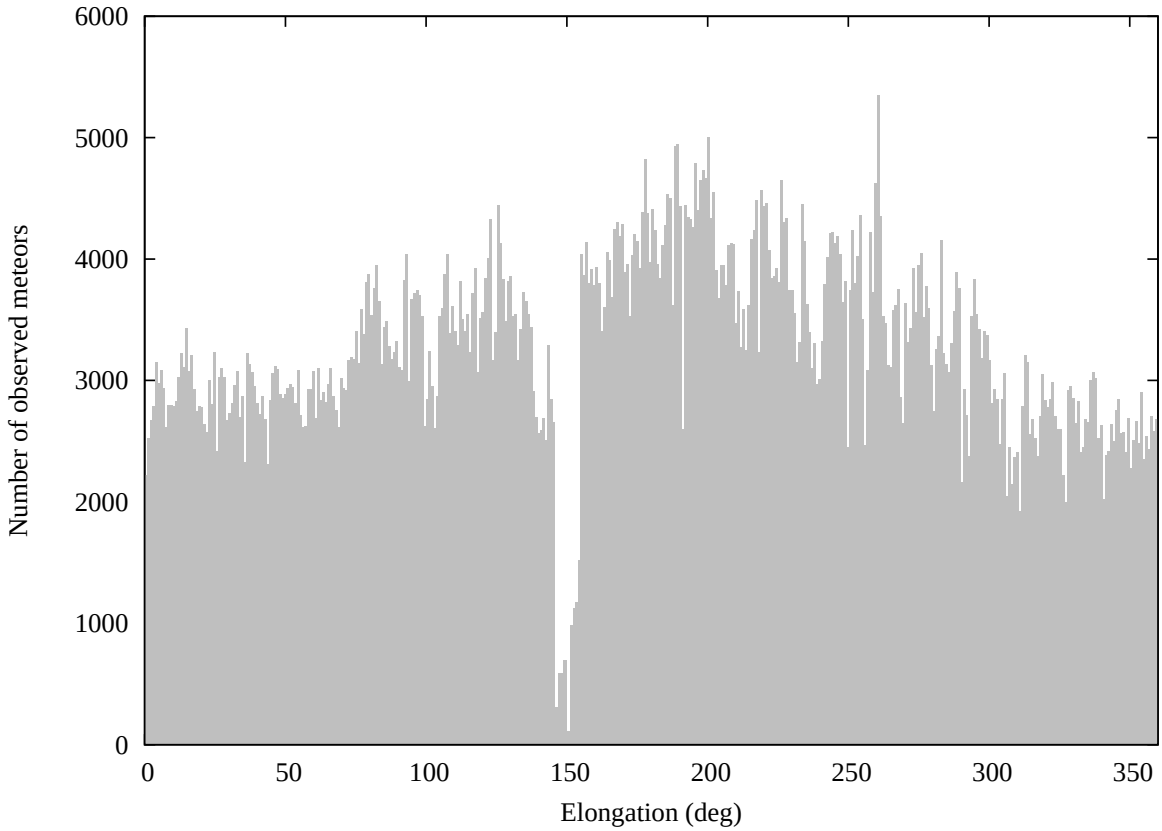

Figure 2.10: Daily impact statistics vs solar longitude λ for all 1.3 million meteors recorded by CMOR system during the year 2012, where all hyperbolic and shower meteors were removed. The sudden drop in daily impacts statistics near $\lambda = 150^{\circ}$ is caused by a malfunction of the system. Even though the streams were removed, we are still able identify number of stream-like structures that will be discussed in the following sections.

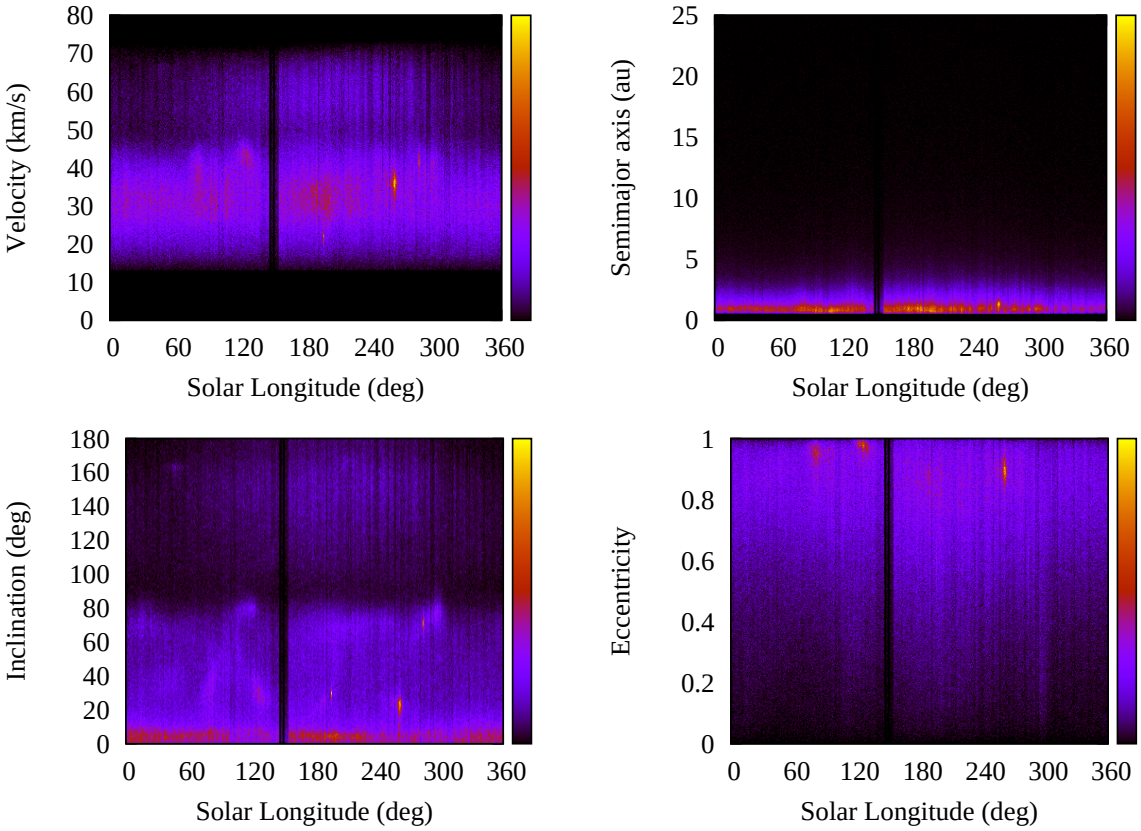

Figure 2.11: Two-dimensional distributions of solar longitude vs geocentric impact velocity (top left), solar longitude vs semimajor axis (top right), solar longitude vs inclination (bottom left), and solar longitude vs eccentricity (bottom right) for 1.3 million meteors measured by CMOR in 2012. The color scale represents number of meteors in each bin that was normalized to unity (the bin with the highest magnitude is equal to unity).

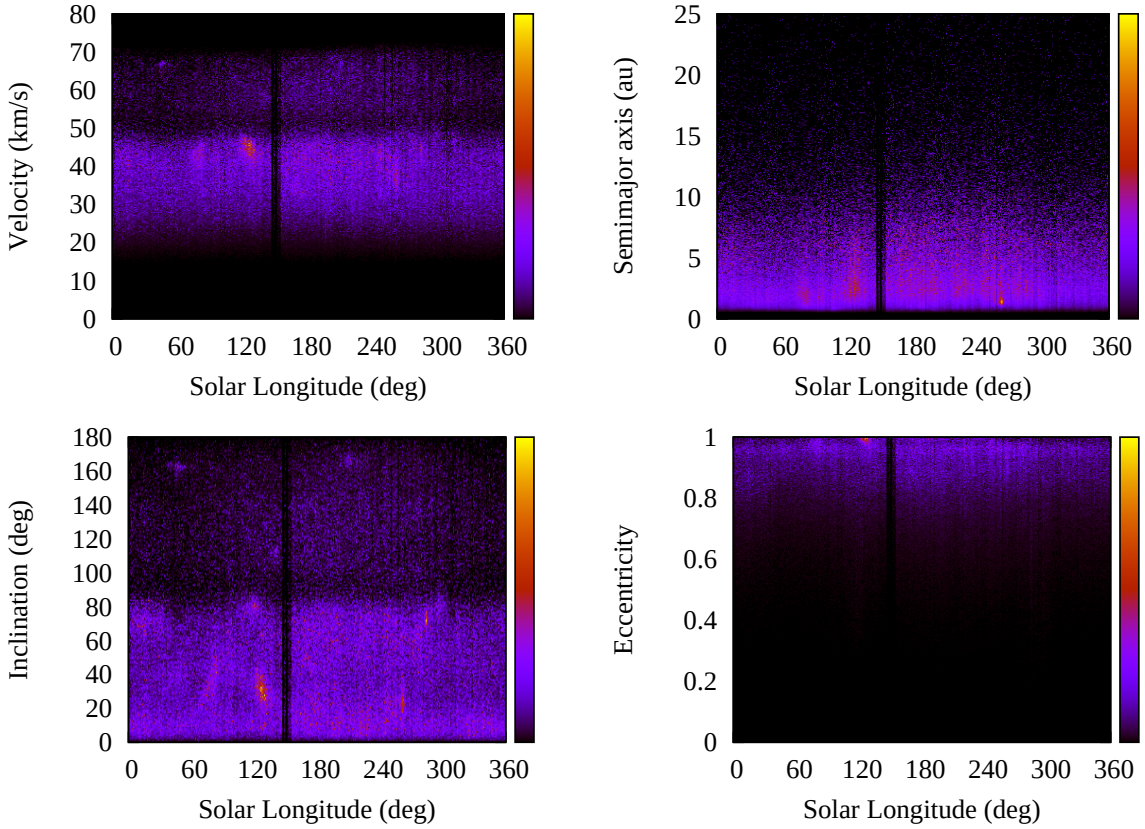

Figure 2.12: The same as in Fig. 2.11 but now weighted for the collisional probability P_{coll}.

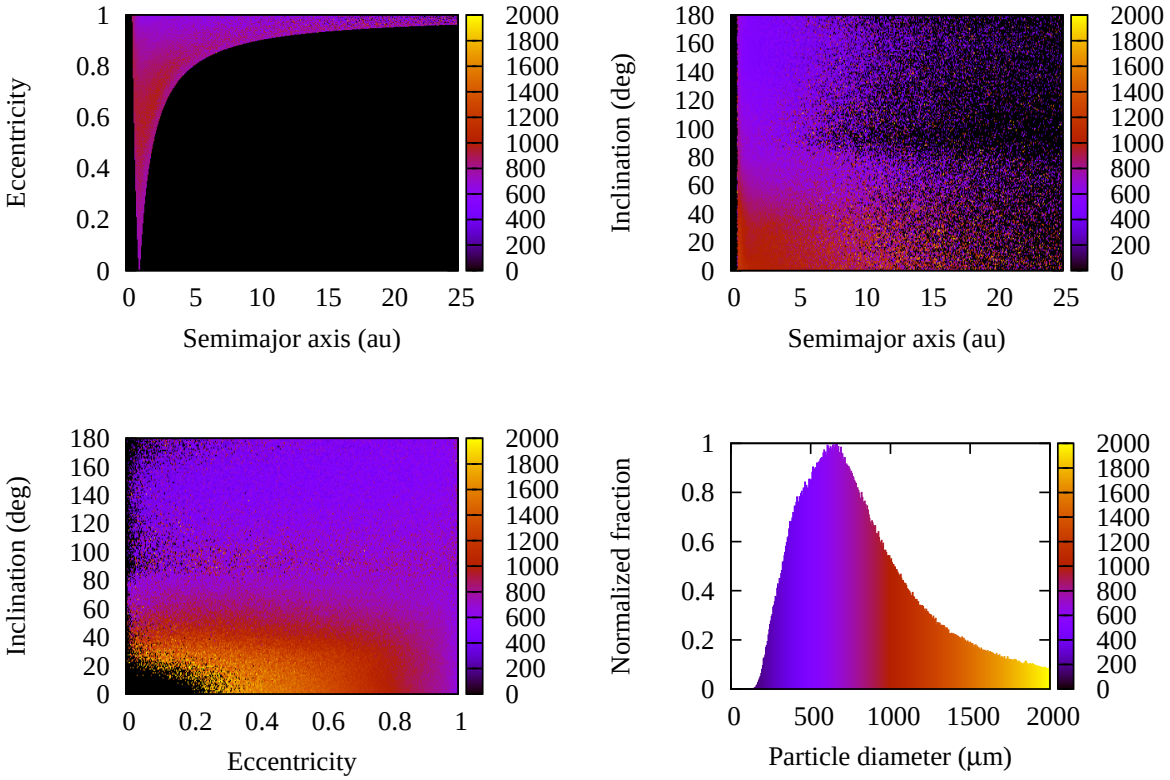

Figure 2.13: Two-dimensional distributions of semimajor axis vs eccentricity (top left), semimajor axis vs inclination (top right), eccentricity vs inclination (bottom left), and distribution of particle diameter for 1.3 million meteors measured by CMOR in 2012. The color scale in two-dimensional plots represents the mean particle diameter for each bin, while the histogram is filled with color that is equivalent to particular value of particle diameter.

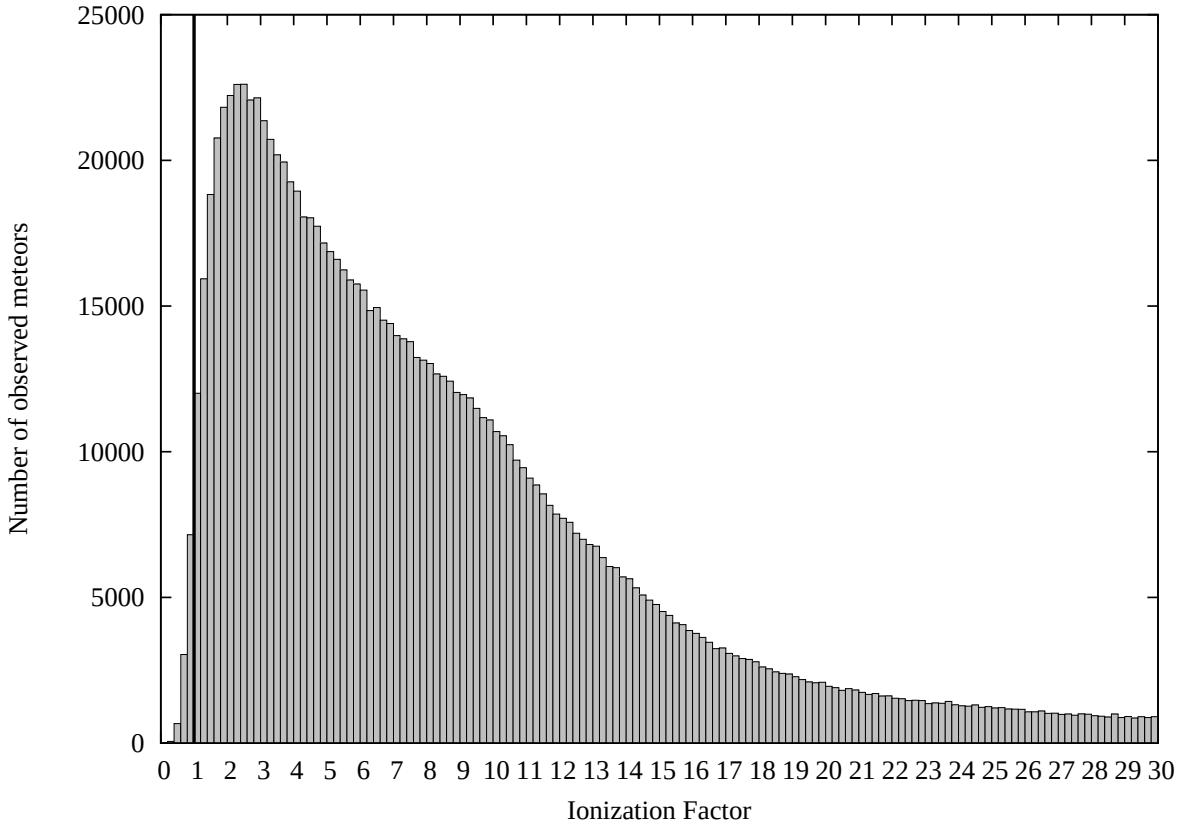

Figure 2.14: Distribution of ionization factor I_{ion} for 1.3 million meteors measured by CMOR in 2012. The black line represents $I_{\text{ion}} = 1$, which is a critical threshold obtained for CMOR system.

2.7 North/south apex source - data

Now, we will discuss particular sporadic meteor sources in more detail. We start with the apex complex that is composed from the north apex source with radiant positions enclosed in a semicircle with radius 40° and center at $(\ell, b) = (0°, 0°)$, and the south apex source, a symmetric counterpart of the north apex with respect to the ecliptic plane. CMOR in 2012 observed 321785 meteors, which is $\sim$ 24.6% of all meteors detected in 2012 by CMOR.

Fig. 2.15 shows distribution of v_g, a, e, and I both for observed and generating populations. Apex meteors are very fast, having a peak of the impact velocity distribution at $v_g \sim 63$ km s^{-1}, with a small fraction of quite slow meteors. From the weighted part of geocentric impact velocity plot we see that the generating population is mostly composed from very fast meteors with speeds near to hyperbolic limit at ~ 72 km s^{-1}. Inclinations of apex meteors are mostly higher than 90°, which is strictly correlated with the v_g distribution. However, CMOR also observes a small fraction of prograde meteors in the apex region. The generating population is almost strictly composed of retrograde particles with peak near $I \sim 140°$. The fraction of observed meteors grows nearly linearly with increasing eccentricity, while the generating population is evidently of cometary origin, since the majority of generating particles have very high eccentricities $e > 0.95$.

Now, we will discuss the distribution of semimajor axis a. The observed population is still concentrated at $a \sim 1$ au, however, the generating population is much more interesting. In Fig. 2.15, we see that number of generating particles is almost constant regardless on a. We extended range of semimajor axis up to 1000 au (Fig. 2.16), to investigate this trend for higher values of a. Even for $a \sim 100$ au the contribution of particular bins is still nearly constant with a slightly decreasing trend after $a \sim 150$ au (bottom left panel in Fig. 2.16). Such large semimajor axes and eccentricities imply cometary origin of apex meteors with a high fraction of contribution from the Oort Cloud comets (OCCs). We investigated dynamics of the dust particles released from OCCs in paper C, reviewed in Sec. 2.8.

Fig. 2.17 represents number of observed meteors vs solar longitude λ, or, in other words, temporal variations of the meteor flux observed by CMOR in 2012. We observe many stream-like structures that are obviously remnants of removed streams in the apex region, where many of them can be distinguished quite easily; Eta Aquarids at $\lambda \sim 45°$, Orionids at $\lambda \sim 207°$, or e.g., Leonids at $\lambda \sim 237°$ (Brown et al., 2008). Let us recall that the correct stream identification requires more precise techniques discussed briefly in Sec. 2.1. Interestingly, all streams seem to lie on a very broad Gaussian-shaped structure with the peak near $\lambda \sim 190°$. Since the sporadic background should be ideally constant with no dependence on λ, this Gaussian-shaped structure may be a remnant of an event that produced enormous amount of dust in the past, where a possible source might be a cometary breakup, that occurred in the recent past. A proper randomization of nodes of the dust particles requires tens of thousands years of dynamical evolution, however, a certain modeling effort is needed for better understanding of this phenomenon. We must admit that we were not aware of this structure, and thus we did not investigate its origin in paper C.

Now, we focus on two-dimensional distributions of orbital elements with respect to solar longitude λ. Observed distributions for apex region are shown in Fig. 2.18. The flux in all orbital elements is dominated by the Gaussian-shaped structure recognized in Fig. 2.17, however, at least one meteor stream is visible with a naked eye without further

processing. The Eta Aquarids stream with $v_g \sim 65$ km s^{-1}, $a \sim 7$ au, $e \sim 0.92$, and $I \sim 163°$, may be recognized in bottom left plot, where its concentration in I is evident. Since the observed population is concentrated near $a = 1$ au, we are not able to obtain a of the parent body. Fig. 2.19 shows the same two-dimensional distributions but now for the generating population that should at least partially represent the positions of the parent bodies. The remnants of the Eta Aquarids stream are more evident in Fig. 2.19, and also at least slight concentration near $a \sim 15$ au, which together with other orbital elements directly points to a Halley-type comet. It is known that the parent body of the Eta Aquarids stream is the comet 1P/Halley (Jenniskens, 2006) with $a = 17.83$ au, $e = 0.967$, $I = 162.26°$ for the J2000 epoch[2].

Figs. 2.20 and 2.21 represent two-dimensional distributions of v_g, a, e, and I with respect to each other, for observed and generating populations, respectively. The majority of observed meteors from the apex source belong to the Gaussian-shaped structure composed of meteors with retrograde orbits. Interestingly, the prograde meteors do not have orbits with $e < 0.5$, while the orbits of their retrograde counterparts fill almost the whole range of e. Another interesting feature of apex meteors can be found in a vs e plot (top left panel Fig. 2.20), where the majority of observed meteors lie on the border of area denoting possible impact configurations, while only a small fraction lies within this area, contrary to distribution from all meteors observed by CMOR in 2012 (Fig. 2.8). The generating population does not provide any surprising facts. The prograde part of meteors observed by CMOR vanish due to their much larger collisional probability with the Earth, the contribution of slower meteors is thus negligible, and the generating population consists of highly eccentric, fast, retrograde dust particles with large semimajor axes.

[2]Orbital elements were obtained via JPL Small-Body Database Browser at JPL solar system dynamics web site `http://ssd.jpl.nasa.gov/`.

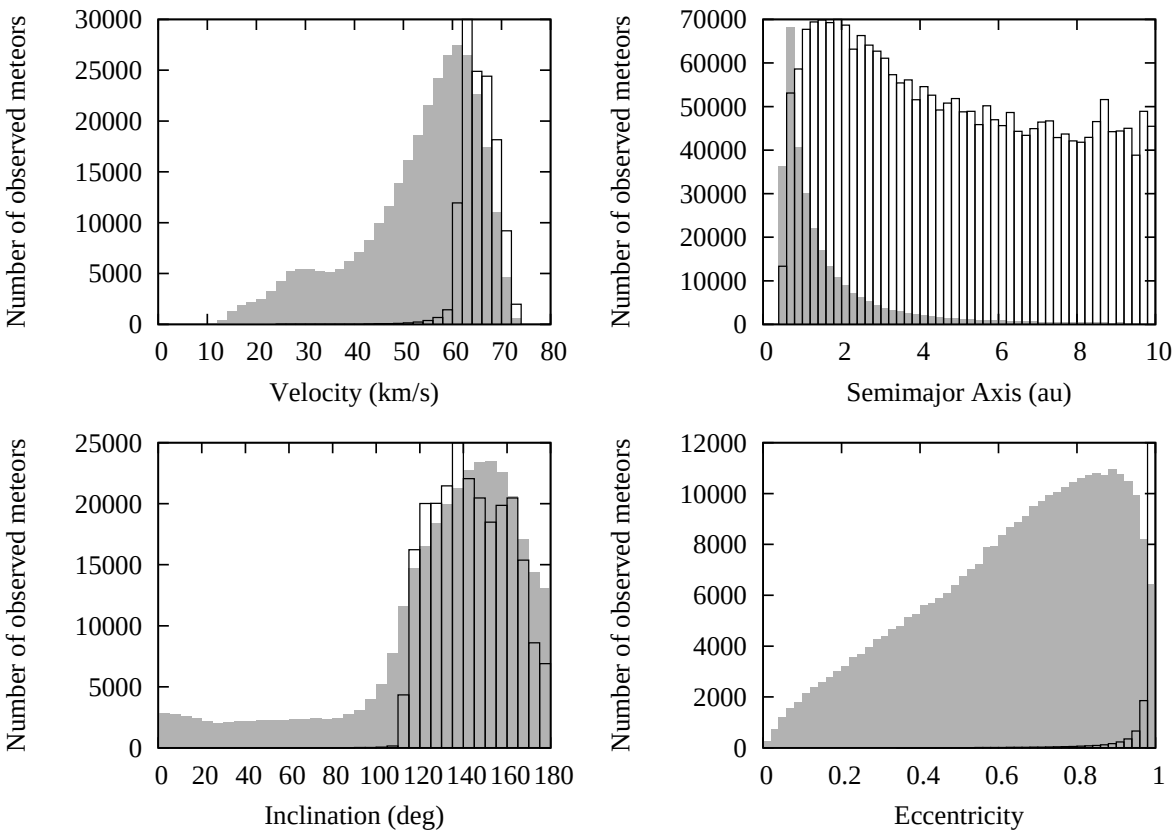

Figure 2.15: The same as in Fig. 2.7 but now for apex meteors only.

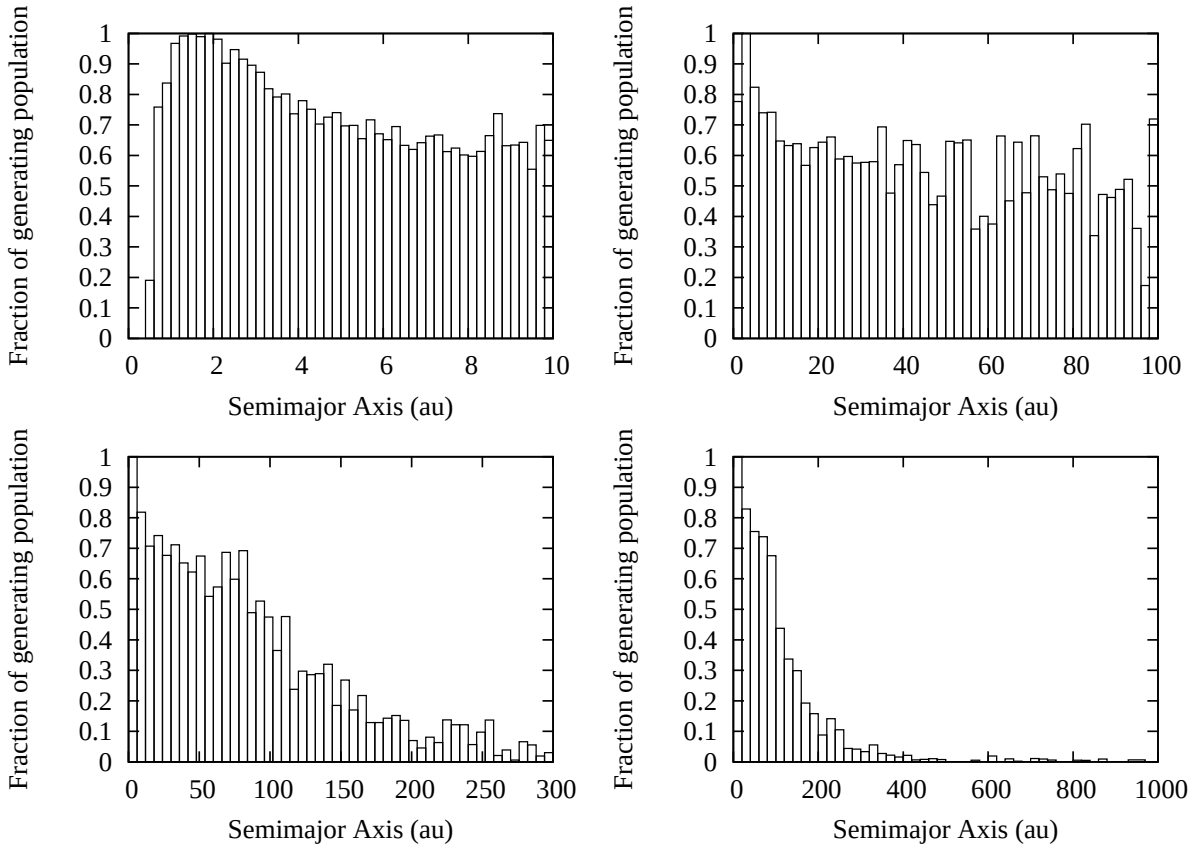

Figure 2.16: Distribution of semimajor axis for the generating population of the apex sporadic meteor complex for four different ranges of semimajor axis a, $0 < a < 10$ au with $\Delta a = 0.2$ au (top left), $0 < a < 100$ au with $\Delta a = 2.0$ au (top right), $0 < a < 300$ au with $\Delta a = 6.0$ au (bottom left), $0 < a < 1000$ au with $\Delta a = 20.0$ au (bottom left), where Δa is the width of the bin.

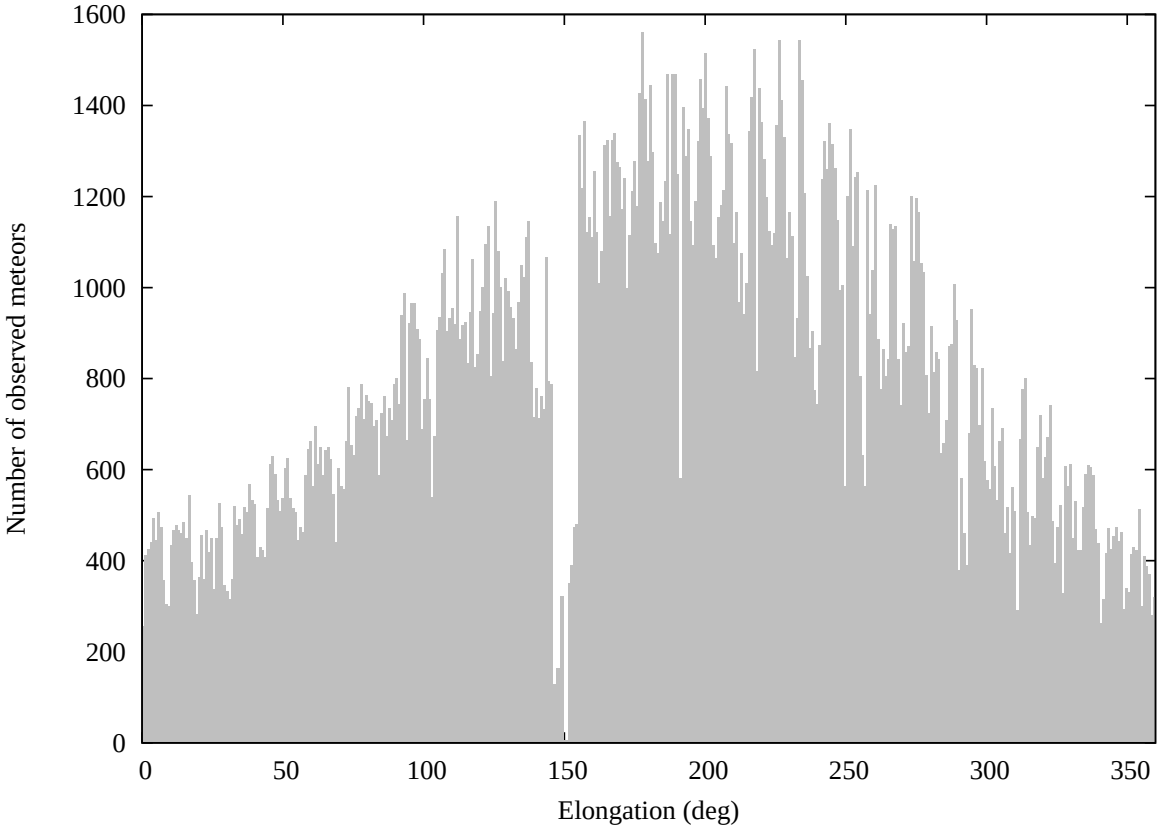

Figure 2.17: The same as in Fig. 2.10 but now for apex meteors only.

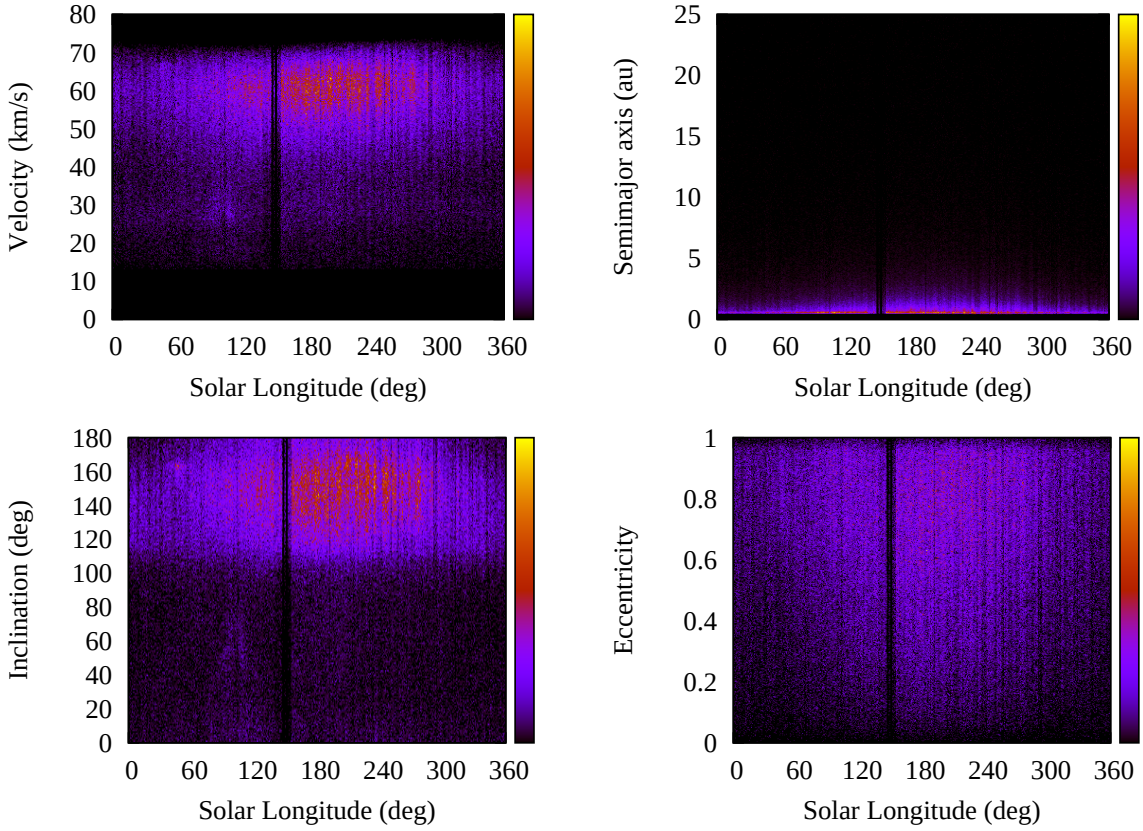

Figure 2.18: The same as in Fig. 2.11 but now for apex meteors only.

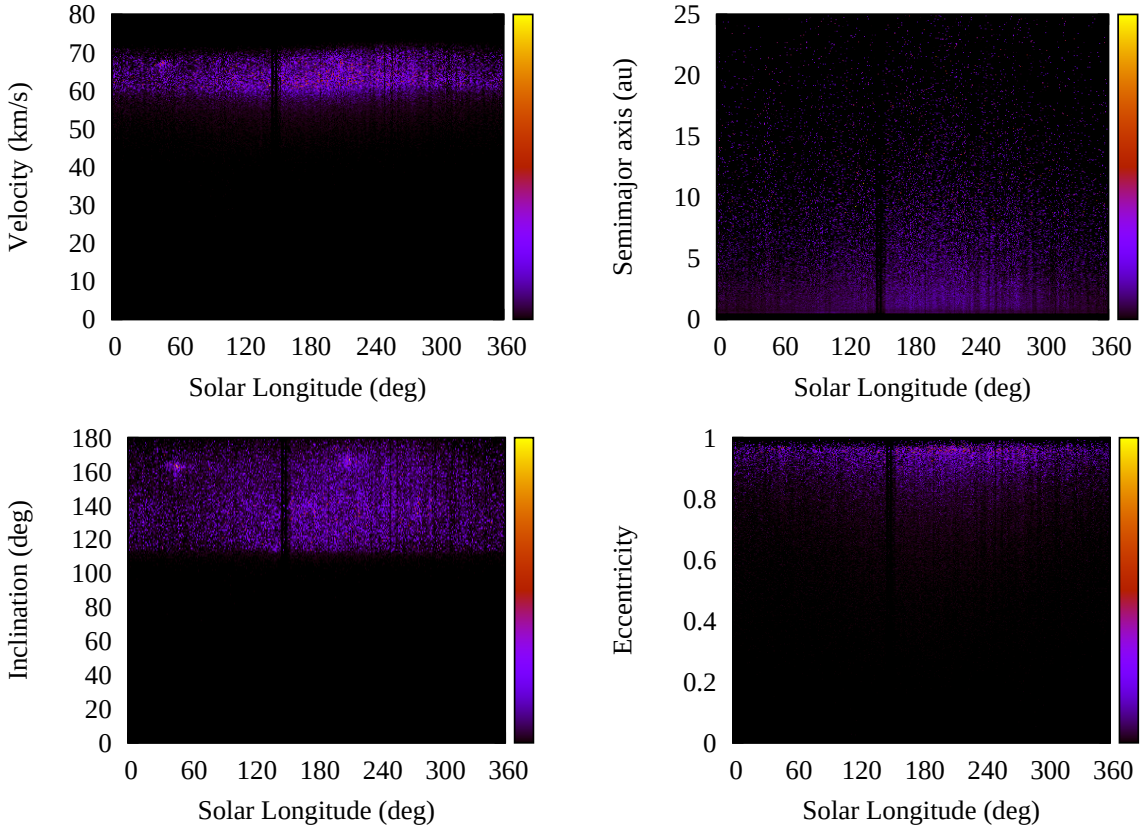

Figure 2.19: The same as in Fig. 2.12 but now for apex meteors only.

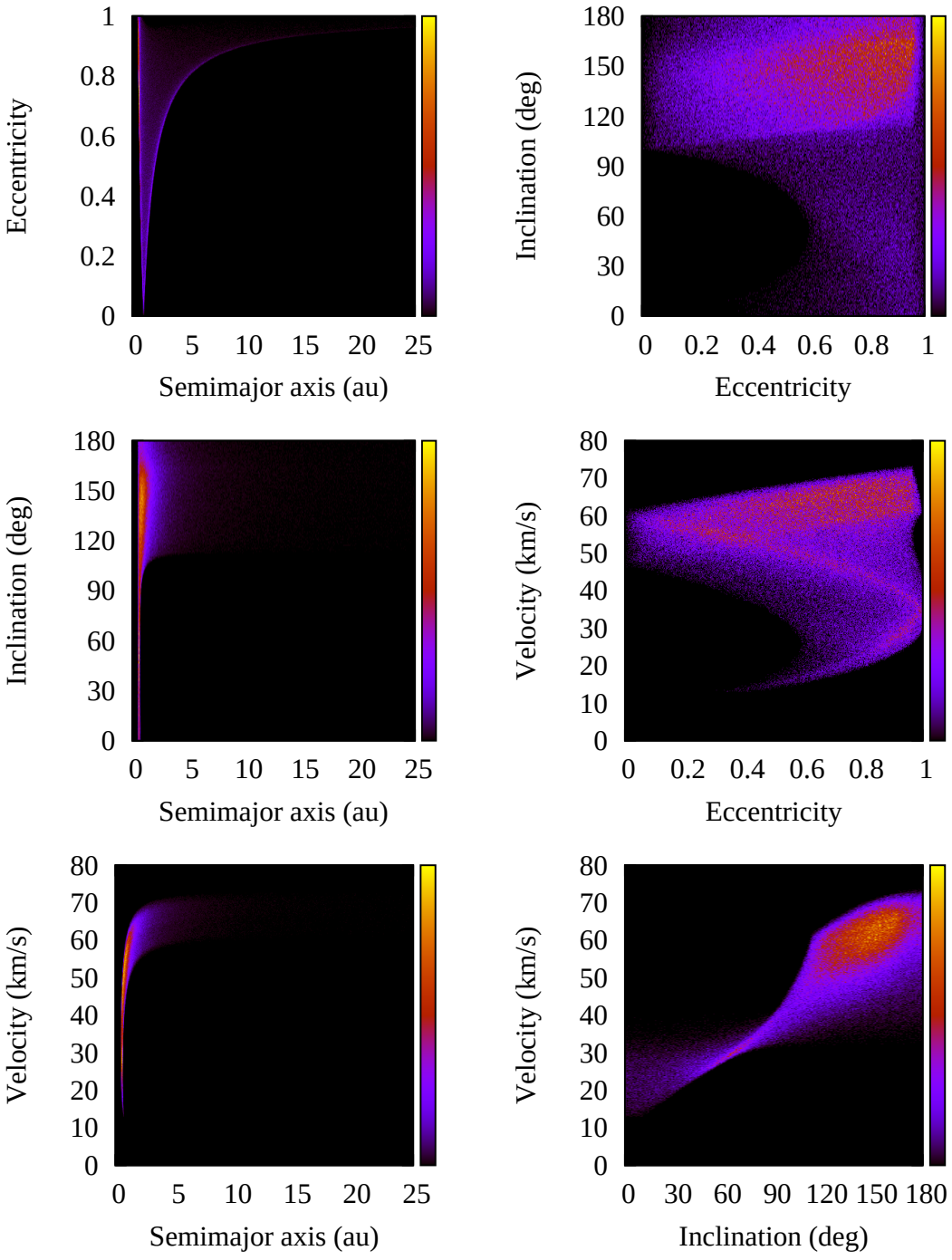

Figure 2.20: The same as in Fig. 2.8 but now for apex meteors only.

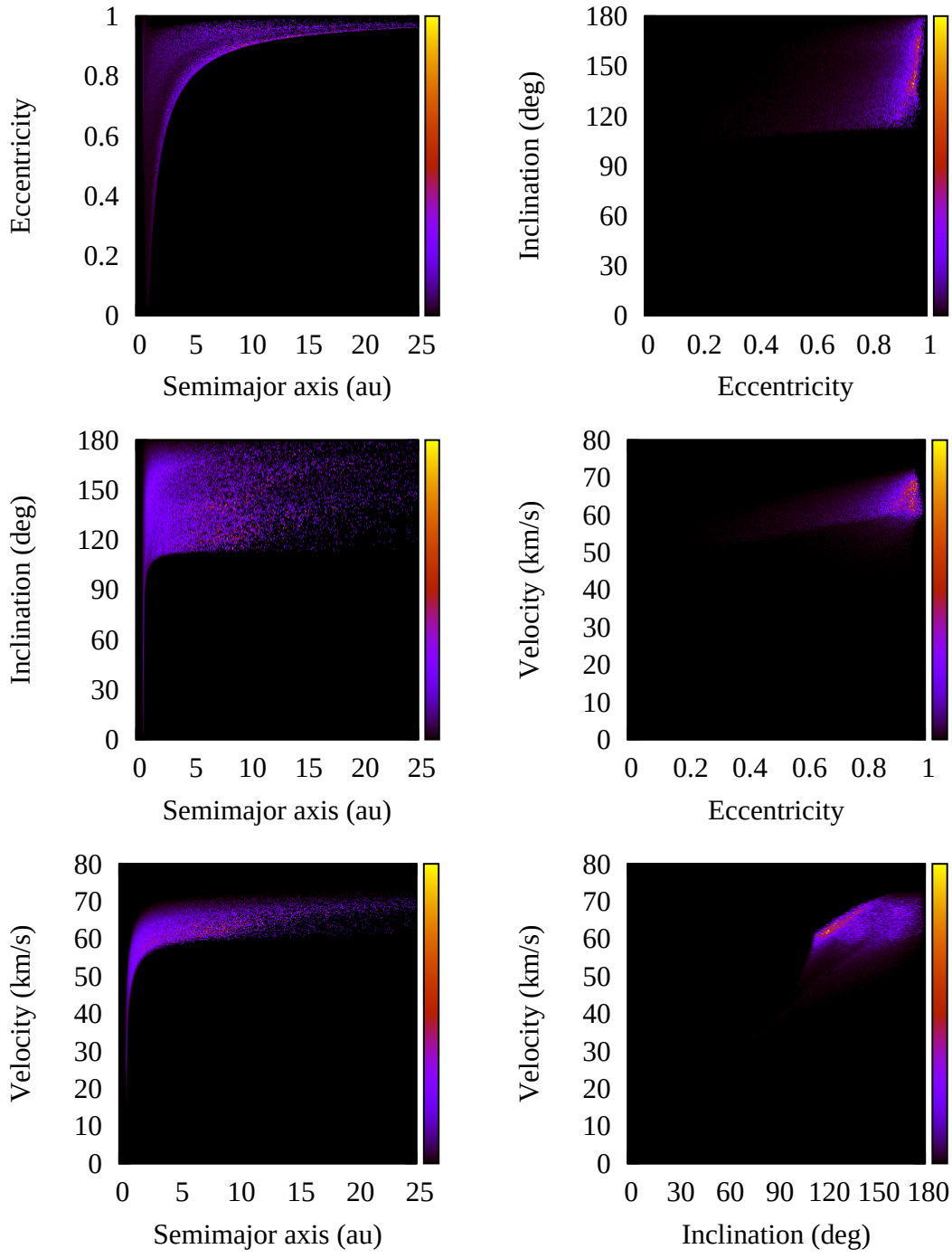

Figure 2.21: The same as in Fig. 2.9 but now for apex meteors only.

2.8 North/south apex source - model - short review - paper C - Dynamics of Dust Particles Released from Oort Cloud Comets and Their Contribution to Radar Meteors

In this section, we recall basic features and results from paper C (Nesvorný et al., 2011a). The main goal of our paper is a development of a model for dust particles released from Oort Cloud Comets (OCCs), find its contribution to the sporadic meteoroid environment, and also try to compare the modeled distributions of orbital elements with the radar observations from AMOR and CMOR.

The Oort Cloud is a cloud of comets with a roughly spherical shape (Oort, 1950) surrounding the Solar System and extending to very large heliocentric distances $r > 30,000$ au. We use the Oort Cloud as a reservoir of comets that come into the inner Solar System at a rate about 12 comets with perihelion distance $q < 3$ au yr^{-3}, where the absolute magnitude of an active comet $H < 10.9$ (Wiegert and Tremaine, 1999). OCCs can be divided into two different populations based on their dynamical histories: (1) dynamically new OCCs, comets on their first passage through the inner Solar System with typical semimajor axis $a \leq 10,000$ au, and (2) returning OCCs, comets that previously passed thought the inner Solar System, and due to the dynamical effects they typically have $a < 10,000$ au.

Model

In our paper, we study only dust particles originating in returning OCCs with $a \sim 1,000$ au. We do not consider comets with $a > 10,000$ au, corresponding to the Oort spike (Wiegert and Tremaine, 1999), because the cometary disruptions that produce the largest amounts of dust do not usually happen at very large heliocentric distance. Since we are dealing with extreme values of a, the criterion for bound dust particles $\beta > r/2a$ from Eqs. (2.12) and (2.14) is very restrictive even for larger particles with $D \sim 300$ μm and $\rho = 2.0$ g cm^{-3}, where heliocentric distance must be $R > 36$ au to keep released particles on bound orbits. Due to the spherical shape of the Oort Cloud we also assume that the initial distribution of I, Ω, and ω, may be considered isotropic for simplicity.

Our model is built in the following steps: (1) dust particles of different diameters D are released from OCCs, (2) their orbit dynamically evolve in the Solar System due to the gravitational and radiation forces, (3) a fraction of particles are thermally or collisionally destroyed, or impact one of the planets in the Solar System, (4) a small fraction of the initial particle population is accreted by Earth, where they produce meteors in the Earth's atmosphere, and (5) radars observe such meteors and allow us to compare observed and modeled distributions of the orbital elements. All processes are in more detail described in Sec.s 2.2, 2.3, 2.4, and also in paper C.

Results

Dust particles ejected from OCCs follow very interesting dynamical pathways. During their passage through the inner parts of the Solar System their semimajor axes a undergo a random walk caused by indirect planetary perturbations, due to the giant planets, mainly by Jupiter. This process occurs during every perihelion passage and may produce

a significant drop in a down to 40 au, where the particles start to interact with exterior mean motion resonances with Neptune. This process is much faster that the decrease of semimajor axis caused by P-R drag (see Fig. 2.4 for reference). However, after the particles reach $a = 40$ au, the dynamics of their orbits are mainly controlled by P-R drag. Many dust particles are not able to pass through Jupiter's barrier, where the mutual interactions and close encounters drive dust particles to very eccentric orbits, that end either by thermal evaporation near the Sun, or on hyperbolic orbits. Only a small fraction of original population is, in fact, able to eventually decouple from Jupiter, and reach aphelion distance $Q < 4$ au. We reported that roughly $0.8\% - 1.5\%$ of particles with diameter $D = 100$ μm are able to decouple from Jupiter. This number decreases with D and for $D = 1$ mm the fraction is really small $\sim 0.02\%$.

Now, we shortly review our modeled distributions of orbital elements and radiant positions for dust particles from OCCs. Decoupling from Jupiter is a very important process, since we found that the main contribution to the density of OCC particles at $R = 1$ au comes from recently decoupled particles, which have also much higher collisional probabilities with the Earth than their non-decoupled counterparts. Fig. 5 in paper C shows the steady state distribution of orbital elements of OCC particles with $D = 100$ μm. The peak near $a = 6 - 7$ au is caused by concentration of orbits in the exterior mean motion resonances with Jupiter, which are able to protect dust particles against the close encounters with Jupiter (Liou et al., 1999). Eccentricity distribution almost linearly increases towards $e = 1$, which is a direct consequence of P-R drag since the orbits originally started with $e > 0.995$. Very interesting is a lack of orbits with $I \sim 90°$, that were initially strongly populated, because we used an isotropic distribution of I. This absence is a consequence of the Kozai oscillations that drive these polar orbits to very high eccentricities, inevitably ending near the Sun, where the particles are thermally destroyed.

Radiants of OCC dust particles are almost exclusively located near Earth's apex location. Since the retrograde particles have very high relative velocities with the Earth (~ 60 km s^{-1}), they fall directly from the apex radiant positions, while prograde particles may populate much wider area. Also, the collisional probability grows significantly with increasing relative velocity, thus, the contribution of retrograde particles tends to be higher than that from prograde particles (Fig. 6 in paper C). Distribution of meteor radiants expresses a lack near the ecliptic, which is caused by absence of meteors with $I \sim 180°$, and is in accordance with AMOR and CMOR observations (e.g., Fig. 2.1 in Sec. 2.1.1).

The distribution of v_g peaks at $\sim$ 60 km s^{-1} (Figs. 8 and 9 in paper C), and provides a very good match to both CMOR (Fig. 2.15 in Sec. 2.7), and AMOR (Galligan and Baggaley, 2005) observations of apex meteors. Also, the semimajor axis distributions are in a good accordance with radar observations having peak at $a \sim 1$ au, and a sudden decrease with a long tail towards very high values of a. Our model also predicts most of meteors on retrograde orbits with $I \sim 100° - 180°$, however, the shape of strongly depends on a size of the dust particles and is not comparable to the measurements yet. This might be caused by small statistics in our model, which is a consequence of strong Jupiter's barrier, and very small probability of particle's decoupling from Jupiter. The most puzzling is the eccentricity distribution that does not match well the CMOR and AMOR measurements.

Conclusions

Our conclusion is that only a small fraction $\sim 10^{-3\div 4}$ of OCC particles is able to decrease its aphelion distances below Jupiter's orbit. This fraction also varies with particle's size, where the smaller particles have higher probability to overcome Jupiter's barrier, and become circularized in the inner Solar System. We find that smaller particles with $D \sim 100$ μm are able to reach Earth crossing orbits with higher probability, and also are able to decrease their semimajor axis a down to the 1 au. Such particles have many orders of magnitude higher collisional probabilities with the Earth, and thus dominate the observed flux by ground-based radars.

We estimate the overall impact probability with the Earth per one particle released from OCC to be $50-80$ times lower than for particles released from Halley-type comets (HTCs), and $200-400$ times lower than for particles released from Jupiter-family comets (JFCs). Thus, only a substantial material production of OCCs will enable a significant contribution of OCC particles to the sporadic meteoroid complex. From (Levison et al., 2002) we roughly estimate that five returning OCCs disrupt in the Solar System every year. This produces a mass input $\sim 3 \times 10^8$ kg s^{-1}, from which only a small fraction will end in bound dust particles that are able to impact the Earth. For comparison, the active JFCs produce ~ 300 kg s^{-1} (Reach et al., 2007).

OCC particles dominantly contribute to the apex regions with a negligible contribution to helion/anti-helion sources and other regions of the sporadic meteoroid complex. However, the observed distributions of the orbital elements cannot be fully reproduced only by particles originating in OCCs, thus we suggest that there must be another significant source of meteors that can populate apex regions. We, indeed, found a significant contribution from particles coming from HTCs in paper E (Pokorný et al., 2014), but a more detailed modeling for the apex population is needed. We leave a development of a more complete model for the apex population for the future work.

Revision of our original results

For the purpose of this thesis, we performed several numerical simulations with a goal to reproduce, and more precisely investigate, the original simulations from paper C. We were motivated by results of our model for the toroidal source of the sporadic meteoroid complex (see Sec. 2.12 and paper E), where we found that the HTCs have an interesting and promising contribution to the apex source. Since our model for OCC dust particles is not perfect and is not able to precisely match observed orbital elements of meteors in the apex source, we started to develop a new, two-component model, for which we show the first results in the following paragraphs.

We used similar initial conditions, however, our population dust particles coming from OCCs was four-times larger than the original one. Figs. 2.22 and 2.23 show distributions of orbital elements and radiant positions for OCCs particles as seen by a radar similar to AMOR with $I_\star = 0.01$ for particle diameter $D = 100$ μm, and $D = 400$ μm, respectively. We take into account only meteors populating the north/south apex source, while the contributions to other regions are omitted[3]. The distribution of geocentric impact speed v_g is dominated by faster meteors with a negligible contribution of slow meteors.

[3]In fact, OCC particles populate also the ring structure, and have a negligible contribution to the helion/anti-helion source and north/south toroidal source. However, the overall flux is dominated by apex meteors.n

We see that 100 μm particles are able to decrease their semimajor axis to very low values, and the majority of them are near $a \sim 1$ au. For particles with $D = 100$ μm the eccentricity distribution is puzzling. Interestingly, the particles tend to be less eccentric, similarly to those in the original model with the peak near $e = 0.3$ (Fig. 8 in paper C), however, our new simulation suggests a lack of highly eccentric meteors near $e \sim 1$. Inclination distribution looks really promising, since it is dominated by retrograde meteors. Larger particles, with $D = 400$ μm, have eccentricity distribution more similar to particles observed by AMOR (Fig. 2.23). Inclinations are dominantly retrograde with a negligible fraction of prograde meteors, however, still not perfectly matching the observed distributions having peak at $\sim 120°$, while the AMOR meteors are concentrated close to $I \sim 150°$. An anomalously high contribution to one of bins (top and bottom right panels in Fig. 2.23) is caused by a single particle with a very high collisional probability with the Earth that remained on the similar orbit for many time steps in the simulation. Statistical significance of such effect may be decreased by increasing the total number of simulated particles, or by a removal of that particles from the processed population.

Radar similar to CMOR with $I_\star = 1$ detects only a negligible fraction of particles with $D = 100$ μm, thus we investigate modeled distributions of orbital elements and radiants for particles with $D = 400$ μm (Figs. 2.24), and $D = 800$ μm (2.25). The distributions are overall very similar to each other, and also to distributions of $D = 400$ μm particles measured by a radar similar to AMOR. Meteors produced by larger particles tend to be more eccentric, and impact with larger v_g, due to the longer P-R drag timescales, and also their ability to overcome Jupiter's barrier decreases with size.

These first results very promising results and provide smoother distributions of orbital elements than those published in paper C due to the increased statistics. However, many weeks of further work lie ahead of us. To develop a plausible two-component model combining contributions of particles from HTCs and OCCs, we need to fit both observations from AMOR[4] and CMOR, find a reasonable ratio between HTC and OCC dust production rates, and obtain a physically acceptable size-frequency distributions for both HTCs and OCCs. Our modeling efforts are at the very beginning, thus a more detailed study is left for future work.

[4]We are in a process of obtaining the raw data from AMOR since the published data (Galligan and Baggaley, 2004, 2005) do not provide any absolute numbers.

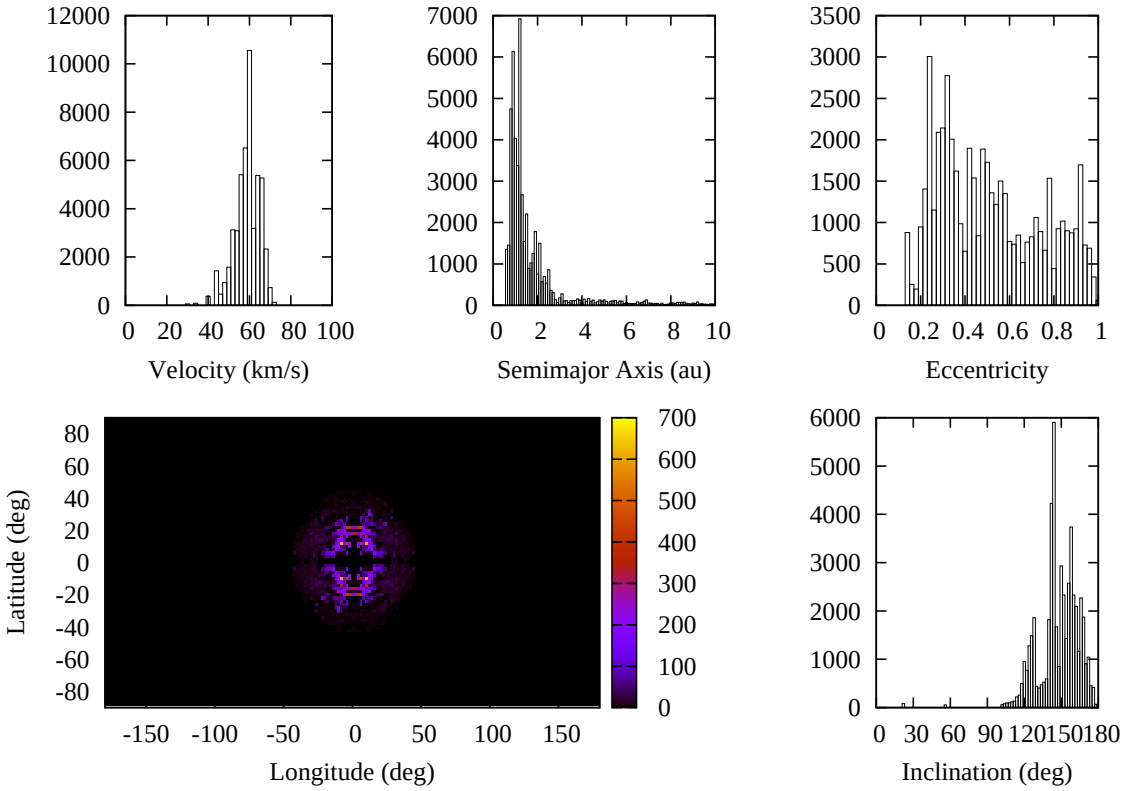

Figure 2.22: Distribution of geocentric impact speed (top left), heliocentric semimajor axis (top middle), eccentricity (top right), inclination (bottom left), and radiant positions (bottom left) of modeled dust particles from Oort Cloud comets with $D = 100$ μm measured by radar with detection threshold similar to AMOR $I_\star = 0.01$ in the north apex region only.

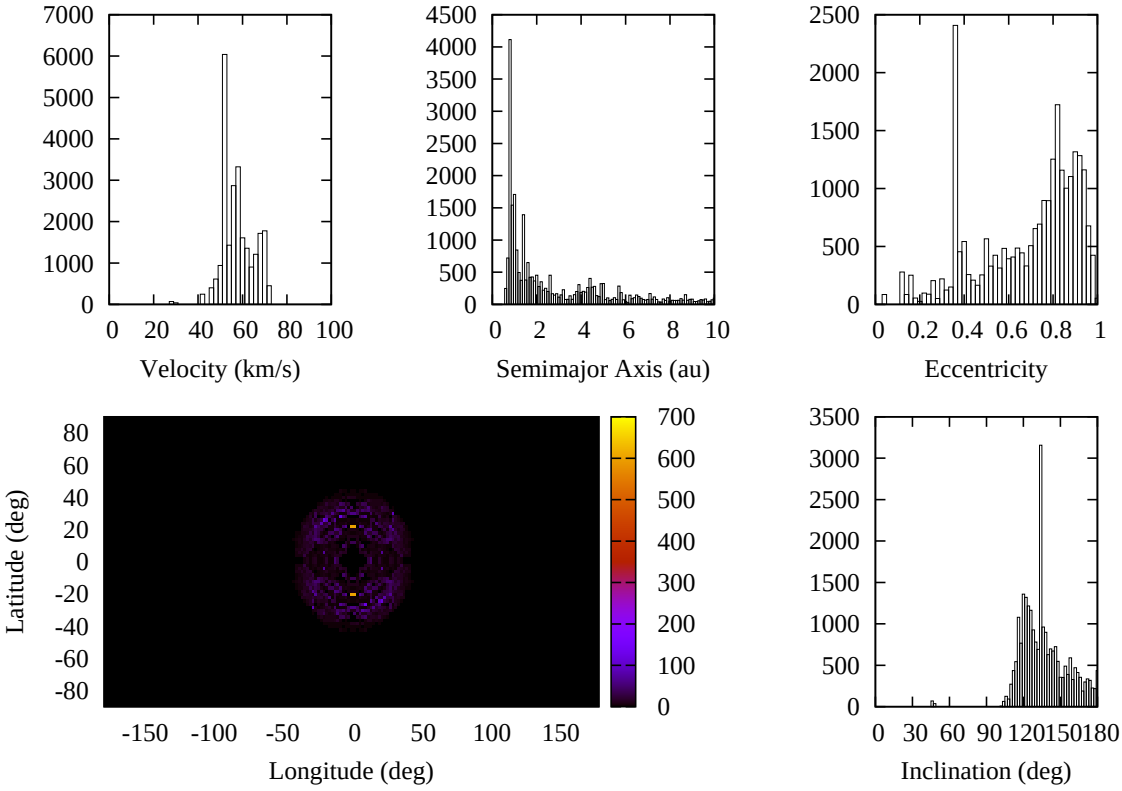

Figure 2.23: The same as in Fig. 2.22 but now for particles with $D = 400$ μm.

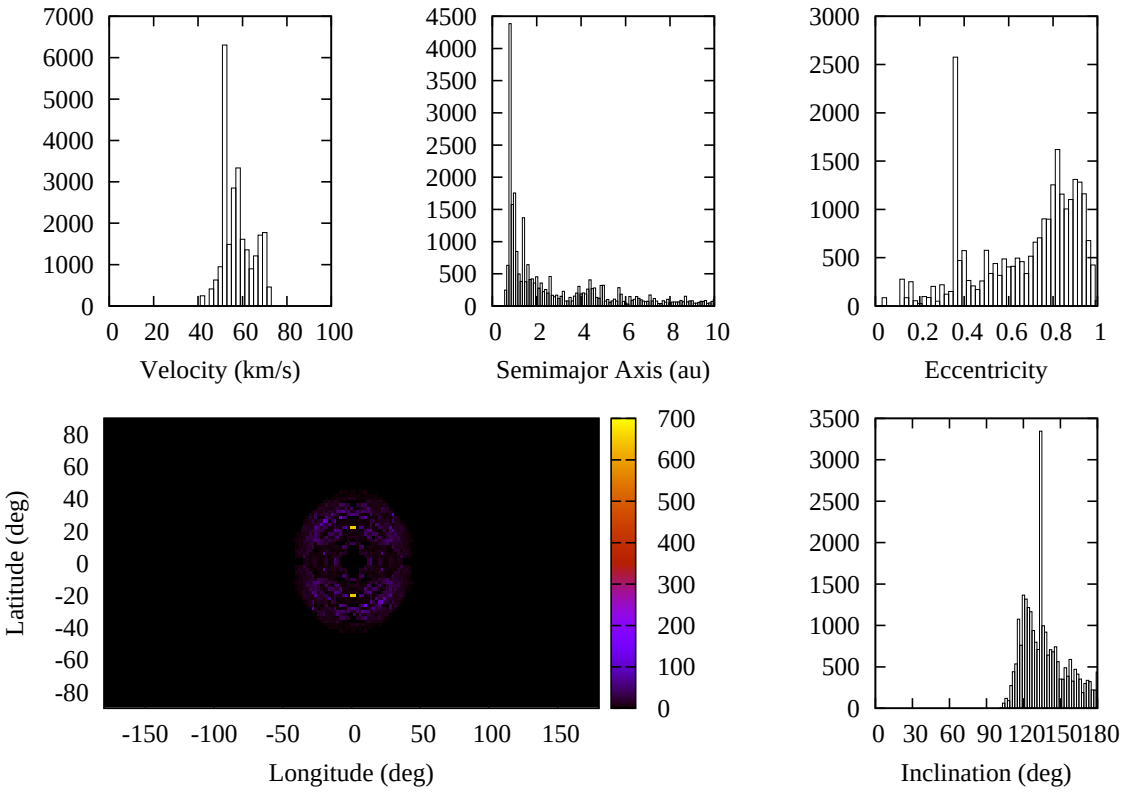

Figure 2.24: The same as in Fig. 2.22 but now for particles with $D = 400$ μm and radar with detection threshold similar to CMOR $I_\star = 1$

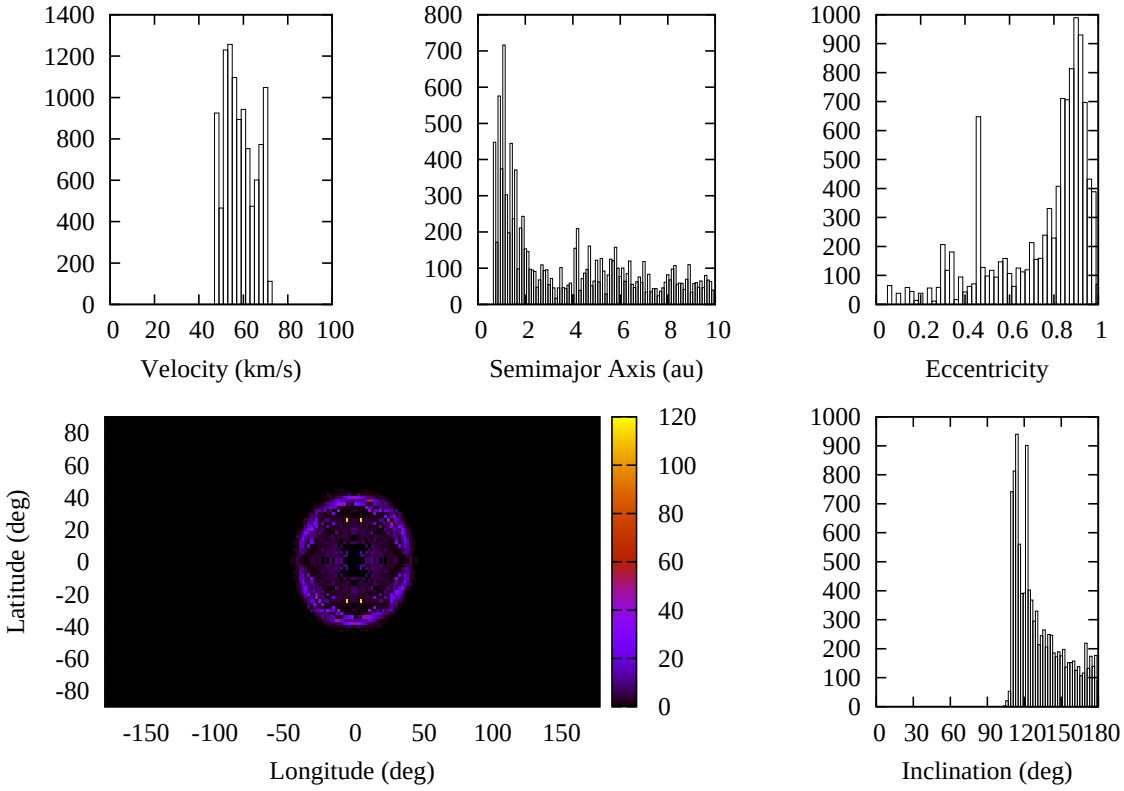

Figure 2.25: The same as in Fig. 2.24 but now for particles with $D = 800$ μm.

2.9 Helion/anti-helion source - data

Helion/anti-helion sources are the prolific components of the sporadic meteoroid complex. First, recognized by Hawkins (1956) using the Jordell Bank meteor-radar system, and later supported by visual observations of strong anti-helion component by Hawkins and Prentice (1957).[5] Helion and anti-helion sources are located near ecliptic approximately 60° in longitudinal distance from the apex (see Fig. 2.2 and Sec. 2.1 for more detailed definition). CMOR observed 451130 meteors in 2012 in both helion and anti-helion sources, which is more than 34.4% of the total amount of all observed meteors in 2012.

Helion/anti-helion sporadic meteors have systematically lower geocentric impact velocities v_g than the apex meteors. Measured v_g distribution peaks at $v \simeq 30$ km s^{-1}, and has almost a Gaussian shape (Fig. 2.26). The semimajor axis peaks at $a \sim 1$ au with a tail beyond 3 au. Helion/anti-helion meteors are known for their low orbital inclinations, where the majority of meteors have $I < 30°$, while eccentricities are dominantly larger $e > 0.7$. The generating population, however, reveals several interesting facts. At least a fraction of helion/anti-helion meteors is retrograde, due to the large $a \geq 8$ au some meteors originate in long-period comets, which is also reflected in extreme values of e, and higher geocentric impact velocities. This might lead us to a preliminary conclusion, that the helion/anti-helion source is populated by at least two different populations of comets, where the majority of meteors come from the short period comets with low inclinations, and the rest is fed by long-period comets, where some of them are on retrograde orbits. Fortunately, Jupiter-family comets and Halley-type comets, one of the most prolific sources of dust in the Solar System, greatly fit into these sought categories, and thus were the first candidates for the parent bodies of the helion/anti-helion source in paper D reviewed in Sec. 2.10.

Variation of number of observed meteors with solar longitude λ is almost constant during the whole year for the helion/anti-helion source, disturbed only by three non-sporadic structures (Fig. 2.27). The first peak at $\lambda \sim 86°$ is associated with Daytime lambda Taurids (DLT) stream, and since its width in λ is about 30°, it must be a result of an event several hundred years old. Brown et al. (2008) suggested, that this stream-like structure was associated with a comet C/1733 K1 which had been observed in 1733 by Dutch and Swedish sailors in the vicinity of the Cape of Good Hope (Koninckx et al., 1995). There is also contribution of the Daytime Arietids (ARI) stream that is associated with a comet SOHO - 2002 R4 (Brown et al., 2008), a sungrazing comet belonging to the Kracht group. The second peak at $\lambda \sim 126°$ is mostly populated by Southern delta Aquariids (SDA) stream. (Brown et al., 2008, 2010) found various sungrazing comets as the parent bodies of this stream. Interestingly, many sungrazing comets are influenced by the Kozai resonance, which significantly changes their orbital elements in time, and subsequently their radiant positions that follow a ring structure with radius $\sim 60°$ with a center at the apex. Radiants of such bodies may, in several thousands years, move from the helion/anti-helion source to the north/south toroidal source (see, e.g., Fig. 3 in paper A). The last peak at $\lambda \sim 261°$ is a remnant of the Geminids streams (GEM) associated with the minor planet 3200 Phaethon (Jenniskens, 2006; Brown et al., 2008).

Figs. 2.28 and 2.29 further confirm our stream recognition. The Geminids are the most prominent structure in both Figs. 2.28 and 2.29, pointing directly at 3200 Phaethon as the

[5] Visual systems are not able to observe the helion source because it is observable only during daytime, and thus the Sun disallows measurements in optical wavelengths.

possible parent body of the stream. Both DLT and ARI streams are convincingly products of cometary activity or breakups of sungrazing comets. Their extreme eccentricities drive these parent bodies to orbits with perihelia very close to the Sun, thus continuous erosion process, fragmentation, and sublimation of the cometary material, allow these comets survive only several passages through perihelion, and thus the original parent bodies of these structures are not observable today (Sekanina, 2003; Knight et al., 2010).

Interestingly, correlations among orbital elements for helion/anti-helion meteors for observed meteors are not completely different from the generating population (Figs. 2.30 and 2.31). There is a shift towards larger values of a and to extreme values of e due to their strong effect on the value of collisional probability P_{coll}, however, overall image remains the same. Helion/anti-helion source is dominated by highly eccentric low inclined meteors with orbits dominated by Jupiter. Generating population reveals a small fraction of retrograde particles with very high eccentricities and significantly larger semimajor axes than their prograde counterparts. This indicates that the helion/anti-helion source is populated by a combination of two different sources of dust particles, where the most of them originate in Jupiter-family comets and the rest is fed by Halley-type comets. Our model for helion/anti-helion source is reviewed in the following section.

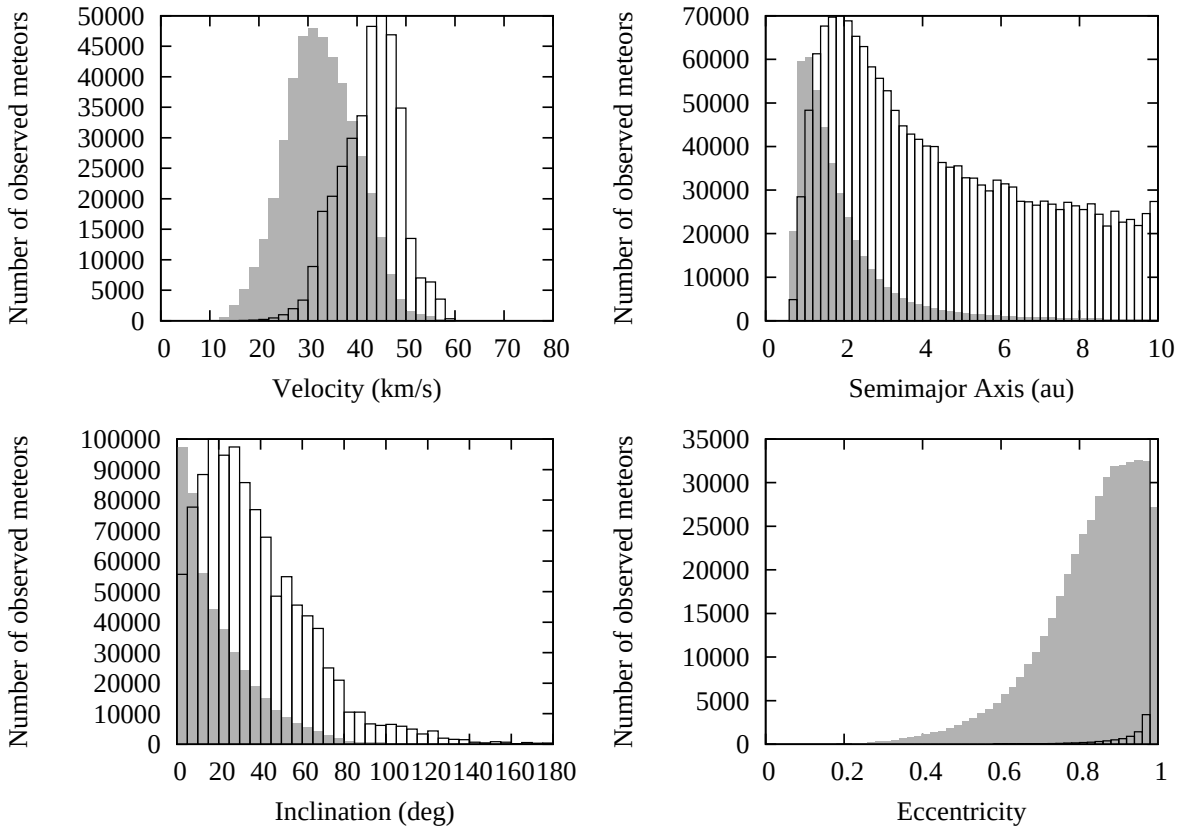

Figure 2.26: The same as in Fig. 2.7 but now for helion/anti-helion meteors only.

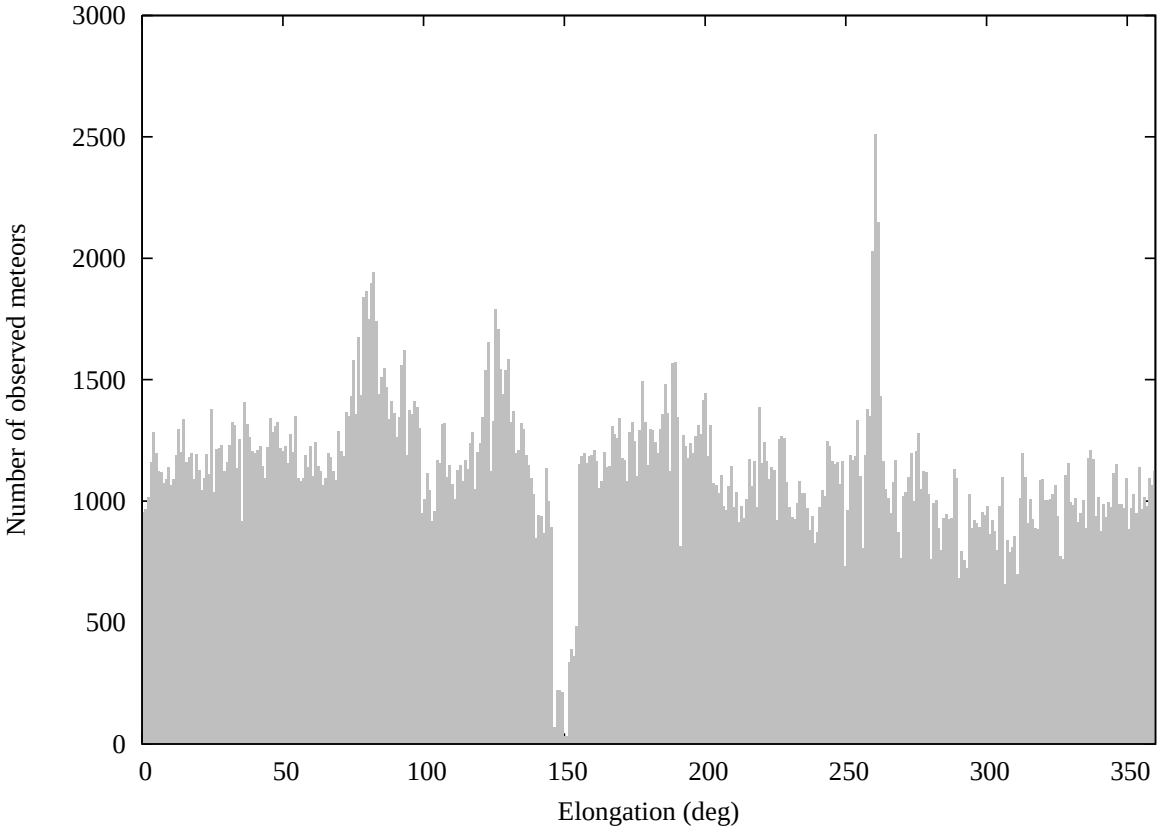

Figure 2.27: The same as in Fig. 2.10 but now for helion/anti-helion meteors only.

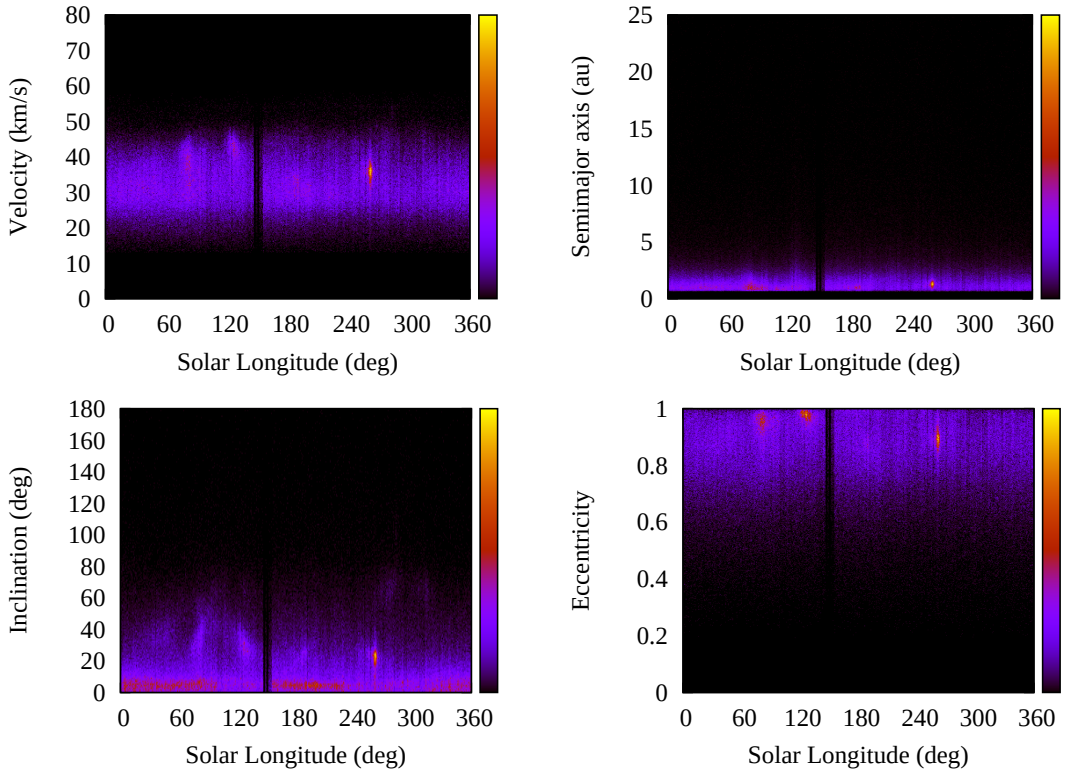

Figure 2.28: The same as in Fig. 2.11 but now for helion/anti-helion meteors only.

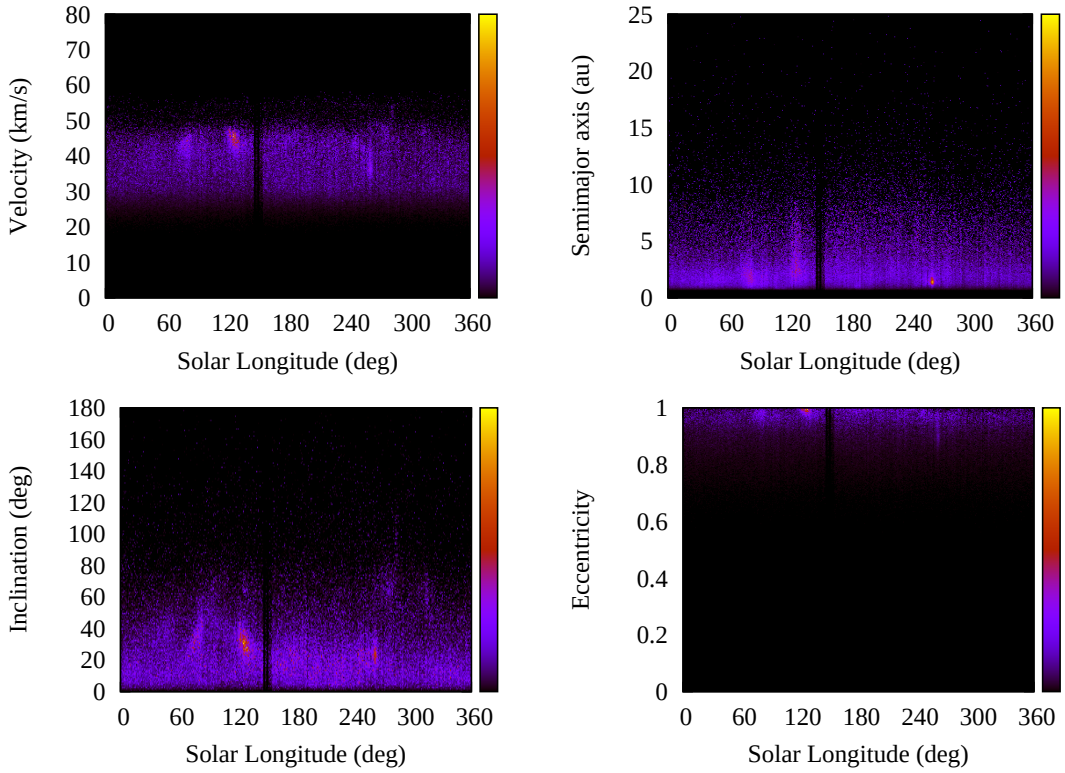

Figure 2.29: The same as in Fig. 2.12 but now for helion/anti-helion meteors only.

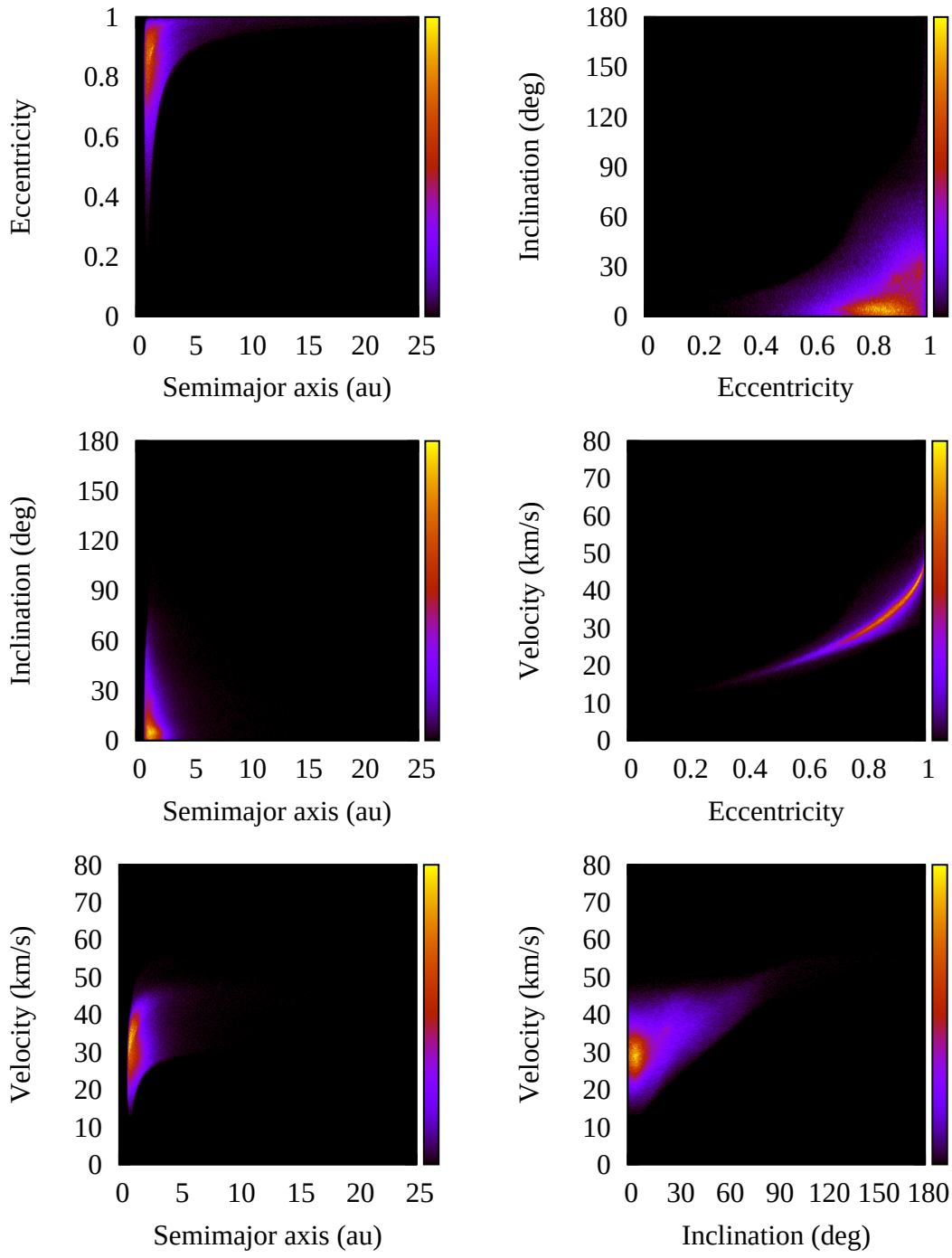

Figure 2.30: The same as in Fig. 2.8 but now for helion/anti-helion meteors only.

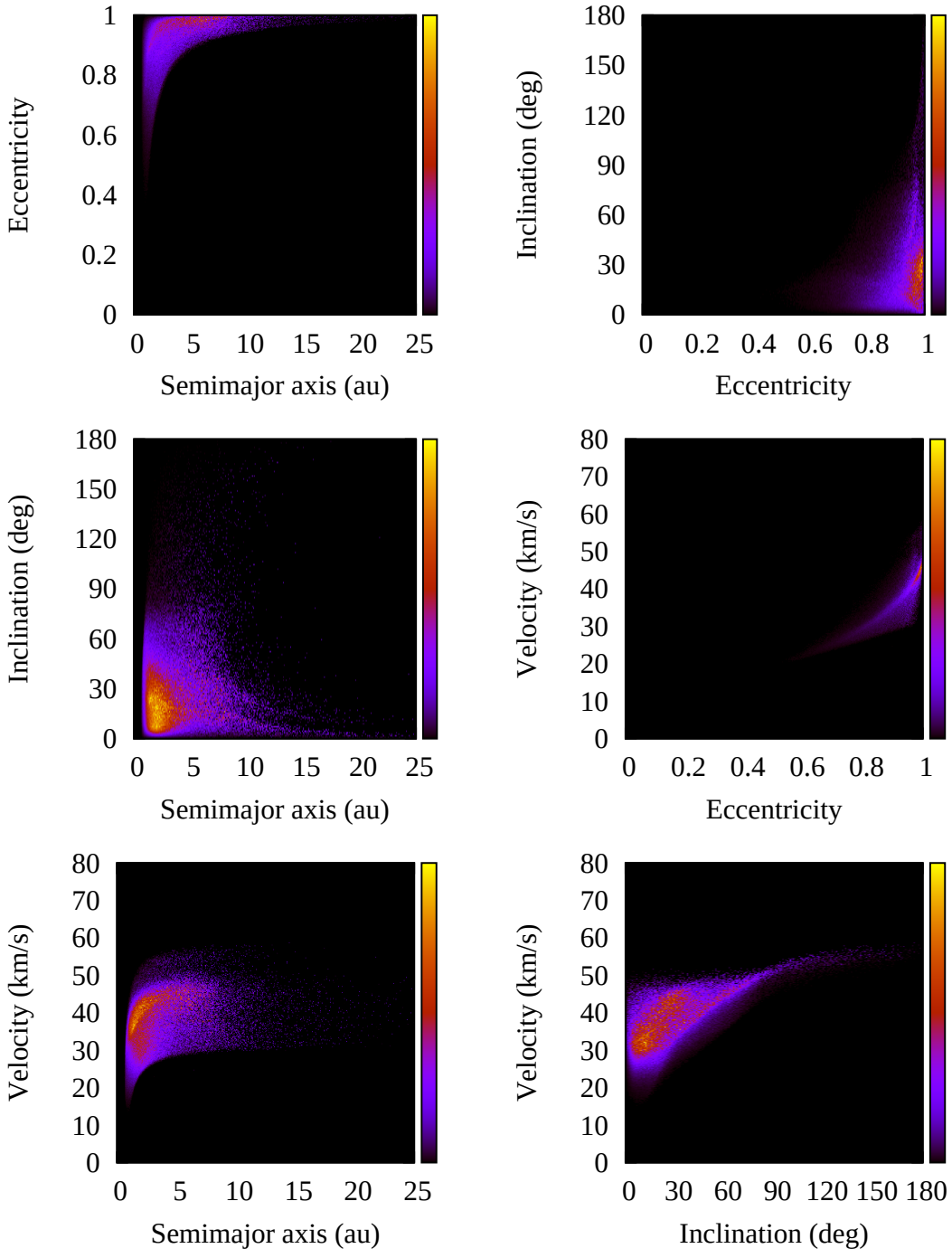

Figure 2.31: The same as in Fig. 2.9 but now for helion/anti-helion meteors only.

2.10 Helion/anti-helion source - model - short review - paper D - Dynamical Model for the Zodiacal Cloud and Sporadic Meteors

Here, we review a our dynamical model for the zodiacal cloud and Solar System meteoroids producing sporadic meteors belonging mainly to the helion/anti-helion source presented in paper D (Nesvorný et al., 2011b). Our model takes Jupiter Family Comets (JFCs) as the main source of the helion/anti-helion sources in the sporadic meteoroid complex. Using *IRAS* observations, we are able to accurately calibrate our model, find the total cross section, and mass of meteoroids in the inner Solar System. We are also able to predict mass influx onto the Earth, which is compared with *LDEF* measurements. y The zodiacal cloud (ZC) is a doughnut-shaped structure in the inner parts of the Solar System populated by small meteoroids produced by asteroid collisions and cometary activity. Nesvorný et al. (2010) developed a dynamical model for particle populations released by asteroids and comets, and used this model to determine the ratio between asteroid and cometary contribution to the ZC meteoroids. They found that the asteroidal particles represent only a small fraction of the the total population of ZC, because the mid-infrared (MIR) emission from asteroidal particles, produced by mutual collision in the asteroid belt, is mostly confined to within latitudes $b \lesssim 30^\circ$ of the ecliptic. However, the ZC has a very broad latitudinal distribution of the thermal emission, where a strong emission is also measured in the direction to the ecliptic poles (Kelsall et al., 1998).

This model proposed that $\gtrsim$ 90% of the ZC's emission at MIR wavelengths comes from dust grains released from JFCs, and the rest comes from other prolific sources of dust particles in the Solar System, the HTCs, OCCs, and asteroidal collisions. Moreover, Nesvorný et al. (2010) also found, that the mass input required to keep the ZC in a steady state exceeds the mass loss in JFCs due to their normal cometary activity (Reach et al., 2007), which may be solved by feeding the dominant mass fraction needed for the steady state of the ZC by spontaneous disruptions or fragmentation of JFCs (e.g., Fernández, 2005; Di Sisto et al., 2009).

The model presented by Nesvorný et al. (2010) seems almost perfect, however, when compared with the radar observations of the sporadic meteoroid background performed by AMOR and CMOR, the model cannot fit measured distributions of orbital elements of sporadic meteors. Thus, we tune the JFCs model with additional constrains introduced by the radar meteor observations. Still, the dominant mass of the ZC is produced by JFCs, however, we include perihelion dependent meteoroid production rate, and the different detection efficiency of the radar systems. These additional constrains allow us to consider a continuous size-frequency distribution (SFD) of meteoroids, and also more precise parametrization of the collisional timescales of the meteoroids in the Solar System.

The modeling phase is very similar to that presented in paper C (Sec. 2.8). Additionally, since the mass and cross section of meteoroids from JFCs dominate the ZC, we calibrate our model using the observations at MIR wavelengths. The model also shows that the accretion rate of the JFC meteoroids at Earth dominates the mass influx measured by *LDEF*, which provides us another constraint for the model calibration.

The orbital distribution of initial orbits of JFCs was taken from Levison and Duncan (1997), who followed the orbital evolution of icy bodies originating in the Kuiper belt from their initial scattering by ice giants, until they evolved into the inner Solar System. We used 10 values of critical perihelion distance $q^\star$, equally spaced between 0.25 au and

2.5 au, to select bodies from the simulations of Levison and Duncan (1997), where we selected bodies when they perihelion distance $q < q^\star$ for the first time. We also use six different sizes of particles in our model with $D = 10, 30, 100, 300, 1000$ and 3000 μm, and with constant particle density $\rho = 2$ g cm^{-3}. This size range covers the majority of the observed meteors by both AMOR and CMOR, and also allows us to interpolate a behavior of particles with intermediate diameters because the orbital dynamics of, let us say, $D = 400$ μm dust particle is very similar to that of $D = 300$ μm particle. Since the dynamics of the dust particles (see Sec. 2.2) depends on the mass of the particles, density variations would only result in the shift in D of the particles. For each $q^\star$ and D we released 10000 particles, which is in total 0.6 million initial orbits.

The dust particles in our model were numerically integrated with `swift_rmvs3` code (Levison and Duncan, 1994), where the effects of radiation pressure and P-R drag were taken into account (see Sec. 2.4). We used a system with seven planets, where the mass of Mercury was added to the Sun, and particles were tracked until their heliocentric distance reached 0.05 au, or the integration time reached 5 Myr. Every 1000 yr we recorded the orbits of both particles and planets.

In Nesvorný et al. (2010) the source particle distributions were parametrized by the "fading time", particle production rate was assumed to be q-independent, and the distribution of the diameters in the population $dN(D)$ was approximated by single size. In our model, we consider that both $dN(q)$ and $dN(D)$ can be approximated by power-law functions. Thus, we introduce four new free parameters. For $dN(q)$, we assume $dN(q) \propto q^\gamma dq$, where γ is a free parameter. For $dN(D)$, we use two-slope SFD[6] with $dN(D) \propto D^{-\alpha_1}$ for $D < D^\star$, and $dN(D) \propto D^{-\alpha_2}$ for $D > D^\star$, where α_1, α_2 and $D^\star$ are free parameters.[7]

Collisional lifetimes of meteoroids $\tau_{\rm coll}$ were taken from Grün et al. (1985). Since the model of Grün et al. (1985) may contain some uncertainties, we introduce a free parameter S, so that $\tau_{\rm coll} = S\tau^\star_{\rm coll}$, where $\tau^\star_{\rm coll}$ is the collisional lifetime from Grün et al. (1985), to test the validity of the collisional model. This allows us to keep meteoroids in our simulation longer, and thus provide them enough time for their dynamical evolution towards the inner parts of the Solar System. See also Sec. 2.3 for further details and another method of determination of $\tau_{\rm coll}$.

Our steady-state model is tested in two different ways. First, we compare MIR emission of the modeled meteoroids with *IRAS* observations, and second, we record impacting particles on the Earth, determine their geocentric impact velocities and orbital elements, and compare them with available data from AMOR and CMOR. All these processes are described in Sec. 2.4, and references therein.

We performed hundreds of tests with different values of free parameters introduced to our model. The main parameters of these tests were: (1) size frequency distribution of JFC particles at the source, as defined by α_1, α_2, and $D^\star$, (2) index γ of the initial perihelion distribution of JFCs, $dN(q) \propto q^\gamma dq$, and (3) parameter S that adjusts the value of collisional lifetime of particles $\tau_{\rm coll}$. Our model was then compared with meteor observations of two radar systems AMOR and CMOR, where we tested different ionization cutoff values for AMOR, while for CMOR we used $I_\star = 1$.

[6] We may also use a single-slope power-law SFD by setting $\alpha_1 = \alpha_2$.

[7] See Eqs. (5)-(10) in paper E (Pokorný et al., 2014) for a detailed definition of the two-slope size frequency distribution.

AMOR

Galligan and Baggaley (2004) states that the limiting diameter of meteor observed by AMOR is roughly $D \sim 40$ μm, and thus the radar is capable of detecting particles that are thought to be dominant in the ZC. Fig. 4 in paper D shows distributions of v_g, a, e, I of JFC meteoroids for $D^\star = 100$ μm, $\gamma = 0, S = 1$, and several values of $I_\star$. The real distribution of particles impacting the Earth is corresponding to $I_\star = 0$, where no cutoff is applied on impact velocity or mass. This distribution is strongly peaked towards Earth's escape speed and is completely different from AMOR and CMOR observations. We assume that $I_\star = 0.003$ is roughly the limiting ionization cutoff of AMOR, for which we obtained velocity distribution with maximum at $v_g \sim 25$ km s^{-1}. This illustrates that only a small fraction of dominating mass is, in fact, detected by radar systems and the real distribution of orbits is very different from the observed one. We, thus, cannot reconstruct the real distribution of meteoroids at 1 au directly from the observations without an important contribution of dynamical modeling of meteoroids.

In similar fashion, the orbits of meteors with no cutoff applied and those observed by radars are very different. Since the geocentric impact speed distribution peaks near $v_g \sim 11.2$ for $I_\star = 0$, orbital elements of such meteors have consequently mostly very small e, and I, and are strongly concentrated near $a = 1$ au. However, AMOR sees completely different image, where the distribution of a is much broader with a tail to larger values of a, eccentricity distribution has maximum at $e \sim 0.8$, and also I distribution is significantly broader.

Interestingly, almost all JFC meteors with $I > I_\star = 0.003$ populate exclusively helion/anti-helion source, while meteors without any mass cutoff, $I_\star = 0$, populate a broad range of radiant positions (Fig. 11 in paper D). Thus, the effect of radiant cutoff for helion/anti-helion source only has a negligible effect for $I_\star = 0.003$ (Fig. 5 in paper D). We also find that our model for $I_\star = 0.003$ shows only a small sensitivity for variation of parameter γ (Fig. 6 in paper D). Effect of variation of $D^\star$ is illustrated in Fig. 7 in paper D. Since we usually use a steeper slope for particles with $D > D^\star$, and a shallower slope for $D < D^\star$, the majority of particles is concentrated near $D^\star$. Thus, for larger particles with $D^\star = 300$ μm slower particles are detected, moving the maximum of v_g towards 20 km s^{-1}, while for smaller particles with $D^\star = 30$ μm the v_g maximum moves up to 40 km s^{-1}, which consequently shifts distribution of eccentricities towards higher values.

We obtain two preferred solutions for AMOR, where both of them have essentially unconstrained values of γ and S. The first solution with $D^\star = 50$ μm, $\alpha_1 = 2$ and $\alpha_2 = 3.5$, better corresponds with impact experiments from Mathews et al. (2001), while the second solution with $D^\star = 200$ μm, $\alpha_1 = 3.5$ and $\alpha_2 = 5$, is closer to the original interpretation of spacecraft impact experiments (Grün et al., 1985; Love and Brownlee, 1993). Fig. 10 in paper D represents our preferred model with $D^\star = 200$ μm. The overall match between model and AMOR observations is good, however, our model cannot reproduce meteors with larger inclinations. We may thus miss a contribution from another prolific source of dust particles. In Sec. 2.12 and paper E, we show that Halley-type comets contribute to helion/anti-helion source, and, thus, may be a solution for a missing part of meteors with large inclinations in our model.

CMOR

As we mentioned before, CMOR with $I_\star = 1$ has the lower overall sensitivity than AMOR, and is not able to detect particles with $D < 200$ μm coming from helion/anti-helion source.

Thus, we deal with larger particles with longer dynamical decay times $\tau_{\rm PR}$, which makes them more vulnerable to collisions with other particles. Using the model of Grün et al. (1985) with $S = 1$ gives results that are at odds with observations of both AMOR and CMOR (Fig. 12 in paper D). The major drawback is a lack of meteors with $e < 0.6$, and also the distribution of semimajor axes a, where we observe a plateau in $a = 1 - 3$ au region. We find that this problem can be resolved by taking significantly longer collisional lifetimes ($S \gtrsim 30$) than those in Grün et al. (1985) (Fig. 13 in paper D). Longer $\tau_{\rm coll}$ allows the larger particles to undergo a larger decay in a, and e, due to the P-R drag, and reach $a \sim 1$ au. On the other hand, our previous models for AMOR do not match the measurements well for $S \gtrsim 30$. This implies that the size dependence of the Grün et al. (1985) model may be incorrect.

Since both values of critical diameter of particles $D^\star = 50$ μm and $D^\star = 200$ μm are beyond CMOR's detection range, we fit only parameter α_2. We find that our model for JFC particles works best with $\alpha_2 = 2$, and $S = 100$ (Fig. 14 in paper D), where we were able to fit data for helion/anti-helion source, and also data without radiant cutoff. We recall, that fitted distributions were corrected for observing biases and mass weighted, thus emphasizing meteors with larger sizes. Our model for helion/anti-helion source has the v_g maximum at 30 km s^{-1}, orbits are concentrated at $a = 1$ au with a tail towards $a = 3$ au, inclinations are still dominated by meteors with $I < 30°$, and eccentricities are rather high with maximum at $e = 0.85$. Radiant distributions of our preferred model for $I_\star = 1$ have dominant concentrations in helion/anti-helion sources, and, interestingly, we also observe a small contribution to apex source (Fig. 15 in paper D). The apex meteors produced by our model have prograde orbits, low impact velocities, and very low a. These impacts happen near the aphelion at 1 au, where the orbital speed of meteoroid is smaller than the Earth's orbital velocity. Only a small fraction ($< 1\%$) of JFC meteoroids can reach retrograde orbits.

IRAS

Next constrains for our model are MIR fluxes of the ZC observed by *IRAS*. The ZC is almost certainly a mixture of several meteoroid populations, with a fractional contribution from asteroids and long-period comets, but, here, we present only MIR emission from the JFC component of the ZC. Our best fits to *IRAS* observations are therefore only approximate and could be modified if missing components of the ZC population are considered.

In general, the model MIR profiles are rather insensitive to variations of free parameters in our models. The ZC emission is dominated by particles with $D < 200$ μm that can survive long enough to experience substantial decrease of a, and e, due to the PR drag, even for $S = 1$. Also variations of the input SFD of the JFC particles have negligible effect. The most of the MIR emission is provided by smaller particles, where all these particles have roughly similar orbital histories, thus produce similar MIR profiles. The model MIR profiles of our solution for AMOR with $D^\star = 100$ μm, $\alpha_1 = 2$, $\alpha_2 = 5$, $\gamma = 0$, and $S = 1$, are slightly narrower than the observed ones, but otherwise the agreement is reasonably good (Fig. 16 in paper D). We estimate that a small, $\lesssim 10\%$, contribution for a source with a more isotropic distribution of inclinations, such as HTCs and/or OCCs, would easily compensate the small difference. With $\gamma < 0$ we can weight the distribution of JFCs toward lower heliocentric distances, which results in a projection to a wider range of ecliptic latitudes, when observed from 1 au. Contrariwise, choosing positive γ leads to narrower MIR emission due to the larger weight of particles with larger heliocentric

distances. Our best match was achieved with $\gamma = -1.3$ (Fig. 17 in paper D).

One of the most desired characteristics of the model is the absolute calibration of the number of particles. *IRAS* data allows us to estimate the total observable cross section $\sigma_{\rm ZC}$ of the ZC particles, which with known SFD and density of the particles is comparable with our model. Nesvorný et al. (2010) found $\sigma_{\rm ZC} = (2.0 \pm 0.5) \times 10^{11}$, while our models have a slightly wider spread with $1.7 \times 10^{11} < \sigma_{\rm ZC} < 3.4 \times 10^{11}$ km^2. Our reference models shown in Figs. 16 and 17 in paper D, however, provide the same result as Nesvorný et al. (2010). Mass of the ZC $m_{\rm ZC}$ is more poorly constrained because of its strong dependency on the SFD (Table 1 in paper D). Our preferred model estimates $m_{\rm ZC} = 3.8 - 3.9 \times 10^{19}$ g, which roughly corresponds to a 33 km diameter sphere with $\rho = 2$ g cm^{-3}. Mass needed for keeping the ZC in the steady state is roughly proportional to $m_{\rm ZC}$, where we expect values between 3000 and 7000 kg s^{-1}. Our model implies that the total mass accreted by the Earth is (15000 ± 3000) tons yr^{-1}, which about two times lower than value found by Nesvorný et al. (2010).

Discussion and Conclusions

We find that meteor radars are not able to detect majority of the overall mass flux considering only constrain posed by ionization cutoff. There are also other observing biases that prevent radar systems to observe all particles even with $I > I_\star$ (see e.g., Campbell, 2002, Chap. 6). Thus, these systems are not suitable for estimating the overall accretion rate. Our model provides terrestrial accretion rate comparable to Love and Brownlee (1993), however, is inconsistent with Mathews et al. (2001).

To match the CMOR measurements in our model, we find $\tau_{\rm coll}$ needs to be significantly longer for $D \sim 1$ mm sized meteoroids than originally suggested by Grün et al. (1985). This results can be, however, difficult to reconcile with the inferred lifetimes of meteor streams that seem to disappear on much shorter timescales (less than a few thousand years; e.g., Jenniskens, 2008). The centimeter-sized meteoroids released from JFCs, which dominate the visual observations of meteor streams, may be physically weaker and disrupt in a few thousand years. The collisional cascade then produces millimeter-sized and smaller population, that is no longer observable by visual systems, and could be more resistant to collisions.

We show that the major problems of Nesvorný et al. (2010) can be resolved if (1) the Nesvorný et al. (2010) model is modified to account for the detection efficiency of meteor radars, (2) meteoroids are released from JFCs over a range of perihelion distances with at least a fraction initially having $q < 1$ au, and (3) the collisional lifetimes for millimeter-sized meteoroids are significantly longer ($\gtrsim 30$) than those estimated by Grün et al. (1985).

Significantly longer collisional lifetimes are, however, incompatible with dynamics of $D \sim 100$ μm meteoroids observed by AMOR. We suggest, that $D \sim 100$ μm and $D \sim 1$ mm meteoroids may have more comparable collisional lifetimes than though before. This may suggest that the observed SFD shape from the spacecraft measurements may be more closely related to the initial SFD of meteoroids at source.

We show that our model is able to match *IRAS* observations of the ZC. We estimate that the cross section and mass of the ZC are $\sigma_{\rm ZC} = (1.7 - 3.4) \times 10^{11}$ km^2 and $m_{\rm ZC} \sim 4 \times 10^{19}$ g. The terrestrial accretion rate of JFC particles is ~ 15000 tons yr^{-1}. To keep the ZC in steady state JFCs must provide $10^3 - 10^4$ kg s^{-1}. This new input mass estimate is ~ 10 times larger than the one suggested by Nesvorný et al. (2010), because of shorter dynamical lifetimes of particles with low initial perihelion distances that need to be

resupplied at faster rates. We suggest that the ZC is dominated by the meteoroids released by disrupting/splitting JFCs, because the observed activity of JFCs cannot provide the needed mass input.

2.11 North/south toroidal source - data

The north toroidal source was first discovered by Hawkins (1962) as a concentration of low eccentricity, and high inclination orbits. Its southern counterpart was recognized after 30 years by Jones and Brown (1993), who surveyed data from the Adelaide meteor radar. Campbell-Brown (2008) in a more detailed study of the north toroidal source determined that CMOR observes $\sim 10\%$ of the total count of sporadic meteors in the north toroidal source, which is approximately two times more than result from a previous study of Brown and Jones (1995). The north toroidal source is located within an ellipse with center at $(0°, 55°)$ with semimajor axis equal to 28° and semiminor axis equal to 15°, while the south toroidal source is a symmetric counterpart of the north toroidal source with respect to the ecliptic plane (see Fig. 2.2 and Sec. 2.1,u for more detailed definition). The north toroidal source is known for its strong seasonal variations (Campbell-Brown and Wiegert, 2009), where several strong stream-like structures have yet to be recognized. CMOR observed 109459 meteors in 2012 in the north toroidal source, which is $\sim 8.4\%$ of the total amount of all observed meteors in 2012.

Meteors coming from the north toroidal source have almost Gaussian-shaped distribution of geocentric impact velocities v_g with peak at ~ 40 km s^{-1} ranging from 11.2 km s^{-1} to 60 km s^{-1} (grey histograms in Fig. 2.32). The semimajor axis distribution has similarly to other sources maximum at $a = 1$ au with a tail exceeding $a > 6$ au. The main characteristic of the north toroidal source is its very specific inclination distribution with a peak at $I \sim 70°$, and small fraction of retrograde orbits. Also, the eccentricity distribution is rather peculiar since the majority of meteor orbits have small eccentricities with maximum at $e \sim 0.3$, and with a decreasing abundance towards higher eccentricities. No potential group of parent bodies with orbital elements similar to the observed distributions of the north toroidal meteors is known in the Solar System, which implies a need of proper dynamical modeling of this peculiar concentration of meteors. Recall, that the bodies with $I > 39.2°$ undergo Kozai oscillations that may significantly change e, and I, in several thousands years (see Sec. 1.2).

The generating population is shifted towards higher v_g with the maximum at ~ 50 km s^{-1} (open histograms in Fig. 2.32). According to the distribution of semimajor axis of the generating population the majority of observed meteors in the north toroidal source originates in long-period comets. A contribution of particles with low inclinations is decreased due to their higher collisional probability with the Earth, and thus the inclination distribution of generating population moves to higher values with maximum at $I \sim 80°$. Interestingly, we see almost no contribution of particles with $e < 0.8$ to the generating population of the north toroidal source that is dominated by extremely eccentric orbits.

Fig. 2.33 shows the number of recorded north toroidal meteors in 2012 as a function of the solar longitude λ at time of their detection. Campbell-Brown and Wiegert (2009) studied extensively the temporal variations of the north toroidal source and provide a great reference for a more detailed description of the problem. The most prolific structures in Fig. 2.33 are two strong streams, namely: (1) Quadrantids at $\lambda \sim 283°$, and (2) θ and ξ Coronae Borealids at $\lambda \sim (285° - 300°)$, that were identified as sources H and I in

Campbell-Brown and Wiegert (2009), respectively. Next, we observe four broader, more dispersed, stream contributions as given in Campbell-Brown and Wiegert (2009), namely: (3) Helion and Antihelion arc and Toroidal at $\lambda \sim 17°$, (4) ψ Cassiopeids and α Lacertids at $\lambda \sim 115°$, (5) Toroidal A and B at $\lambda \sim 216°$, and (6) an underlying Quadrantids extension consisting of the November ι Draconids and December α Draconids, perhaps indicating an old stream complex related to activity of the comet 96P/Machholz (Brown et al., 2010). Perhaps a pure coincidence, however interestingly, (3) and (5) together with (4) and (6) may be actually organized in two pairs with longitude difference of $\sim (180° - 200°)$, which may point out that only two parent bodies are needed for an explanation of these contributions. The pair (4) and (6) have a likely progenitor in the activity of comet 96P/-Machholz several thousand years ago (e.g., Gonczi et al., 1992; Jones and Jones, 1993; Sekanina and Chodas, 2005; Kaňuchová and Neslušan, 2007). The pair (3) and (5) is much broader, indicating to longer dynamical age than previous pair, thus it is perhaps a result of a cometary splitting or disruption $\sim$ ten thousand years ago, since no potential parent body has not been found yet. North toroidal source is also composed of a significant background population that remains almost constant during the whole year implying that a large fraction of observed meteors experienced long dynamical evolution that led to a randomization of their nodes.

Quadrantids ($\lambda \sim 283°$) form a prominent concentration in I vs λ, and v_g vs λ plots (bottom panels in Fig. 2.34), however, interestingly there is no visible concentration in e. Even for generating population, we observe a broad range of eccentric orbits at the same λ as the Quadrantid stream, and a significant concentration is visible at $a \sim 3$ au revealing the comet 96P/Machholz as a possible parent body of this stream (top panels in Fig. 2.34). We are also able to distinguish the pair (4) and (6) that has slightly higher mean inclinations $I \sim 80°$ than Quadrantids, perhaps due to the longer dynamical lifetime of particles, and thus slightly different position in the Kozai cycle. This pair has also slightly smaller a than Quadrantids, which may be results of a small decrease due to the P-R drag. Identification of the second pair (3) and (5) is far more difficult, because no significant concentrations in semimajor axis distribution can be found. This might be a consequence of close encounters with Jupiter that dramatically change all orbital elements, and thus hide away traces leading to possible parent body.

Since the north toroidal meteors measured by CMOR are dominantly coming from low eccentric orbits the generating population is very different to the observed one (Figs. 2.36 and 2.37). Interestingly, CMOR observes no meteors with $e > 0.6$ for inclinations $I < 55°$, which may be a result of existence of two different groups of parent bodies populating the north toroidal source where the low inclined and low eccentric part is, however, only a small fraction of the total number of observed meteors. The generating population is almost exclusively composed from highly eccentric meteoroids with large inclinations favoring a cometary origin of observed meteors. Again, we observe a strong contribution of 96P/Machholz (e.g, middle left panel in Fig. 2.37), and also a significant contribution of long-period comets with inclinations at $I \sim 80°$.

We investigated contribution of Oort Cloud Comets in paper C, and contribution of Jupiter-family Comets in paper D, and none of them could explain the existence of the north toroidal source. This led us to reinvestigation of a contribution of Halley-type Comets (HTCs) to the sporadic meteoroid complex. Our first tests with HTCs were not promising, since the model distributions of orbital elements were completely different from the observed ones, and our tests with the comet 96P/Machholz were also unsuccessful mainly due to inability to circularize initially highly eccentric orbits $e \sim 0.95$

of meteoroids. However, after a proper understanding the north toroidal source and rigorous modeling we succeeded in a development of a plausible model for the background population of the north toroidal complex that is reviewed in the following section.

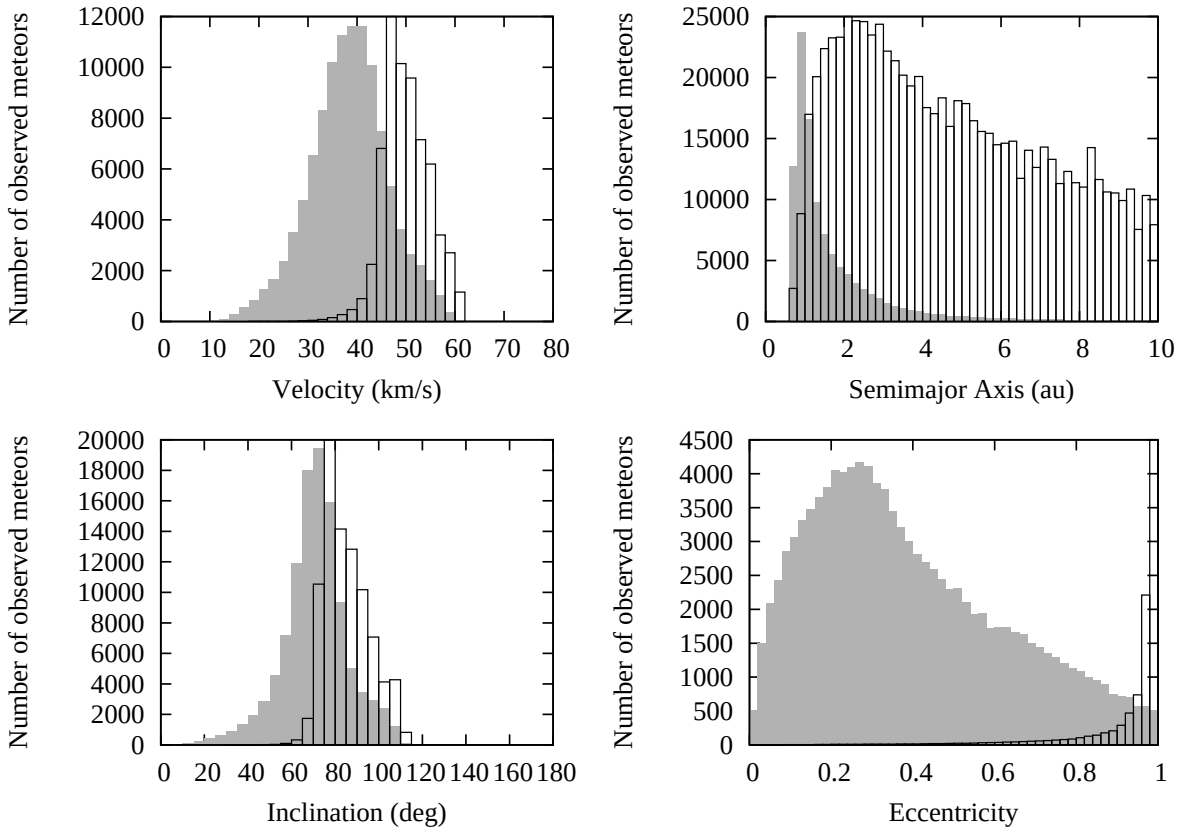

Figure 2.32: The same as in Fig. 2.7 but now for north toroidal meteors only.

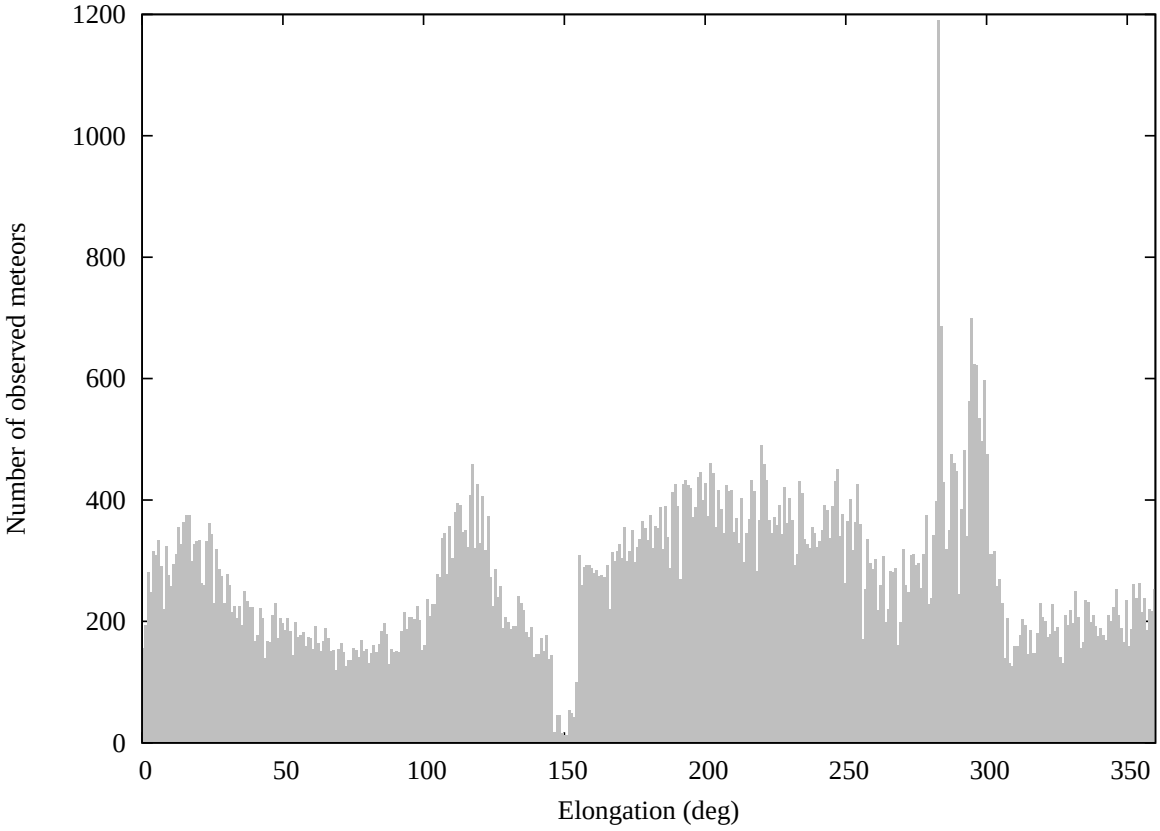

Figure 2.33: The same as in Fig. 2.10 but now for north toroidal meteors only.

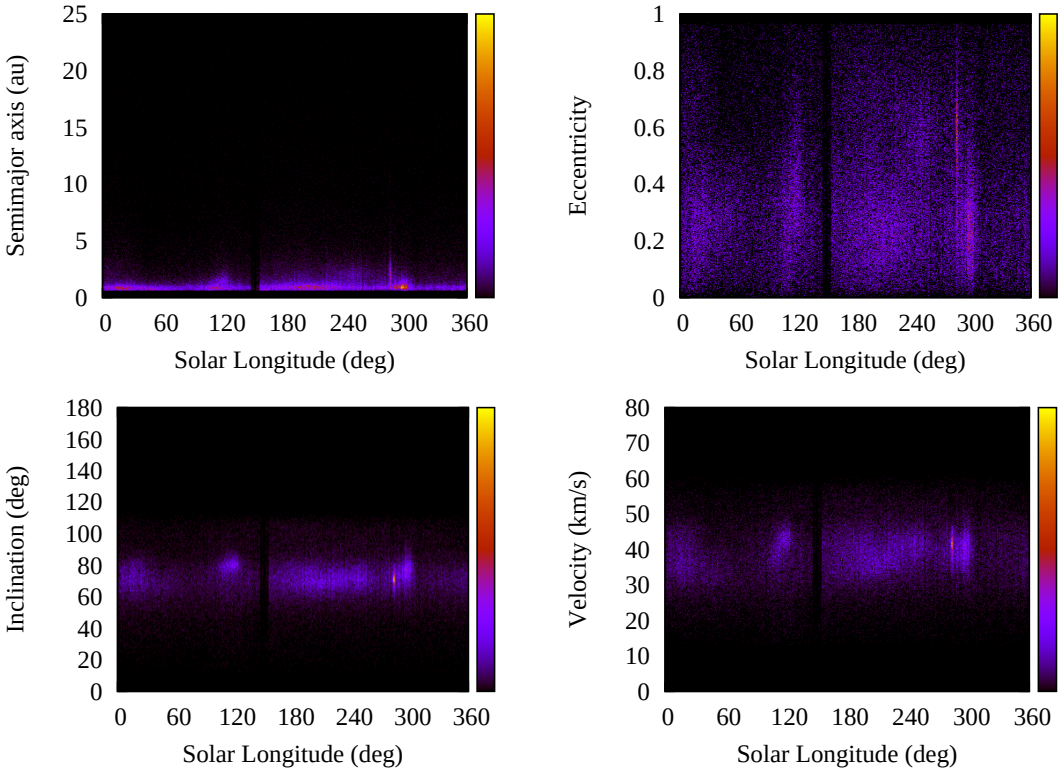

Figure 2.34: The same as in Fig. 2.11 but now for north toroidal meteors only.

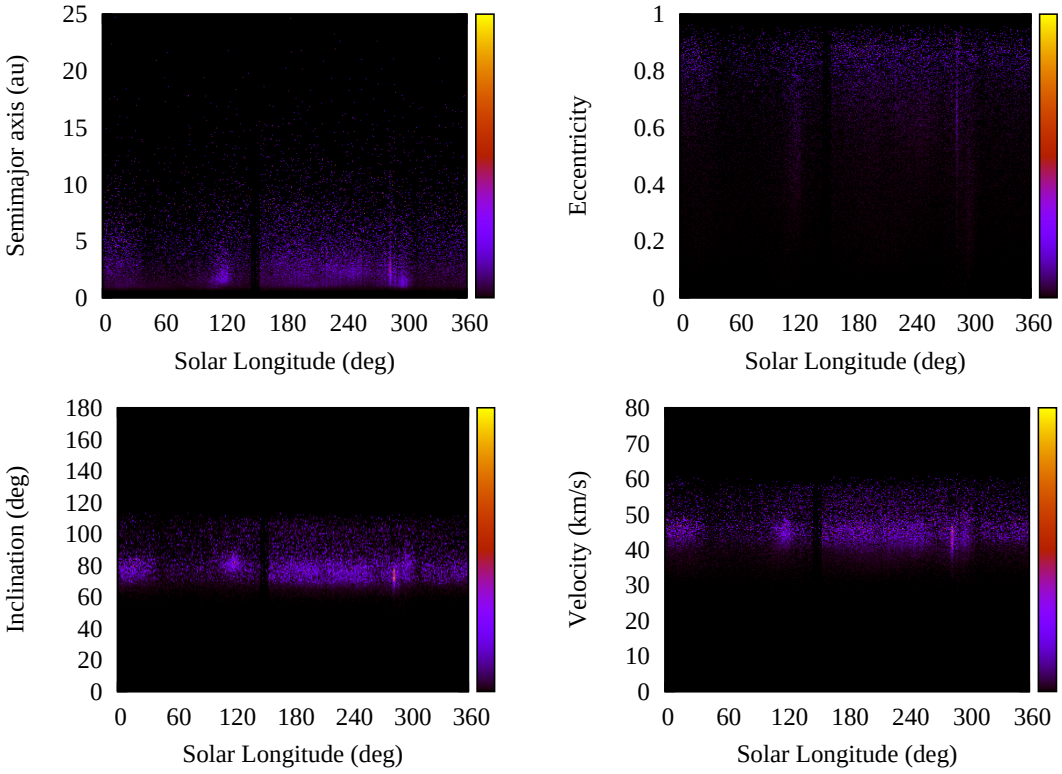

Figure 2.35: The same as in Fig. 2.12 but now for north toroidal meteors only.

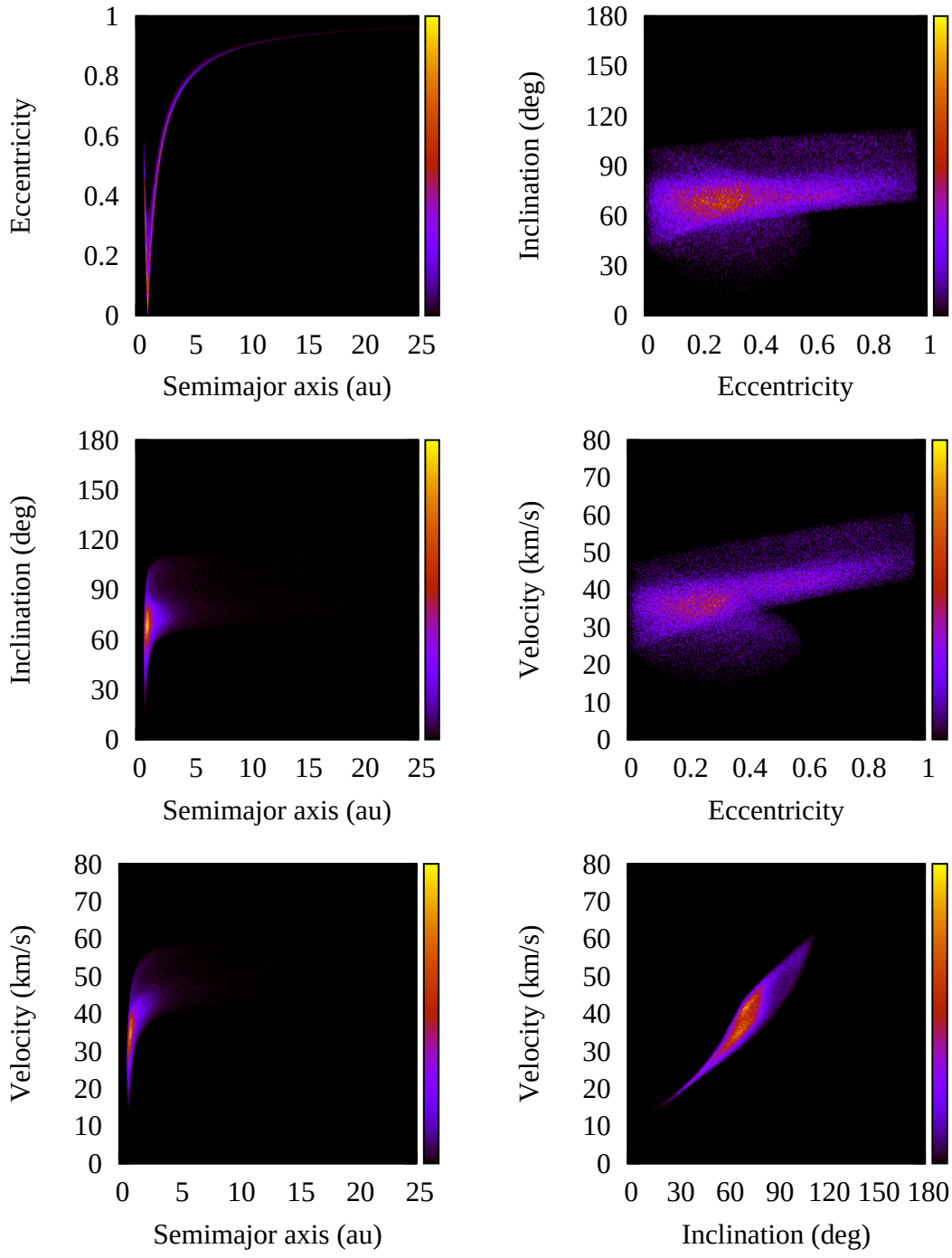

Figure 2.36: The same as in Fig. 2.8 but now for north toroidal meteors only.

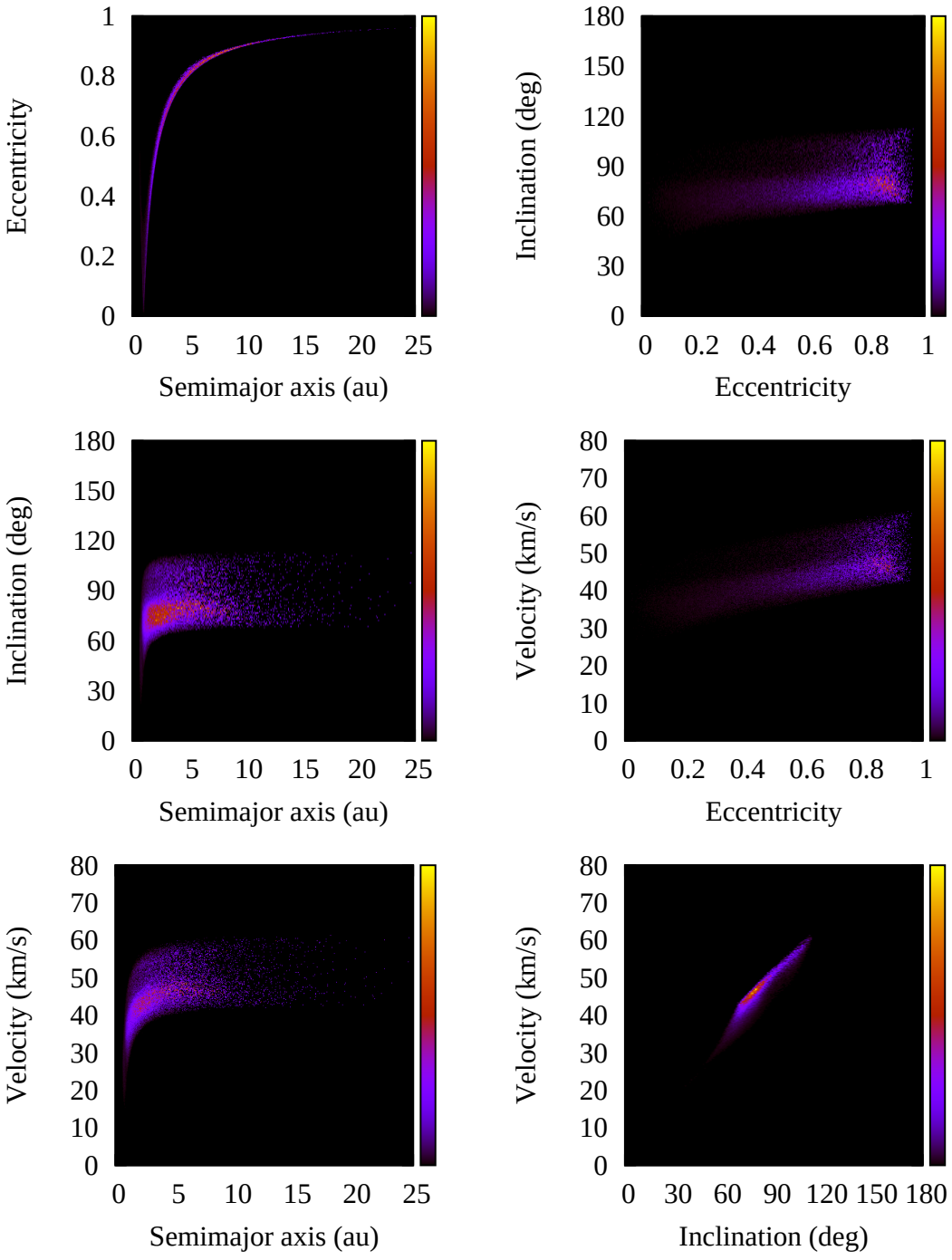

Figure 2.37: The same as in Fig. 2.9 but now for north toroidal meteors only.

2.12 North/south toroidal source - model - short review - paper E - Dynamical Model for the Toroidal Sporadic Meteors

In this paper, we focus on the dynamically most processed meteoroid population, namely the sporadic component of meteoroids hitting the Earth. We were able to develop reasonable models for north/south apex source, and helion/anti-helion source, however, no plausible model for the toroidal meteors has not been published. It is interesting, and to some extend actually puzzling, that understanding the parent source for the toroidal meteors has proved to be the most difficult of all the sporadic sources. The north toroidal particles are characteristic for their high-inclination orbits with respect to ecliptic, $I \sim 70°$, with semimajor axes close to 1 au and a long tail towards larger values, and their broad distribution of eccentricities with a maximum at $e \sim 0.2$ (Fig. 2.32). Taken straight, we do not observe any significant population of parent bodies in the Solar System with similar orbits that could feed the north toroidal source with a observed amount of dust.

Previous studies tried to explain the existence of the north toroidal source by using comet populations with orbits that are not observed in the Solar System, and cannot be reproduced by modeling the potential group of parent bodies, as in Jones et al. (2001). More recent model of Wiegert et al. (2009) provides a reasonable fit for other sources of sporadic meteors, however, their model for the north toroidal source suffers significant drawbacks and potential degeneracies. First, the authors were not able to obtain a good fit of the model to the observed distribution of the north toroidal meteors (Fig. 4 in Wiegert et al., 2009). A more important drawback of the model is a conclusion that the activity of a single or several individual objects may dominantly populate the apparent radiant source. For the north toroidal source Wiegert et al. (2009) found that the dominant contribution comes from several near-Earth asteroids. This is, however, the weakest point of the model because there is no physical justification for significant activity from most near-Earth asteroids. Also, CMOR sees a significant contribution from bodies with larger a, which cannot be explained by activity of near-Earth asteroids.

Our main goal is to develop a model for the background sporadic population of the north toroidal source based on observations of the sporadic meteoroid complex performed by CMOR in 2012. To avoid confusion between background population and contributions of individual sources we selected two intervals in λ apparently devoid of stream activity: (1) $\sim (50° - 90°)$, and (2) $\sim (320° - 360°)$ (Fig. 2 in paper E). As a result, we consider meteors in the first interval (1) to be our primary test sample of the background population. Tests show, however, that orbital data observed in the second interval (2) are very similar to those in the first interval (1), thus we feel justified in checking our results by merging information from both intervals of time. Our restricted sample of background north toroidal source particles contains 3550 individual particle orbits.

In our model, we use an up-to-date synthetic model of HTCs adopted from Levison et al. (2006). These authors developed a steady-state model for HTCs orbital architecture, assuming they originate in the scattered disk. Their model successfully matched the observed distribution of HTC orbits that are preferentially prograde with a median inclination value of $\sim 55°$, and only a small fraction of retrograde comets (Fig. 4 in paper E). Nearly half of HTCs have inclination values between $\sim 40°$ and $\sim 80°$, which is favorable for populating north/south toroidal source. We ran simulations for particles of different diameters D, namely 100 μm, 200 μm, 400 μm, 600 μm, 800 μm, 1000 μm, 1200 μm,

1500 μm, and 2000 μm, all with constant particle density $\rho = 2$ g cm^{-3}. For each D, we randomly generated 20, 000 orbits of particles, and propagated them in time. Most of the runs were completed by integration time $t = 10$ Myr, and only some of the largest particles survived longer in our simulations. We found that trajectories of particles with $D > 2$ mm in a CMOR's observable range are essentially the same, thus the results for particles with $D = 2$ mm could be extrapolated to larger values of D. On the other hand, we omitted to study particles smaller than $D = 100$ μm, because they are below the sensitivity limit of CMOR.

The dust particles in our model were numerically integrated with `swift_rmvs3` code (Levison and Duncan, 1994), where the effects of radiation pressure and P-R drag were taken into account (see Sec. 2.4). Contrary to papers C and D, we used all eight planets of the Solar System. Every 100 yr the orbital elements of particles and planets were recorded, until their heliocentric distance reached 0.05 au, left the Solar System on a hyperbolic orbit, or impacted one of the planets.

Similarly to procedure in paper D (Sec. 2.10), we introduce several free parameters. The starting orbits of our particles have different perihelion distances q (Fig. 4 in paper E), and we assume that comets with smaller q values are generally more active, and may be a subject to splitting/disrupting. In order to account for this bias, we introduce a weighting factor $\propto q^{\gamma}$, where γ is a free parameter. In our model, we consider only particles with $q < 1.3$ au. We performed tests with q extending to 2.6 au, extrapolating the trend from Levison et al. (2006) model, and found that the results are not sensitive to this limit.

In our model, we implemented the collisional model of Steel and Elford (1986) that is described in Sec. 2.3. Model of Steel and Elford (1986) provides the dependence of the collisional lifetime $\tau_{\rm coll}$ on the orbital elements of the particles, including the inclination, which is our largest concern in our model for the north toroidal source. However, similarly to our experience with the model of Grün et al. (1985) in paper D, we introduce a free parameter $F_{\rm coll}$ by which we multiply the estimated collisional lifetime. We use values of $F_{\rm coll}$ between 1 and 30 that allow us to adjust our model to match the CMOR observations.

The last set of free parameters is connected with SFD of particles in our model. In reality, the particle SFD may be a complicated function of diameter D in principle, however, experience shows that a two-slope (broken) power-law representation is a fairly good approximation unless the studied range of D is too large. We determine SFD of particles in range 200 μm$< D < 3$ mm, which is a consequence of CMOR detection sensitivity, because no smaller particles are detected by CMOR in the north toroidal source, and particles larger than $D \sim 3$ mm are rarely detected, or create overdense echoes that prevent a correct determination of their orbit. We introduce four free parameters defining SFD of particles in our model: (1) $D_{\rm mid}$ is the position of midpoint, (2) N_0 fixes the absolute number of particles with $D = 3$ mm, (3) α defining the slope of larger particles with $D > D_{\rm mid}$, and (4) β defining the slope of smaller particles with $D < D_{\rm mid}$ (Eqs. 5-10 in paper E).

This makes in total six free parameters that characterize our model for HTC particles. We found it useful to substitute for the N_0 parameter a parameter $F_{\rm imp} = N_{\rm imp}/N_{\rm obs}$, where $N_{\rm imp}$ is a predicted number of particles impacting in the selected interval of λ, and $N_{\rm obs} = 3550$ is a number of truly detected particles. This allows us to cope with some imperfections of our model while keeping in mind that $F_{\rm imp}$ should be in a reasonable interval around unity.

Our fitting procedure is performed by a highly efficient Bayesian analysis search of

the admitted solutions in the multi dimensional parameter space as described by the multinode nested sampled method efficiently implemented by the `MultiNest` code (e.g., Feroz, 2008; Feroz et al., 2009). A correct representation of effect imposed by variations of parameters $(\gamma, F_{\rm coll})$ introduces high computational demands to our model, thus we opted to pre-compute the modeled distributions of impact speeds and orbital elements for each of the particle sizes and a grid of $(\gamma, F_{\rm coll})$ that was sampled uniformly. The Markov chain walking is thus applied only to the $(\alpha, \beta, D_{\rm mid}, F_{\rm imp})$ space, but we accept this limitation for simplicity.

Model - comparison with CMOR

Before we present our final results, we start with a description of the most important global trends found when changing principal parameters of our model. First, we investigate the importance of proper knowledge of ionization cutoff $I_\star$ for the comparison of our model with observations. Synthetic population of north toroidal particles for $D = 200$ μm observed without no limiting ionization cutoff provides a fairly good match to the observed population (Fig. 5 in paper E). The most prominent feature, the predominance of particles on orbits with low eccentricities, and inclinations near $\sim 60°$, is included in the model population. This result is, indeed, promising since a reasonable SFD would favor smaller particles more than larger ones. However, when the real ionization cutoff for CMOR $I_\star = 1$ is used, the distribution of velocities and orbital elements change drastically (Fig. 6 in paper E). CMOR is able to detect only the fastest particles with $D = 200$ μm, and thus in our model remain only particles with retrograde and very high eccentric orbits, which puts a sever constraint on the slope β of the SFD.

Larger particles with $D = 600$ μm have 30 times larger masses than particles with $D = 200$ μm, which grants them greater potential for a detection by the CMOR system. Orbits of $D = 600$ μm match also the observed distribution fairly well, mostly having orbits with $e \leq 0.4$ and favorable inclination distribution (Fig. 7 in paper E). However, until now, we did not take into account collisional disruptions of the particles. Fig. 8 in paper E shows a simulation for $D = 600$ μm particles as observed by CMOR, but now with collisional disruptions included. We consider a nominal collisional model by Steel and Elford (1986), and show results with varying free parameter $F_{\rm coll}$ in range 1 to 10. Shorter collisional lifetimes do not allow particles to evolve significantly from their initial orbits, pushing thus the typical eccentricities to larger values, which is incompatible with the observed population. We find that $F_{\rm coll} \geq 10$ is needed to properly match the CMOR observations, similarly to our experience with modeling of helion/anti-helion sources (see Sec. 2.10 and paper D).

In the course of testing our fitting procedure we realized that it is more convenient, and also more precise, to use reciprocal value of semimajor axis $1/a$ rather than a of impacting particles. This parameter, equivalent to the heliocentric binding energy, allows us to test our model more severely than using simply a distribution. We search the space of free parameters with the limits defined in Table 1 in paper E.

Our formally best solution with the two-slope SFD was for $(\alpha, \beta, D_{\rm mid}, F_{\rm imp}, \gamma, F_{\rm coll}) = (4.7, 1.1, 950\ \mu{\rm m}, 1.08, 0.0, 20)$ (Fig. 9 in paper E). Our model is able to reproduce all observed features for the north toroidal meteors reasonably well, however, two major, correlated, mismatches occur: our synthetic model provides an unobserved population on high eccentric and orbits with larger semimajor axes (top right and bottom left panels in Fig. 9 in paper E). We find that our model has only slight dependence on the free parameter γ. Shorter collisional lifetimes with $F_{\rm coll}$ produce models inconsistent with

observed data, where at minimum $F_{\rm coll} \geq 10$ is needed, while values over 20 provide statistically equivalent results. Also, our fit has somewhat puzzling shape of SFD, where the parameter β provides a very shallow slope, and the break-point near to 1 mm has not been reported in any of the previous analyses. The missing high eccentric population may be result of the fact that the highest-speed particles are subject to more bias in the CMOR observations. We thus test, how our fit changes, when we discard all orbits with $e > 0.8$. The overall quality of fit improved, except for a mismatch in the inclination fit (Fig. 10 in paper E). However, the final set of free parameters did not change significantly $(\alpha, \beta, D_{\rm mid}, F_{\rm imp}, \gamma, F_{\rm coll}) = (4.8, 1.6, 750\ \mu{\rm m}, 1.11, 0.3, 20)$, still having problems similar to previous fit.

Still unsatisfied, we forced the SFD to be a single-slope power law distribution with a single exponent α. Obviously, we lose two free parameters $D_{\rm mid}$, and β, and thus we apply the Markov chain walking only to the $(\alpha, F_{\rm imp})$ space. Our best-fit model for data without orbits with $e > 0.8$ having $(\alpha, F_{\rm imp}, \gamma, F_{\rm coll}) = (2.1, 1.11, 0.0, 20)$, is formally worse than the broken power-law SFD fit (Fig. 10 in paper E), but the visual check of the results we performed indicated no substantial differences. Our tests with artificial forcing the parameter α to be closer to a more realistic values between $\sim (2.8 - 3)$ still provide visually acceptable, though statistically worse fits.

Model - comparison with *IRAS*

Once we have the SFD parameters $(\alpha, \beta, D_{\rm mid}, F_{\rm imp})$ determined, we can evaluate several interesting quantities. The total mass $M_{\rm tot}$ (Eqs. 13 and 14 in paper E) characterize a validity of our model with regards to the size of the parent population. For our models, we obtain $M_{\rm tot} \simeq (3 - 50) \times 10^{17}$ kg for particles in the size range 200 μm $\leq D \leq$ 3 mm. Assuming a quasi-exponential decay of the population in our integrations with a characteristic timescale of $\tau \simeq 2$ Myr (see Sec. 3.2 in paper E for more details) we need an average flux of $F = M_{\rm tot}/\tau \simeq (1.3 - 25) \times 10^{11}$ kg yr^{-1} to keep our model in the steady state. This value is an order of magnitude smaller than value estimated for JFC population by Nesvorný et al. (2011b), which is consistent with *IRAS* observations. The orbit-averaged activity of large HTCs is estimated to be $\sim (1 - 5) \times 10^9$ kg yr^9 (e.g., Hughes, 1985; Jenniskens, 2002), thus a steady-state population of tens to a hundred such comets would, in the long term, feed interplanetary space with sufficient amount of dust.

One of the constrains of the model of Nesvorný et al. (2011b) was the observed cross section of the zodiacal cloud meteoroids. Model of Nesvorný et al. (2010) proposed that $\gtrsim 90\%$ of the ZC's emission at MIR wavelengths comes from dust grains released from JFCs, while only $\lesssim 10\%$ remains for other sources of the dust particles in the Solar System. Our models estimate that the cross section of particles with a heliocentric distance < 5 au is $\Sigma_{\rm tot}(\leq 5{\rm au}) \simeq (0.03 - 0.25) \times 10^{11}$ km^2 (Eqs. 16 and 17 in paper E), which is $1-2$ orders of magnitude less compared to JFCs (Nesvorný et al., 2011a). Hence, our model for HTC particles is not in conflict with *IRAS* infrared measurements by providing inconsistently large cross sections that would flatten latitudinal profiles of infrared emission measured by *IRAS*.

Other Radiant Source Regions

So far, we have focused on the contribution of the HTC particles exclusively to the north toroidal source. However, these particles do not strictly impact the Earth only in this radiant zone, and their contribution is rather complex. Since we calibrated our model

for the north toroidal source, we might also estimate the contribution of HTCs to other radiant zones as well.

We find that a significant part of HTC particles populate an arc (or ring) structure at about 60° angular distance from the apex direction (left panel in Fig. 12 in paper E), which is in a good agreement with all-sky observations made by CMOR in 2012 for $\lambda = 50° - 90°$ (right panel in Fig. 12 in paper E). We also find a depleted ring structure at about 50° angular distance from the apex direction, where the orbits are efficiently eliminated from our simulations. This is mainly because during their route to the inner parts of the Solar System the perihelia of these particles become too close to the Sun and are eliminated from the simulation. Contrary to Campbell-Brown (2008), who suggested that the existence of the depleted ring is rather a consequence of collision, we find the reason for its existence rather dynamical.

Interestingly, our model particles also contribute to the apex source, having predominantly high eccentric and retrograde orbits. Even though retrograde orbits represented only a small fraction of the total population in our initial conditions, we find the average strength of the apex source ~ 5 to ~ 15 times larger than the strength of the north toroidal source depending significantly on γ. Since the fitting of the north toroidal source was rather insensitive to γ, further work on the relative contribution to apex source may help in refining our model.

Discussion and Conclusions

Our findings show that the background sporadic population of toroidal meteors observed by the CMOR system is likely provided by the activity and/or breakups of HTCs. Our model provides a constraint on several model parameters, such as the mean comet activity in relation to the perihelion distance, and size-frequency distribution function at the source in the ~ 200 μm$- \sim 3$ mm size range.

We find that our model requires longer collisional lifetimes than predicted by standard models (Grün et al., 1985; Steel and Elford, 1986), however, our findings are similar to Nesvorný et al. (2011b). There are several possibilities to explain this difference. First, we do not take into account collisional cascade in our model that may effectively extend the lifetime of the meteoroids. Another solution is to incorporate a more in-depth analysis of the solar wind interactions with the dust grains that may force particles to decay faster. On the other hand, many measurements of the lifetime of cosmic spherules and interplanetary dust particles (e.g., Raisbeck and Yiou, 1989; Olinger et al., 1990; Nishiizumi et al., 1991; Pepin et al., 2001; Kehm et al., 2006) suggest that meteoroid collisional lifetimes are longer than assumed by standard models.

Some of the residual mismatches between observations and our model may originate in our simplified description of the detection limits of the CMOR radar system. Similarly to our previous works, we used a simple ionization factor I defined in Eq. (2.28) to characterize the sensitivity of the radar system. While this simplified treatment captures the most important features of the detection process, the real situation might be more complex. Most importantly, the instantaneous change from non-detectability to detectability of the meteor at a single value $I = I_\star = 1$, might be too simplified. Incorporating more complex function that is taking into account a probabilistic nature of the detection process might improve the precision of our model.

While we succeeded in modeling of the sporadic background of the north toroidal source, many opened issues remain, and are related to our future work. First, we shall analyze the time-variable component of the north toroidal source (Fig. 2.33), search for

the possible individual sources of semi-sporadic structures, and determine, whether these parent bodies still exits or the observed structures are remnants of the asteroidal/cometary disruptions. Second, our finding of the contribution of HTC particles to the apex source is a motivation for revisiting the dynamical modeling of the apex source, we performed in paper C (Nesvorný et al., 2011a). Our findings suggest, that the proper model of the apex source should consider at least two prolific groups of parent bodies, namely HTCs and OCCs.

2.13 Conclusions and further work

The Solar System is a very dusty environment and the Earth is every second showered with dust particles while revolving around the Sun. Many of these particles are detected by ground-based or space-borne systems providing interesting variety of information that allows us to model and predict behavior of various dust populations in the vast region around the Sun. Ground-based radar and visual systems are able to accurately determine radiant locations and velocities of impacting dust particles. Sporadic meteors, dynamically evolved particles without an evident link to their parent bodies, dominate the dust influx on the Earth, while only $\sim 10\%$ remains for the shower meteors. Decades of radar measurements distinguished three broad classes of sporadic meteors according to their radiant positions: the helion and anti-helion source, the north and south apex sources, and the north and south toroidal sources (Sec. 2.1).

Such an abundant population of meteors drew attention of many researchers who sought dynamical model with an ability to explain the observed distribution of radiants, velocities, and orbital elements of sporadic meteors. Despite of complexity of the dynamical evolution of dust particles, time demanding simulations, and yet developing models describing potentially rich sources of dust, many interesting results were discovered (Sec. 2.1.2). However, plausible models with an ability to explain the majority of observed features and characteristics of the sporadic meteoroid complex had yet to be developed.

We reviewed fundamental physical processes dominating the dynamics of dust particles in the Solar System. Except for the gravitational forces, the dynamics of the dust particles are influenced by radiative processes, namely, the radiative pressure, Poynting-Robertson drag, and effect of solar wind (Sec. 2.2). These processes force the majority of dust particles to experience spiraling towards the inner parts of the Solar System, and their final end in the proximity of the Sun, regardless on their initial orbital parameters.

Particles en route to the inner parts of the Solar System may collide with small meteoroids in the zodiacal cloud. In Sec. 2.3 we discuss two standard models, presented by Grün et al. (1985) and Steel and Elford (1986), for the determination of the collisional lifetime of the dust particles in the Solar System. While rather simple, these models are one of the essential parts for development correct steady state model for the sporadic meteoroid population.

Our goal, the development of steady-state models (Sec. 2.5) for each observed source of the sporadic meteoroid complex, cannot be accomplished without many tools and codes we use throughout the whole development process (Sec. 2.4). CMOR system is the longest operating radar facility with over ten million observed orbits. We were fortunate to be able to investigate a very accurate dataset recorded in 2012 by CMOR, determine its basic characteristic, distribution of orbits, and discuss in a more detail some interesting features observed by CMOR (Sec. 2.6).

North/south apex source is populated by the fastest observed meteors near to the hyperbolic limit in the Solar System. Such meteors on mainly retrograde orbits represent approximately one quarter of all meteors orbits (Sec. 2.7) Our dynamical model for the Oort Cloud Comets is able to reproduce the majority of observed features in the north/south apex source (Sec. 2.8). However, our most recent findings of contribution of the Halley-type comets show that a significant amount of north/south apex meteors originates in the Halley-type comets (Sec. 2.12). A steady-state model taking into account two different groups of parent bodies, and a precise determination of the ratio between these two sources is left for the future work.

Helion/anti-helion source, the most abundant source in the sporadic meteoroid complex with more than a third of the total number of observed meteors, is mainly populated by slower and low inclination meteors (Sec. 2.9). We refined the model of Nesvorný et al. (2010) for more complex characteristics of the Jupiter-family comet orbits, size-frequency distribution of model particles, and for more complex collisional models. Our dynamical model for Jupiter-family comets is able to find a good agreement with observations of helion/anti-helion source from AMOR and CMOR systems (Sec. 2.10). Infrared measurements of *IRAS* allowed us to obtain the absolute calibration for our model that provides mass influx of dust particles onto the Earth comparable to space-borne measurements performed by *LDEF*. We find that the model from Grün et al. (1985) provides collisional lifetimes significantly lower than our model requires to fit CMOR data. The mass input needed for keeping our model in steady state is ~ 10 times larger than the one suggested by Nesvorný et al. (2010), and we find that JFC meteoroids form $\gtrsim 90\%$ of the total population of the zodiacal cloud. We suggest that the zodiacal cloud is dominated by the meteoroids released by disrupting/splitting JFCs, because the observed activity of JFCs cannot provide the needed mass input.

North/south toroidal source, characteristic for its high inclination and low eccentricity orbits of observed meteors, and strong seasonal variations, has no evident link to any prolific group of dust producing bodies in the Solar System (Sec. 2.11). Even though known for more than 50 years, no plausible dynamical model that can explain observed distributions of impact velocities and orbital elements with radiant positions at the north/south toroidal source has been published. In Sec. 2.12,q we present our new dynamical model for the background population of the north toroidal source. Using Halley-type comets as the parent bodies of the dust particles we succeeded in matching all observed features. The excellent dataset of 2012 observations provided by CMOR allowed us to obtain the absolute calibration for our model, and to a great degree find constrains for free parameters in our model. We find that the best solution for our model needs collisional lifetimes ~ 20 times larger than the collisional model of Steel and Elford (1986) predicts. We determined that the contribution of HTC particles from our model to the population of the zodiacal cloud is $1-2$ orders of magnitude less than the contribution of JFC particles as found in Sec. 2.10, which is compatible with *IRAS* measurements.

Many interesting projects were left for future work. Our model for the north/south apex source based solely on particles from OCCs was not able to match all observed structures, and also no absolute calibration was established. Our findings of the significant contribution of HTC particles to the north/south apex source suggest that the two-component model should be able to fit the observed population better, and also with the knowledge of the absolute calibration of the HTC particle we may also seek the ratio between OCC and HTC contribution to the north/south apex source, and ultimately obtain the absolute calibration for OCC meteoroids. Once all sources of the sporadic

meteors are calibrated, we may advance to a full-fledged model of the dust environment in the Solar System. With a deeper understanding of the most prolific sources of the dust particles we aspire to create a dynamical model that would match all ground-based and space-borne measurements available to date.

Our modeling efforts has yet been focused only to the background population of the sporadic meteoroid complex. Seasonal variations in all observed source of the sporadic meteors, however, are still not fully understood, and many observed structures have unknown parent bodies. Full dynamical understanding of such structures can tell us many interesting facts about its parent bodies such as, the age of the event that caused the significant production of the dust, the possible link of a non-existent body to a body observed in the past, or the future of these structures in the sporadic meteoroid complex.

Evaluation of the collisional lifetimes of meteoroids in the Solar System was one of the essential parts of our modeling process. We found that values provided by the standard models are not compatible with our dynamical simulations and need to be adjusted to allow our models to match observations properly. New, more advanced, and not necessarily more complicated, model with an ability to determine more precisely the collisional lifetimes among the member of the Solar System dust environment would be greeted by the community.

Final remarks

This thesis summarizes our almost four year lasting effort to improve theories for determination of the collisional probabilities in the Solar System, and also to knowledge of the origin and dynamics of the sporadic meteors in the Solar System.

Our contribution to the problem the collisional probability determination may look minor, but it already proved useful for estimating impact probabilities of the toroidal meteoroids. Our work on this topic is not finished yet, since incorporating target bodies on inclined orbits will further broaden applicability of our research. Moreover, changing our rather simplified scenario with the idealized perturbing body to more complex system with more perturbing bodies on arbitrary orbits may provide more accurate solutions. On the other hand, the main advantages of our current approach, purely analytical solution and consequential speed, may severely suffer during the development process.

The code providing estimates of the collisional probability for various bodies in the Solar System based on our two papers presented in this thesis is already being used by several colleagues.

Our work in the modeling of the sporadic meteoroid complex may seem more complete. Various radar systems recognizes six concentrations in the all-sky radiant map, for which we successfully created dynamical steady-state models based on well-known and at least partially observed populations of comets. However, we focused only on a background sporadic populations, while measurements exhibit seasonal variations that cannot be modeled by steady-state models. These semi-sporadic contributions to the sporadic meteoroid complex are one of the future topics of our work.

Absolute calibration of the steady-state models of the sporadic meteoroid background is another part of research we are really looking forward to. When the models are absolutely calibrated we will obtain a distribution of the majority of micrometer to millimeter sized particles in the whole Solar System.

Further extension of our model from the micrometer sized particles up to centimeter sized meteoroids is what we expect to be possible in the near future. Centimeter sized meteors are not easily detectable by radars, because of several effect such as saturation of the signal or partial fragmentation of the detected body. However, forthcoming projects like CAMS (Cameras for Allsky Meteor Surveillance) measuring meteors in visual spectrum may provide additional repository of information that will allow us to build models for particles of these sizes.

At the very end of this thesis, I hope you enjoyed its reading, and that you find this work worthy of level of the PhD thesis.

Bibliography

Bailey, M. E., Markham, D. J., Massai, S., and Scriven, J. E. (1995). The 1930 August 13 'Brazilian Tunguska' event. *The Observatory*, 115:250–253.

Bertotti, B., Farinella, P., and Vokrouhlický, D. (2003). *Physics of the Solar System - Dynamics and Evolution, Space Physics, and Spacetime Structure.* Kluwer Academic Publishers.

Blaes, O., Lee, M. H., and Socrates, A. (2002). The Kozai Mechanism and the Evolution of Binary Supermassive Black Holes. *ApJ*, 578:775–786.

Bottke, W. F., Morbidelli, A., Jedicke, R., Petit, J.-M., Levison, H. F., Michel, P., and Metcalfe, T. S. (2002). Debiased Orbital and Absolute Magnitude Distribution of the Near-Earth Objects. *Icarus*, 156:399–433.

Bottke, W. F., Vokrouhlický, D., Minton, D., Nesvorný, D., Morbidelli, A., Brasser, R., Simonson, B., and Levison, H. F. (2012). An Archaean heavy bombardment from a destabilized extension of the asteroid belt. *Nature*, 485:78–81.

Bottke, W. F., Vokrouhlický, D., and Nesvorný, D. (2007). An asteroid breakup 160Myr ago as the probable source of the K/T impactor. *Nature*, 449:48–53.

Bottke, W. F., Vokrouhlický, D., Rubincam, D. P., and Nesvorný, D. (2006). The Yarkovsky and Yorp Effects: Implications for Asteroid Dynamics. *Annual Review of Earth and Planetary Sciences*, 34:157–191.

Brown, P. G., Assink, J. D., Astiz, L., Blaauw, R., Boslough, M. B., Borovička, J., Brachet, N., Brown, D., Campbell-Brown, M. D., Ceranna, L., Cooke, W., de Groot-Hedlin, C., Drob, D. P., Edwards, W., Evers, L. G., Garces, M., Gill, J., Hedlin, M., Kingery, A., Laske, G., Le Pichon, A., Mialle, P., Moser, D. E., Saffer, A., Silber, E., Smets, P., Spalding, R. E., Spurný, P., Tagliaferri, E., Uren, D., Weryk, R. J., Whitaker, R., and Krzeminski, Z. (2013). A 500-kiloton airburst over Chelyabinsk and an enhanced hazard from small impactors. *Nature*, 503:238–241.

Brown, P. G. and Jones, J. (1995). A Determination of the Strengths of the Sporadic Radio-Meteor Sources. *Earth Moon and Planets*, 68:223–245.

Brown, P. G., Weryk, R. J., Wong, D. K., and Campbell-Brown, M. D. (2012). The Canadian Meteor Orbit Radar II: A new Facility for Measurement of the Dust Environment in near-Earth space. In *AAS/Division for Planetary Sciences Meeting Abstracts*, volume 44 of *AAS/Division for Planetary Sciences Meeting Abstracts*, page 302.04.

Brown, P. G., Weryk, R. J., Wong, D. K., and Jones, J. (2008). A meteoroid stream survey using the Canadian Meteor Orbit Radar. I. Methodology and radiant catalogue. *Icarus*, 195:317–339.

Brown, P. G., Wong, D. K., Weryk, R. J., and Wiegert, P. (2010). A meteoroid stream survey using the Canadian Meteor Orbit Radar. II: Identification of minor showers using a 3D wavelet transform. *Icarus*, 207:66–81.

Burns, J. A., Lamy, P. L., and Soter, S. (1979). Radiation forces on small particles in the solar system. *Icarus*, 40:1–48.

Campbell, M. D. (2002). *Correcting radar meteor observations for the initial radius effect*. PhD thesis, University of Western Ontario (Canada).

Campbell-Brown, M. D. (2008). High resolution radiant distribution and orbits of sporadic radar meteoroids. *Icarus*, 196:144–163.

Campbell-Brown, M. D. and Wiegert, P. (2009). Seasonal variations in the north toroidal sporadic meteor source. *Meteoritics and Planetary Science*, 44:1837–1848.

Correia, A. C. M., Boué, G., Laskar, J., and Morais, M. H. M. (2013). Tidal damping of the mutual inclination in hierarchical systems. *A&A*, 553:A39.

Cremonese, G., Borin, P., Martellato, E., Marzari, F., and Bruno, M. (2012). New Calibration of the Micrometeoroid Flux on Earth. *ApJ*, 749:L40.

Di Sisto, R. P., Fernández, J. A., and Brunini, A. (2009). On the population, physical decay and orbital distribution of Jupiter family comets: Numerical simulations. *Icarus*, 203:140–154.

Dikarev, V., Grün, E., Baggaley, J., Galligan, D., Landgraf, M., and Jehn, R. (2004). Modeling the Sporadic Meteoroid Background Cloud. *Earth Moon and Planets*, 95:109–122.

Divine, N. (1993). Five populations of interplanetary meteoroids. *J. Geophys. Res.*, 98:17029–17048.

Fabrycky, D. and Tremaine, S. (2007). Shrinking Binary and Planetary Orbits by Kozai Cycles with Tidal Friction. *ApJ*, 669:1298–1315.

Farinella, P. and Davis, D. R. (1992). Collision rates and impact velocities in the Main Asteroid Belt. *Icarus*, 97:111–123.

Fernández, J. A. (2005). *Comets Nature, Dynamics, Origin and their Cosmological Relevance*. Springer.

Feroz, F. (2008). *Bayesian methods for astrophysics and particle physics*. PhD thesis, Cambridge University.

Feroz, F., Hobson, M. P., and Bridges, M. (2009). MULTINEST: an efficient and robust Bayesian inference tool for cosmology and particle physics. *MNRAS*, 398:1601–1614.

Ford, E. B., Kozinsky, B., and Rasio, F. A. (2000). Secular Evolution of Hierarchical Triple Star Systems. *ApJ*, 535:385–401.

Galligan, D. P. and Baggaley, W. J. (2004). The orbital distribution of radar-detected meteoroids of the Solar system dust cloud. *MNRAS*, 353:422–446.

Galligan, D. P. and Baggaley, W. J. (2005). The radiant distribution of AMOR radar meteors. *MNRAS*, 359:551–560.

Gomes, R., Levison, H. F., Tsiganis, K., and Morbidelli, A. (2005). Origin of the cataclysmic Late Heavy Bombardment period of the terrestrial planets. *Nature*, 435:466–469.

Gonczi, R., Rickman, H., and Froeschle, C. (1992). The connection between Comet P/Machholz and the Quadrantid meteor. *MNRAS*, 254:627–634.

Granvik, M., Morbidelli, A., Jedicke, R., Bottke, W. F., Bolin, B., Beshore, E., Vokrouhlicky, D., Nesvorny, D., and Michel, P. (2013). A New Population Model of the Orbits and Absolute Magnitudes of Near-Earth Objects. In *AAS/Division for Planetary Sciences Meeting Abstracts*, volume 45 of *AAS/Division for Planetary Sciences Meeting Abstracts*, page 106.02.

Greenberg, R. (1982). Orbital interactions - A new geometrical formalism. *AJ*, 87:184–195.

Gronchi, G. F. and Milani, A. (1998). Averaging on Earth-Crossing Orbits. *Celest. Mech. Dyn. Astron.*, 71:109–136.

Gronchi, G. F. and Milani, A. (1999). The stable Kozai state for asteroids and comets. With arbitrary semimajor axis and inclination. *A&A*, 341:928–935.

Grün, E., Zook, H. A., Fechtig, H., and Giese, R. H. (1985). Collisional balance of the meteoritic complex. *Icarus*, 62:244–272.

Harris, A. W., Barucci, M. A., Cano, J. L., Drube, L., Fitzsimmons, A., Fulchignoni, M., Green, S. F., Hestroffer, D., Lappas, V., Michel, P., Morrison, D., Meshcheryakov, S. A., Saks, N., and Schäfer, F. (2012). NEOShield: Working towards an international near-Earth object mitigation demonstration mission. In *European Planetary Science Congress 2012*, page 126.

Hawkins, G. S. (1956). Variation in the occurrence rate of meteors. *AJ*, 61:386.

Hawkins, G. S. (1962). Symposium: Small meteoric particles in the earth's neighborhood: Radar determination of meteor orbits. *AJ*, 67:241.

Hawkins, G. S. and Prentice, J. P. M. (1957). Visual determination of the radiant distribution of sporadic meteors. *AJ*, 62:234.

Horvath, H. (2009). Gustav Mie and the scattering and absorption of light by particles: Historic developments and basics. *Journal of Quantitative Spectroscopy & Radiative Transfer*, 110:787–799.

Hughes, D. W. (1985). The size, mass, mass loss and age of Halley's comet. *MNRAS*, 213:103–109.

Jenniskens, P. (2002). More on the dust trails of comet 55P/Tempel-Tuttle from 2001 Leonid shower flux measurements. In Warmbein, B., editor, *Asteroids, Comets, and Meteors: ACM 2002*, volume 500 of *ESA Special Publication*, pages 117–120.

Jenniskens, P. (2006). *Meteor Showers and their Parent Comets*. Cambridge: University Press.

Jenniskens, P. (2008). Mostly Dormant Comets and their Disintegration into Meteoroid Streams: A Review. *Earth Moon and Planets*, 102:505–520.

Jenniskens, P., Gural, P. S., Dynneson, L., Grigsby, B. J., Newman, K. E., Borden, M., Koop, M., and Holman, D. (2011). CAMS: Cameras for Allsky Meteor Surveillance to establish minor meteor showers. *Icarus*, 216:40–61.

Jones, J. and Brown, P. G. (1993). Sporadic meteor radiant distributions - Orbital survey results. *MNRAS*, 265:524.

Jones, J., Brown, P. G., Ellis, K. J., Webster, A. R., Campbell-Brown, M. D., Krzemenski, Z., and Weryk, R. J. (2005). The Canadian Meteor Orbit Radar: system overview and preliminary results. *Planet. Space Sci.*, 53:413–421.

Jones, J., Campbell, M. D., and Nikolova, S. (2001). Modelling of the sporadic meteoroid sources. In Warmbein, B., editor, *Meteoroids 2001 Conference*, volume 495 of *ESA Special Publication*, pages 575–580.

Jones, J. and Jones, W. (1993). Comet Machholz and the Quadrantid meteor stream. *MNRAS*, 261:605–611.

Jopek, T. J., Rudawska, R., and Pretka-Ziomek, H. (2006). Calculation of the mean orbit of a meteoroid stream. *MNRAS*, 371:1367–1372.

Katz, B., Dong, S., and Malhotra, R. (2011). Long-Term Cycling of Kozai-Lidov Cycles: Extreme Eccentricities and Inclinations Excited by a Distant Eccentric Perturber. *Physical Review Letters*, 107(18):181101.

Kaňuchová, Z. and Neslušan, L. (2007). The parent bodies of the Quadrantid meteoroid stream. *A&A*, 470:1123–1136.

Kehm, K., Flynn, G. J., and Hohenberg, C. M. (2006). Noble gas space exposure ages of individual interplanetary dust particles. *Meteoritics and Planetary Science*, 41:1199–1217.

Kelsall, T., Weiland, J. L., Franz, B. A., Reach, W. T., Arendt, R. G., Dwek, E., Freudenreich, H. T., Hauser, M. G., Moseley, S. H., Odegard, N. P., Silverberg, R. F., and Wright, E. L. (1998). The COBE Diffuse Infrared Background Experiment Search for the Cosmic Infrared Background. II. Model of the Interplanetary Dust Cloud. *ApJ*, 508:44–73.

Kero, J., Szasz, C., Nakamura, T., Meisel, D. D., Ueda, M., Fujiwara, Y., Terasawa, T., Nishimura, K., and Watanabe, J. (2012). The 2009-2010 MU radar head echo observation programme for sporadic and shower meteors: radiant densities and diurnal rates. *MNRAS*, 425:135–146.

Kessler, D. J. (1981). Derivation of the collision probability between orbiting objects The lifetimes of Jupiter's outer moons. *Icarus*, 48:39–48.

Kinoshita, H. and Nakai, H. (2007). General solution of the Kozai mechanism. *Celest. Mech. Dyn. Astron.*, 98:67–74.

Knight, M. M., A'Hearn, M. F., Biesecker, D. A., Faury, G., Hamilton, D. P., Lamy, P., and Llebaria, A. (2010). Photometric Study of the Kreutz Comets Observed by SOHO from 1996 to 2005. *AJ*, 139:926–949.

Koninckx, C., Vanouplines, P., and Marsden, B. G. (1995). Comet C/1733 K1–Discovery, rediscovery and orbit. *Vistas in Astronomy*, 39:323–334.

Kozai, Y. (1962). Secular perturbations of asteroids with high inclination and eccentricity. *AJ*, 67:591.

Kramer, E. A., Fernandez, Y. R., Bauer, J. M., Mainzer, A. K., Grav, T., Masiero, J., Walker, R. G., Stevenson, R., Lisse, C. M., and WISE Team (2012). Characterization of Cometary Dust Tails in the WISE/NEOWISE Data Set. In *AAS/Division for Planetary Sciences Meeting Abstracts*, volume 44 of *AAS/Division for Planetary Sciences Meeting Abstracts*, page 514.07.

Krymolowski, Y. and Mazeh, T. (1999). Studies of multiple stellar systems - II. Second-order averaged Hamiltonian to follow long-term orbital modulations of hierarchical triple systems. *MNRAS*, 304:720–732.

Landgraf, M., Liou, J.-C., Zook, H. A., and Grün, E. (2002). Origins of Solar System Dust beyond Jupiter. *AJ*, 123:2857–2861.

Lee, M. H. and Peale, S. J. (2003). Secular Evolution of Hierarchical Planetary Systems. *ApJ*, 592:1201–1216.

Leinert, C., Richter, I., Pitz, E., and Planck, B. (1981). The zodiacal light from 1.0 to 0.3 A.U. as observed by the HELIOS space probes. *A&A*, 103:177–188.

Leinert, C., Roser, S., and Buitrago, J. (1983). How to maintain the spatial distribution of interplanetary dust. *A&A*, 118:345–357.

Levison, H. F. and Duncan, M. J. (1994). The long-term dynamical behavior of short-period comets. *Icarus*, 108:18–36.

Levison, H. F. and Duncan, M. J. (1997). From the Kuiper Belt to Jupiter-Family Comets: The Spatial Distribution of Ecliptic Comets. *Icarus*, 127:13–32.

Levison, H. F., Duncan, M. J., Dones, L., and Gladman, B. J. (2006). The scattered disk as a source of Halley-type comets. *Icarus*, 184:619–633.

Levison, H. F., Morbidelli, A., Dones, L., Jedicke, R., Wiegert, P. A., and Bottke, W. F. (2002). The Mass Disruption of Oort Cloud Comets. *Science*, 296:2212–2215.

Lidov, M. L. (1961). The evolution of orbits of artificial satellites of planets under the action of gravitational perturbations of external bodies. *Artif. Satell. Earth*, 8:5–45.

Liou, J.-C., Zook, H. A., and Jackson, A. A. (1999). Orbital Evolution of Retrograde Interplanetary Dust Particles and Their Distribution in the Solar System. *Icarus*, 141:13–28.

Love, S. G. and Brownlee, D. E. (1993). A Direct Measurement of the Terrestrial Mass Accretion Rate of Cosmic Dust. *Science*, 262:550–553.

Marchi, S., Chapman, C. R., Fassett, C. I., Head, J. W., Bottke, W. F., and Strom, R. G. (2013). Global resurfacing of Mercury 4.0-4.1 billion years ago by heavy bombardment and volcanism. *Nature*, 499:59–61.

Marchi, S., Mottola, S., Cremonese, G., Massironi, M., and Martellato, E. (2009). A New Chronology for the Moon and Mercury. *AJ*, 137:4936–4948.

Mathews, J. D., Janches, D., Meisel, D. D., and Zhou, Q.-H. (2001). The micrometeoroid mass flux into the upper atmosphere: Arecibo results and a comparison with prior estimates. *Geophys. Res. Lett.*, 28:1929–1932.

McNamara, H., Jones, J., Kauffman, B., Suggs, R., Cooke, W., and Smith, S. (2004). Meteoroid Engineering Model (MEM): A Meteoroid Model For The Inner Solar System. *Earth Moon and Planets*, 95:123–139.

Morbidelli, A. (2002). *Modern celestial mechanics : aspects of solar system dynamics*. London: Taylor & Francis.

Mukai, T. and Giese, R. H. (1984). Modification of the spatial distribution of interplanetary dust grains by Lorentz forces. *A&A*, 131:355–363.

Mukai, T. and Yamamoto, T. (1982). Solar wind pressure on interplanetary dust. *A&A*, 107:97–100.

Murray, C. D. and Dermott, S. F. (1999). *Solar system dynamics*. Cambridge University Press.

Naoz, S., Farr, W. M., Lithwick, Y., Rasio, F. A., and Teyssandier, J. (2011). Hot Jupiters from secular planet-planet interactions. *Nature*, 473:187–189.

Nesvorný, D., Janches, D., Vokrouhlický, D., Pokorný, P., Bottke, W. F., and Jenniskens, P. (2011b). Dynamical Model for the Zodiacal Cloud and Sporadic Meteors. *ApJ*, 743:129.

Nesvorný, D., Jenniskens, P., Levison, H. F., Bottke, W. F., Vokrouhlický, D., and Gounelle, M. (2010). Cometary Origin of the Zodiacal Cloud and Carbonaceous Micrometeorites. Implications for Hot Debris Disks. *ApJ*, 713:816–836.

Nesvorný, D., Vokrouhlický, D., Bottke, W. F., and Sykes, M. (2006). Physical properties of asteroid dust bands and their sources. *Icarus*, 181:107–144.

Nesvorný, D., Vokrouhlický, D., Pokorný, P., and Janches, D. (2011a). Dynamics of Dust Particles Released from Oort Cloud Comets and Their Contribution to Radar Meteors. *ApJ*, 743:37.

Nishiizumi, K., Arnold, J. R., Fink, D., Klein, J., Middleton, R., Brownlee, D. E., and Maurette, M. (1991). Exposure history of individual cosmic particles. *Earth and Planetary Science Letters*, 104:315–324.

Olinger, C. T., Walker, R. M., Hohenberg, C. M., and Maurette, M. (1990). Neon measurements of individual Greenland sediment particles - Proof of an extraterrestrial origin and comparison with EDX and morphological analyses. *Earth and Planetary Science Letters*, 100:77–93.

Oort, J. H. (1950). The structure of the cloud of comets surrounding the Solar System and a hypothesis concerning its origin. *Bull. Astron. Inst. Netherlands*, 11:91–110.

Öpik, E. J. (1951). Collision probability with the planets and the distribution of planetary matter. *Proc. R. Irish Acad. Sect. A, vol. 54, p. 165-199 (1951).*, 54:165–199.

Pecina, P. and Ceplecha, Z. (1983). New aspects in single-body meteor physics. *Bulletin of the Astronomical Institutes of Czechoslovakia*, 34:102–121.

Pepin, R. O., Palma, R. L., and Schlutter, D. J. (2001). Noble gases in interplanetary dust particles. II. Excess helium-3 in cluster particles and modeling constraints on interplanetary dust particle exposures to cosmic-ray irradiation. *Meteoritics and Planetary Science*, 36:1515–1534.

Planck Collaboration, Ade, P. A. R., Aghanim, N., Armitage-Caplan, C., Arnaud, M., Ashdown, M., Atrio-Barandela, F., Aumont, J., Baccigalupi, C., Banday, A. J., and et al. (2013). Planck 2013 results. XIV. Zodiacal emission. *ArXiv e-prints*.

Pokorný, P. and Vokrouhlický, D. (2013). Öpik-type collision probability for high-inclination orbits: Targets on eccentric orbits. *Icarus*, 226:682–693.

Pokorný, P., Vokrouhlický, D., Nesvorný, D., Campbell-Brown, M. D., and Brown, P. G. (2014). Dynamical Model for the Toroidal Sporadic Meteors. *ApJ*, 789:25.

Poppe, A., James, D., Jacobsmeyer, B., and Horányi, M. (2010). First results from the Venetia Burney Student Dust Counter on the New Horizons mission. *Geophys. Res. Lett.*, 37:11101.

Press, W. H., Teukolsky, S. A., Vetterling, W. T., and Flannery, B. P. (2007). *Numerical recipes. The art of scientific computing*. Cambridge: University Press, 3nd ed.

Raisbeck, G. M. and Yiou, F. (1989). Cosmic ray exposure ages of cosmic spherules. *Meteoritics*, 24:318.

Reach, W. T., Kelley, M. S., and Sykes, M. V. (2007). A survey of debris trails from short-period comets. *Icarus*, 191:298–322.

Reach, W. T., Morris, P., Boulanger, F., and Okumura, K. (2003). The mid-infrared spectrum of the zodiacal and exozodiacal light. *Icarus*, 164:384–403.

Robertson, H. P. (1937). Dynamical effects of radiation in the solar system. *MNRAS*, 97:423.

Sahu, K. C., Casertano, S., Bond, H. E., Valenti, J., Ed Smith, T., Minniti, D., Zoccali, M., Livio, M., Panagia, N., Piskunov, N., Brown, T. M., Brown, T., Renzini, A., Rich, R. M., Clarkson, W., and Lubow, S. (2006). Transiting extrasolar planetary candidates in the Galactic bulge. *Nature*, 443:534–540.

Sekanina, Z. (2003). Erosion Model for the Sungrazing Comets Observed with the Solar and Heliospheric Observatory. *ApJ*, 597:1237–1265.

Sekanina, Z. and Chodas, P. W. (2005). Origin of the Marsden and Kracht Groups of Sunskirting Comets. I. Association with Comet 96P/Machholz and Its Interplanetary Complex. *ApJS*, 161:551–586.

Southworth, R. B. and Hawkins, G. S. (1963). Statistics of meteor streams. *Smithsonian Contributions to Astrophysics*, 7:261.

Steel, D. I. (1985). Collisions in the solar systems. II - Asteroid impacts upon Mars. *MNRAS*, 215:369–381.

Steel, D. I. and Baggaley, W. J. (1985). Collisions in the solar system. I - Impacts of the Apollo-Amor-Aten asteroids upon the terrestrial planets. *MNRAS*, 212:817–836.

Steel, D. I. and Elford, W. G. (1986). Collisions in the solar system. III - Meteoroid survival times. *MNRAS*, 218:185–199.

Sykes, M. V., Lebofsky, L. A., Hunten, D. M., and Low, F. (1986). The discovery of dust trails in the orbits of periodic comets. *Science*, 232:1115–1117.

Thomas, F. and Morbidelli, A. (1996). The Kozai Resonance in the Outer Solar System and the Dynamics of Long-Period Comets. *Celest. Mech. Dyn. Astron.*, 64:209–229.

Trayner, C. (1997). The Tunguska event. *Journal of the British Astronomical Association*, 107:117–130.

Verniani, F. (1973). An Analysis of the Physical Parameters of 5759 Faint Radio Meteors. *J. Geophys. Res.*, 78:8429–8462.

Vokrouhlický, D., Pokorný, P., and Nesvorný, D. (2012). Öpik-type collision probability for high-inclination orbits. *Icarus*, 219:150–160.

Vondrak, T., Plane, J. M. C., Broadley, S., and Janches, D. (2008). A chemical model of meteoric ablation. *Atmospheric Chemistry & Physics*, 8:7015–7031.

Weryk, R. J. and Brown, P. G. (2004). A search for interstellar meteoroids using the Canadian Meteor Orbit Radar (CMOR). *Earth Moon and Planets*, 95:221–227.

Weryk, R. J., Campbell-Brown, M. D., Wiegert, P. A., Brown, P. G., Krzeminski, Z., and Musci, R. (2013). The Canadian Automated Meteor Observatory (CAMO): System overview. *Icarus*, 225:614–622.

Wetherill, G. W. (1967). Collisions in the Asteroid Belt. *J. Geophys. Res.*, 72:2429.

Wiegert, P. and Tremaine, S. (1999). The Evolution of Long-Period Comets. *Icarus*, 137:84–121.

Wiegert, P., Vaubaillon, J., and Campbell-Brown, M. D. (2009). A dynamical model of the sporadic meteoroid complex. *Icarus*, 201:295–310.

Wilhelms, D. E. (1987). The geologic history of the Moon. *US Geol. Surv. Prof. Pap.*, 1348.

Wisdom, J. and Holman, M. (1991). Symplectic maps for the n-body problem. *AJ*, 102:1528–1538.

Wyatt, S. P. and Whipple, F. L. (1950). The Poynting-Robertson effect on meteor orbits. *ApJ*, 111:134–141.

Appendix A - Source code - Determination of the collisional probability

Here, we present the source for our code based on papers A and B where its main purpose is a determination of the collisional probability between two bodies. See Sec. 1.5 and papers A and B for further reference. Its most recent version is available at `http://sirrah.troja.mff.cuni.cz/~pokorny/Kozai/` .

```
      PROGRAM KOZAIOPIKPROB

! Author:
! Petr Pokorny
!
! LICENCE:
!                ------------
! This program is !!! FREE !!! to use, however, it would be very kind of you to
!                ------------
! put a reference into your article (reference to Vokrouhlicky et al. 2012)
! or better an article with Pokorny, Vokrouhlicky 2013, where is the code cited (^_^)


! Reference publication:
!
! Opik-type collision probability for high-inclination orbits
! Vokrouhlicky, David; Pokorny, Petr; Nesvorny, David
! Icarus, Volume 219, Issue 1, p. 150-160.
!
! Opik-type collision probability for high-inclination orbits: Targets on eccentric orbits
! Pokorny, Petr; Vokrouhlicky, David
! Icarus, Volume 226, Issue 1, p. 682-693

! SUBROUTINE KOZAIOPIK computes impact probabilities between Target and Projectile
! The Target is assumed to be in eccentric and coplanar orbit (i = 0, 0 =< e < 1)
! The Projectile is assumed to be on bound elliptic orbit around the Sun and non-resonant with any other
    planet
! The Projectile is defined by its semimajor axis (AU), eccentricity, Inclination (deg) and argument of
    pericenter (deg)
!
!                             /
!                            /
!                           /                    ---
!                          *                  ,o88888
!                                            ,o8888888'
!                      ,:o:o:oooo.      ,8O88Pd8888"
!                  ,.::.::o:ooooOoOoO. ,oO8O8Pd888'"
!                ,.:.::o:ooOoOoOO8O8OOo.8OOPd8O8O"
!               , ..:.::o:ooOoOOOO8OOOOo.FdO8O8"
!              , ..:.::o:ooOoOO8O888O8O,COCOO"
!             , . ..:.::o:ooOoOOOO8OOOOCOCO"
!              . ..:.::o:ooOoOoOO8O8OCCCC"o
!                 . ..:.::o:ooooOoCoCCC"o:o
!                 . ..:.::o:o:,cooooCo"oo:o:
!              `   . . ..:.:cocoooo"'o:o:::'
!              .`   . ..::ccccoc"'o:o:o:::'
!             :.:.   ,c:cccc"':.:.:.:.:.'
!           ..:.:"'`::::c:"'..:.:.:.:.:.'
!         ...:.'.:.::::"'  . . . . .'
!        .. . ....:."' ` . . . ''
!      . . . ...."'
!      .. . ."'
!     .
!
!!!!!!!!!!!!!!!!!!!!!!!
```

```
      IMPLICIT NONE

      real*8 apl    !  Semimajor Axis of the target [AU]
      real*8 epl    !  Eccentricity of the target

      real*8 a      !  Semimajor Axis of the projectile [AU]
      real*8 e      !  Eccentricity of the projectile
      real*8 inc    !  Inclination of the projectile [deg]
      real*8 omega  !  Argument of pericenter of the projectile [deg]
      real*8 outres !  Total intrinsic collisional probability in au^-2 yr^-1
      real*8 pi

      data pi/3.141592653589793/


!     write(*,*) "Semimajor axis of projectile in [AU]"
      read(*,*) a

!     write(*,*) "Eccentricity of projectile"
      read(*,*) e

!     write(*,*) "Inclination of projectile in (deg)"
      read(*,*) inc

!     write(*,*) "Argument of projectile pericenter (deg)"
      read(*,*) omega

!     Degrees to radians
      inc=inc/180.d0*pi
      omega=omega/180.d0*pi


!     write(*,*) "Semimajor Axis of the target [AU]"
      read(*,*) apl

!     write(*,*) "Eccentricity of the target"
      read(*,*) epl


!     Calling the main subroutine
      call WETKOZ(apl,epl,a,e,inc,omega,outres)


!     Write an output: Total intrinsic collisional probability
      write(*,*) outres

      end

!!!!!!!!!!!!!!!!!!!!!!!!!!!!!!!!!!!!!!!!!!!!!!!!!!!!!!!!!!!!!!!!!!!!!!!!!!!
!        .--..--..--..--..--..--.
!      .' \ (`._   (_)     _   \
!     .'    |  '._)        (_)  |
!     \ _.')\      .----..---.  /   SUBROUTINE AND FUNCTIONS AREA
!     |(_.' |    /    .-\-. \  |
!     \     0|    |   ( O| O) | o|
!      | _  |  .--.____.'._.-. |
!      \ (_) | o         -` .-` |
!       |    \   |`-._ _ _ _ _\ /
!       \    |   |  `. |_||_|  |
!       | o  |    \_      \     |     -.   .-.
!       |.-. \     `--..-'   O |     `.`-' .'
!     _.'  .' |     `-.-'      /-.__   ' .-'
!   .' `-.` '.|='=.='=.='=.='=|._/_ `-'.'
!   `-._  `.  |________/\_____|  `-.'
!      .'   ).| '=' '='\/ '=' |
!      `._.`  '----------------'
!              //___\   //___\
!                ||       ||
!                ||_.-.   ||_.-.
!               (_.--__) (_.--__)
!
!!!!!!!!!!!!!!!!!!!!!!!!!!!!!!!!!!!!!!!!!!!!!!!!!!!!!!!!!!!!!!!!!!!!!!!!!!!
```

```
      SUBROUTINE WETKOZ(apl,epl,apr,e,inc,omega,outres)

      IMPLICIT NONE

      INTEGER n ! Counter for the number of iterations in computing of the integral
      INTEGER it ! Number of steps in the integral
      INTEGER j ! Loop integer
      INTEGER nmax ! Maximal number of iterations in the evaluation of the integral
      INTEGER coef ! Maximal number of steps used for the evaluation in all iterations - defines output
           arrays
      INTEGER l ! Counter determining the position of the element in arrays
      INTEGER k ! Loop integer
      INTEGER ik ! Integer 1 or 2 determining whether the true anomaly of the target is (0,180) or
           (180,360) - we to investigate the whole orbit

      parameter(nmax=7) ! Determines the precision of the evaluation of the integral. The value 7 seems to
           give the best ratio between speed and precision
      parameter(coef=2*2*(3**(nmax-1))) ! Formula for the total number of steps of the integral


!===== INPUTS =====
      real*8 apl   !   Semimajor Axis of the target [AU]
      real*8 epl   !   Eccentricity of the target

      real*8 apr   !   Semimajor Axis of the projectile [AU]
      real*8 e     !   Eccentricity of the projectile
      real*8 inc   !   Inclination of the projectile [radians]
      real*8 omega !   Argument of pericenter of the projectile [radians]
!===== END OF INPUTS =====


!===== OUTPUTS ======
      real*8 outres ! Output: Total intrinsic collisional probability in au^-2 yr^-1
!===== END OF OUTPUTS =====


      real*8 prob(8)! Intrinsic collisional probability for 8 possible impact configurations for one r_0
           of the target
      real*8 prob1 !  Sum of prob(8), total intrinsic collisional probability for one r_0 of the target


      real*8 pi
      real*8 theta(8) ! Theta of the radiants for 8 possible impact configurations
      real*8 phi(8) ! Phi of the radiants for 8 possible impact configurations
      real*8 outk(8) ! k = e*cos(omega) for 8 possible impact configurations
      real*8 outh(8) ! h = e*sin(omega) for 8 possible impact configurations



!===== POSSIBLE OUTPUTS =====
      real*8 outR(coef) ! All heliocentric distances [AU] of the target evaluated in the integral
      real*8 outP(coef,8) ! All intrinsic collisional probabilities [au^-2 yr^-1] evaluated in the
           integral | 8 possible impact configurations for one r_0
      real*8 outTH(coef,8) ! All theta [deg] of the radiants evaluated in the integral | 8 possible impact
           configurations for one r_0
      real*8 outPH(coef,8) ! All phi [deg] of the radiants evaluated in the integral | 8 possible impact
           configurations for one r_0
      real*8 outKK(coef,8) ! All k = e*cos(omega) evaluated in the integral | 8 possible impact
           configurations for one r_0
      real*8 outhh(coef,8) ! All h = e*sin(omega) evaluated in the integral | 8 possible impact
           configurations for one r_0
!===== END POSSIBLE OUTPUTS =====



      real*8 a ! Lower limit of the integral
      real*8 b ! Upper limit of the integral
      real*8 x ! r_0 in the integral
      real*8 del ! Integration step (see Press et al. 1992, chap. 4.1)
      real*8 ddel ! 2 * del
      real*8 s1 ! Intermediate sum of the first integral [a ( 1 - e ) , a ]
```

```
      real*8 s2 ! Intermediate sum of the second integral [ a , a ( 1 + e ) ]

      real*8 aa ! Pericenter of the target
      real*8 bb ! Apocenter of the target
      real*8 tnm ! Number of steps in the integral - denominator in the evaluation of the integral
      real*8 funl ! Function subtitution for the first integral
      real*8 funu ! Function subtitution for the second integral
      real*8 sum ! Intermediate sum in the evaluation of the integrals
      real*8 func ! External function


      EXTERNAL func

      data pi/3.141592653589793/

!     function subtitution
      funl(x) = 2.d0*x*func(aa+x**2,bb,aa)
      funu(x) = 2.d0*x*func(bb-x**2,bb,aa)


!     Zero to variables
      l=0
      outres=0d0



!     Big loop over 2 segments of the orbit because of the true anomaly
      do ik=1,2

!      Pericenter, apocenter and lower and upper integration limits
       aa=apl*(1d0-epl)
       bb=apl*(1d0+epl)
       b=sqrt(apl*epl)
       a=0.d0

!      Zeros to intermediate sums
       s1=0d0
       s2=0d0

!      Loop over the consencutive iterations of the integral
!      FIRST INTEGRAL
       do n=1,nmax
!       The first evaluation, the same as for the circular orbit of the target
        if (n.eq.1) then
        x=0.5*(a+b)
!       Add 1 to the counter
        l=l+1
        CALL KOZAIOPIK(apr,e,inc,omega,apl,epl,aa+x**2,prob,prob1,theta,phi,ik,outh,outk)
        outR(l)=aa+x**2

!       Output flush
        do k=1,8
         outhh(l,k)=outh(k)
         outkk(l,k)=outk(k)
         outP(l,k)=prob(k)
         outTH(l,k)=theta(k)
         outPH(l,k)=phi(k)
        enddo

        s1=(b-a)*funl(x)*prob1

!      Here comes the integral
       else
         it=int(3d0**(n-2))
        tnm=it
        del=(b-a)/(3*tnm)
        ddel=del+del
        x=a+0.5d0*del
        sum=0.d0
        do 11 j=1,it
!       Add 1 to the counter
         l=l+1
         CALL KOZAIOPIK(apr,e,inc,omega,apl,epl,aa+x**2,prob,prob1,theta,phi,ik,outh,outk)
```

```
        outR(l)=aa+x**2

!       Output flush
        do k=1,8
         outhh(l,k)=outh(k)
         outkk(l,k)=outk(k)
         outP(l,k)=prob(k)
         outTH(l,k)=theta(k)
         outPH(l,k)=phi(k)
        enddo

        sum=sum+funl(x)*prob1
        x=x+ddel

!      Add 1 to the counter
        l=l+1
        CALL KOZAIOPIK(apr,e,inc,omega,apl,epl,aa+x**2,prob,prob1,theta,phi,ik,outh,outk)
        outR(l)=aa+x**2

!      Output flush
        do k=1,8
         outhh(l,k)=outh(k)
         outkk(l,k)=outk(k)
         outP(l,k)=prob(k)
         outTH(l,k)=theta(k)
         outPH(l,k)=phi(k)
        enddo

        sum=sum+funl(x)*prob1
        x=x+del
!       Loop end
11      continue
        s1=(s1+(b-a)*sum/tnm)/3.d0
       endif
      enddo

!     Loop over the consencutive iterations of the integral
!     SECOND INTEGRAL
      do n=1,nmax
!     The first evaluation, the same as for the circular orbit of the target
       if (n.eq.1) then

        x=0.5*(a+b)
!      Add 1 to the counter
        l=l+1
        CALL KOZAIOPIK(apr,e,inc,omega,apl,epl,bb-x**2,prob,prob1,theta,phi,ik,outh,outk)
        outR(l)=bb-x**2

!       Output flush
        do k=1,8
         outhh(l,k)=outh(k)
         outkk(l,k)=outk(k)
         outP(l,k)=prob(k)
         outTH(l,k)=theta(k)
         outPH(l,k)=phi(k)
        enddo
        s2=(b-a)*funu(x)*prob1
       else
        it=int(3d0**(n-2))
        tnm=it
        del=(b-a)/(3.*tnm)
        ddel=del+del
        x=a+0.5*del
        sum=0.d0
        do 12 j=1,it
!      Add 1 to the counter
         l=l+1
         CALL KOZAIOPIK(apr,e,inc,omega,apl,epl,bb-x**2,prob,prob1,theta,phi,ik,outh,outk)
         outR(l)=bb-x**2

!      Output flush
         do k=1,8
          outhh(l,k)=outh(k)
```

```
          outkk(l,k)=outk(k)
          outP(l,k)=prob(k)
          outTH(l,k)=theta(k)
          outPH(l,k)=phi(k)
         enddo
         sum=sum+funu(x)*prob1
         x=x+ddel
!       Add 1 to the counter
         l=l+1
         CALL KOZAIOPIK(apr,e,inc,omega,apl,epl,bb-x**2,prob,prob1,theta,phi,ik,outh,outk)
         outR(l)=bb-x**2

!       Output flush
         do k=1,8
          outhh(l,k)=outh(k)
          outkk(l,k)=outk(k)
          outP(l,k)=prob(k)
          outTH(l,k)=theta(k)
          outPH(l,k)=phi(k)
         enddo
         sum=sum+funu(x)*prob1
         x=x+del
12       continue
         s2=(s2+(b-a)*sum/tnm)/3d0
        endif

       enddo

       outres=(s1+s2)+outres

      enddo

      outres=outres/2d0

! SIMPLE ADDITIONAL OUTPUT EXAMPLE
!      write(*,*) outres
!      do j=1,coef
!       do k=1,8
!        if (outP(j,k).gt.(0d0)) then
!         write(*,*)outP(j,k),outR(j),outTH(j,k),
!     &   outPH(j,k),outhh(j,k),outkk(j,k)
!        endif
!       enddo
!      enddo
! END OF EXAMPLE

       end



! Function \psi from the article Pokorny et al. 2013 - needed for
! the total probability

      REAL*8 function func(x,a,b)
      real*8 x,a,b
      func = 1d0/x/sqrt((b-x)*(x-a))*sqrt(a*b)/(asin(1d0)*2)
      end function




! This subroutine computes a collision probability for a target on elliptic
! non-inclined orbit with a projectile on bound heliocentric orbit
!
! The subroutine itself computes a probability only for one heliocentric
! distance of the target rpl, the total probability must be computed as
! an integral of individual probabilities from pericenter to apocenter



      SUBROUTINE KOZAIOPIK(a,e,inc,om,apl,epl,rpl,prob,prob1,theta, phi,ik,outh,outk)
```

```
      IMPLICIT NONE
!     INPUT VARIABLES
      real*8 a ! Semimajor axis of the projectile [AU]
      real*8 e ! Eccentricity of the projectile
      real*8 inc ! Inclination of the projectile [rad]
      real*8 om ! Argument of pericenter of the projectile [rad]
      real*8 apl ! Semimajor axis of the target [AU]
      real*8 epl ! Eccentricity of the target
      real*8 rpl ! Heliocentric distance of the target [AU]
!     END OF INPUT

!     OUTPUT VARIABLES
      real*8 prob(8) ! Intrinsic collisional probabilities for all impact configurations [1D array]
      real*8 prob1 ! Total intrinsic collisional probability = sum of prob(8)
      real*8 outk(8) ! Array of all obtained k=e*cos(omega) in the impact configurations
      real*8 outh(8) ! Array of all obtained h=e*sin(omega) in the impact configurations
      real*8 theta(8) ! Ecliptic latitude of the impact radiants for the impact configurations
      real*8 phi(8) ! Ecliptic longitude of the impact radiants for the impact configurations
!     END OF OUTPUT

      complex*16 x(3) ! Roots of the system of equations (10) and (16) = impact configurations - cubic
          equation

      real*8 Ca ! Coefficients of the cubic Equation
      real*8 Cb
      real*8 Cc
      real*8 Cd

      real*8 y(4) ! Real part of the roots - maximum 8 impact configurations => 4 unique values of
          k=e*cos(omega)
      real*8 z(8) ! h=e*cos(omega) - from EQ (10) in Vokrouhlicky, Pokorny, Nesvorny 2012
      real*8 k ! k=e*cos(omega) - just more convenient and readable variable without array
      real*8 hh(2) ! Array of 2 possible values of h=e*sin(omega) for one unique k=e*cos(omega)
      real*8 h ! Selected h from array hh(2)

      real*8 kk ! Initial value of k=e*cos(omega) from the initial conditions
      real*8 hhh ! Initial value of h=e*sin(omega) from the initial conditions

      real*8 CapC ! Integral of the motion EQ (16) in Pokorny, Vokrouhlicky 2013
      real*8 c ! Integral of the motion c = eta * cos (inc)
      real*8 eta ! \eta = \sqrt{1-e^2}
      real*8 gamm ! Factor Gamma for scaling the lenght of the Lidov-Kozai cycle - see below EQ (28) in
          Vokrouhlicky, Pokorny, Nesvorny 2012

      real*8 dk ! Displacement in k, for an exact impact configuration point - EQ (19) in Vokrouhlicky,
          Pokorny, Nesvorny 2012
      real*8 dh ! Displacement in h, for an exact impact configuration point - EQ (19) in Vokrouhlicky,
          Pokorny, Nesvorny 2012
      real*8 dkdt ! Derivation of k=e*cos(omega) by time - EQ (27) in Vokrouhlicky, Pokorny, Nesvorny 2012
      real*8 dhdt ! Derivation of h=e*sin(omega) by time - EQ (28) in Vokrouhlicky, Pokorny, Nesvorny 2012

      real*8 phk ! EQ (21) in Vokrouhlicky, Pokorny, Nesvorny 2012
      real*8 phh ! EQ (22) in Vokrouhlicky, Pokorny, Nesvorny 2012
      real*8 psk ! EQ (23) in Vokrouhlicky, Pokorny, Nesvorny 2012
      real*8 psh ! EQ (24) in Vokrouhlicky, Pokorny, Nesvorny 2012
      real*8 den ! EQ (20) in Vokrouhlicky, Pokorny, Nesvorny 2012

      real*8 Pom ! T_Kozai - The lenght of the one Lidov-Kozai cycle [yr] - see Kinoshita & Nakai 2007

      real*8 P2 ! EQ (17) in Pokorny, Vokrouhlicky 2013 - Probability part 2

      real*8 aph
      real*8 rho2
      real*8 pi

      real*8 kx
      real*8 hx
      real*8 dkdt1
      real*8 dhdt1
      real*8 dist
      real*8 timm
      real*8 r1
      real*8 r2
```

```
      real*8 aa
      real*8 th
      real*8 ph
      real*8 Ie
      real*8 Iinc
      real*8 Iom

      integer i
      integer j
      integer l
      integer m
      integer m2
      integer nroot
      integer znk(2)
      integer ddd
      integer CUBIC
      integer ik
      data pi/3.141592653589793/

      real*8 err
      real*8 preci

!     Pericenter r1 and apocenter r2 of the target
      r1=apl*(1d0-epl)
      r2=apl*(1d0+epl)

!     Zeros to variables
      theta=0d0
      phi=0d0
      prob=0d0
      prob1=0d0
      ddd=0

!     Determine initial k,h for the projectile
      kk=e*cos(om)
      hhh=e*sin(om)

!     Determine aplha,eta
      aph=rpl/a
      eta=sqrt(1d0-e*e)

!     Evaluate integrals of motion
      c=eta*cos(inc)
      CapC=1./eta/eta*((2d0+3.*e*e)*(3d0*c*c-eta*eta)+15d0*(eta*eta-c*c)*(kk*kk-hhh*hhh))

!     Gamma factor, where 0.0009546 is mass of the Jupiter in Solar Masses
!     and 140.954423151 - this value is not important for the collision probability.
!     However scales the length of Lidov-Kozai cycle
      gamm=2d0*pi*0.0009546*sqrt(a**3)/140.954423151

!     Iteration value
      l=1

!!!   Should be computed only once (CHANGE)
      CALL KINOSHITA(CapC,c,eta,om,gamm,pom)

!     Ascending/Descending node i = 1 Ascending, i = 2 Descending

      do i=1,2

!      Determine coefficients for the Cubic equation

       Ca=(-1.)**(i+1)*30.*aph
       Cb=6.*(3.*aph*aph+5.*aph-5.*c*c)
       Cc=(-1.)**(i+1)*aph*(36.*aph-20.-24.*c*c-CapC)
       Cd=18.*aph*aph-20*aph-24*aph*c*c+30*c*c-CapC*aph

!      Call a routine to solve the cubic equation
       nroot = CUBIC(Ca, Cb, Cc, Cd, x)

!       Loop over the roots of the cubic equation ie. the impact configurations
        do j=1, nroot
```

```
!       We want only non-complex solutions
        if ((aimag(x(j)).eq.(0.)).and.(abs(real(x(j))).lt.(1.))) then
!       Get the real part of the complex root of the equation, k=e*cos(omega)
        y(l)= real(x(j))
!       Evaluate h=e*cos(omega) - EQ (10) in Vokrouhlicky, Pokorny, Nesvorny 2012
        z(2*l-1)=sqrt(1-y(l)**2-aph*(1+(-1.)**(i+1)*y(l)))
        z(2*l-0)=-z(2*l-1)

!       Check if h=e*cos(omega) can exist
        if ((1-y(l)**2-aph*(1+(-1.)**(i+1)*y(l))).lt.(0d0)) then
         goto 200 ! GOTO END OF THE MAIN LOOP (it should never happen, however :))
        endif


!       Assign to more conveniet(readable) variables
        k=y(l)
        hh(1)=z(2*l-1)
        hh(2)=z(2*l-0)
!       Set number of unique h=e*cos(omega)
        m2=2
!       Look whether h=e*cos(omega) is unique, if not m2=1
        if (hh(2).eq.hh(1)) m2=1



!       Forced oscillations - max 4 impact configurations
        if (CapC.lt.(2*(3*c**2-1))) then
         m2=1
         hh(1)=abs(hh(1))
!        See, whether omega is >180, if yes then h must be < 0
         if (om.gt.pi) hh(1)=-hh(1)
        endif

!       Loop over the impact configurations
        do m=1,m2
!       Even more readable variables
        h=hh(m)
        eta=sqrt(1-h**2-k**2)

!       Impact eccentricity,inclination and argument of pericenter
        Ie=sqrt(k**2+h**2)
        Iinc =acos(c/eta)
        Iom = acos(k/Ie)
!       Factor /beta from Eq (21) - see below the equation for a formula
        aa=(-1.)**(ik+1)*sqrt((rpl-r1)*(r2-rpl))/(apl*sqrt(1d0-epl**2))

!       Solution for the ambiquity of acos in the determination of argument of pericenter of the impact
        if (h.lt.(0.0)) Iom = 2*pi - Iom

!       Call Radiant and P2 determination (EQ. 17) - computes also impact velocities, which may be also
    interesting output
        CALL RADIANT_ECC(a,Ie,Iinc,Iom,apl,epl,rpl,th,ph,P2,ik)
!       Outputs from radiants and also k,h for intersections to arrays
        theta(l*2-2+m)=th
        phi(l*2-2+m)=ph
        outh(l*2-2+m)=h
        outk(l*2-2+m)=k
!       Factor /Lambda from EQ 23 (formerly named /rho_2 thus may be misleading (TO BE CHANGED FUTURE)
        rho2=sqrt( &
    &       (eta**2 - c**2) / &
    &       ( &
    &       (1d0+aa**2)*(eta**2-c**2)*(1+(-1.)**(i+1)*k)**2 &
    &     + ( &
    &       (h*eta)+(-1.)**(i+1)*aa*c*(1+(-1.)**(i+1)*k) &
    &       )**2 &
    &       ) &
    &       )
!        EQ 22
         dist=(eta**2-aph*(1+(-1.)**(i+1)*k))*rho2
!        Partial derivations of the distance EQs (21) - (24) in Vokrouhlicky, Pokorny, Nesvorny 2012
    (ICARUS)
         phk=2.*k*(2.*(7.-3.*c*c+3.*h*h-12.*k*k)+CapC)
         phh=2.*h*(2.*(-8.+12.*c*c+3.*k*k+18.*h*h)+CapC)
```

```
          psk=-2.*(k+(-1.)**(i+1)*aph/2.)*rho2
          psh=-2.*(h)*rho2
!         Denominator EQ (20) in Vokrouhlicky, Pokorny, Nesvorny 2012 (ICARUS)
          den=(phh*psk-phk*psh)
!         And finally displacements EQ (19) in Vokrouhlicky, Pokorny, Nesvorny 2012 (ICARUS)
          dk=phh/den/a
          dh=-phk/den/a

          kx=k
          hx=h

          timm=0

!     If Denominator is too small we have to compute the time in the proximity of planet numerically (it
     is a bit slower, but we have quite large steps)
!       if (abs(den).lt.(2E-3)) then
       if (abs(den).lt.(2E-3)) then
!      We do not know the radius of the target, thus we set this value as an approximate value (but should
     be ok for most of cases).
        err=1D-9
        preci=1D-7
!       Set zero values for a special case commented in Vokrouhlicky, Pokorny, Nesvorny 2012 (ICARUS) -
     Appendix
        znk(1)=0
        znk(2)=0


        do while (abs(dist).lt.(err))
         dkdt1=-3d0/2d0*preci*gamm*eta*h*(1- &
     &  5d0/2d0*k*k*(eta*eta-c*c)/(1-eta*eta)/eta/eta+ &
     &  5d0/2d0*(c*c-eta**4d0)/(eta**4d0)*h*h/(1d0-eta*eta))
         dhdt1=3d0/2d0*preci*gamm*eta*k*(1+5d0/2d0*h*h*c*c/eta**4d0)
         k=k-dkdt1
         h=h-dhdt1
         eta=sqrt(1-h*h-k*k)
         dist=(eta*eta-aph*(1+(-1.)**(i+1)*k))* &
     &       sqrt((eta**2 - c**2) / &
     &       ( &
     &       (1d0+aa**2)*(eta**2-c**2)*(1+(-1.)**(i+1)*k)**2 &
     &     + ( &
     &       (h*eta)+(-1.)**(i+1)*aa*c*(1+(-1.)**(i+1)*k) &
     &       )**2 &
     &       ))
!       Dist should be
        if (dist.ge.(0.0)) znk(1)=1
        if (dist.le.(0.0)) znk(2)=1
        timm=timm+preci
            enddo
        if ((znk(1).eq.(1)).and.(znk(2).eq.(1))) ddd=1
        znk(1)=0
        znk(2)=0
!        write(*,*) timm, "END 1", ddd
        k=kx
        h=hx
        eta=sqrt(1-h*h-k*k)
        dist=(eta*eta-aph*(1+(-1.)**(i+1)*k))* &
     &    sqrt((eta**2 - c**2) / &
     &  ( &
     &  (1d0+aa**2)*(eta**2-c**2)*(1+(-1.)**(i+1)*k)**2 &
     &  + ( &
     &     (h*eta)+(-1.)**(i+1)*aa*c*(1+(-1.)**(i+1)*k) &
     &     )**2 &
     &  ))
!        write(*,*) dist
           do while (abs(dist).lt.(err))
        dkdt1=-3./2.*preci*gamm*eta*h*(1- &
     &    5./2.*k*k*(eta*eta-c*c)/(1-eta*eta)/eta/eta+ &
     &    5./2.*(c*c-eta**4.)/(eta**4.)*h*h/(1-eta*eta))
        dhdt1=3./2.*preci*gamm*eta*k*(1+5./2.*h*h*c*c/eta**4.)
        k=k+dkdt1
        h=h+dhdt1
        eta=sqrt(1-h*h-k*k)
        dist=(eta*eta-aph*(1+(-1.)**(i+1)*k))* &
```

```
     &    sqrt((eta**2 - c**2) / &
     &  (  &
     &  (1d0+aa**2)*(eta**2-c**2)*(1+(-1.)**(i+1)*k)**2 &
     &  + (  &
     &     (h*eta)+(-1.)**(i+1)*aa*c*(1+(-1.)**(i+1)*k) &
     &     )**2  &
     &  ))
        if (dist.ge.(0.0)) znk(1)=1
        if (dist.le.(0.0)) znk(2)=1
        timm=timm+preci


!  !        write(*,*) dist,k,h,timm
!       call sleep(0)
            enddo

        if ((znk(1).eq.(1)).and.(znk(2).eq.(1))) ddd=1
        znk(1)=0
        znk(2)=0
!        write(*,*) timm, "END 2",ddd
        k=kx
        h=hx
        if (ddd.eq.(1)) then
        timm=timm/2d0
!       write(*,*) "PRESKOK DRAH", timm,abs(timm)/pom,P2
        else
!        write(*,*) "NEPRESKOK DRAH", timm,abs(timm)/pom,P2
        endif
        timm=timm/err

        prob(l*2-2+m) =  &
     &    abs(timm)/pom*P2/a

!!!! 1/a is from R/a = rho

!     Denominator is OK, so we can go straighforward as in the article
      else
        k=kx
        h=hx

        dkdt=-3./2.*gamm*eta*h*(1- &
     &    5./2.*k*k*(eta*eta-c*c)/(1-eta*eta)/eta/eta+ &
     &    5./2.*(c*c-eta**4.)/(eta**4.)*h*h/(1-eta*eta))
        dhdt=3./2.*gamm*eta*k*(1+5./2.*h*h*c*c/eta**4.)
           prob(l*2-2+m)=abs(dk/dkdt)*2/pom*P2
      endif
      prob1=prob(l*2-2+m)+prob1
      enddo


            l=l+1
         endif
 200  continue
        enddo


      enddo

      END


      SUBROUTINE RADIANT_ECC(a,e,inc,om,apl,epl,rpl,theta,phi,P2,k)
      IMPLICIT NONE

! This subroutine computes radiants of a particle (phi,theta)
! for a eccentric coplanar target and projectile
! apex of the target's motion has theta = 0, phi = 0
! theta means ecliptic latitude
! phi means ecliptic longitude
!!! INPUT/OUTPUT
```

```
! INPUT Variables:
! a ... semimajor axis of the projectile
! e ... eccentricity of the projectile
! inc ... inclination of the projectile in radians
! om ... argument of pericenter of the projectile in radians
! apl ... semimajor axis of the target
! epl ... eccentricity of the target
! rpl ... heliocentric distance of the target

      real*8 a,e,inc,om,apl,epl,rpl
      integer k

! OUTPUT Variables:
! theta ... ecliptic latitude (-pi/2,pi/2)
! phi ..... ecliptic longitude (-pi,pi)
! P2 ..... second term in probability calculation

      real*8 theta,phi,P2

      real*8 eta,etapl,asc,dsc,GM,r1,r2
      real*8 v1,v2,v3,vel,pi,rad,bigR,bigF,P,R2F2

      data pi/3.141592653589793/

! GM = gravitational constat * mass of the gravitational center
! in [astronomical unit**3 * mean solar day ** (-2) * solar mass**(-1)
      GM = 0.2959122104742908d-03
! Some initial computations
      rad=pi/180.0d0
      eta=sqrt(1d0-e*e)
      etapl=sqrt(1d0-epl**2)
      r1=apl*(1d0-epl)
      r2=apl*(1d0+epl)
      bigR=(-1.)**(k+1)*sqrt((rpl-r1)*(r2-rpl))/rpl
      bigF=etapl*apl/rpl
      P=a*eta**2/rpl
      R2F2=bigR**2+bigF**2

      asc = P/(1d0+e*cos(om))
      dsc = P/(1d0-e*cos(om))

!     Zeros to variables
      v1=0d0
      v2=0d0
      v3=0d0
      vel=0d0

!      write(*,*) "RADS ",asc,dsc
      if ((1d0-1e-4.le.asc).and.(asc.le.1d0+1e-4)) then

      v1 = -(sqrt(apl/rpl*P)*(bigF*cos(inc) - e*sin(om)/P*bigR) &
     &     - R2F2) / sqrt(R2F2)
      v2 = (e*sin(om)*bigF/P + bigR*cos(inc)) * sqrt(apl/rpl*P) &
     &     / sqrt(R2F2)
      v3 = - sqrt(apl/rpl*P) * sin(inc)

      vel=sqrt(v1**2+v2**2+v3**2)
      theta=asin(v3/vel)
      phi=atan2(v2,v1)
!      write(*,*)theta/rad,phi/rad, "asc"
      endif


      if ((1d0-1e-4.le.dsc).and.(dsc.le.1d0+1e-4)) then

      v1 = -(sqrt(apl/rpl*P)*(bigF*cos(inc) + e*sin(om)/P*bigR) &
     &     - R2F2) / sqrt(R2F2)
      v2 = ( - e*sin(om)*bigF/P + bigR*cos(inc)) * sqrt(apl/rpl*P) &
     &     / sqrt(R2F2)
      v3 = + sqrt(apl/rpl*P) * sin(inc)


      vel=sqrt(v1**2+v2**2+v3**2)
```

```
      theta=asin(v3/vel)
      phi=atan2(v2,v1)
      endif
      theta=theta/rad
      phi=phi/rad
      P2=1d0/apl/4d0/sqrt(R2F2)*vel/sqrt(vel**2-v1**2)/sqrt(a**3)
      END

!       ================================================

        SUBROUTINE COMELP(HK,CK,CE)

!       ================================================
!       Purpose: Compute complete elliptic integrals K(k)
!                and E(k)
!       Input  : K  --- Modulus k ( 0 ?? k ?? 1 )
!       Output : CK --- K(k)
!                CE --- E(k)
!       ================================================
!
        IMPLICIT NONE
        real*8 PK,HK,CK,CE,AE,BE,AK,BK

        PK=1.0-HK*HK
        IF (HK.EQ.1.0) THEN
           CK=1.0+300.
           CE=1.0
        ELSE
           AK=(((.01451196212*PK+.03742563713)*PK &
     &        +.03590092383)*PK+.09666344259)*PK+ &
     &        1.38629436112
           BK=((((.00441787012*PK+.03328355346)*PK+ &
     &        .06880248576)*PK+.12498593597)*PK+.5
           CK=AK-BK*dLOG(PK)
           AE=(((.01736506451*PK+.04757383546)*PK+ &
     &        .0626060122)*PK+.44325141463)*PK+1.0
           BE=((((.00526449639*PK+.04069697526)*PK+ &
     &        .09200180037)*PK+.2499836831)*PK
           CE=AE-BE*LOG(PK)
           CK=AK-BK*dlog(PK)
        ENDIF

        RETURN
        END

!       ================================================

      SUBROUTINE KINOSHITA(CapC,c,eta,om,gamm,pom)


! Kinoshita-Nakai 2007
!
! Input variables
! CapC .. energy integral in quadrupole Kozai oscillations
! c ..... particle's integral of motion c = eta * cos(i)
! eta ... eta = (1 - e**2)
! om .... argument of pericenter of the particle
!
!         Ms/Mj = 0.0009546, aJ**3 = 140.954423151 AU**3
! gamm ... gamm=2d0*pi*0.0009546*sqrt(a*a*a)/140.954423151
!
      implicit none
      real*8 CapC,c,eta,om,gamm
! Output variables
! pom .... one period of argument of pericenter in years
!         (if in forced libration mode we take only 1/2 of it)

      real*8 pom

! Temp variables

      real*8 C1,C2,x0,x1,x2,DD,tmp,a0,a1,a2,HK,CK,CE,nom,pi
      complex*16 xq(2)
```

```
        data pi/3.141592653589793/

        a0=0d0
        a1=0d0
        a2=0d0
        x1=0d0
        x2=0d0

      C1=5d0+5d0*c*c
      C2=5d0*c*c/eta/eta+eta*eta+5d0*(1-eta*eta)*(1-c*c/eta/eta)* &
     &  cos(2*om)
      x0=1d0/4d0*(C1-C2)

      DD = 1d0/2d0*(C1+C2)*1d0/2d0*(C1+C2)-12d0*5d0*c*c
      if(DD .ge. 0.)then
          xq(1)=cmplx((-1d0/2d0*(C1+C2)+sqrt(DD))/2./(-3d0), 0.)
          xq(2)=cmplx((-1d0/2d0*(C1+C2)-sqrt(DD))/2./(-3d0), 0.)
        else
          xq(1)=cmplx(-1d0/2d0*(C1+C2)/2./(-3d0), +sqrt(-DD)/2./(-3d0))
          xq(2)=cmplx(-1d0/2d0*(C1+C2)/2./(-3d0), -sqrt(-DD)/2./(-3d0))
        endif
           if (aimag(xq(1)).eq.(0.)) x1=real(xq(1))
           if (aimag(xq(2)).eq.(0.)) x2=real(xq(2))
      if (x1.gt.x2) then
      tmp=x1
      x1=x2
      x2=tmp
      endif
      if (x0.le.x1) then
      a0=x0
      a1=x1
      a2=x2

      endif
      if (x0.ge.x2) then
      a0=x1
      a1=x2
      a2=x0
      endif
      if ((x0.ge.x1).and.(x0.le.x2)) then
      a0=x1
      a1=x0
      a2=x2
      endif

!   Complete Elliptic Integral of the First Kind = CK
      HK=sqrt((a1-a0)/(a2-a0))

        CALL COMELP(HK,CK,CE)
!      write(*,*) CK
!       IF (HK.NE.1.0) WRITE(*,*) HK,CK,CE
!       IF (HK.EQ.1.0) WRITE(*,*) HK,CE
      Nom=3d0*sqrt(6d0)*pi/8d0/CK*sqrt(a2-a0)*gamm
      Pom=2d0*pi/nom


!      Variable Pom is a period of one Kozai cycle (see Kinoshita-Nakai 2007)

      if (CapC.lt.(2*(3*c*c-1))) pom=pom/2d0


      END



      FUNCTION quad(a, b, c, x)

! Solve a quadratic equation where a, b, and c are real.
!   a*x*x + b*x + c = 0
! This function returns the number of roots
!
! Public Variables
!   a, b, c    ... coefficients (input)
```

```
!   x(i)       ... two complex*16    solutions (output)
!   nroot      ... number of roots (output)
! ------------------------------------------------------------------------

       IMPLICIT NONE
      complex*16 x(2)
      real*8 a,b,c,DD
      integer QUAD,NROOT

      if(a .eq. 0.)then
        if(b .eq. 0.)then
!          We have a non-equation; therefore, we have no valid solution
          nroot = 0
        else
!          We have a linear equation with 1 root.
          nroot = 1
          x(1) = cmplx(-c/b, 0.)
        endif
      else
!       We have a true quadratic equation. Apply the quadratic formula to find two roots.
      nroot = 2
        DD = b*b-4.*a*c
      if(DD .ge. 0.)then
          x(1) = cmplx((-b+sqrt(DD))/2./a, 0.)
          x(2) = cmplx((-b-sqrt(DD))/2./a, 0.)
        else
          x(1) = cmplx(-b/2./a, +sqrt(-DD)/2./a)
          x(2) = cmplx(-b/2./a, -sqrt(-DD)/2./a)
        endif
      endif

! Return the number of roots
      QUAD = NROOT

      end

! ------------------------------------------------------------------------
      FUNCTION cubic(a, b, c, d, x)
! ------------------------------------------------------------------------
!   Solve a cubic equation where a, b, c, and d are real.
!     a*x**3 + b*x**2 + c*x + d = 0
!   This function returns the number of roots
!
!   Public Variables
!     a, b, c, d ... coefficients (input)
!     x(i)       ... three (generally) complex*16 solutions (output)
!     nroot      ... number of roots (output)
!   Local Variables:
!     y1, y2, y3 ... three transformed solutions
!
!   Formula used are given in Tuma, "Engineering Mathematics Handbook", p7
!     (McGraw Hill, 1978).
!     Step 0: If a is 0. use the quadratic formula to avoid dividing by 0.
!     Step 1: Calculate p and q
!             p = ( 3*c/a - (b/a)**2 ) / 3
!             q = ( 2*(b/a)**3 - 9*b*c/a/a + 27*d/a ) / 27
!     Step 2: Calculate discriminant D
!             D = (p/3)**3 + (q/2)**2
!     Step 3: Depending on the sign of D, we follow different strategy.
!             If D<0, three distinct real roots.
!             If D=0, three real roots of which at least two are equal.
!             If D>0, one real and two complex*16 roots.
!     Step 3a: For D>0 and D=0,
!             Calculate u and v
!             u = cubic_root(-q/2 + sqrt(D))
!             v = cubic_root(-q/2 - sqrt(D))
!             Find the three transformed roots
!
!             y1 = u + v
!             y2 = -(u+v)/2 + i (u-v)*sqrt(3)/2
!             y3 = -(u+v)/2 - i (u-v)*sqrt(3)/2
!     Step 3b Alternately, for D<0, a trigonometric formulation is more convenient
!             y1 =  2 * sqrt(|p|/3) * cos(phi/3)
```

```
!           y2 = -2 * sqrt(|p|/3) * cos((phi+pi)/3)
!           y3 = -2 * sqrt(|p|/3) * cos((phi-pi)/3)
!           where phi = acos(-q/2/sqrt(|p|**3/27))
!                 pi  = 3.141592654...
!     Step 4 Finally, find the three roots
!           x = y - b/a/3
!   ---------------------------------------------------------------------

      IMPLICIT NONE

!   Declare variables
      complex*16 x(3)

      real*8 DD,q,p,temp1,phi,temp2,u,v,y1,y2,y3,y2r,y2i,a,b,c,d,pi

      integer QUAD,NROOT,CUBIC


      data pi/3.141592653589793/
!   Step 0: If a is 0 use the quadratic formula. -------------------------
      if(a .eq. 0.)then
        nroot = QUAD(b, c, d, x)
        CUBIC = NROOT
        return
      endif

!   Cubic equation with 3 roots
      nroot = 3

!   Step 1: Calculate p and q --------------------------------------------
      p  = c/a - b*b/a/a/3.
      q  = (2.*b*b*b/a/a/a - 9.*b*c/a/a + 27.*d/a) / 27.

!   Step 2: Calculate DD (discriminant) ----------------------------------
      DD = p*p*p/27. + q*q/4.

!   Step 3: Branch to different algorithms based on DD -------------------
      if(DD .lt. 0.)then
!        Step 3b:
!        3 real unequal roots -- use the trigonometric formulation
        phi = acos(-q/2./sqrt(abs(p*p*p)/27.))
        temp1=2.*sqrt(abs(p)/3.)
        y1 =  temp1*cos(phi/3.)
        y2 = -temp1*cos((phi+pi)/3.)
        y3 = -temp1*cos((phi-pi)/3.)
      else
!        Step 3a:
!        1 real root & 2 conjugate complex*16 roots OR 3 real roots (some are equal)
        temp1 = -q/2. + sqrt(DD)
        temp2 = -q/2. - sqrt(DD)
        u = exp(log(abs(temp1))/3.)
        v = exp(log(abs(temp2))/3.)
        if(temp1 .lt. 0.) u=-u
        if(temp2 .lt. 0.) v=-v
        y1  = u + v
        y2r = -(u+v)/2.
        y2i =  (u-v)*sqrt(3.)/2.
      endif

!   Step 4: Final transformation -----------------------------------------
      temp1 = b/a/3.
      y1 = y1-temp1
      y1=y1-(d+y1*(c+y1*(b+y1*a))) &
     &  /(c+y1*(2.*b+y1*3.*a))
      y2 = y2-temp1
      y2=y2-(d+y2*(c+y2*(b+y2*a))) &
     &  /(c+y2*(2.*b+y2*3.*a))
      y3 = y3-temp1
      y3=y3-(d+y3*(c+y3*(b+y3*a))) &
     &  /(c+y3*(2.*b+y3*3.*a))
      y2r=y2r-temp1
```

```
!   Assign answers ------------------------------------------------------
      if(DD .lt. 0.)then
        x(1) = cmplx( y1, 0.)
        x(2) = cmplx( y2, 0.)
        x(3) = cmplx( y3, 0.)
      elseif(DD .eq. 0.)then
        x(1) = cmplx( y1, 0.)
      y2r=y2r-(d+y2r*(c+y2r*(b+y2r*a))) &
     &  /(c+y2r*(2.*b+y2r*3.*a))
        x(2) = cmplx(y2r, 0.)
        x(3) = cmplx(y2r, 0.)
      else
        x(1) = cmplx( y1, 0.)
        x(2) = cmplx(y2r, y2i)
        x(3) = cmplx(y2r,-y2i)
      endif

!   Return the number of roots
      CUBIC = NROOT

      end
```

Appendix B - Publications

Here, we list all publications with recorded citations below, as for July 2014.

Peer-reviewed papers

- Nesvorný, D., Vokrouhlický, D. **Pokorný, P.**, & Janches, D., 2011, Dynamics of Dust Particles Released from Oort Cloud Comets and Their Contribution to Radar Meteors, *Astrophysical Journal*, 743, 129.

    1. Vokrouhlický, D., Pokorný, P, & Nesvorný, D., 2012, Öpik-type collision probability for high-inclination orbits, *Icarus*, 219, 150.
    2. Dartois, E., Engrand, C., Brunetto, R., Duprat, J., Pino, T., Quirico, E., Remusat, L., Bardin, N., Briani, G., Mostefaoui, S., Morinaud, G., Crane, B., Szwec, N., Delauche, L., Jamme, F., Sandt, Ch. & Dumas, P., 2013, UltraCarbonaceous Antarctic micrometeorites, probing the Solar System beyond the nitrogen snow-line, *Icarus*, 224, 243.
    3. Withers, Paul, Christou, A. A. & Vaubaillon, J., 2013, Meteoric ion layers in the ionospheres of venus and mars: Early observations and consideration of the role of meteor showers, *Advances in Space Research*, 52, 1207.
    4. Bianchi, S., Piconcelli, E., Pérez-Torres, M. Á., Fiore, F., La Franca, F., Mathur, S. & Matt, G. , 2013, The NGC 3341 minor merger: a panchromatic view of the active galactic nucleus in a dwarf companion, *MNRAS*, 435, 2335.
    5. Langowski, M., von Savigny, C., Burrows, J. P., Feng, W., Plane, J. M. C., Marsh, D. R., Janches, D., Sinnhuber, M. & Aikin, A. C., 2014, Global investigation of the Mg atom and ion layers using SCIAMACHY/Envisat observations between 70 km and 150 km altitude and WACCM-Mg model results, *Atmospheric Chemistry and Physics Discussions*, 14, 1971.
    6. Sekhar, A. & Asher, D. J., 2014, Meteor showers on Earth from sungrazing comets, *MNRAS*, 437, 71.
    7. Janches, D., Hocking, W., Pifko, S., Hormaechea, J. L., Fritts, D. C., Brunini, C., Michell, R. & Samara, M., 2014, Interferometric meteor head echo observations using the Southern Argentina Agile Meteor Radar, *Journal of Geophysical Research: Space Physics*, 119, 2269.
    8. Pokorný, P., Vokrouhlický, D. Nesvorný, D., Campbell-Brown, M. D., & Brown, P. G., 2014, Dynamical Model for the Toroidal Sporadic Meteors, *Astrophysical Journal*, 789, 25.

- Nesvorný, D., Janches, D., Vokrouhlický, D. **Pokorný, P.**, Bottke, W. F., & Jenniskens, P., 2011, Dynamical Model for the Zodiacal Cloud and Sporadic Meteors, *Astrophysical Journal*, 743, 129.

    1. Alonso-Azcárate, J., Madiedo, J. M., Trigo-Rodriguez, J. M., Zamorano, J., Izquierdo, J., Ocaña, F., Sánchez de Miguel, A., Lacruz, J. & Toscano, F. M., 2012, Orbit and Radiant of a Sporadic Fireball Imaged by the Spanish Meteor Network, *Lunar and Planetary Science Conference*, 43, 1177.
    2. Jewitt, D., Ishiguro, M. & Agarwal, J., 2013, Large Particles in Active Asteroid P/2010 A2, *ApJ*, 764, L5.

3. Pifko, S., Janches, D., Close, S., Sparks, J., Nakamura, T. & Nesvorny, D., 2013, The Meteoroid Input Function and predictions of mid-latitude meteor observations by the MU radar, *Icarus*, 223, 444.
4. Withers, Paul, Christou, A. A. & Vaubaillon, J., 2013, Meteoric ion layers in the ionospheres of venus and mars: Early observations and consideration of the role of meteor showers, *Advances in Space Research*, 52, 1207.
5. Langowski, M., von Savigny, C., Burrows, J. P., Feng, W., Plane, J. M. C., Marsh, D. R., Janches, D., Sinnhuber, M. & Aikin, A. C., 2014, Global investigation of the Mg atom and ion layers using SCIAMACHY/Envisat observations between 70 km and 150 km altitude and WACCM-Mg model results, *Atmospheric Chemistry and Physics Discussions*, 14, 1971.
6. Janches, D., Hocking, W., Pifko, S., Hormaechea, J. L., Fritts, D. C., Brunini, C., Michell, R. & Samara, M., 2014, Interferometric meteor head echo observations using the Southern Argentina Agile Meteor Radar, *Journal of Geophysical Research: Space Physics*, 119, 2269.
7. Pokorný, P., Vokrouhlický, D. Nesvorný, D., Campbell-Brown, M. D., & Brown, P. G., 2014, Dynamical Model for the Toroidal Sporadic Meteors, *Astrophysical Journal*,

- Vokrouhlický, D., **Pokorný, P**, & Nesvorný, D., 2012, Öpik-type collision probability for high-inclination orbits, *Icarus*, 219, 150.

1. Vokrouhlický, D. & Nesvorný, D., 2012, Sun-grazing orbit of the unusual near-Earth object 2004 LG, *A&A*, 541, A109.
2. Bottke, W. F., Vokrouhlický, D., Nesvorný, D. & Moore, J. M., 2013, Black rain: The burial of the Galilean satellites in irregular satellite debris, *Icarus*, 223, 775.
3. Tamayo, D., Burns, J. A. & Hamilton, D. P., 2013, Chaotic dust dynamics and implications for the hemispherical color asymmetries of the Uranian satellites, *Icarus*, 226, 655.
4. Pokorný, P, Vokrouhlický, D., 2013, Öpik-type collision probability for high-inclination orbits: Targets on eccentric orbits, *Icarus*, 226, 682.
5. Pokorný, P., Vokrouhlický, D. Nesvorný, D., Campbell-Brown, M. D., & Brown, P. G., 2014, Dynamical Model for the Toroidal Sporadic Meteors, *Astrophysical Journal*, 789, 25.

- **Pokorný, P.**, Vokrouhlický, D., 2013, Öpik-type collision probability for high-inclination orbits: Targets on eccentric orbits, *Icarus*, 226, 682.

1. Pokorný, P., Vokrouhlický, D. Nesvorný, D., Campbell-Brown, M. D., & Brown, P. G., 2014, Dynamical Model for the Toroidal Sporadic Meteors, *Astrophysical Journal*, 789, 25

- **Pokorný, P.**, Vokrouhlický, D. Nesvorný, D., Campbell-Brown, M. D., & Brown, P. G., 2014, Dynamical Model for the Toroidal Sporadic Meteors, *Astrophysical Journal*, 789, 25

Conference abstracts

- Nesvorný, D., Janches, D., Vokrouhlický, D. **Pokorný, P.**, Bottke, W. F., & Jenniskens, P., 2012, Dynamical Model for the Zodiacal Cloud and Sporadic Meteors, *Asteroids, Comets, Meteors*, Niigata, Japan, 6336.

- **Pokorný, P.** & Vokrouhlický, D., 2012, Öpik-type collision probability for high-inclination orbits, *American Astronomical Society, DPS Meeting 44*, Reno, NV, United States of America, 212.05.

- **Pokorný, P.**, Vokrouhlický, D. Nesvorný, D., Campbell-Brown, M. D., & Brown, P. G., 2013, Dynamical Model for the Toroidal Sporadic Meteors, *American Astronomical Society, DPS Meeting 45*, Denver, CO, Uniter States of America, 402.04.

Appendix C - Reprints of papers

Paper A: Vokrouhlický, D., **Pokorný, P**, & Nesvorný, D., 2012, Öpik-type collision probability for high-inclination orbits, *Icarus*, 219, 150.

Paper B: **Pokorný, P.**, Vokrouhlický, D., 2013, Öpik-type collision probability for high-inclination orbits: Targets on eccentric orbits, *Icarus*, 226, 682.

Paper C: Nesvorný, D., Vokrouhlický, D. **Pokorný, P.**, & Janches, D., 2011, Dynamics of Dust Particles Released from Oort Cloud Comets and Their Contribution to Radar Meteors, *Astrophysical Journal*, 743, 129.

Paper D: Nesvorný, D., Janches, D., Vokrouhlický, D. **Pokorný, P.**, Bottke, W. F., & Jenniskens, P., 2011, Dynamical Model for the Zodiacal Cloud and Sporadic Meteors, *Astrophysical Journal*, 743, 129.

Paper E: **Pokorný, P.**, Vokrouhlický, D. Nesvorný, D., Campbell-Brown, M. D., & Brown, P. G., 2014, Dynamical Model for the Toroidal Sporadic Meteors, *Astrophysical Journal*, 789, 25

Paper A

Icarus 219 (2012) 150–160

Contents lists available at SciVerse ScienceDirect

Icarus

journal homepage: www.elsevier.com/locate/icarus

Öpik-type collision probability for high-inclination orbits

David Vokrouhlický [a,*], Petr Pokorný [a], David Nesvorný [b]

[a] Institute of Astronomy, Charles University, V Holešovičkách 2, CZ-18000 Prague 8, Czech Republic
[b] Southwest Research Institute, 1050 Walnut St., Suite 300, Boulder, CO 80302, USA

ARTICLE INFO

Article history:
Received 20 December 2011
Revised 14 February 2012
Accepted 20 February 2012
Available online 3 March 2012

Keywords:
Celestial mechanics
Impact processes
Asteroids
Interplanetary dust

ABSTRACT

The classical Öpik theory provides an estimate of the collision probability between two bodies on bound, heliocentric or planetocentric orbits under restrictive assumptions of: (i) constant eccentricity and inclination, and (ii) uniform circulation of the longitude of node and argument of pericenter. These assumptions are violated whenever either of the orbits has a large inclination with respect to the local Laplace plane or large eccentricity, and their motion is perturbed by an exterior (tidal) gravitational field of a planet or the Sun. In this situation, known as the Lidov–Kozai regime, the eccentricity and inclination values exhibit large and correlated oscillations. At the same time, the longitude of node and the argument of pericenter may have strongly nonlinear time evolution, with the latter being even bound to a small interval of values. Here we develop a new Öpik-type collision probability theory which is valid even for highly inclined and/or eccentric orbits of the projectile. We assume that the orbit of the target is circular and in the local Laplace plane. Such a generalized setting is necessary, as an example, to correctly estimate the terrestrial impact fluxes of sporadic micrometeoroids on high-inclination orbits (notably those from the toroidal source and the associated helion and anti-helion arcs).

1. Introduction

Many problems in planetary science require to determine the collision probability of two bodies residing on the Keplerian orbits with the same focal point. Here we consider the important case in which the collision probability needs to be evaluated in a statistical sense for a large population of bodies. In this case, it is often useful if the probability is averaged over the secular orbital timescale.

The standard theory, used and extended by many researchers, was developed by Öpik (1951) (see also Öpik, 1976; Wetherill, 1967; Greenberg, 1982). In his original formulation, Öpik assumed that the target on a circular orbit is bombarded by a population of bodies on orbits with fixed eccentricity and inclination values.

Öpik's theory was generalized to the case of an eccentric orbit of the target by Wetherill (1967) and Greenberg (1982). A different generalized method was developed by Kessler and Cour-Palais (1978) (see also Kessler, 1981). This more geometrical approach based on the evaluation of the probability density distribution has found a number of applications in planetary science (e.g., Steel and Baggaley, 1985; Steel and Elford, 1986; Sykes, 1990).

In these standard collisional theories, the orbital eccentricity e and inclination i is assumed to be constant during the secular evolution cycle. This is appropriate for small e and i values, where e and i are roughly time-invariant. However, some problems in planetary science require a method that is valid for high eccentricities and/or high inclinations, where the effects of the Lidov–Kozai resonance can be important (e.g., Lidov, 1961, 1962; Kozai, 1962; Morbidelli, 2002).

For example, the dust particles released from long-period comets can be an important component of the zodiacal cloud. If so, it would be important to calculate their impact rates on the Earth (and relate the results to meteor observations), Earth-bound detectors and spacecrafts. Other applications can be found in studies of planetary impact rates in the early Solar System when small bodies were stochastically driven to high-e and -i orbits. In these examples, the secular evolution of orbits clearly violates the assumption of the standard Öpik theory, because e and i are affected by the Lidov–Kozai cycles.

Here we generalize the Öpik theory to account for the Lidov–Kozai cycles of high-i and -e orbits. After mathematical preliminaries in Section 2, we generalize the collisional probability theory in Section 3. In Section 3.3, we test the generalized theory by comparing it with direct N-body integrations of orbits. Conclusions are given in Section 4.

2. Mathematical preliminaries

We start by introducing mathematical concepts and notation that will be used throughout the paper. Assume a particle on an elliptic heliocentric orbit described using an osculating set of

* Corresponding author.
E-mail addresses: vokrouhl@cesnet.cz (D. Vokrouhlický), petr.pokorny@volny.cz (P. Pokorný), davidn@boulder.swri.edu (D. Nesvorný).

0019-1035/$ - see front matter © 2012 Elsevier Inc. All rights reserved.
doi:10.1016/j.icarus.2012.02.021

Keplerian elements: semimajor axis a, eccentricity e, inclination i, longitude of node Ω, argument of pericenter ω and true anomaly f. The angles i, Ω and ω are defined with respect to a chosen inertial frame (X,Y,Z).[1] The orbit intersects the (X,Y) reference plane in ascending and descending nodes, where $f = f_0 \equiv -\omega$ and $f = f_0 \equiv \pi - \omega$, respectively. Denote a' the heliocentric distance at either of the two intersections. Introduce a local reference basis $(\mathbf{e}_r, \mathbf{e}_\phi, \mathbf{e}_z)$ of three orthonormal vectors with the origin at the ascending or descending node, such that $\mathbf{e}_r$ is directed in the radial direction, $\mathbf{e}_\phi$ in the longitude direction and $\mathbf{e}_z$ along the Z axis.[2]

The heliocentric position vector $\mathbf{r}$ describing the elliptic orbit of the particle reads

$$\mathbf{r}(f) = r(f)[\mathbf{a}\cos(\omega+f) + \mathbf{b}\sin(\omega+f)], \tag{1}$$

with $r(f) = a\eta^2/(1+e\cos f)$, $\eta^2 = 1-e^2$, and unit vectors $\mathbf{a}^{\mathrm{T}} = (\cos\Omega, -\sin\Omega, 0)$ and $\mathbf{b}^{\mathrm{T}} = (-\cos i\sin\Omega, \cos i\cos\Omega, \sin i)$. At the ascending node we have $\mathbf{a} = \mathbf{e}_r$ and $\mathbf{b} = \cos i\mathbf{e}_\phi + \sin i\mathbf{e}_z$, while at the descending node $\mathbf{a} = -\mathbf{e}_r$ and $\mathbf{b} = -\cos i\mathbf{e}_\phi + \sin i\mathbf{e}_z$. Expanding $\mathbf{r}(f)$ near the origin in the local $(\mathbf{e}_r, \mathbf{e}_\phi, \mathbf{e}_z)$ system (i.e., near the respective nodal intersection with the (X,Y) reference plane), we obtain $\mathbf{r}(f) = a'\mathbf{e}_r + d\mathbf{r}$ with

$$d\mathbf{r} = a'\mathbf{A}_1\, df + \frac{a'}{2}\mathbf{A}_2\, df^2 + \mathcal{O}(df^3), \tag{2}$$

where df is infinitesimal increment of the true anomaly with respect to the intersection value f_0. Eq. (2) locally describes particle's elliptic orbit, with df being an affine parameter having values suitably close to zero. The first term is the crudest rectilinear approximation, while the second term describes the local curvature of the elliptic orbit. The first- and second-order vectorial coefficients read (upper sign for the ascending node intersection and lower sign for the descending node intersection)

$$\mathbf{A}_1 = \mp\frac{e\sin\omega}{P}\mathbf{e}_r + (\cos i\mathbf{e}_\phi \pm \sin i\mathbf{e}_z), \tag{3}$$

$$\mathbf{A}_2 = -2\left[1 - \frac{3}{2P} + \frac{\eta^2}{P^2}\right]\mathbf{e}_r - 2\frac{e\sin\omega}{P}(\pm\cos i\mathbf{e}_\phi + \sin i\mathbf{e}_z), \tag{4}$$

where $P = a\eta^2/a'$ and $\eta^2 = 1-e^2$.

Consider now an observer moving on a circular heliocentric orbit with radius a' in the (X,Y) reference plane. Eq. (2) may be also used to describe its orbit near the respective nodal intersection with the eccentric orbit, with $\mathbf{A}_1^{\mathrm{circ}} = \mathbf{e}_\phi$ (henceforth also the apex direction), $\mathbf{A}_2^{\mathrm{circ}} = -\mathbf{e}_r$ and $df = df_{\mathrm{circ}}$, a differential in the observer's longitude. Denote V_{circ} the orbital velocity of the observer (given by the third Kepler law) and V the relative velocity of the particle with respect to the observer. It is convenient to introduce a scaled value v of the relative velocity, namely $v = V/V_{\mathrm{circ}}$, and parametrize the complete relative vector $\mathbf{v}^{\mathrm{T}} = (v_r, v_\phi, v_z) = v(\cos b\sin\ell, \cos b\cos\ell, \sin b)$ $v_\phi, v_z) = v(\cos b\sin\ell, \cos b\cos\ell, \sin b)$ with a longitude ℓ and a latitude b of the radiant seen by the observer (henceforth, ℓ is measured from the apex direction and increases toward local radial direction in our notation). We also note that our choice makes $\boldsymbol{v}$ point *toward* the radiant from which the observer sees the particle impact.

The velocity components (v_r, v_ϕ, v_z) may be easily obtained from the linear term in (2), namely by using

$$\boldsymbol{v} = \mathbf{e}_\phi - \frac{1}{V_{\mathrm{circ}}}\left(\frac{d\mathbf{r}}{dt}\right)_{f=f_0} = \mathbf{e}_\phi - \mathbf{A}_1\sqrt{P}. \tag{5}$$

We thus obtain

$$e\cos\omega = \pm(P-1), \tag{6}$$

$$e\sin\omega = \pm\sqrt{P}v_r, \tag{7}$$

$$\sqrt{P}\cos i = 1 - v_\phi, \tag{8}$$

$$\sqrt{P}\sin i = \mp v_z, \tag{9}$$

where the upper sign holds for the ascending node intersection and the lower sign for the descending node intersection. Here the first formula (6) is simply the geometric condition of intersection at heliocentric distance a' (as stated above), and the next three formulas (7)–(9) specify the radiant location and impact velocity (in units of V_{circ}). Obviously, our (v_r, v_ϕ, v_z) are closely related, in fact identical, to the standard velocity components (U_x, U_y, U_z) introduced in the Öpik theory (see, e.g., Öpik, 1951, 1976).

Finally, it will be useful to rewrite beforehand Eq. (6) using the non-singular variables $k = e\cos\omega$ and $h = e\sin\omega$ and parameter $\alpha = a'/a$. In the (k,h) plane the nodal intersection condition (6) reads

$$\left(k \pm \frac{\alpha}{2}\right)^2 + h^2 = 1 - \alpha + \frac{\alpha^2}{4}, \tag{10}$$

which is simply an equation of a circle displaced by $\pm\alpha/2$ on the k-axis for the ascending, resp. descending, node and radius equal to $\sqrt{1-\alpha+\alpha^2/4}$.

3. Öpik collision probability approach

In the Öpik approach, the collision probability of a particle with a target is composed of two independent parts: (i) probability P_1 that during the secular cycle of the particle orbital elements its heliocentric node is close to the target's circular orbit (such that their distance can be small enough), and (ii) probability P_2 that the target is close to the nodal intersection of the particle orbit. A product of these statistically independent partial probabilities provides the total probability of impact per revolution of the particle: $P = P_1P_2$. Dividing this value by the orbital period of the particle then yields total probability per unit of time (this is because we assume an equilibrium distribution of particles along the impacting orbit). Obviously, in this way the resulting collision probability is a long-term averaged value or, equivalently, a population averaged value for a large population of particles in steady-state.

Because we keep the assumption of the circular motion of the target and the rectilinear representation of the particle motion near the nodal configurations (first term in Eq. (2)), analysis of P_2 is the same as in Öpik (1951). In particular, assuming the target with radius R on a circular heliocentric orbit with radius a_{circ}, we have

$$P_2(a,e,i) = \frac{R}{4a_{\mathrm{circ}}}\sqrt{\frac{3-T(a,e,i)}{2-F(a,e,i)}}, \tag{11}$$

with

$$T(a,e,i) = \frac{a_{\mathrm{circ}}}{a} + 2\sqrt{\frac{a}{a_{\mathrm{circ}}}}\eta\cos i, \tag{12}$$

$$F(a,e,i) = \frac{a_{\mathrm{circ}}}{a} + \frac{a}{a_{\mathrm{circ}}}\eta^2\cos^2 i. \tag{13}$$

However, to compute P_1, Öpik's assumed constant values of e and i and uniform circulation of ω. This is an acceptable approximation for low inclination and low eccentricity orbits, but it fails when either of or both these elements are large. Our goal is to extend determination of P_1 for orbits with arbitrary inclination and eccentricity values.

[1] We assume $i \neq 0$, otherwise a non-singular set of orbital elements would be needed. In order to keep a close similarity in notation to the works of Öpik (1951) and Wetherill (1967) we only consider the non-planar case.

[2] Note that the $\mathbf{e}_r$ and $\mathbf{e}_\phi$ vectors at the descending node are opposite to their values in the descending node, and vice versa, in our definition.

3.1. Lidov–Kozai driven secular evolution of the particle orbit

We adopt a secular model for particle dynamics, namely assuming its orbit is not resonant with any of the perturbing massive bodies in the Solar system. For simplicity assume planets move on circular and coplanar orbits. Within this model, the first-order perturbations of particle dynamics are obtained by independent averaging of the perturbing function from an arbitrary number of planets over their mean longitude in orbit and that of the particle (e.g., Morbidelli, 2002). Such an approximation immediately provides two integrals of motion, notably (i) the semimajor axis a of the particle, and (ii) projection of the orbital angular momentum on the symmetry axis of the planetary system (i.e., normal to the Laplace plane). The latter may be most conveniently expressed using a constant $c = \eta \cos i$, which implies that any variation in eccentricity e (or η) is correlated with the corresponding variation of the inclination i. In other words, inclination may be considered as a dependent parameter on the eccentricity. The axial symmetry of the secular (averaged) problem also implies that the longitude of node Ω of the particle orbit is a dummy parameter in the perturbing function $\mathcal{P}$, which – apart from constants – depends only on two orbital parameters: eccentricity e and argument of pericenter ω (or their canonical analogs within a Hamiltonian theory; see, e.g., Morbidelli, 2002). Finally, since averaging over planets' motion about the Sun eliminates time dependence of the perturbing function, its value itself is also an integral of motion: $\mathcal{P}(e,\omega;a,c) = \text{constant}$. This again shows, that any secular variation in ω is reflected in a correlated way in the respective variations of e.

In the most general situation of multiple planets with particle orbit crossing all or some of them, the averaged perturbing function $\mathcal{P}(e,\omega;a,c)$ may be obtained only using numerical quadrature (e.g., Bailey et al., 1992; Thomas and Morbidelli, 1996; Gronchi and Milani, 1998, 1999; Morbidelli, 2002). It should be noted that the problem has, aside to numerical evaluation, also subtle conceptual (mathematical) difficulties related to averaging of perturbing function with singular points (cf., Gronchi and Milani, 1998). Our approach developed below might be applied to this case as well, but it would require to evaluate most of the necessary functions numerically. In order to better understand the situation we prefer to restrict to a simpler case, in which more computations could be developed analytically and thus more directly compared with the traditional Öpik's theory. In particular, we assume only one perturbing planet (Jupiter) and a particle orbit entirely inside its orbit. The Earth as a target is assumed massless, which is a fairly good approximation overall. In this case, $\mathcal{P}(e,\omega;a,c)$ may be obtained in terms of multipole series (e.g., Kozai, 1962), of which we shall retain only the leading quadrupole part. Unless perihelion of the particle orbit is close to Jupiter, this is again a fairly satisfactory assumption, at least for sake of our illustration.[3] Using these approximations, a number of constant terms may be factorized from expression of $\mathcal{P}(e,\omega;a,c)$, resulting then in an integral of motion in the form (e.g., Kozai, 1962; Kinoshita and Nakai, 2007)

$$\mathcal{H}(k,h;c) = \frac{1}{\eta^2}[(2+3e^2)(3c^2-\eta^2)+15(\eta^2-c^2)(k^2-h^2)] = C. \qquad (14)$$

Here, we introduce the non-singular variables k and h from Eq. (10). Topology of the C-conserved isolines in the (k,h) plane for various values of c and C has been extensively studied (e.g., Kozai, 1962; Morbidelli, 2002) and we do not need to discuss it in detail. Suffice it to say that in the limit of $|c|$ large enough the level curves of constant C are ovals about the origin of the (k,h) plane that become near circular for $|c| \to 1$. In this limit, both eccentricity and inclination of the particle orbit are small and nearly conserved, matching thus the assumptions of the original Öpik collisional theory. We also note that for a given c value, the eccentricity can take values up to a maximum $\sqrt{1-c^2}$ (more rigorous specification of the interval of e and i value for given c and C integrals can be found, for instance, in Kinoshita and Nakai, 2007, Eqs. (31) and (32). At the critical value $c^2 = 3/5$, topology of the level curves of the C integral changes, adapting to bifurcation of two new stationary solutions at the h axis (i.e., with $\cos\omega = 0$): (i) for $C > 2(3c^2-1)$ they still circulate about the origin, but may take excursions to a very large eccentricity value on the h axis, and (ii) for $C < 2(3c^2-1)$ they circulate about the stationary points on the h axis. Examples are later seen in Figs. 3 and 4.

3.2. Crossing configurations with a target of a finite size

The exact configurations of orbital intersection with a target on a circular heliocentric orbit with radius $a_{\rm circ}$ are determined as roots $k_\star$ and $h_\star$ of Eq. (10), or equivalently Eqs. (6) and (14) with $\alpha = a_{\rm circ}/a$. All of them can be computed analytically, leading to a problem of roots of a cubic equation for $k_\star$. Because of the inversion symmetry $h_\star \leftrightarrow -h_\star$, there is always an even number of roots with generic number of 4 or 8 (2 and 6 are singular cases).[4] As a result, there can be twice as many impact configurations for orbits with high inclination than in the low inclination regime (only 4). This has been known for a long time, in particular from studies of high-inclination meteoroid streams (e.g., Babadzhanov and Obrubov, 1992). Examples are shown in the left panels of Figs. 3 and 4.

Now, the P_1 probability in the Öpik approach stems from the fact that the target has a small but finite radius R ($R \ll a_{\rm circ}$).[5] This means that also orbits with k and h values in a small neighborhood of $(k_\star,h_\star)$ could pass closer than distance R from the center of the target and should be considered intersecting. The limiting configurations with $k_{\rm lim}$ and $h_{\rm lim}$ values are those for which the particle orbit is grazing at distance R from the target's orbit.

In order to formulate such a condition, we use local description of the particle's elliptic orbits from Section 2, Eq. (2). Consider particle's orbit with nodal intersection of the (X,Y) plane at a heliocentric distance a' close to $a_{\rm circ}$.[6] Define the $(\mathbf{e}_r,\mathbf{e}_\phi,\mathbf{e}_z)$ reference frame with the origin at target's orbit at a longitude identical to particle's intersection point with the (X,Y) plane – see Fig. 1 for illustration. Retaining just the linear representation in (2), the particle's position vector in our reference frame is given by

$$\Delta\mathbf{r}(\lambda) = a'\mathbf{A}_1\lambda + (a'-a_{\rm circ})\mathbf{e}_r + \mathcal{O}(\lambda^2), \qquad (15)$$

where we denoted $\lambda = df$; recall the values near $\lambda = 0$ describe the particle orbit near the nodal line. The vector $\mathbf{A}_1$ is given in Eq. (3) with $P = a\eta^2/a'$. In the same way, we may locally represent target's orbit in the same reference frame with

$$\Delta\mathbf{r}'(\lambda') = a_{\rm circ}\mathbf{e}_\phi\lambda' + \mathcal{O}(\lambda'^2), \qquad (16)$$

where we again retained just the linear term (the target's orbit is thus ϕ axis in our system). The square of the target-particle distance is simply $d^2(\lambda,\lambda') = [\Delta\mathbf{r}(\lambda)-\Delta\mathbf{r}'(\lambda')]\cdot[\Delta\mathbf{r}(\lambda)-\Delta\mathbf{r}'(\lambda')]$, and we seek a minimum orbital distance $d^2_{\rm min}$ as a minimization problem in the

[3] In any case, adding higher-multipole terms in the secular perturbing function is just a matter of more algebraic labor, but does not represent any conceptual obstacle to our approach.

[4] Apart from the mentioned symmetry, stemming from the fact that Eqs. (10) and (14) contain only h^2, there is also $k_\star \leftrightarrow -k_\star$ symmetry for impact configurations in the ascending and descending nodes of the particle orbit.

[5] In fact, the geometric radius R of the target should be augmented by a factor $\sqrt{1+(V_{\rm esc}/V)^2}$, where $V_{\rm esc}$ is the escape velocity from the target and V is the impact speed of the particle at a large distance from the target. This recalibration takes into account focusing effect of the target's gravitational field.

[6] Note, we need now to distinguish particle nodal distance a' from the target's heliocentric distance $a_{\rm circ}$. This has to be kept in mind when consulting formulas from Section 2.

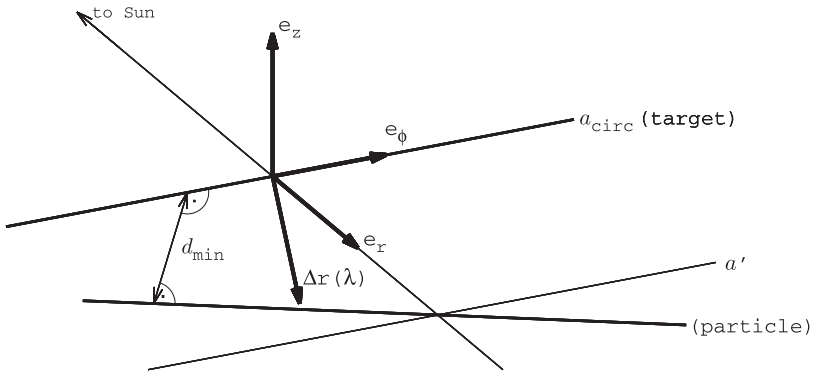

Fig. 1. Geometrical quantities used to represent particle and target motion near the intersection configuration. The reference frame $(\mathbf{e}_r,\mathbf{e}_\phi,\mathbf{e}_z)$ has the origin at the target's orbit: $\mathbf{e}_r$ in the radial direction from the Sun and $\mathbf{e}_\phi$ in the apex direction of the target's heliocentric motion (assumed circular with radius $a_{\rm circ}$). The particle's orbit has a node at heliocentric distance $a' \neq a_{\rm circ}$ and its position $\Delta\mathbf{r}$ in the local frame $(\mathbf{e}_r,\mathbf{e}_\phi,\mathbf{e}_z)$ is given by Eq. (15). We seek minimum distance $d_{\rm min}$ of the particle from target's orbit.

two-parametric (λ,λ') space.[7,8] In the linear representations of $\Delta\mathbf{r}(\lambda)$ and $\Delta\mathbf{r}'(\lambda')$ the task is simple enough and yields

$$d_{\rm min} = (a' - a_{\rm circ})\frac{P\sin i}{\sqrt{P^2\sin^2 i + e^2\sin^2\omega}}, \tag{17}$$

with $a' = a\eta^2/(1\pm e\cos\omega)$ for the ascending and descending node intersections. Scaling $d_{\rm min}$ by a and making it equal to $\rho = R/a$, we obtain for the target-grazing orbits

$$\mathcal{K}(k,h;c) \equiv [\eta^2 - \alpha(1\pm k)]\sqrt{\frac{\eta^2-c^2}{(\eta^2-c^2)(1\pm k)^2 + h^2\eta^2}} = \rho. \tag{18}$$

Here, we used the secular representation of the orbital elements evolution, eliminating in particular inclination i using $c = \eta\cos i$ integral. The $k_{\rm lim}$ and $h_{\rm lim}$ values are obtained by simultaneous solution of Eqs. (14) and (18). Unfortunately, this system of equations does not have simple analytical solutions. However, given that $\rho \ll 1$, we may seek small displacements δk and δh such that $k_{\rm lim} = k_\star + \delta k$ and $h_{\rm lim} = h_\star + \delta h$. Linearizing our problem in δk and δh we obtain

$$\delta k = -\rho\frac{(\partial\mathcal{H}/\partial h)_\star}{\mathcal{D}_\star}, \quad \delta h = \rho\frac{(\partial\mathcal{H}/\partial k)_\star}{\mathcal{D}_\star}, \tag{19}$$

where

$$\mathcal{D}_\star = (\partial\mathcal{K}/\partial h)_\star(\partial\mathcal{H}/\partial k)_\star - (\partial\mathcal{K}/\partial k)_\star(\partial\mathcal{H}/\partial h)_\star. \tag{20}$$

The symbol ★ here means that all derivatives have to be evaluated using the $(k_\star,h_\star)$ values corresponding to the exact intersection condition. After a brief algebra we find

$$(\partial\mathcal{H}/\partial k)_\star = \frac{2k_\star}{\eta_\star^2}\left[2\left(7 - 3c^2 - 12k_\star^2 + 3h_\star^2\right) + C\right], \tag{21}$$

$$(\partial\mathcal{H}/\partial h)_\star = \frac{2h_\star}{\eta_\star^2}\left[2\left(12c^2 - 8 + 3k_\star^2 + 18h_\star^2\right) + C\right], \tag{22}$$

$$(\partial\mathcal{K}/\partial k)_\star = -2\left(k_\star \pm \frac{\alpha}{2}\right)\sqrt{\frac{\eta_\star^2-c^2}{(\eta_\star^2-c^2)(1\pm k_\star)^2 + h_\star^2\eta_\star^2}}, \tag{23}$$

$$(\partial\mathcal{K}/\partial h)_\star = -2h_\star\sqrt{\frac{\eta_\star^2-c^2}{(\eta_\star^2-c^2)(1\pm k_\star)^2 + h_\star^2\eta_\star^2}}. \tag{24}$$

It turns out that the novel property of our approach are mainly the $(\partial\mathcal{H}/\partial k)_\star$ and $(\partial\mathcal{H}/\partial h)_\star$ derivatives, because the condition (18) and its partial derivatives remain formally the same as in the classical Öpik theory (see Appendix A, Eqs. (A7) and (A8)). Note that in the linear approximation, the $(\delta k,\delta h)$ solution is accompanied with a symmetric $(-\delta k,-\delta h)$ solution. Obviously, such displacements are along the tangent to the level line of the $\mathcal{H} = C$ integral at the $(k_\star,h_\star)$ point.

A second novel aspect of our approach, and a generalization of the classical Öpik theory, is that for each possible intersection configuration $(k_\star,h_\star)$ we determine time interval $(\Delta t)_\star$ it takes the particle orbit to evolve from $(k_\star - \delta k, h_\star - \delta h)$ to $(k_\star + \delta k, h_\star + \delta h)$, i.e. across the interval of values it may impact onto the target. The partial P_1 probability from this intersection configuration is then $(\Delta t)_\star/T_{\rm Kozai}$, where $T_{\rm Kozai}$ is the period of whole secular evolution along the level curve of the C integral; $T_{\rm Kozai}$ may be evaluated using a complete elliptic integral of the first kind as shown by Kinoshita and Nakai (2007). We then define the Öpik-type collision probability of impact per revolution of the particle

$$P = \sum\left(\frac{\Delta t}{T_{\rm Kozai}}\right)_\star P_2(a,e_\star,i_\star), \tag{25}$$

which generalizes (A13) recalled in Appendix A. The summation in (25) is performed over all intersection configurations for both ascending and descending nodes. Note that, unlike in the Öpik approach, the orbital eccentricity $e_\star$ and inclination $i_\star$ is now different for different crossing configurations and we need to multiply the partial P_1 probability with the appropriate and individual P_2 probability that the target is near the intersection location. Because the semimajor axis value of the particle is constant, the intrinsic collision probability per unit of time is simply

$$p = P/T_{\rm orb} = (1/2\pi)(\sqrt{GM}/a^{3/2})P, \tag{26}$$

where $T_{\rm orb}$ is the orbital period of the particle and M is the solar mass.

Finally, we return to the issue how to determine $(\Delta t)_\star$. The flow along the C integral isoline is given by the differential equations (e.g., Kozai, 1962; Morbidelli, 2002; Kinoshita and Nakai, 2007)

[7] In our linear approximation things are simpler, and one may drop λ' by just evaluating $\Delta\mathbf{r}(\lambda)$ distance from the ϕ axis. However, the two-parametric formulation might be important to keep in mind when higher-order approximations for $\Delta\mathbf{r}(\lambda)$ and/or $\Delta\mathbf{r}'(\lambda')$ would be used.

[8] Note that $d^2(\lambda,\lambda')$ is quadratic in λ. Its description using the linear approximation (15) might look incomplete, because the corresponding quadratic term (see, e.g., Eq. (2)) would also contribute to the quadratic term in d^2. However, a closer analysis reveals that this addition does not change our results. A more general Öpik collision theory, for instance suitable to describe impacts very close to the pericenter or apocenter of the particle orbit (see Appendix A), would require a complete analysis with $\mathbf{r}(\lambda)$ and $\mathbf{r}'(\lambda')$ represented by higher-order terms beyond the linear approximation used here (and in most previous works).

$$\frac{dk}{dt} = -\frac{3}{2}\gamma\eta h\left[1+\frac{5}{2}\frac{c^2(1-k^2)-\eta^4}{\eta^4}\right], \tag{27}$$

$$\frac{dh}{dt} = \frac{3}{2}\gamma\eta k\left[1+\frac{5}{2}\frac{c^2h^2}{\eta^4}\right], \tag{28}$$

where $\gamma = n\,(m/M)\,(a/a_{\rm Jup})^{3/2}$ with n mean motion of the particle, m mass of the Jupiter and $a_{\rm Jup}$ semimajor axis of its orbit; note we assume that the single perturber of the particle orbit is Jupiter. Given the linear solution of δk and δh above with typical values of the order $\rho(\ll 1)$, we found satisfactory to use a linear discretization of the differential Eqs. (27) and (28), namely representing $dk \to \delta k$, $dh \to \delta h$, $dt \to (\Delta t)_\star/2$ evaluating their right hand sides at $(k_\star, h_\star)$ values. Either of Eqs. (27) and (28) provide the same results, up to terms of the second order in ρ.

This approach only fails when the displacements δk and δh are large, a singular situation when $\mathcal{D}_\star$ is very near 0; this always occurs when $h_\star = 0$, but there might be also other cases in general. In the Öpik formalism limit this singularity happens when the particle's perihelion or aphelion are equal to radius $a_{\rm circ}$ of the target's orbit (see also Appendix A). For that reason, we abandon the simple approach above in this case and we solve Eqs. (14) and (18) numerically when $\mathcal{D}_\star \leqslant 0.05$ in Eq. (20). This provides an accurate determination of all possible intersection configurations. We then determine the corresponding $(\Delta t)_\star$ value using a numerical integration of the secular system (27) and (28) in between the grazing configurations.

3.3. Comparison with the standard Öpik's theory

Here we test the generalized collision probability theory and compare the results with those of the standard Öpik theory (see Appendix A for a comparison of the analytical aspects of the two methods). In our first test case, we calculate the Earth-impact rates for a population of particles that is perturbed by Jupiter (circular orbit, $a_{\rm Jup} = 5.2$ AU). The Earth is assumed to have a circular orbit with $a_{\rm circ} = 1$ AU).

This is a simplified system. In reality there are more perturbing planets, including the Earth itself, whose orbits are also evolving due to their mutual interactions. This latter effect is especially important, because it produces secular resonances in the planet-crossing region (e.g., Michel and Thomas, 1996; Michel and Froeschlé, 1997) and variations of c and C. We will consider this more complicated case later in this section.

We conducted numerical tests to compare the collision probability p from (26), which should be accurate for the high-inclination and/or high-eccentricity orbits, with the predictions of the Öpik theory, which should be only approximate in these cases.

As the secular evolution follows the $\mathcal{H}(k,h;c) = C$ isoline in the (k,h) plane there are typically four or eight intersections with the target orbit. In order to compare p with the collision probability obtained by the Öpik's method, we determine $p_{\rm Opik}(a,e,i)$ from Eq. (A14) at each point of the line defined by $\mathcal{H}(k,h;c) = C$,[9] and compute an average value $p_{\rm eff}$ as

$$p_{\rm eff} = \frac{1}{T_{\rm Kozai}}\int_0^{T_{\rm Kozai}} dt\, p_{\rm Opik}(a,e,i). \tag{29}$$

Here, $T_{\rm Kozai}$ is the period of the Lidov–Kozai cycle. Note that evaluation of (29) needs some care when either pericenter q or apocenter Q of the particle orbit becomes equal to the radius $a_{\rm circ}$ of the target's orbit. This is because

$$p_{\rm Opik} \propto \frac{1}{\sqrt{(a_{\rm circ}-q)(Q-a_{\rm circ})}}, \tag{30}$$

and in both cases Öpik's collision probability has a singularity (see, however, discussion in Appendix A). Nevertheless, as seen from (30), this singularity is integrable and classical numerical tools can be used to accurately evaluate $p_{\rm eff}$ (see, e.g., Press et al., 2007).

3.3.1. Testing the theory: a simple setup

We first test things in the low-e and low-i limit, where the standard Öpik works well. The initial orbital elements of particles were set to be $a = 1.01$ AU, $e = 0.02$, $i = 3°$ and $\omega = 0°$. In this case, the Kozai constant $c \simeq 0.9984$ is very close to unity. We thus expect the eccentricity and inclination should be approximately conserved and the secular angles ω and Ω should uniformly precess. Indeed, Fig. 2 shows that the $\mathcal{H}(k,h;c) = C$ isoline in the (k,h) plane deviates negligibly from a small circle about the origin. As expected, $p \simeq p_{\rm eff}$ in this case. The 0.1%-difference between p and $p_{\rm eff}$ is of the order of variations of $p_{\rm Opik}$ within one secular cycle of the orbital evolution. This difference is partially due to slight variations in e and nonlinearity of time dependence of ω, but may also express a small internal inaccuracy by which we can evaluate both p and $p_{\rm eff}$.

We now move to testing the methods in the Lidov–Kozai regime. We set $a = 1.4$ AU, $e = 0.2$, $i = 65°$, corresponding to $c \simeq 0.414 < \sqrt{0.6}$. Figs. 3 and 4 show the results for $\omega = 0°$ and $\omega = 60°$, respectively. The left panels show nature of the particle orbital evolution using the $\mathcal{H}(k,h;c) = C$ isoline in the (k,h) plane and the two circles characterize nodal impact configurations with the Earth orbit (with $a_{\rm circ} = 1$ AU; see Eq. (10)); symbols at intersections of the respective curves highlight the exact impact geometries that could occur for this orbit during its secular evolution. There are eight of them in Fig. 3 and four of them in Fig. 4. The right panels show formally computed Öpik collision probability values $p_{\rm Opik}$ as a function of time during a timespan of one secular cycle $T_{\rm Kozai}$ of the particle evolution. The discontinuities, when $p_{\rm Opik}$ formally diverge, correspond to configurations of pericentric impact to the target.[10] The solid gray lines are p and $p_{\rm eff}$ values; note, that in both cases $p_{\rm eff}$ is about twice larger than p, indicating that using the standard Öpik theory one would overestimate the collision probability value for these orbits. The middle panels show radiant positions of the impacting particles: the symbols are real radiants corresponding to the true intersection geometries indicated on the left panels, while the gray line are collections of "fake radiants". The latter were obtained by applying assumptions of the Öpik theory, namely constant values of eccentricity and inclinations to the orbit of particle at different phase of its Lidov–Kozai-driven evolution. Obviously such an approach is incorrect, but it has been used in some previous works (e.g., Nesvorný et al., 2011). Note that the angular distance δ of the fake radiants from apex direction is given by $\cos\delta = (\boldsymbol{\nu}\cdot\mathbf{e}_\phi)/v = (1-\sqrt{P}\cos i)/\sqrt{3-T(a,e,i)}$, see Eqs. (7)–(9). As a result, δ depends only on the semimajor axis a and the Kozai constant c of the particle orbit, both conserved during the particle secular evolution, and thus the fake radiants project on arcs of constant angular distance from the apex direction.[11] When a particle or-

[9] Obviously, application of the Öpik approach is not well justified for orbits with low c value associated with significant e and i evolution; nevertheless, it has been used even in these cases in previous works (e.g., Galligan and Baggaley, 2005; Campbell-Brown, 2008; Nesvorný et al., 2011) and part of our work is to see a misfit represented by this inconsistency.

[10] Note, for instance, that the initial values of the orbital elements have a pericenter $q > a_{\rm circ}$ and no impact configuration is possible; it only takes a while during the secular evolution of the particle orbit before the eccentricity increases enough to make $q = a_{\rm circ}$.

[11] This fact has actually been known and used in the meteoritics; see, e.g., Valsecchi et al. (1999), where the secularly invariant value of δ (θ in the notation of this paper) plays a crucial role in defining the similarity function for meteoroid streams.

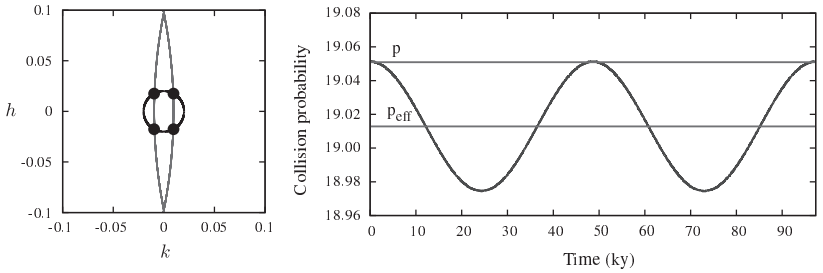

Fig. 2. Secular evolution and intrinsic impact probability for a particle orbit with initial semimajor axis $a = 1.01$ AU, eccentricity $e = 0.02$, inclination $i = 3°$ and argument of pericenter $\omega = 0°$. Left: $\mathcal{H} = C$ isoline in the (k,h) plane of variables (black solid curve) and nodal intersection conditions with $a_{\rm circ} = 1$ AU for ascending and descending nodes (segments of gray circles; see Eq. (10)). Symbols are the four possible impact geometries. Right: Collision probability value $p_{\rm Opik}(a,e,i)$ formally computed using the Öpik formalism for time-dependent values of e and i as given by the secular evolution of the orbit; the abscissa is time in ky during one secular cycle $T_{\rm Kozai}$, and the ordinate is the intrinsic collision probability per AU^2 and yr. The horizontal lines are: (i) $p_{\rm eff}$ defined in Eq. (29), and (ii) the true collision probability p defined in Eq. (25).

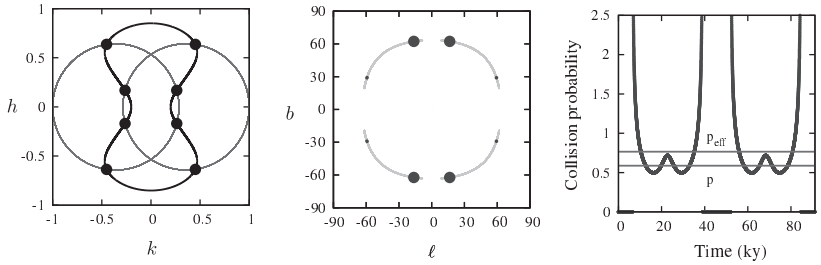

Fig. 3. Secular evolution and impact geometries for a particle orbit with initial semimajor axis $a = 1.4$ AU, eccentricity $e = 0.2$, inclination $i = 65°$ and argument of pericenter $\omega = 0°$. Left: $\mathcal{H} = C$ isoline in the (k,h) plane of variables (solid curve) and nodal intersection conditions with $a_{\rm circ} = 1$ AU for ascending and descending nodes (gray circles; see Eq. (10)). Symbols are the eight possible impact geometries. Middle: Radiant position of the eight impacting configurations as seen by the observer on a circular heliocentric orbit with radius $a_{\rm circ} = 1$ AU; size of the symbol is scaled by the partial collision probability for this particular impact geometry. The gray arcs are collections of "fake radiants" constructed for orbits with constant eccentricities and inclinations, whose values are achieved during the secular evolution of the particle orbit. The abscissa is longitude measured from the apex direction, the ordinate is latitude (both in degrees). Right: Collision probability value $p_{\rm Opik}(a,e,i)$ formally computed using the Öpik formalism for time-dependent values of e and i as given by the secular evolution of the orbit; the abscissa is time in ky during one secular cycle $T_{\rm Kozai}$, and the ordinate is the intrinsic collision probability per AU^2 and yr. The horizontal lines are: (i) $p_{\rm eff}$ defined in Eq. (29), and (ii) the true collision probability p defined in Eq. (25).

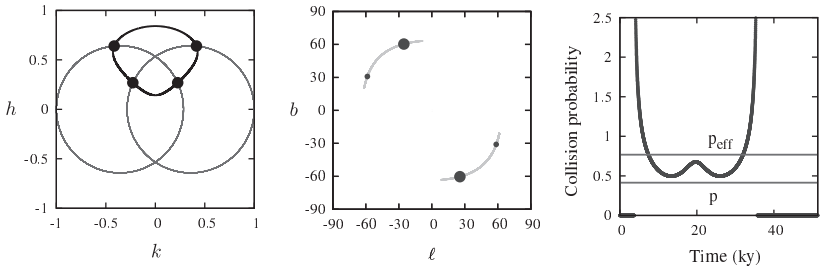

Fig. 4. The same as in Fig. 3 but for an orbit with initial semimajor axis $a = 1.4$ AU, eccentricity $e = 0.2$, inclination $i = 65°$ and argument of pericenter $\omega = 60°$.

bit circulates about a stable point on the h axis, such as seen on Fig. 4, the argument of pericenter is forced to oscillate about 90° or 270° values, and the radiants asymmetrically populate only one quadrant in the longitude vs. latitude plane. The size of symbols denoting the correct radiants is scaled by the partial collision probability – $(\Delta t/T_{\rm Kozai})_\star P_2(a,e_\star,i_\star)$, see Eq. (25) – for this particular impact configuration. Note that the higher-latitude radiants have systematically larger collision probability (e.g., in Fig. 3 three times) than the lower-latitude radiants. This is because the particle orbit spends more time at the large-inclination, and low-eccentricity, state and thus $(\Delta t)_\star$ is larger for the high-inclination radiants.

In the two cases discussed above $p_{\rm eff} > p$, indicating that the true collision probability was smaller than the value given by the Öpik theory. We now consider the same parameters as those used in Fig. 3, but let the semimajor axis a change to see how $p_{\rm eff}/p$ varies in general (Fig. 5). We find that $p_{\rm eff}/p > 1$, except if the impacts occur near the pericenter or apocenter, where $p_{\rm eff}/p < 1$.

Note the unusual extension of the impact probability line in Fig. 5 just below $Q = a_{\rm circ}$. Such a configuration is always an end-state of a sequence of impact possibilities in the Öpik approach, when eccentricity of the particle orbits is assumed constant. Fig. 6 helps to understand the situation. Shrinking the particle orbit semimajor axis makes $\alpha = a_{\rm circ}/a$ increase and the Earth-impact circles from Eq. (10) move toward larger k values and shrink their radius in the (k,h) plane. This would have lead to a "nominal" sequence of impact geometries 3′ to 1′ with no possibility of impact for the smallest a value considered in this figure; in the same time the impact geometry 1′ would be exactly the end-member case with $Q = a_{\rm circ}$. When the secular evolution of the particle orbit is described by the more involved solid line $\mathcal{H}(k,h;c) = C$, impact

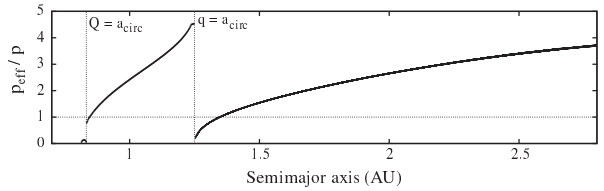

Fig. 5. The ratio $p_{\rm eff}/p$ shown as a function of the semimajor axis a for orbits with fixed initial eccentricity $e = 0.2$, inclination $i = 65°$ and argument of pericenter $\omega = 0°$. The target's heliocentric distance is $a_{\rm circ} = 1$ AU. The discontinuities occur for initial orbits with pericenter q or apocenter Q equal to $a_{\rm circ}$. Only for orbits close to these geometries p becomes larger than $p_{\rm eff}$, otherwise the use of Öpik formulation overestimates the collision probability with the target. The unusual feature below the formal $Q = a_{\rm circ}$ limit is explained using Fig. 6 (see discussion in the text).

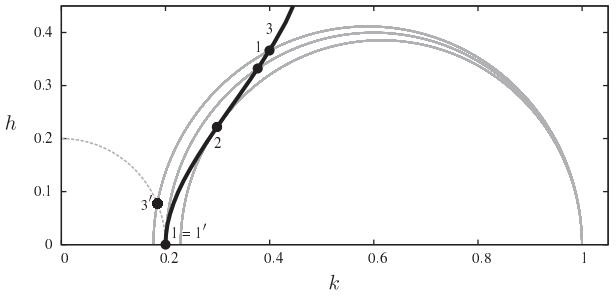

Fig. 6. Conditions for impacts near the apocenter of the particle orbit in the $(k,h) = e(\cos\omega, \sin\omega)$ plane of variables. The gray curves are the descending node impact circles from Eq. (10) for three slightly different values of $\alpha = a_{\rm circ}/a$ (smaller circle for a larger α, thus smaller a, value). The solid black curve is a part of the $\mathcal{H}(k,h;c) = C$ isoline for certain values of c and C integrals of motion, describing secular evolution of a potentially impacting particle. The black symbols are impact geometries for various values of eccentricity of the particle. The impact case labeled $1 = 1'$ with $h = 0$, corresponding to apocenter condition $Q = a_{\rm circ}$, would have been in the Öpik theory an end-member of the possible family of impacts $(3' \to 1')$ along the family of constant eccentricity orbits shown by the dashed circle. For the true orbit an continuation of the impacts is possible up to the limiting case of grazing impact 2.

geometries are possible even after the apocenter geometry 1 has been reached. For smaller a values the impact eccentricity may again increase up to the true end-member of the impact sequence at 2.

3.3.2. Testing the theory: a more realistic setup

We now compare the theory with the statistics of terrestrial impacts as recorded by a numerical integrator. We consider two sets of 500 massless particles having initially $a = 1.4$ AU, $e = 0.2$ and $i = 65°$. The argument of pericenter $\omega = 0°$ in the first set and $\omega = 60°$ in the second set. Nodal and orbit longitudes were taken randomly between 0° and 360°.

We first considered an idealized planetary system consisting of the Sun, Earth and Jupiter (both planets on circular orbits as before). The Earth was given zero mass and its radius was multiplied by a factor of 10 to accelerate the impact rate in the numerical integration ($R_{\rm Earth} = 4.26 \times 10^{-4}$ AU).

We numerically propagated the orbits of all bodies with the `SWIFT_RMVS3` integrator,[12] using a 2-day time step, and recorded the direct impacts of particles on the Earth. Fig. 7 shows the fraction of particles surviving in our simulation as a function of time. For comparison, we also show the expected decay of the population assuming it can be modelled using a Poissonian processes with certain characteristic timescale τ, thus $n_{\rm Pois}(t) = \exp(-t/\tau)$. The decay-curve labeled 1 has $\tau = \tau_1 \simeq 9.4$ Myr (upper panel) and

[12] http://www.boulder.swri.edu/~hal/swift.html.

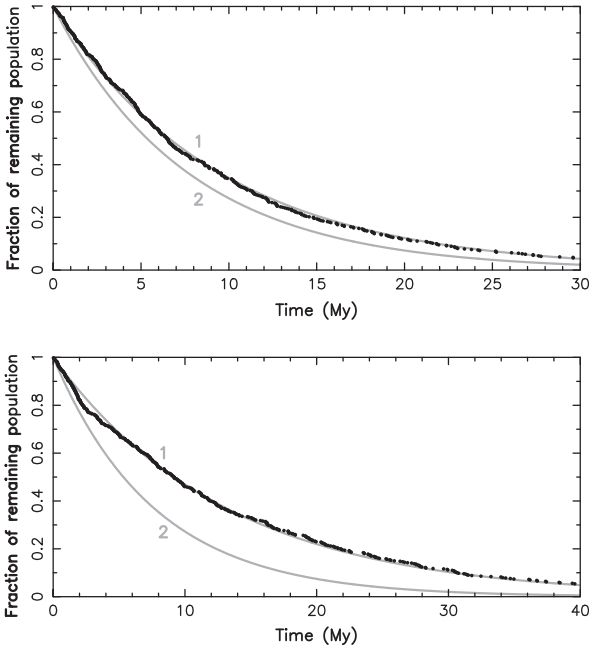

Fig. 7. Fraction of particle population remaining the numerical simulation shown by symbols vs. time t (in Myr). 500 particles were initially put on orbits with semimajor axis $a = 1.4$ AU, eccentricity $e = 0.2$, inclination $i = 65°$ and argument of pericenter $\omega = 0°$ (upper panel) and $\omega = 60°$ (bottom panel); longitude of node and longitude in orbit were set randomly. Their orbital evolution was numerically propagated and direct impacts onto the Earth recorded in a reduced model where only Jupiter was considered on a circular heliocentric orbit (the Earth had zero mass a radius R 10 times larger that the true value). The gray curves simulate results from a Poissonian process with a characteristic timescale τ, thus $\exp(-t/\tau)$: (i) the curve 1 has $\tau \simeq 9.4$ Myr (upper panel) and $\tau \simeq 13.3$ Myr (bottom panel), corresponding to $1/(pR^2)$, and (ii) the curve 2 has $\tau \simeq 7.7$ Myr (both panels), corresponding to $1/(p_{\rm eff}R^2)$.

$\tau = \tau_1 \simeq 13.3$ Myr (bottom panel), while the decay-curves labeled 2 have $\tau = \tau_2 \simeq 7.7$ Myr (both upper and bottom panels).

We find that numerically recorded impact rate on the Earth very nicely matches the decay curves with $\tau = \tau_1$. This is because $\tau_1 = 1/(p\ R^2)$, where $p \simeq 0.586\ {\rm AU}^{-2}\,{\rm y}^{-1}$ (upper panel) and $p \simeq 0.413\ {\rm AU}^{-2}\,{\rm y}^{-1}$ (bottom panel) were determined using our generalized collisional probability theory (see Figs. 3 and 4). The probability p therefore gives a simple and very good approximation for the real collisional decay. For comparison, the Öpik collision probability is $p_{\rm eff} \simeq 0.715\ {\rm AU}^{-2}\,{\rm y}^{-1}$ (upper panel) and $p_{\rm eff} \simeq 0.716\ {\rm AU}^{-2}\,{\rm y}^{-1}$ (bottom panel), and $\tau_2 = 1/(p_{\rm eff}\ R^2)$ decay in Fig. 7. Henceforth, we verified that the standard Opik theory would suggest a stronger decay than the actual one.

We also determined the direction of impacts in the numerical integrations described above. We found that the simulated particles indeed hit the Earth from the two discrete radiant locations shown in Figs. 3 and 4. The impacts from the higher-latitude radiants are approximately three times more numerous than those from the lower-latitude radiants. This is in a very good agreement with expected number of impacts in these radiants from our new theory.

We now consider a more realistic model of the Solar System where we take into account the gravitational perturbations between all planets. To prevent particles from impacting the terrestrial planets other than Earth, we set the physical radii of Mercury, Venus and Mars to zero. The Earth's radius is increased by a factor of 10. We consider the same two particle populations as before. The system was numerically integrated with `SWIFT_RMVS3`.

Now, Jupiter is not the sole perturber of particle orbits, and the planetary orbits undergo secular variations due to mutual perturbations. In addition, close approaches of particles to the terrestrial produce a random walk in their orbits and affect the secular evolution. The evolving system is therefore more complex than the simple Lidov–Kozai model that we used in our generalized theory.

Fig. 8 shows how the fraction of the initial population remaining in the simulation decreases with time for the two simulations. Focusing first on the former case, we note that the particle population decay follows on average the expected Poissonian curve 1 (corresponding to the characteristic collision timescale $\tau = 1/(p R^2) \simeq 9.4$ Myr). However, initially the particles are being eliminated slightly faster while only at later epochs the rate of their elimination becomes slightly slower than shown by the idealized curve 1. We believe this is partly because of the particle-orbit scattering by the terrestrial planets, such that some particles are scattered onto orbits with smaller semimajor axis value and have effectively larger collision probability with the Earth, while the remaining population of particles is biased toward somewhat larger semimajor axis values with smaller collision probability with the Earth.

The situation is somewhat different in the bottom panel of Fig. 8, where the particle orbits had initially $\omega = 60°$. This is the case, when the argument of pericenter ω would circulate about a stationary point on the h axis, making ω oscillate in a limited range of values, in the idealized Lidov–Kozai model (see the left panel on Fig. 4). However, this particular behavior of the orbits is quickly removed by both semimajor axis change due to scattering on terrestrial planets and a complex set of secular perturbations. As a result, the particle orbits more often spend their secular evolution in the mode similar to that seen in Fig. 3, with ω circulating about origin in the (k,h) plane. The collision probability with the Earth then effectively increases and the decay rate approaches that from the above panel (shown by the dashed gray curve).

Finally, we propagated the first set of particles (initial value $\omega = 0°$) in the case where all terrestrial planets were taken as potential targets. To speed up the comparison, we increased the planetary radii by a factor of 10.

We used our collision probability theory to calculate p_i for each planet ($i = 1 \cdots 4$, where 1 stands for Mercury, etc.), Denoting R_i the enhanced radii of the terrestrial planets, the total collisional probability per year is $\Pi_{\rm tot} = \sum_i p_i R_i^2$. The particle population is thus expected to decay with a characteristic timescale $\tau \simeq 1/\Pi_{\rm tot} \simeq 3.9$ Myr. At each instant, the number of impacts on each of the terrestrial planets is weighted using their partial impact probabilities, i.e., $\propto p_i R_i^2/\Pi_{\rm tot}$ for the ith planet. These predictions are confronted with results from the numerical experiment in Fig. 9, where the symbols show the recorded planetary impacts for each of the planet and the dashed gray exponential decay curves are the above described theoretical predictions. While generally showing a good match, the solid gray decay curves slightly better express the population decrease and those have $\tau \simeq 3.2$ Myr.

The small difference between the theory and numerical experiment probably stems from the approximations in our collisional probability approach, where complex planetary perturbations and close encounters of particles to planets are neglected. Obviously, the whole particle population now decays faster than seen in Fig. 8 because more targets are available to destroy them. As expected all planet impacts are fitted by roughly the same decay rate, basically that of the whole population, and their partitioning is roughly that expected from the theory.

Mercury received a large number of impacts, more than it could be expected just based on its relatively small cross-section. This is because the partial impact probability, $p_1 R_1^2$, is increased by a large value of p_1 (nearly three times larger than that of the Earth). This can be explained by realizing that the Mercury impacts always occur near the pericenter of the particle orbits. Such impacts are characterized by large impact probability.

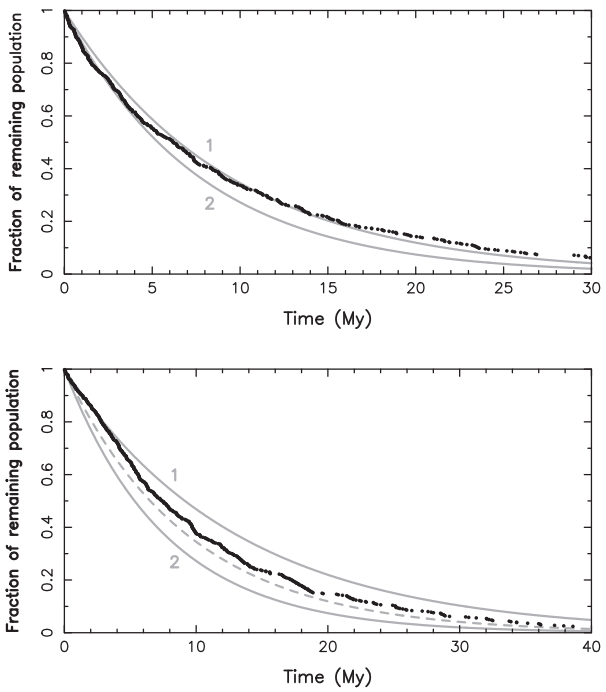

Fig. 8. Fraction of particle population remaining the numerical simulation shown by symbols vs. time t (in Myr). 500 particles were initially put on orbits with semimajor axis $a = 1.4$ AU, eccentricity $e = 0.2$, inclination $i = 65°$ and argument of pericenter $\omega = 0°$ (upper panel) and $\omega = 60°$ (bottom panel); longitude of node and longitude in orbit were set randomly. Their orbital evolution was numerically propagated and direct impacts onto the Earth recorded in a model where perturbations from all planets were taken into account; impacts on Mercury, Venus and Mars were prevented by taking their radii zero and the Earth radius R was 10 times larger that the true value. The gray curves simulate results from a Poissonian process with a characteristic timescale τ, thus $\exp(-t/\tau)$: (i) the curve 1 has $\tau \simeq 9.4$ Myr (upper panel) and $\tau \simeq 13.3$ Myr (bottom panel), corresponding to $1/(pR^2)$, and (ii) the curve 2 has $\tau \simeq 7.7$ Myr (both panels), corresponding to $1/(p_{\rm eff} R^2)$. The dashed gray line in the bottom panel reproduces the solid line 1 from the top panel.

4. Conclusions

We developed a new collision probability theory for the high inclination and high eccentricity orbits for which the Lidov–Kozai cycles are important. The results of this theory agree with those of the standard Öpik theory in the limit of small-eccentricity and small-inclination orbits. For high eccentricities and high inclinations, where the standard Öpik theory falls short in correctly predicting the rates and radiants of the impacts, the generalized theory produces satisfactory results when compared to numerical experiments.

The theory developed in this paper can be generalized further, for example, by relaxing the assumption of the circular orbit of the target (Wetherill, 1967; Greenberg, 1982). Such a formulation may be required, for example, to properly calculate the planetary impact rates of during the early evolution of the Solar system (see, e.g., Bottke et al., 2005).

Another possibility would be to relax the linear approximation (15) and (16) for the local description of motion in the nodal reference system $(\mathbf{e}_r, \mathbf{e}_\phi, \mathbf{e}_z)$, for instance by using the quadratic or higher-order approximations. This may be of some interest for improving the collision probability estimate in cases when the

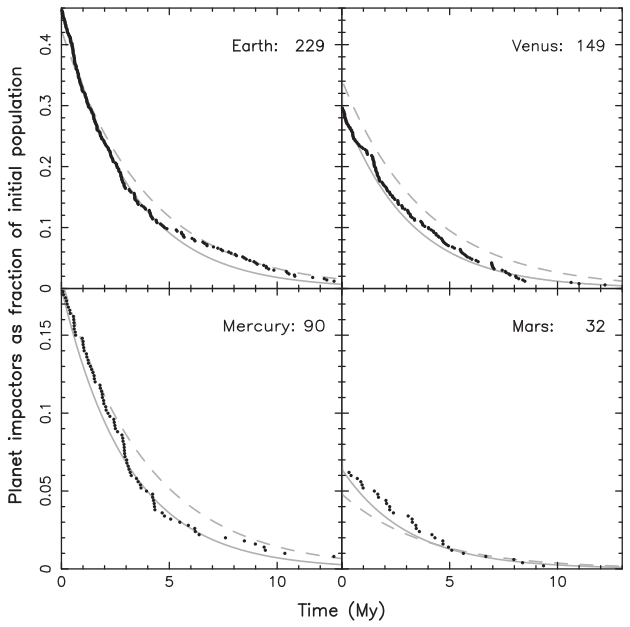

Fig. 9. Fraction of particles impacting the terrestrial planets in the most complete simulation, where all planets were considered as potential targets (their radii were increased by a factor 10 to speed up the simulation). The total number of impacts is indicated by labels. The dashed gray decay curves were obtained by an appropriate partitioning of the total decay of the particle population from our model, and the solid gray decay curves were the best match of the data (see the text).

curvature of orbits becomes important (e.g., for impacts near pericenter or apocenter of the particle orbit).

Acknowledgements

This research was supported by Czech Grant Agency (Grants 205/08/0064 and 205/08/H005) and the Research Program MSM0021620860 of the Czech Ministry of Education. The work of DN was supported by the NASA Planetary Geology and Geophysics program. We thank Giovanni B. Valsecchi and Giovanni F. Gronchi, whose referee comments helped to improve the original version of this paper.

Appendix A. Öpik's approximation

In what follows, we show that the general approach from Section 3.2 reproduces Öpik's results for appropriate assumption about the secular evolution of the particle orbit. In particular, the uniform circulation of the orbit in the (k,h) plane on a circle of constant eccentricity e is generated with

$$\mathcal{H}_{\rm Opik}(k,h) = k^2 + h^2 = C \tag{A1}$$

that follows from (14) in the limit of small e value. When inclination i is also small, conservation of $c = \eta\cos i$ implies i = constant, and nodal circulation decouples from pericenter evolution. The condition (18) of particle grazing the target at a distance equal to its radius R is given by

$$\mathcal{K}_{\rm Opik}(k,h;i) = [\eta^2 - \alpha(1\pm k)]\frac{\sin i}{\sqrt{h^2 + (1\pm k)^2\sin^2 i}} = \rho, \tag{A2}$$

where we recall $\rho = R/a$ and a is the semimajor axis of particle orbit (recall $\alpha = a_{\rm circ}/a$ with $a_{\rm circ}$ heliocentric distance of the target).

First, let us again seek roots of (A1) and (A2) as small displacements δk and δh from exact intersection solution $k_\star$ and $h_\star$ given by (upper sign for the ascending node, lower sign for the descending node impacts)

$$1 \pm k_\star = \frac{\eta^2}{\alpha}, \tag{A3}$$

and

$$h_\star^2 = \frac{\eta^2}{\alpha^2}(\alpha - 1 + e)(1 + e - \alpha). \tag{A4}$$

Obviously, these are just geometrical conditions of intersections of two circles in the (k,h) plane, namely e = constant and (10). The δk and δh are obtained from (19), where now

$$(\partial\mathcal{H}_{\rm Opik}/\partial k)_\star = 2k_\star, \tag{A5}$$

$$(\partial\mathcal{H}_{\rm Opik}/\partial h)_\star = 2h_\star, \tag{A6}$$

$$(\partial\mathcal{K}_{\rm Opik}/\partial k)_\star = -\frac{2(k_\star \pm \alpha/2)\sin i}{\sqrt{h_\star^2 + (1\pm k_\star)^2\sin^2 i}}, \tag{A7}$$

$$(\partial\mathcal{K}_{\rm Opik}/\partial h)_\star = -\frac{2h_\star \sin i}{\sqrt{h_\star^2 + (1\pm k_\star)^2\sin^2 i}}, \tag{A8}$$

and thus

$$\mathcal{D}_\star = \mp\frac{2\alpha h_\star \sin i}{\sqrt{h_\star^2 + (1\pm k_\star)^2\sin^2 i}}. \tag{A9}$$

One easily verifies, that $(\delta k, \delta h)$ are small displacements along tangent to the circle $C = e^2$ = constant. This is because the associated change in e is $\delta e = (k_\star\delta k + h_\star\delta h)/e = 0$. In the same way, the associated change in argument of pericenter ω is $\delta\omega = (k_\star\delta h - h_\star\delta k)/e^2$, or

$$\delta\omega = \frac{\rho}{\alpha\sin i}\sqrt{1 + \frac{(1\pm k_\star)^2}{h_\star^2}\sin^2 i}. \tag{A10}$$

Inserting $k_\star$ and $h_\star$ from (A3) and (A4) above, we have

$$\delta\omega = \frac{R}{a_{\rm circ}\sin i}\sqrt{\frac{2 - F(a,e,i)}{2 - F(a,e,0)}}, \tag{A11}$$

with F-function defined in Eq. (13). The total advancement $\Delta\omega$ of the argument of pericenter between the two extreme, target-grazing configurations is $\Delta\omega = 2\delta\omega$. Because there are four equivalent intersection configurations at the ascending and descending nodes, we have

$$P_{1,\rm Opik} = \frac{2\Delta\omega}{\pi} = \frac{4}{\pi}\frac{R}{a_{\rm circ}\sin i}\sqrt{\frac{2 - F(a,e,i)}{2 - F(a,e,0)}}. \tag{A12}$$

Combining with P_2 from Eq. (11), this finally provides collision probability per revolution

$$P_{\rm Opik} = P_{1,\rm Opik}P_2 = \frac{1}{\pi}\frac{R^2}{a_{\rm circ}^2\sin i}\sqrt{\frac{3 - T(a,e,i)}{2 - F(a,e,0)}}, \tag{A13}$$

which is identical to results given by Öpik (1951) and Wetherill (1967), when restricted to circular orbit of the target (field body). The intrinsic collision probability per unity of time is again

$$p_{\rm Opik} = P_{\rm Opik}/T_{\rm orb} = (1/2\pi)(\sqrt{GM}/a^{3/2})P_{\rm Opik}, \tag{A14}$$

where $T_{\rm orb}$ is the orbital period of the particle (compare with Eq. (26)).

While obtaining identical result as previous authors in the limit of assumptions matching the classical Öpik theory, we finally comment on one of its well-known and often repeated aspects. In particular, the denominator term in the square-root factor in Eq. (A11), and consequently also (A12) and (A13), reads

$$2 - F(a,e,0) = \frac{(a_{\rm circ} - q)(Q - a_{\rm circ})}{a a_{\rm circ}}, \tag{A15}$$

where we denoted $q = a(1-e)$ and $Q = a(1+e)$, i.e., pericenter and apocenter distance of the particle orbit. This produces a singularity of the Öpik collision probability when pericenter or apocenter distances of the particle orbit become equal to the target's heliocentric distance. It seems to have passed unnoticed so far that this apparent singularity may be removed within the Öpik approach by a more thorough analysis of the impact geometries near the pericenter or apocenter configurations. In particular, it stems only from the *linearization* of small displacements about the exact impact geometry at $(k_\star, h_\star)$. However, the system of Eqs. (A1) and (A2) is simple enough to admit exact analytic solution. In particular, the roots in k satisfy a simple quadratic equation $Ak^2 + 2Bk + C = 0$, with coefficients (upper sign for the ascending node, lower sign for the descending node)

$$A = \alpha^2 \sin^2 i + \rho^2 \cos^2 i, \tag{A16}$$

$$B = \pm[\alpha(\alpha - \eta^2) - \rho^2] \sin^2 i, \tag{A17}$$

$$C = (\alpha - \eta^2)^2 \sin^2 i - \rho^2(e^2 + \sin^2 i). \tag{A18}$$

There are obviously two solutions $k_1^\pm$ and $k_2^\pm$

$$k_1^\pm = \frac{\mp[\alpha(\alpha - \eta^2) - \rho^2] \sin^2 i + \rho\sqrt{D(a,e,i)}}{\alpha^2 \sin^2 i + \rho^2 \cos^2 i}, \tag{A19}$$

$$k_2^\pm = \frac{\mp[\alpha(\alpha - \eta^2) - \rho^2] \sin^2 i - \rho\sqrt{D(a,e,i)}}{\alpha^2 \sin^2 i + \rho^2 \cos^2 i}, \tag{A20}$$

with

$$D(a,e,i) = \alpha\eta^2 F(a,e,i) \sin^2 i + \rho^2(1 - \eta^2 \cos^2 i), \tag{A21}$$

and $F(a,e,i)$ from Eq. (13). To each of $k_1^\pm$ and $k_2^\pm$ we have corresponding $h_1^\pm = \sqrt{e^2 - k_1^{\pm 2}}$ and $h_2^\pm = \sqrt{e^2 - k_2^{\pm 2}}$ on the positive side of the h-axis and symmetric values on the negative side of the h-axis. We then simply determine the range $\Delta\omega^\pm$ of the argument of pericenter value around ascending and descending node intersection that still admit impact on the target with

$$\cos\Delta\omega^\pm = \frac{k_1^\pm k_2^\pm + h_1^\pm h_2^\pm}{e^2}. \tag{A22}$$

These values may be then used to compute the partial probabilities $P_{1,\rm Opik} = (\Delta\omega^+ + \Delta\omega^-)/\pi$. Nevertheless, even in this approach a care must be paid to configurations when impacts occur near pericenter or apocenter of the particle orbit. This is because in these cases one of the values k_1^+ or k_2^- may become larger than e, which would prevent to compute the associated h value. The reason for this effect is that the intervals $\Delta\omega$ for the impact configurations with positive and negative h value are no more discontinuous and join together.

An example is seen in Fig. 10, where we show

$$\left(\frac{d_{\rm min}}{R}\right)^2 = \frac{[\eta^2 - \alpha(1+k)]^2 \sin^2 i}{h^2 + (1+k)^2 \sin^2 i}, \tag{A23}$$

as a function of h near values where $h \sim 0$ (i.e., pericentric impacts in the ascending node). For sake of definiteness we took $e = 0.2$, $i = 25°$, $a_{\rm circ} = 1$ AU and R equal to the Earth radius and plotted the left hand side for three different a values of the particle orbit such that the corresponding q value gets very close to $a_{\rm circ}$. Recall that, for a given particle orbit, $d_{\rm min}$ gives a minimum orbit distance from the target as a function of (k,h), such that $d_{\rm min} \leqslant R$ characterize impact configurations. In general, intervals of h values, which are straightforwardly mapped onto intervals of ω values, for which $(d_{\rm min}/R) \leqslant 1$ are disconnected on the positive and negative sides of the axis (light gray curves). But as one approaches the exact pericentric configuration, both intervals join together (black curve). In that case, $P_{1,\rm Opik}$ must be computed only from the common interval of ω values that overlap both impact configurations. Obviously, this way there is no exact singularity even for the pericentric impact.

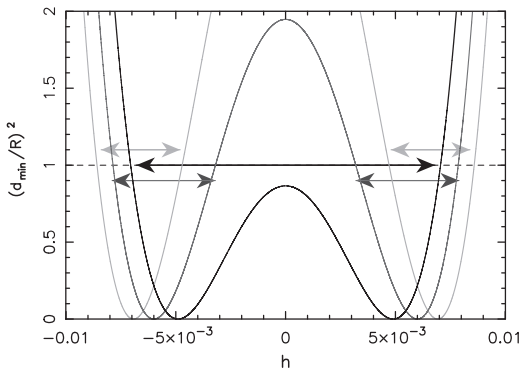

Fig. 10. Behavior of $(d_{\rm min}/R)^2$ function near exact intersection configurations at ascending node vs. h (the k value is constrained by a condition $k^2 + h^2 = e^2 =$ constant). We show the situation for $h \sim 0$, i.e. when the impacts occur very near the pericenter of the particle orbit. Having the target orbit at $a_{\rm circ} = 1$ AU, we show three different cases: (i) $a_{\rm circ} - q = 10^{-4}$ AU (light gray), (ii) $a_{\rm circ} - q = 7.5 \times 10^{-5}$ AU (dark gray), and (iii) $a_{\rm circ} - q = 5 \times 10^{-5}$ AU (black), all for $R = 4.6 \times 10^{-5}$ AU equal to the Earth radius. The $(d_{\rm min}/R)^2 = 0$ condition is for the particle nodal distance exactly at $a_{\rm circ}$, denoted $h_\star$ in the text. The arrows indicate interval of h values near $h_\star$ for which the minimum orbit distance to the target is less than R and oblique impacts occur. There are usually separate h (and correspondingly ω) intervals for $h_\star$ positive and negative, but when $a_{\rm circ} - q$ is less than a critical value they merge into a single interval (such as for the black curve).

Note, however, that $\rho \sim 5 \times 10^{-5}$ in our example, and $\Delta\omega$ for near pericentric impacts is several orders of magnitude larger than ρ (though not infinite). This means that the target-grazing configurations occur very far from the ascending node position of the exact particle impact at a heliocentric distance $a_{\rm circ}$. In this situation, the linear approximations for the particle and target orbits from Eqs. (15) and (16) are not justified and higher-order terms accounting for curvature of the local orbit would be necessary. As a result, our comment about nonexistent singularity in $P_{\rm Opik}$ is rather a curiosity than of real importance.

References

Babadzhanov, P.B., Obrubov, Yu.V., 1992. Evolution of short-period meteoroid streams. Celest. Mech. Dynam. Astron. 54, 111–127.

Bailey, M.P., Chambers, J.E., Hahn, G., 1992. Astron. Astrophys. 257, 315–322.

Bottke, W.F., Durda, D.D., Nesvorný, D., Jedicke, R., Morbidelli, A., Vokrouhlický, D., Levison, H.F., 2005. Linking the collisional history of the main asteroid belt to its dynamical excitation and depletion. Icarus 179, 63–94.

Campbell-Brown, M.D., 2008. High resolution radiant distribution and orbits of sporadic radar meteoroids. Icarus 196, 144–163.

Galligan, D.P., Baggaley, W.J., 2005. The radiant distribution of AMOR radar meteors. Mon. Not. R. Astron. Soc. 359, 551–560.

Greenberg, R., 1982. Orbital interactions – A new geometrical formalism. Astron. J. 87, 184–195.

Gronchi, G.F., Milani, A., 1998. Averaging on Earth-crossing orbits. Celest. Mech. Dynam. Astron. 71, 109–136.

Gronchi, G.F., Milani, A., 1999. The stable Kozai state for asteroids and comets. With arbitrary semimajor axis and inclination. Astron. Astrophys. 341, 928–935.

Kessler, D.J., 1981. Derivation of the collision probability between orbiting objects. The lifetimes of Jupiter's outer moons. Icarus 48, 39–48.

Kessler, D.J., Cour-Palais, B.G., 1978. Collision frequency of artificial satellites: The creation of a debris belt. J. Geophys. Res. 83, 2637–2646.

Kinoshita, H., Nakai, K., 2007. General solution of the Kozai mechanism. Celest. Mech. Dynam. Astron. 98, 67–74.

Kozai, Y., 1962. Secular perturbations of asteroids with high inclination and eccentricity. Astron. J. 67, 591–598.

Lidov, M.L., 1961. Evolution of the planets artificial satellites orbits under effect of the outer bodies gravity perturbations. Artif. Satell. Earth 8, 5–45 (in Russian).

Lidov, M.L., 1962. The evolution of orbits of artificial satellites of planets under the action of gravitational perturbations of external bodies. Planet. Space Sci. 9, 719–759 (the English translation of Lidov's 1961 paper).

Michel, P., Froeschlé, Ch., 1997. The location of linear secular resonances for semimajor axes smaller than 2 AU. Icarus 128, 230–240.

Michel, P., Thomas, F., 1996. The Kozai resonance for near-Earth asteroids with semimajor axes smaller than 2 AU. Astron. Astrophys. 307, 310–318.
Morbidelli, A., 2002. Modern Celestial Mechanics: Aspects of Solar System Dynamics. Taylor & Francis, Cambridge Scientific Publishers, 376pp.
Nesvorný, D., Vokrouhlický, D., Pokorný, P., Janches, D., 2011. Dynamics of dust particles released from Oort cloud comets and their contribution to radar meteors. Astrophys. J. 743, 37, 12pp.
Öpik, E.J., 1951. Collision probabilities with the planets and the distribution of interplanetary matter. Proc. Roy. Irish A 54, 165–199.
Öpik, E.J., 1976. Interplanetary Encounters: Close-Range Gravitational Interactions. Elsevier, Amsterdam, 155pp.
Press, W.R., Teukolsky, S.A., Vetterling, W., Flannery, B.P., 2007. Numerical Recipes: The Art of Scientific Computing. Cambridge University Press, Cambridge, 1256pp.
Steel, D.I., Baggaley, W.J., 1985. Collisions in the Solar System – I: Impacts of the Apollo–Amor–Aten asteroids upon the terrestrial planets. Mon. Not. R. Astron. Soc. 212, 817–836.
Steel, D.I., Elford, W.G., 1986. Collisions in the Solar System: III – Meteoroid survival times. Mon. Not. Roy. Astron. Soc. 218, 185–199.
Sykes, M.V., 1990. Zodiacal dust bands: Their relation to asteroid families. Icarus 85, 267–289.
Thomas, F., Morbidelli, A., 1996. The Kozai resonance in the outer Solar System and the dynamics of long-period comets. Celest. Mech. Dynam. Astron. 64, 209–229.
Valsecchi, G.B., Jopek, T.J., Froeschlé, C., 1999. Meteoroid stream identification: A new approach I. Theory. Mon. Not. R. Astron. Soc. 304, 743–750.
Wetherill, G.W., 1967. Collisions in the asteroid belt. J. Geophys. Res. 72, 2429–2444.

Paper B

Icarus 226 (2013) 682–693

Contents lists available at SciVerse ScienceDirect

Icarus

journal homepage: www.elsevier.com/locate/icarus

Öpik-type collision probability for high-inclination orbits: Targets on eccentric orbits

Petr Pokorný *, David Vokrouhlický

Institute of Astronomy, Charles University, V Holešovičkách 2, CZ-18000, Prague 8, Czech Republic

ARTICLE INFO

Article history:
Received 22 April 2013
Revised 13 June 2013
Accepted 14 June 2013
Available online 28 June 2013

Keywords:
Celestial mechanics
Impact processes
Asteroids
Interplanetary dust

ABSTRACT

Traditional evaluation of collision probability between two bodies on bound heliocentric or planetocentric orbits include assumptions that are often only an approximation of their real motion. In particular, these approaches require (i) the orbital eccentricity and inclination of both target and projectile long-term constant, and (ii) their longitude of ascending node and argument of pericenter precessing uniformly in time. Both conditions (i) and (ii) are satisfied for orbits with very small eccentricities and inclinations only. When either of these two elements is large, a tidal perturbation by planets, or the Sun in a planetocentric configuration, makes these elements oscillate in a correlation with the non-linear evolution of the secular angles. Vokrouhlický et al. (Vokrouhlický, D., Pokorný, P., Nesvorný, D. [2012]. Icarus 219, 150–160) developed an approach which allows the orbit of the projectile undergo such a general secular evolution. An assumption of the circular orbit of the target, however, was a significant drawback of their method. Here, we extend Vokrouhlický et al.'s work to allow a general eccentric and precessing orbit of the target (assuming though fixed orbital plane in space). We test predictions of our new approach, as well as previous theories, against a direct numerical integration and estimate their validity. A particular run is performed for E-belt projectiles impacting terrestrial planets. We conclude a surprisingly good correspondence of the directly obtained impact record from the numerical simulation and the estimate from our theory. Based on these results, we infer that the crater density from E-belt projectiles on Mercury should be roughly comparable (or only slightly larger) to that on our Moon.

1. Introduction

Planets, accompanied with their satellites, are not alone to revolve about the Sun. There is a myriad of smaller bodies, ranging from asteroids and comets down to sizes of dust particles, orbiting the Sun. Some of them may occasionally share the same region in space where planets move, and thus could impact on them. Living in large populations, these smaller bodies may also hit each other. Evaluating the small, though non-zero, probability of these events is often an important information in planetary studies. In this work, we do not deal with an impact probability of a specific projectile over a short timescale. Rather, we have in mind an evaluation of a mean impact probability averaged over a timescale equal or longer than that characterizing a secular evolution of the projectile orbit.

Öpik (1951) was the first to deal with this problem in the modern astronomical literature. This work assumed a target on a circular orbit fixed in space, sweeping through a population of projectiles on bound heliocentric orbits with constant eccentricities and inclinations. Öpik's theory was later generalized for targets on eccentric and inclined orbits by Wetherill (1967) and Greenberg (1982) which themselves undergo a simple secular evolution, again keeping the assumption of a long-term constant values of orbital eccentricity and inclination. A slightly different approach was independently proposed by Kessler (1981).

All these above mentioned approaches are frequently used to determine a collision probability among members of a population of small bodies or with respect to planets and their satellites. For instance, all collisional evolution codes are based on either Wetherill's or Greenberg's variants of the method, some occasionally use the Kessler's approach. All these standard theories assume the orbital eccentricity e and inclination i during the secular evolution of target and projectiles are constant. This assumption is not exactly correct even for moderate values of e and i. Still, the variations of e and i are mostly small enough such that the population average, and often other unknown parameters in the model, make the results grossly justified. However, when either of the projectile or the target orbits have high inclination and/or high eccentricity, application of the traditional collision model is questionable. This is because variations of e and i during the secular cycle may be large, and the secular angles such as the longitude of node and pericenter may exhibit a strongly non-linear evolution with time.

* Corresponding author.
E-mail addresses: petr.pokorny@volny.cz (P. Pokorný), vokrouhl@cesnet.cz (D. Vokrouhlický).

0019-1035/$ - see front matter © 2013 Elsevier Inc. All rights reserved.
http://dx.doi.org/10.1016/j.icarus.2013.06.015

About half a century ago elements of these dynamical phenomena were introduced by Lidov (1961, 1962) in space geodesy and independently by Kozai (1962) in planetary astronomy. Later, more complex theories, allowing for instance a planet crossing, were developed. These results were needed, because certain populations of small bodies reside on such orbits and thus undergo the corresponding orbital evolution: all classes of comets and their related meteoroid streams, meteoroids in the sporadic complex, etc. As a result, the traditional collision probability methods may provide disputable results when evaluating their impact chances with the Earth, for instance.

This situation motivated Vokrouhlický et al. (2012) to formulate a generalized Öpik-type collision probability theory. In their model the projectile orbit was allowed to undergo Lidov–Kozai oscillations, and with a simple generalization even more complex, secular evolution. However, a persisting drawback was the assumption of a circular and fixed orbit of the target. Here we extend this earlier work and allow the target orbit be eccentric and uniformly precessing in space. While not so critical for Earth or Venus, this generalization makes our approach quite more suitable for evaluation of impact probability on Mercury or Mars, as examples.

Mathematical preliminaries are introduced in Section 2.1. Section 2.2 is a brief summary of the Lidov–Kozai dynamics, and the core formulation of our collision probability model is given in Sections 2.3 and 2.4. In Section 3 we provide simple-configuration runs which illustrate our main results and help justify our numerical approach. Finally, Section 4 contains simulation motivated by recent work of Bottke et al. (2012): projectiles originating in today's extinct extension of the main asteroid belt, known as the E-belt, are propagated in the gravity field of the Sun and all planets. We record direct impacts onto terrestrial planets as provided by our numerical simulation and compare them with an estimation from our theory. An emphasis is given to impacts on Mercury which was not included in Bottke et al. (2012).

2. Theory

2.1. Reference frames and notation

In this section we introduce necessary mathematical concepts and notation used throughout the paper. Obviously, both closely follow the work of Vokrouhlický et al. (2012), allowing now an eccentric orbit of the target.

We start with a description of the projectile orbit near the nodal crossings of the target plane (for sake of definiteness we assume both are on heliocentric orbits). Assume the projectile resides on a general elliptic orbit described with osculating Keplerian elements: the semimajor axis a, the eccentricity e, the inclination i, the longitude of node Ω, the argument of pericenter ω and the true anomaly f. The angular parameters i, Ω and ω are defined with respect to the inertial frame (X,Y,Z), whose reference plane (X,Y) coincides with that of the target's fixed orbital plane about the Sun.[1] The projectile orbit intersects the (X,Y) reference plane at the ascending node, where $f=f_{\rm n}=-\omega$, and the descending node, where $f=f_{\rm n}=\pi-\omega$. The description of the orbit near the nodal intersections benefits from introduction of the reference basis $(\mathbf{e}_r,\mathbf{e}_\phi,\mathbf{e}_z)$ composed of the three orthonormal vectors with the origin at the ascending or descending nodes. The vectors $\mathbf{e}_r$ and $\mathbf{e}_\phi$ point to the radial and longitude directions at the respective node, and the vector $\mathbf{e}_z$ along the Z axis of the inertial frame. Thus in our definition, the radial and longitude directions, i.e. $\mathbf{e}_r$ and $\mathbf{e}_\phi$ vectors, at the descending node are opposite to their values at the ascending node.

The heliocentric position vector $\mathbf{r}$ describing the elliptic orbit of the projectile generally reads

$$\mathbf{r}(f)=r(f)[\mathbf{a}\cos(\omega+f)+\mathbf{b}\sin(\omega+f)], \tag{1}$$

with $r(f)=a\eta^2/(1+e\cos f)$ and $\eta=\sqrt{1-e^2}$. The unit vector $\mathbf{a}^T=(\cos\Omega,\sin\Omega,0)$ is directed along the ascending node, and $\mathbf{b}^T=(-\cos i\sin\Omega,\cos i\cos\Omega,\sin i)$ is in the orbital plane, normal to $\mathbf{a}$. As a result, at the ascending node we have $\mathbf{a}=\mathbf{e}_r$ and $\mathbf{b}=\cos i\,\mathbf{e}_\phi+\sin i\,\mathbf{e}_z$, while at the descending node we have $\mathbf{a}=-\mathbf{e}_r$ and $\mathbf{b}=-\cos i\,\mathbf{e}_\phi+\sin i\,\mathbf{e}_z$. Now expand $\mathbf{r}(f)$ near the ascending and descending nodes, where the heliocentric distance is $r=a\eta^2/(1\pm e\cos\omega)$ respectively (the upper sign for the ascending node). Introducing an infinitesimal increment df of the true anomaly, $f=f_{\rm n}+df$, we obtain $\mathbf{r}(f)=r\mathbf{e}_r+d\mathbf{r}$, with

$$d\mathbf{r}=r\mathbf{A}_1\,df+\frac{r}{2}\mathbf{A}_2\,df^2+\mathcal{O}(df^3). \tag{2}$$

Eq. (2) helps to locally describe the elliptic orbit of the projectile with $df=0$ at the respective node. The first term is the crudest rectilinear approximation, while the second term describes the local curvature of the elliptic orbit. The first- and second-order vectorial coefficients read (the upper sign for the ascending node intersection and the lower sign for the descending node intersection)

$$\mathbf{A}_1=\mp\frac{e\sin\omega}{P}\mathbf{e}_r+(\cos i\mathbf{e}_\phi\pm\sin i\mathbf{e}_z), \tag{3}$$

$$\mathbf{A}_2=-2\left[1-\frac{3}{2P}+\frac{\eta^2}{P^2}\right]\mathbf{e}_r-2\frac{e\sin\omega}{P}(\pm\cos i\mathbf{e}_\phi+\sin i\mathbf{e}_z), \tag{4}$$

where $P=a\eta^2/r$.

Next, we use a similar framework to describe motion of the target body. The target body is assumed to move on an elliptic heliocentric orbit with the semimajor axis a_0, the eccentricity e_0 and the argument of pericenter ω_0 in the (X,Y) reference plane. Without loss of generality we set $\omega_0=0$ in our coordinate system. Choosing a certain value f_0 of the true anomaly, the position vector $\mathbf{r}_0$ of the target can again be described as $\mathbf{r}_0(f)=r_0\mathbf{e}_r+d\mathbf{r}_0$ in its orbital vicinity[2] $f=f_0+df$ (r_0 is the target's heliocentric distance for $f=f_0$). We now have

$$d\mathbf{r}_0=r_0\mathbf{A}_{10}\,df+\frac{r_0}{2}\mathbf{A}_{20}\,df^2+\mathcal{O}(df^3), \tag{5}$$

with

$$\mathbf{A}_{10}=\frac{e_0\sin f_0}{P_0}\mathbf{e}_r+\mathbf{e}_\phi, \tag{6}$$

$$\mathbf{A}_{20}=-2\left[1-\frac{3}{2P_0}+\frac{\eta_0^2}{P_0^2}\right]\mathbf{e}_r\pm2\frac{e_0\sin f_0}{P}\mathbf{e}_\phi, \tag{7}$$

where $P_0=a_0\eta_0^2/r_0$ and $\eta_0=\sqrt{1-e_0^2}$. For further use we shall express coefficients in $\mathbf{A}_{10}$ and $\mathbf{A}_{20}$ as a function of r_0 rather than f_0. To that goal we have a relation $e_0\sin f_0=\eta_0 R_\pm$ with $R_\pm=\pm\sqrt{(r_0-r_1)(r_2-r_0)}/r_0$, where $r_1=a_0(1-e_0)$ and $r_2=a_0(1+e_0)$ stand for the perihelion and aphelion distances of the target orbit respectively. The upper and lower sign in $R_\pm$ correspond to f_0 values in the interval $(0,\pi)$ and $(\pi,2\pi)$ respectively, and need to be considered separately.

Previous notation also helps us to express the orbital velocity $\mathbf{v}$ of the projectile at the nodal intersection and the orbital velocity $\mathbf{v}_0$ of the target body. Using arbitrarily $V_0=n_0a_0$ as a velocity normalization (n_0 is the mean motion of the target), we use the linear term

[1] We assume $i\neq0$, otherwise a non-singular set of orbital elements would be needed. As in Vokrouhlický et al. (2012) we keep a close similarity in notation to the works of Öpik (1951) and Wetherill (1967) and thus we only consider a non-planar case.

[2] The unit vectors $\mathbf{e}_r$ and $\mathbf{e}_\phi$ are assumed at the point of the orbit with $f=f_0$.

in Eq. (2) and differentiation by time to obtain

$$\begin{aligned}\mathbf{v} &= V_0\sqrt{\frac{a_0}{r}}\sqrt{P}\mathbf{A}_1 \\ &= V_0\sqrt{\frac{a_0}{r}}\sqrt{P}\left[\mp\frac{e\sin\omega}{P}\mathbf{e}_r + (\cos i\mathbf{e}_\phi \pm \sin i\mathbf{e}_z)\right],\end{aligned} \tag{8}$$

where again the upper and lower sign correspond to the ascending and descending nodes respectively. Similarly, for the target body we have

$$\mathbf{v}_0 = V_0 F\mathbf{A}_{10} = V_0[R_\pm\mathbf{e}_r + F\mathbf{e}_\phi], \tag{9}$$

where $F = \eta_0 a_0/r_0$.

Finally, the relative velocity $\mathbf{V} = \mathbf{v} - \mathbf{v}_0$ of the projectile with respect to the target at the exact intersection condition

$$r_0 = r = \frac{a\eta^2}{1 \pm e\cos\omega} \tag{10}$$

can be obtained from Eqs. (8) and (9). For further convenience we shall express $\mathbf{V}$ in a local frame of rotated vectors $(\mathbf{e}_a, \mathbf{e}_b, \mathbf{e}_z)$, where $\mathbf{e}_a$ is directed to the local apex of target's motion, $\mathbf{e}_b = \mathbf{e}_a \times \mathbf{e}_z$ and $\mathbf{e}_z$ always along the Z axis of the inertial frame. Henceforth

$$\mathbf{e}_a = \frac{R_\pm\mathbf{e}_r + F\mathbf{e}_\phi}{\sqrt{R_\pm^2 + F^2}}, \tag{11}$$

$$\mathbf{e}_b = \frac{F\mathbf{e}_r - R_\pm\mathbf{e}_\phi}{\sqrt{R_\pm^2 + F^2}}, \tag{12}$$

with also $R_\pm^2 + F^2 = 2(a_0/r_0) - 1$. Thus the corresponding velocity components $V_a = \mathbf{V}\cdot\mathbf{e}_a$, $V_b = \mathbf{V}\cdot\mathbf{e}_b$ and $V_z = \mathbf{V}\cdot\mathbf{e}_z$ read

$$V_a = \frac{V_0}{\sqrt{R_\pm^2 + F^2}}\left[\sqrt{\frac{a_0}{r}}\sqrt{P}\left(\mp R_\pm\frac{e\sin\omega}{P} + F\cos i\right) - \left(R_\pm^2 + F^2\right)\right], \tag{13}$$

$$V_b = \frac{V_0}{\sqrt{R_\pm^2 + F^2}}\sqrt{\frac{a_0}{r}}\sqrt{P}\left(\mp F\frac{e\sin\omega}{P} - R_\pm\cos i\right), \tag{14}$$

$$V_z = \pm V_0\sqrt{\frac{a_0}{r}}\sqrt{P}\sin i. \tag{15}$$

2.2. Secular evolution in the Lidov–Kozai model

As mentioned in Section 1, we shall use the Lidov–Kozai model for the secular evolution of the projectile orbit. We shall only briefly recall fundamental facts of this model studied thoroughly in literature (e.g., Lidov, 1961, 1962; Kozai, 1962; Morbidelli, 2002).

We assume a single perturber (such as Jupiter in studies of motion of small bodies in the inner Solar System) on a circular orbit, coplanar with the target. The target is assumed massless, such that it leaves the orbit of perturber fixed. Vice versa, the perturber makes the eccentric orbit of the target uniformly precess in their common orbital plane.

The effect of the perturber on the projectile's orbit are more spectacular. A simple, first-order secular perturbation model, prohibiting mean-motion resonances with the perturber, is obtained by double averaging of the averaged perturbing function over the mean longitude of the perturber and the projectile heliocentric motions (Morbidelli, 2002). Eliminated orbital elements and symmetries of the problem provide three integrals of motion: (i) the semimajor axis a of the projectile heliocentric orbit, (ii) the projection of the projectile's orbital angular momentum on the Z axis, and (iii) the value of the perturbing function $\mathcal{P}$. The second integral (ii) implies $c = \sqrt{1-e^2}\cos i = \text{const.}$, which conveniently helps to eliminate either of the two elements, eccentricity e or inclination i, for the latter and a conserved quantity c. The situation with the third integral (iii) is more complicated because its efficient evaluation may need numerical methods. This is especially true if the projectile's orbit crosses that of the perturber (e.g., Bailey et al., 1992; Thomas and Morbidelli, 1996; Gronchi and Milani, 1998, 1999; Morbidelli, 2002). While our method might be applied in these situations as well, most work would need to be performed numerically. We rather opt for a semi-numerical approach in spite of crude approximations in developing $\mathcal{P}$. In particular, of the multipole series representation used by Kozai (1962) we keep only the lowest-order quadrupole term. Generalizations to higher-order terms are straightforward at the expense of some algebraic effort. In our approximation (iii) above implies first integral (e.g., Kozai, 1962; Kinoshita and Nakai, 2007)

$$\frac{1}{\eta^2}[(2+3e^2)(3c^2-\eta^2) + 15(\eta^2-c^2)(k^2-h^2)] = C, \tag{16}$$

where $k = e\cos\omega$ and $h = e\sin\omega$. The topology of C-isolines in the (k,h) space was extensively studied and does not need to be reminded in detail. When $|c|$ is very close to unity the level curves of constant C are very close to circles about the origin of (k,h) plane. In this limit, the values of e and i are very small and they are well conserved very during the whole Kozai cycle, which is in an accordance with the assumptions of Opik's and Wetherill's collisional theories. Decreasing the value of $|c|$ causes the level curves of constant C to transform from circles to ovals until reaching the critical value $|c| = \sqrt{3/5}$, where the topology adapts to a bifurcation of two different stationary solutions at the h axis (i.e., $k = e\cos\omega = 0$): (i) for $C > 2(3c^2-1)$ the orbits circulate about the origin, but the variations may significantly increase the values e or i leading to very eccentric or inclined orbits, and (ii) for $C < 2(3c^2-1)$ the orbits circulate about the stationary points on the h axis. For a given c value, the maximal values of e and $\cos i$ are limited by $\sqrt{1-c^2}$ (for more rigorous specification of the intervals of e and i for given c and C see, for instance, Kinoshita and Nakai (2007), Eq. (31) and Eq. (32)).

2.3. Evaluating collision probability: target at a given heliocentric distance

In this Section we assume the target body at a given heliocentric distance r_0 on its orbit and consider its collision probability with the projectile. We follow the Öpik–Wetherill method recalled in some detail by Vokrouhlický et al. (2012) (Section 3). In particular, the collision probability Π is composed of two independent parts: (i) the probability Π_1 that during one cycle of secular evolution of the projectile's orbit its nodal crossing is sufficiently close to the target's orbit, and (ii) the probability Π_2 that the target itself is close enough to the nodal crossing of the projectile's orbit. Since our assumptions about the target's orbit are identical to those in Wetherill, namely fixed eccentricity value e_0 and uniformly precessing argument of pericenter ω_0, we can use Wetherill (1967) result for Π_2. Put in our variables, notably using Eqs. (13)–(15), we obtain

$$\Pi_2 = \frac{\tau}{4a_0\sqrt{R_\pm^2 + F^2}}\sqrt{\frac{V^2}{V^2 - V_a^2}}, \tag{17}$$

where $V^2 = V_a^2 + V_b^2 + V_z^2$ is the relative velocity of the projectile and the target at the exact intersection of their orbits and τ is the target's radius (we assume projectile negligibly small, otherwise τ would have been a sum of target and projectile radii). Obviously, Π_2 is to be evaluated at all possible nodal crossings of the projectile and target orbits (see below). The major modification of Wetherill's

approach consists now in an evaluation of Π_1 (see also Vokrouhlický et al., 2012). This is because we consider a more complex secular evolution of the projectile's orbit.

Determination of Π_1 is based on analysis of the orbit geometry near the nodal crossing. This is because the target (and potentially also the projectile) has a finite radius τ and thus the impact occurs not only at the exact orbit crossing expressed by Eq. (10) which we rewrite as (upper and lower sign for the ascending and descending node crossings)

$$\alpha(1 \pm k) = \eta^2 \tag{18}$$

with $\alpha = r_0/a$. Eq. (18) yield circles with a displaced center in the (k,h) space. The orbit-intersection conditions now correspond to a crossing of these circles with the $C = \text{const.}$ lines from Eq. (16) describing the secular evolution of the projectile's orbit. This simple quadrupole approximation of the Lidov–Kozai model yields up to eight such crossings (as compared to maximum of four crossings for two ellipses of fixed eccentricities, e.g. Fig. 1 in Wetherill (1967)).

Consider the local geometry of the target and projectile orbits near the node of the latter. Eqs. (2) and (5), in which we shall retain only linear terms, help us to describe the situation. The reference longitude in the (X,Y) plane at which we construct the radial $\mathbf{e}_r$ and longitudinal $\mathbf{e}_\phi$ vectors of the local reference frame $(\mathbf{e}_r, \mathbf{e}_\phi, \mathbf{e}_z)$ is given by the chosen node of the projectile orbit. We, however, displace the origin of frame to the position of the target at the same longitude. As a result the infinitesimal (rectilinear) arc of the target orbit is given by

$$\Delta\mathbf{r}_0(\lambda') = r_0 \mathbf{A}_{10} \lambda' + \mathcal{O}(\lambda'^2), \tag{19}$$

where r_0 is the heliocentric distance of the origin and λ' parameterizes the orbit. Note that, unlike in Vokrouhlický et al. (2012), $\mathbf{A}_{10}$ from Eq. (6) has now both longitudinal and radial components. This is due to eccentricity of the target's orbit. Similarly, the infinitesimal arc of the projectile's orbit reads

$$\Delta\mathbf{r}(\lambda) = (r - r_0)\ \mathbf{e}_r + r\mathbf{A}_1 \lambda + \mathcal{O}(\lambda^2), \tag{20}$$

in our reference system. Here r is the heliocentric distance of the node crossing. Because generally $r \neq r_0$, we have a radial displacement of the projectile's node expressed by the first term in Eq. (20). Parameter λ again serves to span different orbital locations of the projectile. The square of the projectile-target distance is simply $d^2(\lambda,\lambda') = [\Delta\mathbf{r} - \Delta\mathbf{r}_0] \cdot [\Delta\mathbf{r} - \Delta\mathbf{r}_0]$. We seek a minimum of $d^2(\lambda,\lambda')$ on the (λ,λ') space, a task which leads to a simple system of two linear algebraic equations in our rectilinear approximation for both orbits. Solving them for λ and λ' we obtain the minimum orbital distance $d_{\min}$

$$d_{\min} = \frac{(r - r_0)\sin i}{\sqrt{(1+\beta^2)\sin^2 i + (\gamma - \beta\cos i)^2}}, \tag{21}$$

where $\beta = r_0 R_\pm/(a_0\eta_0)$ and $\gamma = \mp e\sin\omega/P$. Note $d_{\min}$ is a function of assumed fixed r_0 and orbital parameters of the projectile with the nodal distance $r = a\eta^2/(1 \pm e\cos\omega)$. All possibilities with $d_{\min} \leqslant \tau$

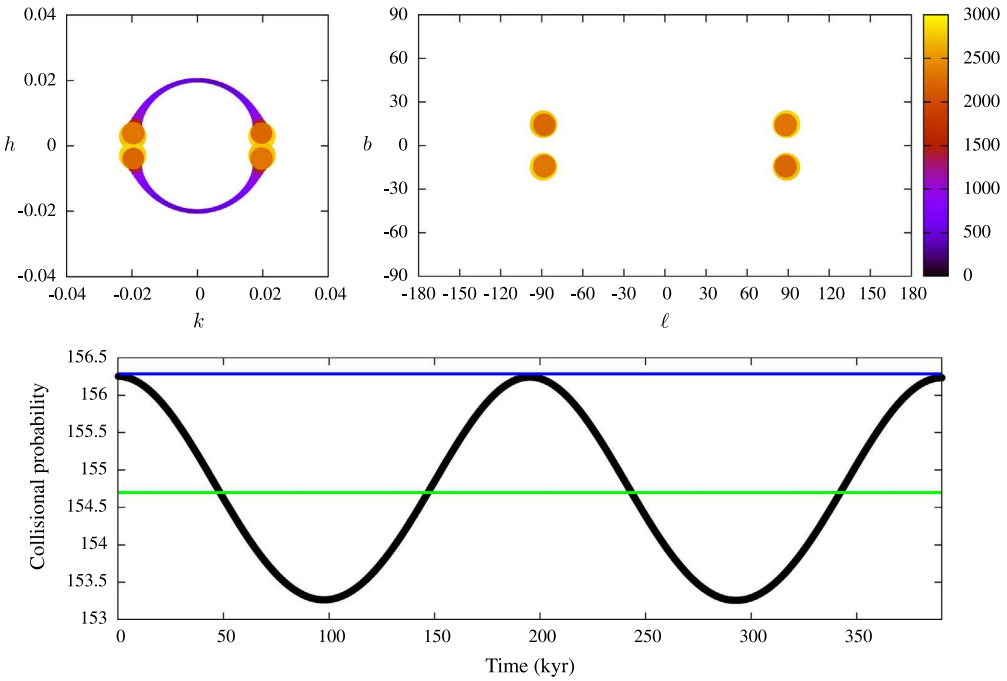

Fig. 1. Secular evolution, impact geometries (radiant position) and intrinsic impact probability. Massless target on Mercury-like orbit with the semimajor axis $a_0 = 0.3871$ AU and the eccentricity $e_0 = 0.2056$. Projectile has the semimajor axis $a = 0.4$ AU, andinitial eccentricity $e = 0.02$, inclination $i = 3°$ and argument of pericenter $\omega = 0°$. Single perturbing planet on a Jupiter-like orbit, coplanar with the target is assumed. Top and left: Secular evolution track of the projectile orbit is a small circle in the $(k,h) = e(\cos\omega, \sin\omega)$ plane (black curve underneath the color-coded pattern). Because the orbit of target is eccentric, true impacts are possible along the whole trajectory characterizing the secular evolution of the projectile – suffice to independently tune the longitude of pericenter of the target. The intrinsic collision probability for that configuration is given by our function $p(r_0)$ from Eq. (25). The color pattern with the color bar on the right gives $p(r_0)$ in $(\text{AU}^{-2}\,\text{y}^{-1})$. The highly increased intrinsic collision probability for $h \simeq 0$ values correspond to near pericentric impacts (see Appendix of Vokrouhlický et al., 2012). Top and right: Radiant positions of impact geometries as seen by observer at the target body; the abscissa is the longitude ℓ measured from the apex direction, the ordinate is the latitude b (both in degrees). Even though there is an infinite number of impact configurations, the small eccentricity of the projectile orbit makes their individual radiants collapse to merely the same position. Color coding according to the intrinsic collision probability as in the left panel. Bottom panel: The formal collision probability $p_{\text{Weth}}(a, e_\star, i_\star; a_0, e_0)$ during a secular (Lidov–Kozai) cycle shown in the top and left panel (black solid line; the abscissa is time in ky and the ordinate is the intrinsic collision probability in $\text{AU}^{-2}\,\text{y}^{-1}$). The Lidov–Kozai cycle averaged intrinsic collision probability from our method p_{fin} (Eq. (28)) is the blue line, the Wetherill's method based average intrinsic collision probability p_{eff} (Eq. (29)) is the green line. (For interpretation of the references to color in this figure legend, the reader is referred to the web version of this article.)

imply an impact on the target, with the limiting configuration given by $d_{\min} = \tau$, or

$$\frac{\tau}{a} = \rho = [\eta^2 - \alpha(1 \pm k)]\Lambda, \tag{22}$$

with

$$\Lambda = \sqrt{\frac{\eta^2 - c^2}{(1+\beta^2)(\eta^2 - c^2)(1 \pm k)^2 + [h\eta \pm \beta c(1 \pm k)]^2}}. \tag{23}$$

Here we used the Kozai integral $c = \eta \cos i$ to eliminate the inclination dependence, and replaced the eccentricity e and argument of pericenter ω with the non-singular (k,h) elements. We now seek the (k,h) values which simultaneously satisfy Eqs. (22), (23), and (16), or in other words those segments on the C-integral of orbital secular evolution that provide minimum orbital distances $d_{\min}$ smaller than the physical size τ of the target. In general, there is a number of such discontinuous segments each near the exact crossing condition (18) with (16). The system of algebraic Eqs. (22), (23) and (16) is too complex to allow an analytic solution. We thus developed a simplified linearization method near the exact crossing to solve them (for details see Vokrouhlický et al. (2012) Section 3.2). Each of such segments is crossed in time Δt over the secular cycle of duration $T_{\rm Kozai}$, such that the partial probability Π_1 of impact is given by relative duration of this window: $\Pi_1 = \Delta t / T_{\rm Kozai}$. Summing up over all exact intersection configurations, each characterized by $(e_\star, i_\star, \omega_\star)$ orbital elements of the projectile, we finally have

$$\Pi(r_0) = \sum \left(\frac{\Delta t(r_0)}{T_{\rm Kozai}} \right)_\star \Pi_2(a, e_\star, i_\star, \omega_\star; r_0). \tag{24}$$

Here we used the principle of uncorrelated partial probabilities Π_1 and Π_2 discussed above. The final expression for the collision probability per unit of time is given by division by the orbital period $T_{\rm orb}$ of the projectile, thus

$$p(r_0) = \frac{\Pi(r_0)}{T_{\rm orb}\,\tau^2} = \frac{\mu^{1/2}}{2\pi a^{3/2}\tau^2}\Pi(r_0), \tag{25}$$

where $\mu = GM$, G is the gravitational constant and M the mass of the center (the Sun). Note $p(r_0)$ has been also normalized to the cross-sectional factor τ^2 of the target, such that it expresses the intrinsic collisional probability (see Öpik, 1951; Wetherill, 1967; Greenberg, 1982). Convenient units of $p(r_0)$ are AU^{-2} y^{-1}.

2.4. Evaluating collision probability: weighted composition of all possible heliocentric distances of the target

In the previous Section we determined the projectile-target collision probability for a particular heliocentric distance r_0 of the target. In order to evaluate the final collision probability $p_{\rm fin}$, we need to consider all possible values of the distance r_0 in the range (r_1, r_2). This basically requires assembling $p(r_0)$ from Eq. (25) with an appropriate weighting, which should express an uniform circulation of the longitude of pericenter of the projectile's orbit.[3] Observing that the true anomaly differential df of an elliptic orbit satisfies $df \propto dr_0/(r_0^2|\mathbf{v}\cdot\mathbf{e}_r|) \propto dr_0/(r_0^2 R_+)$, we identify the necessary weighting factor to be

$$\Psi(r_0) = \frac{a_0\eta_0}{\pi}\frac{1}{r_0\sqrt{(r_0 - r_1)(r_2 - r_0)}}. \tag{26}$$

The explicit value of the constant in the right hand side of Eq. (26) implies the normalization

$$\int_{r_1}^{r_2} \Psi(r_0)\,dr_0 = 1. \tag{27}$$

Henceforth, we obtain the final intrinsic collision probability $p_{\rm fin}$ over all possible impact configurations as

$$p_{\rm fin} = \int_{r_1}^{r_2} \Psi(r_0)\,p(r_0)\,dr_0. \tag{28}$$

Note that the weighting factor $\Psi(r_0)$ is singular at pericenter and apocenter distances, lower and upper integration bounds in Eq. (28). While finite, numerical evaluation of $p_{\rm fin}$ requires some care. Standard methods of integrable singularity removal are briefly recalled in the A.

3. Testing the new approach: A comparison with Wetherill's theory and results of the *N*-body simulations

In this Section we test our approach against results from N-body simulations and perform comparison with predictions of the Wetherill's method (Wetherill, 1967). Both now allow an eccentric orbit of the target, but the latter assumes the eccentricity and the inclination of the projectile orbit are secularly constant, often violated. On the other hand, our approach still assumes the orbit of the target fixed in the inertial space, a drawback which is to be eliminated in the future work. We expect that at least for targets on low-inclination orbits with respect to the local Laplacian plane our results should be meaningful. It is mainly the effects of projectile's high-inclinations and eccentricities which are tested here.

The projectile's orbit approximately follows a trajectory described by a C-isolevel of a function in the left hand side of Eq. (16) in the (k,h) parameter space (see Section 2.2). As recalled by Vokrouhlický et al. (2012), the intersection conditions with a circular orbit of a certain radius r_0, or simply at a given heliocentric distance r_0, is geometrically given by the intersection of this trajectory with two displaced circles given by Eq. (18) for both ascending and descending node impacts. For a circular orbit of the target, r_0 was fixed, and we had exquisitely four or eight intersection configurations (except for singular grazing cases). Now the situation is more complicated, because the eccentricity of the target's orbit makes r_0 change during its orbital and secular cycles, and the radii of the circles by which this is represented in the (k,h) space pulsate (as well as their centers shift). So for a given pair target-projectile we may have the whole set of zero, four and eight intersections over their secular evolution cycle. Obviously, mathematically this is all built in the formulation in Sections 2.3 and 2.4, namely properties of the collision probability $p(r_0)$ from Eq. (25) and the integration in Eq. (28).

A comparison with Wetherill's approach is not a priori given, but we follow the approach in Vokrouhlický et al. (2012). This is based on what in practical terms one would do without having available our theory. Denote, as above in Eq. (24), $(e_\bullet, i_\bullet, \omega_\bullet)$ orbital eccentricity, inclination and argument of pericenter that the projectile's orbit acquires during its secular evolution. Adding the quasi-constant semimajor axis a of the projectile's orbit, and the parameters a_0 and e_0 of the target's orbit, one can formally determine collision probability $p_{\rm Weth}(a, e_\bullet, i_\bullet; a_0, e_0)$ as if the obits would satisfy assumptions of the Wetherill's theory. Performing then an average over the projectile's secular cycle of length $T_{\rm Kozai}$, thus

$$p_{\rm eff} = \frac{1}{T_{\rm Kozai}}\int_0^{T_{\rm Kozai}} p_{\rm Weth}(a, e_\bullet, i_\bullet; a_0, e_0)\,dt, \tag{29}$$

one obtains a proxy for the estimated, long-term collision probability between the projectile and the target. However, $p_{\rm eff}$ may not be equal to our value $p_{\rm fin}$ from Eq. (28). In fact, it is the degree of their difference that interests us in our tests.

[3] See also discussion in Wetherill (1967) and Greenberg (1982). Note that the apparently expected weighting factor $dt \propto dr_0/|\mathbf{v}.\mathbf{e}_r|$, expressing how much time the projectile spends in the interval $(r_0, r_0 + dr_0)$, is already contained in the Π_2 probability.

3.1. Simple validation of our approach

We first validate our new approach using the simplest possible setup, namely considering a target body and a single projectile. For sake of definiteness the target is on a Mercury-like orbit with $a_0 = 0.3871$ AU and $e_0 = 0.2056$. To make the situation as close as possible to the assumptions of our theory, we assume a single perturbing planet, a Jupiter on a circular orbit at 5.2 AU heliocentric distance. The heliocentric orbital planes of the target body and Jupiter are identical, and both Jupiter and the Sun are given their true masses. We the neglect mass of the target body in this section.

In the initial run we took the projectile orbit having the semimajor axis $a = 0.4$ AU, eccentricity 0.02, inclination 3° and argument of pericenter 0°, implying $c = 0.99843$ and $C = 3.98436$. Such a low-eccentricity and low-inclination orbit will undergo only very limited variations due to Jupiter's perturbation, whose major effect will be near steady circulation of the orbital pericenter and node. Indeed, as shown in the upper left panel of Fig. 1 the secular track of the projectile orbit in the (k,h) plane is basically a small circle around the center. The simple secular evolution makes the Wetherill's approach fully applicable and we expect a good correspondence between our results and those based on Wetherill's theory. Fig. 1 confirms this conclusion since $p_{\rm fin} \simeq p_{\rm eff}$ (bottom panel). Their $\simeq$0.01% difference basically reflects the numerical accuracy with which we evaluate both quantities (less so the very small variations of orbital eccentricity and inclination of the projectile's orbit).

Next, we test a configuration where the orbit of the projectile undergoes one of the possible evolutionary regimes described by the Lidov–Kozai theory. In particular, we set the semimajor axis $a = 0.9$ AU. We then consider an orbit with starting eccentricity $e = 0.1$, inclination $i = 55°$ and argument of pericenter $\omega = 0°$, altogether implying $c = 0.5707$ and $C = 0.07446$ constants. Since $c < \sqrt{0.6}$, the secular evolution of the projectile's orbit is characterized by large oscillations of both e and i as seen on the left top panel of Fig. 2. In this case the argument of pericenter circulates about the origin. A more extreme situation occurs for $e = 0.6$, $i = 55°$ and $\omega = 70°$ choice with $c = 0.45886$ and $C = -2.80648$, our second choice of the initial orbit of the projectile. The secular evolutionary track of this orbit is shown in the left top panel of Fig. 3. Here the argument of pericenter oscillates in a limited interval of values about 90° which defines a possible stationary point of the Lidov–Kozai model.

Returning to the first choice of the initial orbit for the projectile, we now focus on Fig. 2. The left top panel shows, apart from the secular track of the projectile's orbit (black curve), also intersection conditions defined by Eq. (18) for all possible values of r_0 in between the pericenter and apocenter of the target's orbit. Each of them is a gray circle, which altogether merge into a 2-D gray area. Unlike in the case of a circular target's orbit, where we have only maximum of 8 intersection configurations, here we formally have an infinite number of them. This is because r_0 ranges a finite interval of values and for each of them we have up to 8 intersections. Some correspond to the grazing configurations for which 8 intersections degenerate to only 4. However, as also discussed by Vokrouhlický et al. (2012), these situations are characterized by a formally large impact probability. This is shown by the color-coded symbols at the top panels of Fig. 2. The top right panel shows location of impact radiants as seen by an observer on the target body (zero longitude fixed at local apex direction). Again, while only a finite number of 8 radiants exist for a circular orbit of the target, we now have an infinity of possibilities (shown by the black rings). Some of them, however, have higher impact probability since they correspond to the grazing configurations of the target-impactor orbits and those are marked by red and yellow symbols. Finally, the bottom panel shows $p_{\rm Weth}(t)$ during one Lidov–Kozai cycle spanning little more than 250 ky (black symbols). These values are computed by Wetherill's approach, assigning formally projectile's orbital elements $(a, e_\bullet, i_\bullet)$ acquired during the orbital evolution along the trajectory shown on the top left panel. These values are sometimes zero for the cases when $e_\bullet$ drops below a critical limit such that the pericenter of the projectile's orbit is above the apocenter of the target's orbit and no intersection configurations exist. The Lidov–Kozai averaged collision probabilities defined by Eqs. (28) and (29) are $p_{\rm fin} \simeq 2.58\,{\rm AU}^{-2}\,{\rm y}^{-1}$ and $p_{\rm eff} \simeq 2.16\,{\rm AU}^{-2}\,{\rm y}^{-1}$, showing only a minor difference in this situation. This is because even in the Lidov–Kozai regime the impacts are possible only over a limited interval of secular evolution cycle, during which eccentricity and inclination values do not change significantly (Fig. 2). A larger difference of the two approaches is exhibited by the apparent impact radiants in the top right panel. The red dots correspond formally to those obtained by Wetherill's theory, the same way as $p_{\rm Weth}(t)$ is computed. These apparent, but fake, radiants span a quite larger region on the local sky of the observer moving together with the target than the true radiants shown by the black loops.

Fig. 3 shows the similar data for the second chosen initial orbit of the projectile. In this case, the orbital argument of pericenter ω oscillates about the 90° stationary point of the Lidov–Kozai model, so apparently assumptions of the Wetherill's approach are strongly violated. The three panels show again evolution of the projectile orbit and intersection conditions in the (k,h) plane, radiant locations with respect to the apex system of the target and $p_{\rm Weth}(t)$ during one Lidov–Kozai cycle. The restricted evolution ω makes now only two radiant locations appear, though formally there is again a continuum of possible radiants distributed along the loop-like region. The averaged collision probabilities are $p_{\rm fin} \simeq 6.54\,{\rm AU}^{-2}\,{\rm y}^{-1}$ and $p_{\rm eff} \simeq 5.72\,{\rm AU}^{-2}\,{\rm y}^{-1}$. Again, their difference is not large, essentially reflecting only small variations of eccentricity and inclination values for impact configurations.

3.2. Comparison with N-body simulations

We further validate conclusions from the previous Section by performing a comparison between the expected number of impacts, based on the collision probability calculation, and their direct record performed by numerical integration. We keep the setup described above, namely considering the Sun and Jupiter as massive bodies and a massless target on a Mercury-like orbit, coplanar with that of Jupiter. In order to accelerate the impact rate in our simple experiment, we assumed the target has ten times larger radius then Mercury (i.e., $\tau \simeq 1.63 \times 10^{-4}$ AU). We considered two sets of projectiles, each consisting of 500 test particles. Instead of starting them from very nearby orbits, we distributed them evenly during the Lidov–Kozai secular cycle of orbits shown in Figs. 2 and 3 (top left panels). The initial data were actually created with the help of integration described in Section 3.1, making an output of orbital elements $(e_\bullet, i_\bullet, \omega_\bullet)$ (recall $a = 0.9$ AU is secularly constant). All integrations were performed using the `SWIFT_RMVS3` package,[4] that is able to record direct impacts onto the target. We used 0.5 day integration timestep to resolve fast motion of the Mercury-like target planet.

In our simplified model there are no other sinks of test particles other than the impact on the target. Since the impacts are probabilistic, Poisson process, we have a simple estimator of the cumulative impactor time profile: $N_{\rm imp}(t) = N_0[1 - \exp(-t/T)]$ ($N_0 = 500$ in our case). Here, T is a characteristic timescale, given by $T = 1/(\tau^2 p)$, where p is the collision probability. We have three alternative formulations of p, namely $p_{\rm fin}$ from our theory, $p_{\rm eff}$ from the formal application of the Wetherill's theory and also we introduce

[4] `http://www.boulder.swri.edu/~hal/swift.html` (Levison and Duncan, 1994).

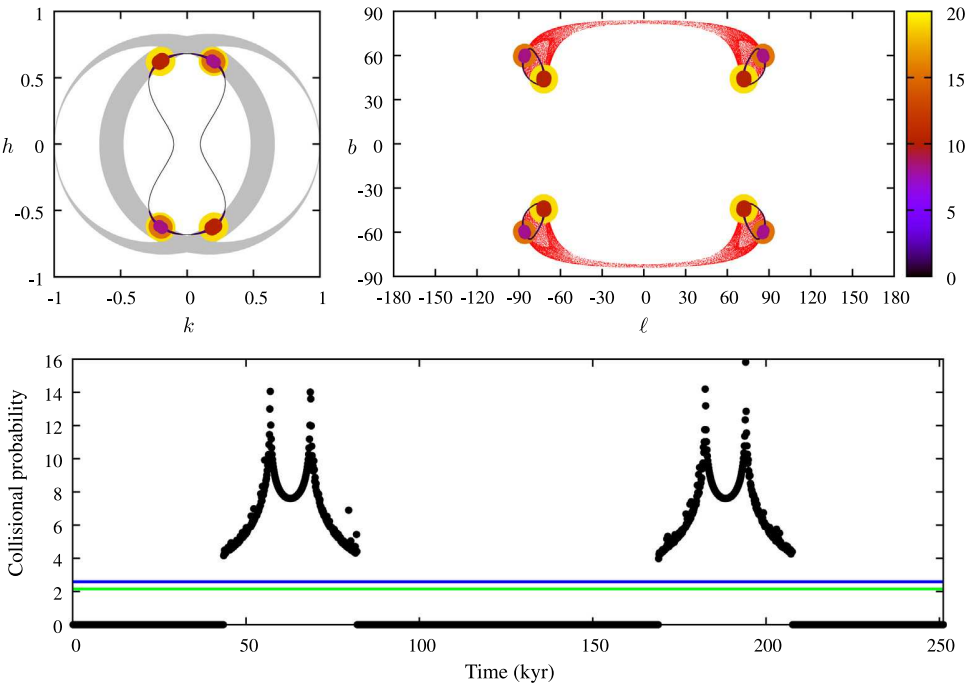

Fig. 2. The same as Fig. 1, but now for the projectile with the semimajor axis $a = 0.9$ AU, the initial eccentricity $e = 0.1$, inclination $I = 55°$ and argument of pericenter $\omega = 0°$. Top and left: The evolution trajectory during one secular, Lidov–Kozai cycle (black line), defined by the $\mathcal{P}(k, h; c) = C$ integral from Eq. (16)), is now different from a simple circle. Exact impact condition with the target body is graphically shown by the set of gray circles (both ascending and descending nodes) and they correspond to solutions of Eq. (18) for all possible target heliocentric distances r_0. Impacts are possible only in the region of black line crossing with gray circles. The color coding corresponds to the individual values of collision probability $p(r_0)$ (see also the bar on the right). Maxima are for the pericentric configurations. Top and right: Radiant position in the apex coordinate system – larger eccentricity of the projectile orbits makes the radiants span four loop-like regions on the local sky of the target-based observer. The set of red dots are fake radiants formally constructed by Wetherill's approach and combinations of $(a, e_\bullet, i_\bullet)$ orbital elements of the projectile and (a_0, e_0) orbital elements of the target. Bottom panel: The formal collision probability $p_{\rm Weth}(a, e_\bullet, i_\bullet; a_0, e_0)$ during a secular (Lidov–Kozai) cycle shown in the top and left panel (black solid line). Zero values for no crossing conditions between the projectile and target orbits. The Lidov–Kozai cycle averaged intrinsic collision probability from our method $p_{\rm fin}$ (Eq. (28)) is the blue line, the Wetherill's method based average intrinsic collision probability $p_{\rm eff}$ (Eq. (29)) is the green line. (For interpretation of the references to color in this figure legend, the reader is referred to the web version of this article.)

$p_{\rm circ}$ for the circular orbit of the target based on Vokrouhlický et al. (2012), so that we can compare the three estimators of the decay timescale $T_{\rm P\&V} = 1/(\tau^2 p_{\rm fin})$, $T_{\rm Weth} = 1/(\tau^2 p_{\rm eff})$ and $T_{\rm VPN} = 1/(\tau^2 p_{\rm circ})$ with the numerically determined value, where $p_{\rm circ}$ is computed formally as if the target had semimajor axis a_0 and zero eccentricity.

Fig. 4 shows results for projectiles on orbits similar to that of Fig. 2. Our estimated decay timescale is $T_{\rm P\&V} \simeq 14.63$ Myr and $T_{\rm Weth} \simeq 17.63$ Myr. In case of the circular target there are no possible impacts, thus $T_{\rm VPN}$ is formally infinite since $p_{\rm circ} = 0$. The corresponding $N_{\rm imp}(t)$ profiles (gray curves) are shown on the left panel and compared with the recorded sequence of impacts (dark symbols). An eye-based comparison would favor results from our recent theory. Indeed, fitting the real impact record with the $N_{\rm imp}(t)$ law would yield $T_{\rm Fit} = 15.46 \pm 0.03$ Myr. Additional support for our conclusions comes from comparison of the predicted impactor radiants and those determined from the numerical simulation. This is shown on the right panel of Fig. 4. Our predicted loop-like radiant distribution is indeed very well matched by the location of numerically recorded radiants (black symbols).

Fig. 5 shows the same for projectiles on orbits similar to that of Fig. 3. Since the collision probabilities were larger now, the decay time constant is shorter and the population fades faster. We obtain $T_{\rm P\&V} \simeq 5.79$ Myr, $T_{\rm Weth} \simeq 6.62$ Myr and $T_{\rm VPN} = 2.64$ Myr, while the fit to numerically-determined $N_{\rm imp}(t)$ provides $T_{\rm Fit} = 5.65 \pm 0.01$ Myr. Again, the radiant distribution shown on the right panel of Fig. 5 indicates an excellent correspondence between the theory prediction and the numerically recorded impacts. Both situations provide a good illustration of differences between new and previous formalisms.

4. A real life application: Impactors from the E-belt

The examples discussed in the previous Section indicated validity of our results, as well as their numerical implementation in our code, but what does it say about their "real-life" applicability. After all, these cases were highly simplified: we used only one disturbing planet in a fixed elliptic orbit, a coplanar massless target, which implied that the particles (projectiles) conserved their initial Lidov–Kozai integrals c and C. In reality, though, the situation is different. All planets are massive and interacting, which complicates the secular evolution of the projectile orbits. Moreover, as the projectile interact with the planets in a short-range close approaches, their orbital semimajor axis is not conserved. Some may be brought close to mean motion resonances with the target orbit. All these effects invalidate, strictly speaking, assumptions of both Wetherill's and ours approaches. Still, we may be interested to know how they perform in such a complex case.

Our "real-life case" is based on the recent work of Bottke et al. (2012) who examined a decay of a putative past extension of the main asteroid belt toward smaller heliocentric distances, bounded basically by the outermost terrestrial planet. Bottke et al. (2012) called this extension the E-belt and found several intriguing facts in favor of this population out of which we mention two outstanding: (i) the E-belt is a natural source of projectiles that impacted terrestrial planets and the Moon during the Archaean period and

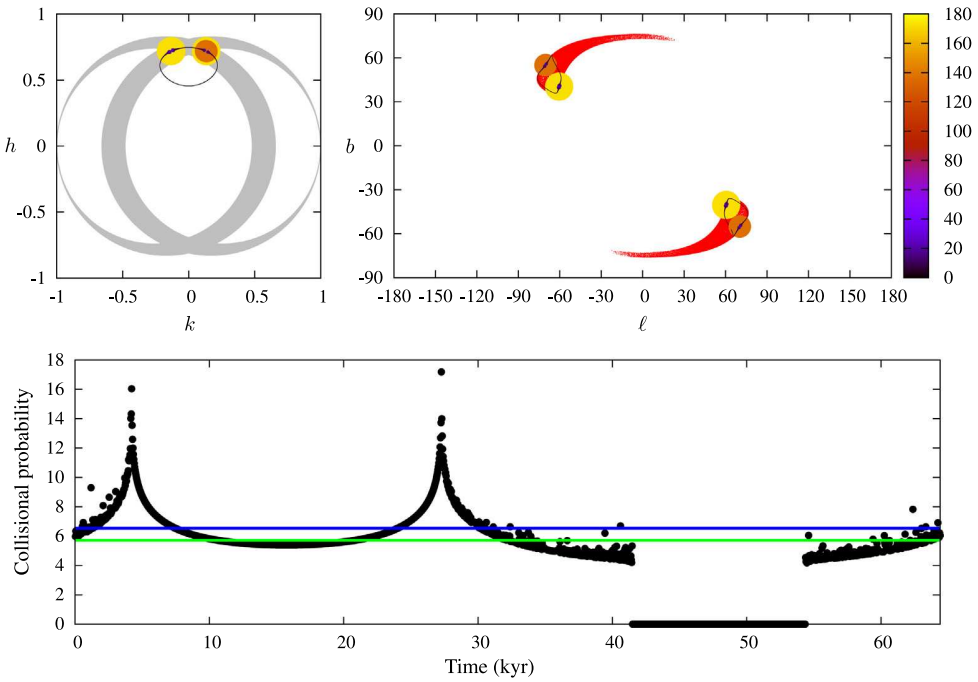

Fig. 3. The same as in Fig. 2, but now for the projectile's orbit with semimajor axis $a = 0.9$ AU, initial eccentricity $e = 0.6$, inclination $i = 55°$ and argument of pericenter $\omega = 70°$. Top and left: The argument of pericenter ω now circulates about the stationary solution offset from the center in the (k,h) plane and thus acquires values from a limited interval of values around 90°. Top and right: Absence of ω values near 180° makes number of radiant locations reduced to two, loop-like structures. Bottom panel: The behavior of the secular-evolution trajectory, black line on the top and left panel, makes the Lidov–Kozai cycle be effectively half of that seen on Fig. 2. Hence, the $p_{\rm Weth}(a,e_\bullet,i_\bullet;a_0,e_0)$ values resemble those from the first part of the bottom panel on Fig. 2. Systematically higher eccentricity $e_\bullet$ offers more chance for the impact configurations, and thus the $p_{\rm Weth}\,(a,e_\bullet,i_\bullet;a_0,e_0) = 0$ interval is shorter. Consequently, also the values $p_{\rm Weth}$ and $p_{\rm eff}$ are larger.

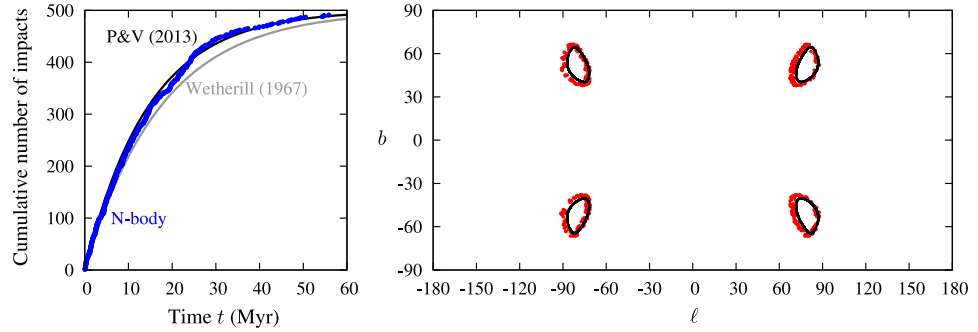

Fig. 4. Impact conditions for a population of $N_0 = 500$ test particles distributed evenly along the secular-cycle trajectory shown by the black line on the top and left panel of Fig. 2. Massless target body on a Mercury-like orbit with $a_0 = 0.3871$ AU and $e_0 = 0.2056$, and radius $\tau \simeq 1.63 \times 10^4$ AU (about ten times larger than that of Mercury). A single, Jupiter-like planet feeds the secular evolution of the projectile population. Left: Cumulative number of impacts onto the target body as a function of time t since the beginning of the numerical simulation. Blue symbols directly from the numerical run, while the black and gray lines are estimators from the collision impact approaches developed here and the Wetherill's method, i.e., $N_{\rm imp}(t) = N_0\,[1 - \exp\,(-t/T)]$ with some T timescale. Our method gives $T_{\rm P\&V} = 14.63$ Myr, Wetherill's approach yields $T_{\rm Weth} = 17.43$ Myr. In absence of other sinks all projectiles eventually hit the target. For the circular orbit of the target, there are no possible impact configurations. Right: Comparison of radiant position as recorded directly from the numerical simulation (red symbols) and predicted from our approach (black lines, see also top and left panel on Fig. 2). The abscissa is the longitude measured from the apex direction as seen by an observer on the target body, the ordinate is latitude in the same system (both in degrees). (For interpretation of the references to color in this figure legend, the reader is referred to the web version of this article.)

dominantly contributed to what is known as the Late Heavy Bombardment (LHB), and (ii) the E-belt provides a natural source of todays small population of Hungaria asteroids.

Similarly to Bottke et al. (2012) we thus considered a population of particles initially located in the E-belt and numerically integrated the post-LHB evolutionary phase. This means planets are assumed to have acquired their current orbits. On the contrary to the work of Bottke et al. (2012), where planet Mercury was neglected, we include it in our current simulation. We thus need to use a considerably shorter integration timestep of 0.5 days. On the other hand, the purpose of our simulation is rather illustrative, so we do not need to develop the model in such a detail as Bottke et al. (2012). For instance, we omit the pre-LHB evolution of the E-belt objects. Luckily, Bottke et al. (2012) have shown that this phase has only limited effects on both number of objects and their orbital distribution in the E-belt. So our starting orbits of the E-belt particles had a uniform distribution of semimajor axes between 1.7 AU and 2.1 AU, eccentricities e and inclinations i distributed using a Maxwellian distribution with the peak values of 0.15, and 8.5° respectively, and the standard deviation values of 0.07, and 7° respectively. We eliminated bodies that would initially cross the orbit of Mars, an expected result of the pre-LHB orbital

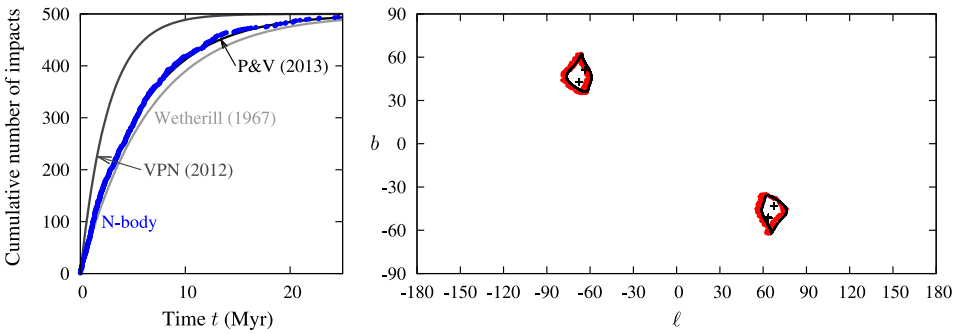

Fig. 5. The same as in Fig. 4 but for a population of particles distributed evenly along the secular-cycle trajectory shown by the black line on the top and left panel of Fig. 3. Left: Because of the larger $p_{\rm fin}$ and $p_{\rm eff}$ values, the characteristic timescale of projectile elimination is shorter now: $T_{\rm P\&V}$ = 5.79 Myr and $T_{\rm Weth}$ = 6.62 Myr. While both are similar, our value slightly better expresses the real track of the impacts (blue symbols). The formal result for the theory where the orbit of the target is circular is represented by dark-gray line with the characteristic timescale $T_{\rm P\&V}$ = 2.64 Myr. In this case it represents the worst estimate of the impact dynamics. Right: As expected, radiants of impacting particles are now fewer and located in only two quadrants on the sky. Directly recorded radiants (red symbols) correspond to their predicted locations (black loops) quite well. The limited number of 4 impact configurations for the circular orbit of the target (dark-gray crosses) cannot express the exact structure of recorded radiants, however it can provide approximate their position. (For interpretation of the references to color in this figure legend, the reader is referred to the web version of this article.)

evolution. Longitudes of node and pericenter, as well as the mean anomaly, were distributed randomly between 0° and 360°. Altogether we started 5000 E-belt particles. Initial values of osculating (a,e,i) are shown on the leftmost panel of Fig. 6. All planets were given their masses and initial orbits as of J2000.0 epoch. In order to speed up the simulation, we multiplied planetary radii by a factor 5, increasing thus their geometric cross-section by a factor 25. We used `SWIFT_RMVS3` package to propagate orbits of planets and particles for 500 Myr and recorded their fate. Few particles survived in heliocentric motion, while majority reached some of the possible end-states: either impacted one of the planets or the Sun, or was pushed onto Jupiter-crossing orbits and was ejected from the Solar System. We output state vectors of all bodies every 100 years, providing us a clue about their orbital evolution. In order to resolve orbital behavior near the Sun, and thus not to miss possible Mercury impacts, we set the minimum heliocentric distance 0.01 AU, about two solar radii. While some projectiles may survive even closer approaches to the Sun, many would tidally or thermally disintegrate.

Thanks to the increased planetary radii in our numerical experiment we have recorded enough impacts onto terrestrial planets directly from the numerical simulation. This information is considered as a ground truth, which is to be compared with predictions from either of the two approaches discussed above. This is to be done as follows. The projectile population $N(t)$ decays with time t according to

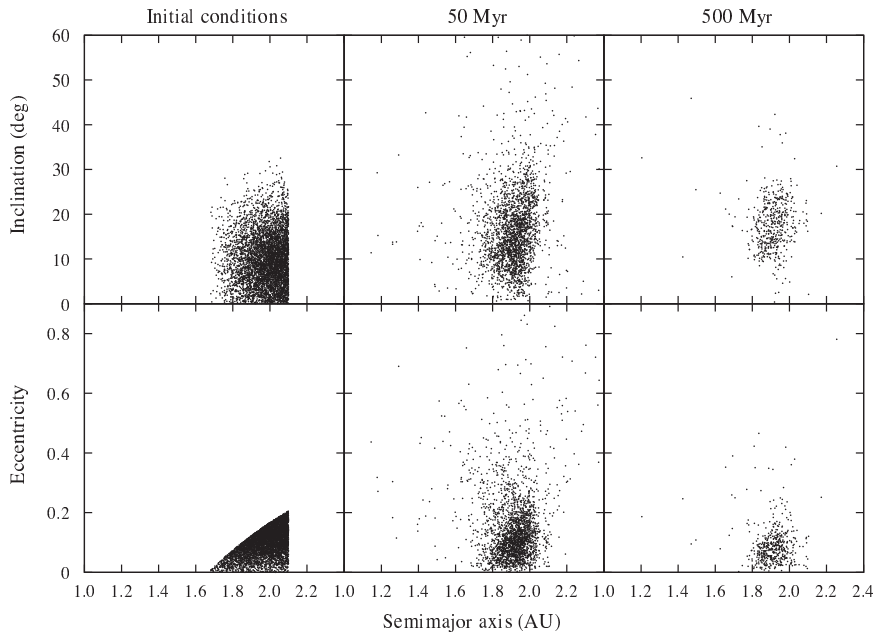

Fig. 6. Post LHB dispersal of the E-belt population. Upper panels show semimajor axis vs inclination, bottom panels show semimajor axis vs eccentricity of the numerically propagated orbits. Left: Initial data of 5000 particles in our simulation. Semimajor axis was distributed uniformly in between 1.6 AU and 2.1 AU. Eccentricity and inclinations had Maxwellian distribution with maxima at 0.15 and 8.5°, and standard deviation of 0.07 and 7°, respectively. All particles having initially Mars-crossing orbits were eliminated (bottom panel). Middle: Population at 50 Myr. Planetary perturbations make the population dispersed. Because of the predominant high inclinations and low eccentricities the characteristic decay timescale is long. At this moment still 46% of particles survive. The remaining were eliminated by several possible orbital end-states: impact on the Sun or the planets, or ejection from the Solar System. Right: Population at 500 Myr has seen depletion at lower inclinations and higher eccentricities (some 10% particles still survived). The surviving orbits converge to what is today observed as the Hungaria population.

Table 1
A summary of cumulative number of impacts on terrestrial planets at the end of simulation, $T = 500$ Myr, obtained by different methods: (i) $N_{\rm direct}$ denotes number of direct impacts recorded by SWIFT code, (ii) $N_{\rm PV}$ is a cumulative number of impacts based on evaluation of intrinsic collisional probability at each time step using our theory (Eq. (31)), (iii) $N_{\rm Weth}$ is the same as $N_{\rm PV}$ but using Wetherill's theory, and (iv) $N_{\rm VPN}$ is the same as $N_{\rm PV}$ but using only the circular orbit of the target.

Planet	$N_{\rm direct}$	$N_{\rm PV}$	$N_{\rm Weth}$	$N_{\rm VPN}$
Mercury	64	58.03	43.65	55.82
Venus	491	491.04	493.09	482.03
Earth	765	808.78	826.69	787.77
Mars	818	884.88	547.99	793.28

$$dN = -(P_{\rm tot} + P')dt. \tag{30}$$

Here $P_{\rm tot}(t) = \sum_i \bar{p}^i_{\rm fin}(t)\tau_i^2$ is the estimate of the composite probability per unit of time to impact one of the terrestrial planets (hence the summation index goes from 1 to 4 spanning Mercury to Mars). The total intrinsic collision probability with respect to the specific target planet $\bar{p}^i_{\rm fin}(t)$ is itself given as a population sum over the projectiles, i.e. $\bar{p}^i_{\rm fin}(t) = \sum_{j=1}^{N(t)} p^i_{{\rm fin}j}$, where the summation here goes over all projectile particles. Their individual intrinsic collision probabilities $p^i_{{\rm fin}j}$ with the target planet i are computed by using Eq. (28) with their current osculating orbital elements (a, e, i, ω). Obviously, due to a more complex long-term orbital evolution of the particles than described in Section 2.2 this is only an approximation. Moreover, the right hand side of Eq. (30) contains also a second part of the probability for particle elimination, namely P'. This is because in our simulation there are now more sinks than impacts on terrestrial planets. First, there is a possibility to impact the Sun, but also some orbits may be pushed to larger heliocentric distance, impact giant planets or be ejected from the Solar System. All these processes are collectively described by P'. However, since we do not dispose with an appropriate formulation of P', we do not solve the Eq. (30), rather we take its solution $N(t)$ as directly given by the SWIFT propagation. Still, we can estimate cumulative number of planetary impacts until time T using (for the ith planet).

$$N^i_{\rm PV}(T) = \int_0^T dt \tau_i^2 \bar{p}^i_{\rm fin}(t), \tag{31}$$

and similarly $N^i_{\rm Weth}(T)$ by replacing $\bar{p}^i_{\rm fin}(t)$ with Wetherill's direct estimator $\bar{p}^i_{\rm Weth} = \sum_{j=1}^{N(t)} p^i_{{\rm Weth}j}$, and $N^i_{\rm VPN}(T)$ for the circular orbit of the target with $\bar{p}^i_{\rm circ}(t)$.

Fig. 6 shows snapshots of the projectile osculating orbits at epochs 0 Myr, 50 Myr and 500 Myr. As expected from Bottke et al. (2012), the E-belt particles are swiftly dispersed with longest lived ones pushed on low-eccentricity orbits with high inclination. Eventually, a tiny residual of such a population survives till now as Hungaria asteroids. In course of Gys though, the remaining part of the E-belt was eliminated. For instance, at 50 Myr (middle panel of Fig. 6) only 46% of particles survived, and at 500 Myr (right panel of Fig. 6) only 10% of particles survived. Most of the eliminated particles impact the Sun, as typical for terrestrial planet crossing orbits, but some hit the planets. Fig. 7 shows the cumulative record of planetary impacts as obtained from our numerical experiment (symbols). We also show the computed functions $N^i_{\rm PV}(T)$ for our theory (green line), $N_{\rm Weth}(T)$ for Wetherill's theory (red line) and $N_{\rm circ}(T)$ for circular orbit of the target (blue line), and make them compared with the true impacts. In spite of minor drawbacks both $N^i_{\rm PV}(T)$ and $N^i_{\rm VPN}(T)$ match the real impacts better than $N_{\rm Weth}(T)$, especially for Mercury and Mars. Earth and Venus impact record is equally well reproduced by $N^i_{\rm PV}(T), N^i_{\rm VPN}(T)$ and $N_{\rm Weth}(T)$. The good coincidence between $N^i_{\rm PV}(T)$ and $N^i_{\rm VPN}(T)$ in the case of these two planets is no surprise because of their very low eccentricity. It is somewhat more surprising that $N^i_{\rm VPN}(T)$ still represents well the impact record on Mars and Mercury (in the Mars case even better than $N^i_{\rm PV}(T)$). This is obviously only formal to a certain degree, because – as we discuss below – the individual particle orbits evolve in a very complicated way which does not satisfy assumptions of any of the approaches. The good performance of the Vokrouhlický et al. (2012) approach is, however, promising, because of much lower CPU requirements than the current theory. A summary of cumulatiive number of impacts on terrestrial planets at the end of the simulation, T = 500 Myr, obtained by different methods is shown in Table 1.

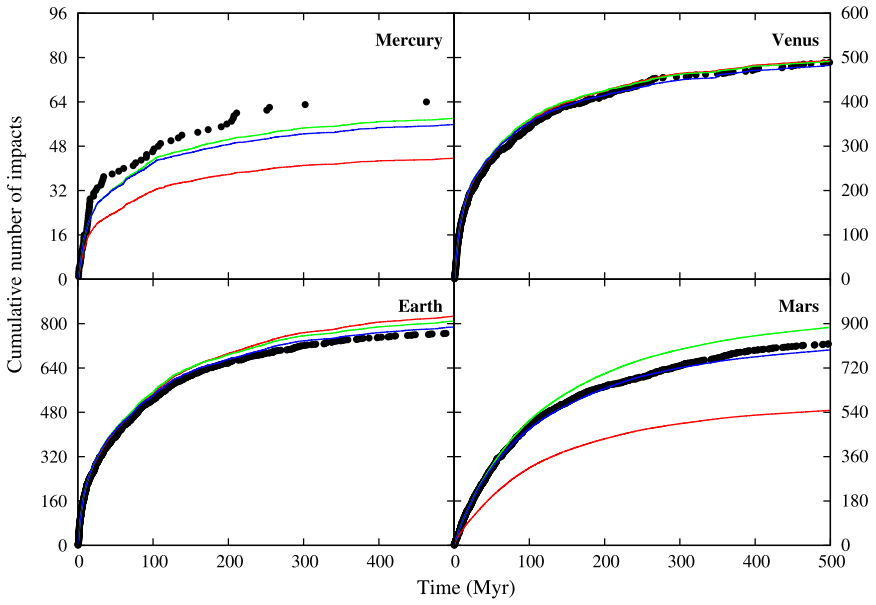

Fig. 7. Cumulative number of E-belt particles impacting terrestrial planets. Time origin at the reconfiguration of giant planets (start of the LHB Bottke et al., 2012). Terrestrial planet had their radii multiplied by a factor 5 in our simulation, so the absolute number of impacts is larger than in reality; their ratio – if corrected for small focusing effects – is however correct. Symbols are directly recorded impacts in our numerical simulation. Green line is prediction $N^i_{\rm PV}(T)$ from our theory, red line is prediction $N^i_{\rm Weth}(T)$ from Wetherill's approach, and blue line is prediction $N^i_{\rm VPN}(T)$ for the circular orbit of the targets (see the text). (For interpretation of the references to color in this figure legend, the reader is referred to the web version of this article.)

Interestingly, Mercury and Venus have the majority of E-belt impact events skewed toward earlier epochs after LHB than Earth and especially Mars. In quantitative terms, 50% of Mercury impacts occur within the first 25 Myr, while 50% of Mars impacts extend over 75 Myr after LHB. In total, Earth receives about 12 times more impacts than Mercury. The ratio of geometric cross section of the Earth and Moon is $\simeq$13.5 and since the post-LHB impact velocities of the E-belt projectiles for Earth are $\simeq$20 km s^{-1} (Bottke et al., 2012), the focusing factor plays a minor role in increasing flux on the Earth with respect to the Moon. In reality, this factor would have been about 1.5, but in our simulation the Earth radius was increased such that the focusation plays virtually no role. From this we infer that Mercury should obtain about the same number of E-belt impacts as the Moon (maybe only 10–20% more). Obviously, since the impact velocity on Mercury is larger – median value of $\simeq$42 km s^{-1} (Marchi et al., 2009) – equal size projectile would create somewhat larger craters on Mercury than on the Moon. The exact factor obviously depends on the scaling law used, but it could be $\simeq\sqrt{2}$. Assuming a collisionally evolved population of impactors, there would be about $\simeq\sqrt{2}^{2.5}\simeq 2.5$ more E-belt produced craters of a given size on Mercury than on the Moon. However, if rescaled to the crater density, one has to take into account an about twice larger surface area of the Mercury, the equal-size E-belt produced craters would have only slightly larger density on Mercury than on the Moon.

We find the Mars impact record interesting, since it has the longest-lived tail of the E-belt bombardment. This is in fact understandable, being just next to the E-belt population. We find also interesting that here the formal application of the Wetherill's approach fails, while results from our theory – while not being perfect – match the data better. This is perhaps because the longer-lived orbits keep having high inclination and low eccentricity, such that impacts on Mars are often nearly pericentric. This increases the collision probability. Another planet, where we observer largest difference between prediction from our model and Wetherill's approach is Mercury. Here again, impactors that make it to Mercury's heliocentric distance likely keep having high-orbital inclination, a situation better described by our approach.

5. Conclusions

We extended the collision probability theory for the high inclination and high eccentricity projectile orbits presented in our previous paper Vokrouhlický et al. (2012). In particular, our present form can handle the target on an elliptic orbit with uniform precession in space. Generalization to target orbits with non-zero inclination and regular node precession, sweeping thus a final volume in space, is left for future work.

We tested our approach using simple projectile-target configurations, mainly to demonstrate the principal phenomena and to verify performance of our numerical code. We also ran a simplified numerical experiment (planetary radii 5 times inflated) of the E-belt population dispersal after planets acquired their final architecture. A full-fledged planetary system, including planet Mercury was used. This allowed us to compare directly recorded planetary impacts with prediction of our collision theory even for this innermost planet. Surprisingly, even that the orbital evolution of the individual E-belt particles is well beyond (and far more complex) the assumptions about secular evolution in our approach, we note rather fair performance of our theory.

The code providing intrinsic collision probability, position of radiants and impact velocities based on our approach written in FORTRAN 77 language is available at `http://sirrah.troja.mff.cuni.cz/~pokorny/Kozai/`.

Acknowledgments

This research was supported by the Czech Grant Agency (Grant P209-13-01308S), the Grant Agency of the Charles University (Grant 602213) and the Project SVV-267301 of the Charles University in Prague. We thank the referees, Giovanni F. Gronchi and Gerhard J. Hahn, for suggestions that helped to improve the original version of this paper.

Appendix A. A comment on numerical evaluation of Eq. (28)

Numerical evaluation of several integrals introduced in Section 2 require specific care. This is because while finite, functions in their integrands may be singular. For instance, the weighting function $\Psi(r_0)$ in the integrand of Eq. (28) diverges when $r_0 = r_1$ and $r_0 = r_2$, the limits of the integration. Obviously, in this case the situation is simple and a standard parameter transformation helps to remove the singularities (see Press et al., 1992, Chapter 4.4). We first split the integral into two pieces, integrating once from r_1 to a_0 and next from a_0 to r_2. In the former case we use the following substitution

$$\int_{r_1}^{a_0}\frac{p(r_0)dr_0}{r_0\sqrt{(r_0-r_1)(r_2-r_0)}}=\int_0^{\sqrt{a_0e_0}}\frac{2p(r_1+t^2)dt}{(r_1+t^2)\sqrt{r_2-r_1-t^2}}, \qquad (A.1)$$

while in the latter case, we have

$$\int_{a_0}^{r_2}\frac{p(r_0)dr_0}{r_0\sqrt{(r_0-r_1)(r_2-r_0)}}=\int_0^{\sqrt{a_0e_0}}\frac{2p(r_2-t^2)dt}{(r_2-t^2)\sqrt{r_2-r_1-t^2}}. \qquad (A.2)$$

We adopted Romberg's method for evaluation of these definite integrals.

The main difficulty now resides in the a priori unknown and potentially ill-behaved course of a function $p(r_0)$, while the rest of the integral is easily evaluated using even a small number of iterations of the Romberg scheme. The potential problems are due to grazing pericentric or apocentric impact configurations for a fixed impactor orbit and varied r_0 value. These situations are typically badly behaved in the linear approximation of the two orbits and result in singularity of apparent $p(r_0)$ (see, e.g., Appendix of Vokrouhlický et al. (2012)). At this moment, we did not optimize our code to deal in detail with all these caveat. Rather, we adopted a pragmatic deal between efficiency and precision of the code. This may degrade its performance at some singular configurations, but overall provides useful tool for most of the situations.

References

Bailey, M.E., Chambers, J.E., Hahn, G., 1992. Origin of sungrazers – A frequent cometary end-state. Astron. Astrophys. 257, 315–322.
Bottke, W.F. et al., 2012. An Archaean heavy bombardment from a destabilized extension of the asteroid belt. Nature 485, 78–81.
Greenberg, R., 1982. Orbital interactions – A new geometrical formalism. Astron. J. 87, 184–195.
Gronchi, G.F., Milani, A., 1998. Averaging on Earth-crossing orbits. Celest. Mech. Dynam. Astron. 71, 109–136.
Gronchi, G.F., Milani, A., 1999. The stable Kozai state for asteroids and comets. With arbitrary semimajor axis and inclination. Astron. Astrophys. 341, 928–935.
Kessler, D.J., 1981. Derivation of the collision probability between orbiting objects. The lifetimes of Jupiter's outer moons. Icarus 48, 39–48.
Kinoshita, H., Nakai, H., 2007. General solution of the Kozai mechanism. Celest. Mech. Dynam. Astron. 98, 67–74.
Kozai, Y., 1962. Secular perturbations of asteroids with high inclination and eccentricity. Astron. J. 67, 591–598.
Levison, H.F., Duncan, M.J., 1994. The long-term dynamical behavior of short-period comets. Icarus 108, 18–36.
Lidov, M.L., 1961. The evolution of orbits of artificial satellites of planets under the action of gravitational perturbations of external bodies. Artif. Satell. Earth 8, 5–45.
Lidov, M.L., 1962. The evolution of orbits of artificial satellites of planets under the action of gravitational perturbations of external bodies. Planet. Space Sci. 9, 719–759.

Marchi, S., Mottola, S., Cremonese, G., Massironi, M., Martellato, E., 2009. A new chronology for the Moon and Mercury. Astron. J. 137, 4936–4948.
Morbidelli, A., 2002. Modern Celestial Mechanics: Aspects of Solar System Dynamics. Taylor & Francis, London.
Öpik, E.J., 1951. Collision probability with the planets and the distribution of planetary matter. Proc. R. Irish Acad. Sect. A 54, 165–199.
Press, W.H., Teukolsky, S.A., Vetterling, W.T., Flannery, B.P., 1992. Numerical Recipes in FORTRAN„ .. The Art of Scientific Computing, second ed. University Press, Cambridge.
Thomas, F., Morbidelli, A., 1996. The Kozai resonance in the outer Solar System and the dynamics of long-period comets. Celest. Mech. Dynam. Astron. 64, 209–229.
Vokrouhlický, D., Pokorný, P., Nesvorný, D., 2012. Öpik-type collision probability for high-inclination orbits. Icarus 219, 150–160.
Wetherill, G.W., 1967. Collisions in the asteroid belt. J. Geophys. Res. 72, 2429–2444.

Paper C

The Astrophysical Journal, 743:37 (12pp), 2011 December 10 doi:10.1088/0004-637X/743/1/37

DYNAMICS OF DUST PARTICLES RELEASED FROM OORT CLOUD COMETS AND THEIR CONTRIBUTION TO RADAR METEORS

David Nesvorný[1], David Vokrouhlický[1,2], Petr Pokorný[1,2], and Diego Janches[3]
[1] Department of Space Studies, Southwest Research Institute, 1050 Walnut Street, Suite 300, Boulder, CO 80302, USA
[2] Institute of Astronomy, Charles University, V Holešovičkách 2, CZ-18000, Prague 8, Czech Republic
[3] Space Weather Laboratory, Code 674, GSFC/NASA, Greenbelt, MD 20771, USA
Received 2011 April 15; accepted 2011 September 5; published 2011 November 21

ABSTRACT

The Oort Cloud Comets (OCCs), exemplified by the Great Comet of 1997 (Hale-Bopp), are occasional visitors from the heatless periphery of the solar system. Previous works hypothesized that a great majority of OCCs must physically disrupt after one or two passages through the inner solar system, where strong thermal gradients can cause phase transitions or volatile pressure buildup. Here we study the fate of small debris particles produced by OCC disruptions to determine whether the imprints of a hypothetical population of OCC meteoroids can be found in the existing meteor radar data. We find that OCC particles with diameters $D \lesssim 10\ \mu$m are blown out from the solar system by radiation pressure, while those with $D \gtrsim 1$ mm have a very low Earth-impact probability. The intermediate particle sizes, $D \sim 100\ \mu$m, represent a sweet spot. About 1% of these particles orbitally evolve by Poynting–Robertson drag to reach orbits with semimajor axis $a \sim 1$ AU. They are expected to produce meteors with radiants near the apex of Earth's orbital motion. We find that the model distributions of their impact speeds and orbits provide a good match to radar observations of apex meteors, except for the eccentricity distribution, which is more skewed toward $e \sim 1$ in our model. Finally, we propose an explanation for the long-standing problem in meteor science related to the relative strength of apex and helion/antihelion sources. As we show in detail, the observed trend, with the apex meteors being more prominent in observations of highly sensitive radars, can be related to orbital dynamics of particles released on the long-period orbits.

Key words: meteorites, meteors, meteoroids – zodiacal dust

1. INTRODUCTION

The Oort Cloud is a roughly spherical cloud of comets (Oort 1950), which surrounds the solar system and extends to heliocentric distances larger than 100,000 AU. The Oort Cloud is currently feeding comets into the inner solar system at a rate of about 12 comets with $q < 3$ AU yr^{-1} with an active comet absolute magnitude $H_{10} < 10.9$ (Wiegert & Tremaine 1999; q is the perihelion distance and H_{10} is a distance-independent measure of the active comet brightness that includes the coma). The Oort Cloud Comets (hereafter OCCs) can be divided into two populations based on their dynamical histories: (1) dynamically new OCCs, which are on their first passage through the inner solar system and typically have $a \gtrsim 10{,}000$ AU and (2) returning OCCs which have previously passed through the inner solar system and typically have $a < 10{,}000$ AU.[4]

The dynamical models of the orbital evolution of new OCCs into returning OCCs predict many times more returning comets than are observed (Wiegert & Tremaine 1999). This is the so-called fading problem, which is thought to be related to the physical evolution of OCCs. To resolve this problem, Levison et al. (2002, hereafter L02) proposed that OCCs must physically disrupt as they evolve inward from the Oort Cloud. Specifically, L02 estimated that, when an OCC becomes inactive, it has only ∼1% chance of becoming dormant, and ∼99% chance of being disrupted. If more OCCs would become dormant, L02 argued, the modern surveys of near-Earth objects would discover a greater number of dormant OCCs passing through perihelion each year than they do. Strong thermal gradients, phase transitions, and volatile pressure buildup experienced by OCCs during their approaches to the Sun are thought to be responsible for disruptions.

If these results are correct, the disrupted OCCs must be a prodigious source of dust particles and larger fragments that may further disintegrate. In particular, the dust production rate from OCC disruptions should be vastly larger than that of active OCCs. On the other hand, the smallest dust particles produced in these disruption events may be lost from the solar system due to the effects of radiation pressure, while the large fragments should be dispersed over enormous radial distances. It is therefore not clear whether the disrupted OCCs can supply a significant amount of material to the inner zodiacal cloud, and whether they could represent a significant source of interplanetary dust particles accreted by the Earth.

Given their large speeds relative to the Earth, the OCC particles plunging into the upper atmosphere could produce meteor phenomena and be detected by optical and radar meteor surveys (e.g., see Steel 1996 for a review). Here we consider the radar meteors. The modern meteor radar surveys produced vast data sets including millions of high-quality orbits covering both the northern and southern hemispheres (e.g., Jones & Brown 1993; Taylor & Elford 1998; Galligan & Baggaley 2004, 2005; Janches et al. 2003; Janches & Chau 2005; Chau et al. 2007; Campbell-Brown 2008). Moreover, the sensitivity of meteor observations broke new grounds with routine measurements of meteor echoes using HPLA[5] radars such as the Arecibo (AO) radar, which is capable of detecting ∼50 μm particles down to ∼20 km s^{-1} (e.g., Janches et al. 2003, 2006; Fentzke et al. 2009). It is natural to ask whether some of these observations can be linked to the particle populations from disrupted OCCs.

[4] See Dybczyński (2001) for an alternative definition.

[5] High Power and Large Aperture.

Meteors are produced by small interplanetary particles, also known as the *meteoroids*, that interact with air molecules upon atmospheric entry. Based on meteor data, the meteoroids can be divided into two groups: sporadic meteoroids and meteoroid streams. The meteoroid streams are prominent concentrations of particles with similar orbits (Whipple & Gossner 1949; Whipple 1951). They are thought to be produced by particles released by active and recently (< few thousand years ago) disrupted comets (e.g., Jenniskens 2008). Sporadic meteoroids are those particles that have evolved significantly from their parent body so that they are no longer easily linked to that parent, or to other meteoroids from the same parent. Notably, the time-integrated flux of meteors at Earth is dominated by about a factor of ~ 10 by sporadics (Jones & Brown 1993).

The radiant distribution of sporadic meteors shows several concentrations on the sky, known as the helion/antihelion, north/south apex, and north/south toroidal sources (e.g., Younger et al. 2009, and references therein). Wiegert et al. (2009, hereafter W09) developed a dynamical model to explain these concentrations. Their main results concern the prominent helion/antihelion sources for which the particles released by Jupiter-family comets (JFCs) such as 2P/Encke provide the best match, in agreement with previous studies (e.g., Jones et al. 2001). As for the north/south apex source, W09 pointed out the potential importance of retrograde Halley-type comets (HTCs) such as 55P/Tempel-Tuttle (or an orbitally similar lost comet). The case for the retrograde HTC particles is compelling, because three prominent retrograde HTCs, namely, 1P/Halley, 55P/Tempel-Tuttle, and 109P/Swift-Tuttle, all have associated streams, known as Orionids/η Aquarids, Leonids, and Perseids, respectively. The sporadic meteoroids with the north/south apex radiants can thus plausibly be a dynamically old component of HTC particles.

Here we consider the possibility that at least some part of the meteoroid complex is produced by disrupting OCCs (L02; see also Jones et al. 2001). We study the effects of radiation pressure on particles released from the highly eccentric OCC orbits, and their dynamical evolution under gravitational perturbations from planets and Poynting–Robertson (P-R) drag (see Section 2 for our model). We show that a significant contribution of OCC particles to the inner zodiacal cloud and meteor record is somewhat problematic, because most small OCC particles are blown out from the solar system by radiation pressure, while most large ones get scattered by planets and never make it into the inner solar system (Section 3). Still, we find that there is a sweet spot at particle sizes $\sim$ 100–300 μm. Our modeling work shows that the orbits and impact speeds of these intermediate-size OCC particles can match those derived from the meteor radar data for apex meteoroids. Furthermore, we find that the preponderance of fast apex meteors in HPLA radar observations (e.g., AO, ALTAIR, Jicamarca) can be linked to the competing effects of P-R drag and Jupiter perturbations, which act as a size filter on populations of the long-period meteoroids (Section 4).

2. MODEL

We studied the following sequence of events: (1) particles of different sizes were released from OCCs (Section 2.1), (2) their orbits evolved under the influence of gravitational and radiation forces (Section 2.2), (3) some particles were thermally or collisionally destroyed (Section 2.3), and (4) a small fraction of the initial particle population was accreted by Earth, producing meteors (Section 2.4). We describe our model for (1)–(4) below.

2.1. Initial Orbits

According to Francis (2005), OCCs have $dN(q) \propto (1 + \sqrt{q})\, dq$ for $q < 2$ AU. For $q > 2$ AU, Francis' result predicts $dN(q)$ being flat or declining, while we would expect the perihelion distribution to increase with q. It probably just shows that the distribution is not well constrained for $q > 2$ AU. We used $dN(q) \propto 2.41(q/2)^{\gamma}\, dq$ for $q > 2$ AU, with $0 \leqslant \gamma \leqslant 1$. The initial values of q in our numerical integrations were set to be uniformly random between 0 and 5 AU, because particles starting with $q > 5$ AU do not reach 1 AU (see Section 3.1), where they could contribute to the Earth-impact record. The results for different $dN(q)$ were obtained by assigning the appropriate weight to particles starting with different qs (i.e., instead of 1 we counted each particle as $dN(q)/dq$).

Upon its release from a larger object, a small particle will feel the effects of radiation pressure. These effects can be best described by replacing the mass of the Sun, $m_{\odot}$, by $m_{\odot}(1-\beta)$, with β given by

$$\beta = 5.7 \times 10^{-5}\, \frac{Q_{\rm pr}}{\rho s}, \qquad (1)$$

where radius s and density ρ of the particle are in cgs units. Pressure coefficient $Q_{\rm pr}$ can be determined using the Mie theory (Burns et al. 1979). We set $Q_{\rm pr} = 1$, which corresponds to the geometrical optics limit, where s is much larger than the incident-light wavelength. We used particles with $D = 2s = 10$, 30, 100, 300, 1000 μm, which should cover the interesting range of sizes, and $\rho = 2.0$ g cm^{-3}.

For large eccentricity e of the parent object and/or for large β, the released particle may become unbound and escape to interstellar space. To stay bound, the heliocentric distance, R, of the released particle must fulfill the following condition (e.g., Kresak 1976; Liou et al. 1999):

$$R > R^* = 2\beta a. \qquad (2)$$

This condition shows that all particles with β released at the orbit's perihelion will be removed, if $2\beta > 1 - e$. The new OCCs have $1 - e \lesssim 10^{-4}$. It follows that particles produced by a new OCC near its perihelion will become unbound for sizes up to $D \sim 1$ cm. The usual near-perihelion activity of OCCs therefore cannot be a major source of small dust particles in the inner solar system.

Motivated by the L02 results, we now consider OCCs disruptions. Interestingly, observations of the disruption events of comets show that there does not seem to be any correlation between the time of disruption and the orbital phase of the parent object. Many comets were seen to disrupt (or suffer outburst/splitting events) at large heliocentric distances. For example, 174P/Echeclus showed an outburst with $R \approx 13$ AU, more than 6 AU beyond its perihelion distance (Choi et al. 2006). It may therefore be possible that OCCs could disrupt at relatively large R and produce particles that, according to Equation (2), will stay on bound orbits.

We release particles with $R > R^*$ in our model. For example, a $D = 100\,\mu$m particle with $\rho = 2.0$ g cm^{-3} ejected from the parent comet with $a = 10^3$ AU will have $\beta \simeq 0.006$ and $R^* = 12$ AU. We thus release these particles with $R > 12$ AU. In addition, we only study particles ejected from orbits similar to those of the *returning* OCCs with $a \sim 10^3$ AU. We do not consider orbits with $a \gtrsim 10^4$ AU, corresponding to the

Oort spike,[6] because we believe it unlikely that disruptions could happen at the very large heliocentric distance implied by Equation (2) for $a \gtrsim 10^4$ AU. For example, a $D = 300\,\mu$m particle with $\rho = 2.0$ g cm^{-3}, released from a parent orbit with $a = 10^4$ AU, would become unbound, unless $R > 36$ AU.

The particle populations studied here have bound initial orbits. They represent only a fraction of all particles released from OCCs. This fraction, denoted f_0 in Section 4, is difficult to estimate, because we do not have a detailed understanding of the processes, and their dependence on R, that govern comet disruptions. We will return to this issue in Section 4. The initial distribution of orbital inclination vectors was set to be isotropic. To simplify things, we neglected the ejection velocities of dust particles from their parent objects (see Jones et al. 2001) and assumed that they will initially follow the parent comet's orbit modified by radiation pressure.

For reference, we also followed meteoroids from 1P/Halley, 2P/Encke, and 55P/Tempel-Tuttle. These comets were suggested to be important sources of the sporadic meteors by W09. The comet's orbits were obtained from the JPL Horizons site. Particles of different sizes were released from the parent orbits and tracked into future. We applied the same procedures/criteria to them that we used for the OCC particles.

2.2. Orbit Integration

The orbits of small particles in the interplanetary space are subject to gravitational perturbations of planets and radiation forces (Robertson 1937; Burns et al. 1979). The acceleration $\vec{F}$ due to radiation forces is

$$\vec{F} = \beta G \frac{m_\odot}{R^2} \left[\left(1 - \frac{\dot{R}}{c} \right) \frac{\vec{R}}{R} - \frac{\vec{V}}{c} \right], \quad (3)$$

where $\vec{R}$ is the heliocentric position vector of particle, $\vec{V}$ is its velocity, G is the gravitational constant, $m_\odot$ is the mass of the Sun, c is the speed of light, and $\dot{R} = dR/dt$. The acceleration Equation (3) consists of the radiation pressure and the velocity-dependent P-R term. Parameter β is related to the radiation pressure coefficient $Q_{\rm pr}$ by Equation (1).

The particle orbits were numerically integrated with the `swift_rmvs3` code (Levison & Duncan 1994), which is an efficient implementation of the Wisdom–Holman map (Wisdom & Holman 1991) and which, in addition, can deal with close encounters between particles and planets. The radiation pressure and drag forces were inserted into the Keplerian and kick parts of the integrator, respectively. The change to the Keplerian part was trivially done by substituting $m_\odot$ by $m_\odot(1-\beta)$. The `swift_rmvs3` integrator is stable even for near-parabolic orbits, and thus well suited for the integrations that we carried out here.

The code tracks the orbital evolution of a particle that revolves around the Sun and is subject to the gravitational perturbations of seven planets (Venus to Neptune; the mass of Mercury was added to the Sun) until the particle impacts a planet, is ejected from the solar system or evolves to within 0.05 AU from the Sun. We removed particles that evolved to $R < 0.05$ AU because the orbital period for $R < 0.05$ AU was not properly resolved by our 1 day integration time step.

Several thousand particles were followed for each D. Their orbital elements were defined with respect to the barycenter of the solar system. The barycentric elements are similar to the heliocentric elements for $R < 5$ AU, but differ for large R, where the Sun's orbital speed about the barycenter of the solar system is not negligible relative to the orbital speed of a particle.

All orbits were followed from the present epoch into the future. Each particle's orbital elements were stored at 10^3 yr intervals. We used the output to construct a *steady state distribution* of OCC particles in the inner solar system. This approach differs from that of Nesvorný et al. (2006) and W09, who started particles at many different past epochs and used these integrations to determine the *present distribution* of particles. The two distributions are expected to be slightly different, expressing mainly the difference between the present configuration of planets, with each planet having a specific secular phase, and the time-averaged system, where all phases are mixed. Since this difference is small, however, we can use the steady state distribution, which is easier to obtain, as a reasonable approximation.

2.3. Physical Effects

Solar system micrometeoroids can be destroyed by collisions with other particles and by solar heating, that can lead to sublimation and vaporization of minerals. Here we describe how we parameterize these processes in our model.

2.3.1. Thermal Destruction

Thermal alteration of grains in the interplanetary grains is a complex process. The OCC particles evolving into the inner solar system will first lose their volatile ices, which will rapidly sublimate once the grains are heated to a critical temperature. We do not model the volatile loss in detail. Instead, we crudely assume that the grains have lost $\sim 50\%$ of their mass/volume when reaching $R \lesssim 5$ AU. We do not include the orbital effects of mass loss in orbital modeling because it should produce only a relatively small perturbation on orbits for large particles that we consider here. The remaining grains will be primarily composed from amorphous silicates and will survive down to very small R.

According to Duschl et al. (1996), silicates are thermally altered at temperatures $T \sim 900$–1600 K, and start to vaporize for $T > 1600$ K. As an example of thermal alteration, Kasuga et al. (2006; see also Čapek & Borovička 2009) studied the thermal desorption of alkali minerals and concluded that micrometeoroids should show evidence of thermal desorption of metals, Na in particular, for $q < 0.1$ AU. Following Moro-Martín & Malhotra (2002), Kessler-Silacci et al. (2007), and others, we adopt a simple criterion for the silicate grain destruction. We will assume that they are destroyed when the grain temperature reaches $T = 1500$ K.

The temperature of a small, fast spinning grain in interplanetary space is set by an equilibrium between the absorbed and re-radiated energy fluxes. While the absorbed flux is a simple function of the particle's size, albedo and heliocentric distance, the re-radiated flux depends on the particle's emissivity, which in turn is a function of the particle's size, shape, and material

[6] The semimajor axis values of most OCCs are $10^4 \lesssim a \lesssim 5 \times 10^4$ AU, which is known as the Oort spike (e.g., Wiegert & Tremaine 1999). Comets in the spike are mostly dynamically new comets, on their first passage into the inner planetary system from the Oort Cloud. A comet that passes through the planetary system receives a gravitational kick from the planets. The typical energy kick, Δx, depends strongly on the perihelion distance of the comet's orbit. According to Wiegert & Tremaine (1999), $\Delta x \sim 10^{-3}$ AU^{-1} for $q \lesssim 6$ AU, while comets in the Oort spike have $x = 1/a \lesssim 10^{-4}$ AU^{-1}. Depending on the sign of the kick, they will either leave the planetary system on unbound orbit, never to return, or be thrown onto a more tightly bound orbit with $a \lesssim 10^3$ AU.

properties. Using the optical constants of amorphous pyroxene of approximately cosmic composition (Henning & Mutschke 1997), we find that a dark $D \gtrsim 100\,\mu$m grain at R has the equilibrium temperature within 10 K of a blackbody, $T(R) \simeq 275/\sqrt{R}$ K. According to our simple destruction criterion, $T(R) > 1500$ K, the silicate grains should thus be removed when reaching $R \lesssim 0.03$ AU. On the other hand, the smallest particles considered in this work, $D = 10\,\mu$m, will reach $T(R) = 1500$ K for $R \simeq 0.05$ AU. Thus, we opted for using a very simple (and conservative) criterion where particles of all sizes were destroyed, and not considered for statistics, if they ever reached $R \leqslant 0.05$ AU. Note that, by design, this limit is the same as the one imposed by the integration time step (Section 2.2).

2.3.2. Disruptive Collisions

The collisional lifetime of meteoroids, $\tau_{\rm coll}$, was taken from Grün et al. (1985, hereafter G85). It was assumed to be a function of particle mass, m, and orbital parameters, mainly a and e. We neglected the effect of orbital inclination on $\tau_{\rm coll}$, because the results discussed in Steel & Elford (1986) suggest that the inclinations should affect $\tau_{\rm coll}$ only up to a factor of $\sim$2–5, which is not overly significant in the context of our work. We assumed that the mass and orbital dependencies of $\tau_{\rm coll}$ can be decoupled, so that

$$\tau_{\rm coll}\,(m, a, e) = \Phi\,(m)\,\Psi\,(a, e)\,, \tag{4}$$

where $\Phi(m)$ and $\Psi(a, e)$ are discussed below.

As for $\Phi(m)$, we used the G85 model based on measurements of various spacecraft and Earth-based detectors. We found that the model can be approximated by a simple empirical fit. Specifically, between $10^{-6.4}$ g and $10^{1.2}$ g, we adopted the quadratic function

$$\log\Phi\,(m) = c_2\,(\log m)^2 + c_1\,(\log m) + c_0, \tag{5}$$

with $(c_0, c_1, c_2) = (4.021, 0.300, 0.083)$, where the values of c_0, c_1, and c_2 were set to fit the G85 collision lifetime for circular orbits at the reference distance $R_0 = 1$ AU. A linear relation between $\log\Phi\,(m)$ and $\log m$ was used outside the quoted mass range to approximate the G85 model down to $m = 10^{-8}$ g. $\Phi(m)$ has a minimum for $m \simeq 0.01$ g, corresponding to $s \simeq 1$ mm for $\rho = 2$ g cm^{-3} (Figure 1). The collisional lifetime of $\sim$1 mm particles in the G85 model is very short, roughly 5000 yr at 1 AU.

$\Psi(a, e)$ is assumed to drop as a power law with R. From Equation (18) in G85 we have

$$\Psi = \left(\frac{R}{R_0}\right)^{\alpha} \frac{v\,(R)}{v_{\rm circ}\,(R)}, \tag{6}$$

where $v(R)$ and $v_{\rm circ}(R)$ are the particle and circular speeds at R, respectively, and $\alpha \simeq 1.8$. The velocity-dependent factor provides an appropriate scaling of $\tau_{\rm coll}$ for eccentric orbits.

Averaging Equation (6) over a Keplerian orbit with semimajor axis a and eccentricity e, we obtain

$$\Psi\,(a, e) = \left(\frac{a}{R_0}\right)^{\alpha} \mathcal{J}\,(e)\,, \tag{7}$$

where

$$\mathcal{J}\,(e) = \frac{1}{\pi}\int_0^{\pi} du \frac{(1 - e\cos u)^{1+\alpha}}{\sqrt{1 + e\cos u}} \tag{8}$$

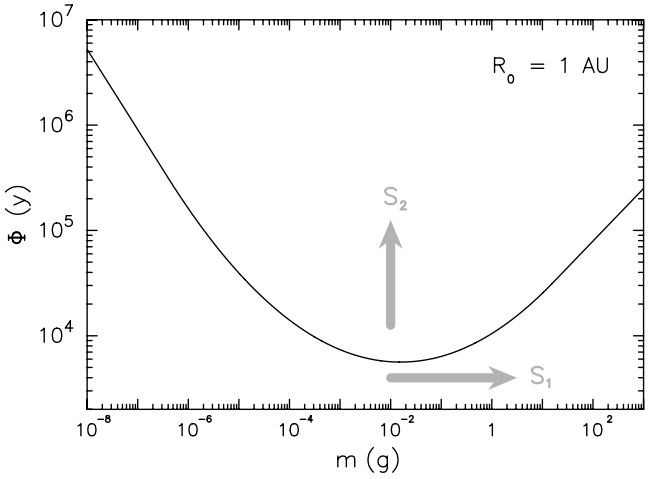

Figure 1. Mass dependence, $\Phi(m)$, of the adopted model for the collisional lifetime of particles. The plot shows $\Phi(m)$ for a particle on the circular orbit at the reference heliocentric distance $R_0 = 1$ AU. Two parameters of the collisional model, S_1 and S_2, were used to test the sensitivity of our results to modifications of $\Phi(m)$.

can be written as a series in e^2 with good convergence. Note that $\mathcal{J} \simeq 1$ for $e \simeq 0$, as required in Equation (7), but can become $\gg 1$ for very eccentric orbits.

The G85 model was calibrated to match the impact fluxes of particles as measured prior to 1985. The more recent measurements indicate lower fluxes (e.g., Dikarev et al. 2005; Drolshagen et al. 2008). Also, to estimate $\tau_{\rm coll}$, assumptions needed to be made in G85 about the strength of particles, and their impact speeds. As a result, $\tau_{\rm coll}$ proposed by G85 may have a significant uncertainty. To test different possibilities, we introduced two free parameters in our model, S_1 and S_2, that were used to shift the $\Phi(m)$ function in $\log m$ and $\log\Phi$, respectively (as indicated by arrows in Figure 1). For example, the positive S_2 values increase $\tau_{\rm coll}$ relative to the standard G85 model, as expected, for example, if particles were stronger than assumed in G85, or if the fluxes were lower.

Collisional disruption of particles was taken into account during processing the output from the numerical integration described in Section 2.2. To account for the stochastic nature of breakups, we determined the breakup probability $p_{\rm coll} = 1 - \exp(-h/\tau_{\rm coll})$, where $h = 1000$ yr is the output interval and $\tau_{\rm coll}$ was computed individually for each particle's orbit. The code then generated a random number $0 \leqslant x \leqslant 1$, and eliminated the particle if $x < p_{\rm coll}$.

We caution that our procedure does not take into account the small debris fragments that are generated by disruptions of larger particles. Instead, all fragments are removed from the system. This is an important approximation, whose validity needs to be tested in the future.

2.4. Model for Meteor Radar Observations

We used the Öpik theory (Öpik 1951) to estimate the expected terrestrial accretion rate of OCC particles in our model. Wetherill (1967), and later Greenberg (1982), improved the theory by extending it more rigorously to the case of two eccentric orbits. Here we used the Fortran program written by W. F. Bottke (see, e.g., Bottke et al. 1994), which employs the Greenberg formalism.

We modified the code to compute the radiants of the impacting bodies. The radiants were expressed in the coordinate system,

where longitude l was measured from Earth's apex in the counterclockwise direction along Earth's orbit and latitude b was measured relative to Earth's orbital plane. Note that our definition of longitude is different from the one more commonly used for radar meteors, where the longitude is measured from the helion direction. The radiants were calculated before the effects of gravitational focusing were applied.

The longitude and latitude values of radiants were binned into 1 deg^2 area segments. For each radiant bin, the code gives information about the distribution of geocentric impact speeds, v_g, and heliocentric orbits prior to the impact, as defined by a, e, and i. Here, v_g is defined as $v_g = (v_\infty^2 + v_{\rm esc}^2)^{1/2}$, where v_∞ is the relative velocity "in infinity" and $v_{\rm esc}$ is the escape speed from Earth's surface. The orbital elements, on the other hand, are the orbital elements that the particle would have in the absence of the gravitational focusing by the Earth. The radiant distribution, v_g, a, e, and i will be compared to meteor radar observations in Section 3.3.

To compare our model with observations, we need to include the meteor radar detection efficiency. This is a difficult problem because the meteor phenomenon itself and radar detection of it involve complex physics. For example, the specular meteor radars (SMRs), such as the Canadian Meteor Orbit Radar (CMOR; Campbell-Brown 2008) and Advanced Meteor Orbit Radar (AMOR; Galligan & Baggaley 2004, 2005), detect the specular reflection of the meteor trail (the plasma formed by the meteoroid's passage). The meteoroid velocities are then derived from the detection of the Fresnel diffraction patterns of the developing trail, or are determined by measuring the time of flight between stations.

The detection efficiency of a meteor should mainly be a function of the particle size and speed, but it also depends on a number of other parameters discussed, for example, in Janches et al. (2008). Following W09, we opt for a simple parameterization of radar sensitivity function, where the detection is represented by an ionization function

$$I(m, v_g) = \frac{m}{10^{-4}\,{\rm g}} \left(\frac{v_g}{30\,{\rm km\,s^{-1}}}\right)^{3.5}. \quad (9)$$

All meteors with $I(m, v_g) \geqslant I^*$ are assumed to be detected in our model, while all meteors with $I(m, v_g) < I^*$ are not detected (see Fentzke et al. 2009 for a similar method applied to head echo radars). The ionization cutoff I^* is different for different SMRs. For example, $I^* \sim 1$ for CMOR (Campbell-Brown 2008) and $I^* \sim 0.001$–0.01 for AMOR (Galligan & Baggaley 2004, 2005). For reference, an OCC particle with $v_g = 60$ km s^{-1} and $m = 10^{-5}$ g, corresponding to $s \sim 100$ μm, will have $I(m, v_g) \simeq 0.1$, i.e., a value intermediate between the two thresholds. These meteoroids would thus be detected by AMOR, according to our definition, but not by CMOR. We will discuss these issues in more detail in Section 3.3.

3. RESULTS

3.1. Orbital Evolution of OCC Particles

Wyatt & Whipple (1950) identified the following constant of motion of P-R drag

$$C = a\frac{(1-e^2)}{e^{4/5}}, \quad (10)$$

where a and e are the particle's semimajor axis and eccentricity (see also Breiter & Jackson 1998). This constant is independent of the particle properties such as its size. The orbit path of any particle in a and e can thus be obtained by calculating C for the initial orbit, and requiring that Equation (10) holds at all times (Figure 2(a)). For $e \sim 1$, the orbit trajectories follow the lines of constant q, because $C \simeq 2q$ for $e \simeq 1$. The semimajor axis of orbits shrinks until reaching a value only several times larger than q. At that point, a more familiar form of P-R drag takes place with both a and q converging to zero.

The timescale of orbital evolution is as follows. For an initial orbit with a, e, and $q = a(1-e)$, the total time of fall to the Sun is (Wyatt & Whipple 1950)

$$\tau_{\rm fall} = 20\,{\rm Myr}\left(\frac{s}{1\,{\rm cm}}\right)\left(\frac{\rho}{2\,{\rm g\,cm^{-3}}}\right)\left(\frac{q}{1\,{\rm AU}}\right)^2 f(e), \quad (11)$$

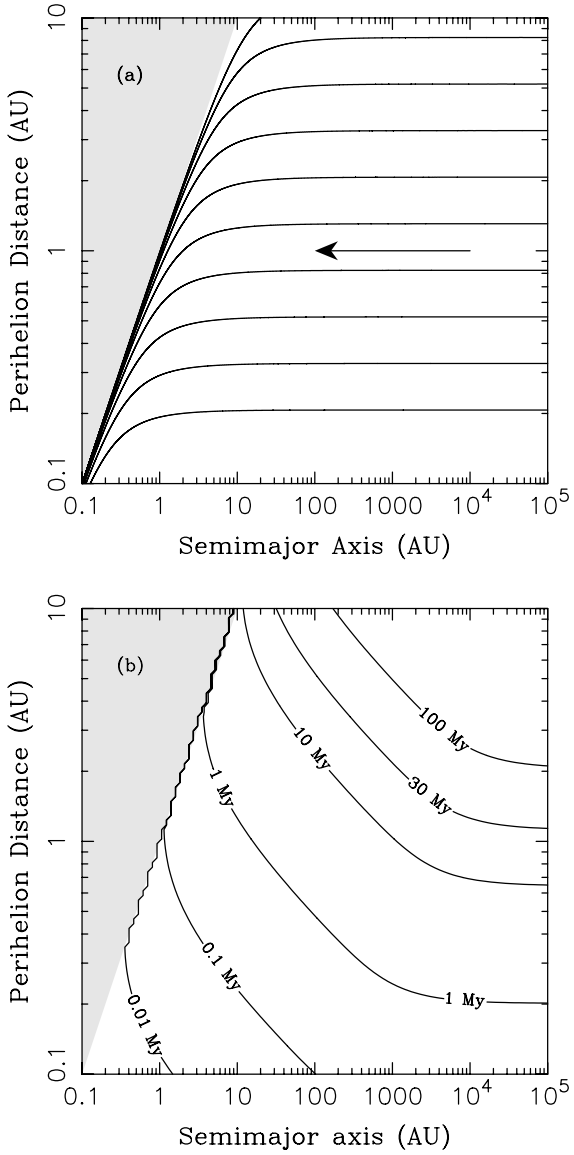

Figure 2. Effects of P-R drag on the highly eccentric orbits of OCC particles. (a) Evolution tracks of particles evolving by P-R drag in semimajor axis and perihelion distance. Particles with $e \simeq 1$ evolve from right to left along the lines of constant perihelion distance. The shaded area is inaccessible to orbits. (b) Evolution timescale for particles with $D = 100\,\mu$m and $\rho = 2$ g cm^{-3}. Contours show the time of fall, $\tau_{\rm fall}$, from the initial orbit with a and q to the Sun. According to Equation (11), $\tau_{\rm fall}$ scales linearly with D (and ρ), so that, for example, the 1 Myr contour for $D = 100\,\mu$m is the 10 Myr contour for $D = 1$ mm.

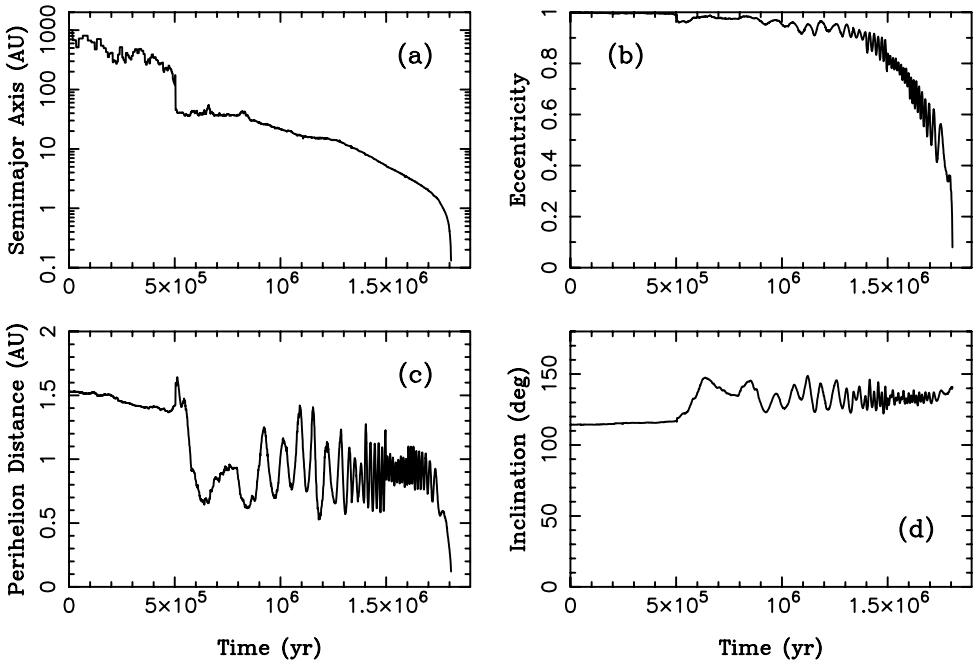

Figure 3. Orbit history of a particle with $D = 100\,\mu$m, initial $a = 10^3$ AU, and $q = 1.53$ AU. After 1.7 Myr, the orbit decouples from Jupiter and moves to $a \sim 1$ AU. The particle ends up having $a < 0.1$ AU, and sublimates upon reaching $R < 0.05$ AU.

where

$$f(e) = 1.13\frac{(1+e)^2}{e^{8/5}}\int_0^e d\eta \frac{\eta^{3/5}}{(1-\eta^2)^{3/2}}. \quad (12)$$

Figure 2(b) shows $\tau_{\rm fall}$ for orbits relevant to OCC particles.

Interestingly, the timescale for large a can be relatively short if q is small. For example, an OCC particle with $D = 100\,\mu$m, $a = 10^4$ AU, and $q = 1$ AU takes about 20 Myr to fall to the Sun. This is only about 20 orbital periods for $a = 10^4$ AU. According to Equation (11), $\tau_{\rm fall}$ scales linearly with particle size. Thus, a $D = 10\,\mu$m particle with the same initial orbit has $\tau_{\rm fall} = 2$ Myr.

One important aspect that cannot be captured by the analytical results discussed above is the effect of planetary perturbations on drifting orbits of OCC particles. To evaluate this effect, as described in Section 2.2, we numerically integrated the orbits of OCC particles as they evolve from large a and interact with the planets.

Figure 3 shows the orbital history of a particle, whose orbit evolved all the way down into the inner solar system. Initially, the particle's semimajor axis underwent a random walk caused by indirect planetary perturbations, mainly from Jupiter, during each perihelion passage (Wiegert & Tremaine 1999). Then, at time $t \simeq 5 \times 10^5$ yr, a single perihelion passage produced a significant drop of a from 150 to 40 AU, where the particle started to interact with the exterior mean motion resonances with Neptune. The following evolution was mainly controlled by P-R drag. Eventually, the orbit decoupled from Jupiter, reached $a \sim 1$ AU, and kept shrinking further toward the Sun, where the particle was thermally destroyed. The large oscillations of q for $0.9 < t < 1.7$ Myr, correlated with those in i, were produced by Kozai dynamics (e.g., Kozai 1962).

The orbit history shown in Figure 3 is typical for an OCC particle that is able to make it into the inner solar system. These particles, however, represent a relatively small fraction of the initial population, with most particles being ejected from the solar system by planetary perturbations. Using $dN(q)$ with $0 \leqslant \gamma \leqslant 1$ (Section 2.1), $a \sim 10^3$ AU and isotropic distribution of inclination vectors, roughly 0.8%–1.5% of particles with $D = 100\,\mu$m evolve down into the inner solar system and decouple from Jupiter (as defined by the aphelion distance $Q = a(1+e) < 4$ AU), without being disrupted by an impact (with standard $S_1 = S_2 = 0$; Section 2.3) or ever having $q < 0.05$ AU (to avoid sublimation). These particles can potentially be important for the terrestrial impact record and interpretation of the meteor radar data. The bulk of OCC particles that do not reach $a \sim 1$ AU, do not significantly contribute to Earth's accretion, because these particles spend most of their lifetimes at $R \gg 1$ AU.

The fraction of OCC particles reaching $a \sim 1$ AU, f_1, normalized to the number of particles whose orbits were initially bound (see Section 2.1), is sensitive to particle size. For $D = 10\,\mu$m, $dN(q)$ described in Section 2.1, and initial $a \sim 10^3$ AU, $f_1 \simeq 0.15$–0.2. For $D = 300\,\mu$m, on the other hand, $f_1 \simeq 2 \times 10^{-3}$. Moreover, for $D = 1$ mm, only one particle out of the total of 5000 reached $a \sim 1$ AU. This trend, with the larger particles having progressively smaller f_1 values, has interesting implications for the observations of sporadic meteors (Section 4).

The above estimates used $\tau_{\rm coll}$ as described in Section 2.3.2. Collisional disruption, however, turned out to have only a modest effect for the standard G85 $\tau_{\rm coll}$ ($S_1 = S_2 = 0$) and the particle sizes considered here. For example, only ~2% of particles with $D = 100\,\mu$m that reached $a \sim 1$ AU in our numerical integration have disrupted prior to decoupling from Jupiter, as detected in post-processing of the integration output, with the standard G85 $\tau_{\rm coll}$. A great majority of particles with $D = 300\,\mu$m also survived. The effect of disruptive collisions becomes more significant for $D \sim 1$ mm, for which $\tau_{\rm coll}$ is significantly shorter (Section 2.3.2) and P-R drag is weaker.

The thermal effects discussed in Section 2.3.1 turned out to be very important for all particle sizes considered here. For example, 75 out of 122 particles (i.e., over 60%) with

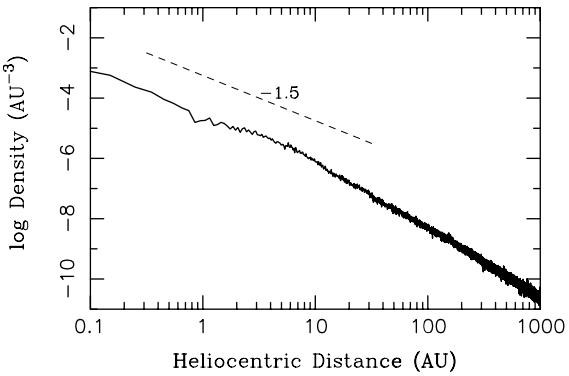

Figure 4. Radial distribution of OCC particles that we obtained in our model. The number density was normalized to the input flux of one particle released on bound orbit per year. We used $D = 100\,\mu$m here. The distribution with $D = 300\,\mu$m looks similar for $R > 5$ AU, but is depleted below 5 AU, relative to the one shown here, because fewer particles with $D = 300\,\mu$m are able to decouple from Jupiter. Particles were released on orbits with $a \sim 10^3$ AU and uniformly random $\sin i$. The initial distribution $dN(q)$ was set as described in Section 2.1 with $\gamma = 0.5$ (the results are not sensitive to γ).

$D = 100\,\mu$m that ever reached $Q < 4$ AU, previously had $q < 0.05$ AU, which is our crude threshold for the thermal destruction of particles. Also, 68 out of 74 $D = 300\,\mu$m particles (over 90%) reaching $Q < 4$ AU previously had $q < 0.05$ AU. The thermally destroyed particles are removed and the orbital histories after their disruption are not used for our analysis.

These fractions are a direct consequence of the relative importance of planetary perturbations and P-R drag on particles with different D and q. The orbital evolution of a large particle on the OCC-like orbit is primarily controlled by planetary perturbations. Sooner or later, the planets will eject the particle from the solar system, unless the orbit shrinks and decouples from Jupiter. To achieve this, q of the particle's orbit must be very low, so that the P-R drag timescale is short (see Figure 2(b)). But if q is low, it may easily drop below $q < 0.05$ AU, where the particle is removed, thus explaining why most *large* particles reaching $Q < 4$ AU previously have $q < 0.05$ AU.

Interestingly, the fraction of particles with $D \simeq 100$–$300\,\mu$m reaching $a \sim 1$ AU is not overly sensitive to the initial perihelion distance, as far as $q \lesssim 5$ AU. This is because it is more likely to decouple if q is low, because P-R drag is stronger, but this trend is nearly canceled, because particles with very low q tend to drop below $q = 0.05$ AU and sublimate before they can decouple. Particles with $D \simeq 100$–$300\,\mu$m and $q > 5$ AU, on the other hand, tend to have very long P-R drag timescales (e.g., $\tau_{\rm fall} > 50$ Myr for initial $a = 10^3$ AU; Figure 2(b)), and are scattered by planets from the solar system.

3.2. Orbital and Spatial Distributions

Here we discuss the expected distribution of OCC particles in the inner solar system. Figure 4 shows the number density of OCC particles as a function of R. As expected, the particle density increases toward the Sun. The radial distribution of $D = 100\,\mu$m particles can be approximated by a power law, $dN(R) \propto R^{-\alpha} dR$, where $\alpha \simeq 1.5$ for $R < 5$ AU, and $\alpha \simeq 2.0$ for $R > 10$ AU. Both these radial dependencies are significantly steeper than $dN(R) \propto R^{-1} dR$, expected for distribution of particles on nearly circular orbits (see, e.g., Dermott et al. 2001).

The relatively steep radial distribution is a consequence of Keplerian motion of particles with $e \sim 1$. For $R < a$, the time

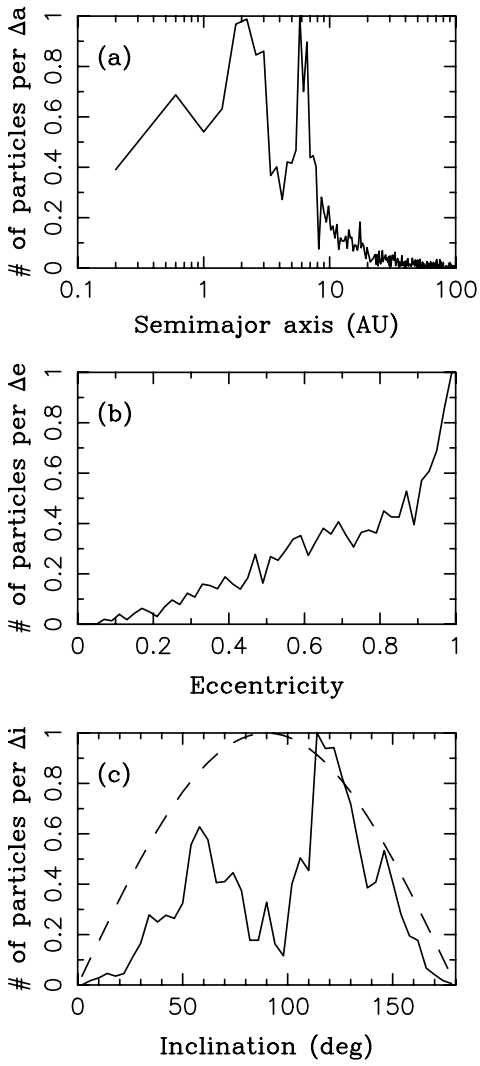

Figure 5. Steady state distribution of orbital elements of particles with $D = 100\,\mu$m: (a) $dN(a)$, (b) $dN(e)$, and (c) $dN(i)$. The distributions shown here ignore particles with $R > 5$ AU. They therefore represent the steady state distribution of orbits in the inner solar system, which is relevant for observations of the inner zodiacal cloud and sporadic meteors.

spent by a particle on the Keplerian orbit between R and $R+dR$ is $dt \propto R^{0.5} dR$. This leads to $dN(R) \propto R^{-1.5} dR$, if the expected number of particles, which is proportional to dt, is divided by volume $4\pi R^2 dR$. For $R > a$, on the other hand, appropriate for large radial distances, $dt \sim$ const. and $dN(R) \propto R^{-2} dR$. Thus, $\alpha \simeq 1.5$–2 is expected for $e \sim 1$ (see also Liou et al. 1999).

We find that the number density of OCC particles at $R \sim 1$ AU is mainly contributed by the particles that orbitally decoupled from Jupiter. This shows the importance of orbital decoupling for the distribution of OCC particles in the inner solar system, and their accretion by the Earth. Specifically, most OCC particles accreted by the Earth are expected to have $a(1+e) < 4$ AU despite the fact that their orbits started with $a \gtrsim 10^3$ AU.

Figure 5 shows the distributions of orbital elements for OCC particles with $D = 100\,\mu$m and $R < 5$ AU. The semimajor axis distribution, $dN(a)$, has a broad maximum centered at 0.5–2 AU with $a \sim 2$ AU being the most common. $dN(a)$ decreases toward larger a, because particles with $a > 3$ AU are coupled to Jupiter, have short dynamical lifetimes, and do not spend

much time at $R < 5$ AU. The peak of $dN(a)$ at $a = 6$–7 AU is produced by orbits in the exterior mean motion resonances with Jupiter, which prolong the dynamical lifetime of particles by phase protecting them against encounters with Jupiter (Liou et al. 1999).

The eccentricity distribution $dN(e)$ increases toward $e \sim 1$, which is expected because all orbits started with $e > 0.995$. The tail extending to the moderate- and low-eccentricity values is due to the dynamically long-lived particles, whose orbits decouple from Jupiter and become circularized by P-R drag.

The inclination distribution is also interesting as it significantly deviates from the initial distribution with $dN(i) \propto \sin(i)di$ (Figure 5(c)). The retrograde orbits are more common than the prograde ones. The preference for retrograde orbits is probably caused by gravitational perturbations from Jupiter that are more effective on prograde orbits, because the encounter speeds are lower, and thus ΔVs are larger. The prograde particles should therefore have shorter dynamical lifetimes than the retrograde particles, which would explain their relative paucity in a steady state $dN(i)$ for $R < 5$ AU. Interestingly, however, the particles that decouple from Jupiter and reach $a \sim 1$ AU by P-R drag do not show a strong preference for retrograde orbits.

In addition, the steady state $dN(i)$ lacks orbits with $i \sim 90°$. We believe that this is a consequence of Kozai dynamics (e.g., Kozai 1962). It is well known that the initially near-polar orbits will suffer large oscillations of q driven by variations of the orbital angular momentum vector. Most of these orbits can therefore reach very low q values, where the particles will be destroyed by thermal effects. Indeed, by studying the orbital histories of particles that started with $i \sim 90°$, we found that most of these orbits had $q < 0.05$ AU prior to reaching $Q < 4$ AU.

The steady state distribution of orbital elements of $D = 300\,\mu$m particles is similar to the one discussed above. Instead of having a single peak at $a = 6$–7 AU, however, $dN(a)$ for $a > 5$ AU is more irregular showing many peaks and dips. Apparently, since the larger $D = 300\,\mu$m particles drift more slowly by P-R drag, they are more susceptible to capture in a large number of resonances (Liou et al. 1999). The second difference concerns $dN(e)$, which is slightly more clumped toward $e \sim 1$ for $D = 300\,\mu$m than for $D = 100\,\mu$m.

3.3. Radiants and Orbits of Particles Accreted by the Earth

The radiants of OCC particles are located near Earth's apex (Figure 6). This is logical because the retrograde OCC particles, which come from the apex direction, have much higher velocity relative to the Earth ($\sim$60 km s^{-1}) than particles on prograde orbits. The retrograde particles therefore also have, according to the usual $n\sigma v$ rule, rather large impact probabilities with the Earth. In addition, the ionization cutoff used here (Equation (9)) poses a rather strict limit on the mass of meteoroids that can be detected by SMRs at low speeds. For example, a $D = 100\,\mu$m particle with $m = 10^{-6}$ g and $v_g = 30$ km s^{-1} has $I = 0.01$, which is near or slightly above the detection limit of AMOR, and way below the detection limit of CMOR.

The model radiants form the south and north apex concentrations, just as observed (e.g., Jones & Brown 1993; Galligan & Baggaley 2005; Campbell-Brown 2008). The lack of radiants within $\sim 10°$ about the ecliptic is due to near absence of OCC meteoroids with $i \simeq 180°$ (see Figure 5(c)). The lack of radiants with $b > 50°$ (or $b < -50°$) is the consequence of the inclination distribution shown in Figure 5(c) that is depleted in orbits with $i \sim 90°$.

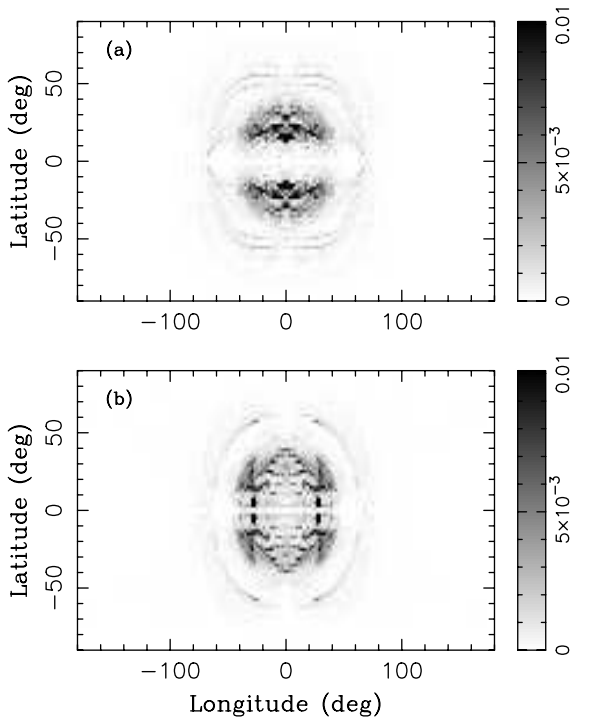

Figure 6. Radiants of OCC meteoroids determined in our model with $I^* = 0.01$: (a) $D = 100\,\mu$m and (b) $D = 300\,\mu$m. The north and south apex sources are clearly visible. In addition, the radiant distribution in panel (b) shows a ring structure centered at $(l, b) = (0, 0)$ and extending to $\simeq 60°$ in l and b. The high-frequency fluctuation of radiant density between neighbor bins is due to insufficient statistics and should be disregarded. The units of the side bar are arbitrary.

Most north (south) radiants fall into an area on the north (south) hemisphere that has the characteristic triangular or half-disk shape. For $D = 100\,\mu$m, the centers of radiant concentrations are at $b \simeq \pm 20°$. For $D = 300\,\mu$m, the centers are at $b \simeq \pm 25°$. This reflects the differences in $dN(i)$ between the populations of particles with $D = 100\,\mu$m and $D = 300\,\mu$m that we obtained in the model. For comparison, observations indicate that $b \simeq \pm 15°$ (e.g., Galligan & Baggaley 2005; Chau et al. 2007; Campbell-Brown 2008). In addition, the apex sources that we obtained in our model tend to be more stretched in both l and b than the observed ones.

While more modeling work will be needed to test things with a better statistic, the issues discussed above may indicate that a better fit to observations could be obtained if the retrograde source had inclinations closer to 180° than the bulk of OCC particles with $100° < i < 160°$. It is not clear how this could be achieved by tweaking the parameters of our model. Instead, clues such as these seem to highlight the importance of known HTCs. Indeed, the two prominent active HTCs, 1P/Halley and 55P/Tempel-Tuttle, both have $i \simeq 162°$. They would therefore be expected to produce apex sources closer to the ecliptic than the bulk of retrograde OCC particles (Figure 7).

An interesting feature in Figure 6(b) is the presence of a ring that stretches to $\pm 60°$ in longitude and latitude. A similar ring has been noted in Campbell-Brown (2008), who suggested that the region inside the ring can be depleted in meteor radiants, except for apex sources, because the retrograde meteoroids with radiants inside the ring would have shorter collisional lifetimes. Our simple collisional model cannot reproduce this effect because $\tau_{\rm coll}$ is independent of i (see Section 2.3.2). In

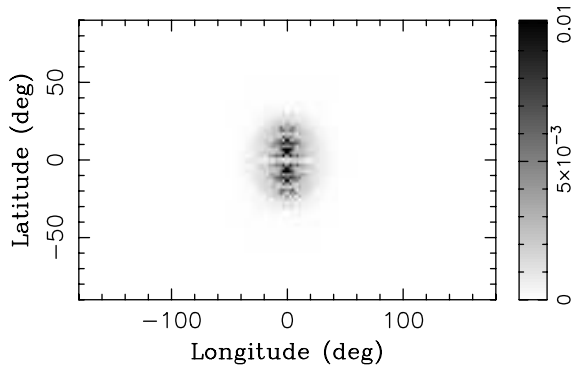

Figure 7. Same as Figure 6 but for $D = 100\,\mu$m particles released from 1P/Halley. The results for 55P/Tempel-Tuttle are similar.

addition, W09 suggested that the origin of the ring can be traced back to Kozai dynamics, which confines the allowed radiants of particles on high-inclination orbits. Here we confirm the W09 result by isolating particles that contribute to the ring, and checking on their orbital behavior.

The impact speed of OCC particles peaks at $v_g \simeq 60$ km s^{-1} (Figure 8 for $D = 100\,\mu$m and Figure 9 for $D = 300\,\mu$m), which is a nice match to observations of apex meteors (Galligan & Baggaley 2005; Campbell-Brown 2008).[7] The width of the peak also looks good (see Figure 13 in Campbell-Brown 2008). In comparison, using a population of meteoroids from 1P/Halley and 55P/Tempel-Tuttle, W09 obtained a peak at $v_g \simeq 70$ km s^{-1}, which is expected for large particles that have not evolved far from their parent comet orbit.

Figures 8 and 9 also show the model distributions of orbital elements of OCC meteoroids. Distributions $dN(a)$, now heavily weighted by the collision probability (see Figure 5), peak at $a \simeq 1$ AU and show a tail extending to $a > 2$ AU. The meteoroids in the peak have orbits that have strongly evolved by P-R drag. The model distributions for $D = 100\,\mu$m and $D = 300\,\mu$m are similar, except for a few wiggles produced by statistical fluctuations. Both provide a good match to the observed semimajor axis distribution of apex meteors (see Figure 11 in Galligan & Baggaley 2005).

According to our model, most apex meteors should have inclinations between $i \sim 100°$ and 180° (Figures 8(c) and 9(c)), which is also the range indicated by observations. Unlike $dN(i)$ measured by radars, which shows a broad peak centered at $i \sim 150°$–160°, our model $dN(i)$ is more spread and noisy. While part of this discrepancy could be blamed on insufficient statistics in our model, it may also point to a more fundamental problem.

The eccentricity distribution is puzzling. For both $D = 100\,\mu$m and $D = 300\,\mu$m, we obtained $dN(e)$ that raises toward $e \sim 1$. This trend is slightly more pronounced for $D = 300\,\mu$m (Figure 9(d)) than for $D = 100\,\mu$m (Figure 8(d)). W09, using selected HTCs for parent bodies of apex meteors, obtained $dN(e)$ that also peaked toward $e \sim 1$. In contrast, the observed apex meteors have nearly flat $dN(e)$ at $0.2 < e < 1$, and show a slight depletion for $e < 0.1$ (Figure 13 in Campbell-Brown 2008).

The cause of these differences is unclear. To obtain lower values of e in our model, the orbits would need to become more circularized by P-R drag before arriving to $a \sim 1$ AU. This could be achieved, for example, if more weight is given to particles starting with $q > 1$ AU. We confirm this by using $\gamma > 1$, but a detailed match to the observed eccentricity distribution remains elusive. A detailed analysis of this problem is left for future studies.

4. RELATIVE IMPORTANCE OF HELION/ANTIHELION AND APEX SOURCES

The observations of sporadic meteors show that the relative importance of helion/antihelion and apex sources depends on

[7] Note that observations by HPLA radars, such as AO or ALTAIR, measure the apex peak speed at $\simeq 55$ km s^{-1}.

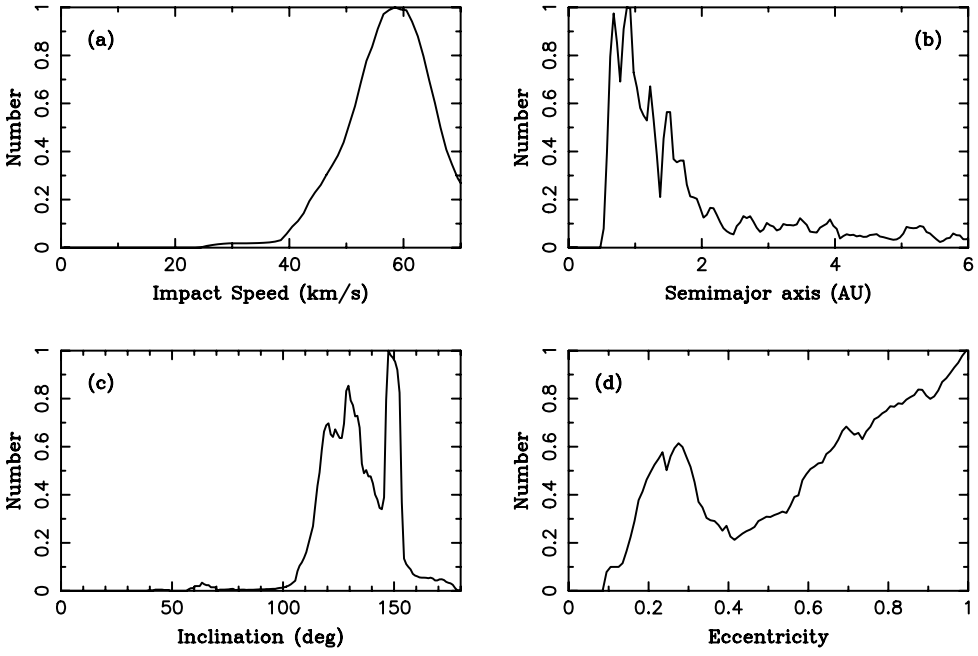

Figure 8. Orbital element distribution of model apex meteoroids: (a) v_g, (b) a, (c) i, and (d) e. Here we used OCC particles with $D = 100\,\mu$m and $I^* = 0.01$. The apex meteoroids were selected by using the following radiant cutoffs: $-40° < l < 40°$ and $-40° < b < 40°$.

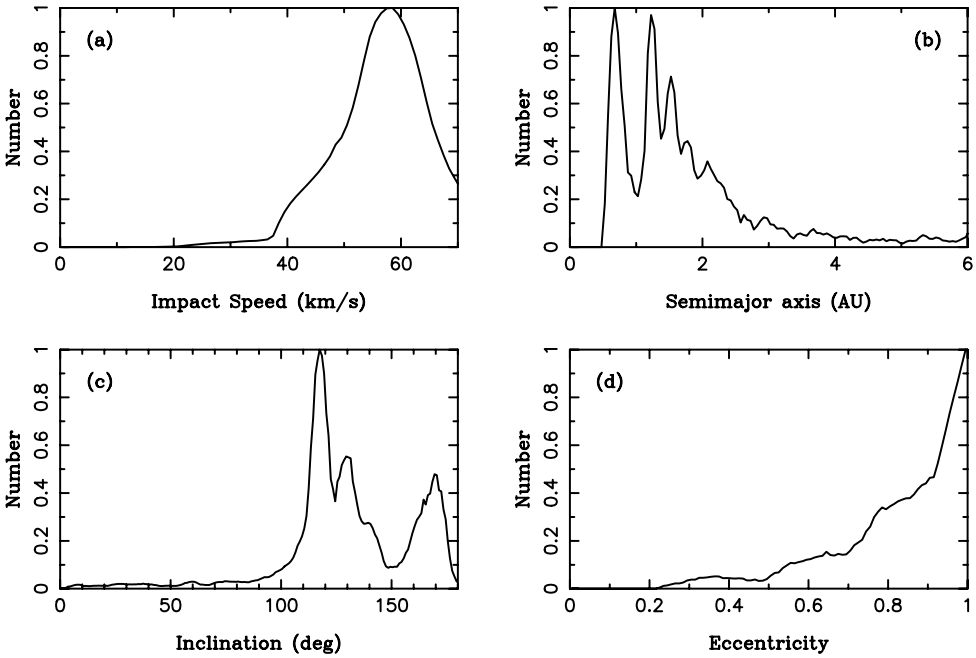

Figure 9. Same as Figure 8 but for $D = 300\,\mu$m OCC particles.

the sensitivity of the radar that is used to carry out such observations. The less sensitive SMRs with $I^* \sim 1$, such as the Harvard Radar Meteor Project (HRMP; Jones & Brown 1993; Taylor & Elford 1998) or CMOR, detect ~3–10 times more helion/antihelion meteors then apex meteors (see, e.g., Campbell-Brown 2008 for comparison of different radars). The more sensitive radars, such as AMOR with $I^* \sim 0.001$–0.01, on the other hand, detect a relatively larger number of apex meteors. Finally, the apex meteors are predominant in observations by the highly sensitive AO radar (e.g., Janches et al. 2003) because of their ability to detect small particles (Fentzke & Janches 2008; Fentzke et al. 2009).

This trend can be explained if the size frequency distribution (SFD) of apex meteoroids is steeper (i.e., if the number of meteoroids increases more sharply with decreasing size) than that of the helion/antihelion meteoroids because radars that are capable of detecting smaller meteoroids would then be expected to see many more apex meteors (Fentzke & Janches 2008). For example, the *initial* SFD of particles produced by disrupted OCCs (or HTCs) could be steeper than the one produced by the sources of the helion/antihelion meteoroids (presumably active and disrupted JFCs; W09; Nesvorný et al. 2010). While this is a possibility that cannot be ruled out by the existing data, there are also no indications that this might be true (McDonnell et al. 1987; Grün et al. 2001; Green et al. 2004; Reach et al. 2007).

We propose that the predominance of apex meteors in AO observations is caused by orbital dynamics of particles released from OCCs (or HTCs). Let us assume that the initial SFD of particles released from OCCs (or HTCs) is $dN_0(D) = N_0 D^{-\zeta} dD$. The SFD of meteoroids accreted by the Earth will then be

$$dN(D) = f_0 P_i N_0 D^{-\zeta} dD, \quad (13)$$

where f_0 is the fraction of particles that remain on bound orbits (see Section 2.1) and P_i is the impact probability of these particles on the Earth. Factor f_0 expresses the removal of small particles by radiation pressure (see Section 2.1). Thus, the size dependence of f_0 is such that it cannot increase the number of small particles relative to the large ones.[8]

Table 1 lists P_i and v_∞ for various sources. For example, the OCC particles with $D = 30\,\mu$m and $D = 300\,\mu$m have $P_i = 2 \times 10^{-6}$ and $P_i = 5 \times 10^{-7}$, respectively. This indicates that $dN(D)$ should have a *steeper* slope than $dN_0(D)$. Specifically, if $dN_0(D)$ can be approximated by $D^{-\zeta} dD$ for $D \sim 30$–$300\,\mu$m, where ζ is a constant, we find that $dN(D) \propto D^{-(\zeta+\delta)} dD$, where $\delta \sim 0.6$ for OCCs. This estimate was obtained with $0 \leqslant \gamma \leqslant 1$, $S_1 \sim S_2 \sim 0$, $q^* = 0.05$ AU, and initial $a \sim 10^3$ AU. The results for $S_2 = 1$, applicable if $\tau_{\rm coll}$ were ~10 times longer than in G85, and for HTCs are similar.

For comparison, W09 suggested that comet 2P/Encke (or an orbitally similar lost comet) is the main source of helion/antihelion meteors. We find that particles released from comet 2P/Encke have $P_i = 6 \times 10^{-5}$ for $D = 30\,\mu$m and $P_i = 2.3 \times 10^{-4}$ for $D = 300\,\mu$m (Table 1). If these estimates are representative for the sources of the helion/antihelion meteors, they suggest that the slope of $dN(D)$ should be *shallower* than that of $dN_0(D)$ ($\delta \sim -0.6$).

We therefore find that $dN(D)$ of apex meteoroids is expected to be steeper than that of helion/antihelion meteoroids, even if the initial SFD of particles released from the respective sources—JFCs and OCCs/HTCs—were similar. This effect is produced by orbital dynamics of particles starting on different initial orbits. As we discussed in Section 3.1, the Earth-impact record of OCC particles is mainly contributed by those particle that decouple from Jupiter. Since the decoupling efficiency, described by factor f_1 in Section 3.1, ramps up toward smaller D, the population of small OCC (or HTC) particles is enhanced, relative to large ones. This effect is weaker for JFC meteoroids, for which the correlation between f_1 and P_i is not as extreme. In the JFC case, the population of small particles accreted by

[8] Factor $f_0(D)$ could presumably be approximated by a step function with $f_0(D) = 0$ for $D < D^*$ and $f_0(D) = 1$ for $D > D^*$, where D^* is the critical diameter implied by Equation (2).

Table 1
The Earth Impact Probability, P_i, and Mean Impact Speed, $\langle v_\infty \rangle$, of Particles Released on Different Orbits

D (μm)	P_i (10^{-6})	$\langle v_\infty \rangle$ (km s^{-1})
OCCs		
10	4.6 (4.6)	52 (52)
30	1.9 (1.9)	47 (47)
100	1.0 (1.4)	46 (46)
300	0.5 (0.6)	55 (54)
1000	0.2 (0.3)	58 (58)
1P/Halley (HTC)		
10	57 (57)	60 (60)
30	100 (110)	59 (59)
100	80 (110)	59 (59)
300	24 (46)	65 (61)
1000	17 (22)	67 (67)
55P/Tempel-Tuttle (HTC)		
10	53 (53)	60 (60)
30	120 (120)	59 (59)
100	80 (120)	60 (59)
300	27 (51)	66 (61)
1000	16 (23)	68 (66)
2P/Encke (JFC)		
10	17 (17)	18.0 (18.0)
30	60 (60)	18.5 (18.5)
100	210 (220)	18.7 (18.4)
300	230 (340)	23.6 (22.0)
1000	120 (300)	30.5 (27.0)

Notes. For each particle's diameter, D, we give our best estimate values for the standard G85 τ_{coll} ($S_1 = S_2 = 0$), and for $S_1 = 0$ and $S_2 = 1$ (values in parenthesis). The longer collisional lifetime in the later case leads to the larger P_i values. The effect of disruptive collisions is significant for $D \gtrsim 300\,\mu$m.

the Earth is suppressed by their short P-R drag timescale, and consequently, lower P_i.

The magnitude of the SFD effects discussed above is just right to explain observations. If the ionization threshold I^* of AMOR is ~ 100 times lower than that of CMOR/HRMP, these more sensitive instruments are expected to detect meteoroids that are ~ 5 times smaller in size. If they detect 3–10 times more apex meteors than the helion/antihelion meteors (e.g., Campbell-Brown 2008), this would suggest that the SFD slope index difference between apex and helion/antihelion meteors is $\delta \sim 0.7$–1.4. We found $\delta \sim 1.2$ above, in good agreement with observations. Figure 10 illustrates the relative strength of sporadic meteor sources expected from our model.

5. CONCLUSIONS

We found that only a very small fraction, $f_1 \lesssim 10^{-4}$, of $D \gtrsim 1$ mm OCC particles can ever make it into the inner solar system. The relevance of these very large OCC particles to observations of sporadic meteors is therefore not obvious. The situation looks more favorable for OCC particles with $D \simeq 100$–$300\,\mu$m. These particles should survive the effects of radiation pressure, if released from returning OCCs at $R \gtrsim 4$–12 AU. Moreover, about 0.2%–1.5% avoid being collisionally disrupted or thermally destroyed, decouple from Jupiter, and finally spiral down to $a \sim 1$ AU, where their Earth-impact probability is increased by orders of magnitude.

We estimated that the overall probability of Earth impact per one particle released on bound orbit from the returning OCC

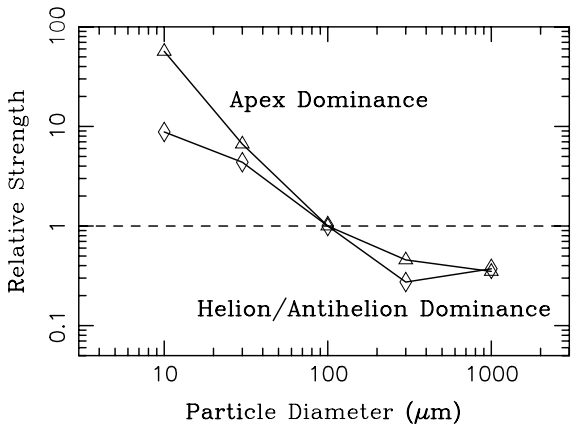

Figure 10. Expected relative strength of the apex and helion/antihelion sources as a function of particle size. The triangles (diamonds) show the result for OCC (1P/Halley) particles. We calculated the relative strength by dividing $P_i(D)$ listed in Table 1 for OCC (1P/Halley) particles (assumed here to represent the apex source) by $P_i(D)$ of 2P/Encke particles (assumed to represent the helion/antihelion source; W09). The $P_i(D)$ ratio is a proxy for the relative strength of meteor sources if $dN_0(D)$ of different initial populations had roughly the same shape. We arbitrarily normalized the ratio to 1 for particles with $D = 100\,\mu$m. As more sensitive radars detect smaller particles, they are expected see more apex meteors, because $P_i(D)$ of OCC (1P/Halley) particles increases while that of JFC particles drops.

is $P_i \sim 0.5$–1×10^{-6} for $D \simeq 100$–$300\,\mu$m. This is 50–80 times lower than P_i expected for particles released from HTCs such as 1P/Halley and 55P/Tempel-Tuttle, and 200–400 times lower than P_i expected for JFCs such as 1P/Encke. The OCC particles will therefore significantly contribute to the sporadic meteor complex only if the mass of material produced by disrupting OCCs is large enough to compensate for these factors. From L02, we can roughly estimate that ~ 5 returning OCCs disrupt per year producing the mass input of perhaps as much as $\sim 10^{18}$ g yr^{-1}, or 3×10^8 kg s^{-1}. Only a small fraction of this mass will end in bound particles with $D \simeq 100$–$300\,\mu$m. For comparison, the active JFCs produce ~ 300 kg s^{-1} (Reach et al. 2007).

We found that the SFD of apex meteoroids, presumably starting on highly eccentric orbits, is expected to be steeper than those of helion/antihelion meteoroids, even if their initial SFDs were similar. The steepening of the SFD slope of apex meteoroids results from the efficiency with which OCC/HTC meteoroids of different sizes decouple from Jupiter. This result has interesting implications for observations of sporadic meteors because it can explain why the north/south apex sources are more represented in observations of highly sensitive radars that are capable of detecting smaller meteoroids.

This article is based on work supported by the NASA's PG&G program. The work of D.V. was partially supported by the Czech Grant Agency (grant 205/08/0064) and the Research Program MSM0021620860 of the Czech Ministry of Education. The work of D.J. was partially supported by NSF Award AST 0908118. We thank W. F. Bottke for sharing with us his Öpik code, M. Campbell-Brown for useful discussions, and Tadeusz Jopek for a very helpful review of this article.

REFERENCES

Bottke, W. F., Nolan, M. C., Greenberg, R., & Kolvoord, R. A. 1994, Icarus, 107, 255
Burns, J. A., Lamy, P. L., & Soter, S. 1979, Icarus, 40, 1

Breiter, S., & Jackson, A. A. 1998, MNRAS, 299, 237
Campbell-Brown, M. D. 2008, Icarus, 196, 144
Čapek, D., & Borovička, J. 2009, Icarus, 202, 361
Chau, J. L., Woodman, R. F., & Galindo, F. 2007, Icarus, 188, 162
Choi, Y.-J., Weissman, P., Chesley, S., et al. 2006, CBET, 563, 1
Dermott, S. F., Grogan, K., Durda, D. D., et al. 2001, in Interplanetary Dust, ed. E. Grün, B. S. Gustafson, S. Dermott, & H. Fechtig (Berlin: Springer), 569
Dikarev, V., Grün, E., Baggaley, J., et al. 2005, Adv. Space Res., 35, 1282
Drolshagen, G., Dikarev, V., Landgraf, M., Krag, H., & Kuiper, W. 2008, Earth Moon Planets, 102, 191
Duschl, W. J., Gail, H.-P., & Tscharnuter, W. M. 1996, A&A, 312, 624
Dybczyński, P. A. 2001, A&A, 375, 643
Fentzke, J. T., & Janches, D. 2008, J. Geophys. Res. (Space Phys.), 113, 3304
Fentzke, J. T., Janches, D., & Sparks, J. J. 2009, J. Atmos. Sol.-Terr. Phys., 71, 653
Francis, P. J. 2005, ApJ, 635, 1348
Galligan, D. P., & Baggaley, W. J. 2004, MNRAS, 353, 422
Galligan, D. P., & Baggaley, W. J. 2005, MNRAS, 359, 551
Green, S. F., McDonnell, J. A. M., McBride, N., et al. 2004, J. Geophys. Res., 109, 12
Greenberg, R. 1982, AJ, 87, 184
Grün, E., Hanner, M. S., Peschke, S. B., et al. 2001, A&A, 377, 1098
Grün, E., Zook, H. A., Fechtig, H., & Giese, R. H. 1985, Icarus, 62, 244
Henning, T., & Mutschke, H. 1997, A&A, 327, 743
Janches, D., & Chau, J. L. 2005, J. Atmos. Sol.-Terr. Phys., 67, 1196
Janches, D., Close, S., & Fentzke, J. T. 2008, Icarus, 193, 105
Janches, D., Heinselman, C. J., Chau, J. L., Chandran, A., & Woodman, R. 2006, J. Geophys. Res. (Space Phys.), 111, 7317
Janches, D., Nolan, M. C., Meisel, D. D., et al. 2003, J. Geophys. Res. (Space Phys.), 108, 1222
Jenniskens, P. 2008, Earth Moon Planets, 102, 505
Jones, J., & Brown, P. 1993, MNRAS, 265, 524
Jones, J., Campbell, M., & Nikolova, S. 2001, in Meteoroids 2001 Conference, ed. B. Warmbein (ESA Special Publication, Vol. 495; Noordwijk: ESA), 575
Kasuga, T., Yamamoto, T., Kimura, H., & Watanabe, J. 2006, A&A, 453, L17
Kessler-Silacci, J. E., Dullemond, C. P., Augereau, J.-C., et al. 2007, ApJ, 659, 680
Kozai, Y. 1962, AJ, 67, 591
Kresak, L. 1976, Bull. Astron. Inst. Czech., 27, 35
Levison, H. F., & Duncan, M. J. 1994, Icarus, 108, 18
Levison, H. F., Morbidelli, A., Dones, L., et al. 2002, Science, 296, 2212
Liou, J.-C., Zook, H. A., & Jackson, A. A. 1999, Icarus, 141, 13
McDonnell, J. A. M., Evans, G. C., Evans, S. T., et al. 1987, A&A, 187, 719
Moro-Martín, A., & Malhotra, R. 2002, AJ, 124, 2305
Nesvorný, D., Jenniskens, P., Levison, H. F., et al. 2010, ApJ, 713, 816
Nesvorný, D., Vokrouhlický, D., Bottke, W. F., & Sykes, M. 2006, Icarus, 181, 107
Oort, J. H. 1950, Bull. Astron. Inst. Neth., 11, 91
Öpik, E. J. 1951, Proc. R. Ir. Acad. A, 54, 165
Reach, W. T., Kelley, M. S., & Sykes, M. V. 2007, Icarus, 191, 298
Robertson, H. P. 1937, MNRAS, 97, 423
Steel, D. 1996, Space Sci. Rev., 78, 507
Steel, D. I., & Elford, W. G. 1986, MNRAS, 218, 185
Taylor, A. D., & Elford, W. G. 1998, Earth Planets Space, 50, 569
Wetherill, G. W. 1967, J. Geophys. Res., 72, 2429
Whipple, F. L. 1951, ApJ, 113, 464
Whipple, F. L., & Gossner, J. L. 1949, ApJ, 109, 380
Wiegert, P., & Tremaine, S. 1999, Icarus, 137, 84
Wiegert, P., Vaubaillon, J., & Campbell-Brown, M. 2009, Icarus, 201, 295
Wisdom, J., & Holman, M. 1991, AJ, 102, 1528
Wyatt, S. P., & Whipple, F. L. 1950, ApJ, 111, 134
Younger, J. P., Reid, I. M., Vincent, R. A., Holdsworth, D. A., & Murphy, D. J. 2009, MNRAS, 398, 350

Paper D

The Astrophysical Journal, 743:129 (16pp), 2011 December 20 doi:10.1088/0004-637X/743/2/129

DYNAMICAL MODEL FOR THE ZODIACAL CLOUD AND SPORADIC METEORS

David Nesvorný[1], Diego Janches[2], David Vokrouhlický[1,3], Petr Pokorný[1,3], William F. Bottke[1], and Peter Jenniskens[4]
[1] Department of Space Studies, Southwest Research Institute, 1050 Walnut St., Suite 300, Boulder, CO 80302, USA
[2] Space Weather Laboratory, Code 674, GSFC/NASA, Greenbelt, MD 20771, USA
[3] Institute of Astronomy, Charles University, V Holešovičkách 2, CZ-18000, Prague 8, Czech Republic
[4] Carl Sagan Center, SETI Institute, 515 N. Whisman Road, Mountain View, CA 94043, USA
Received 2011 May 31; accepted 2011 September 9; published 2011 November 29

ABSTRACT

The solar system is dusty, and would become dustier over time as asteroids collide and comets disintegrate, except that small debris particles in interplanetary space do not last long. They can be ejected from the solar system by Jupiter, thermally destroyed near the Sun, or physically disrupted by collisions. Also, some are swept by the Earth (and other planets), producing meteors. Here we develop a dynamical model for the solar system meteoroids and use it to explain meteor radar observations. We find that the Jupiter Family Comets (JFCs) are the main source of the prominent concentrations of meteors arriving at the Earth from the helion and antihelion directions. To match the radiant and orbit distributions, as measured by the Canadian Meteor Orbit Radar (CMOR) and Advanced Meteor Orbit Radar (AMOR), our model implies that comets, and JFCs in particular, must frequently disintegrate when reaching orbits with low perihelion distance. Also, the collisional lifetimes of millimeter particles may be longer ($\gtrsim 10^5$ yr at 1 AU) than postulated in the standard collisional models ($\sim 10^4$ yr at 1 AU), perhaps because these chondrule-sized meteoroids are stronger than thought before. Using observations of the *Infrared Astronomical Satellite* to calibrate the model, we find that the total cross section and mass of small meteoroids in the inner solar system are (1.7–3.5) $\times 10^{11}$ km^2 and $\sim 4 \times 10^{19}$ g, respectively, in a good agreement with previous studies. The mass input required to keep the zodiacal cloud in a steady state is estimated to be $\sim 10^4$–10^5 kg s^{-1}. The input is up to $\sim$10 times larger than found previously, mainly because particles released closer to the Sun have shorter collisional lifetimes and need to be supplied at a faster rate. The total mass accreted by the Earth in particles between diameters $D = 5$ μm and 1 cm is found to be $\sim$15,000 tons yr^{-1} (factor of two uncertainty), which is a large share of the accretion flux measured by the Long Term Duration Facility. The majority of JFC particles plunge into the upper atmosphere at $<$15 km s^{-1} speeds, should survive the atmospheric entry, and can produce micrometeorite falls. This could explain the compositional similarity of samples collected in the Antarctic ice and stratosphere, and those brought from comet Wild 2 by the *Stardust* spacecraft. Meteor radars such as CMOR and AMOR see only a fraction of the accretion flux ($\sim$1%–10% and $\sim$10%–50%, respectively), because small particles impacting at low speeds produce ionization levels that are below these radars' detection capabilities.

Key words: comets: general – meteorites, meteors, meteoroids – zodiacal dust

1. INTRODUCTION

The zodiacal cloud (ZC) is a circumsolar disk of small debris particles produced by asteroid collisions and comets. Nesvorný et al. (2010, hereafter N10) developed a dynamical model for particle populations released by asteroids and comets, and used the model to determine the relative contribution of asteroid and cometary material to the ZC. They found that the mid-infrared (MIR) emission from particles produced in the asteroid belt is mostly confined to within latitudes $b \lesssim 30^\circ$ of the ecliptic. Conversely, the ZC has a broad latitudinal distribution so that strong thermal emission is observed even in the direction to the ecliptic poles (e.g., Hauser et al. 1984; Kelsall et al. 1998). This shows that asteroidal particles can represent only a small fraction of the ZC.

Based on a comparison of the model with observations of the *Infrared Astronomical Satellite* (*IRAS*), N10 proposed that $\gtrsim$90% of the ZC's emission at MIR wavelengths comes from dust grains released by Jupiter Family Comets (JFCs), and $\lesssim$10% comes from the Oort Cloud Comets (OCCs), Halley-Type Comets (HTCs), and/or asteroid collisions. In addition, it was found that the mass input required to keep the ZC in a steady state largely exceeds the mass loss in JFCs due to their normal activity (e.g., Reach et al. 2007). To resolve this problem, N10 suggested that the dominant mass fraction is supplied to the ZC by spontaneous *disruptions/splittings* of JFCs (e.g., Fernández 2005; Di Sisto et al. 2009).

N10's model implies that the orbits of small meteoroids (diameters $D \lesssim 100$ μm) released by JFCs become significantly circularized by Poynting–Robertson (P-R) drag before they can reach $a \sim 1$ AU and contribute to the Earth impact record. These particles, at the time of their accretion by the Earth, should thus have relatively low impact speeds ($v < 20$ km s^{-1}), low eccentricities, and $a \sim 1$ AU. The large JFC particles ($D \gtrsim 1$ mm), on the other hand, should have a broader distribution of impact speeds, large eccentricities, and $a \sim$ 2–4 AU, mainly because they have presumably short collisional lifetimes (Grun et al. 1985, hereafter G85), and disrupt before they can significantly evolve by P-R drag. As we discuss below, these results appear to be at odds with the observations of sporadic meteors.

Meteors are produced by small interplanetary particles also known as the *meteoroids*. Based on meteor data, the meteoroids can be divided into two groups: sporadic meteoroids and meteoroid streams. The meteoroid streams are prominent concentrations of particles with similar orbits (Whipple 1951). They are thought to be produced by particles released by active and recently (less than a few thousand years ago) disrupted comets

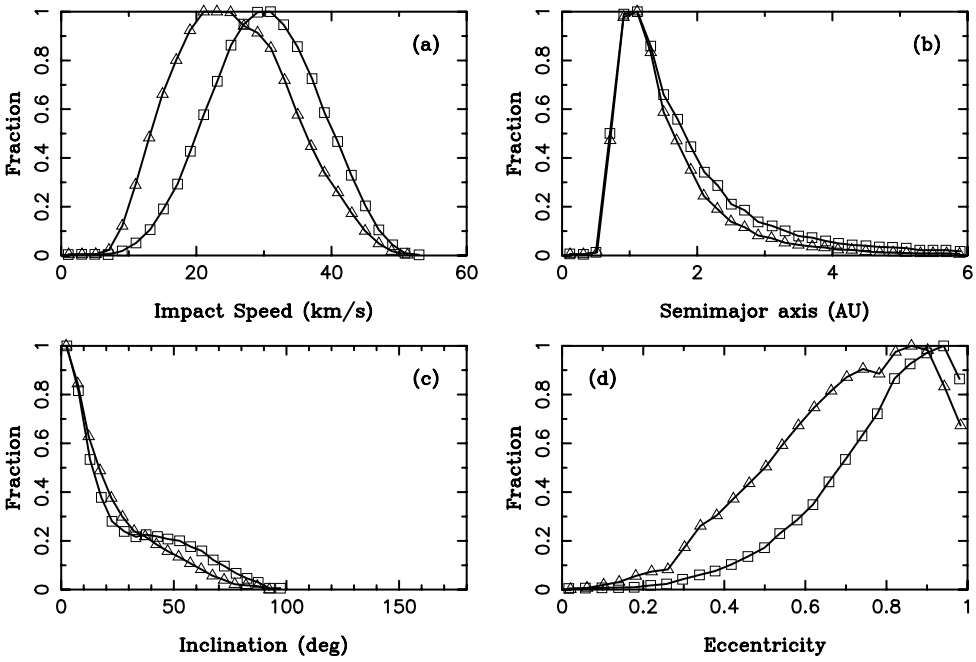

Figure 1. Distributions of impact speeds and orbits of prograde antihelion meteors measured by the Advanced Meteor Orbit Radar (AMOR). According to Galligan & Baggaley (2005), the antihelion meteors were selected using a broad radiant cutoff ($20° < l < 120°$, in our definition of longitude—see Section 2.6— and no condition on b). The squares label the raw distributions obtained by AMOR. The distributions labeled by triangles were corrected for the atmospheric interference and Faraday rotation. The helion meteors, not shown here, have corrected distributions very similar to those plotted here. The impact speeds in panel (a) include effects of the gravitational focusing by Earth. The heliocentric orbital elements shown in panels (b), (c), and (d) do not include these effects. All distributions were normalized to reach 1 at their maximum. Adapted from Figure 8 in Galligan & Baggaley (2005).

(Jenniskens 2008). Sporadic meteoroids are those particles that have evolved significantly from their parent body so that they are no longer easily linked to that parent, or to other meteoroids from the same parent. Notably, the time-integrated flux of meteors at Earth is dominated by about a factor of ~10 by sporadics (Jones & Brown 1993).

The radiant distribution of sporadic meteors shows several concentrations on the sky known as the helion/antihelion, north/south apex, and north/south toroidal sources (e.g., Campbell-Brown 2008, and the references therein). The prominent helion/antihelion source is the concentration of meteors near the helion and antihelion directions. These meteors are believed to originate from the same population of meteoroids. The two groups differ in impact direction because some particles will impact before their perihelion passage, thus producing meteors with the antihelion radiants, while others will impact after their perihelion passage, producing meteors with the helion radiants.

The helion/antihelion meteoroids have a measured impact speed distribution that peaks at $v \simeq 20$–30 km s^{-1}, $a \sim 1$ AU with a tail to 3 AU and beyond, $e > 0.3$, and low inclinations (Figure 1). Wiegert et al. (2009, hereafter W09) developed a dynamical model to explain these observations. They found that particles released by JFCs, mainly by 2P/Encke, provide the best match to the observed properties of the helion/antihelion source (see also Jones et al. 2001).[5]

Comet 2P/Encke has an orbit that is quite unique among JFCs ($a = 2.2$ AU, $e = 0.85$, $i = 11.^\circ8$), because its aphelion distance lies well within Jupiter's orbit ($Q = a(1 + e) = 4.1$ AU). The orbit is relatively stable as it is not affected by close encounters with Jupiter.[6] In addition, the comet has a very low perihelion distance ($q = a(1 - e) = 0.34$ AU) and is expected to fall into the Sun in 10^5–10^6 years (Levison & Duncan 1994), if it physically survived that long. Finally, 2P/Encke is the source of several meteor streams known as Taurids (Whipple 1939), suggesting, as argued in W09, that it can also be an important source of sporadic meteoroids at 1 AU.

The difference between W09 and N10 lies, in part, in different assumptions on the initial distribution of meteoroids. In W09, the meteoroids launched from 2P/Encke initially had a low perihelion distance so that even after having evolved by P-R drag to $a \sim 1$ AU, they still retained a relatively large eccentricity. In N10, on the other hand, most meteoroids were released with $q \sim 2.5$ AU, and greater effects of P-R drag were thus required for particles to reach 1 AU. In addition, N10 did not properly include the detection efficiency of meteor radars in their model. This is a central issue, because most meteor radars are only capable of detecting the relatively large and/or fast meteoroids, and may thus produce measurements of the Earth accretion flux that are heavily biased by their detection capabilities.

The agreement between the W09 model and observations of helion/antihelion meteors is not perfect. For example, the W09 model produced tightly clustered distributions of v and e about $v = 30$ km s^{-1} and $e = 0.85$, and lacked orbits with $a \gtrsim 2.5$ AU (Figure 2 in W09). The observed speeds and eccentricities have larger spreads, perhaps indicating that the helion/antihelion meteors are produced not by one, but many parent comets with a broad distribution of orbits, including those with $a \gtrsim 2.5$ AU. The inclination distribution produced in W09

[5] The north/south apex meteors are most likely produced by meteoroids released from retrograde HTCs and/or OCCs (Jones et al. 2001; W09; Nesvorný et al. 2011). The origin of the toroidal source is unknown.

[6] The dynamical origin of 2P/Encke has yet to be explained, but probably requires non-gravitational forces produced by jets of material escaping from the comet's surface, and gravitational perturbations from the terrestrial planets (Valsecchi 1999).

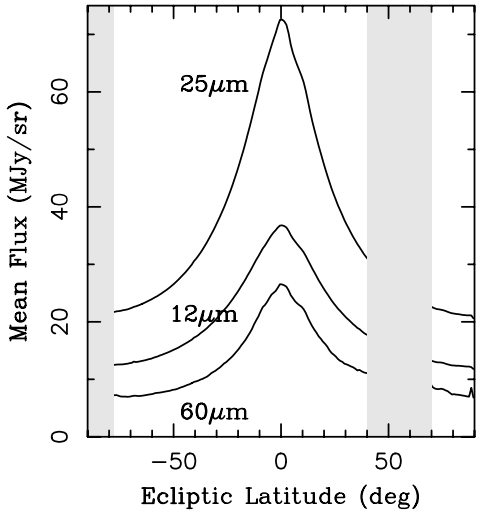

Figure 2. Mean ZC profiles obtained by *IRAS* in 12, 25, and 60 μm wavelengths. To make these profiles, the selected *IRAS* scans obtained with the $\simeq 90^\circ$ solar elongation were centered at the ecliptic, smoothed by a low-pass filter, and combined together (see N10 for details). The gray rectangles at $b < -78^\circ$ and $40^\circ < b < 70^\circ$ block the latitude range where the mean fluxes were significantly affected by the galactic plane emission. We do not use the excluded range in this work. The uncertainties of the mean flux values are not shown here; they are too small to clearly appear in the plot. *IRAS* observations at 100 μm, not shown here, are less useful for probing the thermal radiation of dust particles in the inner solar system, because of the strong interference with the galactic and extragalactic emission at these wavelenghts.

does not have the resolution needed for a careful comparison with data, but it also seems to be narrower than the observed distribution.

While 2P/Encke, or orbitally similar comets, can be an important source for helion/antihelion meteors, comet 2P/Encke itself cannot be a single dominant source of the ZC. This is because studies of the ZC indicate that $\sim$1000 kg s^{-1} of material need to be injected into interplanetary space to keep the ZC in a steady state (e.g., Leinert et al. 1983, N10). Also, according to N10, the present mass of the inner ZC at <5 AU is ~ 1–2×10^{19} g, which is roughly equivalent to that of a 25 km diameter body. For comparison, the mass loss in comet 2P/Encke is only $\sim$26 kg s^{-1}, based on observations of its dust trail (Reach et al. 2007), and the diameter of the nucleus is $\simeq$4.8 km (Fernández et al. 2000; Boehnhardt et al. 2008).

According to N10, the dominant mass fraction is supplied to the ZC by spontaneous disruptions/splittings of JFCs. Since meteoroids in the ZC are also expected to produce meteors, the meteor observations discussed above can place important constraints on the ZC's origin. To take advantage of these constraints, and motivated by the results discussed above, we modify N10's model to include a q-dependent meteoroid production rate,[7] and account for the detection efficiency of meteor surveys. We also improve N10's model to consider a continuous Size Frequency Distribution (SFD) of particles, and more precisely parameterize their collisional disruption in space. We show that, with these modifications of the N10 model, the results match available constraints. We describe the new model in Section 2. The results are reported in Section 3. We estimate the ZC's cross section and mass, meteoroid production rate required to keep the ZC in a steady state, and the terrestrial accretion rate of interplanetary dust.

2. MODEL

Our model includes the following parts: (1) particles of different sizes are released from JFCs (Section 2.1), (2) their orbits evolve under the influence of gravitational and radiation forces (Section 2.2), (3) some particles are thermally or collisionally destroyed (Section 2.3), (4) while in space, particles emit thermal radiation (Section 2.4), which (5) is detected by a telescope observing at MIR wavelengths (Section 2.5), and (6) a small fraction of the initial particle population is accreted by the Earth, producing meteors (Section 2.6). We describe components (1)–(6) below.

Procedures described in Sections 2.5 and 2.6 are mainly required because the raw particle distributions obtained from our numerical integrations of orbits in Section 2.2 do not have a sufficient resolution. We use analytical methods to enhance the resolution in a way that is suitable for (5) and (6).

2.1. Initial Orbits

We only consider JFCs in this paper, because previous works showed that they are the main source of the ZC particles and helion/antihelion meteors (e.g., Jones et al. 2001; W09; N10). The asteroid meteoroids have low impact speeds and are not detected by meteor radars. The meteoroids released from long-period comets contribute to apex meteors and are not modeled here (see Nesvorný et al. 2011 for a discussion of apex meteors).

The orbital distribution of JFCs was taken from Levison & Duncan (1997, hereafter LD97), who followed the orbital evolution of bodies originating in the Kuiper belt as they are scattered by planets, and evolve in small fractions into the inner solar system. For each critical perihelion distance, q^*, we selected bodies from LD97's simulations when they reached $q < q^*$ for the first time. Particles were released from these source orbits.[8] We used 10 values of q^* equally spaced between 0.25 AU and 2.5 AU, particles with $D = 10$, 30, 100, 300, 1000, and 3000 μm, which should cover the interesting range of sizes, and particle density $\rho = 2$ g cm^{-3}. Our tests show that this size resolution is adequate because the orbital dynamics of, say, a $D = 150\,\mu$m particle is similar to that of a $D = 100\,\mu$m particle. The results for a continuous range of sizes were obtained by interpolation. Varying particle density has only a small effect on their orbital dynamics. Ten thousand particles were released for each q^* and D for the total of 0.6 million of the initial orbits.

Upon their release from the parent object, particles will feel the effects of radiation pressure. These effects can be best described by replacing the mass of the Sun, $m_\odot$, by $m_\odot(1-\beta)$,

[7] Direct evidence for JFC disruptions at small heliocentric distances comes from the comparison of dynamical models of JFCs, which follow their transport from the trans-Neptunian region to the inner solar system, with observations (e.g., Levison & Duncan 1997; Di Sisto et al. 2009). If the radial density of JFCs expected from the dynamical model, assuming no disruptions, is normalized so that it matches the observed (complete) sample of active comets with $q \simeq 1.5$ AU, it becomes apparent that the model density profile drops far too slowly for $q < 1.5$ AU to match observations. This means that the comets with small q values must disappear, due to physical effects, more quickly than those with large q values. To match the observed profile, Di Sisto et al. (2009) suggested that the disruption probability of JFCs scales with q as $q^{-\zeta}$, where $\zeta \simeq 0.5$–1.

[8] Note that this method does not properly account for the possibility that JFCs lose mass gradually by recurrent splitting events. For example, Di Sisto et al. (2009) assumed that the splitting events occur with certain frequency, considered to be a free parameter, and that a fixed mass fraction, also a free parameter, is lost in each event. Such a model may be physically more appropriate, but has more free parameters.

with β given by

$$\beta = 5.7 \times 10^{-5} \frac{Q_{\rm pr}}{\rho s} \quad (1)$$

where the particle's radius $s = D/2$ and ρ are in cgs units. Pressure coefficient $Q_{\rm pr}$ can be determined using the Mie theory (Burns et al. 1979). We set $Q_{\rm pr} = 1$, which corresponds to the geometrical optics limit, where s is much larger than the incident-light wavelength. Note that all particles considered here are large enough to stay on bound heliocentric orbits after their release (see, e.g., Nesvorný et al. 2011).

In Section 3, we combine the results obtained with different q^* and D to mimic the continuous distributions $dN(q)$ and $dN(D)$. This is different from N10 where the source particle distributions were parameterized by the "fading time," particle production rate was assumed to be q-independent, and $dN(D)$ was approximated by single size. Here we consider $dN(q)$ and $dN(D)$ that can be approximated by simple power laws. For $dN(q)$, we thus have $dN(q) \propto q^\gamma dq$, where γ is a free parameter. For $dN(D)$, we have $dN(D) = N_0 D^{-\alpha} dD$, where N_0 is a normalization constant and α is the usual slope index (at source). Alternatively, we use the two-slope SFD with $dN(D) \propto D^{-\alpha_1} dD$ for $D < D^*$ and $dN(D) \propto D^{-\alpha_2} dD$ for $D > D^*$, where α_1, α_2, and D^* are free parameters.

Parameter γ can be inferred from the number of JFCs found at each q, and their disruption probability as a function of q. If the former can be approximated by q^ξ, where $\xi \sim 0.5$ (LD97; Di Sisto et al. 2009), and the latter is proportional to $q^{-\zeta}$, where $\zeta \simeq 0.5$–1 (Di Sisto et al. 2009), it would be expected that $\gamma = \xi - \zeta \sim -0.5$–0. We use $\gamma = 0$ as our starting value, and test the sensitivity of results for $\gamma < 0$ and $\gamma > 0$. As for $dN(D)$, we set $\alpha \sim 4$ for the whole size range, as motivated by meteor radar observations (e.g., Galligan & Baggaley 2004), or $D^* \sim 100\,\mu$m, $\alpha_1 < 3$ and $\alpha_2 > 4$, as motivated by space impact experiments (e.g., Love & Brownlee 1993). Given the various uncertainties of these measurements (see, e.g., Mathews et al. 2001), we also test $D^* < 100\,\mu$m and $D^* > 100\,\mu$m.

2.2. Orbit Integration

The particle orbits were numerically integrated with the `swift_rmvs3` code (Levison & Duncan 1994), which is an efficient implementation of the Wisdom–Holman map (Wisdom & Holman 1991) and which, in addition, can deal with close encounters between particles and planets. The radiation pressure and P-R drag forces were inserted into the Keplerian and kick parts of the integrator, respectively. The change to the Keplerian part was trivially done by substituting $m_\odot$ by $m_\odot(1-\beta)$. We assumed that the solar-wind drag force has the same functional form as the P-R term and contributes by 30% to the total drag intensity.

The code tracks the orbital evolution of a particle that revolves around the Sun and is subject to the gravitational perturbations of seven planets (Venus to Neptune; the mass of Mercury was added to the Sun) until the particle impacts a planet, is ejected from the solar system, evolves to within 0.05 AU from the Sun, or the integration time reaches 5 Myr. We removed particles that evolved to $R < 0.05$ AU, because the orbital period for $R < 0.05$ AU was not properly resolved by our one-day integration time step.[9] The particle orbits were recorded at 1000 yr time intervals to be used for further analysis.

[9] We tested an integration time step of 0.3 day. The results were essentially identical to those obtained with the one-day time step.

2.3. Physical Effects

The solar system meteoroids can be destroyed by collisions with other particles and by solar heating that can lead to sublimation and vaporization of minerals. Here we explain how we parameterize these processes in our model.

The JFC particles will rapidly lose their volatile ices. We do not model the volatile loss here. The remaining grains will be primarily composed from amorphous silicates and will survive down to very small heliocentric distances. Following Moro-Martín & Malhotra (2002), Kessler-Silacci et al. (2007), and others, we adopt a simple criterion for the silicate grain destruction. We assume that they are thermally destroyed (sublimate, vaporize) when the grain temperature reaches $T \geqslant 1500$ K.

Using the optical constants of amorphous pyroxene of approximately cosmic composition (Henning & Mutschke 1997), we find that a dark $D \gtrsim 100\,\mu$m grain at R has the equilibrium temperature within 10 K of a black body, $T \simeq 280/\sqrt{R}$ K. According to our simple destruction criterion, $T \geqslant 1500$ K, the silicate grains should thus be removed when reaching $R \lesssim 0.035$ AU. On the other hand, the smallest particles considered in this work ($D = 10\,\mu$m) have $T = 1500$ K at $R \simeq 0.05$ AU. Thus, we opted for a simple criterion where particles of all sizes were instantly destroyed and were not considered for statistics, when they reached $R \leqslant 0.05$ AU. Note that, by design, this limit is the same as the one imposed by the integration time step (Section 2.2).

The collisional lifetime of meteoroids, $\tau_{\rm coll}$, was taken from G85. It was assumed to be a function of particle mass, m, and orbital parameters, mainly a and e. For example, for a circular orbit at 1 AU, particles with $D = 100\,\mu$m and 1 mm have $\tau^*_{\rm coll} = 1.5 \times 10^5$ yr and 7.3×10^3 yr, respectively, where $\tau^*_{\rm coll}$ denotes the collisional lifetime from G85. Also, $\tau^*_{\rm coll}$ increases with a. To cope with the uncertainty of the G85's model, we introduced a free parameter, S, so that $\tau_{\rm coll} = S\tau^*_{\rm coll}$. Values $S > 1$ increase $\tau_{\rm coll}$ relative to $\tau^*_{\rm coll}$, as expected, for example, if particles were stronger than assumed in G85, or if the measured impact fluxes were lower (e.g., Dikarev et al. 2005; Drolshagen et al. 2008). See Nesvorný et al. (2011) for a fuller description.

Collisional disruption of particles was taken into account during processing the output from the numerical integration described in Section 2.2. To account for the stochastic nature of breakups, we determined the breakup probability $p_{\rm coll} = 1 - \exp(-h/\tau_{\rm coll})$, where $h = 1000$ yr is the output interval, and $\tau_{\rm coll}$ was computed individually for each particle's orbit. The code then generated a random number $0 \leqslant x \leqslant 1$ and eliminated the particle if $x < p_{\rm coll}$.

We caution that our procedure does not take into account the small debris fragments that are generated by disruptions of larger particles. Instead, all fragments are removed from the system. This is an important approximation whose validity needs to be tested in the future.

2.4. Thermal Emission of Particles

Meteoroids were assumed to be isothermal, rapidly rotating spheres. The absorption was assumed to occur into an effective cross section πs^2, and emission out of $4\pi s^2$. The infrared flux density (per wavelength interval $d\lambda$) per unit surface area at distance r from a thermally radiating particle with radius s is

$$F_\lambda = \epsilon(\lambda, s) B(\lambda, T) \frac{s^2}{r^2} \quad (2)$$

where ϵ is the emissivity and $B(\lambda, T)$ is the energy flux at $(\lambda, \lambda + d\lambda)$ per surface area from a black body at temperature T:

$$B(\lambda, T) = \frac{2\pi hc^2}{\lambda^5} \left[e^{hc/\lambda kT} - 1\right]^{-1}. \quad (3)$$

In this equation, $h = 6.6262 \times 10^{-34}$ J s is the Planck constant, $c = 2.99792458 \times 10^8$ m s^{-1} is the speed of light, and $k = 1.3807 \times 10^{-23}$ J K^{-1} is the Boltzmann constant.

Since our model does not include detailed emissivity properties of dust grains at different wavelengths, we set the emissivity at 25 μm to be 1 and fit for the emissivities at 12 and 60 μm. We found that the relative emissivities at 12 and 60 μm that match the data best are 0.70–0.75 and 0.95–1, respectively. Such a variability of MIR emissivity values at different wavelengths is expected for small silicate particles with some carbon content. $T(R)$ was set to be $280/\sqrt{R}$ K, as expected for dark $D \gtrsim 10\,\mu$m particles. See Nesvorný et al. (2006) for a more precise treatment of $\epsilon(\lambda, s)$ and $T(R)$ for dust grains composed of different materials.

2.5. MIR Observations

To compare our results with *IRAS* observations illustrated in Figure 2,[10] we developed a code that models thermal emission from distributions of orbitally evolving particles and produces infrared fluxes that a space-borne telescope would detect depending on its location, pointing direction and wavelength. See Nesvorný et al. (2006) for a detailed description of the code.

In brief, we define the brightness integral along the line of sight of an infrared telescope (defined by fixed longitude l and latitude b of the pointing direction) as

$$\int_{a,e,i} da de di \int_0^\infty dr\, r^2 \int_D dD\, F_\lambda(D, r) N(D; a, e, i) K(R, L, B) \quad (4)$$

where r is the distance from the telescope, $F_\lambda(D, r)$ is the infrared flux (evaluated at the effective wavelength of the telescope's system) per unit surface area at distance r from a thermally radiating particle with diameter D. $K(R, L, B)$ defines the spatial density of particles in the Sun-centered coordinates as a function of R, ecliptic longitude, L, and latitude, B. $N(D, a, e, i)$ is the number of particles having effective diameter D and orbits with a, e, and i.

We evaluate the integral in Equation (4) by numerical renormalization (see Nesvorný et al. 2006). $F_\lambda(D, r)$ is calculated as described in Section 2.4. $N(D, a, e, i)$ is obtained from our numerical simulations (Section 2.2). $K(R, L, B)$ uses analytic expressions for the spatial distribution of particles with fixed a, e, and i, and randomized orbital longitudes (Kessler 1981).

We assume that the telescope is located at $(x_t = r_t \cos\phi_t,\ y_t = r_t \sin\phi_t,\ z_t = 0)$ in the Sun-centered reference frame with $r_t = 1$ AU. Its viewing direction is defined by a unit vector with components (x_v, y_v, z_v). In Equation (4), the pointing vector can be also conveniently defined by longitude l and latitude b of the pointing direction, where $x_v = \cos b \cos l$, $y_v = \cos b \sin l$, and $z_v = \sin b$. We fix the solar elongation $l_\odot = 90°$, so that $l = \phi_t + 90°$, and calculate the thermal flux of various particle populations as a function of b and wavelength. The model brightness profiles at 12, 25, and 60 μm are then compared with the mean *IRAS* profiles shown in Figure 2.

2.6. Model for Meteor Radar Observations

We used the Öpik theory (Öpik 1951) to estimate the expected terrestrial accretion rate of JFC particles in our model. Wetherill (1967), and later Greenberg (1982), improved the theory by extending it more rigorously to the case of two eccentric orbits. Here we used a computer code that employs Greenberg's formalism (Bottke et al. 1994).[11]

We modified the code to compute the radiants of the impacting particles. In doing so we properly accounted for all impact configurations and weighted the results by the probability with which each individual configuration occurs, including focusing. The radiants were expressed in the coordinate system, where longitude l was measured from the Earth's apex in counterclockwise direction along the Earth's orbit, and latitude b was measured relative to the Earth's orbital plane. Note that our definition of longitude differs from the one more commonly used for radar meteors, where the longitude is measured from the helion direction. The radiants were calculated before the effects of gravitational focusing were applied.

The meteor radars use different detection methods (i.e., trail versus echo)[12] and have different sensitivities. Their detection efficiency is mainly a function of the particle's mass and speed, but it also depends on a number of other parameters discussed, for example, in Janches et al. (2008). Following W09, we opt for a simple parameterization of the radar sensitivity function, where the detection is represented by the ionization function

$$I(m, v) = \frac{m}{10^{-4}\,\mathrm{g}} \left(\frac{v}{30\,\mathrm{km\,s^{-1}}}\right)^{3.5}. \quad (5)$$

All meteors with $I(m, v) \geqslant I^*$ are assumed to be detected in our model, while all meteors with $I(m, v) < I^*$ are not detected. The ionization cutoff I^* is taken to be different for different radars. For example, $I^* \sim 1$ for the Canadian Meteor Orbit Radar (CMOR; Campbell-Brown 2008) and $I^* \sim 0.01$–0.001 for Advanced Meteor Orbit Radar (AMOR; Galligan & Baggaley 2004, 2005). For reference, a JFC particle with $v = 30$ km s^{-1} and $m = 10^{-6}$ g, corresponding to $D \simeq 100\,\mu$m with $\rho = 2$ g cm^{-3}, has $I(m, v) = 0.01$, i.e., a value intermediate between the two thresholds. These meteoroids would thus be detected by AMOR, according to our definition, but not by CMOR. The particle size detection threshold is shown, as a function of v, in Figure 3.

To study the orbital properties of different meteor sources, these sources need to be isolated. This is typically done by selecting meteors with specific radiants. To test how the radiant cutoff affects the results, we select the helion meteors with $-90° < l < -45°$ and $-30° < b < 30°$, and antihelion meteors with $45° < l < 90°$ and $-30° < b < 30°$. Since our code computes the same impact speed and orbit distributions for

[10] We use *IRAS* because it is the data set we are best familiar with (see Nesvorný et al. 2006; N10). Other, more modern MIR surveys such as the Cosmic Background Explorer (COBE; e.g., Kelsall et al. 1998) have better precision and resolution, but their results do not differ in important ways from those obtained by *IRAS*. The COBE measurements of the extended MIR emission were used to calibrate the *IRAS* fluxes as described in Nesvorný et al. (2006).

[11] The Öpik theory cannot properly account for the capture of particles in orbital resonances (e.g., Dermott et al. 1994; Šidlichovský & Nesvorný 1994). Testing the effect of orbital resonances on particles released by JFCs is left for future work.

[12] Note that the parameterization described here applies to the specular meteor radars, which detect the meteor trails. A similar parameterization can be developed, however, for the more sensitive High Power and Large Aperture (HPLA) Radars (Fentzke & Janches 2008; Fentzke et al. 2009) that detect meteor head echoes.

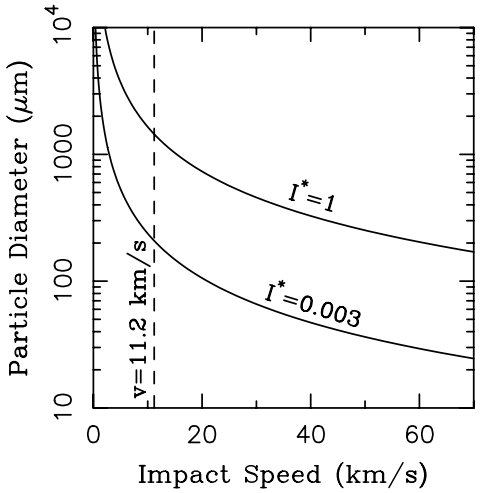

Figure 3. Detection size threshold as a function of the meteor impact speed. All particles above the solid lines are assumed to be detected. The thresholds are $I^* \simeq 1$ for CMOR and $I^* \simeq 0.003$ for AMOR. Meteors occur to the right from the dashed vertical line that denotes the Earth's escape speed ($v_{esc} = 11.2$ km s^{-1}).

the helion and antihelion sources, we combine the results from the two radiant cutoffs together. Note, therefore, that our method cannot capture the suspected asymmetry between the helion and antihelion sources (see, e.g., W09, and the references therein).

3. RESULTS

We performed hundreds of tests with the model described in Section 2. The main parameters of these tests were the (1) size distribution of JFC particles at the source, as defined by D^*, α_1 and α_2, (2) power index of the initial perihelion distribution, $dN(q) \propto q^\gamma dq$, and (3) collisional lifetime of particles, τ_{coll}. To compare our model with meteor observations, we specified the appropriate ionization threshold and applied the usual χ^2 statistics (see, e.g., Nesvorný et al. 2006). To simplify the presentation of results, we first discuss selected cases that illustrate the trends with different parameters. These cases are generally representative for a wide range of parameter values, as explained in the following text.

3.1. AMOR

We start by discussing the results relevant to AMOR, because AMOR is capable of detecting particles with $D \sim 100\,\mu$m (Figure 3), and can thus provide constraints on the particle sizes that are thought to be dominant in the ZC. Figure 4 shows the distributions of impact speeds and orbits of JFC meteoroids for $D^* = 100\,\mu$m, $\gamma = 0$, $S = 1$, and several values of the ionization cutoff. With $I^* = 0$, corresponding to no cutoff on mass or impact speed, the impact speed distribution, $dN(v)$, is strongly peaked toward the Earth's escape speed ($v_{esc} = 11.2$ km s^{-1}). When $I^* = 0.003$ cutoff is applied, as roughly expected for the AMOR detections, $dN(v)$ has a maximum at $v \simeq 25$ km s^{-1}. *This illustrates the crucial importance of the ionization cutoff for the interpretation of meteor radar observations.*

Given the strong effect of the ionization cutoff it is difficult to imagine how the radar observations can be correctly "debiased," based solely on the measurements, corrections, and considerations of the Earth-impact probability of different orbits (e.g., Taylor & McBride 1997; Galligan & Baggaley 2004; Campbell-Brown 2008), to obtain the real distribution of meteoroids at 1 AU. As shown in Figure 4, the real distribution can be very different from the observed one; although meteors at low speeds may dominate the real distribution, only a tiny fraction are detected. This highlights the importance of dynamical modeling.

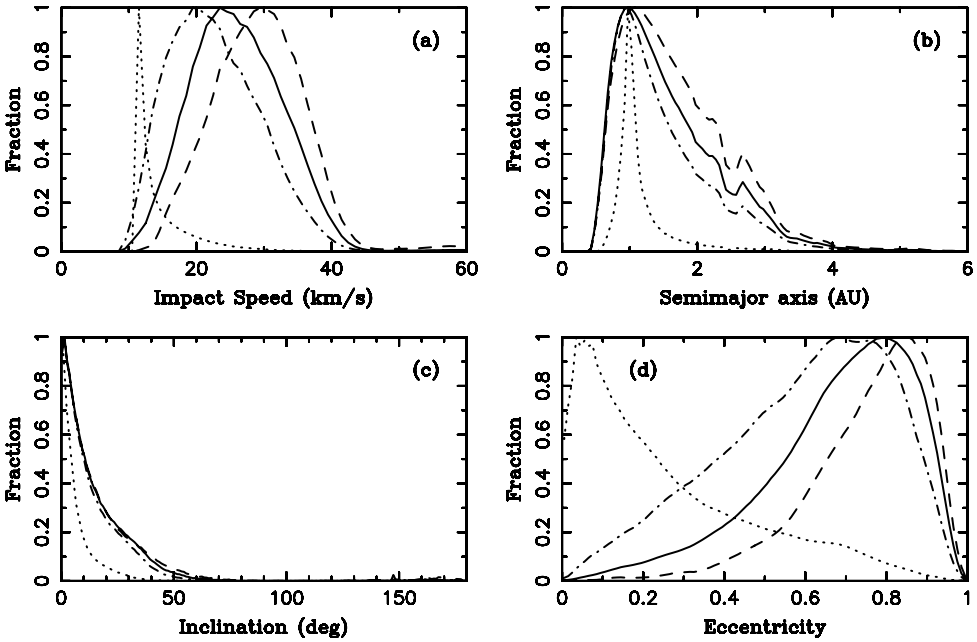

Figure 4. Effect of the ionization cutoff. Different lines show the results for $I^* = 0$ (dotted), $I^* = 0.001$ (dot-dashed), $I^* = 0.003$ (solid), and $I^* = 0.01$ (dashed). As the ionization cutoff increases, the peak of $dN(v)$ shifts to larger values. Here we used $D^* = 100\,\mu$m, $\alpha_1 = 2$, $\alpha_2 = 5$, $\gamma = 0$, and $S = 1$. Most meteoroids accreted by Earth have $v < 15$ km s^{-1}, while most meteoroids detected by AMOR have $v > 15$ km s^{-1}. No radiant cutoff was applied here. The drop of $dN(a)$ near $a = 2.5$ AU corresponds to the gap in the distribution of orbits produced as particles drifting by P-R drag jump over the 3:1 mean motion resonance with Jupiter. All distributions were normalized to reach 1 at their maximum.

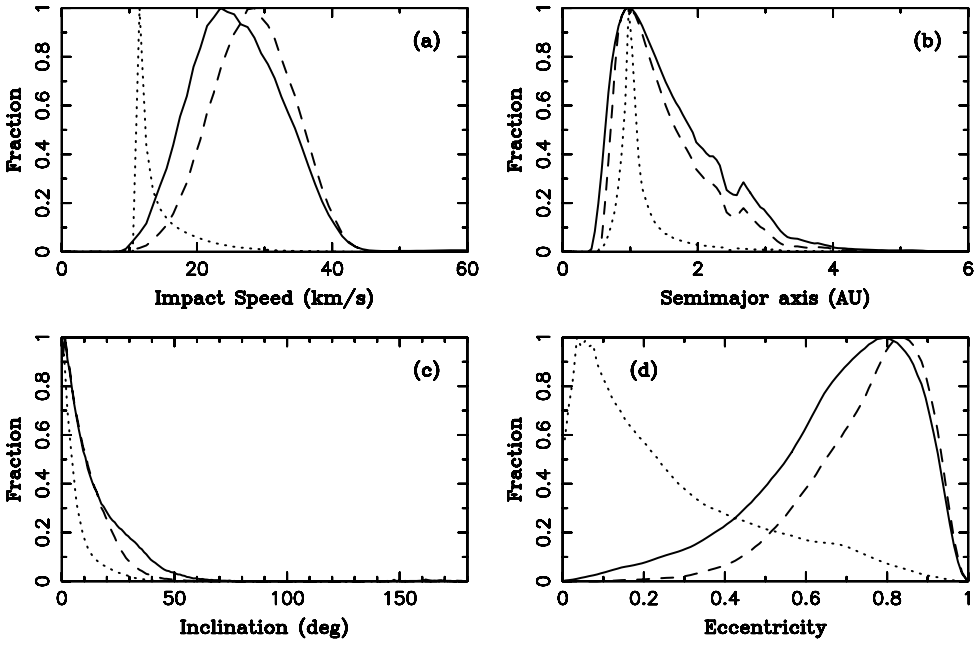

Figure 5. Effect of the radiant cutoff. Different lines show the results for $I^* = 0$ without a radiant cutoff (dotted), $I^* = 0.003$ without a radiant cutoff (solid), and $I^* = 0.003$ with radiant cutoff (dashed). As in Figure 4, we used $D^* = 100\,\mu$m, $\alpha_1 = 2$, $\alpha_2 = 5$, $\gamma = 0$, and $S = 1$.

In a similar fashion, the observed eccentricity distribution, $dN(e)$, is strongly biased toward large values by the ionization cutoff, while the underlying distribution has more small and moderate values (Figure 4(d)). This explains, at least in part, why N10 were unable to obtain meteor-like $dN(e)$, because they did not model the meteor detection in detail. The model semimajor axis and inclination distributions, $dN(a)$ and $dN(i)$, are also strongly affected by the ionization cutoff. With $I^* = 0.003$, both distributions become significantly broader than those computed for $I^* = 0$ (Figures 4(b) and (c)).

The distribution of impact speeds obtained in our model has a peak value of $v = 20$ km s^{-1} for $I^* = 0.001$ and $v = 30$ km s^{-1} for $I^* = 0.01$, in good agreement with the AMOR measurements of helion/antihelion meteors that show a peak at $v = 20$–25 km s^{-1}. The spread of model $dN(v)$ (Figure 4(a)), however, is slightly narrower than the one indicated by observations (Figure 1(a)). We will discuss this difference later in this section and show that it can be related to the initial SFD of particles produced by JFCs.

Figure 5 illustrates the effect of the radiant cutoff for $I^* = 0.003$ and the case described above. The radiant cutoff, as defined in Section 2.6, moves $dN(v)$ to slightly larger values (Figure 5(a)) and leads to narrower distributions of a, e, and i. More aggressive radiant selection criteria, such as the ones used in Campbell-Brown (2008) to define the helion/antihelion sources, would produce a slightly larger effect. On the other hand, Galligan & Baggaley (2005) adopted a very broad radiant cutoff ($-120^\circ < l < -30^\circ$ and $20^\circ < l < 120^\circ$, respectively, for our definition of l, and no condition on b). According to our tests, these broad selection criteria give results that are similar to those with no radiant cutoff.

The effect of the radial distribution of initial orbits is illustrated in Figure 6. As expected, $\gamma < 0$ produces $dN(v)$ that peaks at larger values, and $dN(e)$ that is more skewed toward $e = 1$. This is because more particles are produced with small q values in this case, and these particles tend to have larger v and e values when they impact. The effects of $\gamma > 0$ are opposite to those of $\gamma < 0$. Interestingly, $dN(a)$ and $dN(i)$ obtained with $I^* = 0.003$ are not very sensitive to changes of γ.

Together with Figure 4, these results show that it can be difficult to constrain the value of γ from the fits to the AMOR measurements alone, because the effects of γ are similar to those produced by slight changes in the detection efficiency, and can be confused with them. A detailed knowledge of the instrument sensitivity, that goes beyond the simple concept of the ionization cutoff described in Section 2.6, will be required for a more constrained modeling (see, e.g., Fentzke & Janches 2008; Fentzke et al. 2009).

The effects of initial $dN(D)$ of particles, as discussed below, are in many ways similar to those produced by changes of γ and I^*. Figure 7 illustrates the effect of D^*. Again, $dN(v)$ and $dN(e)$ show more variation than $dN(a)$ and $dN(i)$. While for $D^* = 30\,\mu$m, the velocity peak shifts to $v \simeq 30$ km s^{-1}, it moves to $v \simeq 20$ km s^{-1} for $D^* = 300\,\mu$m. This variation can be linked to the ionization cutoff. For example, with $D^* = 30\,\mu$m, particles tend to be smaller and will be detected with $I^* = 0.003$ only if their speeds are larger.

The distributions $dN(v)$ shown in Figures 4(a)–7(a) are all slightly narrower than the one indicated by observations (see Figure 1(a)). This difference cannot be resolved by varying γ, S, or I^*. Instead, to resolve this problem, we needed to assume that the power index of $dN(D)$ is $3 \lesssim \alpha \lesssim 4$, at least in the size range relevant to AMOR observations. To illustrate this case, Figure 8 shows the distributions for $\alpha = \alpha_1 = \alpha_2 = 3.5$. While $dN(a)$, $dN(e)$ and $dN(i)$ have not changed much relative to Figure 4, the new distribution $dN(v)$ with $I^* = 0.01$–0.001 becomes broader, thus better mimicking the AMOR measurements.

This trend can be easily understood. With a sharp SFD break at $D^* \sim 100\,\mu$m, the particles that produce most meteors with $I > 0.01$–0.001 are those with $D \sim 100\,\mu$m. These particles have similar orbital histories and produce a relatively narrow $dN(v)$. With $\alpha_1 = \alpha_2 \sim 3.5$, on the other hand, the size range of particles significantly contributing to AMOR meteors increases, relative to the previous case, producing a larger variability in

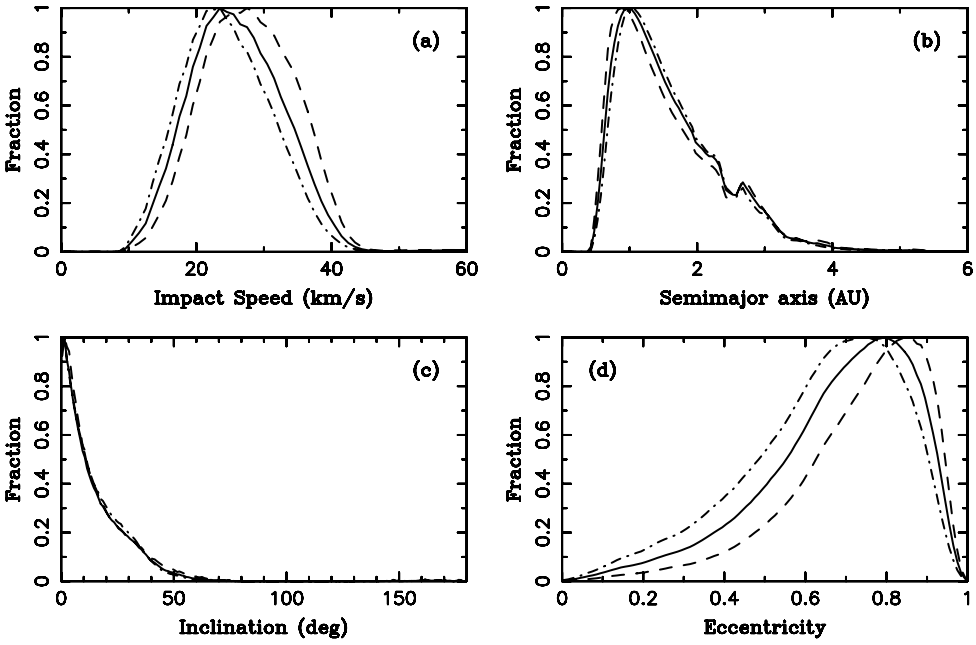

Figure 6. Effect of γ. Different lines show the results for $\gamma = 0$ (solid), $\gamma = -1$ (dashed), and $\gamma = 1$ (dot-dashed). As in Figure 5, we used $I^* = 0.003$, $D^* = 100\,\mu$m, $\alpha_1 = 2$, $\alpha_2 = 5$, and $S = 1$. No radiant cutoff was applied here.

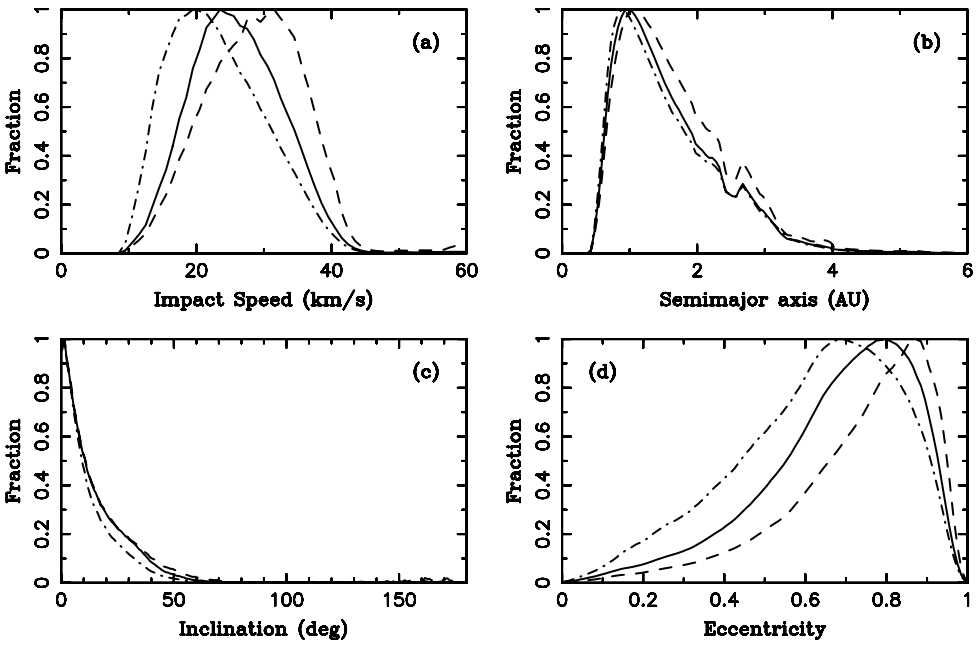

Figure 7. Effect of D^*. Different lines show the results for $D^* = 100\,\mu$m (solid), $D^* = 30\,\mu$m (dashed), and $D^* = 300\,\mu$m (dot-dashed). As in Figure 5, we used $I^* = 0.003$, $\alpha_1 = 2$, $\alpha_2 = 5$, and $S = 1$. No radiant cutoff was applied here.

orbital histories, and thus also a larger spread in v. Figure 9 illustrates these trends.

By experimenting with different SFDs, we found that the best matches to AMOR observations can be obtained with $D^* \lesssim 50\,\mu$m and $\alpha_2 = 3.5$, or with $D^* \gtrsim 200\mu$m and $\alpha_1 = 3.5$, while the values of γ and S are essentially unconstrained (but see Section 3.2 for a discussion of the collisional model). We opt for $D^* = 200\,\mu$m in Figure 10, which illustrates one of our preferred models, because the original interpretation of spacecraft impact experiments indicates a change of slope at $D \simeq 200\,\mu$m (e.g., G85; Love & Brownlee 1993). The solutions with $D^* \lesssim 50\,\mu$m and $\alpha_2 = 3.5$, which would better correspond to the reinterpretation of the impact experiments by Mathews et al. (2001), are also plausible. We will discuss this issue in Section 4.

While our models $dN(v)$, $dN(a)$, and $dN(e)$ in Figure 10 match observations reasonably well, the model $dN(i)$ is slightly narrower than the one measured by AMOR. This indicates that we may be missing sources with larger inclinations. For example, as discussed in Section 2.1, our model for the initial inclinations of JFC particles can be inappropriate if JFCs lose mass gradually by recurrent splitting events (e.g., LD97; Di Sisto

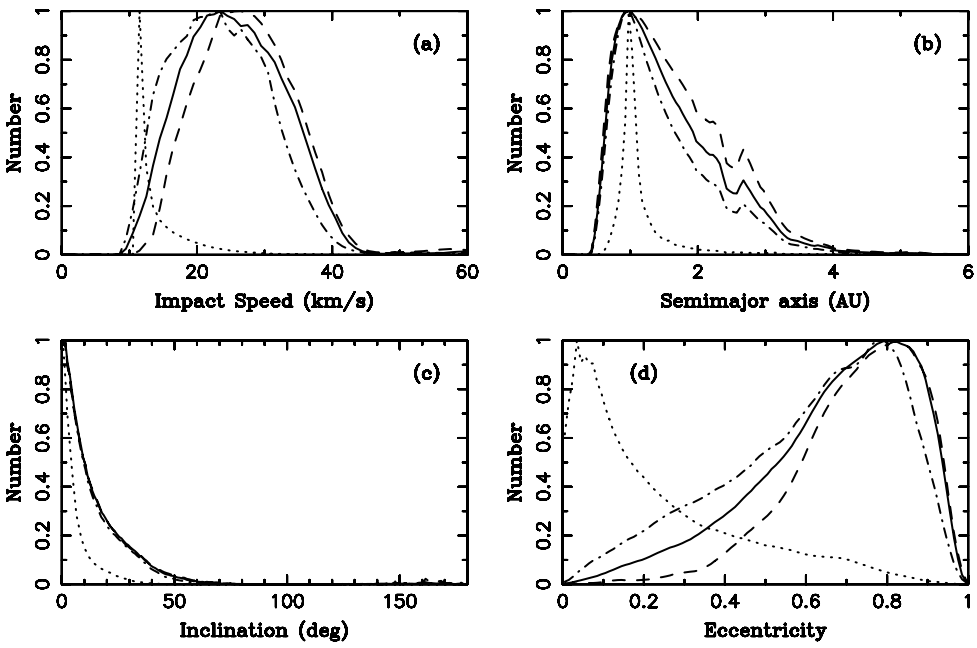

Figure 8. Same as Figure 4 but for $\alpha_1 = \alpha_2 = 3.5$.

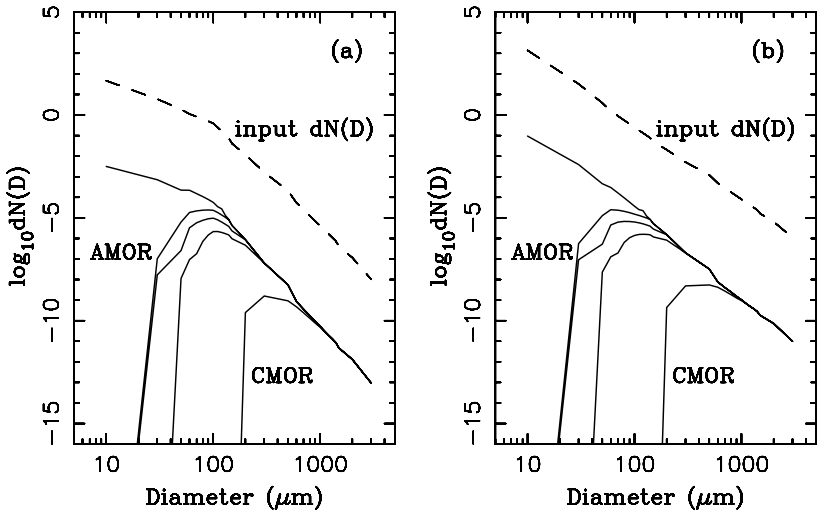

Figure 9. SFDs of different populations for (a) $D^* = 100\,\mu$m, $\alpha_1 = 2$, $\alpha_2 = 5$ and (b) $\alpha_1 = \alpha_2 = 3.5$. The input distributions, shown by dashed lines, correspond to those used in Figures 4 and 8. They were normalized to 1 particle with $D > 100\,\mu$m. The upper solid line in each panel shows the SFD of particles accreted by the Earth ($I^* = 0$). Accreted particles show a slightly steeper slope than the input SFD for $D \gtrsim 100\,\mu$m, because of the effects of disruptive collisions, which eliminate large particles in the G85 model, and a shallower slope for $D \lesssim 100\,\mu$m, because small JFC particles have smaller Earth-accretion probabilities than the larger ones due to their shorter P-R drag lifetimes. The other solid lines show the expected meteor SFD for AMOR (three lines corresponding, from left to right, to $I^* = 0.001$, 0.003, and 0.01) and CMOR ($I^* = 1$).

et al. 2009; N10). It is also possible, however, that the radiant cutoff of Galligan & Baggaley (2004, 2005) is not sufficiently restrictive to pick up JFC meteoroids only, as hinted on by Figure 1(c), where $dN(i)$ seems to follow different trends for $i < 30°$ and $i > 30°$. Note that Campbell-Brown (2008), using a more restrictive radiant cutoff, obtained a relatively narrow $dN(i)$ of helion/antihelion meteors.

Figure 11 shows the radiant distributions for our preferred model shown in Figure 10. With $I^* = 0$, the radiants fill the whole sky and show broad concentrations around $l = -90°$, $l = 90°$, and $b = 0°$. With $I^* = 0.003$, however, the radiants become tightly clustered about $l = -70°$, $l = 70°$, and $b = 0°$. This highlights the importance of the ionization cutoff. For a comparison, Galligan & Baggaley (2005) found that the helion and antihelion sources are centered at $l = \pm 70°$ and their full widths are $\simeq 20°$ in both l and b. The location and spread of our model radiants very closely match these measurements.

3.2. CMOR

The results discussed in Section 3.1 were obtained with the standard G85 model for the collisional disruption of particles. In G85, the large, millimeter-sized particles have very short physical lifetimes ($\sim 10^4$ yr) and disrupt before they can significantly evolve by P-R drag. Small particles, on the other hand, have long collisional lifetimes and evolve faster by P-R drag. The G85 model therefore implies different orbital histories of small and large particles and, as we found here, produces significantly

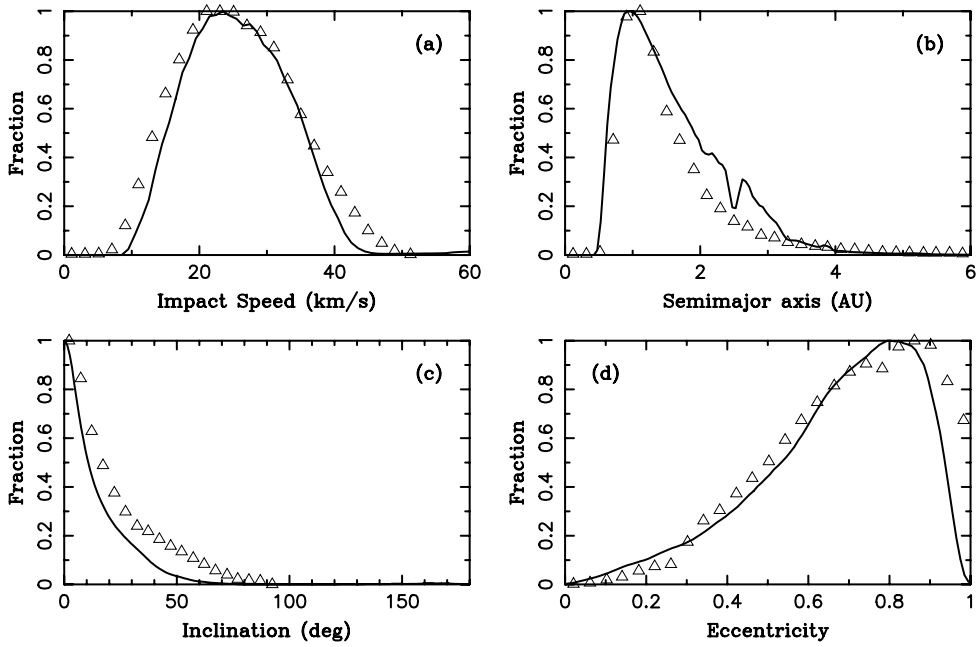

Figure 10. Our preferred model for the AMOR meteors. The triangles label the corrected AMOR data from Galligan & Baggaley (2005). Solid lines show our results obtained with $I^* = 0.003$, $D^* = 200\,\mu$m, $\alpha_1 = 3.5$, $\alpha_2 = 5.0$, $\gamma = 0$, and $S = 1$.

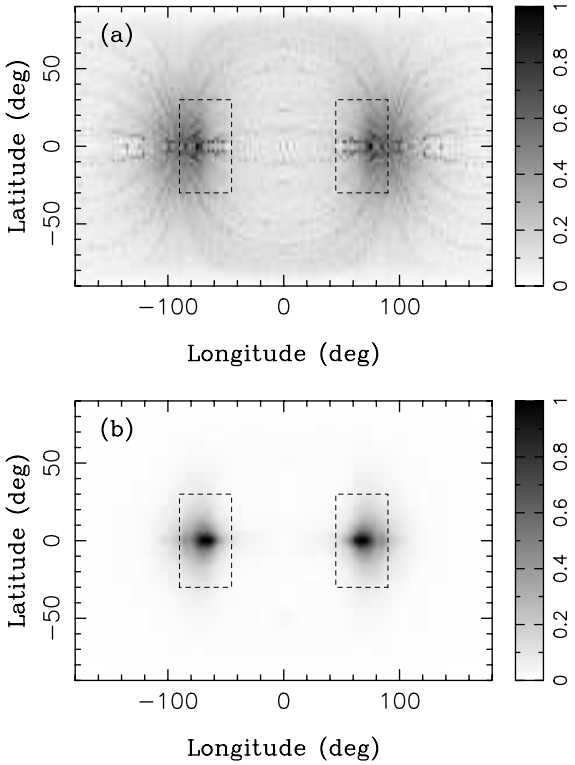

Figure 11. Radiants for $I^* = 0$ (a) and $I^* = 0.003$ (b). The model parameters used here are the same as in Figure 10. The gray scale shows the radiant density that was normalized to 1 at its maximum. The dashed rectangles in both panels show our radiant selection criteria defined in Section 2.6.

different distributions of impact speeds and heliocentric orbits for $I^* = 0.003$ and $I^* = 1$. Figure 12 illustrates the case of $I^* = 1$. These results are at odds with observations, because the distributions measured by AMOR and CMOR are not that different.

To resolve this problem, we needed to assume that $\tau_{\rm coll}$ for $D \sim 1$ mm is significantly longer than in G85 ($S \gtrsim 30$). Figure 13 shows the results for $S = 100$. The main improvement with respect to Figure 12 is that $dN(a)$ now peaks at $a \sim 1$ AU. This is a direct consequence of longer $\tau_{\rm coll}$, which allows the large particles to accumulate larger P-R drifts and reach $a \sim 1$ AU. On the other hand, models with $S \gtrsim 30$ and $I^* = 0.01$–0.001 do not match the AMOR measurements. This shows that the size dependence of the G85 collisional model may be incorrect. Taken together, if $S \gtrsim 30$ is needed to match CMOR, while $S \sim 1$ is needed to match AMOR, $\tau_{\rm coll}(D)$ should be more constant over the relevant size range, $D \sim 30$–$1000\,\mu$m according to Figure 9, than suggested by G85.

We performed a search in parameter space to see whether we can obtain the impact speed and orbit distributions with $S = 100$ that would closely resemble those measured by CMOR (Figure 10– 12 in Campbell-Brown 2008). We found that the model results with $\alpha \sim 2$ work best. With $\alpha \sim 2$, at least locally near $D \sim 500\,\mu$m, which are the most important sizes for CMOR, the model distributions have the characteristic shapes measured by CMOR (Figure 14). When no radiant cutoff is used, $dN(v)$ has the maximum just below $v = 20$ km s^{-1}, and $dN(e)$ peaks at $e \sim 0.7$. When the radiant cutoff is applied, $dN(v)$ has the maximum just below $v = 30$ km s^{-1}, and $dN(e)$ peaks at $e \sim 0.8$. These trends correspond very well to those in Figures 10 and 12 in Campbell-Brown (2008).

The model $dN(a)$ with radiant cutoff becomes more tightly clustered at $a \sim 1$ AU than in the case without cutoff, in a nice correspondence to the CMOR measurements (Figure 14(b)). Our $dN(i)$ with radiant cutoff is slightly broader than the CMOR distribution (Figure 14(c)), which is logical because the radiant cutoff used by Campbell-Brown (2008) is more restrictive than the one used here. Overall, the agreement between the model and observations is very good.

While the meteoroid SFD can be wavy (e.g., Ceplecha et al. 1998), with $\alpha \sim 3.5$ at $D \sim 100\,\mu$m (see Section 3.1) and $\alpha \sim 2$ at $D \sim 500\,\mu$m, these slope determinations can also

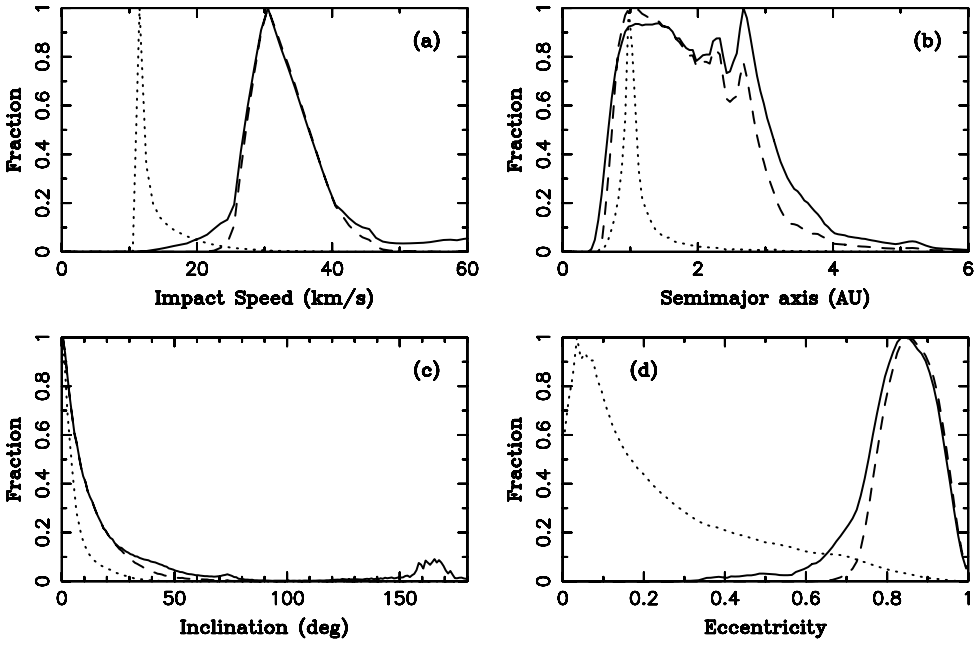

Figure 12. Different lines show the results for $I^* = 0$ (dotted), $I^* = 1$ (solid), and $I^* = 1$ with radiant cutoff (dashed). As in Figure 10, illustrating our preferred fit to the AMOR data, we used $D^* = 200\,\mu$m, $\alpha_1 = 3.5$, $\alpha_2 = 5$, $\gamma = 0$, and $S = 1$. The distributions shown here do not match the CMOR observations of the helion/antihelion meteors (cf. Figures 10 and 12 in Campbell-Brown 2008). They may be more similar to the distributions inferred from the visual meteor surveys that are sensitive to larger, ~1 cm meteoroids (P. Jenniskens et al. 2011, in preparation).

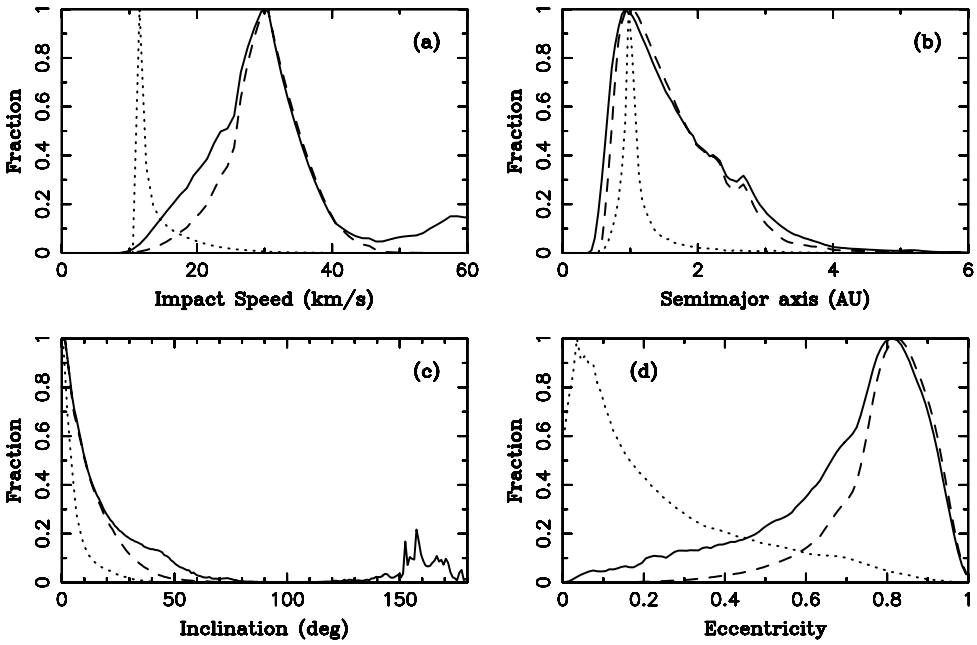

Figure 13. Same as Figure 12 but for $S = 100$.

be artificially imposed on the results by our simple treatment of the radar's detection efficiency.[13] In addition, it is not clear to us whether it is appropriate to compare our results for the helion/antihelion meteors to Figures 10 and 12 in Campbell-Brown (2008), because their Figure 10 shows the CMOR distributions for *all* sporadic sources, and the distributions in Figure 12 were weighted to a constant limiting mass, a correction that is not needed for a comparison with our model.

Finally, Figure 15 shows the CMOR radiant distributions for models illustrated in Figures 12 and 13. With longer $\tau_{\rm coll}$, the radiants are slightly more spread around the helion and antihelion directions. Interestingly, Figure 15 indicates that the JFC meteoroids are capable of producing apex meteors.

[13] The SFD constraints established here were obtained with the simple parameterization of the radar's detection efficiency described in Section 2.6. In reality, the detection efficiency should be a more complex function of the meteoroid mass and speed, other impact parameters, and observing conditions. It is plausible, for example, that the detection probability of a meteor, $D(I)$, goes smoothly from ~0 for $I \leqslant I_0^* < I^*$ to ~1 for $I \geqslant I_1^* > I^*$, and attains some intermediate values from I_0^* to I_1^*. If so, this could broaden the size range of particles that contribute to detections and potentially resolve the problem with the width of $dN(v)$, without the need to resorting to a relatively shallow SFD slope.

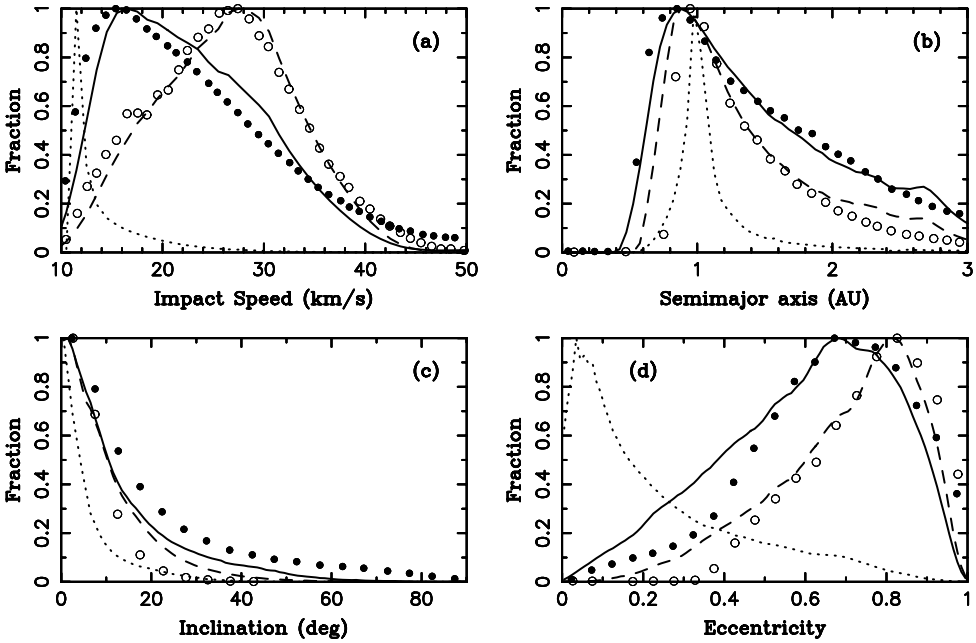

Figure 14. Our preferred model for the CMOR meteors. The filled and unfilled circles label the CMOR data from Figures 10 and 12 in Campbell-Brown (2008). The filled circles are raw CMOR data where no radiant cutoff was applied to separate different sources. The unfilled circles show the distributions, where the antihelion source was isolated by the radiant cutoff defined in Table 1 in Campbell-Brown (2008). These distributions were corrected for the observing biases and mass weighted. The helion meteors, not shown here, have the corrected CMOR distributions very similar to those plotted here. Different lines show the model results for $I^* = 0$ (dotted), $I^* = 1$ (solid), and $I^* = 1$ with radiant cutoff (dashed). We used the same parameters as in Figure 12, except for $S = 100$ and $\alpha = 2$. These assumed parameters are not inconsistent with those used is Figure 10, because they apply to larger particles. Figures 10 and 14 can therefore be thought as a simultaneous fit to the radar data. Note that the X-axis ranges were changed here relative to the previous figures to show things more clearly.

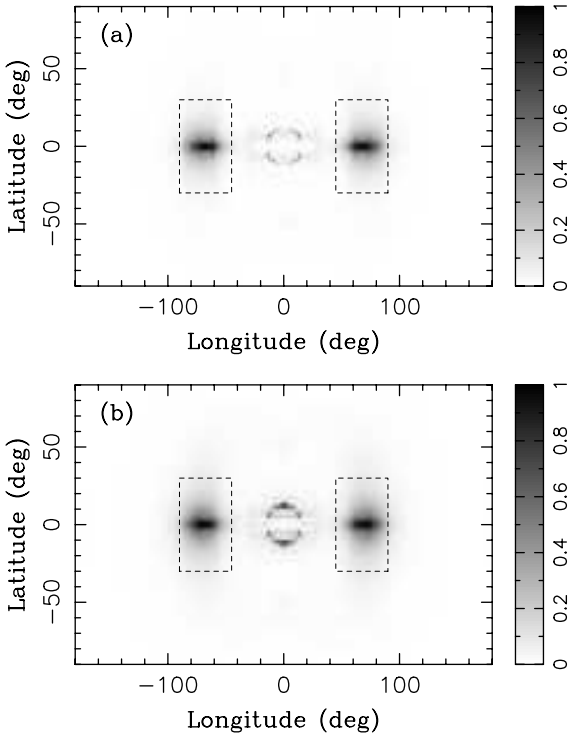

Figure 15. Radiants for $I^* = 1$ and: (1) $S = 1$, and (b) $S = 100$. The model parameters used here are the same as in Figures 12 and 13. The gray scale shows the radiant density that was normalized to 1 at its maximum. The dashed rectangles in both panels denote our radiant selection criteria defined in Section 2.6.

These apex particles have prograde orbits, low impact speeds, and very low semimajor axes. They impact from the apex direction because their orbital speed near the aphelion at 1 AU is smaller that the Earth's orbital speed. The contribution of JFC meteoroids to apex meteors should be small, however, relative to those produced by the retrograde HTC and/or OCC meteoroids. We verified that only a small fraction (<1%) of the JFC meteoroids can reach retrograde orbits.

3.3. IRAS

Using the methods described in Sections 2.4 and 2.5, we computed the MIR fluxes for all models considered in the previous section. Here we illustrate these results and compare them with those obtained by *IRAS*. Before we do so, however, we want to emphasize that the ZC is in all likelihood a mixture of several particle populations, including contribution from asteroids and long-period comets (see, e.g., N10), while here we only model the JFC component. The best fits obtained to *IRAS* observations in this work are therefore only approximate and could be modified if other components of the ZC were considered.

Figure 16 shows our results for $D^* = 100\,\mu$m, $\alpha_1 = 2$, $\alpha_2 = 5$, $\gamma = 0$, and $S = 1$, corresponding to Figures 4 and 5. The model MIR profiles are slightly narrower than the observed ones, but otherwise correspond to *IRAS* measurements reasonably well. For example, a small, $\lesssim$10% contribution from a source with a more isotropic distribution of inclinations, such as HTCs and/or OCCs, would easily compensate for the small difference. See N10 for a discussion of additional sources that were not modeled here.

A different way to bring the model and observations into a closer agreement is to assume that $\gamma < 0$. With $\gamma < 0$, the

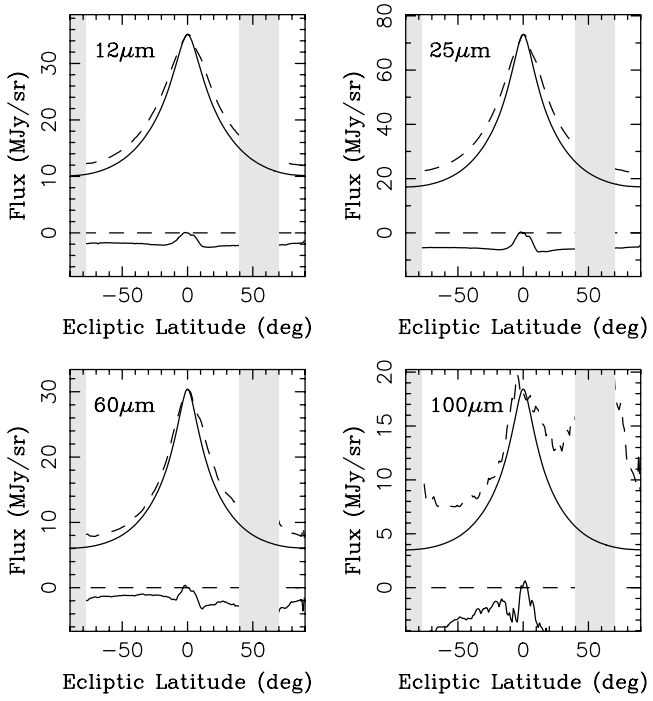

Figure 16. MIR profiles at (a) 12 μm, (b) 25 μm, (c) 60 μm, and (d) 100 μm wavelengths. The dashed line shows the mean *IRAS* profiles for $l_\odot = 90°$. The upper solid curves show the model results for the same wavelength and elongation. The bottom lines show the residual flux obtained by subtracting the model flux from the mean *IRAS* profile. Here we used the same model parameters as in Figure 4: $D^* = 100\,\mu$m, $\alpha_1 = 2$, $\alpha_2 = 5$, $\gamma = 0$ and $S = 1$.

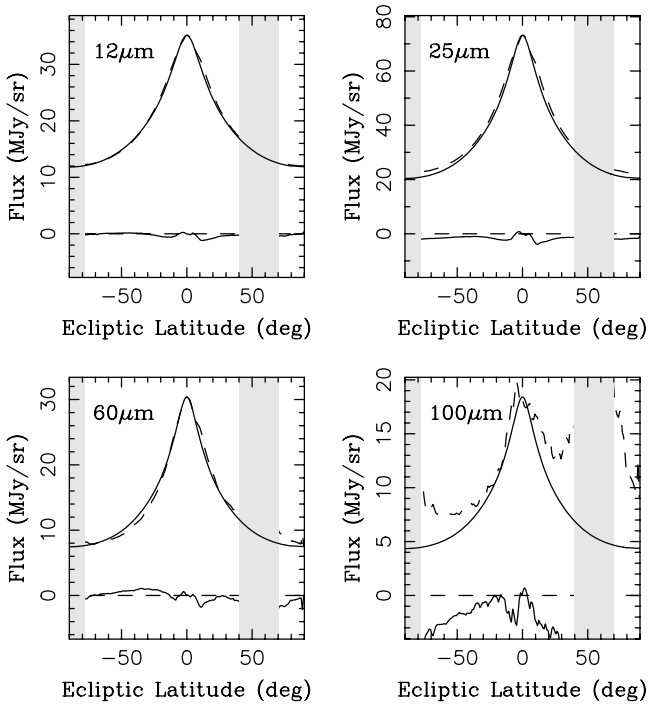

Figure 17. Same as Figure 16, but with $\gamma = -1.3$. The radial distribution obtained with $\gamma = -1.3$ leads to the best fit to *IRAS* observations, at least for the input SFD assumed here. The MIR profiles, however, are not overly sensitive to the assumed SFD.

distribution of JFC particles is weighted toward low R and is projected to a wider range of b when observed from $R = 1$ AU. If $\gamma > 0$, on the other hand, the distribution is weighted toward large R and is seen closer to the ecliptic. We tested a continuous range of γ values and found that $\gamma \simeq -1.3$ provided the best match to the *IRAS* observations (Figure 17).

The effects of additional sources and $\gamma \neq 0$ on the MIR profiles are to some degree degenerate in the *IRAS* model. They would be difficult to separate, based solely on modeling of the *IRAS* observations, if we included additional sources in the present work. For example, as discussed above, the MIR profiles become broader, and more similar to the *IRAS* measurements, if $\gamma < 0$ and/or if sources with a more isotropic inclination distribution are included (N10). On the other hand, a small asteroid contribution at the ~5%–10% level (Nesvorný et al. 2006) would produce slightly narrower profiles than those obtained with the JFCs alone (N10). A two-source model with JFCs and asteroids would thus require $\gamma < 0$.

The MIR profiles obtained in our model are not overly sensitive to the assumptions on the collisional lifetimes of particles. For example, increasing the collisional lifetime of millimeter-sized particles relative to the G85 model, which may be needed to match CMOR observations (Section 3.2), does not affect the results obtained here, because the ZC's cross section is mainly in $D \lesssim 200\,\mu$m particles (N10).

In addition, the model profiles are also insensitive to the input SFD of the JFC particles. This is because the JFC particles with $D \lesssim 200\,\mu$m have $\tau_{\rm coll}$ that exceeds their P-R drag lifetimes. All these particles therefore have roughly similar orbital histories and produce similar MIR profiles. This explains why we obtain nearly identical results for all $D^* < 200\,\mu$m.[14] The effects of α_1 and α_2 are also minor.

3.4. ZC Mass and Cross Section, and Mass Influx on Earth

The comparison of our model with the *IRAS* data is important because it allows us to obtain the absolute calibration of the number of particles in the ZC (or, more precisely, their total cross section). This calibration can then be used to estimate the rate of the terrestrial accretion of interplanetary material, both with and without the ionization cutoff, with the former estimate being relevant to radar observations. Note that it is more difficult to derive the overall terrestrial accretion rate from the meteor radar measurements alone, because different radar instruments have different detection sensitivities, and some, such as the less sensitive CMOR, do not detect the very small and/or slow meteoroids (see discussion in Section 4).

Unless we specify otherwise, all estimates quoted below were obtained for the full size range of particles between $D = 5\,\mu$m and $D = 1$ cm (10^{-10} g to 1 g for $\rho = 2$ g cm^{-3}). These estimates need to be considered with caution because they were obtained with approximate initial SFDs. In reality, the number of particles released by JFCs can be a complicated function of D and should also depend on the circumstances of the splitting/disruption events.

We start by discussing the total cross-section area ($\sigma_{\rm ZC}$) and mass ($m_{\rm ZC}$) of particles in the ZC. For the sake of simplicity, we will assume that $30 \lesssim D^* \lesssim 300\,\mu$m, $\alpha_1 < 3$ and $\alpha_2 > 4$, so that particles with sizes below 30 μm and above 300 μm do not strongly contribute to the cross section or mass, as suggested

[14] We note that the model profiles obtained for $\gamma \simeq -1.3$ and $D^* = 10\,\mu$m are slightly narrower than those shown in Figure 17 for $D^* = 100\,\mu$m, because small particles drift faster and their inclinations are disturbed to a lesser degree by planets and planetary resonances.

Table 1
A Summary of Different Models

D^* (μm)	α_1	α_2	γ	σ_{ZC} (10^{11} km^2)	m_{ZC} (10^{19} g)	$\dot{m}_{ZC}$ (kg s^{-1})	$\dot{m}_0$ (tons yr^{-1})	$\dot{m}_{0.003}$ (tons yr^{-1})	$\dot{m}_1$ (tons yr^{-1})
100	2	5	0	2.1	3.8	4200	15,000	4200	240
100	2.9	4.1	0	2.1	4.6	6200	12,000	4100	860
100	2	5	−1	2.0	3.8	5200	15,000	6100	480
100	2	5	−1.3	2.0	3.9	5800	16,000	7000	590
100	2	5	1	2.3	4.0	4000	14,000	3100	130
30	2	5	0	1.8	1.2	1600	7700	500	27
300	2	5	0	3.4	15	19,000	26,000	19,000	3300
50	2	3.5	0	2.5	12	25,000	18,000	9300	4100
50*	2	3.5	0	2.5	11	13,000	17,000	8500	3300
200	3.5	5.0	0	1.9	2.0	2400	12,000	2900	230
200*	3.5	5.0	0	2.1	3.0	3400	11,000	2,900	220

Notes. See the main text for the definition of parameters shown here. The asterisks denote the cases, where only particles between $D = 10\,\mu$m and $D = 3$ mm were considered.

by the spectral observations of the ZC (e.g., Reach et al. 2003), and various other measurements (see, e.g., Ceplecha et al. 1998, and the references therein).

With these assumptions we find that $1.7 \times 10^{11} < \sigma_{ZC} < 3.5 \times 10^{11}$ km^2, where the larger values correspond to $D^* = 300\,\mu$m. This estimate is in a good agreement with N10 who found that $\sigma_{ZC} = (2.0 \pm 0.5) \times 10^{11}$ km^2. The uncertainty in σ_{ZC} mainly stems from the uncertainty in D^*, with γ producing only a minor effect. For a reference, the models shown in Figures 16 and 17 have $\sigma_{ZC} = 2.1 \times 10^{11}$ and 2.0×10^{11} km^2, respectively (Table 1).

Mass m_{ZC} is more poorly constrained then σ_{ZC}. For $30 \lesssim D^* \lesssim 300\mu$m, $\alpha_1 < 3$, $\alpha_2 > 4$ and $\rho = 2$ g cm^{-3} we estimate that $10^{19} < m_{ZC} < 1.5 \times 10^{20}$ g, with larger values corresponding to $D^* = 300\,\mu$m. For a more restrictive assumption with $D^* \simeq 100\,\mu$m, we find that $3 \times 10^{19} < m_{ZC} < 5 \times 10^{19}$ g, where the exact value depends on α_1, α_2, and γ. For a reference, the models shown in Figures 16 and 17 have $m_{ZC} = 3.8 \times 10^{19}$ and 3.9×10^{19} g, which roughly corresponds to a 33 km diameter sphere with $\rho = 2$ g cm^{-3}.

These results compare well with those reported in N10, where it was found that $2.6 \times 10^{19} < m_{ZC} < 5.2 \times 10^{19}$ g, under the assumption that the continuous SFD can be approximated by a population of the same-size particles with $D = 100$–$200\,\mu$m.

N10 estimated that the input mass rate of $\dot{m}_{ZC} = 1000$–1500 kg s^{-1} is needed to keep the ZC in a steady state. Here we obtain larger values, mainly because the population of particles released with low q has shorter lifetimes and needs to be resupplied at a higher rate. If $D^* \lesssim 100\,\mu$m, $\dot{m}_{ZC}$ ranges between 3000 and 7000 kg s^{-1}, with the largest values corresponding to $\gamma = -1.3$ in the model illustrated in Figure 17. Input rate $\dot{m}_{ZC}$ is also sensitive to D^*, roughly in the same proportion as m_{ZC}. For example, $\dot{m}_{ZC} \sim 1600$ and 19,000 kg s^{-1} for $D^* = 30\,\mu$m and $D^* = 300\,\mu$m, respectively. These estimates are valid for $\alpha_1 < 3$ and $\alpha_2 > 4$. The required input rates can be somewhat smaller or larger if $\alpha_1 \sim 3.5$ and/or $\alpha_2 \sim 3.5$ (see Table 1).

Finally, we consider the terrestrial accretion rate, $\dot{m}_{I^*}$, where $\dot{m}_{I^*}$ denotes the rate for $I > I^*$. We consider cases with $I^* = 0$, $I^* = 0.003$, and $I^* = 1$, with the latter two roughly corresponding to our expectations for AMOR and CMOR, respectively. Using the *IRAS* calibration, we find that our standard model with $D^* \simeq 100\,\mu$m, $\alpha_1 < 3$, $\alpha_2 > 4$ implies that $\dot{m}_0 = (15{,}000 \pm 3000)$ tons yr^{-1}, $\dot{m}_{0.003} = (5000 \pm 2000)$ tons yr^{-1}, and $\dot{m}_1 = (500 \pm 400)$ tons yr^{-1}, where a large part of the quoted uncertainty comes from the poorly constrained γ. Note that the values for $I^* = 0.003$ and $I^* = 1$ do not include any radiant cutoff.

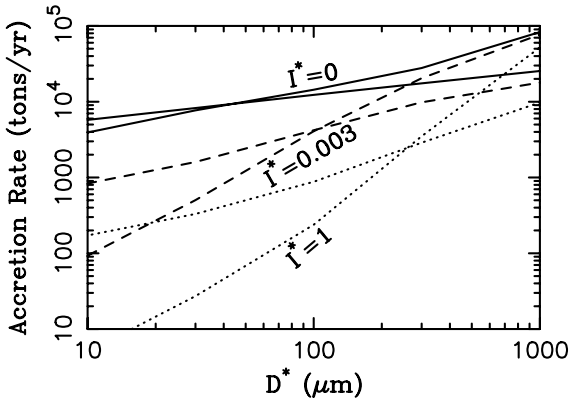

Figure 18. Terrestrial accretion rate of JFC particles as a function of D^* obtained in our model for $\gamma = 0$ and $S = 1$. Different lines denote the results for $I^* = 0$ (solid), $I^* = 0.003$ (dashed), and $I^* = 1$ (dotted). The two lines for each I^* were computed for different values of α_1 and α_2. The more horizontal lines correspond to $\alpha_1 = 3$ and $\alpha_2 = 4$. The more inclined lines correspond to $\alpha_1 = 2$ and $\alpha_2 = 5$. For $D^* \simeq 100\,\mu$m, the overall terrestrial accretion rate for $I^* = 0$ is $\sim$1–2 $\times 10^4$ tons yr^{-1}.

The uncertainty becomes larger if D^* is allowed to vary (Figure 18). For example, with $\alpha_1 = 2$, $\alpha_2 = 5$, and $\gamma = 0$, we obtain $\dot{m}_0 = 26{,}000$ tons yr^{-1}, $\dot{m}_{0.003} = 19{,}000$ tons yr^{-1}, and $\dot{m}_1 = 3300$ tons yr^{-1} for $D^* = 300\,\mu$m, and $\dot{m}_0 = 7700$ tons yr^{-1}, $\dot{m}_{0.003} = 500$ tons yr^{-1}, and $\dot{m}_1 = 27$ tons yr^{-1} for $D^* = 30\mu$m. Also, our preferred model for the AMOR meteors illustrated in Figure 10 gives $\dot{m}_0 = 12{,}000$ tons yr^{-1}, $\dot{m}_{0.003} = 2900$ tons yr^{-1}, and $\dot{m}_1 = 230$ tons yr^{-1}. Similarly, the model with $D^* = 50\,\mu$m, $\alpha_1 = 2$, and $\alpha_2 = 3.5$ gives $\dot{m}_0 = 18{,}000$ tons yr^{-1}, $\dot{m}_{0.003} = 9300$ tons yr^{-1}, and $\dot{m}_1 = 4100$, or $\dot{m}_0 = 17{,}000$ tons yr^{-1}, $\dot{m}_{0.003} = 8500$ tons yr^{-1}, and $\dot{m}_1 = 3300$, tons yr^{-1}, if the size range of the contributing particles is restricted to $10 < D < 3000\,\mu$m (Table 1).

The above estimates with $I^* = 0$ are a factor of several lower than those found by N10. This difference probably stems from some of the crude approximations used by N10. For example, N10 did not use a continuous SFD of particles and

approximated $dN(D)$ by delta functions. Their initial particle orbits had (almost exclusively) $q > 1.5$ AU, and did not take into account the fact that many JFCs can split and/or disrupt with $q < 1.5$ AU. Moreover, N10 did not properly include the collisional lifetimes of JFC particles in their model. The results presented here, which include all these components, and which were validated on meteor observations, can be more trusted and should supersede those reported in N10.

4. DISCUSSION

The results reported in Section 3.4 show that the low-sensitive meteor radars such as CMOR can only detect a few percent of the overall mass flux. It may therefore be difficult to estimate the terrestrial accretion rate from these measurements alone. The more sensitive meteor radars such as AMOR, on the other hand, should detect 10%–50% of the flux, with the exact value mainly depending on the SFD assumptions (Table 1). These more sensitive measurements, especially those obtained with the HPLA radars, are therefore better suited for estimating the overall accretion rate.

The terrestrial accretion rate found here is comparable to that originally inferred by Love & Brownlee (1993) from the Long Term Duration Facility (LDEF) experiment, and much larger than the one suggested by Mathews et al. (2001) from the Arecibo Observatory (AO) measurements of meteor fluxes. As pointed out by Mathews et al. (2001), the difference between the AO and LDEF measurements could be resolved if LDEF data were recalibrated to $v \sim 50$ km s^{-1}, which is the prevailing meteor speed as seen at Arecibo (see Janches et al. 2003, 2006; Fentzke et al. 2009).

We found that $dN(v)$ for $I^* = 0$ peaks at $v \sim v_{\rm esc} = 11.2$ km s^{-1} (see, e.g., Figures 4, 8, and 10). The only parameter choices that we were able to identify, where this was not the case, were those where it was assumed that essentially all dust was produced with $q \lesssim 0.5$ AU, and that $D^* \gtrsim 100\,\mu$m for $S = 1$. Such an extreme q dependence seems unlikely, because not many solar system objects—potential parent bodies of meteoroids—ever reach $q \lesssim 0.5$ AU. (Comet 2P/Encke has $q = 0.34$ AU, but as we discussed in the Section 1, the measured mass loss in comet 2P/Encke is far too low to be dominant.)

The case described above could potentially be interesting, because it could help to explain why the meteor observations at AO, albeit being much more sensitive than AMOR, do not detect a significant population of meteors with $v < 15$ km s^{-1} (e.g., Janches et al. 2008). To allow for $D^* < 100\,\mu$m in this case, and bring our results to a closer agreement with Mathews et al. (2001), $\tau_{\rm coll}$ of $D < 100\,\mu$m particles, mainly for orbits with $q \lesssim 0.5$ AU, would need to be significantly shorter than suggested by G85.

To match the CMOR measurements in our model, the collisional lifetime of meteoroids with $D \sim 1$ mm needs to be significantly longer than suggested by G85. Such a long lifetime, of order of a few times 10^5 yr for a circular orbit at 1 AU, can be difficult to reconcile with the inferred lifetimes of meteor streams that seem to disappear on a much shorter timescale (less than a few thousand years; e.g., Jenniskens 2008). Possibly, the centimeter-sized particles released from JFCs, which appear to be dominant in the visual observations of the meteor streams, are physically weak and disrupt in a few thousand years. They could produce a population of millimeter-sized and smaller particles that, according to our work, could be more resistant to collisions.

As explained in Section 2.3, our model neglects small fragments produced by disruptions of larger particles, because it is difficult to account for numerous debris particles in the N-body code. Since the fragments are small and should be released on the orbits already evolved by P-R drag, we may speculate that this could lead to a steeper SFD of particles with low perihelion distances. To compensate for that, our preferred model for the source population of particles would need to be adjusted. It is unclear, however, if the effect of the collisional cascade is important. Future work will need to address this problem.

5. CONCLUSIONS

The radar observations of sporadic meteors reveal an important population of meteoroids that impact Earth from the helion and antihelion directions. Typically, these particles have heliocentric orbits with $a \sim 1$ AU, $e > 0.3$, $i < 30°$, and dive into the upper atmosphere at speeds $v \sim 20$–30 km s^{-1}. These results were seemingly inconsistent with the model of the circumsolar meteoroid complex developed in N10, which has been calibrated on the *IRAS*'s MIR observations of the ZC's thermal emission.

The N10 model implied that particles impacting Earth from the helion/antihelion directions should either have $a \sim 1$ AU and $e \lesssim 0.3$, or $a \sim 2$–4 AU and $e \gtrsim 0.6$. The former case corresponds to $D \lesssim 100\,\mu$m meteoroids, whose orbits evolved by P-R drag. The latter cases are the large, $D \gtrsim 1$ mm particles that were assumed in N10 to be collisionally disrupted before their orbits could significantly evolve by P-R drag. The different orbital histories of small and large meteoroids in the N10 model would mean that the meteor radars with different detection thresholds should measure very different distributions of the impact speeds and orbits. This is not the case.

Here we showed that the above problem can be resolved if (1) the N10 model is modified to account for the detection efficiency of meteor radars, (2) meteoroids are released from JFCs over a range of perihelion distances with at least some fraction initially having $q \lesssim 1$ AU, and (3) $D \sim 1$ mm particles have significantly longer ($\gtrsim$30 times) collisional lifetimes than those estimated in G85. With these modifications of the N10 model, the results match meteor constraints.

We also found, using the AMOR observations as a constraint, that $D \sim 100$-μm particles cannot have much longer collisional lifetimes than proposed in G85. Together with (3), these results therefore suggest that $D \sim 100\,\mu$m and $D \sim 1$ mm meteoroids may have more comparable collisional lifetimes (a few times 10^5 yr for a circular orbit at 1 AU) than thought before. If so, the SFD shape inferred from the measurements of the spacecraft impact detectors (such as, e.g., *Ulysses*, *Galileo*, *LDEF*; G85, Love & Brownlee 1993) may be more closely related to the initial SFD of particles released at sources then to the collisional destruction of particles in space.

We showed that the modified N10 model can successfully match the telescopic observations of the ZC. Using *IRAS* to calibrate the model, we estimated that the cross section and mass of the ZC are $\sigma_{\rm ZC} = (1.7$–$3.5) \times 10^{11}$ km^2 and $m_{\rm ZC} \sim 4 \times 10^{19}$ g. The terrestrial accretion rate of JFC particles was found to be $\sim$15,000 tons yr^{-1}, of which only a few percent should be detected by CMOR, and 10–50% should be detected by the more sensitive AMOR.

Moreover, some 10^3–10^4 kg s^{-1} of material must be provided by JFCs to keep the ZC in a steady state. This new input mass estimate is up to $\sim$10 times larger than the one suggested by N10 (see also Leinert et al. 1983), because particles starting

with low q have shorter lifetimes, and need to be resupplied at a faster rate. This new estimate resonates with the N10 model in which the ZC is dominated by the meteoroids released by disrupting/splitting JFCs, because the observed activity of JFCs cannot provide the needed input.

This article is based on work supported by the NASA's Planetary Geology and Geophysics and Planetary Astronomy programs. D.J.'s participation in this work was supported through the NSF Award AST 0908118. The work of D.V. and P.P. was partially supported by the Czech Grant Agency (grants 205/08/0064 and 205/08/H005) and the Research Program MSM0021620860 of the Czech Ministry of Education. We thank Margaret Campbell-Brown, Jack Baggaley, and Hal Levison for useful discussions. We also thank the anonymous reviewer for excellent suggestions to this work.

REFERENCES

Boehnhardt, H., Tozzi, G. P., Bagnulo, S., et al. 2008, A&A, 489, 1337
Bottke, W. F., Nolan, M. C., Greenberg, R., & Kolvoord, R. A. 1994, Icarus, 107, 255
Burns, J. A., Lamy, P. L., & Soter, S. 1979, Icarus, 40, 1
Campbell-Brown, M. D. 2008, Icarus, 196, 144
Ceplecha, Z., Borovička, J., Elford, W. G., et al. 1998, Space Sci. Rev., 84, 327
Dermott, S. F., Jayaraman, S., Xu, Y. L., Gustafson, B. Å. S., & Liou, J. C. 1994, Nature, 369, 719
Dikarev, V., Grün, E., Baggaley, J., et al. 2005, Adv. Space Res., 35, 1282
di Sisto, R. P., Fernández, J. A., & Brunini, A. 2009, Icarus, 203, 140
Drolshagen, G., Dikarev, V., Landgraf, M., Krag, H., & Kuiper, W. 2008, Earth Moon Planets, 102, 191
Fentzke, J. T., & Janches, D. 2008, J. Geophys. Res. (Space Physics), 113, 3304
Fentzke, J. T., Janches, D., & Sparks, J. J. 2009, J. Atmos. Sol.-Terr. Phys., 71, 653
Fernández, J. A. 2005, in Comets: Nature, Dynamics, Origin and Their Cosmogenic Relevance (Dordrecht: Springer), 249
Fernández, Y. R., Lisse, C. M., Käufl, H. U., et al. 2000, Icarus, 147, 145
Galligan, D. P., & Baggaley, W. J. 2004, MNRAS, 353, 422
Galligan, D. P., & Baggaley, W. J. 2005, MNRAS, 359, 551
Greenberg, R. 1982, AJ, 87, 184
Grun, E., Zook, H. A., Fechtig, H., & Giese, R. H. 1985, Icarus, 62, 244 (G85)
Hauser, M. G., Gillett, F. C., Low, F. J., et al. 1984, ApJ, 278, L15
Henning, T., & Mutschke, H. 1997, A&A, 327, 743
Janches, D., Nolan, M. C., Meisel, D. D., et al. 2003, J. Geophys. Res. (Space Physics), 108, 1222
Janches, D., Heinselman, C. J., Chau, J. L., Chandran, A., & Woodman, R. 2006, J. Geophys. Res. (Space Physics), 111, 7317
Janches, D., Close, S., & Fentzke, J. T. 2008, Icarus, 193, 105
Jenniskens, P. 2008, Earth Moon Planets, 102, 505
Jones, J., & Brown, P. 1993, MNRAS, 265, 524
Jones, J., Campbell, M., & Nikolova, S. 2001, Meteoroids 2001 Conf., 495, 575
Kelsall, T., Weiland, J. L., Franz, B. A., et al. 1998, ApJ, 508, 44
Kessler, D. J. 1981, Icarus, 48, 39
Kessler-Silacci, J. E., Dullemond, C. P., Augereau, J.-C., et al. 2007, ApJ, 659, 680
Leinert, C., Roser, S., & Buitrago, J. 1983, A&A, 118, 345
Levison, H. F., & Duncan, M. J. 1994, Icarus, 108, 18
Levison, H. F., & Duncan, M. J. 1997, Icarus, 127, 13 (LD97)
Love, S. G., & Brownlee, D. E. 1993, Science, 262, 550
Mathews, J. D., Janches, D., Meisel, D. D., & Zhou, Q.-H. 2001, Geophys. Res. Lett., 28, 1929
Moro-Martín, A., & Malhotra, R. 2002, AJ, 124, 2305
Nesvorný, D., Vokrouhlický, D., Bottke, W. F., & Sykes, M. 2006, Icarus, 181, 107
Nesvorný, D., Jenniskens, P., Levison, H. F., et al. 2010, ApJ, 713, 816 (N10)
Nesvorný, D., Vokrouhlický, D., Pokorný, P., & Janches, D. 2011, ApJ, in press
Öpik, E. J. 1951, Proc. R. Irish Acad. Sect. A, 54, 165
Reach, W. T., Morris, P., Boulanger, F., & Okumura, K. 2003, Icarus, 164, 384
Reach, W. T., Kelley, M. S., & Sykes, M. V. 2007, Icarus, 191, 298
Šidlichovský, M., & Nesvorný, D. 1994, A&A, 289, 972
Taylor, A., & McBride, N. 1997, Second European Conference on Space Debris, 393, 375
Valsecchi, G. B. 1999, in IAU Colloq. 173, Evolution and Source Regions of Asteroids and Comets, ed. J. Svoren, E. M. Pittich, & H. Rickman (Tatranska Lomnica: Astronomical Institute of the Slovak Academy of Sciences), 353
Wetherill, G. W. 1967, J. Geophys. Res., 72, 2429
Whipple, F. L. 1939, Publ. Am. Astron. Soc., 9, 235
Whipple, F. L. 1951, ApJ, 113, 464
Wiegert, P., Vaubaillon, J., & Campbell-Brown, M. 2009, Icarus, 201, 295 (W09)
Wisdom, J., & Holman, M. 1991, AJ, 102, 1528

Paper E

The Astrophysical Journal, 789:25 (20pp), 2014 July 1 doi:10.1088/0004-637X/789/1/25

DYNAMICAL MODEL FOR THE TOROIDAL SPORADIC METEORS

Petr Pokorný[1], David Vokrouhlický[1], David Nesvorný[2], Margaret Campbell-Brown[3], and Peter Brown[3]
[1] Institute of Astronomy, Charles University, V Holešovičkách 2, CZ-18000 Prague 8, Czech Republic; petr.pokorny@volny.cz, vokrouhl@cesnet.cz
[2] Department of Space Studies, Southwest Research Institute, 1050 Walnut Street, Suite 300, Boulder, CO 80302, USA; davidn@boulder.swri.edu
[3] Department of Physics and Astronomy, University of Western Ontario, London, ON N6A 3K7, Canada; margaret.campbell@uwo.ca, pbrown@uwo.ca
Received 2014 January 21; accepted 2014 May 13; published 2014 June 10

ABSTRACT

More than a decade of radar operations by the Canadian Meteor Orbit Radar have allowed both young and moderately old streams to be distinguished from the dispersed sporadic background component. The latter has been categorized according to broad radiant regions visible to Earth-based observers into three broad classes: the helion and anti-helion source, the north and south apex sources, and the north and south toroidal sources (and a related arc structure). The first two are populated mainly by dust released from Jupiter-family comets and new comets. Proper modeling of the toroidal sources has not to date been accomplished. Here, we develop a steady-state model for the toroidal source of the sporadic meteoroid complex, compare our model with the available radar measurements, and investigate a contribution of dust particles from our model to the whole population of sporadic meteoroids. We find that the long-term stable part of the toroidal particles is mainly fed by dust released by Halley type (long period) comets (HTCs). Our synthetic model reproduces most of the observed features of the toroidal particles, including the most troublesome low-eccentricity component, which is due to a combination of two effects: particles' ability to decouple from Jupiter and circularize by the Poynting–Robertson effect, and large collision probability for orbits similar to that of the Earth. Our calibrated model also allows us to estimate the total mass of the HTC-released dust in space and check the flux necessary to maintain the cloud in a steady state.

Key words: interplanetary medium – meteorites, meteors, meteoroids – zodiacal dust

1. INTRODUCTION

The Earth is permanently showered with dust particles born in space. Cometary activity and both cometary and asteroidal breakup events are the natural source processes for these meteoroids. Particles with sizes in the tens of microns to millimeter range are most efficiently detected with powerful radar systems (e.g., Jones et al. 2005). The specular meteor radars (SMRs), such as the Canadian Meteor Orbit Radar (CMOR) and the Advanced Meteor Orbit Radar (AMOR), have provided the most complete information so far in terms of raw numbers of individual orbits for meteoroids impacting the Earth. This is because their observations cover long and often continuous time intervals, and their measurements are able to resolve both the radiant location and velocity of each impacting particle. If properly understood, such observations may tell us much about the source populations of meteoroids, and particularly constrain the overall strength of cometary activity and/or the pace of their breakups.

Analysis of SMR observation data sets allows two components of Earth-impacting meteoroids to be readily distinguished: (1) particles associated with streams concentrated in interplanetary space (e.g., Jenniskens 2006, 2008a, 2008b; Brown et al. 2008, 2010), thus impacting the Earth at discrete and well-defined time windows lasting typically days, and (2) particles belonging to a sporadic background (e.g., Jones & Brown 1993) for an excellent data compilation and a historic perspective). It is believed that the sporadic component is actually composed of particles which originated in streams, which over the course of time have dispersed and become interwoven so much with other sources that they cannot be individually distinguished anymore. Indeed, fine analysis of high-quality data (e.g, Brown et al. 2008, 2010; Campbell-Brown & Wiegert 2009), has allowed an intermediate evolutionary stage between the stream and sporadic components to be identified, namely very broad radiants of long duration, which are still recognizable, particle showers. In this case, the activity from a large but coherent radiant zone in the sky can last up to several months.

In this paper, we focus on the dynamically most processed meteoroid population, namely the sporadic component of meteoroids hitting the Earth. In spite of the fact that sporadic meteoroids impact the Earth from various directions on the sky during the whole year, the geometry of their flux, as seen from Earth, is not isotropic (e.g., Jones & Brown 1993; Campbell-Brown 2008). Rather, they are grouped into certain concentrations of radiants and impact with specific ranges of speeds. This is due to a limited number of source populations for the sporadic particles, combined with Earth's heliocentric motion. Thus, most of the particles observable at the Earth in the sporadic complex belong to one of the three groups: (1) the helion and anti-helion sources, (2) the north and south apex sources, and (3) the north and south toroidal (NT/ST) sources.

The helion and anti-helion sources are the dominant mass flux and therefore they were first to be discovered (e.g., Hawkins 1956). Their radiant concentrations peak on the ecliptic some $\pm 70^\circ$ away from the apex direction, hence nearly pointing toward and away from the Sun. This component has been convincingly interpreted as particles released from the population of Jupiter-family comets (JFCs; e.g., Jones et al. 2001; Wiegert et al. 2009; Nesvorný et al. 2011a). This is only natural, since JFCs are the closest vast population of solar system bodies with significant dust production. It has also been shown that the JFC-produced dust particles contribute dominantly to the thermal flux from the zodiacal cloud as seen by space surveys such as the *InfraRed Astronomical Satellite* (*IRAS*) or *Cosmic Background Explorer* spacecraft (e.g., Nesvorný et al. 2010, 2011a).

The apex source radiants are located at ecliptic latitude $\simeq \pm 20^\circ$ north and south from the apex direction. These particles have been associated with some long-period comets (HTCs) or even new (Oort cloud) comets (OCCs; e.g., Jones et al. 2001;

Wiegert et al. 2009; Nesvorný et al. 2011b; and Section 4.3 here). This is also unsurprising, because both HTCs and OCCs—while being more distant from the Earth—are also very prolific sources of dust in the solar system.

In what follows, we consider the third of the source regions for sporadic meteoroids, namely the toroidal particles. The north toroidal source was first discovered and fully described in the early 1960s from the analysis of Harvard Radio Meteor Project (Hawkins 1962, 1963), with hints coming from earlier projects such as at Jodrell Bank (e.g., Davies 1957; Davies & Gill 1960). Its counterpart, the south toroidal source was confirmed in a study of meteor orbit surveys by Jones & Brown (1993), and later in the more detailed study of AMOR data by Galligan & Baggaley (2005), or Jicamarca high-power large-aperture radar by Chau et al. (2007). The most detailed study of the north toroidal complex so far was presented by Campbell-Brown & Wiegert (2009). An optical component of the north toroidal source was also identified (see, e.g., Hashimoto et al. 2011).

It is interesting, and to some extent actually puzzling, that understanding the parent source for the toroidal particles has proved to be the most difficult of all the sporadic sources. Their apparent source zone on the sky is characterized by high-latitude radiants of $\simeq \pm(55^\circ$–$60^\circ)$, both north and south from the apex direction. The toroidal particles impact the Earth with a typical velocity of $\simeq$35 km s^{-1}. When translated to the parameters of the pre-atmospheric heliocentric orbits, the toroidal particles seen by radars reside on high-inclination orbits with respect to the ecliptic ($\simeq 70^\circ$), have semimajor axes close to 1 au, but with a long tail to larger values, and have a broad distribution of eccentricities with a maximum at $\simeq$0.2 (e.g., Campbell-Brown & Wiegert 2009 and Figure 3 below). Taken straight, there is clearly no significant population of solar system bodies with similar orbits that could provide a significant amount of dust.

Hence, this made previous workers to speculate that either (1) the toroidal particles may come from a single or few, unusual source(s), some of which may be presently extinct, or (2) to conclude that the observed toroidal particle orbits must have significantly evolved from their source regions. The latter might make the source identification somewhat problematic, but there is no a priori reason to believe that the problem should be more complicated than for the helion/anti-helion or apex sources. We shall see in Section 2.1 that an important step before further tracking the zone of origin for the toroidal particles is to apply a proper debiasing, specifically to take into account the collision probability with the Earth for particles on different heliocentric orbits.

1.1. Previous Models

As far as modeling efforts for the origin of toroidal particles are concerned, we note that Jones et al. (2001), in a short but interesting conference paper, assumed the source of the toroidal particles could be interpreted as a high-inclination tail of the JFC-released particles. To prove the concept, they modeled a simple analytic Poynting–Robertson (PR) drag driven evolution from JFC population, but noted that in order to obtain toroidal-source particles they need to significantly push the initial inclination values of this comet population. In particular, instead of having a Gaussian inclination distribution with a standard deviation of $\simeq 11.8^\circ$ (observed), they needed to unrealistically increase this value to $\simeq 28^\circ$ so that the toroidal concentration of radiants would appear in their simulation. While interesting, there is no real physical justification for such a large inclination component among JFCs. Interestingly though, what they started with is roughly an evolutionary phase in our simulations below that identify the starting orbits of the toroidal particles with the HTCs.

Wiegert et al. (2009) presented an effort to explain all major sources of sporadic meteoroids. As far as the toroidal component is concerned, they considered both long-period comets and near-Earth asteroids (NEAs) with high-inclination orbits as potential (immediate) source bodies. Even though interesting, the conclusion from this model suffers significant drawbacks and potential degeneracies. First, the authors did not perform any quantitative fit to the data and hence the modeled orbital distribution of the toroidal particles did not match the observations except in a broad qualitative manner (Figure 4 in Wiegert et al. 2009). More importantly, though, the authors were led to conclude—in contradiction with their initial assumptions—that activity of a single or a few individual objects may dominantly contribute to either of the apparent radiant source regions of meteoroids on the sky. In the case of the NT source region they in fact preferred contribution from several NEAs. This is, however, the weakest point of their model because there is no justification for significant activity from most NEAs as far particle production is concerned (even in the most famous case of 3200 Phaeton, for which a solid evidence of the dust production has been found, e.g., Jewitt et al. 2013, the contemporary amount of dust produced is far too small to account for the associated Geminid stream and in Phaeton's case only occurs because of its unusually small perihelion distance).

In an earlier work, Wiegert (2008) studied the orbital evolution of faint streams with radiants located in the arc structures connecting the toroidal region on the sky with the north and south apex regions (see also Brown et al. 2010). By performing backward integration in time for several of such streams, Wiegert (2008) was able to track their evolution to JFC-like orbits with high inclinations affected by the Kozai–Lidov oscillations. When running forward simulations for particles from such starting orbits (somewhat similar to simpler modeling work of Jones et al. 2001), he concluded that some of them were also capable of populating the toroidal source regions. However, sparse sampling of the initial orbits and/or unavailability of a more advanced collision probability scheme made him conclude that the observed and modeled eccentricity distribution in the NT source still do not match perfectly.

In our work, we revisit the problem of the ultimate source of background particles seen in the toroidal source regions. We are simply returning to the idea qualitatively outlined by Davies & Gill (1960) but equipped with modern observations and better computational speed. These authors hypothesized that the high-inclination and low-eccentricity sporadic NT component ultimately originates from long-period comets. Particles released from them would have a higher chance of overcoming Jupiter's barrier at larger inclinations and would thus be able to migrate into the inner parts of the solar system. Along the way, their orbits would have been circularized by the effects of PR drag. Once on orbits close to the Earth, their collision probability would be so high that they would overwhelm the contribution of their sister particles still residing on high-eccentricity orbits having much longer orbital periods.

1.2. Paper Outline

Our goal is to create a theoretical steady-state model that provides a distribution of orbital elements and velocities of meteors in agreement with observations from CMOR (a brief overview and introductory data analysis is presented in

Section 2). Our numerical model tracks the dynamical evolution of thousands of dust particles in the 100 μm to mm size range released from a synthetic population of HTCs (Section 3.1). We include both gravitational perturbations by planets and relevant non-gravitational effects, namely direct radiation pressure and PR drag. The particle evolution is followed for millions of years until particles reach end of their life, either by being scattered from the solar system by giant planets (mostly Jupiter), hitting one of the terrestrial planets, or evolving too close to the Sun.

The main assumptions and features of the dynamical-evolution model are presented in Section 3.2. Particles in our simulation can also be destroyed because of a collision with other particles of the zodiacal cloud (a simple model is described in Section 3.3). Confining the radiant zone to the NT source as defined by previous studies (e.g., Campbell-Brown 2008), we attempt to adjust free parameters in our model, including the size distribution of the particles at their source (see Section 3.4), to match the observations.

We also attempt to use the CMOR data to absolutely calibrate the population of our modeled particles from HTCs, though we find that this can be presently done only within an order of magnitude (see Section 4). We finally relax the restriction in the model to test particles having to occur in the toroidal-source radiant zone and check the contribution of our modeled HTC dust population to the other source radiant regions on the sky, in particular the north and south apex sources and the arc structure connecting the toroidal sources to the north and south apex sources (Section 4.3). We also check that our estimate of the absolute number of particles from HTCs in interplanetary space does not violate constraints from thermal observations by *IRAS* spacecraft (Section 4.4). General conclusions and an outlook for future work are in the final Section 5.

We note that the architecture of our approach most closely matches the work of Nesvorný et al. (2011a), who considered particles released from JFCs in an attempt to model the helion/anti-helion meteoroid sources, and Nesvorný et al. (2011b), who considered particles released from OCCs in an attempt to model the north and south apex sources.

We should also note that the sporadic toroidal source is known to have the largest temporal variability (even upon removal of the obvious meteor streams; e.g., Campbell-Brown & Wiegert 2009). What we aim to model here is the long-term, time invariant background part of the source, acknowledging that the variable parts need contributions from one or few individual dust-producing bodies (such as the unusual comet 96P/Machholz). Analysis of the time-variable part of the NT source is left to future work. While our model is compared here with data from the CMOR system that can see only the NT source, we believe our results apply equally to the ST source. Consequently, by combining CMOR data with a more sensitive survey, which can also observe the ST sky region (such as the AMOR system), one could potentially improve our results in the future.

2. OBSERVATIONS

We use data recorded in 2012 by the CMOR system (e.g., Jones et al. 2005; upgrades described in Brown et al. 2012), where a filter to remove major meteor showers was applied. We selected radiant and speed information about particles emanating from the NT source, which we define here in accordance with Campbell-Brown (2008), namely, a region centered at 57° north of the apex direction width 15° with in the ecliptic longitude and 9° width in the ecliptic latitude. While there might be slight differences in definition of the NT location across the literature, we believe this is not important for our work provided we use a consistent definition for the data and the model in our analysis. More importantly, our definition clearly separates our sample of NT orbits from the other important sporadic source zones on the sky.

Having made this selection, we are left with a little more than one hundred thousand recorded particles in the NT source by CMOR in 2012. However, to be conservative, we opted to discard all inputs that have (1) geocentric velocity uncertainty $\geqslant$4 km s^{-1} and (2) radiant position uncertainty $\geqslant 2^\circ$. Here the individual radiant and speed uncertainties are found using a Monte Carlo procedure described in Weryk & Brown (2012).

Using this quality filter, the sample dropped by roughly one half to 56,898 meteors detected during the calendar year 2012. Most of the discarded particles had low signal-to-noise ratios and were at the edge of detectability of the CMOR system (generally small particles). In order to characterize the detection sensitivity of the system, Wiegert et al. (2009) introduced an ionization factor

$$I = \frac{m}{10^{-7}\,\mathrm{kg}} \left(\frac{V}{30\,\mathrm{km\,s^{-1}}} \right)^{3.5}, \quad (1)$$

where m is the particle mass and V its apparent velocity at the Earth (composed of the relative velocity at intersection of the particle's heliocentric orbit with the Earth and the planet's velocity vector including acceleration due to gravity). Particles with I larger than some critical threshold $I_\star$ are detected, while those with I smaller than $I_\star$ produce too little ionization in the atmosphere to be detected by the radar. While necessarily approximate, the ionization factor-based detection criterion is a useful tool for our modeling work in order to select modeled impacting particles that could be recorded by the system. We note that $I_\star$ actually varies over the sky, being a function of echo range and position in the CMOR antenna beam pattern—here we refer to the absolute minimum $I_\star$, which for CMOR occurs at the zenith. The numerical constants in (1) have been purposely chosen such that $I_\star \simeq 1$ for the CMOR system. While upgrades may decrease somewhat this value a little, we observe that the ionization factor values of the selected NT particles that passed our tightened criterion on radiant and impact velocity uncertainties sharply drop at $\simeq$1. This confirms that the limiting value $I_\star \simeq 1$ is appropriate for our work.

Figure 1 shows a correlation between the size D of the detected NT particles and their apparent impact velocity V. We assumed a bulk density of 2 g cm^{-3} to convert the reported masses m to effective particle sizes. Masses are computed by calculating the electron-line density q of the echo based on its received power, location in the radar beam and range. The mass–velocity–ionization relation of Verniani (1973) is then used to convert from q to m. Particles smaller than $\sim$200 μm were not detected in the NT source because their typical impact speeds make the ionization factor I smaller than $I_\star$. Indeed, we observe a strong D versus V correlation whose low-end closely follows the $I \simeq I_\star \simeq 1$ limit. This prevents small particles with $D \leqslant 500\,\mu$m traveling at low speeds, from being detected. The recorded data does not show any signs of an upper ionization cutoff, which indicates that CMOR detects large and fast particles as well.

Figure 2 shows the number of recorded NT particles in our sample as a function of the solar longitude λ at detection, or equivalently, the temporal flux of the NT particles in 2012. Previous studies (e.g., Campbell-Brown & Wiegert 2009 and

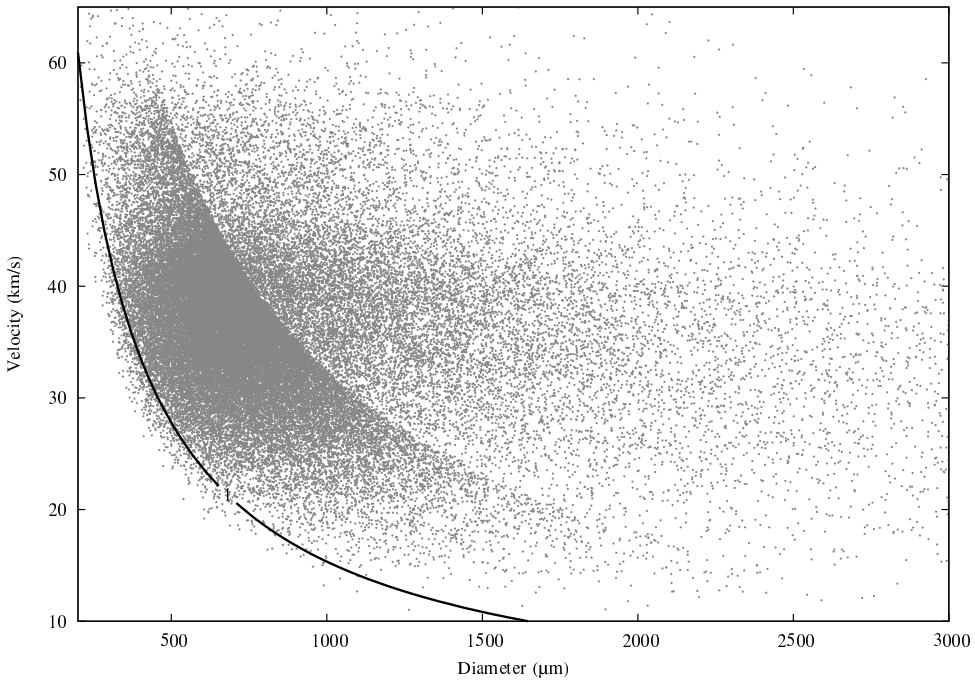

Figure 1. Selected north toroidal source particles recorded by the CMOR system during the year 2012: effective size D (in μm) vs. impact velocity V (in km s^{-1}). Isoline of a constant ionization factor (Equation (1)) for $I = I_\star = 1$, shown by the solid line, roughly delimit the range of detected particles. The discontinuity in apparent numbers running parallel to the $I_\star = 1$ line represents the approximate transition point between underdense and overdense echoes.

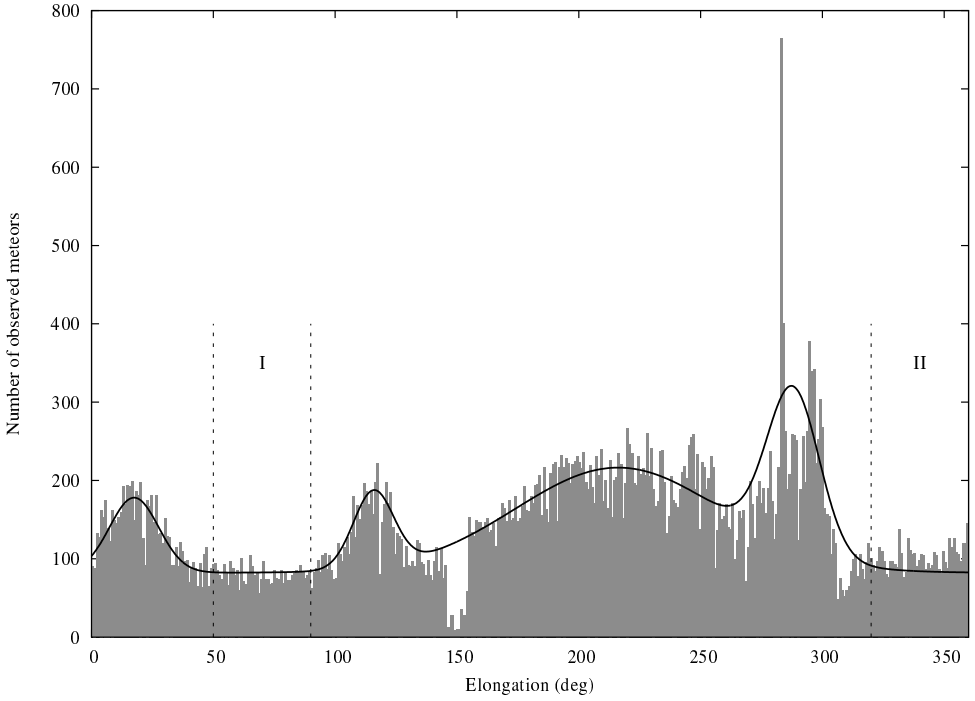

Figure 2. Selected north toroidal source particles recorded by the CMOR system during the year 2012: daily impact statistics vs. solar longitude λ. The solid black line, composed of a constant—background—term and four broad Gaussian contributions, depict an envelope model for activity in the NT source (compact streams such as Quadrantids at $\lambda \simeq 283°$, and θ and ξ Coronae Borealids at $\lambda \simeq (285°–300°)$ are not considered in this fit). The intervals labeled I and II, delimited by dashed lines, are our primary representation of the background, steady-state component in the source.

references therein) noticed and characterized significant variability in the source which is also immediately seen in this figure. However, in this work, we shall not study fine details of the source variability. Our assumption is that the source has its own permanent (steady-state) activity over which contributions from individual source(s) overlays. In this work we plan to model the primary, presumably long-term stable, component. Obviously, it is not easy (if even possible) to rigorously separate the steady and variable components. Here we take a simple approach and proceed as follows.

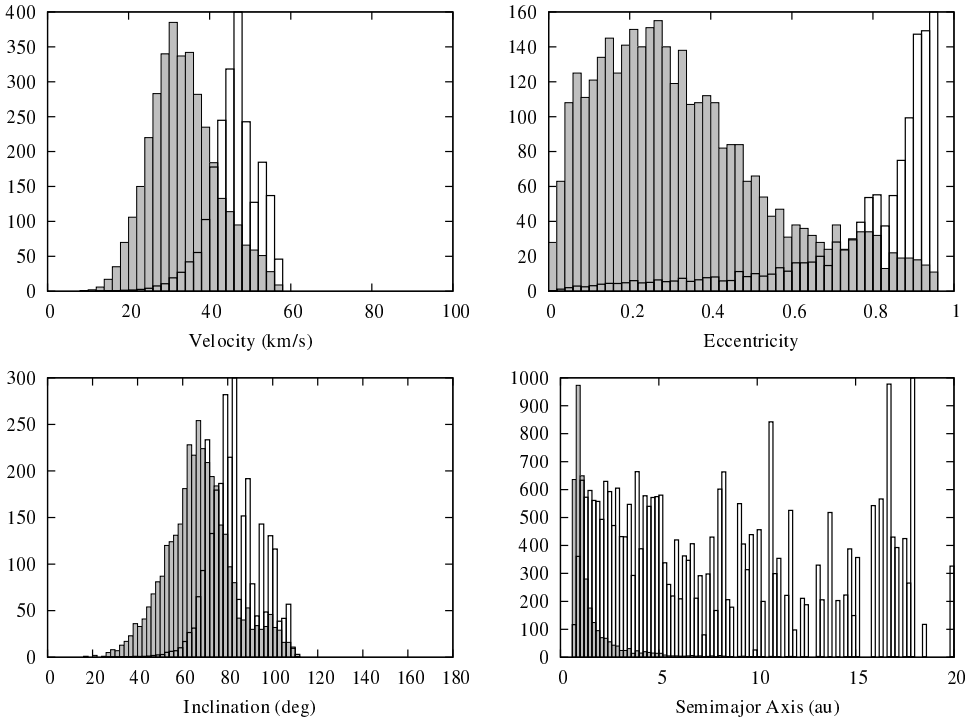

Figure 3. Distribution of geocentric impact speed (top left), eccentricity (top right), inclination (bottom and left), and heliocentric semimajor axis (bottom right) for 3550 selected particles of the background population of NT particles. The gray histograms correspond to the observed data from CMOR. The unfilled black histograms were constructed using the methods described in Section 2.1 and approximate the distribution of the population with an ability of generating observed NT particles normalized to unity. The raw and generating distributions are significantly different, implying there are strong selection effects in the observed population. The parameters of the generating population led us to choose HTCs as the most promising source of NT particles.

First, we recognize that there are two principal strong stream contributions in the NT source, namely: (1) Quadrantids at $\lambda \simeq 283^\circ$, and (2) θ and ξ Coronae Borealids at $\lambda \simeq (285^\circ$–$300^\circ)$. These are the sources H and I described in Campbell-Brown & Wiegert (2009). Next, there are roughly four broader, more dispersed stream contributions named Helion and Antihelion Arc and B as given in Campbell-Brown & Wiegert (2009) throughout the course of the year. In our data (Figure 2) we can see them as roughly Gaussian features at solar longitude of $\sim 17^\circ$, $\sim 115^\circ$, $\sim 216^\circ$ and $\sim 280^\circ$ (the last has been also described by Brown et al. 2010, as an underlying Quadrantids extension consisting of the November ι Draconids and December α Draconids, perhaps indicating an old stream complex related to activity of the comet 96P/Machholz). The total duration of this complex is one to two months. We find it interesting that these four broad features may actually be organized in two pairs with longitude difference of $\simeq(180^\circ$–$200^\circ)$. Hence at least two different individual sources are needed, out of which the pair consisting of the toroidal D stream and the Quadrantid broad underlying stream have a likely progenitor in the activity of comet 96P/Machholz several thousand years ago (e.g., Gonczi et al. 1992; Jones & Jones 1993; Sekanina & Chodas 2005; Kaňuchová & Neslušan 2007). We shall address this issue in a forthcoming study.

To avoid confusion between background and individual sources we are then left with two longitude intervals apparently devoid of stream activity: (1) $\simeq(50^\circ$–$90^\circ)$, and (2) $\simeq(320^\circ$–$360^\circ)$. Campbell-Brown & Wiegert (2009) describe a weak and very broad toroidal source C in the latter interval, while no recognizable individual source is seen in the first interval. As a result, we shall consider NT particles in the first interval (1) to be our primary test sample of background population. Tests show, however, that orbital data for particles in the second interval (2) are very similar to those in the first interval (1), so we feel justified in checking our results by merging information from both intervals of time. Our restricted sample of background NT-source particles contains 3550 individual meteoroid orbits, roughly 90 particles hitting the Earth per day.

Figure 3 (gray histogram) shows the distribution of the apparent impact speed of the selected NT particles and distributions of the orbital elements, namely semimajor axis, eccentricity and inclination. Our results are very similar to those of Campbell-Brown (2008) or Campbell-Brown & Wiegert (2009). The most distinct features are: (1) semimajor axis distribution peaked at 1 au, (2) broad eccentricity distribution with a predominance of low-eccentricity orbits (eccentricities smaller than ~ 0.4), and (3) characteristic inclinations between 60° and 70° with a tail to retrograde orbits (correlated with a velocity-distribution tail to values larger than ~ 45 km s^{-1}). Data in the second interval (2) described above show only a very small excess of larger-eccentricity orbits relative to period (1). A more detailed study of the data set may be found in the Appendix.

2.1. Searching for the Generating Population

Before we formulate our model and compare its results with the observations of the background NT particles, we first perform a simple analysis of the observed NT meteoroid sample selected in the previous section.

Our first step is to debias the observed population for impact probability with the Earth. This is an important factor because a body on a given heliocentric orbit with semimajor axis a, eccentricity e and inclination i has a mean collision probability $P_{\rm coll}$ with the Earth that strongly depends on these parameters. Since we aim to model the steady-state, background

population, we can use collision probability values averaged over a long-enough time interval (characteristic of the variation of the orbital longitudes of node and pericenter—typically of order 10^4 yr for NT particles). Obviously, an underlying hierarchy in the orbital time evolution is assumed here, notably that the secular angles change faster than the semimajor axis changes due to radiation drag. While this may not always be satisfied for individual particle orbits, such an assumption holds population-wise.

Traditionally, workers adopted Öpik-type theory for $P_{\rm coll}$ (e.g., Öpik 1951), or equivalent variants that only allow for slight eccentricity of the target planet (e.g., Wetherill 1967; Greenberg 1982). However, the dynamics of the high-inclination orbits which dominate in the NT source violate the assumptions of all these approaches by being strongly affected by the Kozai–Lidov cycles (e.g., Kozai 1962). This motivated us to formulate a new secular collisional probability approach that takes into account at least the fundamental elements of the Kozai–Lidov effect (Vokrouhlický et al. 2012; Pokorný & Vokrouhlický 2013). While still approximate (it does not take into account the orbit's ability to be scattered by Jupiter if close encounters to that planets are possible), the new theory represents an important improvement over previous ones. Not only is a refined value of $P_{\rm coll}$ obtained, which for some sets of orbital elements may be similar to unrefined value and for another set the difference may be higher than an order of magnitude, but also a correct representation of the radiant position at intersection with the Earth is calculated.

For that reason we always use our new formulation of $P_{\rm coll}$ in this paper. In fact, a faster variant from Vokrouhlický et al. (2012), where the target planet is assumed to be on a circular orbit, is fully sufficient for our work.

We can now debias the population of particles observed from the NT source by representing a single input of each particle seen to impact from a heliocentric orbit with (a, e, i) elements with a weight $\propto 1/P_{\rm coll}$ and obtain a population of particles with an ability to generate observed NT orbits. Figure 3 (black open histograms) shows the results. The generating population is very different from the observed one. The semimajor axis values distribution is basically flat up to Jupiter's heliocentric distance of $\simeq$5 au, followed by a slow decrease in numbers at larger values. There is still a fair contribution of orbits with a beyond 10 au, though both noise (due to few observed orbits with those values of a) and imperfection in $P_{\rm coll}$ determination affect the distribution trend. In the same way, the generating eccentricity steadily increases to large values, indicating the low-eccentricity population is just a minor part of the whole distribution. The inclinations, while constrained by the relatively tight radiant zone on the sky, are also slightly shifted to larger values, now having a higher contribution of retrograde orbits. This is also reflected in systematically larger impact velocities for the generating population. All these findings point to a cometary origin of the NT particles. Since JFC orbital parameters are not compatible with the orbital elements of generating particles seen in Figure 3, especially as far as the semimajor axis and inclination are concerned, we are left with the long-period comet population. The contribution of the new comets has been studied by Nesvorný et al. (2011b), who showed that the isotropic and more distant initial orbits preferentially led the dust particles impacting in the apex sources. We thus suggest that the prime candidate source population for the NT particles are HTCs. In Sections 3 and 4 we explore this hypothesis with a detailed numerical model.

3. MODEL: THEORETICAL BASIS

Our model contains the following elements. We start with a description of the assumed ultimate population of source bodies from which the NT particles are initially released. To that end we use an up-to-date synthetic model of HTCs (Section 3.1). The orbital evolution of particles with different sizes is numerically propagated until it reaches one of several possible end-states (ejection from the solar system or impact on the Sun or planets; Section 3.2). The integrator accounts for both gravitational perturbations due to planets and radiative effects (direct solar radiation pressure and PR drag). Evolutionary paths for all particles are stored and used for further analysis. The effects of collisional destruction by impacts of other zodiacal cloud particles are modeled separately using a Monte Carlo probabilistic scheme (Section 3.3). Proper weighting of the contribution from particles with different sizes is also needed (Section 3.4). Merging the data together to simulate the synthetic impact population at NT source and comparison with observations is covered in Section 4.

3.1. HTC Model: Initial Particle Orbits

We adopt results from Levison et al. (2006). These authors developed a steady-state model for HTC orbital architecture, assuming they originate in the scattered disk. Tracking the orbital evolution of a large number of test particles, their model was able to successfully match the observed distribution of HTC orbital elements, including the most problematic case of the inclination distribution that was not reproduced in previous efforts. This is because the observed inclination distribution of HTCs contains preferentially prograde orbits with a median inclination value of $\sim$55° and only a small fraction of comets on retrograde orbits (Figure 4). In relation to the HTC dust it is thus interesting to note that previous works, such as Wiegert et al. (2009), appeared to focus on the role of famously known long-period comets such as 1P/Halley or 55P/Tempel-Tuttle, whose orbits are actually outliers in their group. We also note that nearly half of HTCs have inclination values between $\sim$40° and $\sim$80°, which additionally favors them as a source for NT (and ST) particles.

The starting orbits for our particles are those of the synthetic, steady-state population of HTCs from Levison et al. (2006). Since we take into account radiation forces, including direct radiation pressure and PR drag, in the particle dynamics, the osculating orbits upon release from the parent comet change (e.g., Dermott et al. 2001). This is because radiation pressure effectively changes the solar mass M to $M\,(1-\beta)$, with

$$\beta = 1.15\,\frac{Q_{\rm pr}}{\rho D}\,, \tag{2}$$

for a particle of a bulk density ρ (in g cm^{-3}) and size D (in μm). Details of the radiation interaction with the particle are included in the pressure coefficient $Q_{\rm pr}$. In all our simulations below we take $\rho = 2$ g cm^{-3} and set $Q_{\rm pr} = 1$ for simplicity. One of the solar mass recalibration aspects is that particle orbits may become unbound when released from a high-eccentricity cometary orbit (Figure 4). To stay initially bound in the solar system, a particle with a beta factor β must be released at heliocentric distance R

$$R > R^\star = 2\beta a\,, \tag{3}$$

for a cometary orbit with a semimajor axis a (e.g., Dermott et al. 2001). Since the particles of interest for us have typically

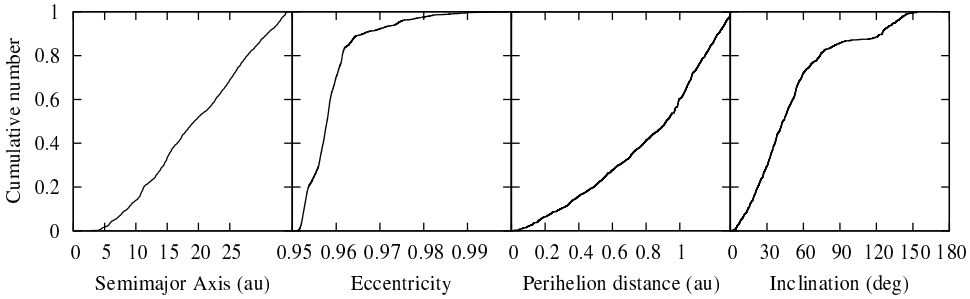

Figure 4. Distribution of the heliocentric orbital elements of the synthetic population of HTCs: semimajor axis a (left), eccentricity e (second from left), perihelion distance q (second from right), and inclination i (right). Most notably, the inclination is unevenly distributed about 90°: the median inclination of HTCs is ∼55° and only ∼20% of orbits have inclination larger than 90°. This favorably directs particles surviving the Jupiter barrier to the toroidal source zone.

$D \geqslant 200\ \mu$m, as suggested by Figure 1, the condition (3) is not very restrictive (it only prohibits release very near perihelion for comets with the largest a and our smallest particles). To keep things simple, since our model contains enough free parameters of more importance, we release particles uniformly in mean longitude along the cometary orbits (not seeking thus an additional parameterization to model their ejection as more concentrated toward perihelion). We also give the particles zero ejection velocity with respect to the comet, accounting only for the radiation pressure effects mentioned above.

The starting orbits of our particles have different perihelion distances q in accord with the distribution shown on the third panel in Figure 4. Comets with smaller q values are generally more active and may deliver more dust particles to interplanetary space. In order to account for this bias, we introduce a weighting factor W_a, assigned to each of the particles as

$$W_a = q^{-\gamma}\ . \tag{4}$$

Here q is in astronomical units and γ is an adjustable parameter of our model. We nominally set $\gamma = 0$, but test the sensitivity of the results to adopting positive γ values.

It is also important to note that we consider a population of starting orbits with perihelion q up to a maximum value of 1.3 au (Figure 4). However, selecting a limited number of particle sizes, we also tested a solutions with q extending to 2.6 au, extrapolating the trend from the Levison et al. (2006) model. We found that the results are not sensitive to this limit and are comparable to our main results. For that reason we believe that the limitation of $q \leqslant 1.3$ au does not represent a limitation of our model.

3.2. Orbital Evolution Propagator and Results of Particle Integrations

The particle orbits were numerically propagated using the `swift_rmvs3` code (e.g., Levison & Duncan 1994; http://www.boulder.swri.edu/~hal/swift.html) which allows an efficient long-term integration of test bodies in the solar system. Gravitational perturbations from all planets, whose initial orbits were obtained from the JPL DE405 ephemerides, were taken into account. The radiation forces were implemented in two steps upon evaluation of the β-factor for particles of a specified size (Equation (2)): (1) the direct radiation pressure was represented as the appropriate recalibration of the solar mass, and (2) the PR drag was introduced as a perturbation like the gravitational effects of planets. The code was tested and successfully used in previous studies (e.g., Nesvorný et al. 2006, 2010, 2011a, 2011b). We also take into account the drag effect of the solar wind which is, on average, believed to increase the PR drag by some 30% (e.g., Dermott et al. 2001).

Since we aim to model a steady-state population of HTC-related particles in interplanetary space, once started on their initial orbits, the particles were followed until the whole population was eliminated. There were several orbital end-states in our simulations. Close encounter with giant planets, mainly Jupiter, could eject the particles from the solar system (we consider this condition to be when the heliocentric distance of the particle becomes larger than 10,000 au). Particles may also hit the Sun or its immediate vicinity. We eliminate them when the heliocentric distance becomes smaller than 0.05 au, roughly ten solar radii. Below that distance the effective temperature of the particles exceeds ∼1300 K and the particles are deemed to evaporate or be torn by thermal stresses (e.g., Čapek & Vokrouhlický 2010). Some particles may even hit a planet, including the Earth, but the likelihood is small given a limited number of integrated bodies. We do not make use of the directly simulated Earth impacts in our analysis.

Since all planets, including Mercury, are propagated together with the dust particles in our simulations, we use a short timestep of 1 day. In order to prevent disk overflow, the particle orbits are exported, and used for further analysis, once every 100 yr in all our simulations. We ran simulations for particles of different sizes D, namely, 100 μm, 200 μm, 400 μm, 600 μm, 800 μm, 1000 μm, 1200 μm, 1500 μm, and 2000 μm. Each time, we had 20,000 randomly generated orbits of particles, giving altogether nearly 200,000 propagated particles. Most of the runs were completed by $t = 10$ Myr, and only some of the largest particles lasted longer in our simulations. We found that the dynamics of particles in our two largest-size bins is sufficiently similar to bin them together. This means trajectories of our largest particles, 2 mm in size, could be taken as a good template for dynamics of any other particles with larger size. Data shown in Figure 1 indicate that we do not need to integrate orbits for particles with sizes smaller than 100 μm for this project as this is below the sensitivity limit for CMOR. With our choice, and computer-power limitations, we believe we sufficiently covered the necessary interval of particle sizes for the population size distribution analysis (Section 3.4).

In the zero approximation, the population depletion with time t in our runs may be matched by an exponential law $\propto \exp(-t/\tau)$, where τ is some characteristic timescale. For our smallest particles of 100 μm and 200 μm we found $\tau \simeq 0.67$ Myr and $\tau \simeq 1.07$ Myr, respectively. For all larger particles, the τ value ranged between ∼1.48 Myr and ∼1.85 Myr, quickly approaching a limiting value of ∼1.9 Myr. This information is necessary when estimating the production rate of HTC

particles at the source to maintain a steady-state situation (see Section 4).

Another interesting piece of information that we obtain from our simulations relates to the particles ability to decouple from the gravitational influence of Jupiter and migrate inward to the terrestrial planet zone. We find that ∼25% particles of 200 μm size decouple from Jupiter, while only ∼5% of 1 mm particles are able to do so. These percentages are large and promising for the modeling of the toroidal sources. Note that similar integrations for particles released from the Oort cloud comets revealed that less than ∼0.1%–0.5% of particles decouple from Jupiter in this size range (e.g., Nesvorný et al. 2011b). This is more than a factor of 10 fewer particles than in our simulations of HTC-born particles.

3.3. A Simple Implementation of the Particle Collisional Lifetime

Particles may also be removed on their way toward the inner solar system because of a collision with another particle in the interplanetary space. This effect is not directly modeled in our numerical simulations and must be considered separately. Indeed, the estimated collisional lifetime for particles in the relevant size range (Figure 1) may be shorter than the characteristic dynamical lifetime mentioned above, especially when particles move to inside part of the Jupiter's orbit. For reference, a $D \sim 1$ mm particle on $a \sim 1$ au orbit, typical for the NT source zone (Figure 3), has an estimated collisional lifetime $\lesssim 10^5$ yr (e.g., Steel & Elford 1986; Grün et al. 1985). This may be up to an order of magnitude shorter than the dynamical transport time from its initial, HTC-like orbit.

Similarly to Wiegert et al. (2009), we used the collisional model of Steel & Elford (1986, hereafter SE86), first checking that similar results would also have been obtained with the model by Grün et al. (1985) that has been used by Nesvorný et al. (2011a, 2011b). Conveniently, the SE86 model provides the dependence of the collisional lifetime on the orbital elements of the particle, including the inclination value, which was our largest concern in this study. In order to estimate the collisional lifetime of a particle, SE86 use a technique of volume integration of partial space–density distribution functions of (1) the zodiacal cloud model, and (2) that of particle-orbits swept during one secular cycle of node and pericenter longitudes (see Kessler 1981). There are obviously large approximations taken both in (1) and (2). As far as (1) is concerned, SE86 use a very simple density distribution model of the zodiacal cloud (Equation (2) in SE86). We adopt this model as well. As far as (2) is concerned, SE86 assume constant eccentricity and inclination values during the secular cycle. This is particularly violated for the high-eccentricity and high-inclination orbits studied here, and thus we have slightly modified the SE86 technique. In particular, we evaluate an instantaneous collision probability of the particle orbit with the zodiacal cloud performing simply a one-dimensional averaging orbit revolution about the Sun (some details are given in Supplementary materials). This result better suits our model, because we can now fully account for nontrivial secular variations of the particle orbit as provided by our numerical integrator. Moreover, we model the collisional dynamics of the particles using a Monte Carlo model with a timestep shorter than the orbital secular cycle, so the estimate of a collisional lifetime for the instantaneous orbit would be needed anyway. As far as the size dependence of the collisional lifetime is concerned, we assumed that projectile capable of breaking a given particle is one ∼30 times smaller in size (SE86) and used the zodiacal cloud size distribution from Grün et al. (1985). Obviously, all these assumptions are grossly simplified. For that reason we also used an empirical factor $F_{\rm coll}$ by which we multiply the estimated collisional lifetime. Values of $F_{\rm coll}$ between 1 and 30 are allowed in our procedure and adjusted to obtain the best match between the observations and the model (Section 4; Nesvorný et al. 2011a, 2011b have used a similar scheme of extending the canonical collisional lifetime values).

We implement the effects of a finite collisional lifetime in the following way. Our numerical integration of the particle-orbital evolution treats them as indestructible bodies and outputs the state vectors once every $dt = 100$ yr. In the modeling phase, we load these orbital histories and follow the particles anew. At this phase, though, we assume a finite collisional lifetime $\tau_{\rm cl}$ and at each timestep dt we consider a probability $1 - \exp(-dt/\tau_{\rm cl})$ that the particle collisionally disrupts. At each timestep we thus consider a randomly generated number, compare it with the disruption probability and decide whether the particle is to be eliminated from further analysis. Since such a Monte Carlo procedure brings a stochastic element in our work, and computer power allows only a small number of particles to be analyzed, we typically repeat the analysis 25 times and average over the results.

We should also point out that in this work, as well in all previous works, the particles deemed to collisionally disrupt are fully eliminated. In reality, though, disruption events form fragments that themselves continue orbital evolution and eventually may contribute to the observed signal at the Earth. We believe that the $F_{\rm coll} > 1$ values which best suit in our model (Section 4) effectively account for the fragment contribution at the zero level. In other words, the $F_{\rm coll} > 1$ values might not be in great conflict with the $\tau_{\rm cl}$ values estimated by SE86 and Grün et al. (1985).

3.4. Assumptions About the Size Distribution of Particles at Their Source

Particles of different size D may take different orbital evolution paths and thus contribute in an uneven way to our results. We thus need to run our simulations for a set of different sizes and then combine the data. The underlying weighting procedure has to account for the size frequency distribution (SFD) of the particle population. Except for Section 2.1, we always work in this paper with the SFD at the ultimate source in the solar system, i.e., corresponding to the particle population freshly released from the parent comets. The source SFD reported here is not equal to that of the Earth-impacting particles that is affected by both dynamical (PR drag) and physical (collisions) effects. Our model takes these alterations into account.

While the particle SFD may be a complicated function of D in principle, experience shows that a broken power-law representation is a fairly good approximation unless the size range ($D_{\rm min}$, $D_{\rm max}$) is too large. Figure 1 provides guidance for the selection of these limits. Namely, we consider $D_{\rm min} \simeq 200\,\mu$m, because basically no smaller particles are recorded in our sample due to the ionization factor cutoff $I \geqslant I_\star$ described above. Similarly, we take $D_{\rm max} \simeq 3$ mm, because particles larger than this value are rarely detected by CMOR or have long-duration echo characteristics which do not allow automatic orbit determination by CMOR in the NT source.

The most general SFD we test in our work allows a breakpoint between piece-wise power laws at a midpoint[4] $D_{\rm mid} \in$

[4] We may also use a single-slope power-law SFD by setting $\alpha = \beta$ in all formulas in Sections 3.4 and 4.2; one easily verifies that $D_{\rm mid}$ is either arbitrary or drops out of the equations in that case.

($D_{\rm min}$, $D_{\rm max}$). In particular, at larger sizes ($D_{\rm mid}$, $D_{\rm max}$) we assume a power law with a differential size distribution exponent α:

$$dN = N_\alpha \left(\frac{D_{\rm max}}{D}\right)^{\alpha} \frac{dD}{D_{\rm max}} , \quad (5)$$

while at smaller sizes ($D_{\rm min}$, $D_{\rm mid}$) we assume a power law with a differential size distribution exponent β:

$$dN = N_\beta \left(\frac{D_{\rm mid}}{D}\right)^{\beta} \frac{dD}{D_{\rm mid}} . \quad (6)$$

To ensure continuity in population statistics we must choose $N_\beta = N_\alpha\,(D_{\rm max}/D_{\rm mid})^{\alpha-1}$. Cumulative SFD functions, compatible with differential distribution laws from Equations (5) and (6), are given by

$$N(>D) = N_0 \left(\frac{D_{\rm max}}{D}\right)^{\alpha-1} , \quad (7)$$

for $D \in (D_{\rm mid}, D_{\rm max})$ and

$$N(>D) = \frac{N_\beta}{\beta-1}\left(\frac{D_{\rm mid}}{D}\right)^{\beta-1} + C_1 , \quad (8)$$

for $D \in (D_{\rm min}, D_{\rm mid})$. Here we introduced a constant

$$C_1 = \frac{N_\beta}{\beta-1}\frac{\beta-\alpha}{\alpha-1} , \quad (9)$$

and additionally made a choice $N_\alpha = N_0\,(\alpha-1)$ with a free parameter N_0 in Equation (9). One convenience of doing so is good behavior of the cumulative SFD at $D = D_{\rm max}$. The SFD model is three-parameter, with adjustable constants being (1) N_0, fixing the absolute number of particles with $D = D_{\rm max}$, and (2) exponents α and β. We only require (and expect) both α and β be larger than unity, with an expected value between 3 and 4. A starting point for these values come both from direct comet observations (see, e.g., compilation of data by Fulle 2004) and mass–index calculations for the core of young meteoroid streams (e.g, Blaauw et al. 2011). The total number of particles $N_{\rm tot}$ in the specified range of sizes reads $N_{\rm tot} = C_1 + C_2$, with

$$C_2 = \frac{N_\beta}{\beta-1}\left(\frac{D_{\rm mid}}{D_{\rm min}}\right)^{\beta-1} . \quad (10)$$

While the above formulation enforces continuity of the cumulative SFD across the whole range of sizes, the finite range of the two intervals ($D_{\rm min}$, $D_{\rm mid}$) and ($D_{\rm mid}$, $D_{\rm max}$) produce boundary effects. In particular, performing a least squares fit of the single power-law exponent in each of the intervals may not result in either α of β values, which formally define our broken power-law SFD. The effective power-law exponent may be steeper or shallower, and the boundary effect is larger for a smaller range of sizes (and example of the phenomenon is discussed in the Supplementary materials). We shall bear this in mind when commenting on our formal solutions for α and β in Section 4.

In our procedure, we follow the orbital evolution of a set of sizes ($D_i, i = 1, \ldots, n$) $\in$ ($D_{\rm min}$, $D_{\rm max}$).[5] The population weight assigned to each of the sizes is determined as follows: (1) we divide intervals between the neighbor sizes in half, taking a logarithmic size scale, and (2) use the cumulative SFD in (7) and (8) to determine the number of population particles N_i in the interval centered at the chosen size D_i. Were we able to integrate a large number of sizes, and the SFD were just a single power law with and index α, we would have $N_i \propto D_i^{1-\alpha}$ (compare with Wiegert et al. 2009, Section 2.2.1). The finite number of sizes D_i, and the assumed broken power law of SFD, may change this simple dependence. The estimated population number N_i is used in our fitting procedure as a weighting factor $W_{\rm d}$ assigned to each of the particles of a given size D_i: $W_{\rm d} = N_i$.

[5] In our case, $n = 9$ and the individual sizes D_i were listed in Section 3.2.

3.5. Particle Weighting Together and Fitting Model Parameters

Summarizing the information above, a total weight W is assigned to each particle in our simulation, composed of three partial terms:

$$W = W_{\rm a}\, W_{\rm c}\, W_{\rm d} . \quad (11)$$

The first contribution, $W_{\rm a}$, represents the activity of the source comet in terms of particle production (Section 3.1). The second contribution, $W_{\rm c}$, is the collision probability of the particle orbit at a given time with respect to the Earth. We take $W_{\rm c} = P_{\rm coll}$, where $P_{\rm coll}$ is from Vokrouhlický et al. (2012). The last contribution, $W_{\rm d}$, expresses the increasing number of small particles in the population through the SFD modeling described in Section 3.4. Recall that the fitted SFD is representative of the source population of particles released from HTC.

We assume that our modeled particle population from HTC is in an approximate steady state. This allows us to neglect the time evolution of the individual particles in our simulation since any time should be equally representative of the population state. Rather, we just perform a direct summation of the particle contributions to the impacting population onto the Earth over all computer-stored orbital states of all particles.

Our goal is to examine the hypothesis that the particles released from HTCs represent a viable explanation of the background population of NT meteoroids as seen by the CMOR system. To that end we match the observed particle population, as described in Section 2, to the synthetic population, as obtained with our model in Section 3. In doing so we adjust several free parameters introduced above, namely, (1) SFD slope parameters α and β, break-point location $D_{\rm mid}$ and number N_0 of particles with the largest size $D_{\rm max} = 3$ mm (if fitting only a single-slope power-law SFD we adjust α and N_0), (2) particle production slope parameter γ from Equation (4), and (3) empirical adjustment parameter $F_{\rm coll}$ of the collisional lifetime of particles in the interplanetary space (Section 3.3). This makes in total six free parameters at most (fewer if we decide, for instance, to use just a single-slope power-law SFD representation). We also found it useful to substitute for the N_0 parameter a parameter $F_{\rm imp}$ defined as follows. Having chosen a set of the above mentioned parameters we predict $N_{\rm imp}$ particles impacting in the selected interval of solar longitudes (Section 2) and being detected by CMOR (more of the detection sensitivity in Section 4.2). Ideally, N_0 should assure $N_{\rm imp}$ equals number of truly detected particles $N_{\rm obs} = 3550$ (Section 2). However, to cope with small imperfections of the model and our simplifications in fully modeling the CMOR system response function, we introduce a scaling factor $F_{\rm imp} = N_{\rm imp}/N_{\rm obs}$ and allow its values to range in some reasonable interval around unity.

Our target function may be either one (or a combination) of the orbital element or velocity distributions shown on Figure 3. Denoting R_i the observed data and S_i the modeled data, we use of a chi-square function

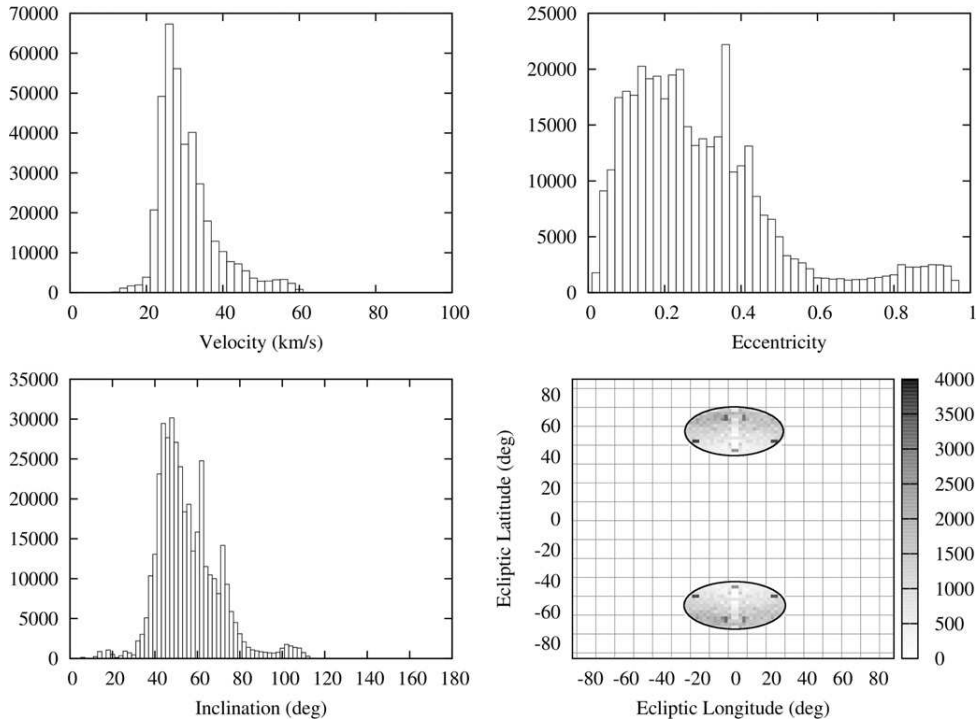

Figure 5. Synthetic NT population of particles with $D = 200\,\mu$m from the sole dynamical transport of HTC-like orbits at origin: infinite collisional lifetime are assumed and no lower cutoff in the ionization factor I at impact (i.e., effectively $I_\star = 0$). Distribution of geocentric impact speed V (top left), eccentricity e (top right), and inclination (bottom left) at impact, all weighted by the collision probability $P_{\rm coll}$. Distribution of radiant locations restricted to the NT and ST zones (bottom and right). Only meteors in two elliptical regions in the bottom and right panel are taken into account. The grid shows the radiant locations that were not considered. PR drag makes the orbital eccentricity decrease significantly from the initial values, and orbits with larger than $\sim 80^\circ$ inclination typically impact the Sun on their way to the inner solar system due to the Kozai–Lidov effect.

$$\chi^2 = \sum_i \frac{(R_i - S_i)^2}{R_i} \qquad (12)$$

to evaluate the similarity of the observed and modeled data (see also Press et al. 2007). The goodness of fit is best represented with ξ^2 normalized by $N - m$, where N is number of data (bins) and m is the number of fitted parameters. Generally, values $\xi \leqslant 1$ indicate a statistically good fit. However, because of possible uncertainty in both the observations and the model (such as data selection by the simplified ionization function I; see Section 2.1), we accept values slightly larger than unity as reasonable.

We use the highly efficient Bayesian analysis search of the admitted solutions in the parameter space as described by the multimode nested sampled method efficiently implemented by the `MultiNest` code (e.g., Feroz 2008; Feroz et al. 2009). The different nature of the adjustable parameters in our model adds a slight complication in our effort. This is because while the SFD parameters (α, β, $D_{\rm mid}$, N_0) and the particle production parameter γ project onto the results in a deterministic way, the effect of the collisional lifetime adjustment parameter $F_{\rm coll}$ is statistical in nature. As mentioned in Section 3.3, the collisional breakup of the particles is a random process. A single simulation has stochastic variations, so we always perform 25 different runs for the same $F_{\rm coll}$ and average the results. This part is computationally demanding, because it needs to follow the orbital evolution of hundreds of thousands of particles from our integration output files. In fact, we opted to pre-compute the modeled distributions of impact speeds and orbital elements for each of the particle sizes and a grid of (γ, $F_{\rm coll}$) values. These results are then combined in the fitting model when trying to constrain the SFD parameter. In this way the SFD parameters are analyzed separately from the (γ, $F_{\rm coll}$). While the Markov chain walking is applied to the (α, β, $D_{\rm mid}$, N_0) parameter space, or alternately (α, β, $D_{\rm mid}$, $F_{\rm imp}$), the grid of (γ, $F_{\rm coll}$) is sampled uniformly within some preset values. The inconvenience is that no correlation of (γ, $F_{\rm coll}$) with the four SFD parameters is obtained, but we accept this limitation for simplicity.

4. MODEL: SYNTHETIC DATA AND COMPARISON WITH THE AVAILABLE OBSERVATIONS

4.1. Testing the Parameter Dependence of the Results

Before we present of our final results, we describe the most important global trends found when changing principal parameters. This helps better understand the problems and the parameter dependencies.

First, we consider separately runs with particles of a different size D and observe how they potentially contribute to the NT source. Figure 5 shows the synthetic population of NT particles for $D = 200\,\mu$m when no limiting cutoff of the ionization factor I is assumed (i.e., $I_\star = 0$). No collisional disruptions were modeled in this test. This reveals the potential impacting population of particles from HTCs as if the instrument had infinite sensitivity and the particles were indestructible (limited only by the dynamical transport from their ultimate source). To the zero order, the results match the observed population of NT particles (Figure 3), including the most prominent feature, the predominance of particles on orbits with low eccentricities. This is caused by a combination of the particle-orbits' ability to decouple from Jupiter (Section 3.2), and efficient circularization by PR drag. Since a reasonable SFD would favor small particles more than large ones, we consider the result to be promising.

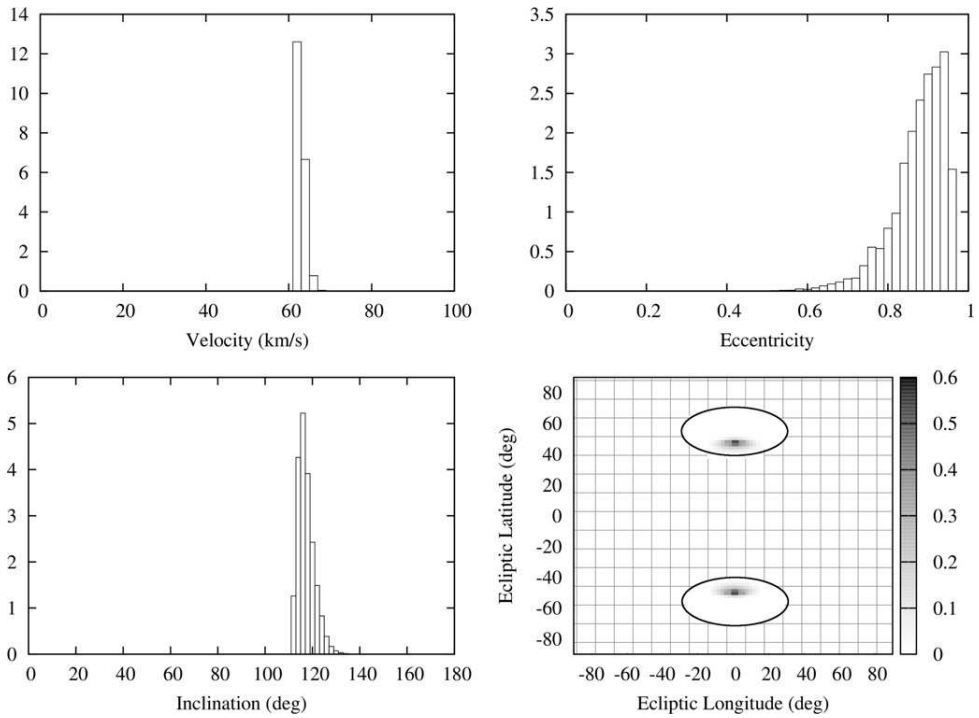

Figure 6. Same as in Figure 5, but now the lower cutoff of the ionization factor I is set to unity ($I_\star = 1$). Only a negligible tail population of particles impacting the Earth satisfy the ionization cutoff criterion $I \geqslant I_\star$, namely atypical orbits with high e and i values (both implying high impact speeds). Because of required high-inclination orbits, the radiants are shifted to lower latitudes. None of these features is compatible with the parameters of the observed NT particles (Figure 3).

However, the limited instrument sensitivity—as expressed here by the minimum ionization factor needed for detection—complicates these first results. Figure 6 is similar to Figure 5 but now takes into account the $I_\star = 1$ limit. Small masses and predominantly low impact velocity made most of the particles contributing to the signal in Figure 5 undetectable with this ionization factor cutoff. What remains is just the high-speed tail of particles impacting from retrograde and high-eccentricity orbits, which are not typical in the population. Moreover, the signal seen in Figure 6 is now not compatible with the observations and this leads to a potential problem. If the SFD of the impacting particles steeply increased toward small sizes (i.e., the weighting factor W_d large enough for $\leqslant$200 μm particles), even the tail contribution would corrupt the model. This puts a severe constraint on the slope β of the SFD (see Section 2.1 for some hints).

Figure 7 shows the same exercise but now for larger particles with $D = 600\,\mu$m. Their nearly 30 times larger mass makes them overcome the $I_\star = 1$ cutoff, and all particles are potentially detected by the CMOR system. It is still very promising that even the $D = 600\,\mu$m particles decouple from Jupiter for the most part and circularize their orbits to $e \leqslant 0.4$ values. Interestingly, the eccentricity range between ~0.5 and ~0.8 is underpopulated. We believe this is a result of the Kozai–Lidov effect, which makes eccentricity and inclination oscillate in a correlated way. The NT zone requires high orbital inclination values, and this requires the eccentricities to be smaller. Above $e \sim 0.8$ the eccentricity distribution again slightly increases, which is the contribution of the population of particles freshly released from the parent HTCs and those lately scattered by Jupiter.

Next, we probe the importance of collisional disruptions of the particles. Figure 8 shows a simulation for $D = 600\,\mu$m particles exceeding the $I_\star = 1$ cutoff (as in Figure 7), but now their losses due to breakups on the way to the Earth are included. We consider a nominal collisional model by Steel & Elford (1986), and also extended particle lifetimes with $F_\mathrm{coll} = 1$ to 10. As expected, shorter lifetimes do not allow particles to evolve much from their initial orbits, pushing thus the typical eccentricities to large values. The inclination values are also discordant with the observations (being systematically larger), indicating that more dynamical evolution is needed to extend their range. This is likely due to scattering by Jupiter and effects of multiple secular resonances in the intra-Jovian region. Clearly, $F_\mathrm{col} \geqslant 10$ values are needed to match the observations (see also a similar results from Nesvorný et al. 2011b).

4.2. Fitting the Model to the Observations

We now attempt to estimate parameters of the synthetic model that would best match the selected observations shown in Figure 3. Before doing so, it is useful to comment on the special status of the population parameter N_0 (Section 3.4, alternately, the F_imp parameter). Having the absolute daily number of observed meteoroids, we may in principle, estimate the total population of HTC particles (thus N_0). However, there is a suite of additional factors which bias the observations, and each of them may add some uncertainty.

First, we selected data from only a $\simeq$1/9 fraction of the 2012 year. The collision probability W_c in the synthetic model normalized estimate is effectively to a year in length, so we have to account for this selection. Second, there is a visibility bias of the source zone on the sky as seen by CMOR (e.g., Campbell-Brown 2008). Luckily, the northern location of the NT source means it is nearly always visible from Canada. We ran a simple simulator of the observations, taking into account the latitude of the CMOR system, the location of the NT source on the sky, and Earth's revolution about the Sun, and found

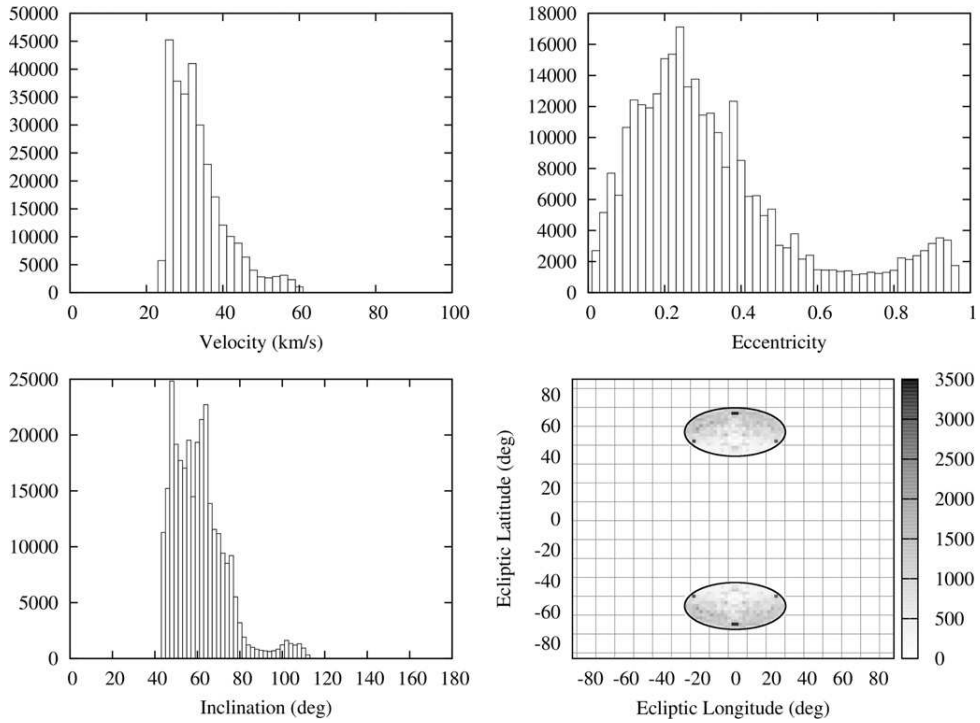

Figure 7. Same as in Figure 6, but now for particles of size $D = 600\,\mu$m. The corresponding figure for $I_\star = 0$ looks basically the same, indicating that virtually all $600\,\mu$m particle pass the ionization cutoff criterion for their typical impact speed of 30–40 km s^{-1}. The gross features of the distributions are now compatible with the parameters of the observed NT particles (Figure 3).

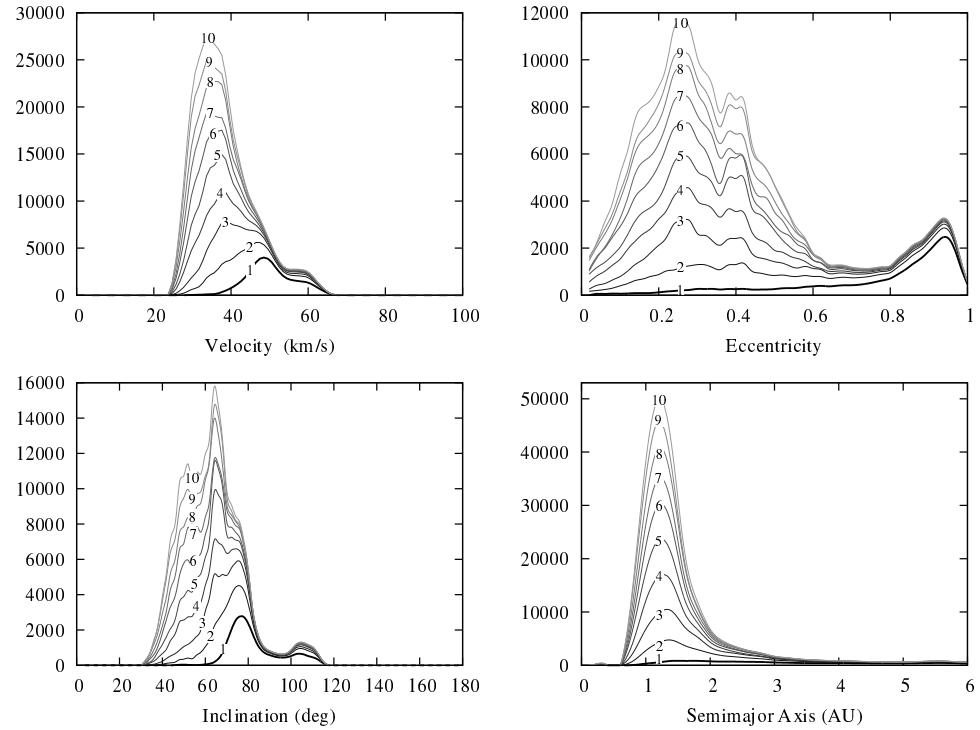

Figure 8. Same as in Figure 7, but now finite collisional lifetime of the particles is also modeled. The black line is for the nominal value of the collisional lifetime as given by the Steel & Elford (1986) model (i.e., $F_{\rm coll} = 1$). The sequence of gray lines assume longer collisional lifetime values than nominal by factors $F_{\rm coll} = 1$–10 from darker to lighter.

that the NT source region receives ≃40% visibility in the time interval we are using. We also used an actual collecting area for CMOR taking into account the true gain pattern of CMOR with mass index equal to 2. Most importantly, CMOR can effectively collect data from a limited surface area on the Earth (e.g., Brown & Jones 1995), while again the particle weighting W_c referred to impacts on the whole Earth surface. We estimate the ratio of the instantaneous surface area having detectable NT meteoroids ablating in the atmosphere as seen by CMOR and that of the Earth to be $\sim 6 \times 10^{-7}$, where the uncertainty of our estimate

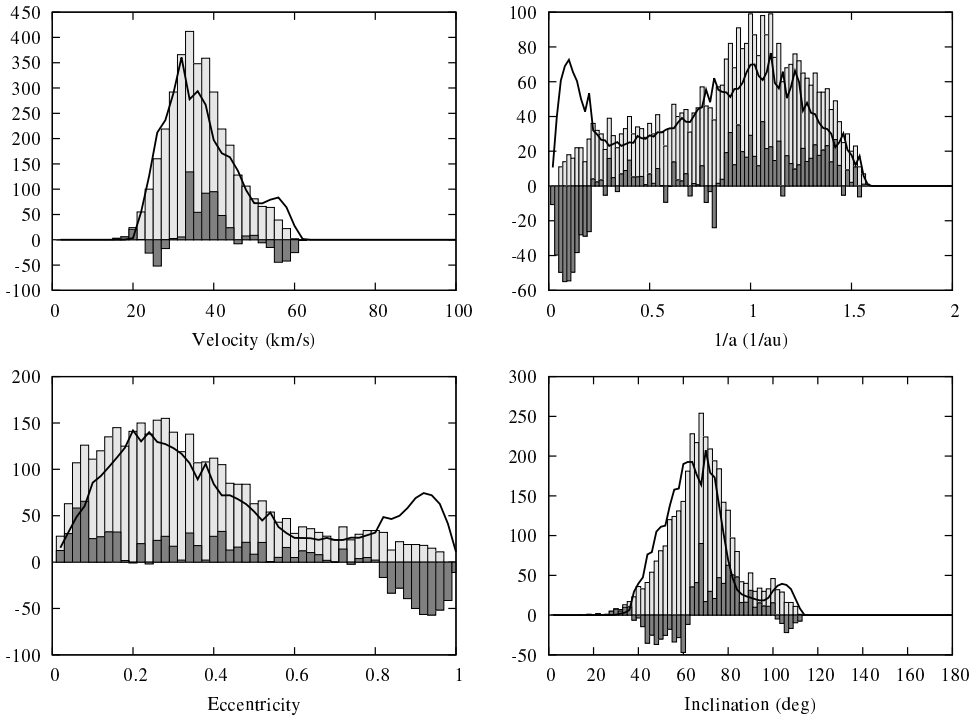

Figure 9. Comparison of the selected data set of NT meteoroids (gray histograms) with the results of our synthetic model (solid line) for the following set of parameters (broken power-law SFD model allowed): (α, β, $D_{\rm mid}$, $F_{\rm imp}$) = (4.7, 1.1, 950 μm, 1.08), γ = 0.0 (comet activity parameter, Equation (4)), and $F_{\rm coll}$ = 20 (fudge factor, by which we have to stretch the nominal values of the particle collisional lifetimes). The dark-gray filled histogram shows a difference between the observed and modeled signal in the particular bin. From this figure on, the semimajor axis a distribution has been replaced with a distribution of $1/a$ that contains a more detailed information.

is about an order of magnitude. We also apply a correction for echo height ceiling effect by multiplying our results by a factor of 2.5; according to (Section 6.5 in Campbell 2002) the NT meteors are detected with 35%–40% efficiency. Putting these factors together, CMOR can see in the spring months selected only 6.5×10^{-8} of the yearly load on the whole Earth. Therefore, we must apply this factor to recalibrate the fitted N_0 parameter in order to obtain information about the whole population of HTC particles.

In the course of testing our fitting procedure we also realized that it is not convenient, nor actually correct, to use semimajor axis distribution (see, e.g., Figure 3) of the impacting particles as a equal-weight data set. This is because the information in this parameter is too concentrated to the few bins around the 1–1.4 au range, while in other parameters, such as eccentricity, inclination and impact speed, the information is fairly distributed over a large range of values and thus data-bins. After experimenting with the data and model, we decided to fit $1/a$ rather than a of the impacting particles (see Figure 9, right and top panels). With that parameter, equivalent to the heliocentric binding energy, the information contained in the data expands and the model is, in fact, tested quite more severely than using simply the semimajor axis distribution.

We used a numerical code to search a parameter space with the limits[6] given in Table 1. As mentioned above, the (α, β, $D_{\rm mid}$, $F_{\rm imp}$) subspace was efficiently scanned by the Bayesian statistics procedure used by the `MultiNest` code, while the (γ, $F_{\rm coll}$) parameters were sampled with steps 0.1 and 5.

[6] For completeness we mention that we also probed an extended range for the β parameter down to negative values of −4 and found local minima of the χ^2 function for negative β values. Here we discard them, though, for lack of physical justification.

Table 1
Parameter Range in the Fitting Runs

Parameter	Minimum	Maximum
α	2.0	5.0
β	0.5	4.0
$D_{\rm mid}$	200 μm	1800 μm
$F_{\rm imp}$	0.8	1.2
γ	0.0	1.6
$F_{\rm coll}$	1	30

Notes. In the case of γ and $F_{\rm coll}$ parameters, for which we do not use the `MultiNest` search, we sample their values with 0.1 and 5 equal steps. Runs for each $F_{\rm coll}$ value were performed 25 times and results averaged to avoid flukes.

Our formally best solution with a broken power-law SFD was for (α, β, $D_{\rm mid}$, $F_{\rm imp}$) = (4.7, 1.1, 950 μm, 1.08), γ = 0.0 and $F_{\rm coll}$ = 20. The match to the data is shown in Figure 9. Overall, the fit is reasonable, matching the major features observed for NT meteoroids, there are, however, two major, and correlated, mismatches: our synthetic model provides an unobserved population of high-eccentricity and large semimajor axis orbits. Clearly, this is a population of freshly ejected particles that has still not evolved far from the HTC source orbits. Additionally, we find that the results only very weakly depend on the γ parameter but do depend on the $F_{\rm coll}$. As discussed above, values of $F_{\rm coll} \leqslant 5$ yield a synthetic model inconsistent with the data (Figure 8); $F_{\rm coll} \geqslant 10$ is needed, while values over 20 provide statistically equivalent results. Finally, our formal fit has a shallow SFD slope at the small-size end of the spectrum (i.e., β). The later seems somewhat puzzling, though hints are

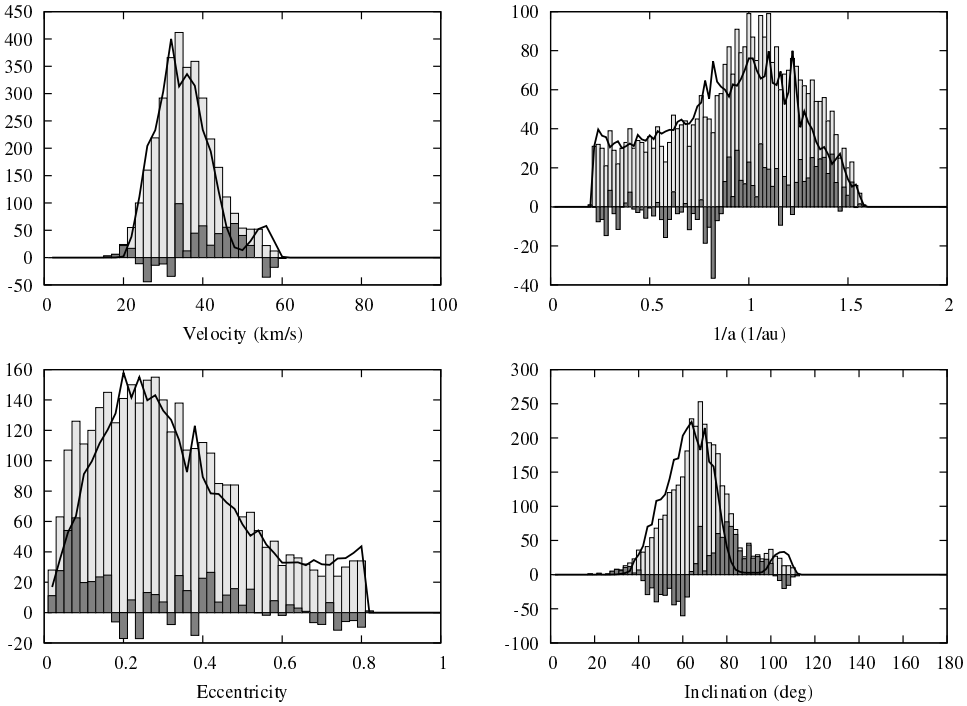

Figure 10. Same as in Figure 9, but now for the data set where all particles with observed heliocentric eccentricity values larger than 0.8 were eliminated. The best-fit parameters are $(\alpha, \beta, D_{\rm mid}, F_{\rm imp}) = (4.8, 1.6, 750\,\mu{\rm m}, 1.11)$, $\gamma = 0.3$ and $F_{\rm coll} = 20$.

already contained in the nature of the data set (see Section 2.1), and it is difficult to get around. The SFD break-point near to 1 mm and its shallow branch below this value has not been reported in any of the previous analyses.

While a "long collisional lifetime" of the particles is a required condition of satisfactory fits, we shall now test the sensitivity of the results with regards to two effects: (1) "selective-subjective" removal of the possibly undetected high-eccentricity orbits, and (2) necessity of the broken power-law SFD.

First, we note that the highest-speed particles are subject to more bias in the CMOR observations than the lower-speed particles (Section 6.5 in Campbell 2002). It may thus happen, that the "missing population" of the toroidal particles in the CMOR data, that we would predict from our synthetic model in Figure 9 (i.e., large-a and large-e heliocentric orbits), were removed (or were not detected) in the CMOR data and are not thus present in our final data set. To test this possibility, we rerun our fit on the data, where we artificially discarded all data with heliocentric eccentricity larger than 0.8 (where the data and models start to diverge in Figure 9). By doing this we obtained the results shown in Figure 10. The quality of fit improved, except for a small mismatch in the inclination fit (more lower-inclination particles predicted than observed and vice versa). From this test we conclude that the $e > 0.8$ particles may be incompletely detected, since the model otherwise fits the data well.

Now, we examine how much we can relax the shallowness of the particle SFD for small particles before the fit becomes worse. To that end we force the SFD be a single-slope power-law distribution with the exponent α in the range 1–5. Obviously, in this attempt we do not have the break-point size $D_{\rm mid}$ and the only fitted parameters, except for γ and $F_{\rm coll}$, are $(\alpha, F_{\rm imp})$ (the latter again standing for N_0). We used the CMOR data set where all particles with $e > 0.8$ were excluded as above. The best-fit model, $(\alpha, F_{\rm imp}) = (2.1, 1.11)$ with $\gamma = 0$ and $F_{\rm coll} = 20$, is formally worse in terms of χ^2 value than with the broken power-law SFD, but the visual check of the results we performed indicated no substantial differences. The top two panels in Figure 11 show the posterior distribution in Bayesian statistics of the α and $F_{\rm imp}$ parameters as determined by the `MultiNest` code. We also note the lack of correlation of the two parameters. Even when forcing α to be closer to a more realistic value between ~(2.8–3), we still get visually acceptable, though statistically worse fits. We recall that, given the simple nature of our treatment of the CMOR biases (such as a more complete understanding of the detection probability as a function of the ionization factor I and a complete treatment of the radar response function), a nominally statistically imperfect data fit may still be physically quite acceptable.

4.2.1. Total Mass of the Particle Population

With the population parameters estimated, we can now evaluate several interesting quantities. For instance, having the calibrated SFD parameters $(N_0, \alpha, \beta, D_{\rm mid})$ available, we can evaluate the total mass $M_{\rm tot}$ of the particles in the $(D_{\rm min}, D_{\rm max})$ range as (assuming both α and β smaller than 4)

$$\frac{M_{\rm tot}}{M_{\rm max}} = \frac{N_\alpha}{4-\alpha}\left[1 - \frac{\alpha-\beta}{4-\beta}\left(\frac{D_{\rm mid}}{D_{\rm max}}\right)^{4-\alpha} - \frac{4-\alpha}{4-\beta}\left(\frac{D_{\rm mid}}{D_{\rm max}}\right)^{4-\alpha}\left(\frac{D_{\rm min}}{D_{\rm mid}}\right)^{4-\beta}\right]. \quad (13)$$

We have assumed both α and β are smaller than a critical value of 4, and introduced mass $M_{\rm max} = \pi\rho D_{\rm max}^3/6$ of the largest particles with size $D_{\rm max}$ and bulk density ρ. Obviously, we may only expect to get an order of magnitude estimate because of several factors. First, the obtained parameters $(N_0, \alpha, \beta, D_{\rm mid})$ have large, and not fully established, uncertainties. Second, for slope exponents sufficiently smaller than 4, the largest particles dominate the mass, hence $M_{\rm tot} \sim M_{\rm max} N_\alpha/(4-\alpha)$. However,

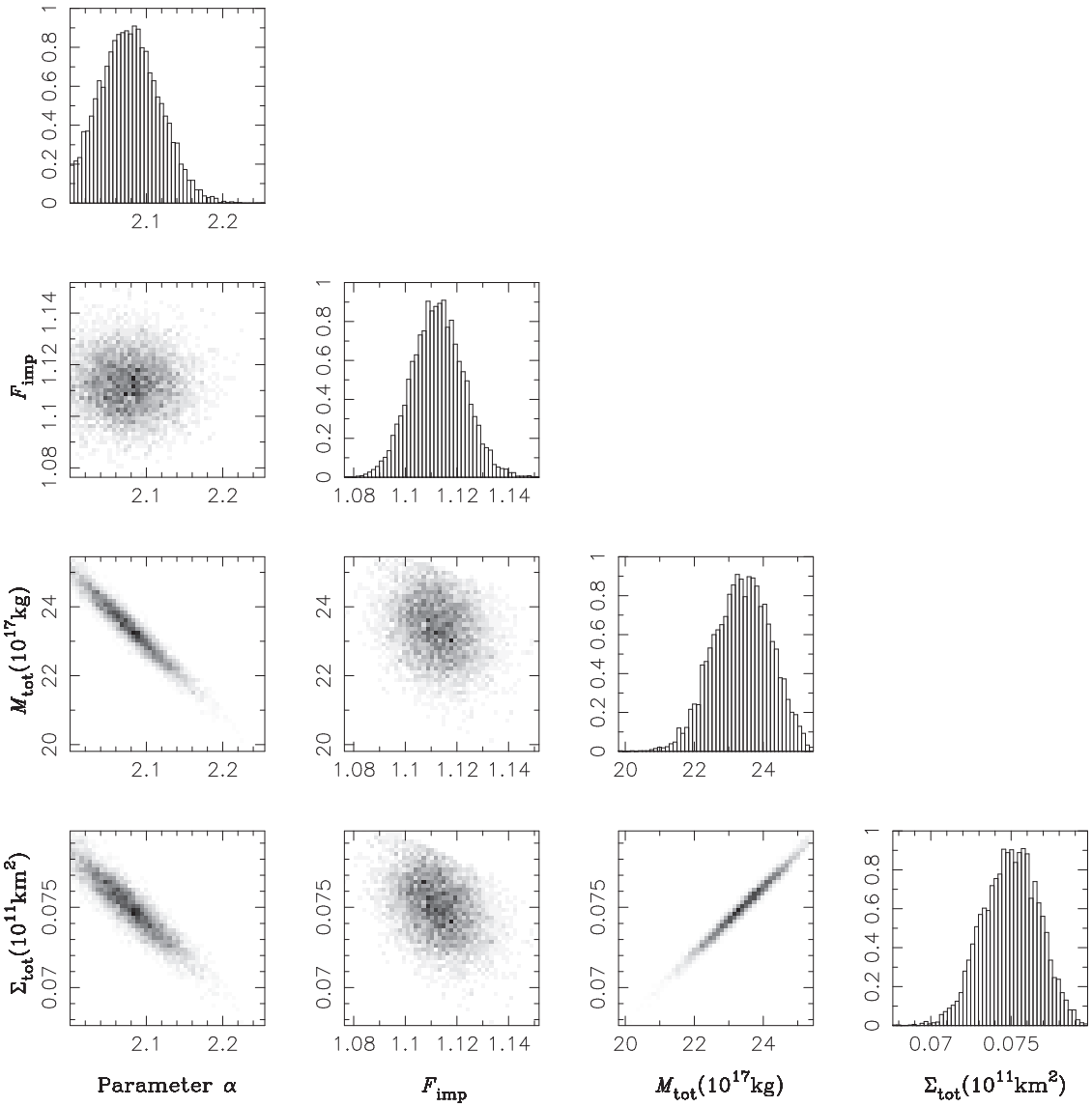

Figure 11. Posterior distribution of four parameters used in our model. Panels in the upper two lines show the fitted parameters α (SFD slope, top) and F_{imp} (population fudge factor, second line), with fixed values of $\gamma = 0$ and $F_{coll} = 20$. Histograms in the outer plots show a distribution of statistically equivalent solutions, while the plot inside the triangular structure show projection of these solutions onto a two-dimensional planes of two selected parameters, where levels of gray scale represent density of solutions. This representation helps to understand possible correlations between the parameters. The bottom two rows show computed (using Equations (13)–(17)), not fitted, parameters discussed in Sections 4.2.1 and 4.2.2: (1) estimated mass M_{tot} of the steady-state HTC particle population in the interplanetary space within the fitted range $(D_{min}, D_{max}) = (200\,\mu m, 3\,mm)$ (in 10^{17} kg; third row), and (2) estimated cross-section $\Sigma_{tot}(\leqslant 5au)$ of the steady-state HTC particle population in the interplanetary space within the 5 au heliocentric distance (in 10^{11} km^2; bottom row).

these particles only weakly contributed to the model fit because of their small number. On the other hand, this approximation shows that the break-point location D_{mid} and the slope exponent β at smaller sizes only weakly influence the estimated mass M_{tot}. This is well understood, because for shallow SFDs, the largest particles and the local slope of the SFD dominate the mass determination.

Since our formal solutions also admit $\alpha > 4$, we give here the population mass in this case (still assuming $\beta < 4$):

$$\frac{M_{tot}}{M_{mid}} = \frac{N_\alpha}{\alpha - 4}\left(\frac{D_{max}}{D_{mid}}\right)^{\alpha-1}\left[\frac{\alpha-\beta}{4-\beta} - \left(\frac{D_{mid}}{D_{max}}\right)^{\alpha-4} - \frac{\alpha-4}{4-\beta}\left(\frac{D_{min}}{D_{mid}}\right)^{4-\beta}\right], \quad (14)$$

with the mass of particles at the SFD break-point size now $M_{mid} = \pi\rho D_{mid}^3/6$ (obviously, the scaling uses the mass of the particles dominating the total mass of the population). The case $\alpha = 4$ would have to be treated separately, but we do not give the result here because of its singular nature in the α parameter solution.

Running formulas (13) and (14) through our solutions, we obtain $M_{tot} \simeq (3\text{–}50) \times 10^{17}$ kg in our fitted particle size range between 200 μm and 3 mm. The third-row panel in Figure 11 gives the computed values of M_{tot} in the case where we fitted a single-slope power-law SFD. We note M_{tot} is anti-correlated with the slope parameter α, such that steeper-slope SFDs would yield smaller total particle mass M_{tot}. This is easily understood because of by conservation of the number of impacting particles at the Earth.

With this order-of-magnitude estimate of HTC particle mass in interplanetary space, we can now attempt to constrain the long-term mass flux from HTCs needed to sustain the assumed steady-state population (for concepts of the flux computation see, e.g., Bottke et al. 2002, Section 4.3.1). Assuming a quasi-exponential decay of the population in our integrations with a characteristic timescale of $\tau \simeq 2$ Myr (Section 3.2), we need an average flux of

$$F = \frac{M_{\rm tot}}{\tau} \simeq (1.3\text{–}25) \times 10^{11}\ {\rm kg\ yr^{-1}}\ , \qquad (15)$$

about an order of magnitude smaller than the mass influx estimated for the JFC population by Nesvorný et al. (2011a). This finding seems justifiable, since Nesvorný et al. (2010) found from the analysis of *IRAS* infrared observations of the zodiacal cloud that HTCs contribute about an order of magnitude less than JFCs at most. Similarly, the orbit-averaged activity of large HTCs is estimated to be $\sim$(1–5) $\times$ 10^9 kg yr^{-1} (e.g., Hughes 1985; Jenniskens 2002). A steady-state population of several tens to a hundred of such comets would, in the long term, feed interplanetary space with sufficient dust for our findings. Additionally, modeling of direct dust detections beyond Jupiter requires a contribution from HTCs of about the same order of magnitude (e.g., Landgraf et al. 2002). These independent studies support our results and validate our approach.

4.2.2. Total Cross-section of the Particle Population

In a similar way, we may also estimate the total cross-section of the HTC-released population of particles in space. Assuming a particular case of $\alpha > 3$ and $\beta < 3$, we obtain

$$\frac{\Sigma_{\rm tot}}{\Sigma_{\rm mid}} = \frac{N_\alpha}{\alpha-3}\left(\frac{D_{\rm max}}{D_{\rm mid}}\right)^{\alpha-1}\left[\frac{\alpha-\beta}{3-\beta} - \left(\frac{D_{\rm mid}}{D_{\rm max}}\right)^{\alpha-3} - \frac{\alpha-3}{3-\beta}\left(\frac{D_{\rm min}}{D_{\rm mid}}\right)^{3-\beta}\right], \qquad (16)$$

where we have introduced $\Sigma_{\rm mid} = \pi D_{\rm mid}^2/4$, the cross-section of the particles at the break-point of the SFD. The assumed arrangement of the slope indexes for $D \geqslant D_{\rm mid}$ and $D \leqslant D_{\rm mid}$ makes these particles dominate the total cross-section. In fact, an order of magnitude estimate is given by $\Sigma_{\rm tot} \sim \Sigma_{\rm mid} N_\alpha (D_{\rm max}/D_{\rm mid})^{\alpha-1}/(\alpha-3)$, and it is weakly sensitive to both extreme sizes, $D_{\rm min}$ and $D_{\rm max}$ in the spectrum.

Again, we formally need a total cross-section solution for $\alpha < 3$ (with $\beta < 3$), which reads

$$\frac{\Sigma_{\rm tot}}{\Sigma_{\rm max}} = \frac{N_\alpha}{3-\alpha}\left[1 - \frac{\alpha-\beta}{3-\beta}\left(\frac{D_{\rm mid}}{D_{\rm max}}\right)^{3-\alpha} - \frac{3-\alpha}{3-\beta}\left(\frac{D_{\rm mid}}{D_{\rm max}}\right)^{3-\alpha}\left(\frac{D_{\rm min}}{D_{\rm mid}}\right)^{3-\beta}\right], \qquad (17)$$

with $\Sigma_{\rm max} = \pi D_{\rm max}^2/4$. The critical value case $\alpha = 3$ is effectively not needed.

To compare our result to Nesvorný et al. (2010, 2011a) we also restricted the cross-section analysis to the population of particles with a heliocentric distance <5 au. For that purpose we went through the record of steady-state particle orbits used in our fitting procedure, and for each of them, evaluated a fraction of the orbit where the heliocentric distance was <5 au, and applied this factor to each individual orbit with an appropriate weight with which it contributes to the whole population. With that scheme our fitted particle populations provided $\Sigma_{\rm tot}(\leqslant 5{\rm au}) \simeq (0.03\text{–}0.25) \times 10^{11}$ km^2, which is 1–2 orders of magnitude less compared to JFCs (Nesvorný et al. 2011a). The last-row panel in Figure 11 gives $\Sigma_{\rm tot}(\leqslant 5{\rm au})$ in the fitting run with a single-slope SFD model.

4.3. HTC Contribution to Other Radiant Source Regions

So far, we have focused on the contribution of the HTC particles to the NT zone. However, these particles do not impact the Earth only in this radiant zone on the sky; rather, they contribute to other zones as well. Having calibrated our model, we can now estimate the contribution of HTC particles elsewhere.

It has long been suggested that the particles whose radiants are arranged in arc (or ring) structures at about 50° angular distance from the apex direction are related to the toroidal source (e.g., Wiegert 2008; Wiegert et al. 2009; Campbell-Brown & Wiegert 2009; Brown et al. 2010). These authors also noted that the structure is formed with the help of the Kozai–Lidov mechanism perturbing heliocentric orbits of the impacting particles. Indeed, assuming the Earth heliocentric orbit has zero eccentricity (and unitary radius) and denoting with δ the angular distance from the apex of a radiant for an impacting particle, we have

$$\cos\delta = \frac{1-\sqrt{a}c}{\sqrt{3-T(a,c)}}\ . \qquad (18)$$

Here, we define $c = \cos i\sqrt{1-e^2}$ and $T(a,c) = (1/a) + 2\sqrt{a}\,c$ with a, e and i being the heliocentric semimajor axis, eccentricity and inclination of the impacting particle orbit. Note that both c and T are conserved parameters of the Kozai–Lidov model (e.g., Kozai 1962). Obviously, a given orbit intersects the Earth at only a specific (and finite in number) radiants, but considering a set of orbits with slightly evolving a and c values, such as by the PR drag, the radiants will fill an arc structure characterized by a limited range of δ values.[7] Because the impact speed at infinity $V = \sqrt{3-T(a,c)}$ is also nearly Kozai–Lidov-preserved, the observed impact speeds for the arc-radiant orbits are expected to be close to those observed in the NT source region. On the other hand, the individual orbital elements, especially eccentricity and inclination, undergo large variations and they are expected to have different distributions.

We have plotted the radiant distribution for all our modeled HTC particles and found a significant part of them populates the arc structure. Our model arc ensemble ranges from apex angular distances between $\delta \simeq 55°$ and about $\delta \simeq 65°$ bf (left panel in Figure 12), and is in a good agreement with all-sky observations made by CMOR in 2012 for solar longitudes between 50°–90° (right panel in Figure 12). Summarized all-sky observations were presented for instance, in Campbell-Brown (2008; see also Campbell-Brown & Wiegert 2009; Brown et al. 2010). We find that the depletion for δ smaller than our minimum value, described by Campbell-Brown (2008) as the depleted ring, is also due to the Kozai–Lidov mechanism. Equation (18) indicates that polar orbits with semimajor axis values between 1 and 2 au, which are most likely to hit the Earth, would have their radiants at $\simeq$ (45°–50°). However, these orbits are efficiently eliminated from our simulations en route to the inner solar system because

[7] We note that the Wyatt & Whipple (1950) integral for PR-evolving orbits implies that for a small c value a leading order relation reads $a \propto c^{-2}$. This means that δ changes only very moderately even if the orbits undergo large evolution driven by the PR drag.

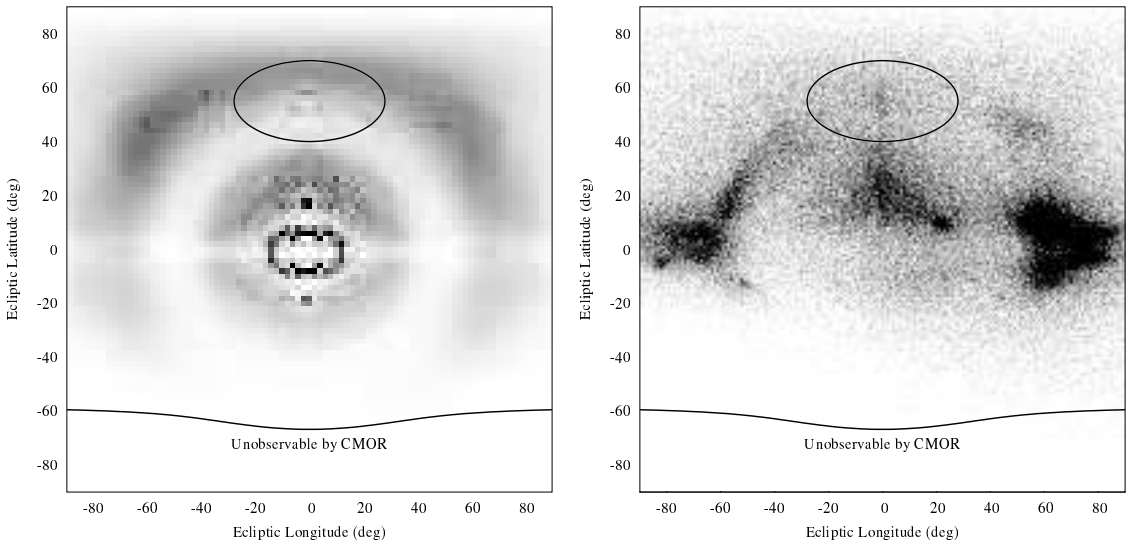

Figure 12. Distribution of radiant positions of our modeled population of micrometeoroids released from HTCs (left panel) and distribution of radiant positions of CMOR 2012 observations restricted to 50°–90° solar longitude (right panel); ecliptic longitude measured from the apex direction at the abscissa and ecliptic latitude at the ordinate. Gray-scale corresponds to the synthetic/observed particle flux. The oval zone centered at 57° ecliptic latitude indicates the NT region. We used our visibility simulator to compute a fraction of the year by which each of the latitude–longitude bin is observable from CMOR. This coefficient has been used to multiply the synthetic particle flux in each of the bins. The bottom solid curve delimits sky region that is not visible from CMOR at any time.

their perihelia would become too close to the Sun. In this way, our explanation for the depleted ring is mainly of a dynamical, rather than collisional, origin (see Campbell-Brown 2008). The few orbits whose radiants are seen in the zone of the depleted ring are prograde in nature and have mainly semimajor axis values smaller than 1 au and small eccentricities. They represent an unusual end-state, not efficiently fed by any evolutionary path and, obviously, they also have short collisional lifetimes. This is, however, only a secondary aspect of the depletion, the primary being dynamical origin.

While the impact speed distribution of arc orbits resembles that of the NT orbits (Figure 3), we see very different e and i distributions: (1) the median inclination is $\simeq$45° and extends from nearly zero to $\simeq$110°, and (2) the eccentricity distribution steadily increases to a value of $\simeq$0.8–0.9. The latter confirms our previous finding that very low e values in the NT source are the result of a selection effect: NT radiants simply require high inclination and the Kozai–Lidov dynamics then makes the eccentricity small. When the radiant-location is relaxed from the NT zone, the arc orbits have inclination distribution similar to the HTC orbits, with only slight preference for lower inclinations because of the higher collision probability with the Earth. The lower latitude radiants imply higher eccentricity values (e.g., Vokrouhlický et al. 2012).

We find that the HTC-released particles also contribute to the apex sources. Having $\delta \leqslant 30°$, they require predominantly retrograde or high eccentricity orbits. The first represents a minority of cases among our starting conditions for HTC-released dust particles, but retrograde orbits may be produced during their orbital evolution by scattering off Jupiter and/or the effects of secular resonances. With their larger impact speeds (median value $\simeq$55 km s^{-1} and a tail up to 70 km s^{-1}), the apex zone may see somewhat smaller particles than the NT zone. For instance, we find that particles between 100 and 200 μm contribute to the apex, while their input into the NT zone was negligible (Figure 1). For this reason it is problematic to use our calibrated population of the HTC particles and compute their exact flux at the apex zone (unless an uncertain extrapolation to smaller sizes is used). Since the impact speed, semimajor axis, eccentricity and inclination distributions from our 100 and 200 μm synthetic population resembles closely the observed data (see, e.g., Campbell-Brown 2008), we find it promising that our model predicts the HTC particles are contributors to the apex zone too. Additionally, our simulations show that the average strength of the apex source is ~5 to ~15 times larger than the NT source and depends, among other factors, also on the γ exponent of the cometary dust production function (4). Since the NT signal is largely insensitive to γ, further work on how the HTC dust contributes both in NT and apex sources may help in refining our model. Re-evaluation of the relative weight at which this dust component and dust from new (Oort cloud) comets contribute at apex (as advocated by Nesvorný et al. 2011b), however, needs a separate, dedicated study. It would be advantageous to combine CMOR data with other radars that have different limiting sensitivity for instance the AMOR system (e.g., Galligan & Baggaley 2005) or the MU system (e.g., Kero et al. 2012).

4.4. Contribution to IR Flux of the Zodiacal Cloud

Nesvorný et al. (2010, 2011a) have calibrated the zodiacal cloud parameters using a combination of a dynamical model and infrared measurements from the *IRAS* spacecraft. In particular, they found that the total cross-section of the cloud inside Jupiter's orbit (heliocentric distances $\leqslant$5 au) is ~ (1–2) × 10^{11} km^2, with the dominant contribution from particles in the 100–200 μm size range. This is because they also used a broken power-law SFD with a $D_{\rm mid}$ value in this size interval.

Nesvorný et al. (2010) also included a model of the HTC dust contribution in the zodiacal cloud. Their HTC model, though somewhat simpler, was comparable to ours. They estimated that HTC dust contributes less than 10% in the quoted total cross-section. Because it is calibrated by an entirely different data set, it is interesting to check our solution for the HTC dust yields with their constraints. Note that this comparison is somewhat problematic, because out data are insensitive to the smallest

possible sizes contributing to the zodiacal cross-section. If anything, the cross-sectional estimate from our population must be even smaller than the mentioned 10% value.

In Section 4.2.2 we determined that our HTC particle populations that generally match the toroidal source provide $\Sigma_{\rm tot}(\leqslant 5\,{\rm au}) \simeq (0.03\text{–}0.25) \times 10^{11}$ km^2. This is indeed at most 10% of the JFC particle population cross-section found by Nesvorný et al. (2010). Hence our HTC particles should not cause a conflict in fitting the *IRAS* infrared measurements by providing inconsistently large cross-sections that would flatten latitudinal profiles of IR emission measured by *IRAS*. A more detailed modeling of the HTC dust contribution to the thermal emission of the zodiacal cloud is left for future work.

5. DISCUSSION AND CONCLUSIONS

We have shown that the steady-state population of toroidal meteoroids as observed by the CMOR radar is likely provided by the activity or breakups of HTCs. The model provides a constraint on several parameters, such as the mean comet activity in relation to the perihelion distance and parameters of the particle size distribution at the source in the ~200 μm–~3 mm size range.

A stronger constraint is imposed on the collisional lifetime of particles in the millimeter size range. In order to dynamically transport particles to the vicinity of the Earth, we find that our model requires a longer lifetime than predicted by standard models (e.g., Grün et al. 1985). We think there are several possibilities to explain this difference. For example, we do not take into account fragments from collisional disruptions of the particles on their way toward the inner parts of the solar system. The resulting collisional cascade may effectively extend the lifetimes of their parent particles.

Another possible solution is to accelerate the dynamical evolution of the particle orbits. For instance, we assumed particle bulk density of 2 g cm^{-3}, but if the cometary dust has a lower value the orbits would evolve faster. It is also possible that a more in-depth analysis of the solar wind interaction with microscopic particles at large heliocentric distances may exceed this canonical value and contribute thus to faster orbital decay.

Finally, we note that several measurements of the lifetime of cosmic spherules and interplanetary dust particles (e.g., Raisbeck & Yiou 1989; Olinger et al. 1990; Nishiizumi et al. 1991; Pepin et al. 2001; Kehm et al. 2006) suggest the ultimate resolution to this dilemma may simply be that meteoroid collisional lifetimes are longer than previously assumed. Some of the residual mismatches between the observed data and our model may also originate in our ability to describe the detection limits of the radar system. In this work, similar to previous workers, we used the simple ionization factor I defined in Equation (1) to characterize the detectability of the modeled impacting particles. This captures the most important features, such as the particle's ability to ionize the atmospheric constituents, but may disregard others. Most importantly, we suspect that the instantaneous change from non-detectability to detectability at a single value $I_\star = 1$ is too simplified. In reality, there should be a range of I values about this critical limit where a particle detection should be a probabilistic event with the probability slowly increasing from zero (at small I) to unity (at large I). We believe that having the ability to properly model this feature would also improve fits with single power-law SFD, since the SFD break and small β values formally found in Section 4.2 is just another face of the same problem. Additionally, the need to disregard high-eccentricity orbits ($e \geqslant 0.8$) in our best fits is likely related to preferential rejection of those inputs from the data set.

Our next efforts will focus on two projects related to this work. First, we shall analyze the time-variable component in the NT source (Figure 2) searching for possible individual sources (if they still exist and are known in our catalogs). The prime candidate for some, but not all, is the activity of the peculiar comet 96P/Machholz and the complex of related objects (e.g., Sekanina & Chodas 2005). Second, the results of this paper motivate us to revisit dynamical modeling of the origin of apex source particles. Nesvorný et al. (2011b) found that dust released from new (Oort cloud) comets may contribute to this region. Unsurprisingly, we find that this is so for the dust released from HTCs as well. The exact proportion of these two potentially contributing source populations of dust is, however, yet to be determined.

This research was supported by Czech Grant Agency and the Grant Agency of the Charles University (grants P209-13-01308S, SVV-260089, and GAUK 602213). The work of D.N. was supported by NASA's PGG Program. CMOR measurements were supported by funding from NASA's Meteoroid Environment Office through co-operative agreement NNX11AB76A. The work of M.C.B. and P.B. were supported by the Natural Sciences and Engineering Research Council of Canada and the Canada Research Chairs program.

APPENDIX

PRELIMINARY ANALYSIS OF CMOR DATA SET

In order to gain more understanding of the data, and to set the stage for construction of the full model in Section 3, we additionally performed the following simple test. We randomly sampled the NT radiant sky zone and associated with it an impacting particle with a speed modeled by a Gaussian distribution (no correlation between the radiant and the impact speed was assumed). The Gaussian distribution was characterized with two parameters, namely, (1) a mean value $V_{\rm g}$, and (2) a standard deviation $\delta V_{\rm g}$. Having chosen the radiant and impact speed, we easily obtain the necessary heliocentric orbital elements for computation of the related impact probability $P_{\rm coll}$ of this synthetic impactor (e.g., Vokrouhlický et al. 2012). Next we characterized the impactor population with a broken power-law SFD described in Section 3.4 below in the size range $(D_{\rm min}, D_{\rm max}) = (200, 3000)\,\mu$m. This brings another three parameters, notably (1) size $D_{\rm mid} \in (D_{\rm min}, D_{\rm max})$ at which the power-law index changes, and (2) power-law indexes α and β of the two slopes (parameter N_0 from SFD definition in Section 3.4 is fixed by the absolute number 3550 of selected background-population NT particles). With this simple model we fit (1) the observed velocity distribution from Figure 3, and (2) the observed size distribution of the NT-impacting particles (note that this is different from the SFD fitting in Section 3 where we consider parameters at the source rather than those of the impacting population on the Earth). In fact, the latter was computed from the reported mass distribution using a constant bulk density of 2 g cm^{-3}. Obviously, the $(V_{\rm g}, \delta V_{\rm g})$ adjustment basically follows from the velocity-distribution fit and $(D_{\rm mid}, \alpha, \beta)$ adjustment basically follows from the size distribution fit, but the fitting procedure is not uncorrelated. This is because we only accept particles that could have been detected by CMOR, by constraining the ionization factor I of the impacting synthetic particle to be higher than the $I_\star$ limit described above.

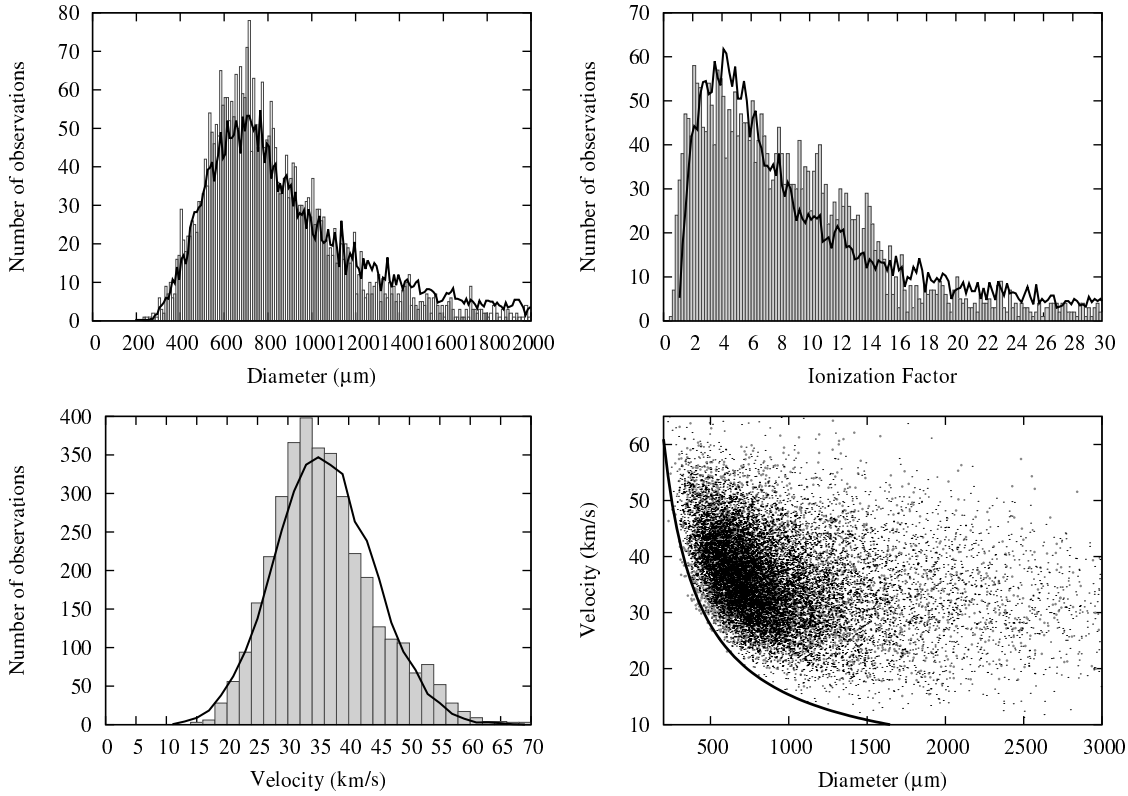

Figure 13. Results from a simple, five-parameter fitting analysis described in Section 2.1: gray histograms are for 3550 observed particles from the background population of NT particles, black line is the adjusted model. Left panels show the fitted data, size distribution of the particles (top), and geocentric impact speed (bottom). Both are matched very well by the model. The top right panel shows a comparison of the data and the model for the ionization factor I; here a slight mismatch is seen at low I values. The bottom right panel shows the observed particles (black symbols) and modeled particles (gray symbols) projected onto the size vs. velocity plane.

The results are shown in Figure 13. Unsurprisingly, the velocity fit is fairly good with only a small mismatch due to a large-velocity tail in the observed distribution (related to a small contribution of retrograde impactors from Figure 3). The adjusted values read $V_g = 31.8 \pm 0.3$ km s^{-1} and $\delta V_g = 9.2 \pm 0.3$ km s^{-1}. The fit of the observed size distribution is also rather good (the normalized χ^2 parameter from Equation (12) is $\sim$0.8). The formal solution of the adjusted parameters is $D_{\rm mid} = (750 \pm 20)\,\mu$m, $\alpha = 3.0 \pm 0.1$ and $\beta = 1.0 \pm 0.2$. Of these values, only α matches the expected value (see references in Section 3.4), while the value β is quite shallow and the break-point at $\simeq$750 μm has not been reported in the literature. Recall that the observed-population SFD maps to the source-population SFD in a non-trivial way due to size-dependent dynamical (PR drag) and physical (collisional lifetime) effects. However, understanding of some elements of the model may not be entirely correct, as indicated by the poor match between the distribution of the observed and modeled ionization factor (top left panel on Figure 13). This may be due to an unmodeled correlation between the radiant position and impact speed (which is, however, not strongly seen in the data). The problem may, however, also be deeper and indicate that (1) either the ionization factor from (1) is just too simplified, and does not accurately capture all the fine details of particle detections, or (2) the sharp transition from non-detected to detected particles as I crosses the critical value $I_\star = 1$ is unrealistic. The latter issue (2) is an especially important factor in our opinion. In fact, there should be some interval of ionization factor values, say between 1 and 3–5, where particles are detected with a probability smaller than unity (increasing toward the larger I values). This may well explain why we are forced to assume the shallow distribution below the break-point $D_{\rm mid}$ in our simple test. However, at this moment we do not have available an in-depth analysis of detection efficiency as a function of I near the critical value $I_\star$, nor a replacement of I with another quantity that would more realistically capture the particle detectability. With such warnings we thus proceed toward the full numerical model for the background population of the NT particles. We should note, that the break-point may be related to the simplified nature of the mass determination, in particular in the intermediate scattering region between underdense and overdense echoes that are treated as a step function rather than through a full-wave model approach such as Poulter & Baggaley (1978). Refinements in the radar mass scale in future may change the results, but the general mechanics of our model should not be significantly affected.

REFERENCES

Blaauw, R. C., Campbell-Brown, M. D., & Weryk, R. J. 2011, MNRAS, 412, 2033
Bottke, W. F., Morbidelli, A., Jedicke, R., et al. 2002, Icar, 156, 399
Brown, P. G., & Jones, J. 1995, EM&P, 68, 223
Brown, P. G., Weryk, R. J., Wong, D. K., & Campbell-Brown, M. D. 2012, DPS, 44, 302.04
Brown, P. G., Weryk, R. J., Wong, D. K., & Jones, J. 2008, Icar, 195, 317
Brown, P. G., Wong, D. K., Weryk, R. J., & Wiegert, P. 2010, Icar, 207, 66
Campbell, M. D. 2002, PhD thesis, Univ. Western Ontario (Canada)
Campbell-Brown, M. D. 2008, Icar, 196, 144
Campbell-Brown, M. D., & Wiegert, P. 2009, M&PS, 44, 1837

Čapek, D., & Vokrouhlický, D. 2010, A&A, 519, A75
Chau, J. L., Woodman, R. F., & Galindo, F. 2007, Icar, 188, 162
Davies, J. G. 1957, in IAU Symp. 4, Radio Astronomy, ed. H. C. van de Hulst (Cambridge: Cambridge Univ. Press), 390
Davies, J. G., & Gill, J. C. 1960, MNRAS, 121, 437
Dermott, S. F., Grogan, K., Durda, D. D., et al. 2001, in Orbital Evolution of Interplanetary Dust, ed. E. Grün, B. A. S. Gustafson, S. Dermott, & H. Fechtig (Berlin: Springer), 569
Feroz, F. 2008, PhD thesis, Cambridge Univ.
Feroz, F., Hobson, M. P., & Bridges, M. 2009, MNRAS, 398, 1601
Fulle, M. 2004, in Motion of Cometary Dust, ed. M. C. Festou, H. U. Keller, & H. A. Weaver (Tuscon, AZ: Univ. Arizona Press), 565
Galligan, D. P., & Baggaley, W. J. 2005, MNRAS, 359, 551
Gonczi, R., Rickman, H., & Froeschle, C. 1992, MNRAS, 254, 627
Greenberg, R. 1982, AJ, 87, 184
Grün, E., Zook, H. A., Fechtig, H., & Giese, R. H. 1985, Icar, 62, 244
Hashimoto, T., Watanabe, J., Sato, M., & Ishiguro, M. 2011, in Meteoroids: The Smallest Solar System Bodies, ed. W. J. Cooke, D. E. Moser, B. F. Hardin, & D. Janches (Washington, DC: NASA), 82
Hawkins, G. S. 1956, AJ, 61, 386
Hawkins, G. S. 1962, AJ, 67, 241
Hawkins, G. S. 1963, SCoA, 7, 53
Hughes, D. W. 1985, MNRAS, 213, 103
Jenniskens, P. 2002, in ESA Special Publication, Vol. 500, Asteroids, Comets, and Meteors: ACM 2002, ed. B. Warmbein (Noordwijk, Netherlands: ESA), 117
Jenniskens, P. 2006, Meteor Showers and their Parent Comets (Cambridge: Cambridge Univ. Press)
Jenniskens, P. 2008a, EM&P, 102, 505
Jenniskens, P. 2008b, Icar, 194, 13
Jewitt, D., Li, J., & Agarwal, J. 2013, ApJL, 771, L36
Jones, J., & Brown, P. G. 1993, MNRAS, 265, 524
Jones, J., Brown, P. G., Ellis, K. J., et al. 2005, P&SS, 53, 413
Jones, J., Campbell, M., & Nikolova, S. 2001, in Proceedings of the Meteoroids 2001 Conference, ed. B. Warmbein (ESA SP-495; Noordwijk: ESA), 575
Jones, J., & Jones, W. 1993, MNRAS, 261, 605
Kaňuchová, Z., & Neslušan, L. 2007, A&A, 470, 1123
Kehm, K., Flynn, G. J., & Hohenberg, C. M. 2006, M&PS, 41, 1199
Kero, J., Szasz, C., Nakamura, T., et al. 2012, MNRAS, 425, 135
Kessler, D. J. 1981, Icar, 48, 39
Kozai, Y. 1962, AJ, 67, 591
Landgraf, M., Liou, J.-C., Zook, H. A., & Grün, E. 2002, AJ, 123, 2857
Levison, H. F., & Duncan, M. J. 1994, Icar, 108, 18
Levison, H. F., Duncan, M. J., Dones, L., & Gladman, B. J. 2006, Icar, 184, 619
Nesvorný, D., Janches, D., Vokrouhlický, D., et al. 2011a, ApJ, 743, 129
Nesvorný, D., Jenniskens, P., Levison, H. F., et al. 2010, ApJ, 713, 816
Nesvorný, D., Vokrouhlický, D., Bottke, W. F., & Sykes, M. 2006, Icar, 181, 107
Nesvorný, D., Vokrouhlický, D., Pokorný, P., & Janches, D. 2011b, ApJ, 743, 37
Nishiizumi, K., Arnold, J. R., Fink, D., et al. 1991, E&PSL, 104, 315
Olinger, C. T., Walker, R. M., Hohenberg, C. M., & Maurette, M. 1990, E&PSL, 100, 77
Öpik, E. J. 1951, PRIAA, 54, 165
Pepin, R. O., Palma, R. L., & Schlutter, D. J. 2001, M&PS, 36, 1515
Pokorný, P., & Vokrouhlický, D. 2013, Icar, 226, 682
Poulter, E. M., & Baggaley, W. J. 1978, P&SS, 26, 969
Press, W. H., Teukolsky, S. A., Vetterling, W. T., & Flannery, B. P. 2007, Numerical Recipes. The Art of Scientific Computing (3rd ed.; Cambridge: Cambridge Univ. Press)
Raisbeck, G. M., & Yiou, F. 1989, Metic, 24, 318
Sekanina, Z., & Chodas, P. W. 2005, ApJS, 161, 551
Steel, D. I., & Elford, W. G. 1986, MNRAS, 218, 185
Verniani, F. 1973, JGR, 78, 8429
Vokrouhlický, D., Pokorný, P., & Nesvorný, D. 2012, Icar, 219, 150
Weryk, R. J., & Brown, P. G. 2012, P&SS, 62, 132
Wetherill, G. W. 1967, JGR, 72, 2429
Wiegert, P., Vaubaillon, J., & Campbell-Brown, M. 2009, Icar, 201, 295
Wiegert, P. A. 2008, EM&P, 102, 15
Wyatt, S. P., & Whipple, F. L. 1950, ApJ, 111, 134